DYNAMIC MODELLING AND SIMULATION OF TURBULENT BUBBLY FLOW IN BUBBLE COLUMN REACTORS

by

WEIBIN SHI

A thesis submitted to the University of Nottingham in partial fulfilment of the requirements for the degree of

Doctor of Philosophy

Under the supervision of

Prof Xiaogang Yang

Dr Buddhi Hewakandamby

JULY 2018

DECICATION

To my wife, Yayun Xie, my parents and my parents-in-law for their love, support and encouragement.

ACKNOWLEDGEMENT

I would like to express my gratitude to my supervisor, Professor Xiaogang Yang, for his consistent help, encouragement, physical insight, creative influence and patient guidance in my entire PhD study. Also, my thanks go to the thesis' two referees, Professor Ning Yang, Institute of Process Engineering, Chinese Academy of Sciences and Dr Yong Ren, Department of Mechanical, Materials and Manufacturing Engineering, the University of Nottingham Ningbo China.

I would like to thank the FAST group members, Dr Guang Li, Dr Jie Yang, Dr Luming Chen, Dr Collins Ezeh, Dr Bin Dong, Ms Xiani Huang, Mr Chenyang Xue, Ms Lu Liu, Mr Xingyi Qian, Ms Xinyue Cai, Ms Yanqing Guo, and Ms Shanshan Long for their assistance and pleasurable discussions.

Finally, I would especially like to thank my wife for her understanding and full support through duration of this project.

This work was financially supported by the National Natural Science Foundation of China (Grant Nos. 91534118, 21761132026). I would also like to acknowledge the Ph.D. scholarship of the International Doctoral Innovation Centre (IDIC) of the University of Nottingham Ningbo China and the support of EPSRC (Grant no. EP/G037345/1).

SYNOPSIS

Considerable progress in understand and predicting turbulent bubbly flow in bubble column reactors has been advanced over the last two decades or so using a combination of model development, computational techniques and well-designed experiments. However, there remain many modelling uncertainties mainly associated with inadequate physical prescriptions rather than numerical schemes. The present project addresses some of these questions, in particular in relation to the interactions between the deformable rising bubbles and the turbulent eddies, with the later which from liquid shear flow or in the wakes of bubbles.

Recent literature on existing models and experimental studies of bubble column reactors is reviewed in Chapter 1. It appears that the correlations and phenomenal models developed from early-stage experimental studies have been implemented into CFD modelling, and in return, accelerates the developments of theoretical understandings of the flow characteristics in the bubble columns. The research efforts made from both CFD modelling and experimental studies to understand the complicated mechanisms of gas-liquid interactions have been summarised in this chapter.

In chapter 2, the inlet conditions, as one of the important issues in the CFD simulations of bubble columns, have been addressed. A kinetic inlet model is proposed, which considers the effects of number and size of holes on the gas spargers, the volume flow rate, and the gas-phase velocity profile. The proposed model achieves similar accuracy as modelling the real sparger holes while the computational costs have been significantly reduced.

Chapter 3 applies a CFD-PBM method to investigate the influence of various shapes of bubbles on the bubble breakage rate and bubble size distribution. Bubbles are classified into spherical, ellipsoidal and spherical-capped shapes, and explicitly calculated in the breakage kernel. The correlation of aspect ratio of ellipsoidal bubbles is developed base on dimensionless numbers, summarising the effect of buoyancy, surface tension, and viscosity. The surface energy and pressure head have been adopted as two competing breakage mechanisms with the energy density constraint has been used as the breakage criterion. The simulation results demonstrate improvements in the estimations of gas holdup, liquid velocity, and bubble size distribution, as well as strong enhancements in mass transfer prediction.

The effects of the turbulent kinetic energy spectrum for the turbulent bubbly flow on the bubble breakage are considered in Chapter 4. The κ^{-3} power law scaling behaviour of bubble induced turbulence is considered together with the Kolmogorov -5/3 law to characterise the turbulent eddies that interact with the subsequent bubbles. A characteristic length scale Λ is used to approximately separate the shear turbulence and bubble induced turbulence. The implementation of the modified breakage model into CFD modelling shows a great improvement in the prediction of bubble breakage rate, which believes to be competitive to the results obtained from Chen et al. (2004) that has artificially increase of breakage rate by 10 times.

In Chapter 5, the approaching velocities of collision bubbles that are under the influence of shear turbulence and bubble induced turbulence are clearly distinguished. The turbulence dissipation rate that strongly affects the estimation of collision time has been calculated by taking into account the turbulence generation and dissipation in the wakes of bubbles, especially considering the anisotropic feature of bubble induced turbulence in the Reynolds stress turbulence model by using extra source terms. The modified coalescence model properly addresses the coalescence rate for different sizes of binary bubble coalescence.

Chapter 6 presents the experimental study of the spatial velocity fluctuations and the turbulence energy spectrum in the wakes of bubbles by using PIV and highspeed imaging techniques. The experimental results clearly demonstrate the existence of the κ^{-3} power law scaling region due to bubble induced turbulence. The theoretical analysis successfully shows that the scaling exponent of -3 to be robust from three different aspect.

In sum, some important issues of the gas-liquid interactions in turbulent bubbly flows have been addressed in this project. The implication is that the liquid phase turbulence is strongly affected by the size and shape of rising bubbles. Meanwhile, it can be found from the turbulence energy spectrum that the behaviours of turbulent eddies in the wakes of bubbles are very different from those in shear flow, thereby strongly influencing the kernels of bubble coalescence and breakage and hence the model predicted bubble size distributions.

TABLE OF CONTENTS

CHAPTER 4: AN IMPROVED BUBBLE BREAKAGE MODEL ACCOUNTING THE EFFECT OF BUBBLE INDUCED TURBULENCE ENERGY SPECTRUM DISTRIBUTION

CHAPTER 5: MODELLING OF BUBBLE COALESCENCE IN BUBBLE COLUMNS ACCOUNTING FOR BUBBLE INDUCED TURBULENCE

LIST OF FIGURES

CHAPTER 1

CHAPTER 2

CHAPTER 3

CHAPTER 4

CHAPTER 5

CHAPTER 6

LIST OF TABLES

NOMENCLATURE

a = long half axis length of an ellipse, m

c = short half axis length of an ellipse, m

C_D = effective drag coefficient for a bubble around a swarm, dimensionless

D = bubble column diameter, m

d = bubble diameter, m

d_{32} = equivalent bubble diameter, m

d_{eq} = equivalent bubble diameter, m

d_V = length of virtual axis, m

$\bar{e}$ = mean turbulence kinetic energy, kg·m^2/s^2

e_s = increase in surface energy, kg·m^2/s^2

Eo = Eötvös number, dimensionless

E = aspect ratio, dimensionless

F = force, N

F^D = drag force, N/m^3

F_{Lift} = lift force, N/m^3

F_{VM} = virtual mass force, N/m^3

f_V = breakage volume fraction, dimensionless

f_i = fraction of i-th bubble class of total fraction

f_λ = number density of bombarding eddies, m^{-4}

g = gravity acceleration, m/s^2

H = distance from the bottom surface, m

k = turbulence kinetic energy, m^2/s^2

k_l = liquid side mass transfer coefficient, m/s

l = length scale, m

Mo = Morton number, dimensionless

n = number density per unit volume, m^{-3}

N = number of bubbles per unit volume, dimensionless

P_T = total pressure, MPa

P_S = vapour pressure of the liquid, MPa

r = radius / distance, m

Rc = radius of curvature, m

Re = Reynolds number, dimensionless

S = surface area, m^2

t = time, s

U = superficial velocity, m/s

U_r = rising velocity, m/s

U_{Slip} = slip velocity, m/s

U_t = terminal velocity, m/s

$\bar{u}_\lambda$ = mean velocity of turbulent eddies, m/s

u = velocity vector, m/s

u' = fluctuation velocity in u-direction, m/s

V = volume, m^3

v' = fluctuation velocity in v-direction, m/s

w' = fluctuation velocity in w-direction, m/s

X^W = weight fraction of the primary liquid in the mixture

Greek letters

α = phase volume fraction, gas holdup

Γ = gas distributor parameter

ε = turbulence dissipation rate, m^2/s^3

η = Kolmogorov length scale, m

κ = wave number, m^{-1}

λ = eddy length scale, m

Λ = characteristic length scale, m

μ = molecular dynamic viscosity, Pa·s

μ_t = turbulence dynamic viscosity, Pa·s

μ_{eff} = effective turbulence dynamic viscosity, Pa·s

υ = kinematic viscosity, m^2/s

ξ = ratio of eddy length scale to bubble diameter, dimensionless

ρ = fluid density, kg/m^3

σ = surface tension, N/m

τ = shear stress, Pa

Superscripts/Subscripts

b = bubble

B = breakage

BIT = bubble induced turbulence

C = column / coalescence

Coal = coalescence

col = collision

eff = effective

g = gas

i = i-th class bubble

j/k = daughter bubble

l = liquid / long axis

m = mixture

R = Reynolds stress

rel = relative

s = short axis / surface

td = turbulent dispersion

vm= virtual mass

w = wake

wl = wall lubrication

z = vertical direction

CHAPTER 1: A LITERATURE REVIEW ON CFD MODELLING OF TURBULENT BUBBLY FLOWS AND EXPERIMENTAL STUDIES OF BUBBLE COLUMN REACTORS

SUMMARY

The experimental and numerical investigations of bubble column reactors have made considerable progress in the last few decades. The studies at early stages focused on the experimental investigations of the global parameters and the time-averaged characteristics. These studies have formed the most basic understandings of the bubble columns. With the rapid development of different experimental devices from the 90s last century, the capture of dynamic structures and behaviour of local flow field has become more and more accurate, and the in-depth study of the multiphase nature of the bubble columns have become possible. Based on the experimental findings, a lot of correlations and phenomenal models have been developed and implemented into the CFD modelling, which in return, accelerates the development of theoretical understandings of the flow characteristics in the bubble columns. However, the fluid dynamics in the bubble columns are very complex. The multi-scale behaviours, especially the gas-liquid two-phase interactions, have not been fully revealed, which has become a key issue in the design and scale-up of bubble column reactors. Therefore, this chapter reviews some efforts that many researchers have made, in both experimental investigations and CFD modelling, towards the understanding of multi-phase flow characteristics in the bubble column reactors.

1. Introduction

Bubble column reactors are widely used as multiphase contactors for carrying out gas-liquid two-phase or gas-liquid-solid three-phase reactions in chemical, petrochemical, biochemical, pharmaceutical and metallurgical industries, primarily due to the lower requirements of both the labour cost and the capital cost in the construction, operation, and maintenance. On the contrary to its low-cost, bubble columns exhibit excellent heat and mass transfer characteristics. One important application of bubble column reactor in the energy industry is the Fischer-Tropsch process, which is a collection of gasification and liquefaction reactions to produce synthetic lubrication oil, low-sulphur transportation fuels and other synthetic fuels from coal, natural gas or biomass, addressing environmental advantageous over petroleum derivatives (Krishna and Sie, 2000, Degaleesan et al., 2001). Typical examples can also be found in p-xylene oxidation (Jin et al., 2005), wine fermentation (Schmidt and Velten, 2016), wastewater treatment (Smith et al., 1996), and algae growing for high-value products extraction (Manjrekar et al., 2017). A simple bubble column reactor usually consists of a vessel with a gas distributor at the bottom. Gas is injected in the form of bubbles into either liquid or liquid with solid suspensions in the main body of the column. Some bubble columns have equipped with different kinds of internals for their specific industrial applications, which includes vertical or horizontal tube bundles, draft tubes, rotating disks and multi-layer seize plates (Youssef et al., 2013). The types of gas distributors that are commonly found include nozzles, perforated plates, seize plates, porous media, membrane, ring type distributors and arm spargers (Kulkarni and Joshi, 2005).

Despite the general simplicity of bubble columns in mechanical design, fundamental characteristics of the gas-liquid two-phase hydrodynamics associated with the performance of bubble column reactors, which are essential for scale-up and process optimisation, are still not fully understood because of the complex nature of multiphase flow. The main concerns focus on the physical mechanisms of the gas-liquid two-phase interactions, such as the interfacial forces, the turbulence interactions, and the bubble coalescence and breakup phenomena. In the last few decades, the interphase interactions have been widely studied by many researchers and different models have been developed and validated based on well-designed experiments and computational fluid dynamics (CFD) modelling. The developments in the open literature that attempts to understand the flow characteristics in the bubble column reactors are reviewed in this chapter from both the experimental studies and CFD modelling aspects respectively.

2. FUNDAMENTALS OF BUBBLE COLUMN REACTORS

The bubble column reactor is a typical multiscale system, which consists of macroscale or reactor scale structures such as large-scale liquid circulation, mesoscale interactions such as bubble-eddy or bubble-bubble collision, and microscale behaviours such as mass or momentum transfer across the bubble surface. Although the complicated multiphase and multiscale nature has not yet been fully and thoroughly revealed due to the limitations of the more advanced experimental device and the development of turbulence theory, the fundamental understandings of turbulent bubbly flow in the bubble columns have been established and generally accepted on the basis of experimental studies. Some common understandings of the turbulent bubbly flows in bubble column reactors include the flow structures and flow regime transitions, as well as bubble deformations and interfacial mass transfer.

2.1 Flow structures

The flow regimes in the bubble column can be defined as homogeneous bubbly flow, transition range, slug flow the heterogeneous churn-turbulent range, depending on the superficial velocity of the gas phase and the column diameter. The approximate distinction of the flow regimes in the bubble columns is sketched in Figure 1-1. A very comprehensive study on the flow regime transitions in the bubble columns, as shown in Figure 1-2, has been presented by Chen et al. (1994), which identifies the flow regimes as dispersed bubble, vortical-spiral flow, and turbulent flow. The typical 3-D macroscopic flow structures in the vortical-spiral flow regime have been clearly illustrated, which include descending flow, vortical-spiral flow, fast bubble flow, and central plume. These illustrations have greatly extended the understandings in the dynamic characteristics and the coherent eddy structures in the bubble columns, which further provide very important guidelines to the design and scale-up of bubble columns. It seems that the flow regime transitions are influenced by various parameters including bubble column diameter, liquid dispersion height, liquid phase properties, operating pressure, and gas distributor designs. In the recent studies, it has been found that the homogeneous flow regime can be further distinguished into the mono-dispersed homogeneous regime and the poly-dispersed homogeneous flow regime, depending on the superficial velocities and the associated bubble size distributions (Besagni and Inzoli, 2016b). The mono-dispersed homogeneous regime may not exist if the large bubbles are aerated due to large diameter orifices on the sparger (Besagni and Inzoli, 2016a). The transition from the homogeneous regime to the transition region is due to the presence of the large bubbles, and the transition flow regime is characterised by a macroscopic flow structures with large eddies and a widened bubble size distribution (Guedon et al., 2017), in which case, the turbulent eddies induced by the “coalescence-induced” large bubbles may make increasingly significant contributions to the turbulence generated in the column.

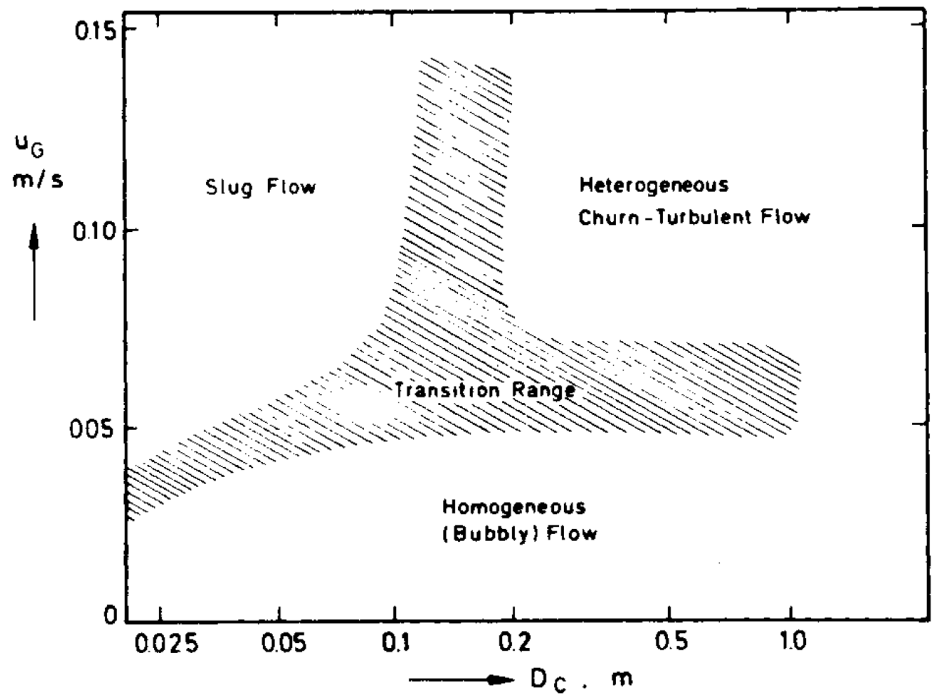

Figure 1-1 Approximate dependence of flow regime on gas superficial velocity and the bubble column diameter (taken from Shah et al. (1982)).

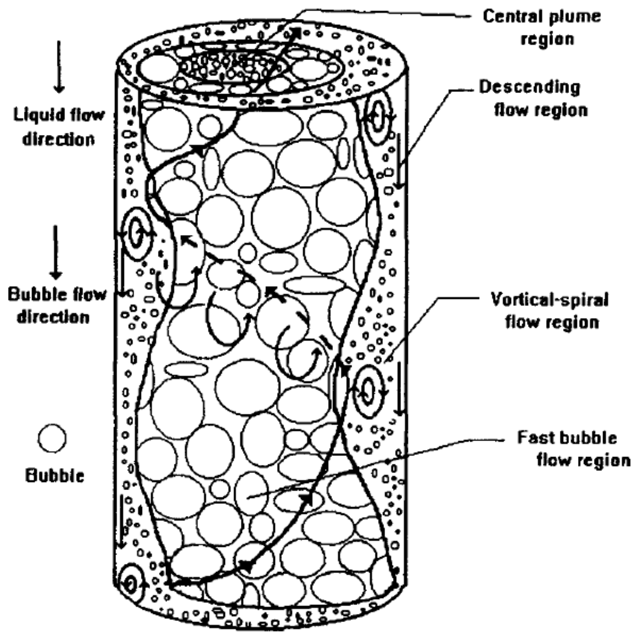

Figure 1-2 Flow structure in the vortical-spiral flow regime in a 3-D gas-liquid bubble column (taken from Fan et al. (1994)).

2.2 <u>Interfacial Mass transfer</u>

The interfacial mass transfer in the bubble column reactors mainly subject to two aspects: the interfacial area that the mass transfer can take place and the mass transfer rate between the two fluids. As the gas is usually the discrete phase in the bubble columns, the interfacial mass transfer takes place at the bubble surface. Therefore, the interfacial area can be determined by the size and shape of bubbles.

As shown in Figure 1-1, when the superficial gas velocities are small, the overall flow structure is within the homogeneous regime that bubbles rising in orders once being sparged into the column. At the homogeneous regime, the bubble coalescence and breakage phenomena are rarely found, mainly due to the weak turbulence intensity. In this case, spherical bubbles with constant bubble size may be an appropriate approximation. With the increase of superficial gas velocity, the flow enters transition regime that the bubble coalescence and breakage sometimes occur at local regions. Once the flow enters the heterogeneous regime or churn-turbulent regime, the bubble-bubble and eddy-bubble collision take place very frequently at the entire column. The colliding eddies and bubbles that carry with sufficient turbulent kinetic energy will result in the quick changes of the bubble size and shape. Ellipsoidal bubbles and spherical-cap bubbles that are with much larger surface often appear at the transitional regime and heterogeneous regime, which may facilitate the interfacial mass transfer. If the slug flow regime is presented due to the restriction of the column diameter, the interfacial mass transfer is greatly reduced due to the limited contact surface between the carrier fluid and the bubble slug, which is the case that usually needs to be avoided in bubble column design.

The influence of physical properties such as viscosity and surface tension has also been found to be very significant on the size and shapes of bubbles. Although the surfaces of bubbles are oscillating and the shapes of bubbles are fast-changing, Clift et al. (1978) summarised the regime map of bubble shapes on the basis of a large number of experimental observations, as shown in Figure 1-3. The shape of bubbles is divided into three types, such as spherical, ellipsoidal and capped bubbles, by using three dimensionless numbers, including Reynolds number *Re*, Eötvös number *Eo* and Morton number *Mo*. However, bubbles in wobbling, skirted or dimpled spherical-cap have also been found in the bubble columns, due to the surface oscillations. The interpretations on the physical meanings of these dimensionless numbers suggest that the influencing factors mainly include the inertial force, the viscous force, the gravitational force, and the surface tension. Further discussions on the dimensionless numbers that have been developed in the open literature are presented in next section.

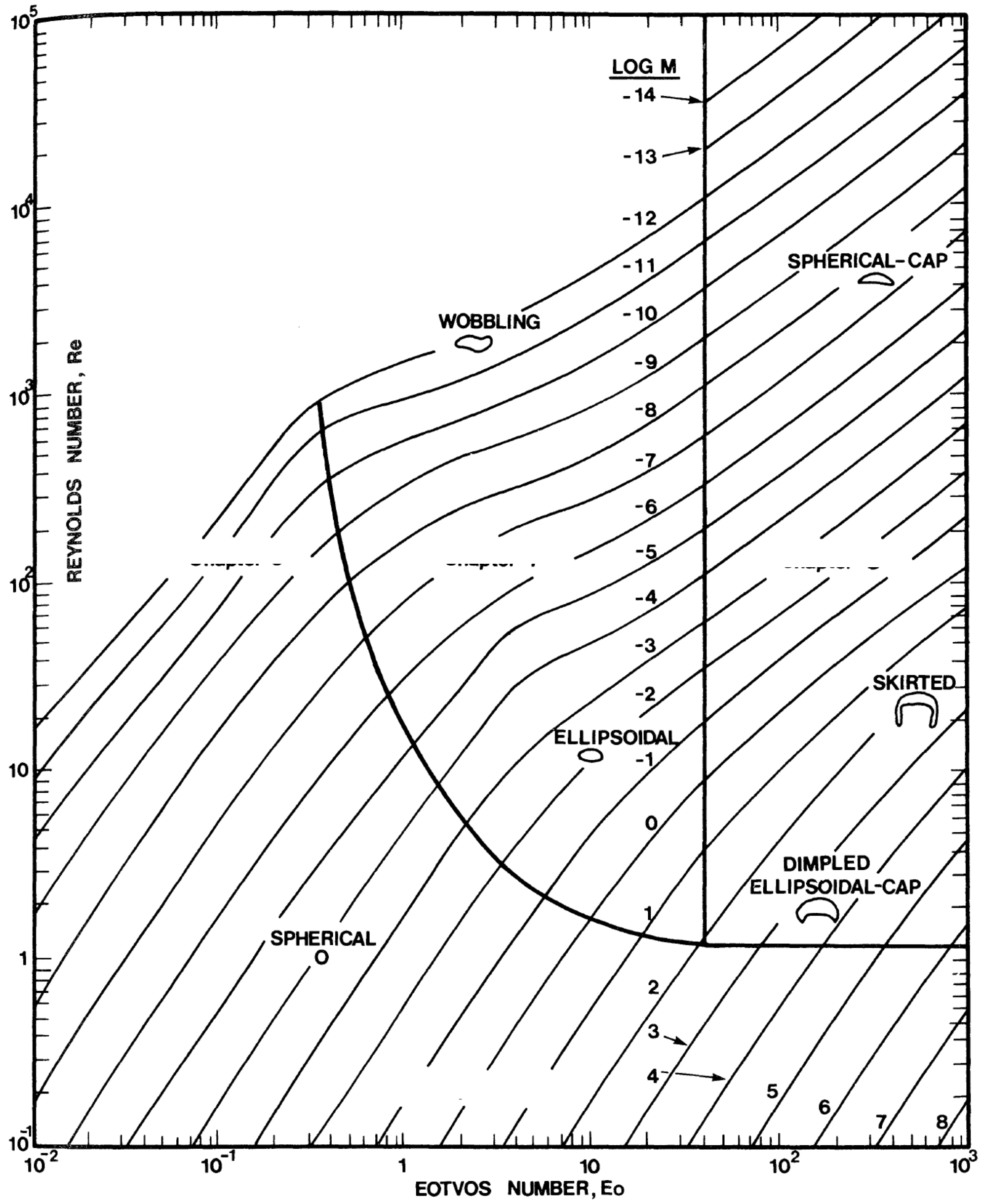

Figure 1-3 Regime map of bubble shapes (taken from Clift et al. (1978)).

When a bubble rises in a liquid, the mass transfer resistance is mainly on the liquid side. The two-film model by Lewis and Whitman (1924), the penetration model by Higbie (1935) and the surface renewal model by Danckwerts (1951) are three classical approaches to describe the liquid side mass transfer coefficient. The two-film theory assumes that the mass transfer is a steady-state process and there is a stagnant film near the interface. However, the mass transfer between a rising bubble and its surrounding liquid is unsteady. In this case, the Higbie's penetration theory and its extension (the surface renewal theory) are more suitable for the description of mass transfer. Both the Higbie's penetration and surface renewal theories assume that the mass transfer coefficient is controlled by the rate of surface renewal. The liquid-side mass transfer coefficient k_l for a bubble with mobile surface can be expressed as:

$$k_l = \frac{2}{\sqrt{\pi}}\sqrt{\frac{D_l}{t_c}} \qquad (1\text{-}1)$$

where t_c is the contact time and D_l is the molecular diffusivity.

The penetration model proposed by Higbie (1935) has assumed a dynamic liquid film and a down-flowing laminar flow. The contact time can be estimated as:

$$t_c = \frac{d_b}{U_r} \qquad (1\text{-}2)$$

where U_r is the rising velocity of the bubble

Danckwerts (1951) further assumed that the main contribution of surface renewal is due to the turbulence eddies and their positive effect on the mass transfer. Based on the surface renewal theory, the liquid side mass transfer coefficient can be expressed as:

$$k_l = c_r\sqrt{\frac{D_l}{t_r}} \qquad (1\text{-}3)$$

where c_r is a model parameter and t_r is the mean time between renewal events. The latter variable is assumed to be proportional to the Kolmogorov time scale $(\nu_l/\varepsilon)^{1/2}$, where ν_l is the liquid kinematic viscosity and ε is the turbulence dissipation rate.

It seems that the surface renewal model may be appropriate for describing the mass transfer in turbulent bubbly flows, as it is based on the turbulent eddies while the penetration model assumes the flow is laminar. However, the mass transfer coefficient predicted by the surface renewal model is independent of the bubble size and bubble motion, which seems to be insufficient especially when the bubbles are quite large. By contrast, Higbie's model has taken these parameters into account and Alves et al. (2006) have found the penetration model could adequately predict the mass transfer coefficient of single bubbles up to d_b = 6 mm in clean water when the turbulent dissipation rate is up to ε = 0.04 m^2/s^3.

The addition of surfactant may change the physical properties of the liquid phase and lead to a nearly totally rigid bubble-liquid interface. In this case, the dynamic behaviour of bubbles are significantly altered, which may result in a decrease in the mass transfer coefficient. (Frössling, 1938) proposed a theoretical model of mass transfer for a rigid bubble from the laminar boundary layer theory, which gives that:

$$k_l = c\sqrt{U_r/d_b}D_l^{2/3}\nu_l^{-1/6} \tag{1-4}$$

where c is the model coefficient and usually takes the value of 0.6.

2.3 Critical Issues on Studies of Bubble Column Reactors

It seems that no matter the flow structures or the interfacial mass transfer in the bubble column reactors is strongly associated with the bubble sizes and shapes, the bubble motion and the turbulence in the wake or the surrounding of the bubbles. Although numerous research efforts have been made, the complex multiscale and multiphase nature of the bubble column reactors have not been fundamentally revealed. It seems that the key issues focus on the mechanism of gas-liquid interactions, such as different interfacial momentum transfer or bubble coalescence and breakage phenomena. In particular, the understanding of turbulence in the bubble columns is still very limited from both CFD modelling and experimental point of views. In general, the description of turbulence in the bubble columns is usually based on the analogy to isotropic homogeneous single-phase turbulence in pipe flows. This is due to the ongoing debates on the experimental findings of bubble motions, surface oscillations and deformations, bubble wakes and the turbulence generated in the wakes of bubbles. Therefore, the research works including CFD modelling and experimental studies on these critical issues of bubble column reactors will be presented in section 3 and section 4 respectively. A short recapitulation and implication will be presented in section 5.

3. CFD MODELLING

Numerical methods for two-phase flows can be categorised into two general groups, time-averaged models and time-dependent (including direct numerical simulation; DNS) models. There are also two ways of calculating the dispersed phase variables: Lagrangian tracking or Eulerian two-fluid methods.

The direct numerical simulations for gas-liquid two-phase flows solve the governing equations for the liquid phase flow and the gas flow field in every single bubble. The interface between two phases should be represented explicitly with sharp interfacial properties and should be free to move, deform, breakup and coalesce as how an actual interface would behave. Therefore, the two-phase coupling and the momentum exchange rely on the interface-tracking methods. The interface-tracking methods that have been developed mainly include Particle-In-Cell method, Marker-and-Cell method, volume of fluid method, level-set method, boundary-fitted grid method and front tracking method (Tryggvason et al., 2001). It is one of the greatest advantages of the DNS method for gas-liquid two-phase flow simulations that the changes on the bubbles interface can be clearly illustrated, such as Krishna and van Baten (1999). Also, the DNS method for two-phase flow can be used as a tool to study the liquid phase turbulence under the influence of gas bubbles, such as Metrailler et al. (2017). Although there are not interphase force model or turbulence models required as model closure, the computational demanding is so high that DNS is limited to low Reynolds numbers and few bubbles, which makes the simulation of real industrial processes almost impossible.

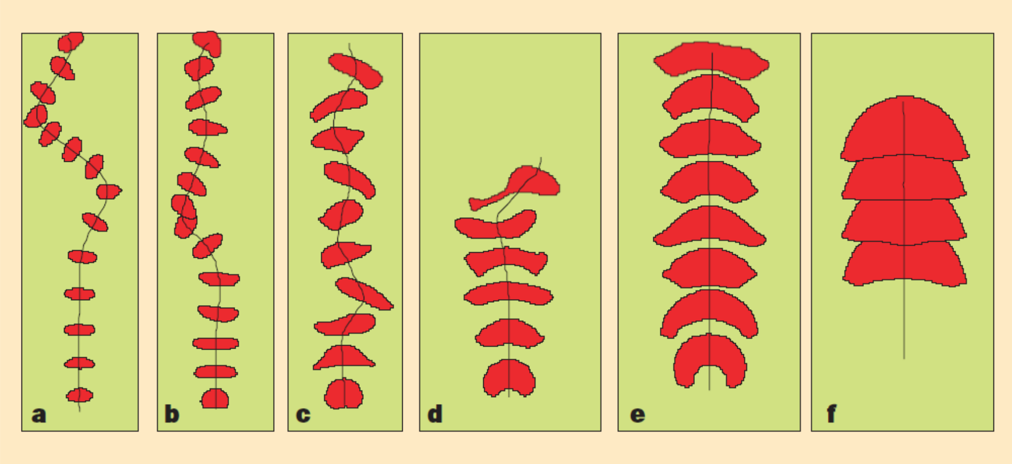

Figure 1-4 Two-dimensional VOF simulations of the rise trajectories and the interface changes of bubbles (taken from Krishna and van Baten (1999)).

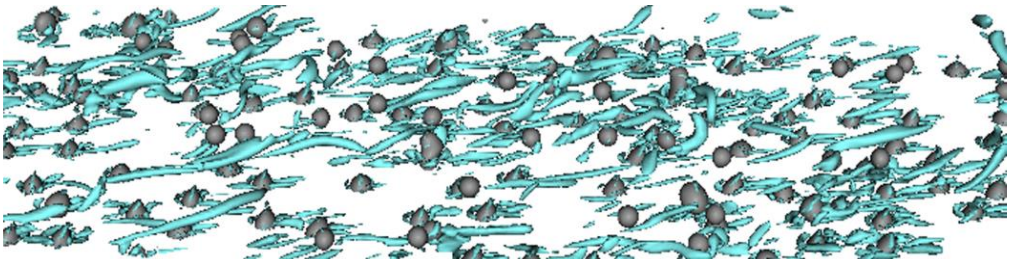

Figure 1-5 Turbulent coherent structures affected by the bubbles while detaching from the wall (taken from Metrailler et al. (2017)).

The Eulerian-Lagrangian method is a more promising approach. This method considers the dispersed phase as discrete particles, and the appropriate equation of motion is solved for each particle under Lagrangian frame of reference. The particle-particle interactions can be clearly described, such as hard-sphere models or soft-ball model for bubble collision and coalescence. The continuous phase is calculated as time-averaged flow field using a grid-based Eulerian method. When the dispersed phase particles are very small in size and low in concentration, it can be assumed that the movement of the dispersed phase particles does not change the flow field of the continuous phase. However, when the particle concentration can no longer be neglected, the discrete particles and the continuous phase can be coupled by using a source term of interphase momentum exchange equations. Some researchers have used this method to study the gas-liquid two-phase flow in the bubble columns and have shown more promising results, such as Delnoij and Kuipers (2000), Sokolichin et al. (1997), Lain and Sommerfeld (2003), Deen et al. (2004) and Buwa et al. (2006). As turbulence description in the continuous phase by Eulerian method only leads to averaged velocity and turbulence statistics, as required by the equation of motion, assumptions have to be made to obtain the instantaneous velocity of the continuous phase at bubble position from its mean value. The Euler-Lagrangian method is quite suitable for fundamental investigations since it allows for direct consideration of various effects related to bubble-bubble and bubble-liquid interactions. The use of this method is often limited not only by the spatial resolution of the meshes but also the number of bubbles that are tracked. Although the computational cost is still very high for industrial-scale simulations, the physical interpretations still make sense while the considered models in this method are simpler than the DNS method.

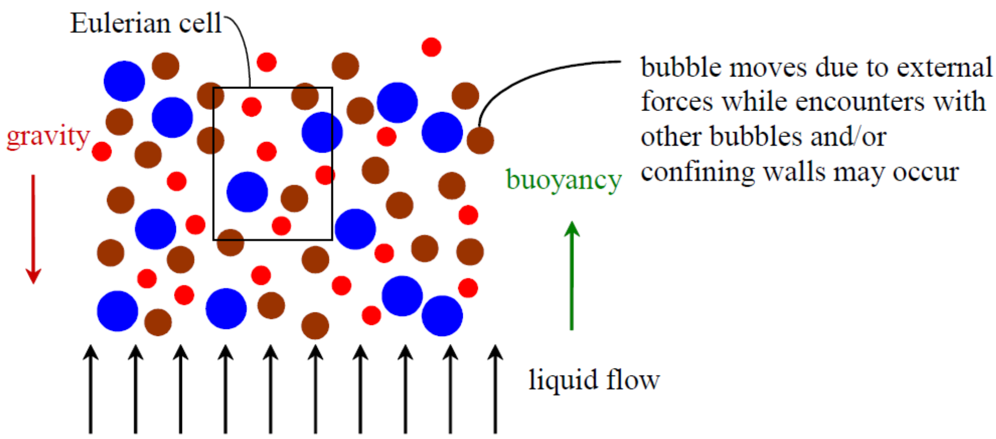

Figure 1-6 Schematic diagram of Eulerian-Lagrangian method (taken from Chen (2004)).

The Eulerian-Eulerian method, also called two-fluid model, is the most widely used approach in numerical simulations of multiphase flow. Not only the continuous phase but also the dispersed phase is treated as statistical continua. The two-fluid model is developed to describe the motion for each phase in a macroscopic sense. As there are two 'fluids' present, the void fraction is used to represent the concentration of each phase. Although the void fraction is not possible to resolve every point in time or space, it is rather necessary to average over a specific time and space. The mass and momentum conservations are expressed as

$$\frac{\partial(\rho_k \alpha_k)}{\partial t} + \nabla \cdot (\rho_k \alpha_k \boldsymbol{u}_k) = 0 \tag{1-5}$$

$$\frac{\partial(\rho_k \alpha_k \boldsymbol{u_k})}{\partial t} + \nabla \cdot (\rho_k \alpha_k \boldsymbol{u_k} \boldsymbol{u_k}) = -\alpha_k \nabla p + \nabla \cdot \bar{\bar{\tau}}_k + \alpha_k \rho_k \boldsymbol{g} + \boldsymbol{F_k} \tag{1-6}$$

where ρ_k, α_k, $\boldsymbol{u}_k$, $\bar{\bar{\tau}}_k$, $\boldsymbol{g}$ and $\boldsymbol{F}_k$ represent the density, volume fraction, velocity vector, viscous stress tensor, gravity vector and the inter-phase momentum exchange term for the k (liquid or gas) phase respectively. The sum of the volume fractions for both phases is equal to 1.

The governing equations of the two-fluid model can be treated based on averaging methods. For example, the most commonly used averaging method that has been accepted by many commercial CFD codes is the Reynolds (ensemble) averaging, which decomposes instantaneous flow variable into the time-averaged mean component and the fluctuating component. The averaged governing equations and the different turbulent correlations of fluctuation terms have been discussed by Joshi (2001) in details. Due to the averaging process, the information regarding the microscopic scale has been lost, which inevitably leads to the closure problems that have been extensively studied by many researchers. It seems that the most required terms to numerically solve the governing equations of two-fluid model are the interphase forces and the Reynolds stresses terms, and different closure models have been developed to close these two terms. Also, some of the interphase force closures, such as the drag force and the lift force, are the function of the bubble diameter, which further arises the need of appropriate closure of the bubble size distributions. When the bubble column is operated at the homogeneous regime with the bubble size distribution being very narrow, using a volume-averaged bubble diameter seems to be acceptable. However, in most industrial processes when the bubble columns are operated at the churn-turbulent flow regime, the bubble sizes are broadly distributed due to intensive bubble coalescence and breakage phenomenon. In this case, the uniform bubble diameter assumption is no longer appropriate, and the local bubble sizes can be calculated with the help of bubble population balance equations.

It should be noted that there are other multiphase models under the framework of the Euler-Euler approach, such as the volume of fluid model (VOF) and the mixture model. However, these models are not as much appropriate as the two-fluid model for the numerical investigations that will be presented in the following chapters. For example, the VOF model is a surface-tracking technique applied to a fixed Eulerian mesh. It is designed for two or more immiscible fluids where the position of the interface between the fluids is of interest. In the VOF model, a single set of momentum equations is shared by the fluids, and the volume fraction of each of the fluids in each computational cell is tracked throughout the domain. It is suggested that the VOF model can be used in stratified flows, free-surface flows, filling, sloshing, the motion of large bubbles in a liquid, the motion of liquid after a dam break, the prediction of jet breakup (surface tension), and the steady or transient tracking of any liquid-gas interface. However, for the turbulent bubbly flows, the dispersed-phase volume fractions usually exceed 10% and the interface between fluids is not much of the main concern, the mixture model or the two-fluid model is suggested. Further considering the inhomogeneity and the significant effects of interphase drag laws for the gas-liquid two-phase flows in the bubble columns, the two-fluid model seems to be a better choice.

3.1 Interphase Forces

The interphase forces term is required by the two-fluid model as the model closure to describe the momentum exchange between the gas phase and the liquid phase. The interphase forces include the drag force, lift force, virtual mass force, turbulent dispersion force, wall lubrication force and Basset force. All these forces are essentially originated from local pressure variations on the bubble surface. The forces acting on a motionless bubble in a stagnant liquid are pressure and gravity. Since there is usually a relative motion between the bubble and liquid, the liquid flow surrounding individual bubbles leads to local variations in pressure and hence producing shear stresses. If the slip velocity is uniform, the force acting on the bubbles is only the drag force. If the bubbles accelerate relative to the liquid motion, the virtual mass force takes effect. If the bubbles flow in non-uniform liquid phase flow field, there are also the lateral lift forces. Due to the liquid phase turbulent fluctuations, the bubble moves transversely under the effect of turbulent dispersion force. When the bubble is approaching the vessel wall, the higher pressure gradient caused by the low velocity in the boundary layer makes the direction of the wall lubrication force towards the centre of the bubble column. Basset force is a historical force, which greatly affects the bubble motion in a very short time. However, the time step is usually much larger than the influencing time of the Basset force. Therefore, the Basset force is usually neglected in the Eulerian-Eulerian simulations.

Drag Force

Drag force is one of the most important interphase forces. The drag force is caused by the relative motion of bubbles and the surrounding liquid flow. The accurate estimation of the drag force is the key to the simulation of gas-liquid two-phase flow in the bubble columns. For a single spherical bubble rising at steady state, the drag force can be expressed by

$$\boldsymbol{F_{D,bubble}} = C_D \left(\frac{\pi}{4} d_b^2\right) \frac{\rho_l}{2} (\boldsymbol{u_l} - \boldsymbol{u_g}) |\boldsymbol{u_l} - \boldsymbol{u_g}| \tag{1-7}$$

where C_D is the drag coefficient, d_B is the bubble diameter and $(\boldsymbol{u_l} - \boldsymbol{u_g})$ is the slip velocity. It appears that the drag coefficient and the bubble diameter are required to calculate the drag force.

For a swarm of bubbles, the formulation of the drag force is complicated by the presence of other surrounding bubbles. The idealised drag force for a bubble swarm can be considered as linear superposition of single bubbles. If there are N number of bubbles per unit volume within the swarm, the drag force of the bubble swarm can be expressed as

$$\boldsymbol{F_{D,swarm}} = N \cdot C_D \left(\frac{\pi}{4} d_b^2\right) \frac{\rho_l}{2} (\boldsymbol{u_l} - \boldsymbol{u_g}) |\boldsymbol{u_l} - \boldsymbol{u_g}| \tag{1-8}$$

Since N is the number of bubbles per unit volume, which can be expressed by $N = {\alpha_g}\Big/{\frac{\pi}{6} d_b^3}$, Equation (1-8) can be rewritten as

$$\boldsymbol{F}_{\boldsymbol{D},\boldsymbol{swarm}} = C_D \frac{3\alpha_g}{4}\frac{\rho_l}{d_b}\left(\boldsymbol{u}_l - \boldsymbol{u}_g\right)\left|\boldsymbol{u}_l - \boldsymbol{u}_g\right| \qquad (1\text{-}9)$$

To ensure the drag force returns to zero when the gas holdup in a computational cell is 1 or 0, Equation (1-9) should be multiplied by α_l, which gives

$$\boldsymbol{F}_{\boldsymbol{D},\boldsymbol{swarm}} = C_D \frac{3\alpha_g\alpha_l}{4}\frac{\rho_l}{d_b}\left(\boldsymbol{u}_l - \boldsymbol{u}_g\right)\left|\boldsymbol{u}_l - \boldsymbol{u}_g\right| \qquad (1\text{-}10)$$

Although the drag coefficient has been extensively studied by many researchers, its formulations are mostly still based on empirical or semi-empirical correlations. The most commonly used models of drag coefficients in CFD studies of bubble columns include Schiller and Naumann (1935), Ishii and Zuber (1979), Grace et al. (1978) and Tomiyama (1998). The expressions for the drag models are presented in Table 1-1.

Table 1-1 Expressions for a single bubble drag coefficient

Model	Description	Expressions
Schiller and Naumann (1935)	A rigid spherical particle in an infinite stagnant fluid	$C_D = \begin{cases} \frac{24}{Re_b}(1+0.15Re_b^{0.687}) & Re_b \le 1000 \\ 0.44 & Re_b > 1000 \end{cases}$; $Re_b = \frac{\rho_l \lvert \boldsymbol{u}_g - \boldsymbol{u}_l \rvert d_B}{\mu_l}$
Grace et al. (1978)	Non-spherical bubbles	$C_D = max\left(C_{D,sphere}, min\left(C_{D,ellipse}, C_{D,cap}\right)\right)$; $C_{D,sphere} = \begin{cases} \frac{24}{R_{eb}} & Re_b < 0.01 \\ \frac{24}{R_{eb}}(1+0.15R_{eb}^{0.687}) & Re_b \ge 0.01 \end{cases}$; $C_{D,cap} = \frac{8}{3}$; $C_{D,ellipse} = \frac{4}{3}\frac{gd_b}{U_t^2}\frac{(\rho_l-\rho_g)}{\rho_l}$; $Re_b = \frac{\rho_l \lvert \boldsymbol{u}_g - \boldsymbol{u}_l \rvert d_b}{\mu_l}$; $U_t = \frac{\mu_l}{\rho_l d} M_O^{-0.149}(J-0.857)$; $M_O = \frac{\mu_l^4 g(\rho_l-\rho_g)}{\rho_l^2\sigma^3}$; $J = \begin{cases} 0.94H^{0.757} & 2 < H < 59.3 \\ 3.42H^{0.441} & H \ge 59.3 \end{cases}$; $H = \frac{4}{3}E_O M_O^{-0.149}\left(\frac{\mu_l}{\mu_{ref}}\right)^{-0.14}$; $\mu_{ref} = 0.0009\ kg/(ms)$
Ishii and Zuber (1979)	Bubble and droplet	$C_D = \max\left\{\frac{24}{Re_b}(1+0.15Re_b^{0.687}), min\left[\frac{2}{3}\sqrt{Eo}, \frac{8}{3}\right]\right\}$
Tomiyama (1998)	A single bubble at various conditions ($10^{-2} < Eo < 10^3$,	For purified water: $C_D = max\left\{min\left[\frac{16}{Re_b}(1+0.15Re_b^{0.687}), \frac{48}{Re_b}\right], \frac{8}{3}\frac{Eo}{Eo+4}\right\}$; For slightly contaminated water:

$10^{-14} < Mo < 10^{7}$ and $10^{-3} < Re_b < 10^{5}$)	$C_D = max\left\{min\left[\frac{24}{Re_b}(1 + 0.15Re_b^{0.687}), \frac{72}{Re_b}\right], \frac{8}{3}\frac{Eo}{Eo+4}\right\}$; For contaminated water: $C_D = max\left[\frac{24}{Re_b}(1 + 0.15Re_b^{0.687}), \frac{8}{3}\frac{Eo}{Eo+4}\right]$;

In the CFD simulations using two-fluid model, the drag coefficient has been considered in different ways according to the nature of the two-fluid flows. For example, using the drag coefficient of the single bubble by ignoring the bubble interactions and the bubble deformations. Alternatively, to modify the drag coefficient of the spherical bubble by taking the shape factors into account or to consider the bubble interactions by assuming the drag coefficient of bubble swarm to that of the single bubble as a function of the gas holdup. However, it is noticed that none of these drag models is applicable to all complex flow conditions in real industrial processes, and different kinds of lumping parameters are proposed to adjust the drag coefficients from case to case.

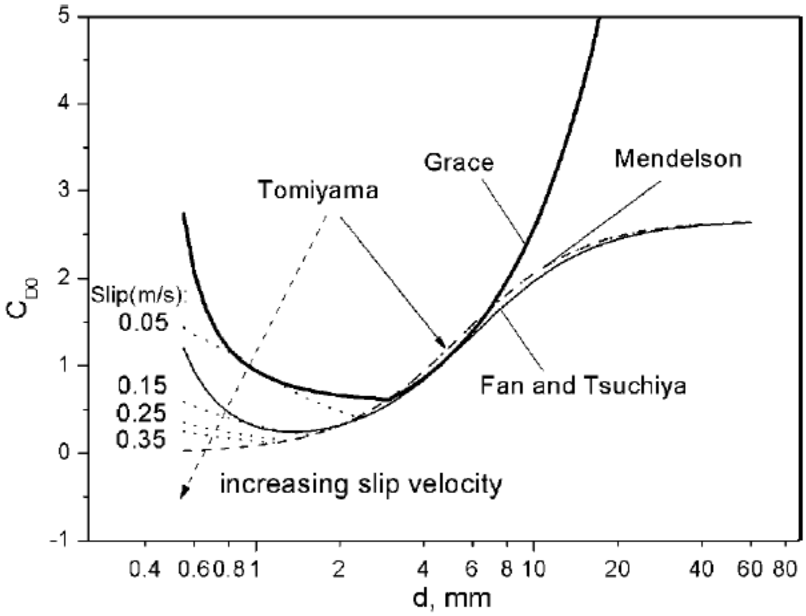

Figure 1-7 Comparison of different drag coefficient correlations (taken from Chen et al. (2009b)).

Added mass Force

When a single bubble accelerates or decelerates, some volume of the surrounding liquid must be moved or deflected as the bubble moves through it. Due to the acceleration induced by the bubble motion, the surrounding liquid experiences an extra force. This is like the mass of bubble has been added.

It seems that a concrete conclusion has not yet been made regarding the effect of added mass force in the CFD studies of gas-liquid two-phase flows in the bubble columns (Krishna and Van Baten, 2001b, Joshi, 2001, Tabib et al., 2008). Mudde and Simonin (1999) have shown when the drag and the virtual mass forces are used together, the values of the amplitude and the time period of the bubble plume oscillations in 3-D simulations are satisfactorily comparable with the experimental observations. However, from the same research group, Oey et al. (2003) investigated the influence of interfacial closures and numerics on the hydrodynamics of the same bubble column, but they could not reproduce the same results. However, the right magnitude of the oscillations of the meandering plume has been found without using the virtual mass.

The mathematical expressions of virtual mass force have derived by Auton et al. (1988). The virtual mass force model implanted in most CFD codes can be expressed as

$$\boldsymbol{F}_{\boldsymbol{VM,l}} = \alpha_g \rho_l C_{VM} \left(\frac{D\boldsymbol{u}_{\boldsymbol{g}}}{Dt} - \frac{D\boldsymbol{u}_{\boldsymbol{l}}}{Dt} \right) \tag{1-11}$$

where C_{VM} is the virtual mass coefficient. The value of the virtual mass coefficient of spherical bubble in potential flow is 0.5. However, in the reality, the bubbles are not perfectly spherical and the interactions among neighbouring bubbles make the virtual mass coefficient deviated from the theoretical value. For example, Cook and Harlow (1986) have used a value of 0.25 and Tomiyama (2004) has used a tensor for the virtual mass coefficient for ellipsoidal bubbles to represent the different values in horizontal and vertical directions.

Lift force

The lift force is one of the most significant driving forces for the radial movement of bubbles. The mechanisms for the lift force are quite complicated, including the Magnus lift force due to the bubble rotation, the Saffman lift force due to the velocity gradient of the carrier fluid, and the lift force due to the bubble deformation. The different flow conditions that lead to the generation of lift forces have been clearly illustrated by Tomiyama et al. (1995) and summarised by Chen (2004).

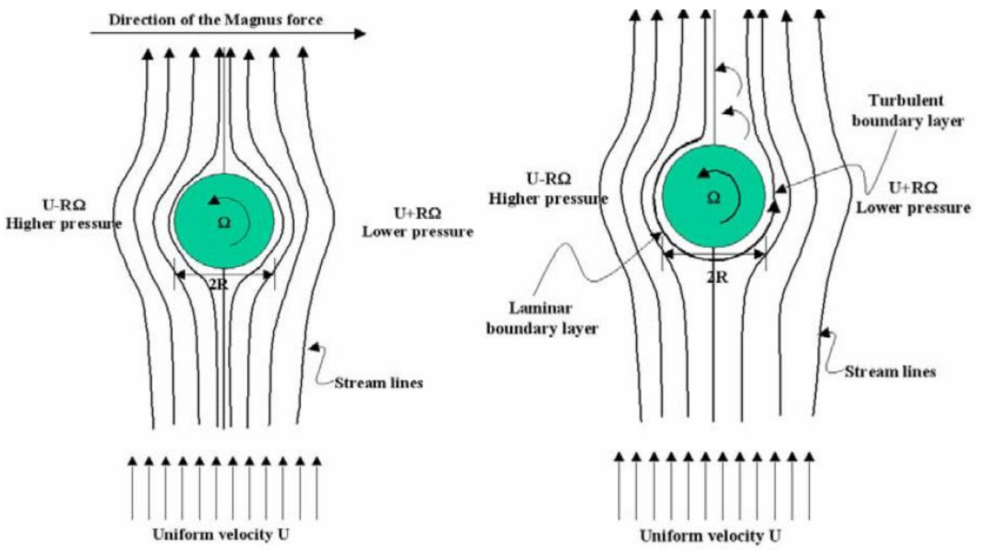

(a) (b)

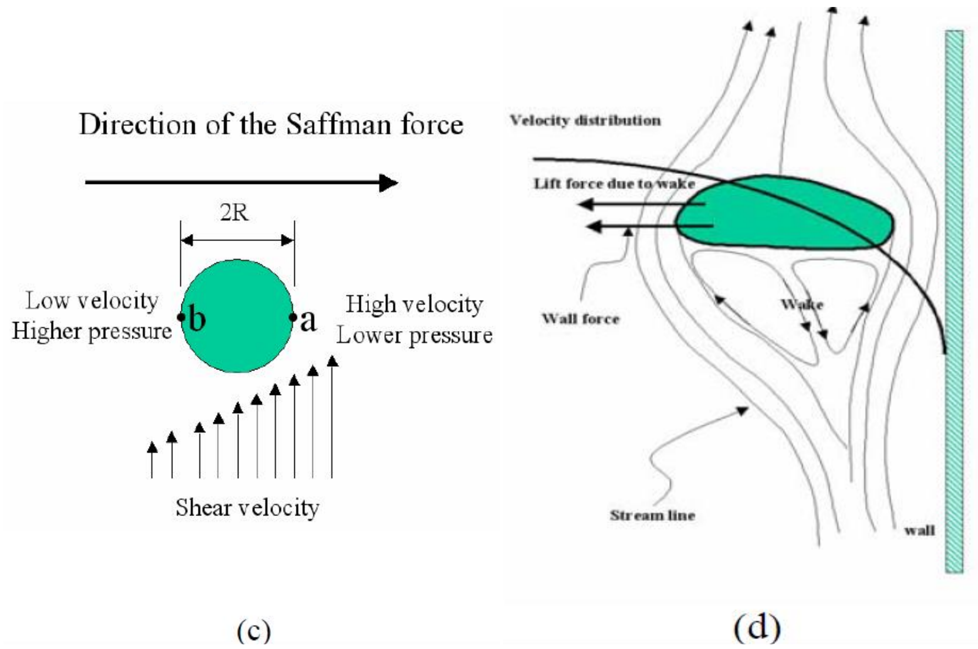

Figure 1-8 Schematic diagram of lift force (taken from Chen (2004)): (a) Magnus lift force in uniform flow field; (b) Magnus lift force with laminar boundary layer on one side and turbulent boundary layer on the other side of the bubble; (c) Saffman lift force; (d) lift force due to bubble deformation (U: uniform velocity; R: radius; Ω: rotational speed).

It seems that the lift force acting on the bubbles mainly due to the velocity gradient of the liquid phase flow in the bubble columns. The lift force acting on the dispersed phase can be expressed as

$$\boldsymbol{F_{lift}} = -C_L \rho_l \alpha_g (\boldsymbol{u_l} - \boldsymbol{u_g}) \times (\nabla \times \boldsymbol{u_l}) \tag{1-12}$$

where C_L is the lift coefficient. In the open literature, successful simulations have been reported both for including lift (Tabib et al., 2008, Zhang et al., 2006, Rampure et al., 2007, Deen et al., 2001) and isolating the effect of lift force (Deen et al., 2000b, Krishna and van Baten, 2001a, Ranade and Tayalia, 2001). The different values of lift coefficient have been found in the open literature, such as Zhang et al. (2006) and Bhole et al. (2008). It is generally believed that the effect of lift coefficient is more significant at high superficial velocities. The positive value of lift force makes the bubbles move outwards towards the column wall, which leads to a flatter hold-up profile and lower centreline velocity. Therefore, the value of lift coefficient should be chosen depending on the bubble size distribution, rather than using a constant value for averaged bubble size for the entire bubble column.

Based on large numbers of experimental statistics, Tomiyama (1998) has correlated the lift coefficient with the bubble size, which considers the bubble shape variations by using the bubble Eotvos number.

$$C_L = \begin{cases} \min[0.288\tanh(0.121Re),\, f(Eo')] & Eo < 4 \\ 0.00105Eo'^3 - 0.0159Eo'^2 - 0.0204Eo' + 0.474 & 4 \le Eo \le 10 \\ -0.29 & Eo > 10 \end{cases}$$

(1-13)

where the $Eo' = \frac{g(\rho_l - \rho_g)d_h^2}{\sigma}$ and the long axis of deformable bubble $d_h = d_b(1 + Eo^{0.757})^{\frac{1}{3}}$.

It can be found from Equation (1-13) that value of lift coefficient becomes negative when the bubble diameter larger than 5.8 mm in the air-water system, which drives the large ellipsoidal bubbles to move towards the core region of the bubble column.

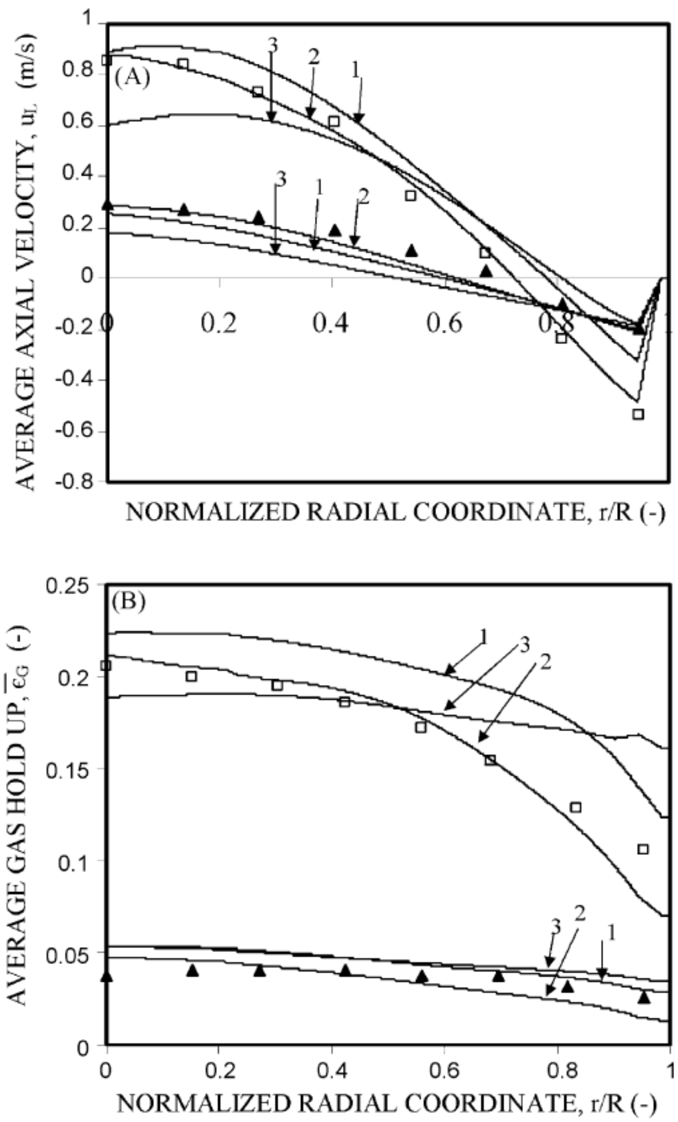

Figure 1-9 Effect of lift force, (A) average liquid velocity; (B) gas holdup. (▲) Experimental data of Menzel *et al.* (1990) [U_g = 0.012 m/s], (□) experimental data of Menzel *et al.* (1990) [U_g = 0.096 m/s]; (1) C_L = 0 (2) C_L: negative value (3) C_L: positive value [taken form Tabib *et al.* (2008)].

Turbulent Dispersion Force

The effect of the turbulent fluctuations of liquid velocity on the bubbles can be described by the turbulent dispersion force. Yang et al. (2002) have demonstrated that the significant effect of the turbulent eddies, which are with approximately the same size as the bubbles, on the entrapment and transport of bubbles. However, the turbulent fluctuations at small scales have been smoothed out in the two-fluid model. Based on the analogy with molecular movement, the turbulent diffusion of the bubbles by the turbulent eddies can be approximated by Lopez de Bertodano (1992),

$$\boldsymbol{F_{td,l}} = -\boldsymbol{F_{td,g}} = C_{TD}\rho_l k_l \nabla\alpha_g \tag{1-14}$$

where C_{TD} is the turbulent dispersion coefficient with recommended values between 0.1 and 0.5, k_l is the liquid phase kinetic energy per unit mass, $\nabla\alpha_g$ is the gradient of gas phase volume fraction.

Based on the Favre averaging of the interphase momentum exchange due to drag force, Burns et al. (2004) derived an explicit expression of the turbulent dispersion force.

$$\boldsymbol{F_{td,l}} = -\boldsymbol{F_{td,g}} = C_{TD}\frac{3\alpha_g}{4}\frac{\rho_l}{d_b}\left(\boldsymbol{u_l} - \boldsymbol{u_g}\right)\frac{\nu_t}{\sigma_{TD}}\left(\frac{\nabla\alpha_l}{\alpha_l} - \frac{\nabla\alpha_g}{\alpha_g}\right) \tag{1-15}$$

where ν_t is the turbulent kinematic viscosity, and σ_{TD} is referred as Schmidt number. In principle, it should be possible to obtain its value from single bubble experiments also for this force by evaluating the statistics of bubble trajectories in well characterized turbulent flows (Rzehak and Krepper, 2013a). However, due to the absence of a deeper understanding, a constant value of $\sigma_{TD} = 0.9$ is typically used.

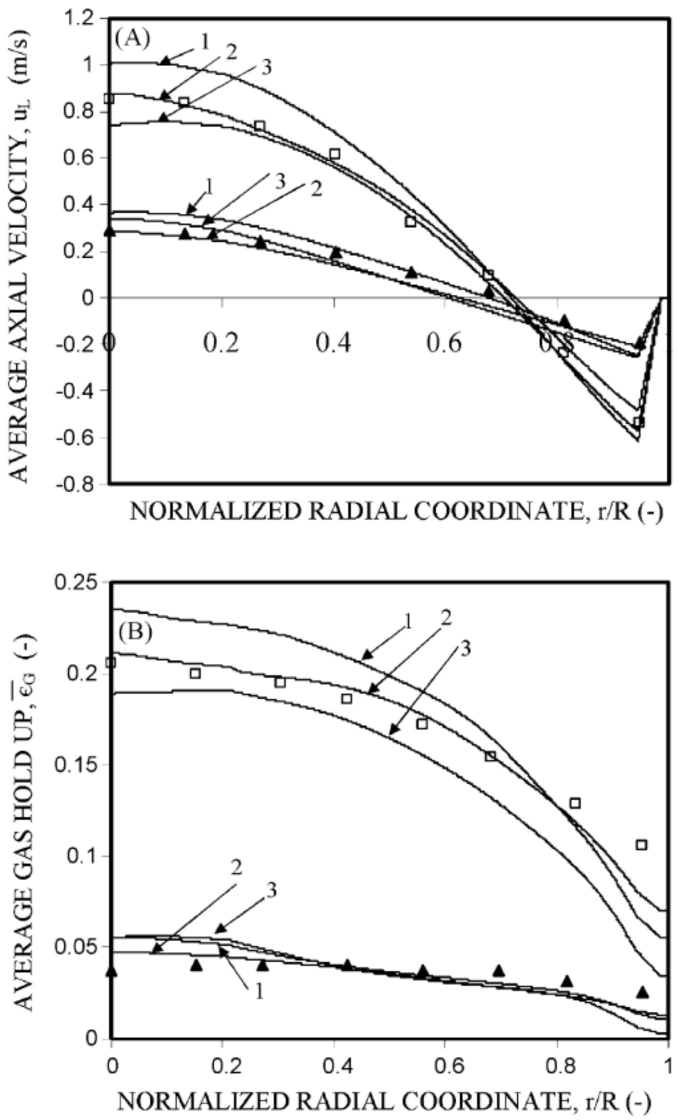

Figure 1-10 Effect of turbulent dispersion force, (A) average liquid velocity; (b) gas holdup. (▲) Experimental data of Menzel *et al.* (1990) [U_g = 0.012 m/s], (□) experimental data of Menzel *et al.* (1990) [U_g = 0.096 m/s]; (1) C_{TD} = 0 (2) C_{TD} = 0.2 (3) C_{TD} = 0.5 [taken form Tabib *et al.* (2008)].

Wall lubrication Force

When rising bubbles being translated approaching to the bubble column wall, the asymmetric fluid flow around the bubbles in the vicinity of the wall due to the fluid boundary layer will lead to the wall lubrication force. The wall lubrication force tends to push the bubbles away from the wall. The general form of the wall lubrication force can be expressed by

$$\boldsymbol{F_{wl}} = C_{wl}\rho_l\alpha_g \left|\left(\boldsymbol{u_l} - \boldsymbol{u_g}\right)_{||}\right|^2 \boldsymbol{n_w} \tag{1-16}$$

where C_{wl} the wall lubrication coefficient, $\left|\left(\boldsymbol{u_l} - \boldsymbol{u_g}\right)_{||}\right|$ the phase relative velocity component tangential to the wall surface, and n_w the unit normal pointing away from the wall.

Antal et al. (1991) have derived an expression for the wall lubrication coefficient, such as

$$C_{wl} = max\left(0, \frac{C_{w1}}{d_b} + \frac{C_{w2}}{y_w}\right) \tag{1-17}$$

where commonly used values for the dimensionless coefficients C_{w1} = -0.01 and C_{w2} = 0.05, and y_w the distance to the nearest wall.

The wall lubrication force is only effective in a thin layer adjacent to the wall, as a model cut-off, $y_w \leq \left(\frac{C_{w2}}{C_{w1}}\right) d_b$.

Based on the correlations developed in the experiments, Tomiyama (1998) have improved the model for wall lubrication coefficient and make the formulation associated with pipe diameter. Also, based on Tomiyama (1998), Frank et al. (2008) have further improved the model of wall lubrication coefficient by removing the dependence of the pipe diameter and achieved better agreements with experimental data.

3.2 <u>Turbulence Models</u>

Turbulence widely exists in the fluid flows of industrial processes. However, accurate modelling of turbulence is very difficult, as its behaviour is extremely complex. The bubble column reactors are usually operated in heterogeneous regime with high superficial gas velocities to achieve high productivity. In this case, the turbulence in the bubble columns is multiphase turbulence, which is a very important question that cannot be disregarded in the CFD studies. Theoretically, with sufficient small grid size and timestep, direct numerical simulation can predict the turbulence behaviour in all scales. However, the length scale ratio is inversely proportioned to $Re^{3/4}$ (Kolmogorov, 1991), which means the higher turbulence intensity the smaller grid size should be used. It is obvious that the computational demanding of using DNS for turbulence in practical engineering systems is tremendous and nearly impossible with current technology. The DNS is only capable of low Reynolds number flows and with few numbers of bubbles. Therefore, engineering solutions are needed to deal with turbulence modelling in industrial processes.

To avoid resolving the turbulence structures in all scales, approximate treatment has been employed to model the contributions of turbulent eddies at specific length scales, such as larger eddy simulations (LES) and Reynolds averaging. The LES only computes large-scale turbulent eddies directly. The information of eddies at small length scales can be removed by filtering operation, while the effect of these eddies smaller than the cutoff width is considered using sub-grid models. Some researchers have used LES for numerical modelling of bubble columns, such as Deen et al. (2001), Dhotre et al. (2008), Niceno et al. (2008), Ma et al. (2016), and Liu and Li (2018). Comparing with the DNS, the computational demanding of LES is much reduced. It is likely that the pace of developments of LES for industrially relevant complex flows will increase as computing resources become more powerful.

Reynolds averaging is the most preferred method in the studies of industry-relevant reactors, as its computational cost is believed to be the least expensive. The main concern is the Reynolds stress term τ, resulting from the Reynolds averaging. The Reynolds stress term needs to be modelled correctly in order to achieve accurate results. Different models have been developed to model the Reynolds stress term, such as one equation Spalart-Allmaras model, two-equation models, and Reynolds stress models. Two-equation models are the most widely studied and commonly used method, which include Algebraic stress model, $k \sim \omega$ model, $k \sim \varepsilon$ model and their variants such as shear stress transport (SST) $k \sim \omega$, RNG $k \sim \varepsilon$ and Realisable $k \sim \varepsilon$ models.

Two-equation k ~ ε model

The two-equation $k \sim \varepsilon$ model includes two extra transport equations to represent the turbulent properties of the flow. This allows the convection and diffusion of turbulent energy to be taken into account. The transported variable k is the turbulent kinetic energy and ε is the turbulent dissipation rate. The standard $k \sim \varepsilon$ model for the liquid phase flow can be expressed by

$$\frac{\partial(\alpha_l \rho_l k_l)}{\partial t} + \nabla \cdot (\alpha_l \rho_l k_l \boldsymbol{u_l}) = \nabla \cdot \left[\alpha_l \left(\mu_l + \frac{\mu_t}{\sigma_k}\right) \nabla k_l\right] + \alpha_l \left(G_{k,l} - \rho_l \varepsilon_l\right) + S^k \tag{1-18}$$

$$\frac{\partial(\alpha_l \rho_l \varepsilon_l)}{\partial t} + \nabla \cdot (\alpha_l \rho_l \varepsilon_l \boldsymbol{u}_l) = \nabla \cdot \left[\alpha_l \left(\mu_l + \frac{\mu_t}{\sigma_k}\right) \nabla \varepsilon_l\right] + \alpha_l \frac{\varepsilon_l}{k_l} \left(C_{1\varepsilon} G_{k,l} - C_{2\varepsilon} \rho_l \varepsilon_l\right) + S^\varepsilon \tag{1-19}$$

where the eddy viscosity $\mu_t = C_\mu k^2/\varepsilon$. S^k and S^ε are the source terms for the turbulence generation in the wakes of bubbles. If there are not source terms in these two equations, it means that only the liquid shear turbulence is considered. On the contrary, by adding the source terms S^k and S^ε, the effects of the bubble induced turbulence can be partially included in the turbulence model, even though the source term S^k is still limited to the isotropic turbulence assumption set by the two-equation turbulence model. The detailed expressions of source terms S^k and S^ε are discussed in the bubble induced turbulence section.

G_k in Equation (1-18) and (1-19) represents the production of turbulent kinetic energy and can be expressed by

$$G_k = -\rho\overline{u'_i u'_j}\frac{\partial u_j}{\partial x_i} \tag{1-20}$$

The Reynolds stress terms are new unknowns that are introduced into the averaged equations by the Reynolds averaging, which inevitably lead to the closure problem. The Reynolds stress terms are not solved directly in the two-equation model but being approximated by using the Boussinesq's turbulent viscosity hypothesis, which can be expressed by

$$-\rho\overline{u'_i u'_j} = 2\mu_t S_{ij} - \frac{2}{3}\rho k\delta_{ij} \tag{1-21}$$

where S_{ij} is the mean strain rate tensor, and δ_{ij} is the Kronecker delta. The mean strain rate tensor is defined by

$$S_{ij} = \frac{1}{2}\left(\frac{\partial U_i}{\partial x_j} + \frac{\partial U_j}{\partial x_i}\right) \tag{1-22}$$

Therefore, Equation (1-20), the production of turbulent kinetic energy can be rewritten as

$$G_k = 2\mu_t S_{ij} S_{ij} \tag{1-23}$$

The Boussinesq hypothesis is one of the fundamental basis of solving the two-equation models, as it is a huge simplification which allows one to think of the effect of turbulence on the mean flow in the same way as molecular viscosity affects a laminar flow. However, by rewriting Equation (1-20) into Equation (1-23), the isotropic assumption of the normal Reynolds stresses has been used implicitly, which may not be necessarily true in the multiphase turbulence in the bubble column. Also, the postulation of the Reynolds stress tensor being proportional to the mean strain rate tensor by the Boussinesq hypothesis may not in general valid. It is true in simple flows like straight boundary layers, but in complex flows, such as flows with strong curvature, or strongly accelerated or decelerated flows, the Boussinesq hypothesis is simply not valid.

The dispersed turbulence model is the appropriate model when the concentrations of the secondary phases are dilute, or when using the granular model. Fluctuating quantities of the secondary phases can be given in terms of the mean characteristics of the primary phase and the ratio of the particle relaxation time and eddy-particle interaction time. Predictions for turbulence quantities for the dispersed phases are obtained using the Tchen theory of dispersion of discrete particles by homogeneous turbulence (Hinze, 1975). The model is applicable when there is clearly one primary continuous phase and the rest are dispersed dilute secondary phases. By contrast, the mixture turbulence model is an extension of the single-phase $k \sim \varepsilon$ model, and it is applicable when phases separate, for stratified (or nearly stratified) multiphase flows, and when the density ratio between phases is close to 1. In these cases, using mixture properties and mixture velocities is sufficient to capture important features of the turbulent flow. The mixture density, molecular viscosity and velocity can be computed from

$$\rho_m = \sum_{i=1}^{N} \alpha_i \rho_i \tag{1-24}$$

$$\mu_m = \sum_{i=1}^{N} \alpha_i \mu_i \tag{1-25}$$

$$\boldsymbol{u}_m = \frac{\sum_{i=1}^{N} \alpha_i \rho_i \boldsymbol{u}_i}{\sum_{i=1}^{N} \alpha_i \rho_i} \tag{1-26}$$

where the α_i, ρ_i, and $\boldsymbol{u}_i$ are respectively the volume fraction, density, viscosity and velocity of the i^{th} phase.

Reynolds Stress Model

The turbulence generated in the bubble column can be thought of being the joint superposition of shear turbulence and bubble-induced turbulence. The bubble-induced turbulence is mainly influenced by the wake formed by shedding vortices from the bubbles and decays quite quickly. In this case, it seems that the flow features of interest in the present study are the result of anisotropy, and hence the Boussinesq hypothesis of isotropic turbulent eddy viscosity may not be appropriate for the modelling of Reynolds stresses. Therefore, the Reynolds stress model (RSM) is required to reflect the anisotropic nature. In the RSM model, individual Reynolds stresses $\overline{u'_i u'_j}$ are calculated by the Reynolds stress transport equations. The RSM model solves six Reynolds stress transport equations with an additional equation for the turbulence dissipation rate. The exact transport equations for the transport of the Reynolds stresses may be expressed as

$$\frac{\partial\left(\alpha_l \rho_l \overline{u_i' u_j'}\right)}{\partial t} + \frac{\partial\left(\alpha_l \rho_l u_k \overline{u_i' u_j'}\right)}{\partial x_k} = \frac{\partial}{\partial x_k}\left(\alpha_l\left(\mu_l + \frac{\mu_t}{\sigma_k}\right)\frac{\partial \overline{u_i' u_j'}}{\partial x_k}\right)$$
$$+\alpha_l P_{ij} + \alpha_l \phi_{ij} - \tfrac{2}{3}\delta_{ij}\alpha_l \rho_l \varepsilon + \alpha_l S_{ij}^{BIT} \qquad (1\text{-}27)$$

where P_{ij} is the turbulence production that is given by

$$P_{ij} = -\rho_l\left(\overline{u_i' u_k'}\frac{\partial u_j}{\partial x_k} + \overline{u_j' u_k'}\frac{\partial u_i}{\partial x_k}\right) \qquad (1\text{-}28)$$

and ϕ_{ij} is the pressure-strain correlation accounting for pressure fluctuations that redistribute the turbulent kinetic energy amongst the Reynolds stress components. It can be modelled according to the formulation proposed by Launder (1989):

$$\phi_{ij} = \phi_{ij,1} + \phi_{ij,2} + \phi_{ij,1}^{W} + \phi_{ij,2}^{W}$$

$$= -C_1 \rho_l \frac{\varepsilon}{k}\left(\overline{u_i' u_j'} - \frac{2}{3} k \delta_{ij}\right) - C_2 \rho_l \frac{\varepsilon}{k}\left(P_{ij} - \frac{1}{3} tr(P) \delta_{ij}\right)$$

$$-C_1^W \rho_l \frac{\varepsilon}{k}\left(\overline{u_k' u_m'} n_k n_m \delta_{ij} - \frac{3}{2}\overline{u_k' u_i'} n_k n_j - \frac{3}{2}\overline{u_k' u_j'} n_k n_i\right)\left(\frac{k^{3/2}}{\varepsilon}\frac{1}{C_l y_W}\right)^2$$

$$-C_2^W \left(\phi_{km,2} n_k n_m \delta_{ij} - \frac{3}{2}\phi_{ik,2} n_k n_j - \frac{3}{2}\phi_{jk,2} n_k n_i\right)\left(\frac{k^{3/2}}{\varepsilon}\frac{1}{C_l y_W}\right)^2$$

(1-29)

As the scalar turbulence dissipation rate is used in Equation (1-27), a model transport equation is used to calculate ε, such as

$$\frac{\partial(\alpha_l \rho_l \varepsilon)}{\partial t} + \frac{\partial}{\partial x_i}(\alpha_l \rho_l \varepsilon \boldsymbol{u}_i) = \frac{\partial}{\partial x_j}\left[\alpha_l\left(\mu_l + \frac{\mu_t}{\sigma_\varepsilon}\right)\frac{\partial \varepsilon}{\partial x_j}\right] + \alpha_l \rho_l \frac{\varepsilon}{k}\left(C_{1\varepsilon}\overline{u'_i u'_j}\frac{\partial \boldsymbol{u_i}}{\partial x_k} - C_{2\varepsilon}\varepsilon\right) + \alpha_l S_\varepsilon^{BIT} \tag{1-30}$$

where the turbulent kinetic energy k is calculated from the solved values of normal stress using the Reynolds stress transport equation, such as

$$k = \frac{1}{2}\left(\sum_{i=1,2,3} u'_i u'_j\right) \tag{1-31}$$

Several studies used the RSM model to predict flow characteristics in the bubble column reactors. In comparison with $k \sim \varepsilon$ model, RSM can predict the swirling behaviours of the flow more appropriately. Also, RSM is able to better address the characteristics of the turbulent bubbly flow in the bubble columns where the bubble-induced turbulence and anisotropy of turbulence are significant (Gupta and Roy, 2013, Tabib et al., 2008, Silva et al., 2012, Bhole et al., 2008, Ekambara et al., 2008, Parekh and Rzehak, 2018, Liu and Hinrichsen, 2014, Chahed et al., 2003). Silva et al. (2012) used the RSM model to study the heterogeneous regime in bubble column reactor to predict the local gas hold-up inside the bubble column especially toward the centre and walls. Tabib et al. (2008) compared various turbulence models such as RSM, $k \sim \varepsilon$ and LES model to study flow pattern inside the cylindrical bubble column. It the study of Tabib et al. (2008), the RSM demonstrates a good performance to show anisotropic flows involving swirls, acceleration and deceleration and buoyancy in the bubble column. Furthermore, the RSM has shown to be much more successful in predicting the averaged liquid velocity profiles than the $k \sim \varepsilon$ model.

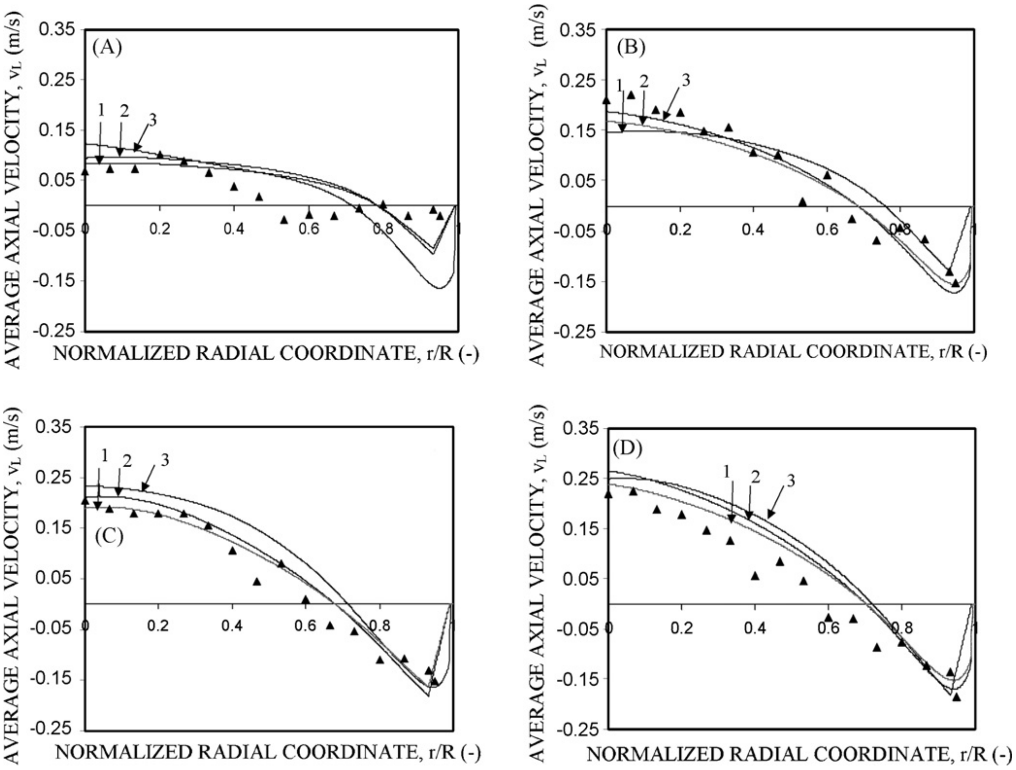

Figure 1-11 Comparison between the simulated and experimental profiles of axial liquid velocity at different axial positions in a 150mm (i.d.) bubble column with sieve plate sparger at U_g = 20 mm/s (A) H/D= 1; (B) H/D= 2; (C) H/D= 3; (D) H/D=4. (▲) Experimental; (1) LES model; (2) RSM model and (3) k–ε model (taken from Tabib et al. (2008)).

Bubble Induced Turbulence

Due to the momentum transfer occurring at the bubble interphase, the multiphase turbulence in the bubble column reactors becomes more complicated. The dispersed bubbles in the bubble columns surely affect the liquid phase turbulence, even though the effects have not been fully understood. In order to consider the influence of bubbles on the liquid phase turbulence, some modifications have been made based on the two-equation models. Sato and Sekoguchi (1975) have assumed that the effective viscosity of the liquid phase turbulence is connsist of the molecular viscosity, turbulent viscosity due to shear, and the due to bubble-induced turbulence, such as $\mu_{eff} = \mu_l + \mu_t + \mu_{BIT}$. However, opinions about the effect of using the Sato model in the numerical studies of bubble columns are different. For example, Pan et al. (1999) have achieved simulation results that are in good agreement with experimental data, while Deen et al. (2001) have shown that the differences for with and without using the bubble-induced turbulence model are not significant.

Pfleger and Becker (2001), Troshko and Hassan (2001), and Simonin (1990) have considered the effect of bubbles by adding different source terms to the *k* and *ε* equations of the liquid phase turbulence. Rzehak and Krepper (2013a) have developed an isotropic bubble-induced turbulence model by adding source term S^k and S^ε or S^ω in the *k*- and *ε*- or *ω*-equation. The source term S^k in the k-equation describes the additional generation of turbulent kinetic energy due to the presence of the gas bubbles. It is assumed that all energy lost by the bubble due to drag is converted to turbulent kinetic energy in its wake, which is in accordance with Troshko and Hassan (2001). The source term S^k can be expressed by

$$S^k = \boldsymbol{F}_L^{drag} \cdot (\boldsymbol{u}_G - \boldsymbol{u}_L) \tag{1-32}$$

The source term S_L^ε in the *ε*-equation is derived using similar heuristics as for the single-phase model, which is to divide the k-source by certain time scale *τ*,

$$S^\varepsilon = C_{\varepsilon B} \frac{S_k}{\tau}. \tag{1-33}$$

In this case, it is very important to select appropriate time scale τ, which represents the lifetime of turbulent eddies. In single-phase flow, there are only two relevant variables, k and ε, resulting in the only combination $\tau = k / \varepsilon$. For bubble-induced turbulence in two-phase flows, it seems that the time scale τ has different possible expressions. It is hard to conclude which one is correct with absolute confidence, as the characteristics of bubble-induced turbulence are much more complicated than isotropic homogeneous turbulence and these characteristics have not been fully understood. However, Rzehak and Krepper (2013a) and Rzehak and Krepper (2013b) have used $\tau = d_B / k^{0.5}$ in the simulations together with $C_{\varepsilon B} = 1$ and achieved very good results.

It seems that the bubble-induced turbulence is strongly anisotropic, which can be more appropriately described by the Reynolds stress model, as the Reynolds stress terms are directly calculated in three directions. However, the isotropic bubble-induced turbulence model cannot be directly used with the Reynolds stress model. Therefore, in a recent study, Parekh and Rzehak (2018) have proposed a source term $\boldsymbol{S}^R$ to represent the turbulent kinetic energy generated by bubbles in the Reynolds stress model. In which case, the magnitude of the source term $\boldsymbol{S}^R$ should be different between the direction of bubble's relative motion and its perpendicular directions. This effect has been clearly shown in the experiments of Hosokawa and Tomiyama (2013). It seems well-accepted that the source term S^R may be decomposed as

$$\boldsymbol{S}^R = S^k(a[\hat{\boldsymbol{u}}_{rel} \otimes \hat{\boldsymbol{u}}_{rel}] + b[\hat{\boldsymbol{u}}_{rel} \otimes \hat{\boldsymbol{u}}_{rel}])\,, \qquad (1\text{-}34)$$

where $\otimes$ is a projection operator and $\hat{\boldsymbol{u}}_{rel}$ is a unit vector in the direction of the relative velocity,

$$\hat{\boldsymbol{u}}_{rel} = \frac{\boldsymbol{u}_G - \boldsymbol{u}_L}{|\boldsymbol{u}_G - \boldsymbol{u}_L|}\,. \qquad (1\text{-}35)$$

The projection operation $\hat{\boldsymbol{u}}_{rel} \otimes \hat{\boldsymbol{u}}_{rel}$ and $1 - \hat{\boldsymbol{u}}_{rel} \otimes \hat{\boldsymbol{u}}_{rel}$ can be written in matrix form in a coordinate system with the x-axis aligned with $\hat{\boldsymbol{u}}_{rel}$, such as

$$\hat{\boldsymbol{u}}_{rel} \otimes \hat{\boldsymbol{u}}_{rel} = \hat{\boldsymbol{x}} \otimes \hat{\boldsymbol{x}} = \begin{bmatrix} 1 & 0 & 0 \\ 0 & 0 & 0 \\ 0 & 0 & 0 \end{bmatrix}$$

$$[1 - \hat{\boldsymbol{u}}_{rel} \otimes \hat{\boldsymbol{u}}_{rel}] = [1 - \hat{\boldsymbol{x}} \otimes \hat{\boldsymbol{x}}] = \begin{bmatrix} 0 & 0 & 0 \\ 0 & 1 & 0 \\ 0 & 0 & 1 \end{bmatrix}. \tag{1-36}$$

According to Parekh and Rzehak (2018), $\hat{\boldsymbol{x}}$ can be simply considered corresponding to the vertical direction for bubble column or pipe flows. For more complex flows arising in other industrial applications, such as static mixers or stirred tanks, this kind of simple correspondence is invalid, which has imposed further difficulties in applying the anisotropic bubble induced turbulence model with the Reynolds stress model as the turbulence closure in CFD simulations.

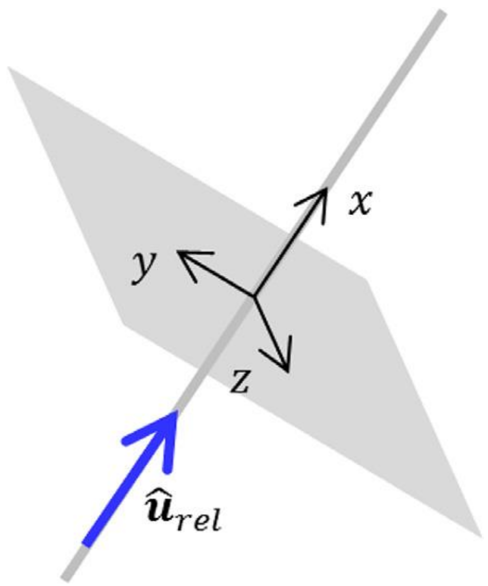

Figure 1-12 Illustration of projections on the subspaces parallel and perpendicular to relative velocity vector (taken from Parekh and Rzehak (2018)).

The remaining two coefficients a and b in Equation (1-34) represent the proportional contributions of BIT to the turbulent kinetic energy in three directions. One relation between the two derives from the requirement that the BIT should contribute the same energy as defined by the k-source S^k above, such as $tr(S^R) = 2S^k$. This requirement yields $a + 2b = 2$. A second relation defines the degree of anisotropy. The experiments of Hosokawa and Tomiyama (2013) performed in BIT dominated conditions have shown that the liquid phase turbulent fluctuations along the relative motion are twice as intensive as fluctuations in its perpendicular directions, which can be expressed as $a = 2b$. Combining these two relations, it is easy to find the value of $a = 1$ and the value of $b = 1/2$. For comparison, an "isotropic" bubble-induced turbulence requires $a = b$, which gives the value of a = 2/3 and the value of b = 2/3. By doing so, the effect of bubble-induced turbulence S^R reflected in the Reynolds stress models is the same as the isotropic term S^k in two-equation models.

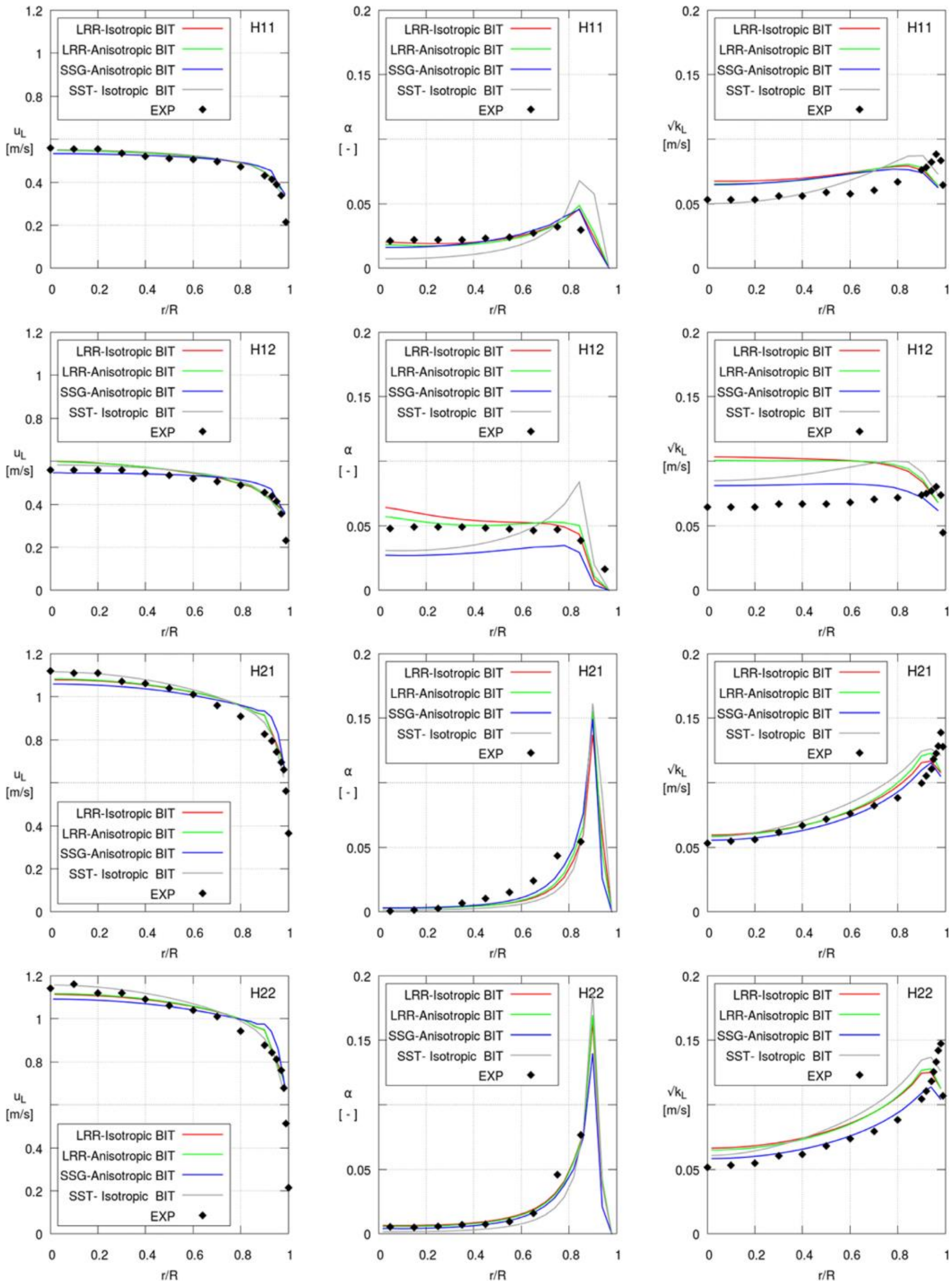

Figure 1-13 Comparison between simulations and experimental data for the tests from Hosokawa and Tomiyama (2009). The columns give from left to right the radial profiles of the mean liquid velocity, the gas fraction, and the turbulent kinetic energy.

Since the Reynolds stress terms or k and ε terms of bubble-induced turbulence have been included in the turbulence closure by using as the source terms, the dissipation rate of BIT can be considered as the generations due to the energy lost by the rising bubbles. In particular, the drag force can be considered as the only source of turbulence generation due to bubbles (Kataoka and Serizawa, 1989, Troshko and Hassan, 2001, Rzehak and Krepper, 2013a, Parekh and Rzehak, 2018). Thus, all the energy lost by the bubbles due to the drag can be assumed to be only converted into turbulence kinetic energy inside the bubble wakes. Kataoka and Serizawa (1989) have indicated that generation of turbulence kinetic energy due to bubbles is directly related to the work of the interfacial force density per unit time. Interfacial work contributed from the drag force has been confirmed to be largely dominant in bubbly flows (Troshko and Hassan, 2001). Following these arguments, it has been suggested by Joshi *et al.* (2017) that the force and energy balances of a single bubble can be approximately expressed by

$$C_D \frac{\pi}{4} d_b^2 \rho_l \left|\boldsymbol{U}_{slip}\right| \boldsymbol{U}_{slip} = V_b \left(\rho_l - \rho_g\right) \boldsymbol{g} \quad (1\text{-}37)$$

$$C_D \frac{\pi}{4} d_b^2 \rho_l \left|\boldsymbol{U}_{slip}\right|^2 \boldsymbol{U}_{slip} = V_b \left(\rho_l - \rho_g\right) \boldsymbol{g} \left|\boldsymbol{U}_{slip}\right| \quad (1\text{-}38)$$

For a bubble swarm, the number of bubble per unit volume is

$$N = \alpha_g / \frac{\pi}{6} d_b^3 \quad (1\text{-}39)$$

Therefore, the frictional energy dissipation rate per unit liquid volume can be obtained by multiplying the LHS of Equation (1-38) by Equation (1-39), which gives

$$E_D / V_l = 1.5 \rho_l \alpha_g C_D \left|\boldsymbol{U}_{slip}\right|^3 / d_b \alpha_l \quad (1\text{-}40)$$

where V_l is the volume of the liquid phase. The energy dissipation per unit mass is thus given by

$$\varepsilon_w = 1.5 \alpha_g C_D \left|\boldsymbol{U}_{slip}\right|^3 / d_b \alpha_l \quad (1\text{-}41)$$

where ε_w is the turbulence energy dissipation rate due to the drag force and mainly dissipated in the wakes of bubbles. It is noticed that other forces may have also contributed to the turbulence intensity in the wakes of bubbles, especially for those bubbles that rise in zigzag trajectories where the added mass and lift forces may have important contributions. Since the understandings to these non-drag forces are still limited and their inclusion in the modelling will further impose the complexity for the estimation of the dissipation in the wakes of bubbles, the effects of these forces will be excluded and the turbulence dissipation of the wakes due to drag is considered.

It seems that a concrete conclusion has not yet been reached on the appropriate descriptions of the bubble-induced turbulence in the CFD modelling. The reasons for these differences should be contributed to the limited understanding of the nature of the multiphase turbulence in the bubble columns, especially the statistically characteristics of the bubble-induced turbulence. Although fully resolved simulations of freely rising deformable bubbles, such as those by Sugiyama *et al.* (2001), Bunner and Tryggvason (2003), Roghair *et al.* (2011) and Riboux *et al.* (2013), have clearly shown different power-law scaling factors from the homogeneous isotropic turbulence, the efforts of coupling these behaviours directly into the turbulence modelling of gas-liquid two-phase flows have rarely been documented in the open literature. Meanwhile, it needs to be pointed out that the effect of bubble-induced turbulence has been shown to be important in the bubble breakup and coalescence models to determine the bubble size distribution, which could be strongly required in the industrial applications especially when interfacial heat and mass transfer processes are involved. This will be further discussed in the following section.

3.3 Bubble Size Distribution

The prediction of bubble sizes is essential in the numerical studies of bubble columns, as it is required by both the interphase force closure, such as drag and lift force, and the turbulence closure due to bubble's contribution. Some early-stage CFD studies have used the averaged bubble size, which can only be obtained from experimental measurements or determined by repetitive trial-and-error simulations. However, not only the predictive nature of CFD modelling has been lost by doing so, but more importantly, an averaged bubble size usually cannot reflect the real inhomogeneity of bubble sizes in time and space. Especially when the bubble columns are operated at the heterogeneous regime with high gas holdup and superficial velocity, the bubble sizes can be widely distributed. Different models have been developed to cope with this issue. For example, rather than explicitly using the bubble diameter, Thakre and Joshi (1999), Vitankar et al. (2002), and Dhotre and Joshi (2007) have used the ratio of drag coefficient and bubble diameter C_D / d_B as a lumping coefficient to close the interphase momentum exchange term. However, the values of the lumping coefficient are usually determined based on semi-empirical or empirical correlations that developed from experiments, and which leaves further difficulties for other closure terms. Krishna and van Baten (2001a) have proposed the two bubble groups model based on experimental observations by using dynamic gas disengagement technique. The two bubble groups concept has also been adopted by Guedon *et al.* (2017) which explicitly classifies the bubbles into large and small groups in the simulations. Although the two bubble groups model has significantly improved the simulation results especially at high superficial velocities (Krishna and van Baten, 2001a, Krishna et al., 1999), it is still a static model that the momentum exchange between the large and small bubbles as well as the dynamic changes of the bubble sizes cannot be properly addressed.

A more direct way to determine the bubble sizes is to use the population balance model. The population balance model with kernel functions accounting for the bubble coalescence and breakage phenomenon can be used to describe the dynamic changes of the number density of bubble groups. On the development and implementation of the population balance models as well as the bubble coalescence and breakup models, many researchers have made significant contributions (Fu and Ishii, 2003a, Fu and Ishii, 2003b, Sun et al., 2004, Ishii et al., 2004, Lehr and Mewes, 2001, Olmos et al., 2001, Buwa and Ranade, 2002, Wang et al., 2006, van den Hengel et al., 2005, Jakobsen et al., 2005, Liao et al., 2015, Bhole et al., 2008, Hagesaether et al., 2002, Kumar and Ramkrishna, 1996).

The interfacial area transport models such as developed by Wu et al. (1998) and Fu and Ishii (2003b) are actually the simplification of the population balance model, and these models can be conveniently used in large diameter vessels such as Schlegel et al. (2015), due to the number of equations to be solved are less than the population balance equations. These models have neglected the influence of the daughter bubbles on the coalescence and breakage rate and not being able to predict the bubble size distributions. However, with the development of computational resources, using the complete population balance equations for the grids with a large number of cells are made possible, such as the work by Yang and Xiao (2017) have performed CFD-PBM modelling with approximately 400-thousand cells and 20 discrete bubble classes.

Population Balance Model

The population balance equations can be numerically solved via different solution methods, such as the discrete method (DM) (Hounslow et al., 1988, Lister et al., 2004), the quadrature method of moments (QMOM) (Marchisio et al., 2003), and the direct quadrature method of moments (DQMOM) (Fan et al., 2004). It seems that all these solution methods are capable of mathematically resolving the population balance equations with different levels of complexity for each method. Therefore, the main concerns of the population balance modelling of bubble columns still fall on the understanding and description of the physical phenomenon of bubble coalescence and breakup, with the nature of which are recognised as the bubble-bubble and the eddy-bubble interactions respectively.

When the bubble size distribution is modelled by the population balance equations with consideration of bubble coalescence and breakage, the discrete method requires the classification of bubbles into different size groups and d_i is the diameter of bubbles for i-th group. The population balance equation is expressed by

$$\frac{\partial n_i}{\partial t} + \nabla \cdot \left(\boldsymbol{u}_{b,i} \cdot n_i\right) = S_i \qquad (1\text{-}42)$$

where n_i is the number density of bubbles for i-th group, $\boldsymbol{u}_{b,i}$ is the bubble velocity vector for the i-th group, and S_i is the source term. The source term can be expressed as the birth and death of bubbles due to coalescence and breakage respectively, such as

$$S_i = B_{coalescence,i} - D_{coalescence,i} + B_{breakup,i} - D_{breakup,i}$$
$$= \sum_{V_j=V_{min}}^{V_i/2} \Omega_C(V_j : V_i - V_j) - \sum_{V_j}^{V_{max}-V_i} \Omega_C(V_j : V_i) + \sum_{V_j=V_i}^{V_{max}} \Omega_B(V_j : V_i) - \Omega_B(V_i)$$

(1-43)

The local gas volume fraction can be calculated by

$$\alpha_g f_i = n_i V_i \tag{1-44}$$

where f_i is the i-th class fraction of total volume fraction, and V_i is the volume for the i-th class.

The Sauter mean diameter d_{32} for the equivalent phase can be calculated by

$$\frac{1}{d_{32}} = \sum_{i=1}^{N} \frac{f_i}{d_i} \tag{1-45}$$

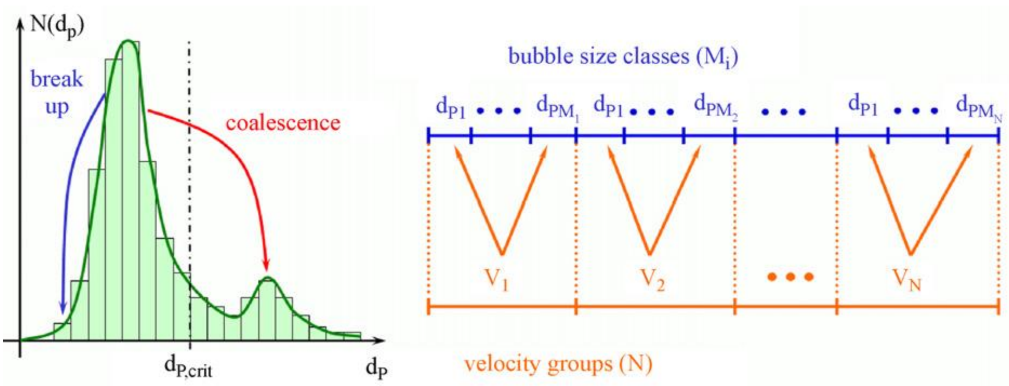

Figure 1-14 Bubble size classes and velocity groups distribution (taken from Frank et al. (2008)).

Bubble Coalescence

For the bubble coalescence process, the occurrence of direct contact and collisions between bubbles is the essential criteria for the coalescence. Shinnar and Church (1960) proposed the classic film drainage model. According to the film drainage model, a liquid film is initially formed when two bubbles contact and deform due to the surrounding pressure; the liquid film begins to drain sequentially, leading to the film rupture and bubble coalescence. If the surrounding pressure is insufficient to overcome the viscous force of the thin film, the bubbles bounce back without coalescence. Therefore, the coalescence probability depends on the intrinsic contact time and drainage time between the bubbles. The expression of collision density was derived by analogy with molecule collision in the kinetic theory of gases, which considers a bubble travelling in a relative speed with respect to the other bubbles enclosed in the collision tube that has been virtually imagined to be stationary. Prince and Blanch (1990) proposed a collision model considering the effects of turbulent eddy fluctuation, buoyancy-driven and liquid viscous shear. In some cases, the effects of turbulence fluctuation may be considered to be more significant compared to the effects of buoyancy-driven and liquid viscous shear. Luo (1993) adopted this deduction and proposed a collision model which further considers the changes in the relative position of the mass centres of the two colliding bubbles during the liquid film drainage process. The coalescence models proposed by Prince and Blanch (1990) and Luo (1993) can be respectively expressed by

$$\Omega_{C,P\&B} = n_i n_j \frac{\pi}{4}\left(\frac{d_i+d_j}{2}\right)^2 \left(\bar{u}_i^2 + \bar{u}_j^2\right)^{1/2} \exp\left(-\frac{t_{coal}}{\tau_{col}}\right) \quad (1\text{-}46)$$

$$\Omega_{C,L} = n_i n_j \frac{\pi}{4}\left(d_i + d_j\right)^2 \left(\bar{u}_i^2 + \bar{u}_j^2\right)^{1/2} \exp\left(-c_1 \frac{\left[0.75\left(1+x_{ij}^2\right)\left(1+x_{ij}^3\right)\right]^{1/2}}{\left(\rho_g/\rho_l+0.5\right)^{1/2}\left(1+x_{ij}\right)^3} We_{ij}^{1/2}\right)$$

(1-47)

where t_{coal} the coalescence time, τ_{col} the collision time, the size ratio of two colliding bubbles $x_{ij}=d_i / d_j$ and We_{ij} the Weber number.

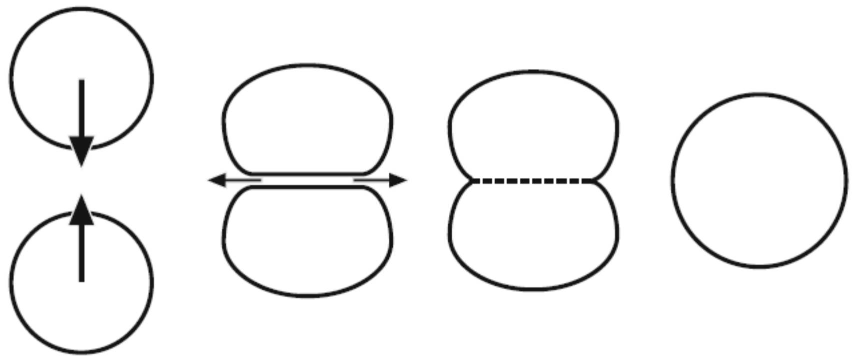

Figure 1-15 A sketch of the three consecutive stages of the binary coalescence process described by liquid file drainage model (taken from Jakobsen et al. (2005)).

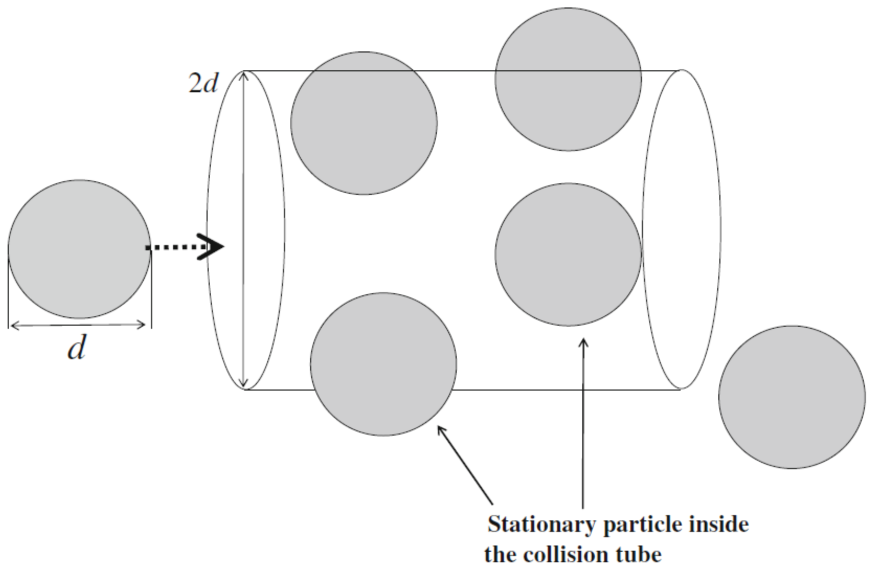

Figure 1-16 A sketch of a collision tube of an entering bubble moving through the tube (taken from Jakobsen et al. (2005)).

When the coalescence models are implemented into CFD simulations together with the breakage model, a mismatch is often found for the bubble coalescence rate and the breakage rate, and hence empirical correlations are required to obtain acceptable agreements with experimental results. Chen (2004) and Chen *et al.* (2005) have reported that in churn-turbulent flow regimes, the model predicted bubble coalescence rate is about one order of magnitude higher than the predicted breakage rate. Wang *et al.* (2005a) and Wang *et al.* (2005b) have proposed correlations to consider two effects that are related to the prediction of bubble coalescence rate. The distance between bubbles may be larger than the bubble turbulent path length and a coefficient less than 1 should be multiplied in the coalescence rate. On the contrary, the reduction of free space due to the bubbles occupying a specified volume may increase the coalescence rate. Bhole *et al.* (2008) have considered the slip velocity between the bubble and liquid eddy and have used a coefficient that is related to the bubble Stokes number to prevent the over-prediction of the bubble coalescence rate. Nguyen *et al.* (2013) have addressed the turbulent suppression phenomena in the coalescence model. It is believed that part of the energy of turbulent eddies has been dissipated by the surface of bubbles without causing breakage. In this case, the size of eddies that has been chosen as the characteristic length scale for bubble-bubble collision is greatly reduced, which further reduces the contact time and the coalescence efficiency. Yao and Morel (2004) and Mukin (2014) have suggested that coefficients for adjusting the model predicted coalescence rate are required in dense bubbly flows. Mitre *et al.* (2010) have addressed that the use of coefficients should depend on the combination of coalescence and breakup models as well as the superficial velocities. Xu *et al.* (2013) have used a coefficient of 0.5 for the coalescence model and have suggested the use of RNG $k \sim \varepsilon$ turbulence model to avoid the overprediction of coalescence rate. Liao *et al.* (2015) summarised various previously proposed mechanisms of bubble collision induced coalescence including turbulence fluctuation, viscous shear stress, capture in turbulent eddies, buoyancy and wake interaction. When the coalescence frequency is derived, in addition to the inertial collision, Liao *et al.* (2015) have also adopted the viscous shear-induced collision as presented by Lo and Zhang (2009). It seems that most of these considerations on the bubble coalescence focus on the bubble motions, whereas the effect of turbulent eddies, especially the ones induced by rising bubbles which are caused by bubble wakes and are encountered in bubble columns and bubble swarms, has rarely been considered. Of particular relevance to this study, Sun *et al.* (2004) have considered the effect of bubble wakes in a cylinder-wise tail region of ellipsoidal and spherical-cap bubbles. However, it seems that their considerations on the wake entrapment are still more favourable of using the empirical correlations rather than strictly following the turbulent kinetic energy of eddies as defined by turbulence energy spectrum.

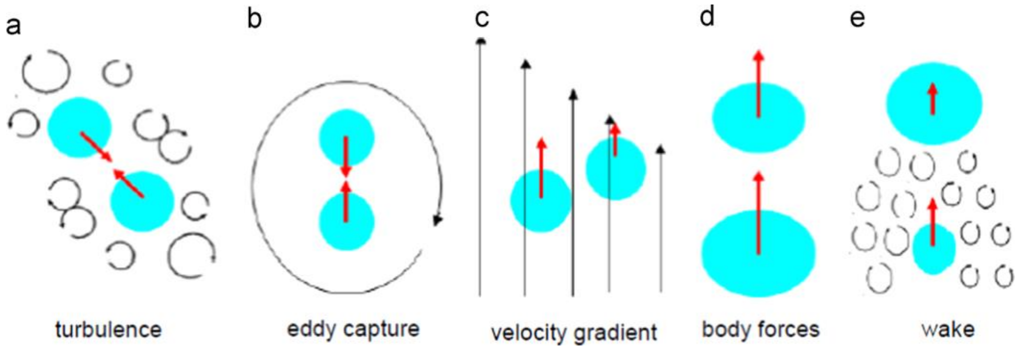

Figure 1-17 Various mechanisms leading to bubble collision in a turbulent flow (taken from Liao *et al.* (2015)).

Bubble Breakage

For the bubble breakup process, Coulaloglou and Tavlarides (1977) assumed that the breakup process would occur if the energy carried by turbulent eddies impacting on the bubble is more than the surface energy contained by the bubble. Prince and Blanch (1990) acknowledged bubble breakup to be caused by eddy-bubble collision but they proposed that the bubble breakup can only be induced by eddies with approximately the same characteristic size as the bubbles. Eddies at a much larger length scale only transport the bubbles without causing breakage. Luo and Svendsen (1996) described the bubble breakup by considering both the length scale and the amount of energy contained by the arriving eddies. The minimum length scale of eddies that are responsible for breakup equals to 11.4 times those eddies corresponding to the dissipation with the Kolmogorov scale. The probability for bubble breakup is related to the critical ratio of surface energy increase of bubbles after breakup and the mean turbulent kinetic energy of the colliding eddies. When applying their model, it was found that very small eddies do not contain sufficient energy to cause the bubble breakup. Lehr et al. (2002) proposed a slightly different breakup mechanism from that proposed by Luo and Svendsen (1996). They considered the minimum length scale of eddies to be determined by the size of the smaller bubble after breakup, and the breakup process to be dependent on the inertial force of the arriving eddy and the interfacial force acting on the bubble. The breakage models proposed by Luo and Svendsen (1996) and Lehr et al. (2002) can be respectively expressed by

$$\Omega_{B,L\&S} = 0.923\left(1-\alpha_g\right)n_i\left(\varepsilon/d_i^2\right)^{1/3}\int_{\xi_{min}}^{1}\frac{(1+\xi)^2}{\xi^{11/3}}\exp\left(-\frac{12\sigma C_f}{\beta\rho_l\varepsilon^{2/3}d_i^{5/3}\xi^{11/3}}\right)d\xi \tag{1-48}$$

$$\Omega_{B,Lehr} = 1.19\varepsilon^{-1/3}d_i^{-7/3}\sigma\rho^{-1}f_V^{-1/3}\int_{\xi_{min}}^{1}\frac{(1+\xi)^2}{\xi^{13/3}}\exp\left(-\frac{2\sigma We_{crit}}{\rho_l\varepsilon^{2/3}d_i^{5/3}f_V^{1/3}\xi^{2/3}}\right)d\xi \tag{1-49}$$

where $\xi = \lambda / d_i$, the increase coefficient of surface area $C_f = f_V^{2/3} + (1 - f_V)^{2/3} - 1$, the breakage volume fraction $f_V = d_j^3 / d_i^3$, and critical Weber number We_{crit}.

Based on the results of Luo and Svendsen (1996) and Lehr et al. (2002), Wang et al. (2003) proposed the model for bubble breakup, for which the constraints both the energy and the capillary pressure are imposed. The energy constraint requires the eddy energy to be greater than or equal to the increase of surface energy of bubbles after the breakage. The capillary constraint requires the dynamic pressure of the arriving eddy to exceed the capillary pressure of the bubble. The use of these two breakup criteria actually restricted the minimum size of the bubbles that can break, and hence could yield the results that are accorded with practical observation and more interpretable than those obtained using Luo and Svendsen (1996). These two breakup criteria have also been adopted and extended in the recent studies reported by Zhao and Ge (2007) and Liao et al. (2015).

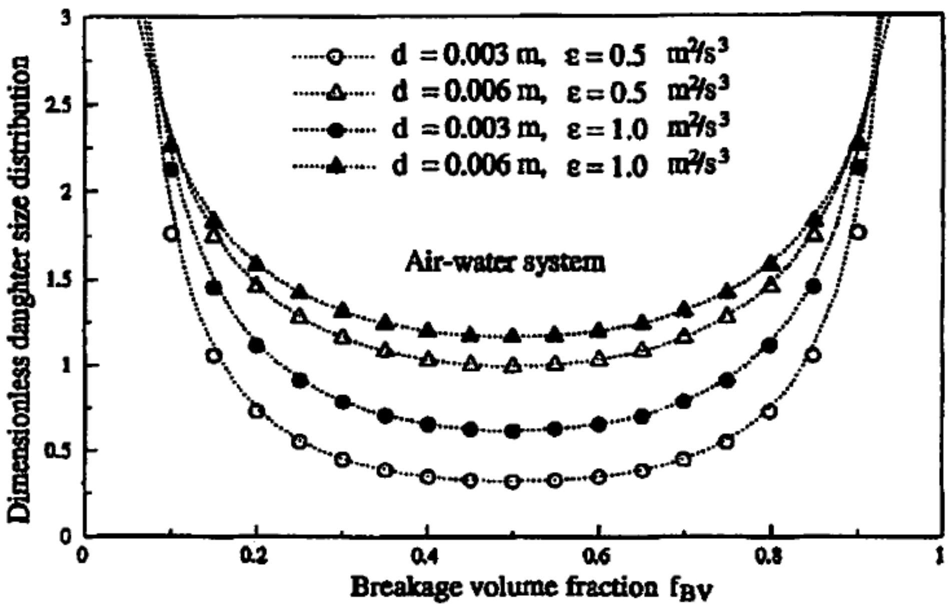

Figure 1-18 Effect of bubble size and energy dissipation rate per unit mass on

the dimensionless daughter bubble sized distribution for the air-water system (taken from Luo and Svendsen (1996)).

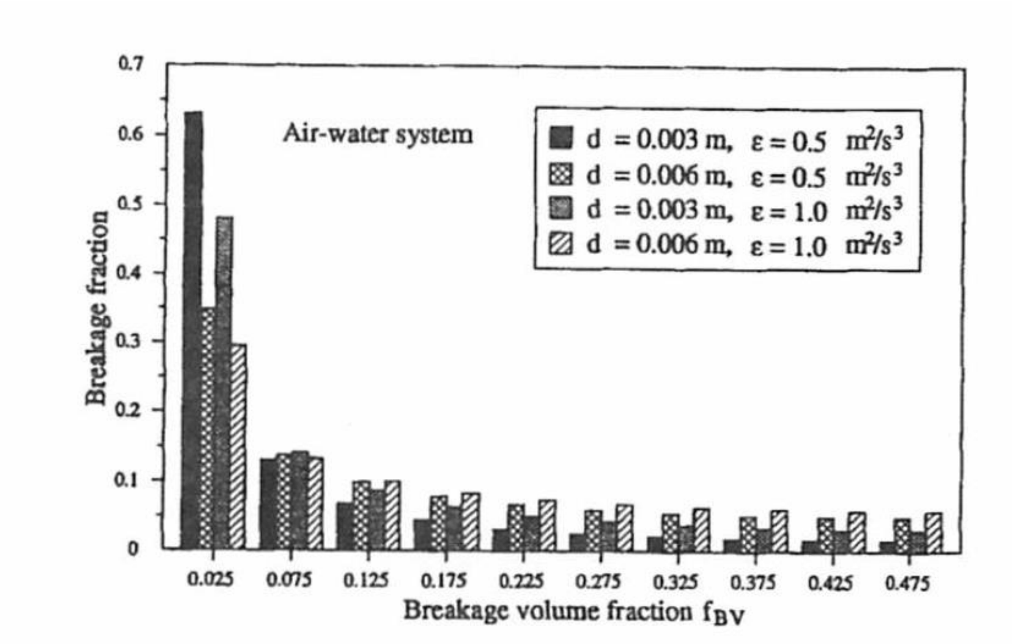

Figure 1-19 Effect of bubble size and energy dissipation rate per unit mass on the breakage fraction as a function of the breakage volume fraction for the air-water system (taken from Luo and Svendsen (1996)).

As discussed above, the surface of bubbles may subject to different forces as they are exposed to the turbulent eddies. The deformation of bubble shapes has a fundamental impact on the estimation of the interfacial area of bubbles. In return, this will have major implications when applying the population balance model for CFD modelling of bubble coalescence and breakage. Few studies have considered the bubble shapes in bubble column CFD modelling especially for the cases of large elliptical or cap bubbles. Clark (1988) proposed a model to describe the deformation and surface oscillation of droplets. The model assumed the motion of the mass centre of the deformed drop to be acted by those interfacial forces. However, the model did not include the buoyancy force and added mass, which occurs when the drop or bubble accelerates relative to the continuous phase. For a gas-liquid system such as bubble columns, added mass force and buoyancy force are dominant factors and have to be taken into account. Andersson and Andersson (2006) considered the deformations of bubbles during the breakage process and suggested that the bubble breakage is strongly associated with the difference of the pressure in the neck due to interfacial tension and at the ends. Han *et al.* (2016) considered the surface deformation and oscillation of bubble to be axisymmetric, i.e. the dynamics of bubble are formulated based on the motion of the centre of mass of the half bubble, and all interfacial forces act upon the centre of mass similar to the analogy of a translational mechanical system with a spring linking two parts with equal mass. This treatment method is still constrained to the cases of ellipsoidal bubbles without considering the actual shapes of the bubbles.

It seems that the mechanism of bubble breakage considered in the open literature is mostly due to the eddy-bubble collision. The other contributions such as bubble stretching and deformation due to liquid velocity gradient or bubble breakage due to Rayleigh-Taylor instabilities are rarely considered. Comparing with the liquid film drainage model for bubble coalescence, the considerations of the physics during the entire breakup process, such as the bubble oscillation and deformation, have less frequently been reported. Moreover, in most of the existing bubble breakage models, a very important parameter that characterises the energy carried by the bombarding eddy, the mean turbulent eddy velocity, is usually considered within the inertial subrange and approximately derived by using the Kolmogorov -5/3 scaling law for homogeneous isotropic liquid shear turbulence. Of the particular relevance to this work, Han et al. (2011) proposed a multi-scale bubble breakage model that considered the wide energy spectrum. However, it seems that the evaluation of the mean turbulent eddy velocity is still based on the shear turbulence rather than the bubble-induced turbulence, which may play a significant role in the bubble columns but not being appropriately addressed in the bubble breakup model.

Though there is still no consensus reached for the power law scaling of bubble-induced turbulence in the bubble columns, most of the recent progress on bubble-induced turbulence have shown the convincing evidence that the scaling law of the pseudo-turbulence induced by the rising bubbles is different from the Kolmogorov -5/3 scaling, as has been demonstrated by Risso and Ellingsen (2002), Roig and de Tournemine (2007) and Risso *et al.* (2008). In particular, Risso *et al.* (2008) analogised the attenuation of wakes in a fixed array of spheres randomly distributed in space to that of bubbles within a homogeneous swarm, and have shown that the bubbles' wakes in pseudo-turbulence decay faster than standard turbulent flow with the same energy and integral length scale, even when the gas volume fraction is increased to 13%. In addition, different experimental approaches have been used to obtain the energy spectrum of the pseudo-turbulence induced by rising bubbles. Mercado *et al.* (2010) used a phase-sensitive constant-temperature anemometry (CTA), which is simultaneously calibrated by LDA, to measure the energy spectrum within the wake of the bubble swarm and obtained the energy spectrum of pseudo-turbulence with a κ^{-3} scaling. Riboux *et al.* (2010) measured the energy spectrum in the wake of a bubble swarm using PIV and also confirmed the scaling to be very close to -3. Risso (2011) proposed a theoretical model to explain the -3 scaling, which argues that the signals from the wakes of bubbles can be treated as the collective effect of localised random bursts with statistically independent strength and size. Prakash *et al.* (2016) also used a phase sensitive CTA probe to measure the velocity fluctuations of the liquid phase, and they again reaffirmed that the κ^{-3} scaling is not only to hold for description of bubble-induced turbulence but also to be suitable for defining the generic feature of turbulent bubbly flows. Based on their experimental findings, they proposed an energy balance between the energy production due to the presence of bubbles and the viscous dissipation, i.e. the dissipation due to the bubbles counterbalances the production rate, a result consistent with the milestone finding of Lance and Bataille (1991).

The above-mentioned literature clearly indicates that the bubble-induced turbulence indeed has a very different scaling behaviour from the liquid shear turbulence on the turbulent kinetic energy spectrum. Since the expression of the turbulence energy spectrum function is essential in deriving the number density of the bombarding eddy, it seems necessary to include these differences in scaling behaviours on the turbulence energy spectrum into the bubble breakup model.

3.4 <u>Mesoscale mechanism</u>

Understanding mesoscale mechanism is critical in the study of multiscale behaviour of turbulent bubbly flows in bubble column reactors. The macroscale or reactor scale flow is strongly influenced by the complex mesoscale hydrodynamics involving bubble swarm dynamics, bubble-bubble or bubble-eddy interactions which are several orders of magnitude smaller than that of the bulk flow in terms of spatial scales. The mesoscale hydrodynamics also affect the interfacial dynamics (such as the gas-liquid interface) at the microscale or bubble scale much smaller than that of mesoscale phenomena. The microscale interactions between a bubble and its surrounding liquid are reflected by various interfacial forces and interfacial heat and mass transfer. However, the collective effect of a bubble swarm at the mesoscale either hinders or accelerates the rising of bubbles and thus has a large influence on the hydrodynamics or mass transfer. Furthermore, the bubble-bubble or bubble-liquid interactions at the mesoscale lead to the coalescence or breakage of bubbles and the change of bubble sizes.

The change of bubble sizes not only affects the motion or mass transfer behaviour of the bubble swarm, but also leads to the flow regime transition at the macroscale or reactor scale. Weak bubble breakage and coalescence often results in a narrow bubble size distribution which leads to the homogeneous flow regime. Conversely, strong bubble breakage and coalescence results in a wider bubble size distribution which leads to heterogeneous flow regime with a strong liquid circulation. Therefore, the core issue focuses on understanding the mesoscale mechanisms (such as gas-liquid interactions at mesoscale) to fundamentally investigate the turbulent bubbly flow in the bubble column reactors.

Rather than studying the microscale and macroscale mechanisms separately, a more promising way to fill up the gap between the microscale and macroscale is the Energy-Minimization Multi-Scale (EMMS) model, a paradigm initially applied to gas-solid fluidization and gaining in popularity. This model links the multiscale phenomena through the energy consumption and the stability condition, which was recognized to be subject to the compromise between solid/liquid dominance and gas dominance (Li et al., 2010). Following this approach, the DBS (Dual Bubble Size) model, an extension of the EMMS paradigm for gas-liquid systems, has been successfully applied to predict the flow regime transition and help the traditional CFD to improve the accuracy in the prediction of the gas hold-up (Chen et al., 2009a, Yang et al., 2007, Yang et al., 2011).

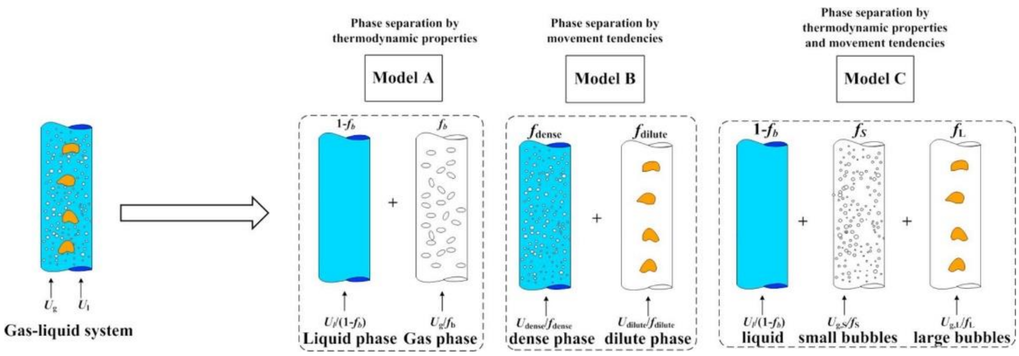

Figure 1-20 Phase separation of three stability-constrained multi-fluid models under DBS conceptual framework (taken from Xiao et al. (2017)).

The DBS model decomposes the gas-liquid system into gas phase and liquid phase, dense phase and dilute phase, or large bubbles and small bubbles, according to the thermodynamic properties and the movement tendencies. The total energy dissipation has been decomposed into different scales with the dissipation in each scale can all be calculated. When the system tends to be steady, the stability constraint requires the micro-scale energy dissipation tends to be minimum and the mesoscale dissipation tends to be maximum (Xiao et al., 2013, Xiao et al., 2017). By doing so, the bubble sizes and shapes can be implicitly considered by using a lumping coefficient C_D/d_B to replace the traditional drag coefficient closures for gas-liquid systems. Different from empirical models that based on experimental statistics and correlations, the DBS drag model has been developed on the basis of optimisation theory and hence no artificial adjustments have been used for the model parameters. The DBS drag models have been implanted into CFD simulations with the use of the two-fluid model, and have achieved greatly improved results for various gas-liquid systems, such as Xu et al. (2015), Jiang et al. (2016), and Zhou et al. (2017).

Based on these previous work, Qin *et al.* (2016) and Yang and Xiao (2017) have developed EMMS-PBM model and successfully employed into CFD simulations of liquid-liquid and gas-liquid systems. Since the mesoscale energy dissipation can be estimated on the basis of the bubble breakage kernels, the EMMS-PBM model has been developed on the basis of the same stability constraint of DBS model, which is the minimisation of microscale dissipation or maximisation of mesoscale dissipation. Therefore, by balancing the birth and death of bubbles due to bubble coalescence and breakup, the EMMS-PBM model provides a unique way to close the equilibrium state of the mesoscale dissipation calculated by DBS model and the dissipation calculated by PBM model considering bubble coalescence and breakage.

4. Experimental studies

The fundamental understandings of turbulent bubbly flow in the bubble columns come from numerous experimental studies at early stages. The experimental studies of bubble column reactors have been through the development from overall characteristics to local characteristics and from steady state to dynamic behaviours. Early stage investigations focus more on the time-averaged overall characteristics, such as large-scale liquid circulation. The experimental approaches are simple, such as bed expansion to measure total gas holdup, conductivity or optical fibre probe for local gas holdup measurement and Pitot tube for time-average liquid velocity. However, many new measurement devices have been rapidly developed since the 1980s, such as hot-wire/file anemometry, Particle Imaging Velocimetry (PIV), Laser Doppler Velocimetry (LDV), High-Speed Camera, Computational Tomography (CT), Electric Resistance Tomography (ERT) /Electric Capacitance Tomography (ECT), and Computer Aided Radioactive Particle Tracing (CARPT). Although different limitations still exist on these new devices and measurement techniques, the in-depth study of flow structures and dynamic behaviours under various conditions can be satisfyingly achieved by choosing the appropriate experimental tools.

4.1 Measurement of Gas Holdup

The measurement of the overall gas holdup in the bubble columns can often be done with simple techniques. Comparing the dynamic liquid height with the static liquid height is the commonly used one, especially when the flow regime is within the bubbly and the transition ranges. For a simple bubble column operation procedure, the liquid is not fully filled into the bubble column and remains static before the gas phase is injected. Once the gas phase has been pumped into the column, the bubbles will be formed and occupy the spaces that are originally full of the carrier fluid. In this case, the gas-liquid interface at the top surface will be lifted up to a dynamic height that keeps fluctuating slightly. Since the cross-sectional area of the bubble column is constant, the volume of the gas being injected into the volume of the liquid phase can be calculated by their heights respectively. The overall gas holdup measured by this method can be expressed by

$$\alpha = \frac{H_{dynamic} - H_{static}}{H_{dynamic}} \tag{1-50}$$

where $H_{dynamic}$ and H_{static} are the dynamic and static liquid height respectively. Since the gas-liquid interface at the top surface keeps oscillating all the time, the dynamic liquid height can only be obtained from taking average of the readings by multiple observations. Although the errors are partially reduced by averaging the recorded data, a specific height seems to be difficult to determine only by eye observations, especially when the gas-liquid interface at the top surface is changing quickly and intensely.

A pressure-based method can also be used to obtain the overall gas holdup in the bubble columns. Two pressure sensors are mounted at the side wall of the top and the bottom of the testing section, away from each other for a certain distance ΔH. The pressure difference ΔP of the testing section can also be measured by a simpler instrument, U-tube pressure gauge, with its two ends respectively connected to the same positions as the pressure sensors. The schematic diagram of using the U-tube to measure the pressure difference of the testing section is shown in Figure 1-21. Since the density of the gas phase is much smaller than the liquid phase, the pressure changes resulting from the gas phase in the testing section can often be neglected under this circumstance. Thus, the change in pressure difference is mainly owing to the volumes that originally occupied by the liquid phase are now replaced by the gas bubbles. Therefore, the overall gas holdup measured by this method can be expressed by

$$\alpha = \frac{\Delta P}{\rho_L g \Delta H} \tag{1-51}$$

where ρ_L is the density of the liquid phase.

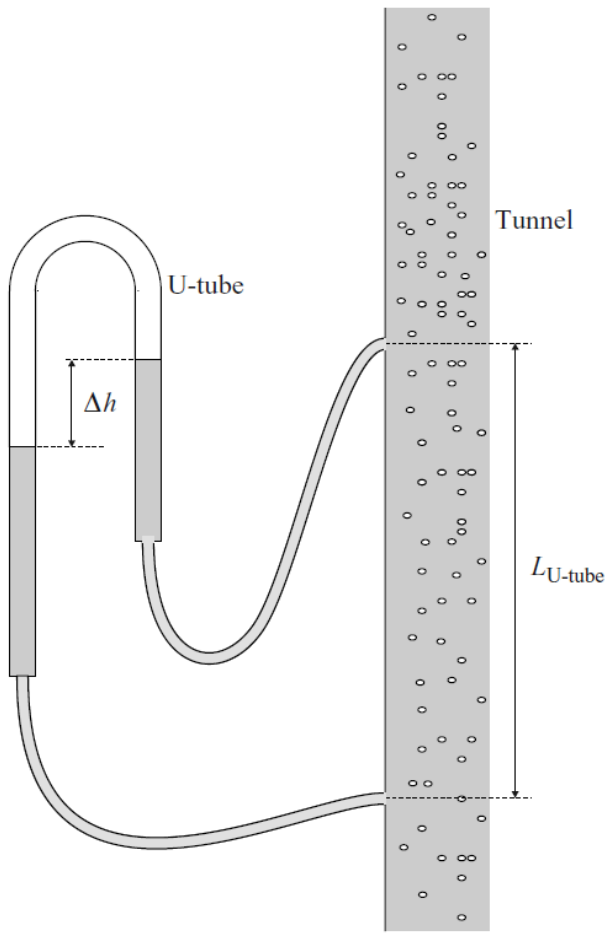

Figure 1-21 Schematic diagram of using a U-tube to measure the pressure difference of the testing section (taken from Rensen et al. (2005)).

There are more complex techniques for total gas holdup measurement, such as dynamic gas disengagement technique (DGD), imaging analysis and cross-sectional averaging from local gas holdup. For example, DGD requires measuring the liquid level or the pressure at different levels in the bubble column when the aeration is stopped. If the dispersion is axially homogeneous when the gas feed is interrupted and no bubble coalescence and breakup happening during disengagement, the liquid level decreases as a function of time can be interpreted as caused by the bubbles disengaged in different rise velocities that corresponding to their bubble classes (Camarasa et al., 1999). However, this method can only be applied when the bubble column is operated in homogeneous regime mainly due to the complex assumptions (Lee et al., 1999). It seems that small relative errors have always existed within these methods. Yet still, the measurement results will be reasonably accurate if a suitable method is chosen for different testing conditions.

It is found that the influencing factors for overall gas holdup include gas superficial velocity, column diameter, gas distributor design, height to diameter ratio, physical properties and operating conditions. The overall gas holdup increases with the gas superficial velocity almost linearly at homogeneous regime while the increasing rate becomes lower at heterogeneous regime due to the large bubbles with higher rising velocities that are formed by the bubble-bubble interactions. A typical example of the increase in overall gas holdup with superficial velocity is shown in Figure 1-22.

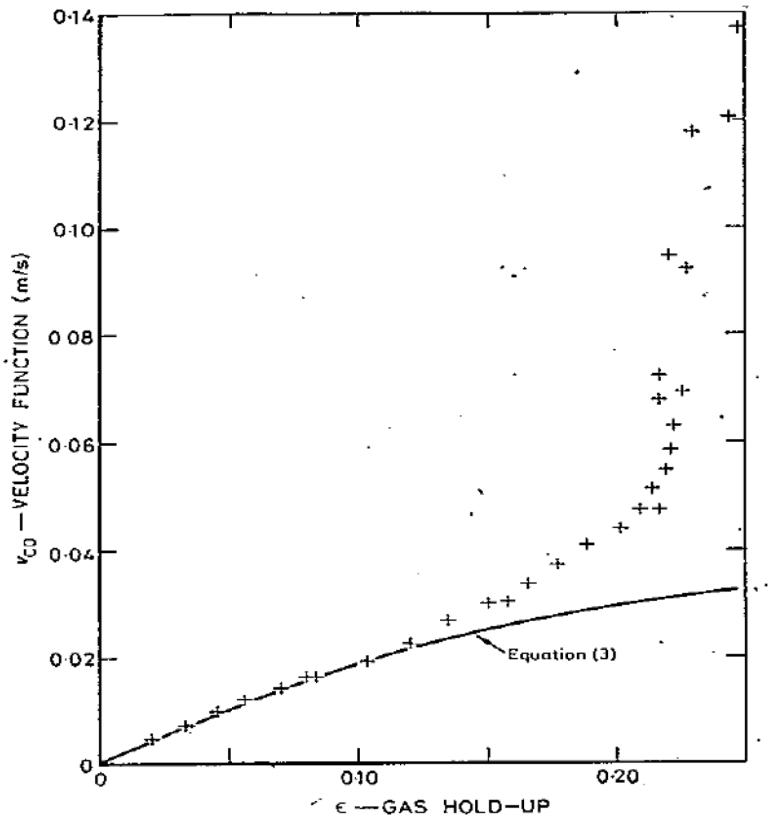

Figure 1-22 Effect of gas superficial velocity on overall gas holdup (taken from Hills (1974)).

Daly et al. (1992) have used DGD method for bubble columns with diameters 0.05 m and 0.21 m respectively and finds that the overall gas holdup in the small column is slightly larger in the large column under the same superficial velocity. The experimental results of Forret et al. (2003) have shown that the overall gas holdup increases with the column diameter while the differences are within 5%. Shah et al. (1982) claim that the effect of column diameter on the overall gas holdup can be neglected once the column diameter is larger than 10 to 15 cm. Vandu and Krishna (2004) finds that the overall gas holdup reduces with the increase of column diameter. They conclude that this is due to the enhanced liquid circulation in bubble columns with large diameters has fastened the bubble rising velocity. It seems that there are different conclusions on the effect of column diameter on the overall gas holdup. However, it is generally believed that the influence is not very significant if the column diameter is larger than 10 cm. Thorat et al. (1998) have comprehensively investigated the effect of sparger design and liquid dispersion height to bubble column diameter ratio on the averaged gas holdup. It is found that the averaged gas holdup decreases as the *H/D* ratio increases from 1 to 5 for perforated plate with hole diameter smaller than 3 mm, but no significant changes when *H/D* > 5. It seems that the *H/D* ratio has almost no effect on the averaged gas holdup for the spargers with hole diameters from 3 mm to 6 mm. For the sparger hole diameter larger than 10 mm, the overall gas holdup increases with the *H/D* ratio due to the large initial bubble size that requires sufficient liquid height to allow bubble breakage. It seems that the free area has not much effect on the overall gas holdup for perforated plate with smaller hole diameters. Yet still, for spargers with larger holes, the overall gas holdup increases reversely with the free area. It seems that the overall gas holdup is increased as the elevated pressure leads to smaller average bubble size(Luo et al., 1999). Also, experimental results show that electrolyte can suppress the bubble coalescence and hence increase the gas holdup (Zahradnik et al., 1995). The liquid viscosity is a parameter that greatly affects the gas holdup. The overall gas holdup is obviously lower in high viscosity systems, such as air-oil system (Chen et al., 1999) or Air-Aqueous Solution of Carboxymethyl Cellulose (Thorat et al., 1998).

The local gas holdup distribution can be measured in different ways, including probes, Computational Tomography (CT), Electric Resistance Tomography (ERT) /Electric Capacitance Tomography (ECT) and high-speed imaging. Among these methods, using needle probes is one of the simplest and the most cost-effective ways to obtain the local gas holdup at the queasy-steady state. Depending on the types of signals that the probes based on, single-tip optical fibre or conductivity probes lead to the measurement of gas fraction and bubbling frequency. In addition to the results that can be obtained by single-tip probes, dual-tip conductivity probes allow measurements of bubble velocity, time-average local interfacial area, and mean bubble chord length. A typical configuration of the dual-tip conductivity probe is shown in Figure 1-23.

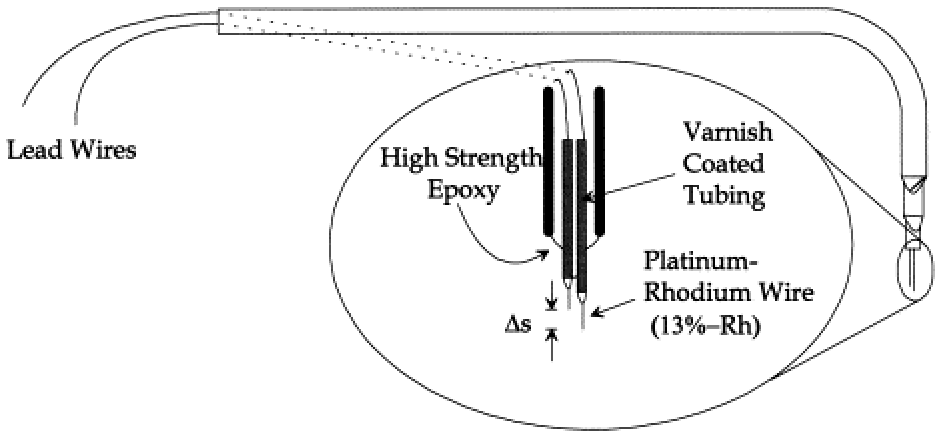

Figure 1-23 Schematic diagram of a dual-tip conductivity probe (taken from Hibiki et al. (1998)).

The measurement of the local gas holdup by the conductivity probe is based on the conductivity difference between the gas and the liquid phase. Since the conductivity probe has to be inserted into the bubble column and fixed at the radial positions that are about to be measured, the two tips of the probe are supposed to be as thin as possible (0.5 mm – 5 μm) to avoid causing too much interference to the flow field (Thang and Davis, 1979). The two tips are separated from each other with a short distance (0.5 - 5 mm) and the sampling frequency should be fast enough (1-10 kHz) to capture the instant transition of the gas and liquid phase without causing long delays and hence large measuring errors (Boyer et al., 2002). Also, the sampling time should be long enough in order to reflect the time-averaged characteristics. When a tip of the probe is immersed in the liquid, due to the high conductivity of the liquid, the signal should appear to be near 1. When the tip is in contact with a gas bubble, the signal will drop to 0 almost instantly. Once the gas bubble leaves the tip, the conductivity signal recovers to 1. Ideally, if no deformation or distortion happened and the gas bubble passes the two tips through the same path, the time durations obtained from two tips for the gas bubble should be exactly the same. However, the reality is far more complicated than the assumptions. For instance, the gas bubble may not come from the normal direction to hit the measuring tips or the gas bubble that attacked the first tip may not necessary hit the second tip. Therefore, the signals obtained from both tips can be used for statistical analysis to reduce the system errors. Output signals for bubble detection by dual-tip probe under different conditions are shown in Figure 1-24.

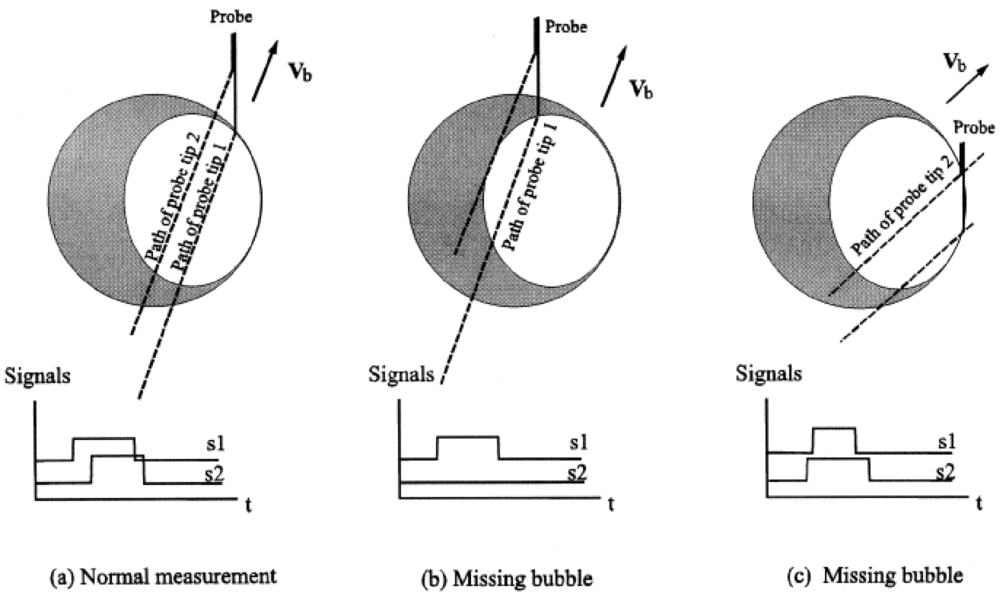

Figure 1-24 Normal measurement and missing bubble of a dual-tip conductivity probe (taken from Wu and Ishii (1999)).

The conductivity probe should be placed at several radial locations, and the collection of data should be repeated sufficiently for each location. Once the conductivity signals have been properly processed, the gas holdup for each local position can be expressed by

$$\alpha_g = \frac{\sum \Delta T_0}{\Delta T_n} \tag{1-52}$$

where ΔT_0 is the time duration for the probe surrounded by the gas bubbles and ΔT_n is the total time duration of each measurement.

Some researchers have proposed multi-point probes, such as Burgess and Calderbank (1975), Yao et al. (1991) and Manjrekar and Dudukovic (2015). Theoretically, all components of the velocity vectors can be obtained by using multi-point probes and hence the measurements become more accurate. However, practical problems have limited the application of these multi-point probes. For instance, multiple tips may cause bubble deformation easily when some of them piercing through the liquid film at the same time. Also, the interaction of trapping of the bubbles with the multiple tips can no longer be neglected. Furthermore, the algorithm for calibration and signal processing is inevitable complicated due to the numbers of the measuring tips.

Although the tips are made as thin as possible, using the probes are still an intrusive method that inevitably affects the surrounding flow field. Also, the measurement results can only represent the gas holdup for a small range around the measuring point. However, non-intrusive measurements on the entire flow field are required for the interest of both the industry and academia. These non-intrusive methods for gas holdup measurement include X-ray/γ-ray CT, ERT, ECT, and high-speed imaging. By using these methods, the spatial distribution of gas holdup for an entire (horizontal or vertical) cross-section can be obtained in time sequence. The non-intrusive measurements have no interference to the fluid flow and as well as not being affected by the operating conditions such as high temperature, high pressure and corrosive fluid, and hence made the accurate on-line measurement of local characteristics possible.

Electrical Capacitance/Resistance Tomography is widely used for void fraction measurement of two-phase flow systems. Based on the differences in capacity/resistivity of the gas-phase and liquid-phase, the ECT/ERT measurement system uses an array of electrodes that attach to the bubble column wall to receive the electrical signals. A data acquisition system is directly connected to the electrodes. The collected data are processed by image reconstruction algorithms to plot the cross-sectional distribution of void fractions. Circumferential arrangement of electrodes, calibration images of different fluids and typical results of a 2-layer ECT/ERT measurement are shown in Figure 1-25.

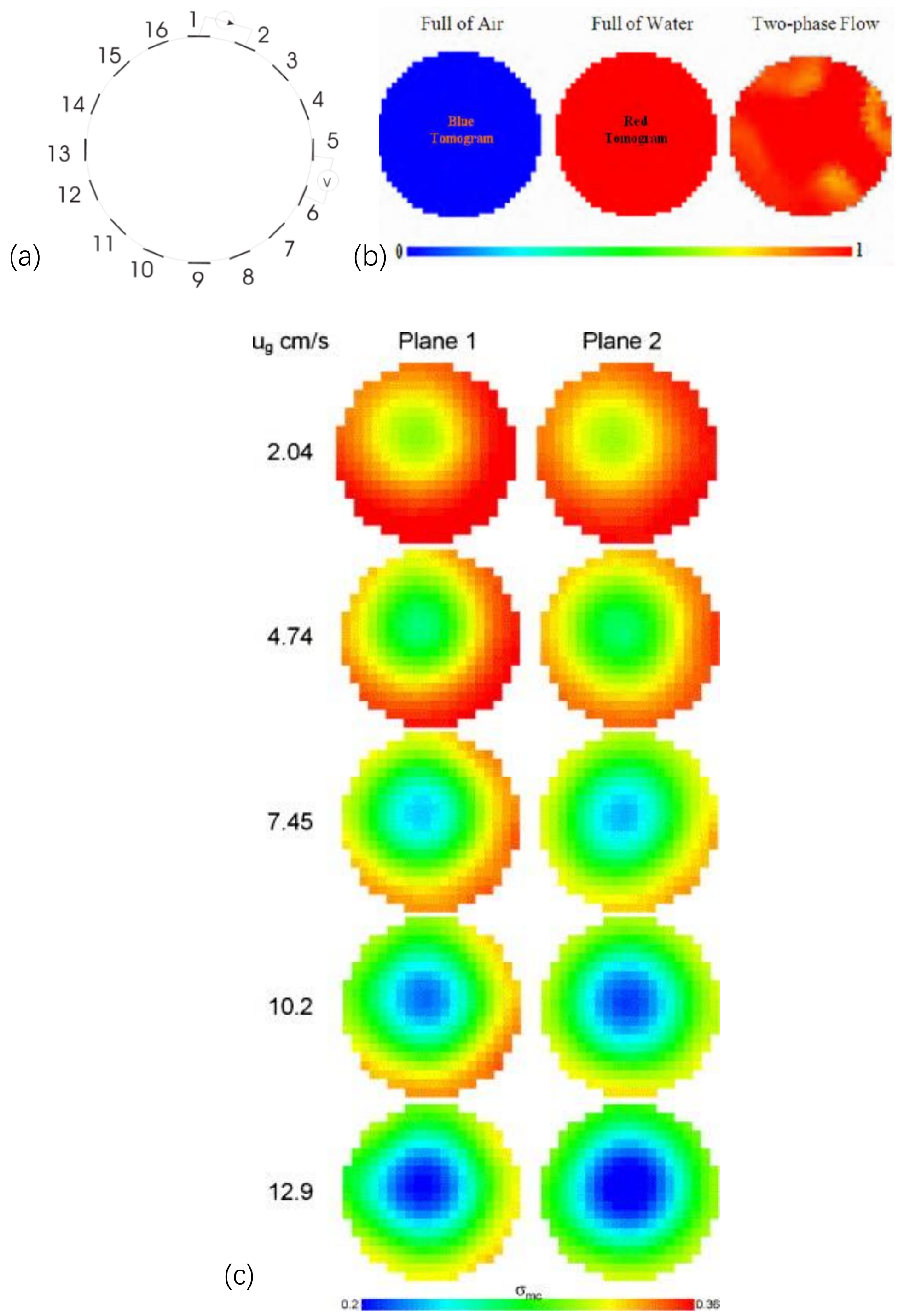

Figure 1-25 (a) Typical arrangement of 16 electrodes (taken from Toye et al. (2005)); (b) calibration images of air-water system (taken from Ismail et al. (2011)); (c) gas holdup distributions of 2-layer ERT measurements for different superficial velocities (taken from Jin et al. (2007)).

It seems that the resolution of ECT/ERT is largely depended on the number of electrodes being deployed, the diameter of the vessel to be measured, and the image reconstruction algorithm. Theoretically, the more electrodes are used the higher resolution will be obtained for the same bubble column. However, in practice, the number of electrodes to be used is limited to the diameter of the bubble column to be measured. Also, increasing the number of electrodes means more time and computing effort for the image reconstruction algorithm, usually linear back projection algorithm, to convert the collected data into the final void fraction images. Moreover, most of these ECT/ERT systems are 2-D based measurement. Although 3-D plots can be obtained such as Al-Masry et al. (2010), it seems that these 3-D plots are generated from interpolation of 2-D measurements. Considering all these disadvantages, a 3-D real-time electrical capacitance volume tomography (ECVT) has been developed recently (Warsito et al., 2007). The ECVT system uses upgraded 3-D capacitance sensors with different shapes and configurations and a volume image reconstruction technique called the neural-network multi-criterion optimisation image reconstruction (NN-MOIRT). The sensor designs and the reconstruction results for the ECVT system are shown in Figure 1-26.

The ECT/ERT measurement systems have used the electrical signals measured on the vessel wall to inversely estimate the image in the centre. It is believed that this is not a direct measurement in the core region of the flow field. However, Computational Tomography uses a narrow beam of X-ray/γ-ray to penetrate the multiphase system along a straight path. Radiative decay flies off during this process primarily by absorption and scattering, and resultant intensity can be detected by scintillation detectors placed on the opposite side of the source (Chen et al., 1998, Patel and Thorat, 2008, Kumar et al., 1997, Hubers et al., 2005).

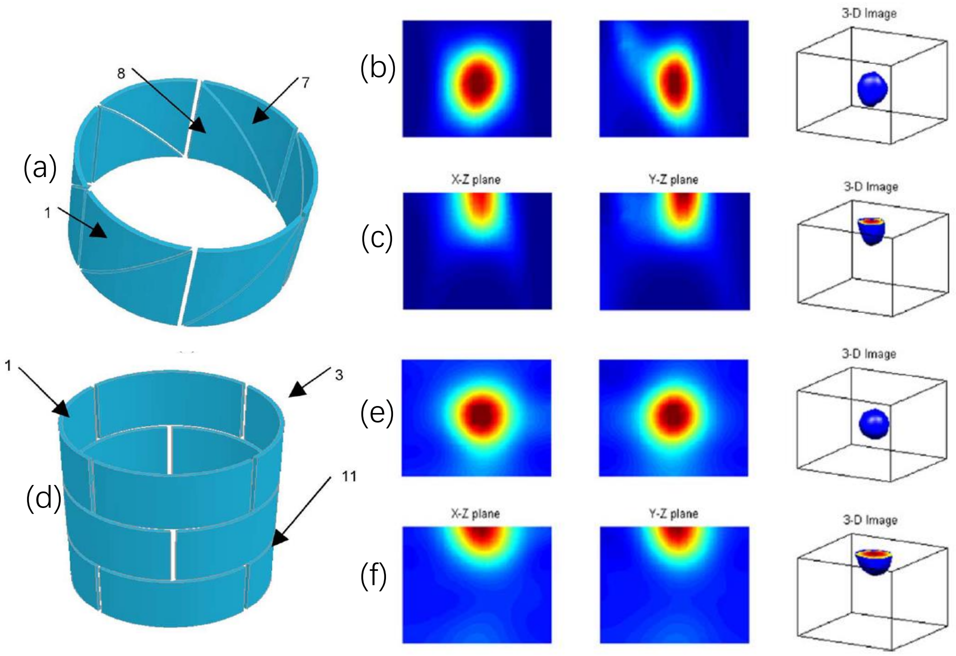

Figure 1-26 ECVT Sensor designs and reconstruction results of a sphere in the centre of a cubic domain using NN-MOIRT algorithm: (a), (b), (c) single-plane triangular sensor; (d), (e), (f) triple-plane rectangular sensor (taken from Warsito et al. (2007)).

(a)

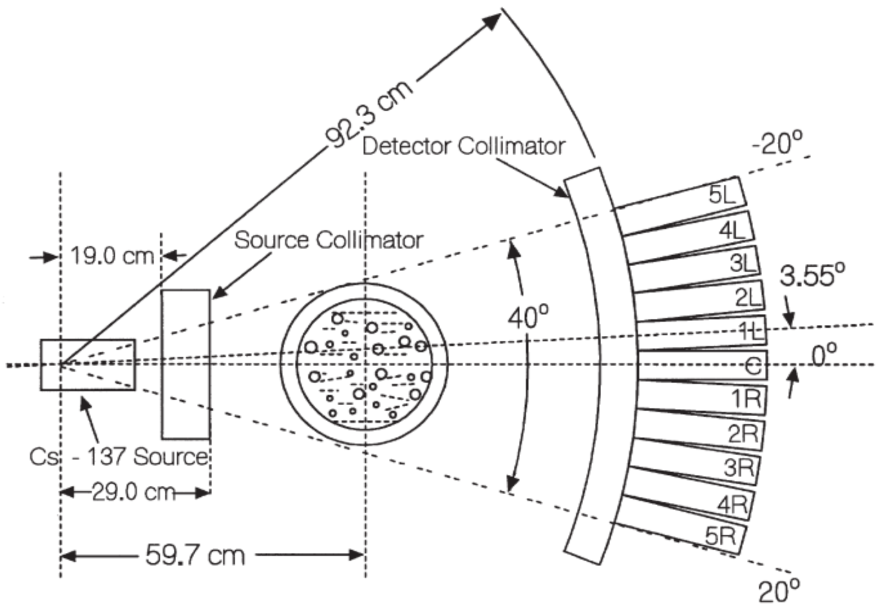

(b)

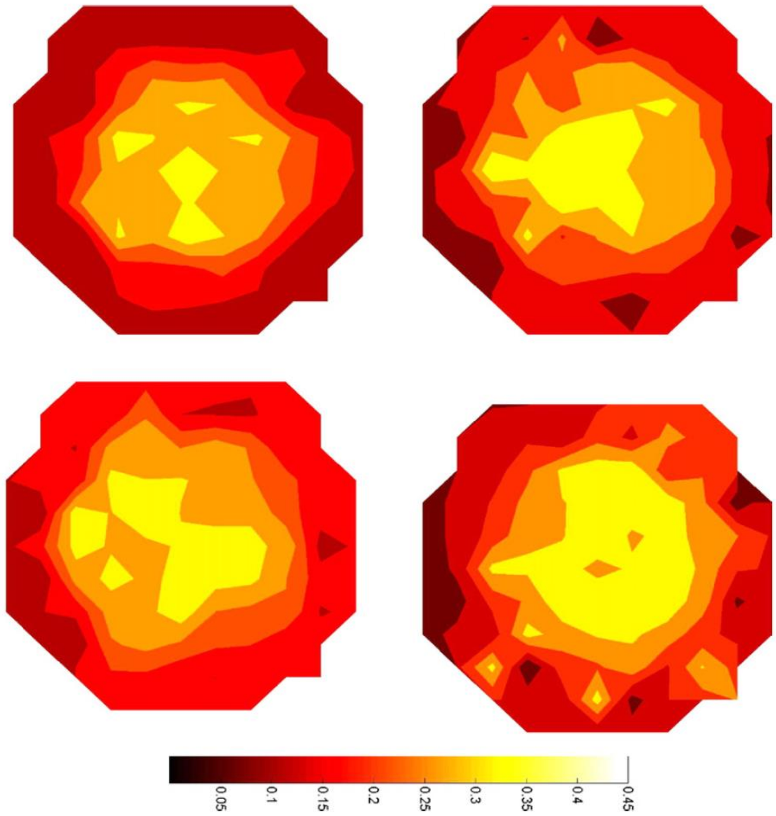

Figure 1-27 (a) Typical source-detector configuration of CT systems (taken from Chen et al. (1998)); (b) Gas holdup profile at different cross sections measured by a γ-ray CT (taken from Patel and Thorat (2008)).

Figure 1-27 (a) presents a typical source-detector configuration of CT systems, the source and detectors are mounted on a gantry that is capable of being rotated about the axis of the test section through a stepper motor. The spatial resolution based on the rotational scanning of CT measurement is generally higher than ECT/ERT. However, different from the instantaneous measurement with some delays from the image reconstruction of ECT/ERT, the gas holdup profile measured by CT can only reflect the time-averaged characteristics, as the maximum rotational speed is limited by the weights of the scanning assembly and the number of projection measurements required for a complete 360-degree rotation.

With the development of those measurement devices, the local characteristics of the bubble columns have been widely studied. For example, an early study by Hills (1974) has used conductivity probe to investigate the radial distribution of time-averaged gas holdup under different superficial velocities and with perforated plate distributors that have different size and number of holes. It is found that the local gas holdup is generally shown to be a normal distribution and it is strongly affected by the distributor configurations. In order to further study the effect of free area and hole diameter of gas distributors, Patel and Thorat (2008) measured radial distribution of gas holdup in a 0.2 m diameter bubble column. It seems that the gas holdup distribution is strongly associated with the flow regime of bubbles at the outlet of gas distributor. When the free area is decreased, the flow regime of bubbles is easier to transform into bubble jetting. In this case, the high-velocity jets will disappear quite quickly under the influence of liquid-phase, large coalesced bubbles are easier to be formed due to the downstream interaction of jets, and hence the gas holdup will be reduced. When the free area is kept the same, increase the hole diameter will also decrease the gas holdup, because of the increased initial bubble size (Kumar et al., 1997). Veera and Joshi (2000) comprehensively measured the local gas holdup distribution for different sparger hole diameters, liquid dispersion height, and liquid phase properties. Similar conclusion with Kumar et al. (1997) has been drawn on the gas distributor design, and they further show that the decrease of gas holdup distribution is due to the bubble coalescence by comparing the measurement results for coalescence inhabiting and coalescence promoting liquids. These experimental findings are shown in Figure 1-28.

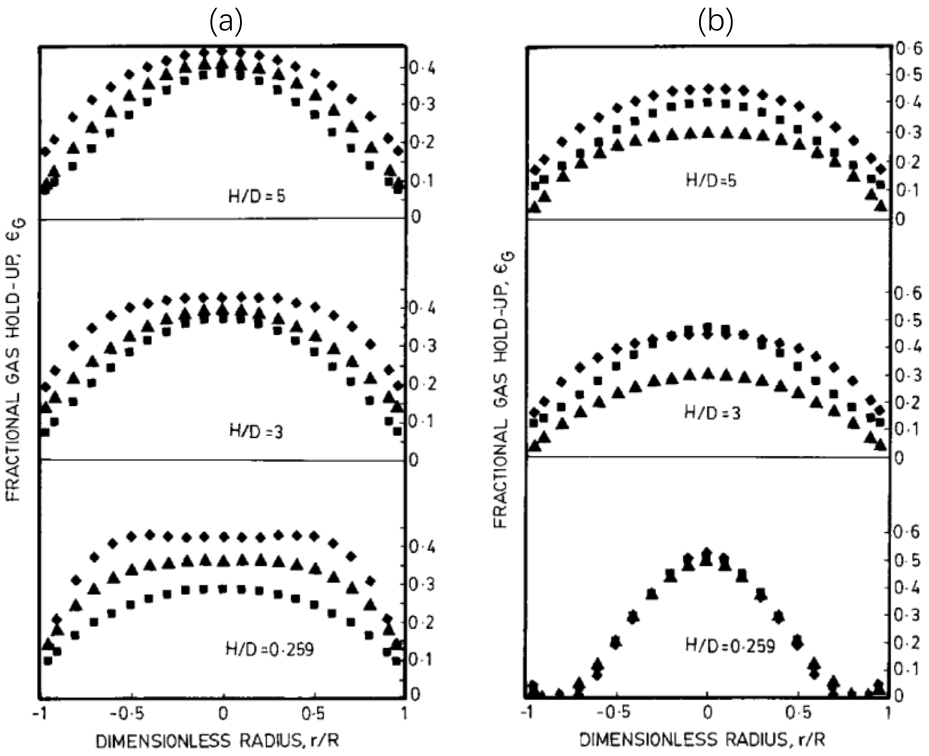

Figure 1-28 Radial gas holdup profiles at various axial locations at Ug = 0.24 m/s for various liquid phases for the sparger plate: (a) d_o = 1 mm, and (b) d_o = 25 mm; ♦Coalescence inhabiting ▲Air-Water, ■ Coalescence promoting. (taken from Veera and Joshi (2000))

The gas holdup distribution is also associated with the axial height position and bubble column diameter. The experimental results of Veera and Joshi (2000) have shown that the gas holdup in the centre of the bubble column increases along the axial direction for a large bubble column with a diameter of 0.38 m. Chen et al. (1998) have found a similar trend for a larger bubble column with a diameter of 0.44 m and at a superficial velocity of 0.1 m/s. Kumar et al. (1997) have measured gas holdup distribution for both large and small bubble columns (diameters of 0.26 m and 0.1 m). Different from the large bubble columns, the evolution of gas holdup distribution in the small bubble column at high superficial velocity is shown to be increased with the axial position in an entry region and then decrease gradually until it reaches an equilibrium state. The effects of axial distance to the gas distributor for both small and large bubble columns are shown in Figure 1-29.

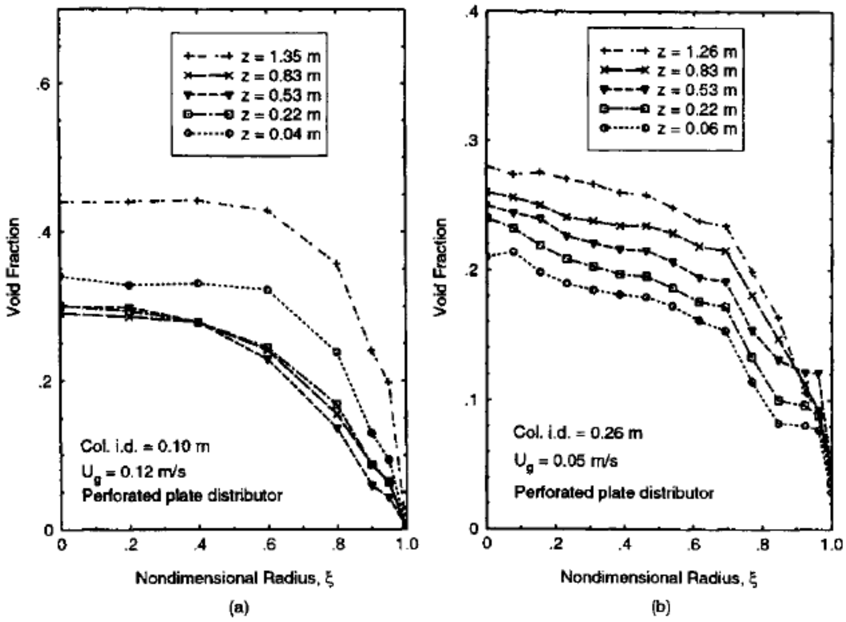

Figure 1-29 Effect of axial distance on the radial distribution of gas holdup with bubble column diameter: (a) 0.1 m; (b) 0.26 m. (taken from Kumar et al. (1997))

The local gas holdup is also influenced by the operating pressure of the bubble columns. It is found by Kemoun et al. (2001) the effect of operating pressure becomes significant especially at high superficial velocities. As shown in Figure 1-30(d), the gas holdup is about 70% higher at 0.7 MPa than at atmospheric pressure, even though the elevated pressure decreases the radial gradient of the gas holdup distribution.

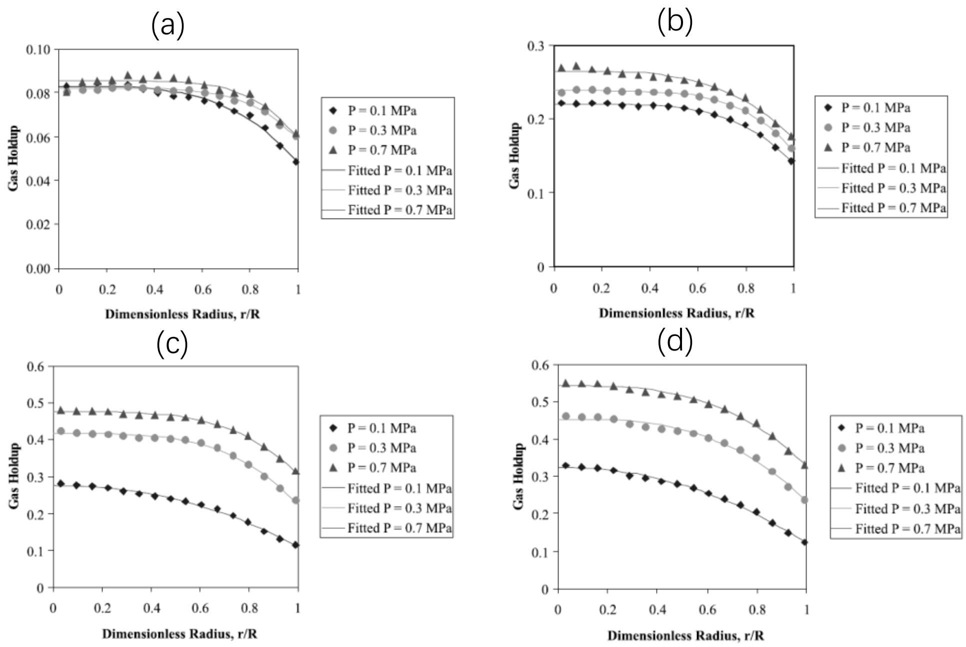

Figure 1-30 Influence of different operating pressure on the radial distribution of gas holdup at different superficial gas velocities: (a) *Ug* = 0.02 m/s; (b) *Ug* = 0.05 m/s; (c) *Ug* = 0.12 m/s; (d) *Ug* = 0.18 m/s; (taken from Kemoun et al. (2001))

4.2 <u>Bubble Dynamics</u>

The bubble characteristics in gas-liquid two-phase flows have been intensively studied. In the bubble column reactors, the rising of bubbles leads to the large-scale circulation of the liquid phase, and the turbulence is generated due to the liquid shear and the wake formed by shedding vortices from the bubbles. The bubble motions in the liquid flow can be considered as flow over moving objects that are under dynamic oscillation and deformation due to the surrounding pressure. The dynamic behaviour of the bubbles is closely associated with the flow of the bubble’s boundary layer and the shedding of vortices. It seems that there are very strong interactions between the bubbles and the carrier fluid. Therefore, investigations on the bubble characteristics lead to understandings of the gas-liquid interactions in the bubble columns.

The influence of liquid viscosity and surface tension has been found to be very significant on the size and shapes of bubbles. Based on a large amount of experimental observations, Clift et al. (1978) summarised the regime map of bubble shapes, as shown in Figure 1-31. The shape of bubbles is divided into three types, such as spherical, ellipsoidal and capped bubbles, by using three dimensionless numbers, including Reynolds number *Re*, Eötvös number *Eo* and Morton number *Mo*. Many researchers have been using different dimensionless numbers to describe the bubble characteristics. The commonly used dimensionless numbers in the gas-liquid system have been listed in Table 1-2.

Table 1-2 Commonly used dimensionless numbers in gas-liquid system.

Dimensionless number	Expression	Physical Meaning	Relation
Re	$\frac{\rho_l u_b d_b}{\mu_l}$	the ratio of inertial forces to viscous forces	-
Eo	$\frac{g d_b^2 \left(\rho_l - \rho_g\right)}{\sigma}$	the ratio of gravitational forces to surface tension forces	-
We	$\frac{\rho_l u_b^2 d_b}{\sigma}$	the ratio of inertia to surface tension	$We = \frac{\mathrm{Re}^2 Mo^{1/2}}{Eo^{1/2}}$
Fr	$\frac{u_b}{\sqrt{g d_b}}$	the ratio of inertia to gravitational forces	-
Mo	$\frac{g \mu_l^4 \left(\rho_l - \rho_g\right)}{\rho_l^2 \sigma^3}$	combination of physical properties	$Mo = \frac{We^3}{Fr^2 \mathrm{Re}^4}$

A crude estimation on the range of these dimensionless numbers are $10^1 < \mathrm{Re} < 10^5$, $10^{-1} < \mathrm{Eo} < 10^3$, $10^{-3} < \mathrm{We} < 10^3$, $10^{-1} < \mathrm{Fr} < 10^1$, and $10^{-11} < \mathrm{Mo} < 10^{-10}$.

For a specific gas-liquid system, such as air-water system, the physical properties of the liquid phase can be regarded as constants. Under this circumstance, the shape of bubbles is only related to the bubble diameters. Mendelson Harvey (1967) specified the shape of bubbles according to the bubble diameters while classifying the terminal velocities into 4 regions. The bubbles are in spherical shape when they are smaller than 1.4 mm. When bubbles become larger, they are no longer spherical and tend to follow a zigzag or helical rising path. According to Mendelson Harvey (1967), the bubbles begin to assume a spherical cap shape when they are larger than 6 mm. However, it has been argued that this transition size to spherical-cap bubble is not accurate. Clift et al. (1978) present that the bubbles are shown to be spherical-capped when the diameter is approximately large than 20 mm, which makes a better agreement with the experimental observations by Batchelor (1967). The terminal velocity map of air bubbles of different sizes has been presented in Figure 1-31. Based on a large number of experimental statistics, Tomiyama (1998) proposed a semi-empirical model for bubble shapes variations, which has given 1.36 mm and 17.3 mm as the boundaries between spherical/ellipsoidal bubbles and ellipsoidal/spherical capped bubbles respectively in a slightly contaminated air-water system.

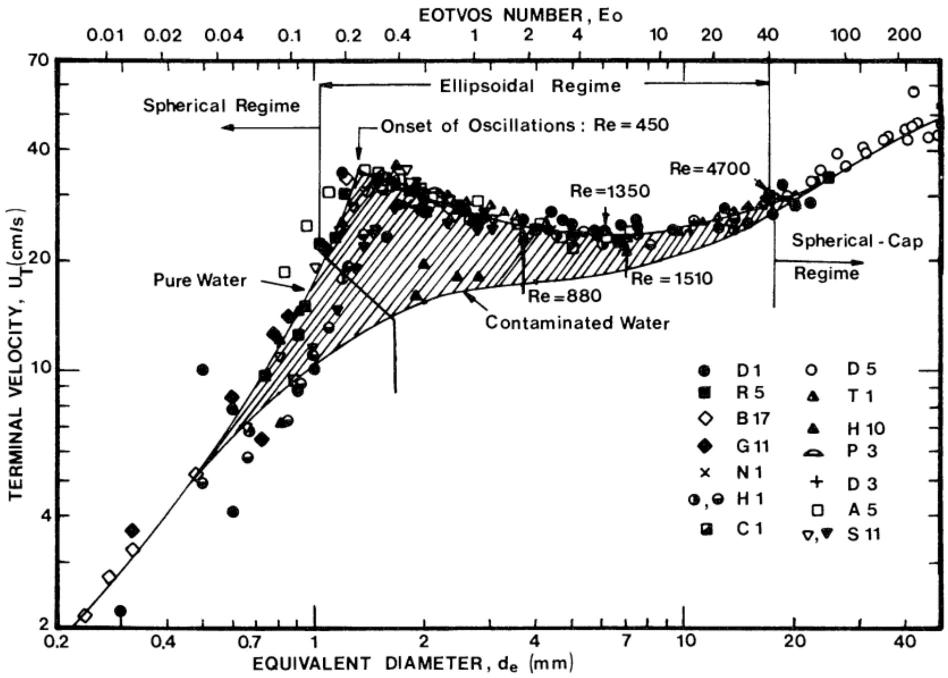

Figure 1-31 Terminal velocity of air bubbles in water (taken from Clift et al. (1978)).

It seems that a large proportion of the bubbles in the bubble column reactors are in ellipsoidal shapes. These medium-size ellipsoidal bubbles have very significant surface oscillations and also the most complex rising trajectories. Reichardt and Sommerfeld (2008) present the oscillation and rising characteristics of single ellipsoidal air-bubble in the stagnant liquid by applying particle tracking velocimetry, as shown in Figure 1-32.

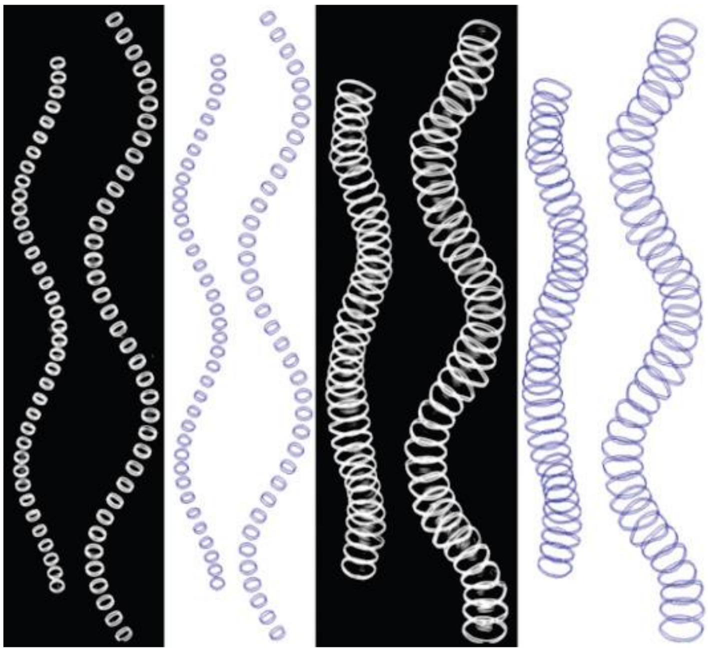

Figure 1-32 Stereo imaging of bubble rise in stagnant liquid about 700 mm above the injection location for two bubble sizes given with their volume equivalent diameter, two images left) 2.3 mm, two images right) 5.2 mm (taken from Reichardt and Sommerfeld (2008)).

For ellipsoidal bubbles, the aspect ratio is a major characterisation of the dynamic deformations. Wellek et al. (1966) proposed an empirical correlation to approximate the deformation of bubbles, which is consisted of dimensionless parameters including Weber number *We*, Reynolds number *Re*, Eötvös number *Eo*, Froude number *Fr*, and the ratio of dynamic viscosity. After a multiple regression process, they found the *Eo* number is the most important parameter and being able to approximate the bubble deformation in low viscosity systems. The idea of using *Eo* number to characterise the bubble deformation has been adopted by Okawa et al. (2003), Tomiyama et al. (2002), Tsuchiya et al. (1990) and Besagni and Inzoli (2016a). Moore (2006) derived an expression of the aspect ratio using the Webber number, based on the balance of the dynamic pressure and the capillary pressure at the bubble nose and side edge respectively. This idea has also been extended by Sugihara et al. (2007) and Legendre et al. (2012). Also, some studies about the bubble deformations have attempted to introduce additional dimensionless parameters (Bozzano and Dente, 2001, Tripathi et al., 2015, Tsamopoulos et al., 2008, Clift et al., 1978, Legendre et al., 2012, Aoyama et al., 2016), such as Morton number *Mo*, Bond Number *Bo*, Archimedes number *Ar* and Tadaki number *Ta*, to correlate the aspect ratio or as the conditions to distinguish different deformed bubbles. By viewing all these dimensionless numbers mentioned above, it can be conjectured that the influencing factors on the bubble deformations are mainly buoyancy, surface tension, and viscosity. Therefore, the dimensionless numbers used to correlate the aspect ratio should be able to reflect the effects of these three influencing factors at least.

It is believed that the rising of non-spherical bubbles is largely affected by the bubble wakes. Mendelson Harvey (1967) considers that the drag force being imposed on the non-spherical bubbles is increased due to the vortices or eddies induced in the bubble’s wake. Since the spherical-cap bubbles vertically rise in water almost along a straight line with relatively constant speed, the flow behind the spherical-cap bubbles seems to be easier to be captured, as shown in Figure 1-33. For Reynolds number less than about 360, the wake behind the bubble is laminar and takes the form of a toroidal vortex; while the Reynolds number is larger than 360, the wake behind the bubble becomes turbulent. It seems that this kind of bubble-induced turbulence decays quite quickly due to liquid viscosity in the downstream of bubbles, which may be very different from the turbulence generated due to the liquid shear. In the bubble columns, the wake of bubbles not only affects the drag force but also interacts very strongly with the subsequent bubbles. To be more specific, both the bubble coalescence and breakup phenomena, which are due to bubble-bubble collision and eddy-bubble collision, will be greatly affected due to the eddies or bubbles that are under the influence of bubble-induced turbulence. Therefore, understanding the bubble-induced turbulence must be one of the key points for accurately describing the gas-liquid interactions in the bubble columns.

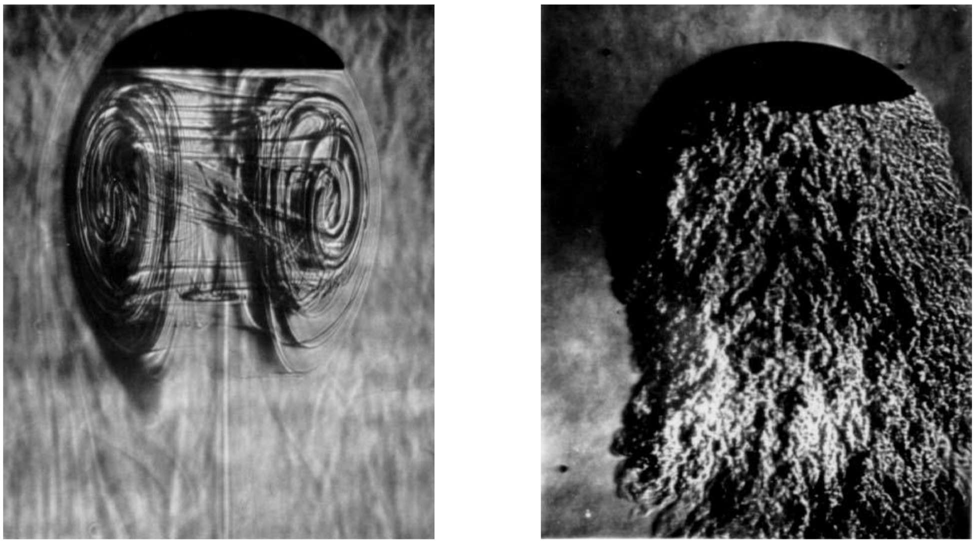

Figure 1-33 Flow visualizations of spherical-cap bubbles: left) laminar wake at *Re* ≈ 180 (taken from Wegener and Parlange (1973)), and right) turbulent wake at Re ≈ 17,000 (taken from Wegener et al. (1971)).

4.3 <u>Liquid Flow Field Characteristics</u>

There are many studies on the liquid flow field characteristics in the bubble column reactors, and most of the early studies focus on the time-averaged liquid velocity distribution, flow structures, and flow regime transitions. The time-averaged liquid velocity distributions can be simply measured by modified Pitot tube, such as Hills (1974). One of the key findings of these studies is the large-scale liquid circulation driven by rising bubbles. However, in-depth understandings of the transient behaviour of the both the local and the entire flow field, such as instantaneous liquid velocity and dynamic flow regime transitions, are still insufficient at this stage.

With the development of Particle Imaging Velocimetry (PIV), Laser Doppler Anemometry (LDA), Computer Aided Radioactive Particle Tracing (CARPT) and high speed imaging, as well as in combined with other measurement techniques including pressure measurements, bed expansion method, and optical probes, the flow regime transitions have been systematically studied by various researchers (Chen et al., 1994, Zahradnik et al., 1997, Camarasa et al., 1999, Ruzicka et al., 2001, Ruzicka et al., 2003, Ruzicka et al., 2008, Reilly et al., 1994, Krishna and Ellenberger, 1996, Manjrekar and Dudukovic, 2015, Thorat and Joshi, 2004). It seems that the flow regime transitions are influenced by various parameters including bubble column diameter, liquid dispersion height, liquid phase properties, operating pressure, and gas distributor designs.

The flow regimes in the bubble column can be defined as homogeneous bubbly flow, transition range, slug flow the heterogeneous churn-turbulent range, depending on the superficial velocity of the gas phase and the column diameter. The sketch of approximate distinction of the flow regimes in the bubble columns has been shown in Figure 1-1. A very comprehensive study on the flow regime transitions in the bubble columns has been presented by Chen et al. (1994), which identifies the flow regimes as dispersed bubble, vortical-spiral flow, and turbulent flow. The typical 3-D macroscopic flow structures in the vortical-spiral flow regime have been clearly illustrated, which include descending flow, vortical-spiral flow, fast bubble flow, and central plume. These illustrations have greatly extended the understandings in the dynamic characteristics and the coherent eddy structures in the bubble columns, which further provide very important guidelines to the design and scale-up of bubble columns. It seems that the transition of the flow regimes and the macroscopic flow structures are found to be analogous to the Taylor instabilities, which characterised flow between two concentric rotating cylinders. In the recent studies, it has been found that the homogeneous flow regime can be further distinguished into the mono-dispersed homogeneous regime and the poly-dispersed homogeneous flow regime, depending on the superficial velocities and the associated bubble size distributions (Besagni and Inzoli, 2016b). The mono-dispersed homogeneous regime may not exist if the large bubbles are aerated due to large diameter orifices on the sparger (Besagni and Inzoli, 2016a). The transition from the homogeneous regime to the transition region is due to the presence of the large bubbles, and the transition flow regime is characterised by macroscopic flow structures with large eddies and a widened bubble size distribution (Guedon et al., 2017), in which case, the turbulent eddies induced by the "coalescence-induced" large bubbles may make increasingly significant contributions to the turbulence generated in the column.

The turbulence in the bubble columns is different from the single-phase turbulence in pipe flows. With the gas phase and liquid phase simultaneously existed in the bubble columns, the two-way interactions are inevitable between the liquid phase flow and the gas bubbles of different sizes and shapes. Apart from the shear turbulence due to the velocity gradient of the liquid phase flow, the interactions between the gas bubbles and the carrier fluid certainly make great contributions to the turbulence in the bubble columns. From a slightly different perspective, bubbles are the energy source of the bubble columns. There is no turbulence when the liquid is remained static before the bubble column start operation. Once the bubbles are aerated into the column, the turbulent eddies are induced at the wake of bubbles. This kind of bubble-induced turbulence is expected to decay in a different way from the single-phase turbulence. However, different from individual bubbles, the structures and behaviours of the turbulent eddies are more difficult to be described, which leads to more problems in understanding the influence of gas bubbles on the liquid-phase turbulence. Therefore, a statistic tool, the turbulence energy spectrum, can be used to characterise different behaviours of the turbulence in the bubble columns.

The turbulence energy spectrum can be approximately divided into energy-containing range and universal equilibrium range, which includes inertial subrange and dissipation range, based on the frequency or wave number of turbulent eddies. The turbulent kinetic energy cascades from large eddies to small eddies in sequence. The Kolmogorov -5/3 law for the inertial subrange, which can be expressed as $E(\kappa)\sim\varepsilon^{2/3}\kappa^{-5/3}$, has already been widely accepted for homogeneous and isotropic turbulence in single-phase flow. However, there are some pioneering work that has shown that the pseudo-turbulence induced by rising bubbles is different from the single-phase turbulence. Batchelor (1967) presented the analytical description of axisymmetric irrotational flow due to a moving sphere and he deduced that the stream function behind the sphere decays with distance to the power of -3. Lance and Bataille (1991) measured the energy spectrum of bubbles rising through an imposed turbulence flow using hot-wire and Laser Doppler anemometry (LDA). They found that the

Kolmogorov power law scaling of -5/3 was gradually replaced by a slope of approximately -8/3 with the increase of the volume fraction of the gas phase. They attributed the change of slope to the wakes of bubbles, in which eddies produced were dissipated extremely rapidly before the spectral transfer had even taken place. Therefore, based on Karman-Howarth equation, they analysed the spectral energy balance of dissipation and production and concluded that the exponent of power law scaling was approximately -3, which was close to the value of -8/3 they found experimentally.

In contrast, a few experimental studies have reported the -5/3 behaviour for pseudo-turbulence, such as Mudde *et al.* (1997) and Cui and Fan (2004), These studies show the same slope on the energy spectrum as the homogeneous and isotropic turbulence in the single-phase flow. Rensen *et al.* (2005) reported a slope close to but slightly less steep than -5/3. They attributed this to the energy enhancement at small scales, which is caused by the presence of microbubbles. However, Mercado *et al.* (2010) have used a phase-sensitive constant-temperature anemometry (CTA) to separate the velocity signals of bubbles from the liquid flow field, and hence re-confirmed the -3 scaling for bubble-induced turbulence.

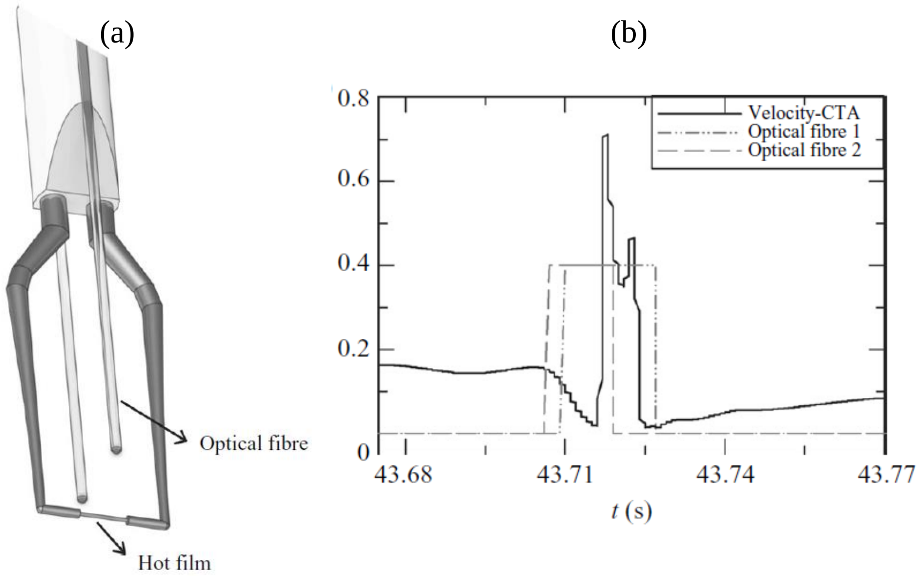

Figure 1-34 Phase-sensitive CTA: (a) structure of the probe; (b) typical signals for bubble detection. (taken from Mercado *et al.* (2010))

The phase-sensitive CTA was developed by van den Berg (2006), who has used optical an optical fibre attached to the hot-film probe. When a bubble collides with the hot-film sensor, it can also be detected by the optical fibre. The detection of bubbles is similar to that by using conductive probes, only the objective signal is the light intensity rather than conductivity. As mentioned by Mercado *et al.* (2010), the signals from the bubbles should be separated from the liquid phase signal, and more importantly, the energy spectrum has to be calculated based on individual segments to reflect the liquid fluctuations rather than being calculated based on averaging. Mendez-Diaz et al. (2013) have used flying hot-film anemometry to perform measurements with gas fractions up to 6% and confirmed the power density distributions decay with a power of -3.

As pointed out by Risso (2011), the κ^{-3} scaling obtained from CTA measurements is based on the time fluctuation of velocities. For the spatial fluctuation of velocities, it requires simultaneous measurements of the liquid velocity insufficient number of locations, which cannot be done by using LDA or CTA probes. Therefore, Riboux et al. (2010) measured the turbulence energy spectrum in the wake of a bubble swarm using PIV and also confirmed that the power law scaling is very close to -3. It should be noticed that their measurements focus on the unsteady flow that evolves as the bubbles just rise away from the fixed measuring window of one high-speed PIV camera. Another synchronised camera is placed at a perpendicular position to trace the bubble trajectories so that the exact timing of the bubbles rise away from the measuring window can be found. Although this technique has successfully measured the velocities induced at the bubbles rising passage, it is essentially the measurement of the single phase. Therefore, the measured velocities are with short delays and whether the characteristics of the bubble swarm’s wake are significant of the flow within the homogeneous swarm are hard to be determined. A typical two-camera PIV system for simultaneous 2-D measurement of the bubbles and the liquid phase in the bubble columns has been presented by Broder and Sommerfeld (2002). The working principle has been explained in details by Poelma et al. (2007).

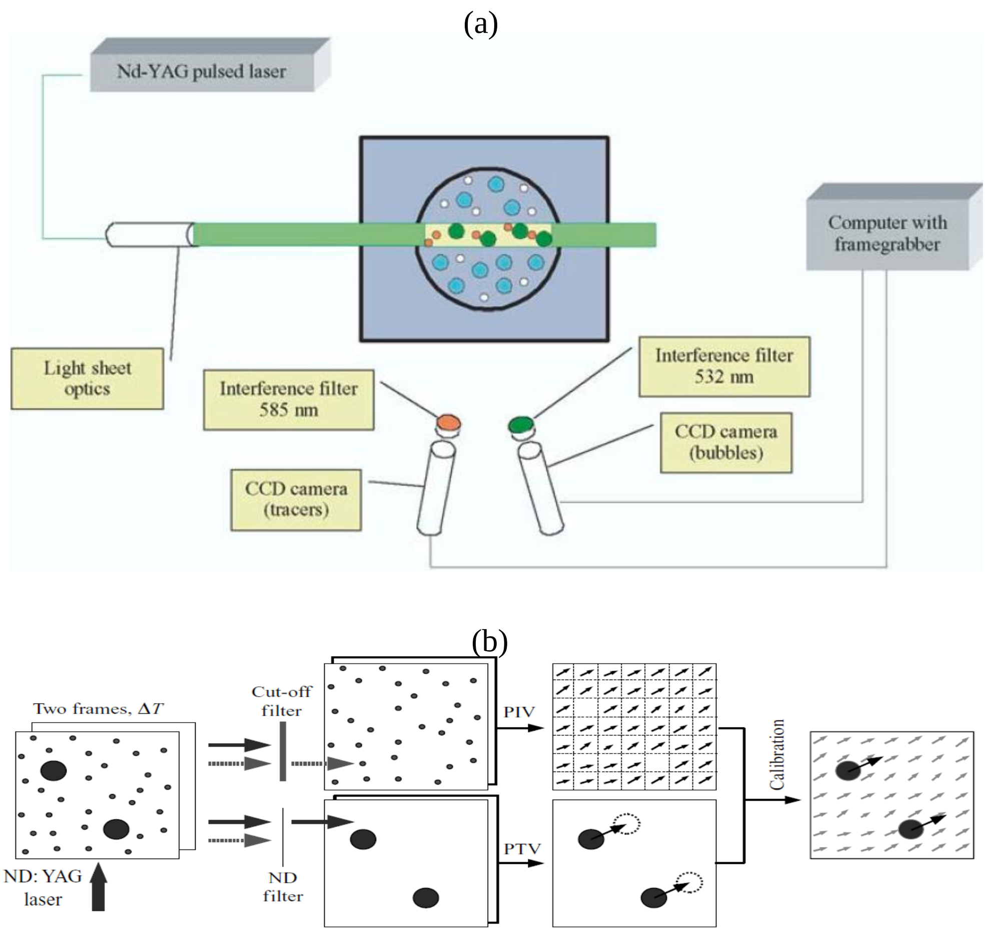

Figure 1-35 Two-camera PIV system for bubble columns: (a) optical arrangement (taken from Broder and Sommerfeld (2002)); (b) schematic diagram of data processing (taken from Poelma et al. (2007)).

The neutral buoyant fluorescing particles are added into the bubble column as tracer particles. The testing section is illuminated by a pulsed Nd:YAG laser which created a light sheet of approximately 0.5 mm. The two CCD cameras are usually placed at non-perpendicular positions, with one records the tracer particles signal and the other records the bubbles. The emission spectrum of the fluorescing particles should be different from the wavelength of the scattered light from the bubbles so that different filters can be applied to both cameras to allow light with a different particular wavelength to pass through for each camera. By doing so, the signals for both phases can be separated. Classic iterative algorithms incorporating a successive refinement of the interrogation area can be used for the image pairs of the tracer particles while the bubble detection algorithm can be applied along with the Particle Tracking Velocimetry (PTV) algorithm to obtain the bubbles velocity vectors (Sommerfeld and Broder, 2009). Deen et al. (2000a) used a similar two-camera PIV to measure the velocity field in a square bubble column and compare the results with that of a single-camera ensemble-averaged PIV measurement. The results revealed clearly a proper discrimination of the displacement vectors for both phases is not possible in a single-camera setup, as the velocity difference between the phases is relatively small in the bubble columns. Therefore, it is emphasised that the separation of the signals from two phases is very important as the main concern is to only investigate the statistical characteristics of liquid phase turbulence (under the influence of bubbles). Based on the separation concept, similar PIV measurement results of -3 scaling turbulence energy spectrum have been obtained by Murai et al. (2000) and Bouche et al. (2014) in both 2-D and 3-D bubble columns.

Although the simultaneous measurement of both phases can be obtained by using the two-camera PIV system, the velocity vectors for the liquid phase at the regions that being occupied by the bubbles are still very difficult to obtain. However, the spatial resolution is strongly required to obtain the turbulence energy spectrum, because the length of the smallest interrogation cell should be small enough to represent the highest wavenumber that intended to be covered. In other words, limited to the resolution of PIV cameras, the measuring window cannot be too big. Therefore, the liquid velocity signals are often blocked by the existence of bubbles in this small measuring window, which may be a difficult problem for obtaining the turbulence energy spectrum from two-camera simultaneous measurements. Considering all these difficulties, a special camera with even higher resolutions and high capturing speed may be required to allow sufficient spatial resolution in a larger measuring window for completed and simultaneous measurements.

Apart from the limitations of experimental devices, the understanding of the -3 pow law scaling behaviour of the bubble-induced turbulence is still insufficient. Theories formed based on the experimental observations and measurements are mostly speculations or conjectures. Arguments and debates on the existence, the active range, the characteristic length and time scales and the energy cascade processes of the -3 power scaling behaviours are still lasting, which has become an obstacle from applying these characteristics of the bubble-induced turbulence into numerical studies, such as coupling with the bubble coalescence and breakup kernels or including the contribution of bubble-induced turbulence into turbulence modelling in gas-liquid two-phase flows.

5. RECAPITULATION AND IMPLICATIONS

This chapter has reviewed the experimental and numerical investigations of the turbulent bubbly flow in the bubble column reactors. Various experimental techniques on the measurements of the gas holdup, bubble characteristics, and liquid phase flow fields have been outlined. It seems that the investigations on the gas holdup, bubble behaviours, and the liquid flow field have trended towards the dynamic and local characteristics. With the development of high-speed and high-resolution measurement device and technique, the importance of the structures of bubbles and eddies that are under the influence of each other has been gradually recognised. For CFD modelling, the two-fluid model is considered as the most cost-effective numerical modelling method for the simulation of turbulent bubbly flows in the bubble columns, especially with the requirement of describing a large number of bubble's coalescence and breakage phenomenon. However, closure problems such as interphase forces, turbulence modelling, and bubble size distribution have been brought into concern in this case. The most crucial conclusion to be drawn from both experimental and numerical studies reviewed in this chapter is that the understanding of gas-liquid interactions in the bubble column reactors is still limited. In particular, the liquid phase turbulence characteristics under the influence of deformable rising bubbles have not been fully revealed from an experimental point of view, and the effects of the bubble-induced turbulence have not been appropriately considered in the CFD modelling. The statistic characteristic of homogeneous isotropic turbulence is still used as an approximation in the most existing models to describe the bubble-bubble and eddy-bubble interactions. It is clear from the foregoing reviews that with a gradually intensified understanding of the power law scaling behaviour of the turbulent bubbly flows, new models that properly reflect the bubble-induced turbulence in bubble column reactors are strongly required.

In the following chapters, the investigations on the influence of deformable rising bubbles on turbulent bubbly flows in bubble column reactors are conducted. A kinetic inlet model accounting for the gas distributor configurations for the simulation of large-scale bubble columns will be presented in Chapter 2. Chapter 3 will investigate the effect of bubble deformation including the bubble shape variation and the internal pressure concentration on the prediction of bubble breakage rate and bubble size distribution. Chapter 4 and 5 will focus on how the κ^{-3} power law scaling behaviour of the bubble-induced turbulence affects the bubble breakage and coalescence respectively in the numerical simulations. Chapter 6 will present experimental study and theoretical analysis of the turbulence energy spectrum of bubbly flow in a 15-cm-diameter bubble column. Finally, Chapter 7 will present the main conclusions derived from previous chapters to deepen the understanding of the turbulent bubbly flows in the bubble column reactors and provide recommendations for future works on this aspect.

References

AL-MASRY, W. A., ALI, E. M., ALSHEBEILI, S. A. & MOUSA, F. M. 2010. Non-invasive imaging of shallow bubble columns using electrical capacitance tomography. *Journal of Saudi Chemical Society,* 14**,** 269-280.

ALVES, S. S., VASCONCELOS, J. M. T. & ORVALHO, S. P. 2006. Mass transfer to clean bubbles at low turbulent energy dissipation. *Chemical Engineering Science,* 61**,** 1334-1337.

ANDERSSON, R. & ANDERSSON, B. 2006. On the breakup of fluid particles in turbulent flows. *Aiche Journal,* 52**,** 2020-2030.

ANTAL, S. P., LAHEY, R. T. & FLAHERTY, J. E. 1991. Analysis of phase distribution in fully developed laminar bubbly two-phase flow. *International Journal of Multiphase Flow,* 17**,** 635-652.

AOYAMA, S., HAYASHI, K., HOSOKAWA, S. & TOMIYAMA, A. 2016. Shapes of ellipsoidal bubbles in infinite stagnant liquids. *International Journal of Multiphase Flow,* 79**,** 23-30.

AUTON, T. R., HUNT, J. C. R. & PRUDHOMME, M. 1988. The Force Exerted on a Body in Inviscid Unsteady Non-Uniform Rotational Flow. *Journal of Fluid Mechanics,* 197**,** 241-257.

BATCHELOR, G. K. 1967. *An Introduction to Fluid Dynamics*, Cambridge University Press.

BESAGNI, G. & INZOLI, F. 2016a. Bubble size distributions and shapes in annular gap bubble column. *Experimental Thermal and Fluid Science,* 74**,** 27-48.

BESAGNI, G. & INZOLI, F. 2016b. Comprehensive experimental investigation of counter-current bubble column hydrodynamics: Holdup, flow regime transition, bubble size distributions and local flow properties. *Chemical Engineering Science,* 146**,** 259-290.

BHOLE, M. R., JOSHI, J. B. & RAMKRISHNA, D. 2008. CFD simulation of bubble columns incorporating population balance modeling. *Chemical Engineering Science,* 63**,** 2267-2282.

BOUCHE, E., ROIG, V., RISSO, F. & BILLET, A. M. 2014. Homogeneous swarm of high-Reynolds-number bubbles rising within a thin gap. Part 2. Liquid dynamics. *Journal of Fluid Mechanics,* 758**,** 508-521.

BOYER, C., DUQUENNE, A. M. & WILD, G. 2002. Measuring techniques in gas-liquid and gas-liquid-solid reactors. *Chemical Engineering Science,* 57**,** 3185-3215.

BOZZANO, G. & DENTE, M. 2001. Shape and terminal velocity of single bubble motion: a novel approach. *Computers & Chemical Engineering,* 25**,** 571-576.

BRODER, D. & SOMMERFELD, M. 2002. An advanced LIF-PLV system for analysing the hydrodynamics in a laboratory bubble column at higher void fractions. *Experiments in Fluids,* 33**,** 826-837.

BUNNER, B. & TRYGGVASON, G. 2003. Effect of bubble deformation on the properties of bubbly flows. *Journal of Fluid Mechanics,* 495**,** 77-118.

BURGESS, J. M. & CALDERBANK, P. H. 1975. The measurement of bubble parameters in two-phase dispersions—I: The development of an improved probe technique. *Chemical Engineering Science,* 30**,** 743-750.

BURNS, A. D., FRANK, T., HAMILL, I. & SHI, J.-M. The Favre Averaged Drag Model for Turbulent Dispersion in Eulerian Multi-Phase Flows. Fifth International Conference on Multiphase Flow, ICMF-2004, 2004 Yokohama, Japan.

BUWA, V. V., DEO, D. S. & RANADE, V. V. 2006. Eulerian-Lagrangian simulations of unsteady gas-liquid flows in bubble columns. *International Journal of Multiphase Flow,* 32**,** 864-885.

BUWA, V. V. & RANADE, V. V. 2002. Dynamics of gas-liquid flow in a rectangular bubble column: experiments and single/multi-group CFD simulations. *Chemical Engineering Science,* 57**,** 4715-4736.

CAMARASA, E., VIAL, C., PONCIN, S., WILD, G., MIDOUX, N. & BOUILLARD, J. 1999. Influence of coalescence behaviour of the liquid and of gas sparging on hydrodynamics and bubble characteristics in a bubble column. *Chemical Engineering and Processing,* 38**,** 329-344.

CHAHED, J., ROIG, V. & MASBERNAT, L. 2003. Eulerian-Eulerian two-fluid model for turbulent gas-liquid bubbly flows. *International Journal of Multiphase Flow,* 29**,** 23-49.

CHEN, J. H., YANG, N., GE, W. & LI, J. H. 2009a. Computational Fluid Dynamics Simulation of Regime Transition in Bubble Columns Incorporating the Dual-Bubble-Size Model. *Industrial & Engineering Chemistry Research,* 48**,** 8172-8179.

CHEN, J. H., YANG, N., GE, W. & LI, J. H. 2009b. Modeling of Regime Transition in Bubble Columns with Stability Condition. *Industrial & Engineering Chemistry Research,* 48**,** 290-301.

CHEN, J. W., GUPTA, P., DEGALEESAN, S., AL-DAHHAN, M. H., DUDUKOVIC, M. P. & TOSELAND, B. A. 1998. Gas holdup distributions in large-diameter bubble columns measured by computed tomography. *Flow Measurement and Instrumentation,* 9**,** 91-101.

CHEN, J. W., LI, F., DEGALEESAN, S., GUPTA, P., AL-DAHHAN, M. H., DUDUKOVIC, M. P. & TOSELAND, B. A. 1999. Fluid dynamic parameters in bubble columns with internals. *Chemical Engineering Science,* 54**,** 2187-2197.

CHEN, P. 2004. *Modeling the fluid dynamics of bubble column flows. Ph.D. Thesis.* Ph.D. Thesis.

CHEN, P., SANYAL, J. & DUDUKOVIC, M. P. 2005. Numerical simulation of bubble columns flows: effect of different breakup and coalescence closures. *Chemical Engineering Science,* 60**,** 1085-1101.

CHEN, R. C., REESE, J. & FAN, L. S. 1994. Flow Structure in a 3-Dimensional Bubble-Column and 3-Phase Fluidized-Bed. *Aiche Journal,* 40**,** 1093-1104.

CLARK, M. M. 1988. Drop Breakup in a Turbulent-Flow .1. Conceptual and Modeling Considerations. *Chemical Engineering Science,* 43**,** 671-679.

CLIFT, R., GRACE, J. R. & WEBER, M. E. 1978. *Bubbles, Drops, and Particles,* Academic Press.

COOK, T. L. & HARLOW, F. H. 1986. Vortices in Bubbly 2-Phase Flow. *International Journal of Multiphase Flow,* 12**,** 35-61.

COULALOGLOU, C. A. & TAVLARIDES, L. L. 1977. Description of Interaction Processes in Agitated Liquid-Liquid Dispersions. *Chemical Engineering Science,* 32**,** 1289-1297.

CUI, Z. & FAN, L. S. 2004. Turbulence energy distributions in bubbling gas-liquid and gas-liquid-solid flow systems. *Chemical Engineering Science,* 59**,** 1755-1766.

DALY, J. G., PATEL, S. A. & BUKUR, D. B. 1992. Measurement of Gas Holdups and Sauter Mean Bubble Diameters in Bubble Column Reactors by Dynamic Gas Disengagement Method. *Chemical Engineering Science,* 47**,** 3647-3654.

DANCKWERTS, P. V. 1951. Significance of Liquid-Film Coefficients in Gas Absorption. *Industrial & Engineering Chemistry,* 43**,** 1460-1467.

DEEN, N., HJERTAGER, B. & SOLBERG, T. 2000a. *Comparison of PIV and LDA Measurement Methods Applied to the Gas-Liquid Flow in a Bubble Column*.

DEEN, N. G., SOLBERG, T. & HJERTAGER, B. H. 2000b. Numerical simulation of gas–liquid flow in a square cross section bubble column. *14th International congress of chemical and process engineering (CHISA).* Praha, Czech Republic.

DEEN, N. G., SOLBERG, T. & HJERTAGER, B. H. 2001. Large eddy simulation of the gas-liquid flow in a square cross-sectioned bubble column. *Chemical Engineering Science,* 56**,** 6341-6349.

DEEN, N. G., VAN SINT ANNALAND, A. & KUIPERS, J. A. M. 2004. Multi-scale modeling of dispersed gas-liquid two-phase flow. *Chemical Engineering Science,* 59**,** 1853-1861.

DEGALEESAN, S., DUDUKOVIC, M. & PAN, Y. 2001. Experimental study of gas-induced liquid-flow structures in bubble columns. *Aiche Journal,* 47**,** 1913-1931.

DELNOIJ, E. & KUIPERS, J. A. M. 2000. Reply to comments on "Dynamic simulation of dispersed gas-liquid two-phase flow using a discrete bubble model". *Chemical Engineering Science,* 55**,** 2345-2346.

DHOTRE, M. T. & JOSHI, J. B. 2007. Design of a gas distributor: Three-dimensional CFD simulation of a coupled system consisting of a gas chamber and a bubble column. *Chemical Engineering Journal,* 125**,** 149-163.

DHOTRE, M. T., NICENO, B. & SMITH, B. L. 2008. Large eddy simulation of a bubble column using dynamic sub-grid scale model. *Chemical Engineering Journal,* 136**,** 337-348.table

EKAMBARA, K., NANDAKUMAR, K. & JOSHI, J. B. 2008. CFD Simulation of Bubble Column Reactor Using Population Balance. *Industrial & Engineering Chemistry Research,* 47**,** 8505-8516.

FAN, J. R., ZHOU, D. D., HUA, Q. & CEN, K. F. 1994. Numerical Computation of Particle-Laden Gas-Flows Past Staggered Tube Banks Undergoing Erosion. *Powder Technology,* 80**,** 1-10.

FAN, R., MARCHISIO, D. L. & FOX, R. O. 2004. Application of the direct quadrature method of moments to polydisperse gas-solid fluidized beds. *Powder Technology,* 139**,** 7-20.

FORRET, A., SCHWEITZER, J. M., GAUTHIER, T., KRISHNA, R. & SCHWEICH, D. 2003. Influence of scale on the hydrodynamics of bubble column reactors: an experimental study in columns of 0.1, 0.4 and 1 m diameters. *Chemical Engineering Science,* 58**,** 719-724.

FRANK, T., ZWART, P. J., KREPPER, E., PRASSER, H. M. & LUCAS, D. 2008. Validation of CFD models for mono- and polydisperse air-water two-phase flows in pipes. *Nuclear Engineering and Design,* 238**,** 647-659.

FRÖSSLING, N. M. 1938. The Evaporation of Falling Drops. *Gerlands Beitr. Geophys.,* 52**,** 170-216.

FU, X. Y. & ISHII, M. 2003a. Two-group interfacial area transport in vertical air-water flow I. Mechanistic model. *Nuclear Engineering and Design,* 219**,** 143-168.

FU, X. Y. & ISHII, M. 2003b. Two-group interfacial area transport in vertical air-water flow II. Model evaluation. *Nuclear Engineering and Design,* 219**,** 169-190.

GRACE, J. R., CLIFT, R. & WEBER, M. E. 1978. *Bubbles, Drops, and Particles,* Academic Press.

GUEDON, G. R., BESAGNI, G. & INZOLI, F. 2017. Prediction of gas-liquid flow in an annular gap bubble column using a bi-dispersed Eulerian model. *Chemical Engineering Science,* 161**,** 138-150.

GUPTA, A. & ROY, S. 2013. Euler-Euler simulation of bubbly flow in a rectangular bubble column: Experimental validation with Radioactive Particle Tracking. *Chemical Engineering Journal,* 225**,** 818-836.

HAGESAETHER, L., JAKOBSEN, H. A. & SVENDSEN, H. F. 2002. A model for turbulent binary breakup of dispersed fluid particles. *Chemical Engineering Science,* 57**,** 3251-3267.

HAN, L. C., FU, J., LI, M., GONG, S. G., GAO, N. N., ZHANG, C. & LUO, H. A. 2016. A theoretical unsteady-state model for k(L) of bubbles based on the framework of wide energy spectrum. *Aiche Journal,* 62**,** 1007-1022.

HAN, L. C., LUO, H. A., LIU, Y. J., YOU, K. Y. & LIU, P. L. 2011. A Multi-Scale Theoretical Model for Gas-Liquid Interface Mass Transfer Based on the Wide Spectrum Eddy Contact Concept. *Aiche Journal,* 57**,** 886-896.

HIBIKI, T., HOGSETT, S. & ISHII, M. 1998. Local measurement of interfacial area, interfacial velocity and liquid turbulence in two-phase flow. *Nuclear Engineering and Design,* 184**,** 287-304.

HIGBIE, R. 1935. The rate of absorption of a pure gas into a still liquid during short periods of exposure. *Transactions of the American Institute of Chemical Engineers,* 31**,** 365-389.

HILLS, J. H. 1974. Radial Nonuniformity of Velocity and Voidage in a Bubble Column. *Transactions of the Institution of Chemical Engineers,* 52**,** 1-9.

HINZE, J. O. 1975. *Turbulence,* McGraw-Hill.

HOSOKAWA, S. & TOMIYAMA, A. 2009. Multi-fluid simulation of turbulent bubbly pipe flows. *Chemical Engineering Science,* 64**,** 5308-5318.

HOSOKAWA, S. & TOMIYAMA, A. 2013. Bubble-induced pseudo turbulence in laminar pipe flows. *International Journal of Heat and Fluid Flow,* 40**,** 97-105.

HOUNSLOW, M. J., RYALL, R. L. & MARSHALL, V. R. 1988. A Discretized Population Balance for Nucleation, Growth, and Aggregation. *Aiche Journal,* 34**,** 1821-1832.

HUBERS, J. L., STRIEGEL, A. C., HEINDEL, T. J., GRAY, J. N. & JENSEN, T. C. 2005. X-ray computed tomography in large bubble columns. *Chemical Engineering Science,* 60**,** 6124-6133.

ISHII, M., PARANJAPE, S. S., KIM, S. & SUN, X. 2004. Interfacial structures and interfacial area transport in downward two-phase bubbly flow. *International Journal of Multiphase Flow,* 30**,** 779-801.

ISHII, M. & ZUBER, N. 1979. Drag Coefficient and Relative Velocity in Bubbly, Droplet or Particulate Flows. *Aiche Journal,* 25**,** 843-855.

ISMAIL, I., SHAFQUET, A. & KARSITI, M. N. Application of electrical capacitance tomography and differential pressure measurement in an air-water bubble column for online analysis of void fraction. 2011 Fourth International Conference on Modeling, Simulation and Applied Optimization, 19-21 April 2011 2011. 1-6.

JAKOBSEN, H. A., LINDBORG, H. & DORAO, C. A. 2005. Modeling of bubble column reactors: Progress and limitations. *Industrial & Engineering Chemistry Research,* 44**,** 5107-5151.

JIANG, X. D., YANG, N. & YANG, B. L. 2016. Computational fluid dynamics simulation of hydrodynamics in the riser of an external loop airlift reactor. *Particuology,* 27**,** 95-101.

JIN, H., WANG, M. & WILLIAMS, R. A. 2007. Analysis of bubble behaviors in bubble columns using electrical resistance tomography. *Chemical Engineering Journal,* 130**,** 179-185.

JIN, H. B., YANG, S. H., HE, G. X., GUO, Z. W. & TONG, Z. M. 2005. An experimental study of holdups in large-scale p-xylene oxidation reactors using the gamma-ray attenuation approach. *Chemical Engineering Science,* 60**,** 5955-5961.

JOSHI, J. B. 2001. Computational flow modelling and design of bubble column reactors. *Chemical Engineering Science,* 56**,** 5893-5933.

JOSHI, J. B., NANDAKUMAR, K., EVANS, G. M., PAREEK, V. K., GUMULYA, M. M., SATHE, M. J. & KHANWALE, M. A. 2017. Bubble generated turbulence and direct numerical simulations. *Chemical Engineering Science,* 157**,** 26-75.

KATAOKA, I. & SERIZAWA, A. 1989. Basic equations of turbulence in gas-liquid two-phase flow. *International Journal of Multiphase Flow,* 15**,** 843-855.

KEMOUN, A., ONG, B. C., GUPTA, P., AL-DAHHAN, M. H. & DUDUKOVIC, M. P. 2001. Gas holdup in bubble columns at elevated pressure via computed tomography. *International Journal of Multiphase Flow,* 27**,** 929-946.

KOLMOGOROV, A. N. 1991. The Local-Structure of Turbulence in Incompressible Viscous-Fluid for Very Large Reynolds-Numbers. *Proceedings of the Royal Society of London Series a-Mathematical Physical and Engineering Sciences,* 434**,** 9-13.

KRISHNA, R. & ELLENBERGER, J. 1996. Gas holdup in bubble column reactors operating in the churn-turbulent flow regime. *Aiche Journal,* 42**,** 2627-2634.

KRISHNA, R. & SIE, S. T. 2000. Design and scale-up of the Fischer-Tropsch bubble column slurry reactor. *Fuel Processing Technology,* 64**,** 73-105.

KRISHNA, R., URSEANU, M. I., VAN BATEN, J. M. & ELLENBERGER, J. 1999. Influence of scale on the hydrodynamics of bubble columns operating in the churn-turbulent regime: experiments vs. Eulerian simulations. *Chemical Engineering Science,* 54**,** 4903-4911.

KRISHNA, R. & VAN BATEN, J. M. 1999. Simulating the motion of gas bubbles in a liquid. *Nature,* 398**,** 208-208.

KRISHNA, R. & VAN BATEN, J. M. 2001a. Eulerian simulations of bubble columns operating at elevated pressures in the churn turbulent flow regime. *Chemical Engineering Science,* 56**,** 6249-6258.

KRISHNA, R. & VAN BATEN, J. M. 2001b. Scaling up bubble column reactors with the aid of CFD. *Chemical Engineering Research & Design,* 79**,** 283-309.

KULKARNI, A. A. & JOSHI, J. B. 2005. Bubble formation and bubble rise velocity in gas-liquid systems: A review. *Industrial & Engineering Chemistry Research,* 44**,** 5873-5931.

KUMAR, S. & RAMKRISHNA, D. 1996. On the solution of population balance equations by discretization .1. A fixed pivot technique. *Chemical Engineering Science,* 51**,** 1311-1332.

KUMAR, S. B., MOSLEMIAN, D. & DUDUKOVIC, M. P. 1997. Gas-holdup measurements in bubble columns using computed tomography. *Aiche Journal,* 43**,** 1414-1425.

LAIN, S. & SOMMERFELD, M. 2003. Turbulence modulation in dispersed two-phase flow laden with solids from a Lagrangian perspective. *International Journal of Heat and Fluid Flow,* 24**,** 616-625.

LANCE, M. & BATAILLE, J. 1991. Turbulence in the Liquid-Phase of a Uniform Bubbly Air Water-Flow. *Journal of Fluid Mechanics,* 222**,** 95-118.

LAUNDER, B. E. 1989. Second-moment closure and its use in modelling turbulent industrial flows. *International Journal for Numerical Methods in Fluids,* 9**,** 963-985.

LEE, D. J., LUO, X. & FAN, L. S. 1999. Gas disengagement technique in a slurry bubble column operated in the coalesced bubble regime. *Chemical Engineering Science,* 54**,** 2227-2236.

LEGENDRE, D., ZENIT, R. & VELEZ-CORDERO, J. R. 2012. On the deformation of gas bubbles in liquids. *Physics of Fluids,* 24.

LEHR, F. & MEWES, D. 2001. A transport equation for the interfacial area density applied to bubble columns. *Chemical Engineering Science,* 56**,** 1159-1166.

LEHR, F., MILLIES, M. & MEWES, D. 2002. Bubble-size distributions and flow fields in bubble columns. *Aiche Journal,* 48**,** 2426-2443.

LEWIS, W. K. & WHITMAN, W. G. 1924. Principles of Gas Absorption. *Industrial & Engineering Chemistry,* 16**,** 1215-1220.

LI, J. H., GE, W., WANG, W. & YANG, N. 2010. Focusing on the meso-scales of multi-scale phenomena-In search for a new paradigm in chemical engineering. *Particuology,* 8**,** 634-639.

LIAO, Y. X., RZEHAK, R., LUCAS, D. & KREPPER, E. 2015. Baseline closure model for dispersed bubbly flow: Bubble coalescence and breakup. *Chemical Engineering Science,* 122**,** 336-349.

LISTER, J. D., SMIT, D. J. & HOUNSLOW, M. J. 2004. Adjustable discretized population balance for growth and aggregation. *AIChE Journal,* 41**,** 591-603.

LIU, Y. F. & HINRICHSEN, O. 2014. Study on CFD-PBM turbulence closures based on k-epsilon and Reynolds stress models for heterogeneous bubble column flows. *Computers & Fluids,* 105**,** 91-100.

LIU, Z. Q. & LI, B. K. 2018. Scale-adaptive analysis of Euler-Euler large eddy simulation for laboratory scale dispersed bubbly flows. *Chemical Engineering Journal,* 338**,** 465-477.

LO, S. & ZHANG, D. 2009. *Modelling of Break-Up and Coalescence in Bubbly Two-Phase Flows*.

LOPEZ DE BERTODANO, M. 1992. *Turbulent bubbly two-phase flow in a triangular duct.* Ph.D. thesis, Rensselaer Polytechnic Institute, Troy, New York.

LUO, H. 1993. *Coalescence, Breakup and Liuqid Circulation in Bubble Column Reactors.* PhD thesis PhD thesis, PhD thesis from the Norwegian Institute of Technology.

LUO, H. & SVENDSEN, H. F. 1996. Theoretical model for drop and bubble breakup in turbulent dispersions. *Aiche Journal,* 42**,** 1225-1233.

LUO, X. K., LEE, D. J., LAU, R., YANG, G. Q. & FAN, L. S. 1999. Maximum stable bubble size and gas holdup in high-pressure slurry bubble columns. *Aiche Journal,* 45**,** 665-680.

MA, T., ZIEGENHEIN, T., LUCAS, D. & FROHLICH, J. 2016. Large eddy simulations of the gas-liquid flow in a rectangular bubble column. *Nuclear Engineering and Design,* 299**,** 146-153.

MANJREKAR, O. N. & DUDUKOVIC, M. P. 2015. Application of a 4-point optical probe to a Slurry Bubble Column Reactor. *Chemical Engineering Science,* 131**,** 313-322.

MANJREKAR, O. N., SUN, Y. J., HE, L., TANG, Y. J. & DUDUKOVIC, M. P. 2017. Hydrodynamics and mass transfer coefficients in a bubble column photo-bioreactor. *Chemical Engineering Science,* 168**,** 55-66.

MARCHISIO, D. L., VIGIL, R. D. & FOX, R. O. 2003. Quadrature method of moments for aggregation-breakage processes. *Journal of Colloid and Interface Science,* 258**,** 322-334.

MENDELSON HARVEY, D. 1967. The prediction of bubble terminal velocities from wave theory. *AIChE Journal,* 13**,** 250-253.

MENDEZ-DIAZ, S., SERRANO-GARCIA, J. C., ZENIT, R. & HERNANDEZ-CORDERO, J. A. 2013. Power spectral distributions of pseudo-turbulent bubbly flows. *Physics of Fluids,* 25.

MENZEL, T., WEIDE, T. I. D., STAUDACHER, O., WEIN, O. & ONKEN, U. 1990. Reynolds Shear-Stress for Modeling of Bubble Column Reactors. *Industrial & Engineering Chemistry Research,* 29**,** 988-994.

MERCADO, J. M., GOMEZ, D. C., VAN GILS, D., SUN, C. & LOHSE, D. 2010. On bubble clustering and energy spectra in pseudo-turbulence. *Journal of Fluid Mechanics,* 650**,** 287-306.

METRAILLER, D., REBOUX, S. & LAKEHAL, D. 2017. Near-wall turbulence-bubbles interactions in a channel flow at Re-tau=400: A DNS investigation. *Nuclear Engineering and Design,* 321**,** 180-189.

MITRE, J. F., TAKAHASHI, R. S. M., RIBEIRO, C. P. & LAGE, P. L. C. 2010. Analysis of breakage and coalescence models for bubble columns. *Chemical Engineering Science,* 65**,** 6089-6100.

MOORE, D. W. 2006. The velocity of rise of distorted gas bubbles in a liquid of small viscosity. *Journal of Fluid Mechanics,* 23**,** 749-766.

MUDDE, R. F., GROEN, J. S. & VANDENAKKER, H. E. A. 1997. Liquid velocity field in a bubble column: LDA experiments. *Chemical Engineering Science,* 52**,** 4217-4224.

MUDDE, R. F. & SIMONIN, O. 1999. Two- and three-dimensional simulations of a bubble plume using a two-fluid model. *Chemical Engineering Science,* 54**,** 5061-5069.

MUKIN, R. V. 2014. Modeling of bubble coalescence and break-up in turbulent bubbly flow. *International Journal of Multiphase Flow,* 62**,** 52-66.

MURAI, Y., SONG, X. Q., TAKAGI, T., ISHIKAWA, M., YAMAMOTO, F. & OHTA, J. 2000. Inverse energy cascade structure of turbulence in a bubbly flow (PIV measurement and results). *Jsme International Journal Series B-Fluids and Thermal Engineering,* 43**,** 188-196.

NGUYEN, V. T., SONG, C. H., BAE, B. U. & EUH, D. J. 2013. Modeling of bubble coalescence and break-up considering turbulent suppression phenomena in bubbly two-phase flow. *International Journal of Multiphase Flow,* 54**,** 31-42.

NICENO, B., DHOTRE, M. T. & DEEN, N. G. 2008. One-equation sub-grid scale (SGS) modelling for Euler-Euler large eddy simulation (EELES) of dispersed bubbly flow. *Chemical Engineering Science,* 63**,** 3923-3931.

OEY, R. S., MUDDE, R. F. & VAN DEN AKKER, H. E. A. 2003. Sensitivity study on interfacial closure laws in two-fluid bubbly flow simulations. *Aiche Journal,* 49**,** 1621-1636.

OKAWA, T., TANAKA, T., KATAOKA, I. & MORI, M. 2003. Temperature effect on single bubble rise characteristics in stagnant distilled water. *International Journal of Heat and Mass Transfer,* 46**,** 903-913.

OLMOS, E., GENTRIC, C., VIAL, C., WILD, G. & MIDOUX, N. 2001. Numerical simulation of multiphase flow in bubble column reactors. Influence of bubble coalescence and break-up. *Chemical Engineering Science,* 56**,** 6359-6365.

PAN, Y., DUDUKOVIC, M. P. & CHANG, M. 1999. Dynamic simulation of bubbly flow in bubble columns. *Chemical Engineering Science,* 54**,** 2481-2489.

PAREKH, J. & RZEHAK, R. 2018. Euler-Euler multiphase CFD-simulation with full Reynolds stress model and anisotropic bubble-induced turbulence. *International Journal of Multiphase Flow,* 99**,** 231-245.

PATEL, A. K. & THORAT, B. N. 2008. Gamma ray tomography - An experimental analysis of fractional gas hold-up in bubble columns. *Chemical Engineering Journal,* 137**,** 376-385.

PFLEGER, D. & BECKER, S. 2001. Modelling and simulation of the dynamic flow behaviour in a bubble column. *Chemical Engineering Science,* 56**,** 1737-1747.

POELMA, C., WESTERWEEL, J. & OOMS, G. 2007. Particle-fluid interactions in grid-generated turbulence. *Journal of Fluid Mechanics,* 589**,** 315-351.

PRAKASH, V. N., MERCADO, J. M., VAN WIJNGAARDEN, L., MANCILLA, E., TAGAWA, Y., LOHSE, D. & SUN, C. 2016. Energy spectra in turbulent bubbly flows. *Journal of Fluid Mechanics,* 791**,** 174-190.

PRINCE, M. J. & BLANCH, H. W. 1990. Bubble Coalescence and Break-up in Air-Sparged Bubble-Columns. *Aiche Journal,* 36**,** 1485-1499.

QIN, C. P., CHEN, C., XIAO, Q., YANG, N., YUAN, C. S., KUNKELMANN, C., CETINKAYA, M. & MULHEIMS, K. 2016. CFD-PBM simulation of droplets size distribution in rotor-stator mixing devices. *Chemical Engineering Science,* 155**,** 16-26.

RAMPURE, M. R., KULKARNI, A. A. & RANADE, V. V. 2007. Hydrodynamics of bubble column reactors at high gas velocity: Experiments and computational fluid dynamics (CFD) Simulations. *Industrial & Engineering Chemistry Research,* 46**,** 8431-8447.

RANADE, V. V. & TAYALIA, Y. 2001. Modelling of fluid dynamics and mixing in shallow bubble column reactors: influence of sparger design. *Chemical Engineering Science,* 56**,** 1667-1675.

REICHARDT, T. & SOMMERFELD, M. Stereoscopic Imaging for Analysing Bubble Oscillation in Turbulence. 14th International Symposium Application of Laser Techniques to Fluid Mechanics, 2008 Lisbon.

REILLY, I. G., SCOTT, D. S., DEBRUIJN, T. J. W. & MACINTYRE, D. 1994. The Role of Gas-Phase Momentum in Determining Gas Holdup and Hydrodynamic Flow Regimes in Bubble-Column Operations. *Canadian Journal of Chemical Engineering,* 72**,** 3-12.

RENSEN, J., LUTHER, S. & LOHSE, D. 2005. The effect of bubbles on developed turbulence. *Journal of Fluid Mechanics,* 538**,** 153-187.

RIBOUX, G., LEGENDRE, D. & RISSO, F. 2013. A model of bubble-induced turbulence based on large-scale wake interactions. *Journal of Fluid Mechanics,* 719**,** 362-387.

RIBOUX, G., RISSO, F. & LEGENDRE, D. 2010. Experimental characterization of the agitation generated by bubbles rising at high Reynolds number. *Journal of Fluid Mechanics,* 643**,** 509-539.

RISSO, F. 2011. Theoretical model for k(-3) spectra in dispersed multiphase flows. *Physics of Fluids,* 23.

RISSO, F. & ELLINGSEN, K. 2002. Velocity fluctuations in a homogeneous dilute dispersion of high-Reynolds-number rising bubbles. *Journal of Fluid Mechanics,* 453**,** 395-410.

RISSO, F., ROIG, V., AMOURA, Z., RIBOUX, G. & BILLET, A. M. 2008. Wake attenuation in large Reynolds number dispersed two-phase flows. *Philosophical Transactions of the Royal Society a-Mathematical Physical and Engineering Sciences,* 366**,** 2177-2190.

ROGHAIR, I., MERCADO, J. M., ANNALAND, M. V., KUIPERS, H., SUN, C. & LOHSE, D. 2011. Energy spectra and bubble velocity distributions in pseudo-turbulence: Numerical simulations vs. experiments. *International Journal of Multiphase Flow,* 37**,** 1093-1098.

ROIG, V. & DE TOURNEMINE, A. L. 2007. Measurement of interstitial velocity of homogeneous bubbly flows at low to moderate void fraction. *Journal of Fluid Mechanics,* 572**,** 87-110.

RUZICKA, M. C., DRAHOS, J., FIALOVA, M. & THOMAS, N. H. 2001. Effect of bubble column dimensions on flow regime transition. *Chemical Engineering Science,* 56**,** 6117-6124.

RUZICKA, M. C., DRAHOS, J., MENA, P. C. & TEIXEIRA, J. A. 2003. Effect of viscosity on homogeneous-heterogeneous flow regime transition in bubble columns. *Chemical Engineering Journal,* 96**,** 15-22.

RUZICKA, M. C., VECER, M. M., ORVALHO, S. & DRAHOS, J. 2008. Effect of surfactant on homogeneous regime stability in bubble column. *Chemical Engineering Science,* 63**,** 951-967.

RZEHAK, R. & KREPPER, E. 2013a. CFD modeling of bubble-induced turbulence. *International Journal of Multiphase Flow,* 55**,** 138-155.

RZEHAK, R. & KREPPER, E. 2013b. Closure models for turbulent bubbly flows: A CFD study. *Nuclear Engineering and Design,* 265**,** 701-711.

SATO, Y. & SEKOGUCHI, K. 1975. Liquid velocity distribution in two-phase bubble flow. *International Journal of Multiphase Flow,* 2**,** 79-95.

SCHILLER, L. & NAUMANN, A. 1935. A drag coefficient correlation. *Z. Ver. Deutsch. Ing,* 77**,** 318-320.

SCHLEGEL, J. P., HIBIKI, T. & ISHII, M. 2015. Two-group modeling of interfacial area transport in large diameter channels. *Nuclear Engineering and Design,* 293**,** 75-86.

SCHMIDT, D. & VELTEN, K. 2016. Numerical simulation of bubble flow homogenization in industrial scale wine fermentations. *Food and Bioproducts Processing,* 100**,** 102-117.

SHAH, Y. T., KELKAR, B. G., GODBOLE, S. P. & DECKWER, W. D. 1982. Design Parameters Estimations for Bubble Column Reactors. *Aiche Journal,* 28**,** 353-379.

SHINNAR, R. & CHURCH, J. M. 1960. Statistical Theories of Turbulence In ... Predicting Particle Size in Agitated Dispersions. *Industrial and Engineering Chemistry,* 52**,** 253-256.

SILVA, M. K., D'AVILA, M. A. & MORI, M. 2012. Study of the interfacial forces and turbulence models in a bubble column. *Computers & Chemical Engineering,* 44**,** 34-44.

SIMONIN, O. Eulerian formulation for particle dispersion in turbulent two-phase flows. Proceedings of the Fifth Workshop on Two-Phase Flow Predictions, Erlangen, Germany, 1990.

SMITH, J. S., VALSARAJ, K. T. & THIBODEAUX, L. J. 1996. Bubble column reactors for wastewater treatment .1. Theory and modeling of continuous countercurrent solvent sublation. *Industrial & Engineering Chemistry Research,* 35**,** 1688-1699.

SOKOLICHIN, A., EIGENBERGER, G., LAPIN, A. & LUBBERT, A. 1997. Dynamic numerical simulation of gas-liquid two-phase flows - Euler/Euler versus Euler/Lagrange. *Chemical Engineering Science,* 52**,** 611-626.

SOMMERFELD, M. & BRODER, D. 2009. Analysis of Hydrodynamics and Microstructure in a Bubble Column by Planar Shadow Image Velocimetry. *Industrial & Engineering Chemistry Research,* 48**,** 330-340.

SUGIHARA, K., SANADA, T., SHIROTA, M. & WATANABE, M. 2007. Behavior of single rising bubbles in superpurified water. *Kagaku Kogaku Ronbunshu,* 33**,** 402-408.

SUGIYAMA, K., TAKAGI, S. & MATSUMOTO, Y. 2001. Multi-scale analysis of bubbly flows. *Computer Methods in Applied Mechanics and Engineering,* 191**,** 689-704.

SUN, X. D., KIM, S., ISHII, M. & BEUS, S. G. 2004. Modeling of bubble coalescence and disintegration in confined upward two-phase flow. *Nuclear Engineering and Design,* 230**,** 3-26.

TABIB, M. V., ROY, S. A. & JOSHI, J. B. 2008. CFD simulation of bubble column - An analysis of interphase forces and turbulence models. *Chemical Engineering Journal,* 139**,** 589-614.

THAKRE, S. S. & JOSHI, J. B. 1999. CFD simulation of bubble column reactors: importance of drag force formulation. *Chemical Engineering Science,* 54**,** 5055-5060.

THANG, N. T. & DAVIS, M. R. 1979. Structure of Bubbly Flow through Venturis. *International Journal of Multiphase Flow,* 5**,** 17-37.

THORAT, B. N. & JOSHI, J. B. 2004. Regime transition in bubble columns: experimental and predictions. *Experimental Thermal and Fluid Science,* 28**,** 423-430.

THORAT, B. N., SHEVADE, A. V., BHILEGAONKAR, K. N., AGLAWE, R. H., VEERA, U. P., THAKRE, S. S., PANDIT, A. B., SAWANT, S. B. & JOSHI, J. B. 1998. Effect of sparger design and height to diameter ratio on fractional gas hold-up in bubble columns. *Chemical Engineering Research & Design,* 76**,** 823-834.

TOMIYAMA, A. 1998. Struggle with computational bubble dynamics. *Multiphase Science and Technology, Vol 10 Issue 4 1998***,** 369-405.

TOMIYAMA, A. 2004. *Drag, lift and virtual mass forces acting on a single bubble*.

TOMIYAMA, A., SOU, A., ZUN, I., KANAMI, N. & SAKAGUCHI, T. 1995. Effects of Eötvös Number and Dimensionless Liquid Volumetric Flux on Lateral Motion of a Bubble in a Laminar Duct Flow A2 - Serizawa, Akimi. *In:* FUKANO, T. & BATAILLE, J. (eds.) *Multiphase Flow 1995.* Amsterdam: Elsevier.

TOMIYAMA, A., TAMAI, H., ZUN, I. & HOSOKAWA, S. 2002. Transverse migration of single bubbles in simple shear flows. *Chemical Engineering Science,* 57**,** 1849-1858.

TOYE, D., FRANSOLET, E., SIMON, D., CRINE, M., L'HOMME, G. & MARCHOT, P. 2005. Possibilities and limits of application of electrical resistance tomography in hydrodynamics of bubble columns. *Canadian Journal of Chemical Engineering,* 83**,** 4-10.

TRIPATHI, M. K., SAHU, K. C. & GOVINDARAJAN, R. 2015. Dynamics of an initially spherical bubble rising in quiescent liquid. *Nature Communications,* 6.

TROSHKO, A. A. & HASSAN, Y. A. 2001. A two-equation turbulence model of turbulent bubbly flows. *International Journal of Multiphase Flow,* 27**,** 1965-2000.

TRYGGVASON, G., BUNNER, B., ESMAEELI, A., JURIC, D., AL-RAWAHI, N., TAUBER, W., HAN, J., NAS, S. & JAN, Y. J. 2001. A front-tracking method for the computations of multiphase flow. *Journal of Computational Physics,* 169**,** 708-759.

TSAMOPOULOS, J., DIMAKOPOULOS, Y., CHATZIDAI, N., KARAPETSAS, G. & PAVLIDIS, M. 2008. Steady bubble rise and deformation in Newtonian and viscoplastic fluids and conditions for bubble entrapment. *Journal of Fluid Mechanics,* 601**,** 123-164.

TSUCHIYA, K., SONG, G. H. & FAN, L. S. 1990. Effects of Particle Properties on Bubble Rise and Wake in a 2-Dimensional Liquid-Solid Fluidized-Bed. *Chemical Engineering Science,* 45**,** 1429-1434.

VAN DEN BERG, T. H. 2006. *The effect of bubbles on developed turbulence.* PhD Thesis, University of Twente, The Netherlands.

VAN DEN HENGEL, E. I. V., DEEN, N. G. & KUIPERS, J. A. M. 2005. Application of coalescence and breakup models in a discrete bubble model for bubble columns. *Industrial & Engineering Chemistry Research,* 44**,** 5233-5245.

VANDU, C. O. & KRISHNA, R. 2004. Influence of scale on the volumetric mass transfer coefficients in bubble columns. *Chemical Engineering and Processing,* 43**,** 575-579.

VEERA, U. P. & JOSHI, J. B. 2000. Measurement of gas hold-up profiles in bubble column by gamma ray tomography - Effect of liquid phase properties. *Chemical Engineering Research & Design,* 78**,** 425-434.

VITANKAR, V. S., DHOTRE, M. T. & JOSHI, J. B. 2002. A low Reynolds number k-epsilon model for the prediction of flow pattern and pressure drop in bubble column reactors. *Chemical Engineering Science,* 57**,** 3235-3250.

WANG, T. F., WANG, J. F. & JIN, Y. 2003. A novel theoretical breakup kernel function for bubbles/droplets in a turbulent flow. *Chemical Engineering Science,* 58**,** 4629-4637.

WANG, T. F., WANG, J. F. & JIN, Y. 2005a. Population balance model for gas-liquid flows: Influence of bubble coalescence and breakup models. *Industrial & Engineering Chemistry Research,* 44**,** 7540-7549.

WANG, T. F., WANG, J. F. & JIN, Y. 2005b. Theoretical prediction of flow regime transition in bubble columns by the population balance model. *Chemical Engineering Science,* 60**,** 6199-6209.

WANG, T. F., WANG, J. F. & JIN, Y. 2006. A CFD-PBM coupled model for gas-liquid flows. *Aiche Journal,* 52**,** 125-140.

WARSITO, W., MARASHDEH, Q. & FAN, L. S. 2007. Electrical capacitance volume tomography. *Ieee Sensors Journal,* 7**,** 525-535.

WEGENER, P. P. & PARLANGE, J. Y. 1973. Spherical-Cap Bubbles. *Annual Review of Fluid Mechanics,* 5**,** 79-100.

WEGENER, P. P., SUNDELL, R. E. & PARLANGE, J. Y. 1971. Spherical Cap Bubbles Rising in Liquids. *Zeitschrift Fur Flugwissenschaften,* 19**,** 347-&.

WELLEK, R. M., AGRAWAL, A. K. & SKELLAND, A. H. 1966. Shape of Liquid Drops Moving in Liquid Media. *Aiche Journal*, 12**,** 854-&.

WU, Q. & ISHII, M. 1999. Sensitivity study on double-sensor conductivity probe for the measurement of interfacial area concentration in bubbly flow. *International Journal of Multiphase Flow,* 25**,** 155-173.

WU, Q., KIM, S., ISHII, M. & BEUS, S. G. 1998. One-group interfacial area transport in vertical bubbly flow. *International Journal of Heat and Mass Transfer,* 41**,** 1103-1112.

XIAO, Q., WANG, J., YANG, N. & LI, J. H. 2017. Simulation of the multiphase flow in bubble columns with stability-constrained multi-fluid CFD models. *Chemical Engineering Journal,* 329**,** 88-99.

XIAO, Q., YANG, N. & LI, J. H. 2013. Stability-constrained multi-fluid CFD models for gas-liquid flow in bubble columns. *Chemical Engineering Science,* 100**,** 279-292.

XU, L. J., YUAN, B. R., NI, H. Y. & CHEN, C. X. 2013. Numerical Simulation of Bubble Column Flows in Churn-Turbulent Regime: Comparison of

Bubble Size Models. *Industrial & Engineering Chemistry Research,* 52**,** 6794-6802.

XU, T. T., JIANG, X. D., YANG, N. & ZHU, J. H. 2015. CFD simulation of internal-loop airlift reactor using EMMS drag model. *Particuology,* 19**,** 124-132.

YANG, N., CHEN, J. H., ZHAO, H., GE, W. & LI, J. H. 2007. Explorations on the multi-scale flow structure and stability condition in bubble columns. *Chemical Engineering Science,* 62**,** 6978-6991.

YANG, N., WU, Z. Y., CHEN, J. H., WANG, Y. H. & LI, J. H. 2011. Multi-scale analysis of gas-liquid interaction and CFD simulation of gas-liquid flow in bubble columns. *Chemical Engineering Science,* 66**,** 3212-3222.

YANG, N. & XIAO, Q. 2017. A mesoscale approach for population balance modeling of bubble size distribution in bubble column reactors. *Chemical Engineering Science*, 170**,** 241-250.

YANG, X., THOMAS, N. H., GUO, L. J. & HOU, Y. 2002. Two-way coupled bubble laden mixing layer. *Chemical Engineering Science,* 57**,** 555-564.

YAO, B. P., ZHENG, C., GASCHE, H. E. & HOFMANN, H. 1991. Bubble Behavior and Flow Structure of Bubble-Columns. *Chemical Engineering and Processing,* 29**,** 65-75.

YAO, W. & MOREL, C. 2004. Volumetric interfacial area prediction in upward bubbly two-phase flow. *International Journal of Heat and Mass Transfer,* 47**,** 307-328.

YOUSSEF, A. A., AL-DAHHAN, M. H. & DUDUKOVIC, M. P. 2013. Bubble Columns with Internals: A Review. *International Journal of Chemical Reactor Engineering,* 11.

ZAHRADNIK, J., FIALOVA, M., KASTANEK, F., GREEN, K. D. & THOMAS, N. H. 1995. The Effect of Electrolytes on Bubble Coalescence and Gas Holdup in Bubble-Column Reactors. *Chemical Engineering Research & Design,* 73**,** 341-346.

ZAHRADNIK, J., FIALOVA, M., RUZICKA, M., DRAHOS, J., KASTANEK, F. & THOMAS, N. H. 1997. Duality of the gas-liquid flow regimes in bubble column reactors. *Chemical Engineering Science,* 52**,** 3811-3826.

ZHANG, D., DEEN, N. G. & KUIPERS, J. A. M. 2006. Numerical simulation of the dynamic flow behavior in a bubble column: A study of closures for turbulence and interface forces. *Chemical Engineering Science*, 61**,** 7593-7608.

ZHAO, H. & GE, W. 2007. A theoretical bubble breakup model for slurry beds or three-phase fluidized beds under high pressure. *Chemical Engineering Science,* 62**,** 109-115.

ZHOU, R. T., YANG, N. & LI, J. H. 2017. CFD simulation of gas-liquid-solid flow in slurry bubble columns with EMMS drag model. *Powder Technology,* 314**,** 466-479.

CHAPTER 2: A KINETIC INLET MODEL FOR CFD SIMULATION OF LARGE-SCALE BUBBLE COLUMNS

SUMMARY

For the simulation of industrial-scale bubble column reactors, current approach adopted for modelling the gas distributor as uniform inlets usually oversimplifies the inhomogeneity introduced by the inlets. Direct simulation of the full geometry of gas distributor or sparger brings about enormous pre-processing work and huge computational cost. To circumvent these difficulties in CFD modelling of bubble column flow, a new inlet model has been therefore proposed in this chapter to simplify the modelling of gas distributor without losing the flow features and simulation accuracy. The proposed inlet model is validated by the comparison of the model prediction with the experimental data available based on a number of experiments reported in the open literature and the CFD simulation incorporating the full geometry of gas distributor for bubble columns of small or large diameters. Three different inlet boundary conditions, i.e., the direct simulation of gas distributor, the uniform inlet, and the new inlet model, are compared through the simulation of the total gas holdup, the radial profiles of gas holdup at different cross-sections along the column height, and the axial velocity of liquid at various superficial gas velocities. The simulation results clearly indicate that the new inlet model is capable of achieving a good balance between simulation accuracy and computational cost for the CFD simulation of large-scale bubble column reactors.

1. INTRODUCTION

Bubble columns and their variants have been extensively utilized in chemical or process industries for gas-liquid or gas-liquid-solid reactions, such as oxidation, chlorination, alkylation, polymerization, hydrogenation, and fermentation. These reactors provide higher heat and mass transfer rates while maintaining lower operation and maintenance costs. For the design and scale-up of various processes, a large number of experimental studies have been carried out to investigate the hydrodynamics of gas-liquid flow in bubble columns at different operational parameters. However, these experimental studies(Deckwer, 1992) are usually carried out in lab-scale columns of diameters less than 0.5 m. Experiments on large-diameter columns are seldom reported due to the difficulty or complexity in experimental measurements. With the rapid development of computer technology and computational science in the past two decades, CFD is becoming a powerful tool in understanding the complexity of hydrodynamics. A number of studies have been conducted on various aspects of CFD simulation, e.g., the impact of turbulence models (Masood et al., 2014, Sokolichin and Eigenberger, 1999, Laborde-Boutet et al., 2009), drag forces(Yang et al., 2011, Xiao et al., 2013, Li and Zhong, 2015), lift forces (Wang and Yao, 2016, Lucas et al., 2016)and bubble breakage and coalescence models(Chen et al., 2005b, Bordel et al., 2006, Wang et al., 2006), and the coupling of CFD simulation with mass transfer(Wiemann and Mewes, 2005, Bao et al., 2015) or reaction kinetics(Van Baten and Krishna, 2004, Rigopoulos and Jones, 2003, Troshko and Zdravistch, 2009). Hitherto there are two main issues in CFD simulation of bubble columns. The first one is the sensitivity of simulation on closure models of interfacial momentum exchange, in particular, the drag force and other forces including lift or virtual mass force exerted by the surrounding liquid to the bubbles. There have been some studies regarding the effects of the lift coefficient C_L (Sankaranarayanan and Sundaresan, 2002, Tomiyama, 1998, Delnoij et al., 1997, Sokolichin et al., 2004, Lucas et al., 2005, Lucas and Tomiyama, 2011), and of the virtual mass force(Hunt et al., 1987, Delnoij et al., 1997). However, successful simulations have been reported in literature for either including lift and virtual mass forces(Tabib et al., 2008, Zhang et al., 2006, Rampure et al., 2007, Deen et al., 2001) or only using the drag force (Deen et al., 2000, Krishna and van Baten, 2001, Ranade and Tayalia, 2001). Actually the lift coefficient or lift force, as a result of pressure or velocity gradient, can generally be used to adjust the simulation of radial distribution of gas holdup, especially when the uniform inlet condition is applied. The physical basis of these non-drag forces still requires further investigation. In this study we temporarily isolate these effects from that of drag force and inlet conditions. The second issue is the simplification of gas distributor or sparger as a uniform inlet or the high computational cost arising from the direct modelling of the full geometry of gas distributors. The latter issue is less covered in literature but still a challenge for the simulation of industrial-scale columns.

Gas distributors or spargers are reported to have great influence on flow behaviours. Hills (1974) and Camarasa et al. (1999) showed that the gas holdup, liquid velocity, bubble size and bubble velocity altered significantly when using different gas distributors, e.g., the sieve plates of various configurations, the porous plates, the multi- or single- orifice nozzles. Mudde et al. (2009)

presented a densely arranged multi-needle sparger to obtain a uniform bubble injection, and found that the homogeneous flow regime was extended up to a gas fraction of 55%. Haque et al. (1986) reported that the mixing time and total gas holdup were significantly affected by sparger designs. Moreover, Dhotre and Joshi (2007) stated that the distributor of different configurations generated the initial bubbles of a certain size and gas holdup, which in turn influenced the overall flow pattern. Some researchers have studied the effect of distributors by using CFD modelling. Ranade and Tayalia (2001) modelled a shallow bubble column of single- or double-ring spargers, and the simulation indicated that the fluid dynamics and mixing in shallow bubble column reactors were controlled by sparger configuration. Akhtar et al. (2006) simulated the perforated plates with different open areas, indicating that including the real gas distributors in simulation can lead to asymmetric flow patterns which were otherwise smoothened when a uniform gas source was used in CFD simulation. Dhotre and Joshi (2007) studied the influence of the size, location, opening area and hole diameter of nozzles on the flow pattern of CFD simulation. They analysed the flow pattern within the gas chamber under the distributor and velocities through all the holes, and found that the chamber configurations affected the uniformity of gas distribution in the sparger region of bubble columns. It appears that an interaction exists between the chamber and sparger, which may affect the stability of the plume. Bahadori and Rahimi (2007) investigated the influence of the number of orifices on gas hold-up and liquid phase velocity by CFD modelling. They reported that increasing the number of orifices in the sparger increased the total gas holdup in a shallow bubble column and each local orifice contributed to liquid circulation and mixing. Li et al. (2009) reported that the distributor configurations had strong impact on the asymmetric flow and mixing characteristics in the vicinity of gas distributor. Rampure et al. (2009) included the plenum area under the gas distributor into the CFD simulation. They modelled the perforated plate as a porous zone and adopted empirical correlations to obtain the model input parameters. Compared to the cases using uniform inlet conditions or directly modelling the gas distributors, the purpose of this study is to develop a new kinetic inlet model which could equivalently reflect the kinetic information of gas velocity gradient and the inhomogeneity introduced through the inlet, without the need to directly model the real inlet geometry. It may provide a simpler way without the necessity to simulate the perforated plate as well as the gas chamber underneath, while the simulation accuracy is still guaranteed.

Direct modelling of the full geometry of gas distributor or specifying the mass sources at the real positions of holes has been reported in literature (Ziegenhein et al., 2013, Tabib et al., 2008). However, this may also lead to a significant increase in pre-processing work, grid number and complexity as well as computational cost. For example, when the number of holes in a gas distributor is around 60 and the hole diameter is larger than 2 mm, it is possible to include every single hole in the simulation of lab-scale bubble columns. Nevertheless, the gas distributors used in industrial-scale columns are far more complicated, involving hundreds of holes with the size around 1 mm. Chen et al. (2005a) used 0.7 mm- or 1.32 mm-diameter holes on perforated plate and stated that it was impossible to include the gas distributor into the simulation due to the fact that the direct modelling of gas distributor would require millions of cells. The computational cost would become unaffordable if more complicated geometries (e.g., heat exchange tubes or internals) need to be investigated, or more transport equations need to be solved, e.g., the three-fluid model for gas, liquid and solid phases, or the population balance equations for bubble coalescence and break-up, or species transport equations to incorporate mass transfer and reaction kinetics.

Some previous CFD studies attempted to simplify the gas distributor as a uniform inlet across the whole bottom surface since this may greatly reduce the number of grids and computational cost. However, this simplification may cause some under-prediction of gas holdup for large diameter columns, which will be further elucidated in this study. Therefore, as a compromise of these two methods, the objective of this work is to propose a new inlet model which is able to reflect the non-uniformity of the gas inlet and achieve the reasonable simulation and meanwhile reduce the computational cost. Section 2 will present the computational models to be used in the simulations and demonstrate the new inlet model. Numerical details in CFD simulations conducted in this work will be given in Section 3. Section 4 provides the simulations utilizing the new inlet model in small- and large-diameter columns. The simulation validates the new model function, demonstrating its capability to achieve the balance between simulation accuracy and computational cost in CFD simulation of large-scale bubble column reactors.

2. MATHEMATICAL FORMULATION

2.1 Computational models

The equations of Eulerian-Eulerian approach used in this work are given as below, consisting of mass and momentum balance equations to describe the hydrodynamics of the continuous liquid or disperse gas phases:

$$\frac{\partial(\rho_k \alpha_k)}{\partial t} + \nabla \cdot (\rho_k \alpha_k \boldsymbol{u}_k) = 0 \tag{2-1}$$

$$\frac{\partial(\rho_k \alpha_k \boldsymbol{u}_k)}{\partial t} + \nabla \cdot (\rho_k \alpha_k \boldsymbol{u}_k \boldsymbol{u}_k) = -\alpha_k \nabla p + \nabla \cdot \boldsymbol{\tau}_k + \rho_k \alpha_k \boldsymbol{g} + \boldsymbol{F}_k \tag{2-2}$$

Closure laws are required for the phase interaction forces. In this study, only the drag force is employed as it is considered to be the predominant interfacial force in gas-liquid flows in bubble columns (Laborde-Boutet et al., 2009, Larachi et al., 2006). The drag force is formulated as:

$$\boldsymbol{F}_D = \frac{3}{4}\frac{C_D}{d_b}\rho_l \alpha_g \left|\boldsymbol{u}_g - \boldsymbol{u}_l\right| \left(\boldsymbol{u}_g - \boldsymbol{u}_l\right) \tag{2-3}$$

In the equation above, C_D/d_b is a critical lumped parameter in CFD simulation. It can be either calculated from several correlations in literature, or be derived from the DBS drag model(Yang et al., 2011, Yang, 2012). The DBS model extended the energy minimization multi-scale (EMMS) approach for gas-solid fluidization to gas-liquid flows, and its physical background and further details can be found in the previous publications(Yang et al., 2011, Xiao et al., 2013, Yang, 2012, Yang et al., 2007, Chen et al., 2009). The lumped ratio was formulated by Xiao et al. (2013) as:

$$C_D / d_b = \begin{cases} 431.14 - 6729.02U_g + 35092.2U_g^2, & U_g \le 0.101\ m \cdot s^{-1} \\ 122.49 - 553.94U_g + 741.24U_g^2, & U_g > 0.101\ m \cdot s^{-1} \end{cases} \tag{2-4}$$

The standard k-ε model for the two-phase mixture is employed as given below:

$$\frac{\partial(\alpha_l\rho_l k_l)}{\partial t} + \nabla\cdot(\alpha_l\rho_l k_l \boldsymbol{u}_k) = \nabla\cdot\left[\alpha_l\left(\mu_l + \frac{\mu_{eff,l}}{\sigma_k}\right)\nabla k_l\right] + \alpha_l\left(G_{k,l} - \rho_l\varepsilon_l\right) \tag{2-5}$$

$$\frac{\partial(\alpha_l\rho_l \varepsilon_l)}{\partial t} + \nabla\cdot(\alpha_l\rho_l \varepsilon_l \boldsymbol{u}_k) = \nabla\cdot\left[\alpha_l\left(\mu_l + \frac{\mu_{eff,l}}{\sigma_k}\right)\nabla \varepsilon_l\right] + \alpha_l\frac{\varepsilon_l}{k_l}\left(C_{1\varepsilon}G_{k,l} - C_{2\varepsilon}\rho_l\varepsilon_l\right) \tag{2-6}$$

2.2 A new inlet model

As mentioned in the introduction section, the CFD modelling of large-scale bubble columns by employing the actual geometry of gas distributor may impose an insurmountable difficulty due to the constraint of mesh generation and computational cost. It would be desired and practical if a kinetic model could be introduced to incorporate the flow behaviour but avoid modelling the actual geometry of gas distributor. A new inlet model is proposed here to account for the effect of entrance velocity gradient with an attractive benefit of significant reduction of the number of mesh cells. This model attempts to take the number and size of the perforated holes into consideration for a particular type of gas distributor, i.e., the perforated plates. For this type of distributor, the gas flows through each perforated hole to form jet arrays, generating a velocity fluctuation around the holes along the radial direction due to the entrainment of the carrier fluid. Although these local jet flows may not essentially affect the hydrodynamic behaviours if the height to dimension ratio *H/D* is larger enough, there can be a very strong influence on the flow pattern in the non-fully-developed region. Moreover, Guan et al. (2015) reported that the flow pattern in bubble columns with internal tubes was always not fully developed due to the existence of internal tube banks. In this case, the inlet condition may play important roles.

Behkish et al. (2006) proposed a correlation of gas holdup in bubble columns or slurry bubble columns based on 3881 experimental data points. The model parameters included the pressure, temperature, gas superficial velocity, solid concentration, particle density/concentration, reactor size, and gas sparger characteristics. Rearranging the correlation of Behkish et al. (2006) leads to

$$\tilde{u}_s = 2.24\times 10^2 \times \alpha^{1.8} \times \left(\frac{\mu_L^{0.313} \sigma_L^{0.486}}{\rho_L^{0.747} \rho_G^{0.319}} \right) \times \left(\frac{P_T - P_S}{P_T} \right)^{0.365} \times \left(\frac{D_C}{D_C + 1} \right)^{0.211} \times \Gamma^{-0.095} \times e^{0.436\, X_W} \tag{2-7}$$

where u_s is the superficial gas velocity, α is the gas holdup, and Γ represents the gas distributor parameter. Other parameters are either the physical properties or operational parameters. The local gas holdup is a function of radial position and can be correlated by an exponential function of radial position, as will be demonstrated in Equation (2-14) in the following sections. Hence if we apply Equation (2-7) to the local radial positions, it can be deduced that the local gas velocity could also be expressed as an exponential function of radial position. In general, the fluctuating trend and magnitude of local jet flows could be averaged and approximated by a normal distribution-like function which defines the local gas velocity at a given point on the inlet boundary. Thus, it may be reasonable to assume that the entrance velocity for the gas distributor could be approximated by the exponential function. Based on this consideration, we thus propose the simplified inlet model. It should be pointed out that this approximate approach should be distinguished from the method of modelling the real holes. The new inlet model for a perforated plate could then be formulated as:

$$\tilde{u}_s = \begin{cases} \left(1.5 + \frac{\Gamma}{100}\right) U_g \cdot e^{\frac{-r^2}{b}}, & Ug \le 0.12 m/s \\ \left(0.75 + \frac{\Gamma}{100}\right) U_g \cdot e^{\frac{-r^2}{b}}, & Ug > 0.12 m/s \end{cases} \tag{2-8}$$

which is also subject to the continuity function:

$$Q = \sum \frac{\pi}{4} d_i^2 \cdot u_i = \frac{\pi}{4} D^2 \cdot U_g = \int_0^R \tilde{u}_s \cdot 2\pi r dr \tag{2-9}$$

where d_i and u_i are the diameter and the through hole velocity of i-th inlet hole respectively, r is the non-dimensional radial position, and the parameter b can be determined by solving the continuity function Equation (2-9). Γ is a lumped coefficient representing the influence of gas distributor configurations and defined by Behkish et al. (2006) as:

$$\Gamma = K_d \times N_O d_O^{\alpha} \tag{2-10}$$

K_d is the distributor coefficient that equals 1.364 for perforated plates, N_O is the number of orifice holes on the plate, and d_O is the diameter of orifice holes. The index α depends on the value of ζ, the free area of the distributor:

$$\zeta = N_O \left(\frac{d_O}{D_C}\right)^2 \times 100 \tag{2-11}$$

For perforated plates,

$\alpha = 0.017$, when $\zeta < 0.055$;

$\alpha = 0.303$, when $0.055 \le \zeta \le 0.3$;

$\alpha = 0.293$, when $\zeta > 0.3$.

Table 2-1 lists the distributor parameters for five typical perforated plates. The gas velocity distribution at the inlet is illustrated in Figure 2-1 for five different gas distributors at U_g = 0.1 m/s, and Figure 2-2 shows the velocity profile of distributor 5 at different superficial velocities.

It should be pointed out that an exact inlet model could also be correlated from the CFD simulation of the actual configuration including the gas plenum chamber and the gas distributor with consideration of the liquid height above the gas distributor, such as the work of Rampure et al. (2009). However, Dhotre and Joshi (2007) reported that the gas velocity profile at the holes was not only dependent on the superficial velocity and the number and diameter of orifice holes, but also on the pressure drop of distributor and liquid bulk phase as well as the chamber geometry. Actually an exact simulation of the velocity profile around holes also requires the inclusion of the two-phase flow above the distributor or even an iteration process between the gas chamber and the bulk region of two-phase flow, which is far more complicated and beyond the scope of this study. Here we propose a simplified function to replace the inlet velocity distribution which is only a function of distributor geometry and superficial gas velocity for engineering application.

Table 2-1 Parameters of 5 typical perforated plates.

Configuration	**Hole number**	**Do (mm)**	**Dc (m)**	**do/Dc**	ζ	Γ	**Umax (m/s)**	***b***
1	61	0.4	0.14	0.0029	0.0498	72.8416	0.2228	0.0026
2	121	1.32	0.14	0.0094	1.0757	23.6553	0.1737	0.0038
3	225	1.32	0.19	0.0069	1.086	43.9871	0.1940	0.0060
4	241	3	0.45	0.0067	1.0711	59.9278	0.2099	0.0280
5	301	0.77	0.45	0.0017	0.0881	46.7722	0.1968	0.0326

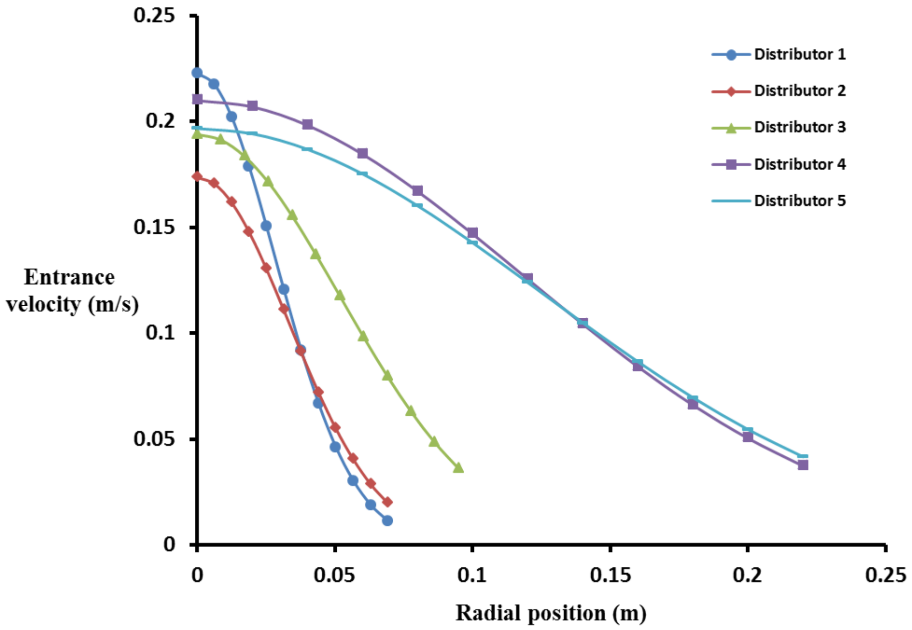

Figure 2-1 Inlet gas velocity profile for different geometrical parameters (*Ug* = 0.1 m/s).

For these five perforated plates with different geometrical configurations, the maximum at the centre of the column are approximately twice the superficial velocity according to the Hagen-Poiseuille's Law.

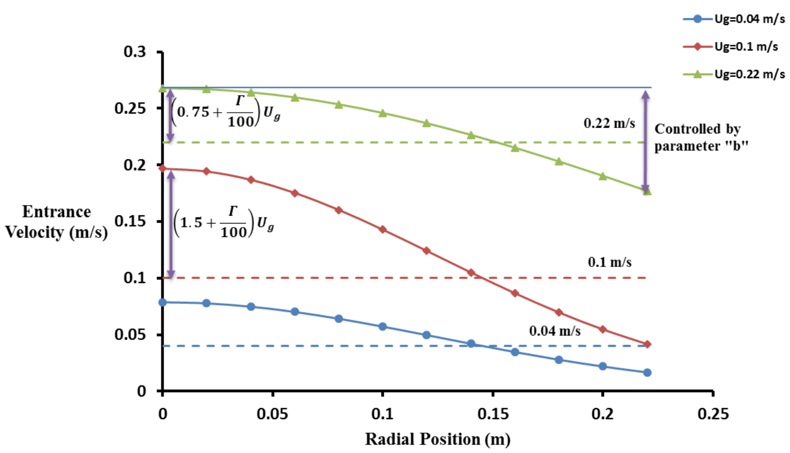

Figure 2-2 Inlet gas velocity profile for Distributor 5 (*Ug* = 0.04, 0.1, 0.22 m/s).

The effects of model parameters are illustrated in Figure 2-2 The maximum value is determined by geometrical parameters, i.e., the ratio $(0.75 + \Gamma/100)$ or $(1.5 + \Gamma/100)$. The slopes of the curve are dependent on the parameter b which can be obtained by solving the continuity function. We may assume that the flow near the distributor region could be approximated by a free-stream flow in a pipe. When the flow rate is relatively lower (0.04～0.1 m/s), the pressure loss is linear to the velocity so that the steepness of the profiles increases. According to Law of Blasius, the sum of viscous shear stress and turbulent stress τ_w can be expressed as $\tau_w = 0.03325\rho U^{7/4}(\upsilon / R)^{1/4}$. Hence when the flow enters the fully-developed heterogeneous (churn-turbulent) regime (U_g > 0.12 m/s), the velocity profiles in the cross-sections close to the entrance of bubble columns tend to be flat and the velocity gradient is restricted to the near wall region.

It should also be pointed out that the new inlet model proposed here has only been tested for perforated plates in which holes are uniformly distributed at the whole cross-section in concentric circles or in a triangular pitch, with the size of holes not exceeding 4 mm and the number of holes more than 60. Although further validation is required, the proposed model is potentially capable of representing distributor configurations beyond this range or other types of gas distributors such as porous plates or multiple-orifice nozzles.

3. SIMULATION DETAILS

To validate the effect of the new inlet model, simulations have been carried out for the air-water bubble columns of Hills (1974). The detail information is listed in Table 2-2.

Table 2-2 Details of experimental setup in Hills (1974).

Column Diameter (m)	Column Height (m)	Observation Height (m)	No. of holes on distributor	Diameter of holes (mm)	ζ	Superficial gas velocity (m/s)
0.138	1.37	0.6	61	0.4	0.0498	0.038~0.127

The average size of cells is about 7 mm for the case of Grid 1 (Figure 2-3) which is equivalent to $14(r) \times 36(\theta) \times 150(z)$ nodes and results in approximately sixty thousand cells in total. The grid sensitivity was further tested in the two stages with a grid refinement of a factor of about 1.3 in all directions. Grid 2 generates twice the total number of cells of Grid 1, and Grid 3 doubles the total number of cells of Grid 2 in a similar manner.

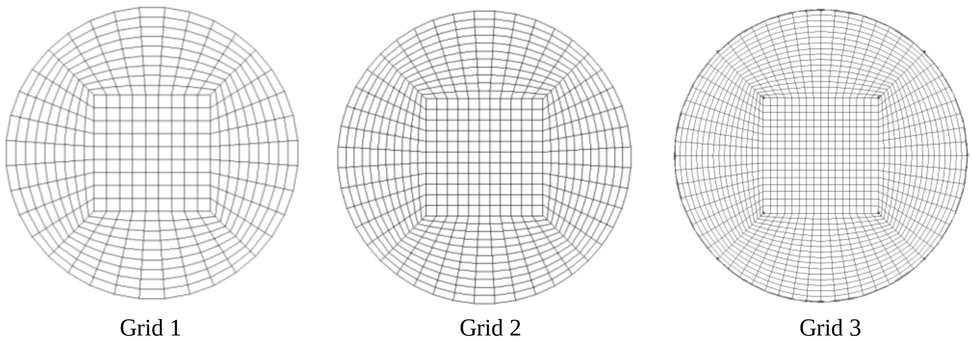

Figure 2-3 Mesh set-up at bottom surface.

3D pressure-based solver of Ansys Fluent® is used in this work. The time step is set to be 0.0005 s in the beginning. When the physical time reaches 10 s, the time step increases to 0.001 s till the flow time reaches 30 s, and then the time step is fixed to be 0.005 s. The quasi-steady state is considered to be achieved after 80 s. Data sampling statistics for the next 80 s is considered to be sufficient to illustrate the time-averaged characteristics of the flow fields. The new inlet model is integrated into the user define function (UDF). The volume fraction of gas phase is set to be 1 at inlet. The outlet boundary is set as a pressure outlet at the top. Non-slip conditions are applied for both liquid and gas phases at the vessel wall. A grid sensitivity test has been conducted for Grid 1, Grid 2 and Grid 3, and they can yield quantitatively the similar results (Figure 2-4), and Grid 2 is used in the succeeding simulations to investigate the effects of inlet models.

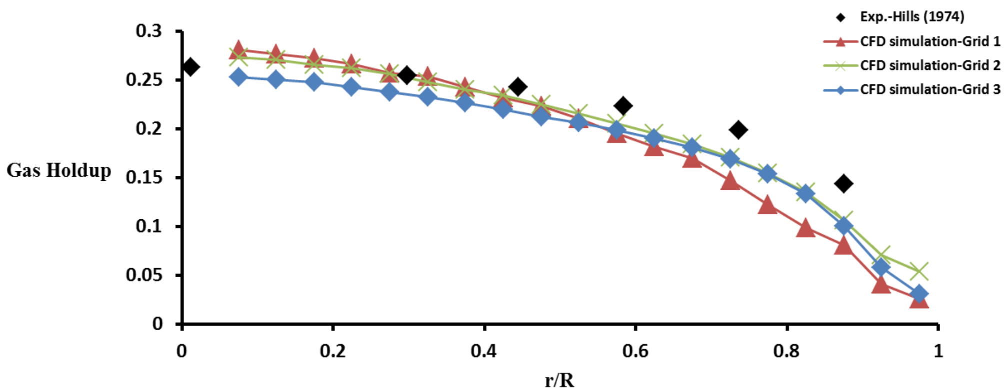

Figure 2-4 Comparison of simulated gas holdup profile with three different grids (Ug = 0.064 m/s).

4. RESULTS AND DISCUSSION

4.1 Validation of the new inlet model

Three cases for different superficial gas velocities are simulated for the Hills system: 0.038, 0.095 and 0.127 m/s, representing the homogenous, transitional, or heterogeneous regimes respectively. The prediction of gas holdup distribution by using the new inlet model is compared with experimental data of Hills (1974) and the simulation of Yang et al. (2011) and Xiao et al. (2013) in which all the gas inlet holes were included.

Figure 2-5 compares the time-averaged gas holdup distribution for three different inlet models at superficial gas velocity U_g=0.095m/s. “Holes” means that all the orifices at the gas distributor are modelled so that the gas is introduced through each orifice holes. “Uniform Inlet” means that the distributor geometry is not modelled and the gas is introduced uniformly through the whole bottom surface of the column. “New Inlet Model” denotes that the gas is introduced through the profile functions of the new inlet model, such as Equation (2-8). Although all the three inlet models achieved reasonable agreements with experimental data, it can be seen that the gas holdup distribution curve tends to be flat for the “Uniform Inlet” case whereas the other two fit the experimental data better.

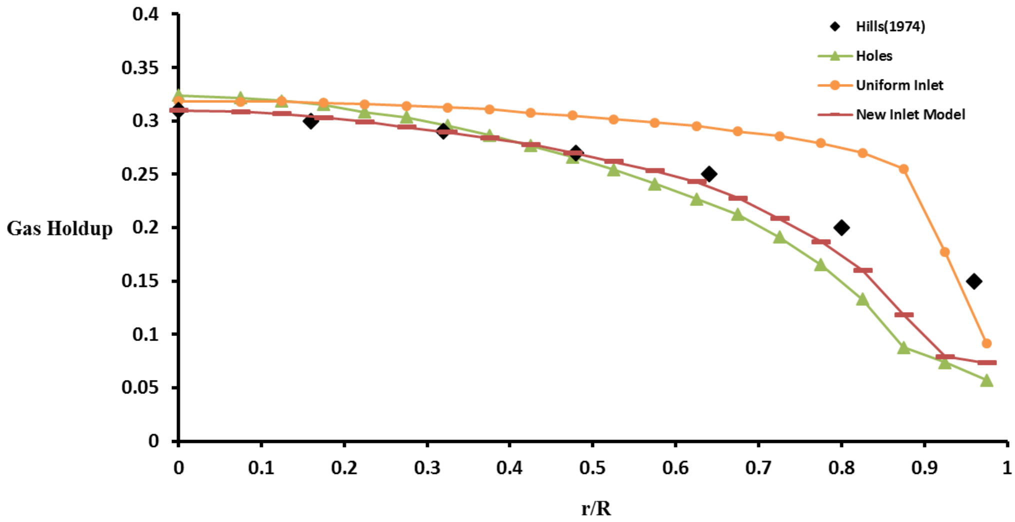

Figure 2-5 Radial distribution of gas holdup using different inlet conditions (Ug = 0.095 m/s, H = 0.6 m, H / D = 4.35).

Figure 2-6 presents the evolution of gas holdup profiles along the column height for the three gas inlet conditions. Since the experimental data of lower H / D ratios is not available, only the simulation results are plotted in the figure. For the "Holes" case, the gas holdup turns out to be a monotonous parabolic profile when H / D = 0.5. This reflects the influence of gas momentum distribution formed by the orifice holes on the sparger. The parabolic profile holds coherently and even rises slightly as a whole with increasing the H / D ratio. On the one hand, for the uniform inlet condition, it allows the gas to be introduced from the entire bottom surface, and the gas holdup profile is shown to be consistently flat at all cross-sections, showing the uniform momentum distribution. On the other hand, the performance of new inlet model is between the "Holes" and "Uniform Inlet" cases. For the new inlet model, it captures the performance of the "Holes" case to some extent, especially the pattern of inlet gas momentum distribution and the resulting parabolic shape of gas holdup profile, even though the absolute magnitudes are not exactly the same. The reason for the difference is that the direct simulation of holes on the sparger actually introduces much higher gas injection velocity at each inlet hole and consequently affects the sparging region. However, the difference becomes smaller for higher *H/D*, as shown in Figure 2-5 (*H*=0.6m, *H/D*=4.35).

The simulations in Figure 2-5 and 2-6 also indicate that, for the new inlet model, the difference in radial profiles for $H / D = 2$ and $H / D = 4.35$ is smaller. This implies that the influence of the inlet condition (or gas distributor) is marginal for higher *H/D*, and the evolution of radial distribution along the height does not change noticeably for each specific distributor.

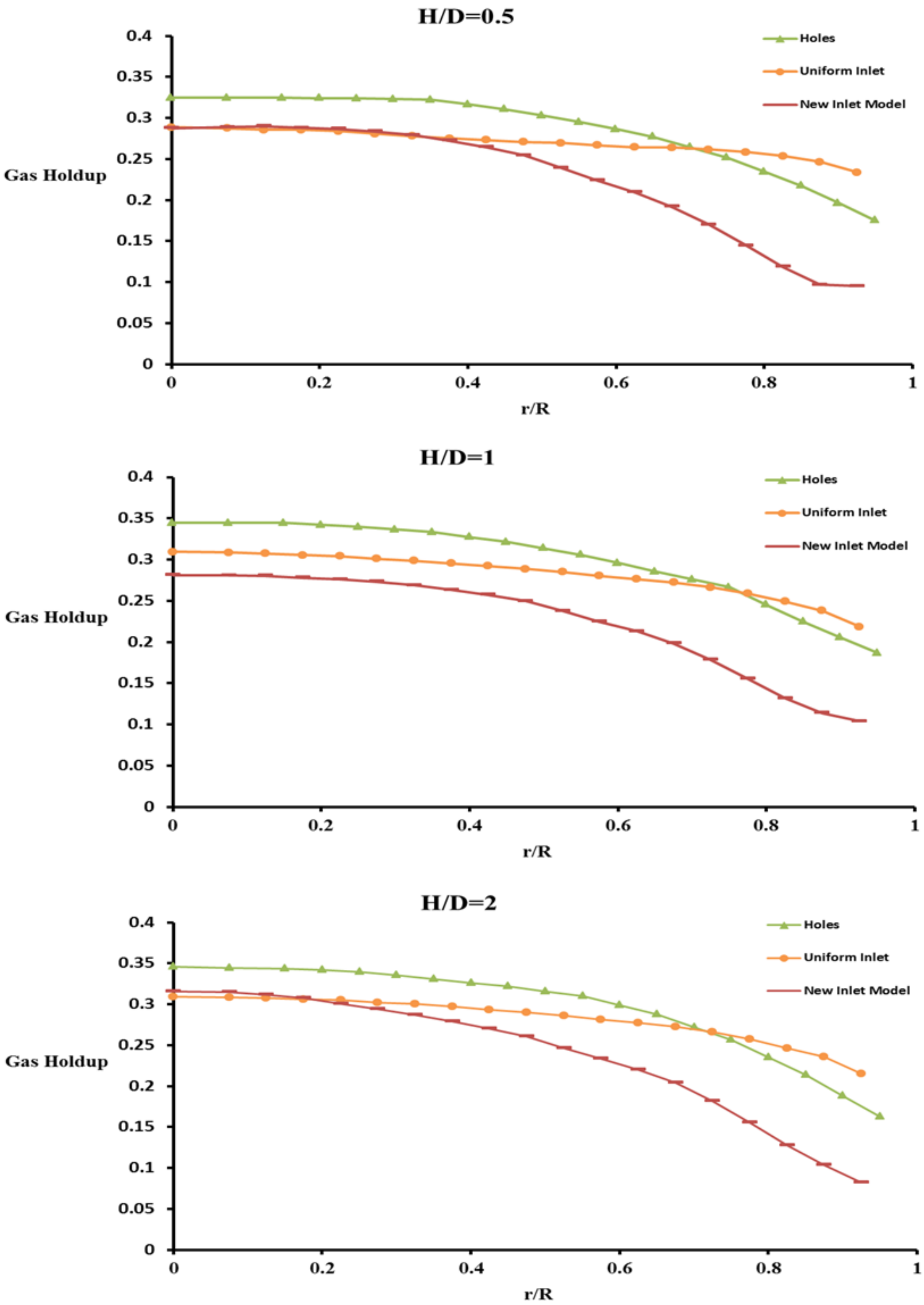

Figure 2-6 Gas holdup radial distribution along the column height (from the top to bottom: H / D =0.5, 1, 2; Ug = 0.095 m/s).

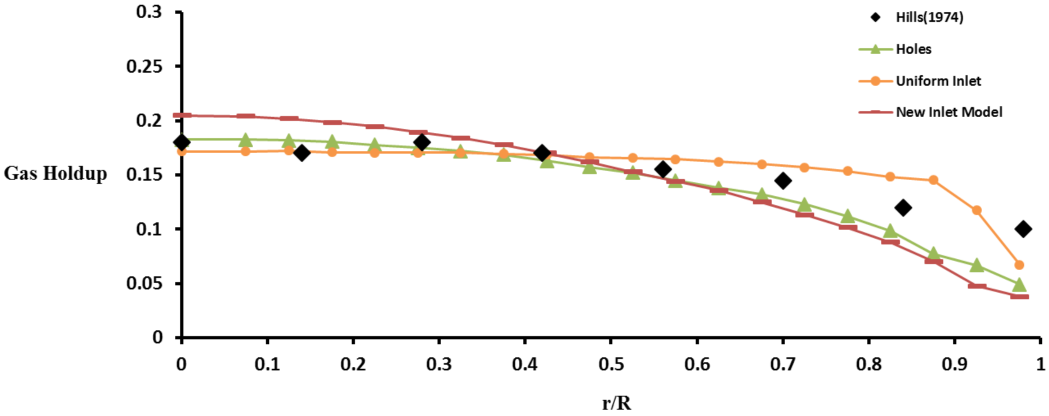

Figure 2-7 Radial distribution of gas holdup using different inlet conditions (Ug = 0.038 m/s, H = 0.6 m).

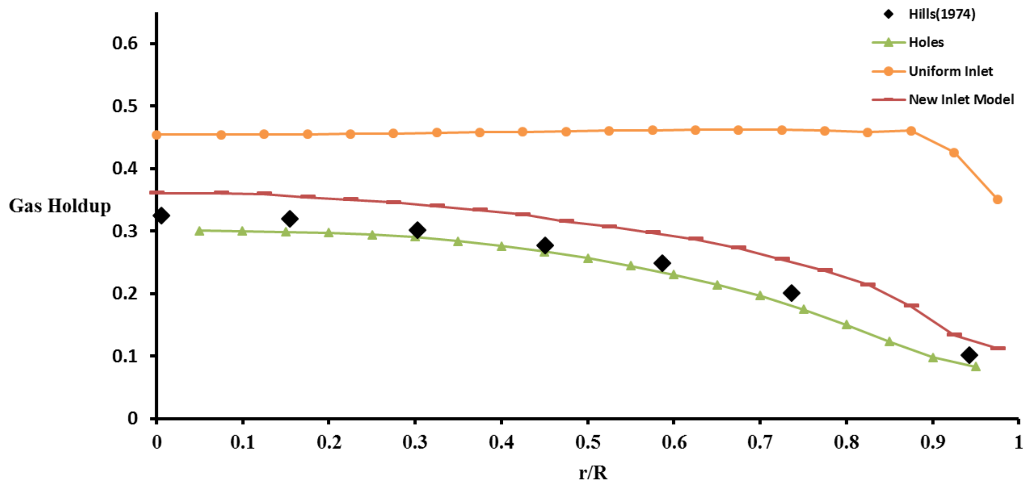

Figure 2-8 Radial distribution of gas holdup using different inlet conditions (Ug = 0.127 m/s, H = 0.6 m).

Figure 2-7 and Figure 2-8 present the radial distribution of gas holdup at Ug=0.038 m/s and Ug=0.127 m/s respectively. The results indicate that the uniform inlet overestimates the gas holdup at higher gas flow rate. While the “Holes” model performs the best, the new inlet model can also yield reasonable simulation. It should be pointed out that some previous studies have used the uniform inlet condition and also obtained good simulation results. This issue is complicated and, to our knowledge, it is related to two aspects. Firstly, the performance of uniform inlet is problem-dependent and a critical evaluation is still lacking on the simulation of different operating conditions and column geometries. Secondly, the simulation is also pertinent to the models of drag force or non-drag forces such as lift and virtual mass force. Some studies involved the lift force for the cases of the uniform inlet conditions, and hence the radial profile of gas holdup becomes parabolic. However, the simulation is also sensitive to the choice of lift coefficient. This article only focuses on the inlet conditions and the effects of non-drag forces have been omitted. We cautiously point out that the interaction between inlet conditions and physical models may be important but has not yet been analyzed or reported in literature. Although the simulation of the new inlet model in Figure 2-7 and Figure 2-8 did not perfectly fit the experimental data, acceptable agreement is achieved with the error less than 20% for the majority part of the curves. The new inlet model reasonably allocates the gas momentum onto the cross-section at the bottom by the distribution profile functions, and hence the prediction can qualitatively capture the main characteristics of the experiments and the "Holes" case.

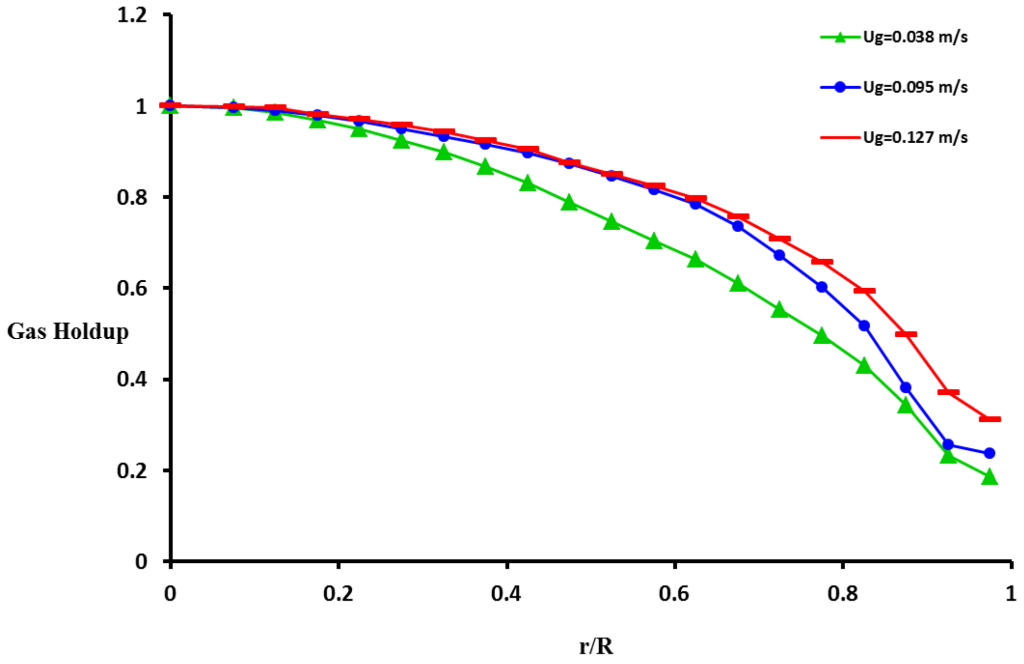

Figure 2-9 Radial distribution of normalized gas holdup profile using new inlet model (H = 0.6 m).

Figure 2-9 presents the gas holdup profile normalised by the centre line values at three different superficial gas velocities (Ug = 0.038, 0.095 and 0.127 m/s). It can be seen that the three profiles of gas holdup bear some analogy. In this case, it is reasonable to establish the following equation for gas holdup:

$$\frac{\partial \alpha}{\partial t} + \boldsymbol{u} \cdot \nabla \alpha = D \nabla^2 \alpha \tag{2-12}$$

The first term vanishes in the fully developed region, and hence in radial direction

$$u_r \cdot \frac{\partial \alpha}{\partial r} = D \frac{\partial}{\partial r}\left(\frac{\partial \alpha}{\partial r}\right) \tag{2-13}$$

By solving Equation (2-13), we obtain:

$$\frac{\partial \alpha}{\partial r} = C \cdot e^{\frac{u_r}{D} r} \tag{2-14}$$

where C and D are constants that come from mathematical manipulations. Equation (2-14) indicates that the gas holdup gradient in radial direction can be expressed in the form of an exponential function. It is reasonable to deduce that the similar expression holds for the inlet condition. It is noted the above manipulations are just for theoretical analysis but not involved in the numerical modelling.

Figure 2-10 shows the profile of normalized axial liquid velocity (relative to the centreline liquid velocity) along the radial direction. The normalized axial liquid velocity profiles are very similar and all of them are close to the experiment results, indicating that inlet conditions do not affect the flow pattern of liquid-phase. However, it should be pointed out that the simulated absolute centreline liquid velocities with all inlet conditions are lower than experiments. This may be relevant to the simplified treatments for holes of sparger. For the "Holes" case, the hole diameter of the distributor was enlarged from 0.4 to 2 mm while maintaining the original number of holes in order to decrease the mesh number and mesh skewness. Therefore, the gas velocity at holes is actually lower than that of real cases, which may lead to the underestimation of liquid axial centreline velocity. The simulation is similar to the results ofYang et al. (2011).

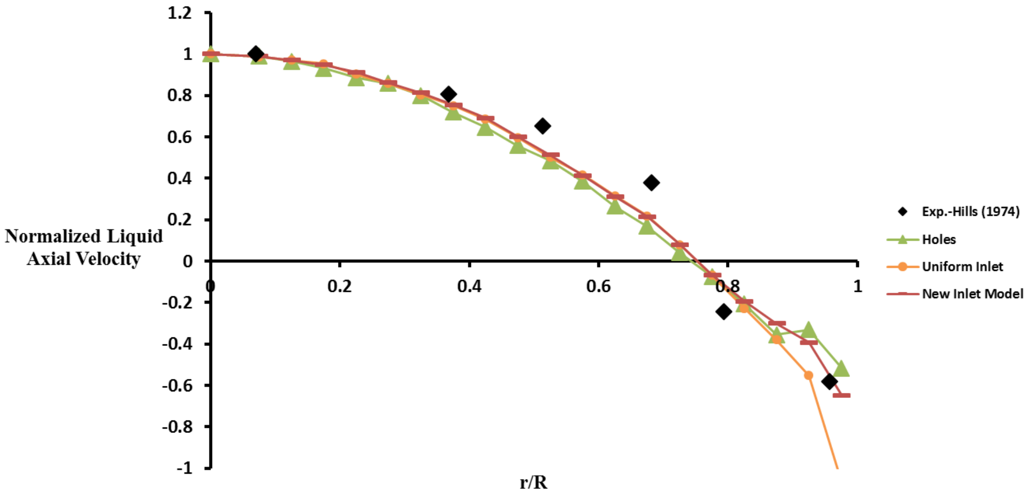

Figure 2-10 Radial distribution of normalized axial liquid velocity (*Ug* = 0.95 m/s, *H* = 0.6 m).

Figure 2-11 compares the simulated total gas holdup and the experiments for three different gas inlet models. The uniform inlet overestimates the total gas holdup especially at higher superficial gas velocities, whereas the other two models give good simulation. In the "Holes" case, the increase of gas holdup slows down with increasing superficial gas velocity. In the meantime, unlike the uniform inlet case, the new inlet model does not change this dampening tendency and can achieve similar effect that can only be obtained by the multi-hole inlet boundary. In conjunction with the DBS drag model, the new inlet model shows great adaptability for the prediction of both the total and the radial distribution of gas holdup without the need of adjusting modelling parameters.

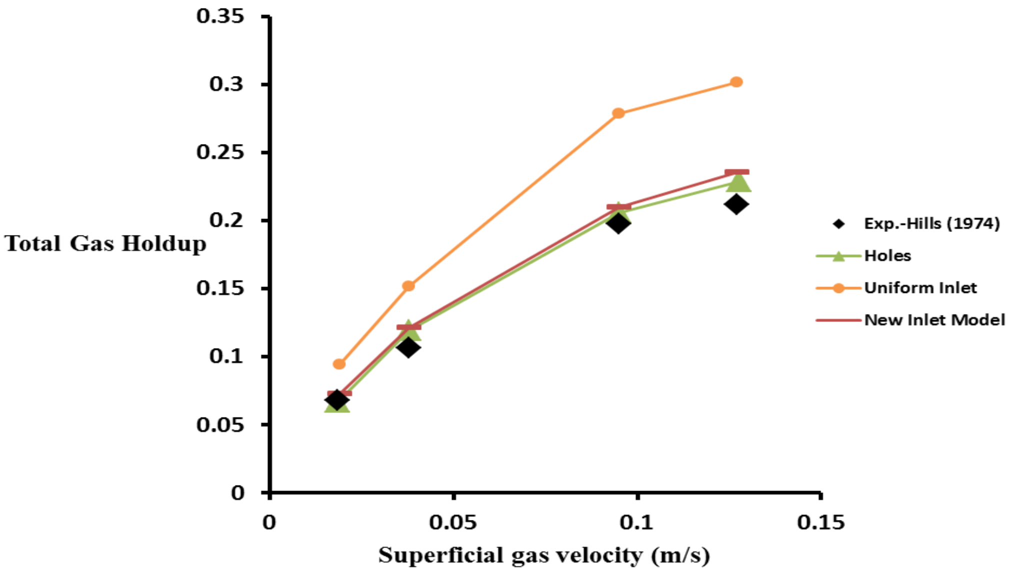

Figure 2-11 Comparison of simulated total gas holdup profiles with experiments of Hills (1974).

It can be inferred from Figure 5-11 that, on one hand, including exactly the real number and size of holes into the simulation is necessary to acquire accurate prediction for all the three superficial velocities, but this requires approximately 700,000 cells for a lab-scale hollow bubble column. On the other hand, utilizing the new inlet model as an approximation can achieve acceptable agreements with experimental data in all the three cases, and the total cell number is reduced to approximately 60,000. The computational cost was apparently reduced to a great extent (approximately one tenth of the "Holes" case) without much sacrifice of the simulation accuracy. This may be of more significance for pilot- or industrial-scale bubble column reactors in which a large number of internals of complex geometry may reside, and in such cases the total number of cells could easily soar up to as many as tens of millions or even hundreds of millions. The new inlet model greatly reduces the grid number and unbearable computational cost by orders-of-magnitude.

It should be pointed out that the drag model is the predominant factor for the accuracy of simulation compared to the inlet boundary conditions. For example, the Schiller-Naumann (S&N) drag model still largely under-predicts the gas holdup, even if the "Holes" model or the new inlet model is employed, as shown in Figure 2-11. For the two different inlet boundary conditions, the DBS drag model consistently shows the better agreement with the experiments than the Schiller-Naumann drag model, which was also reported in our previous publications (Yang et al., 2011, Xiao et al., 2013, Yang, 2012).

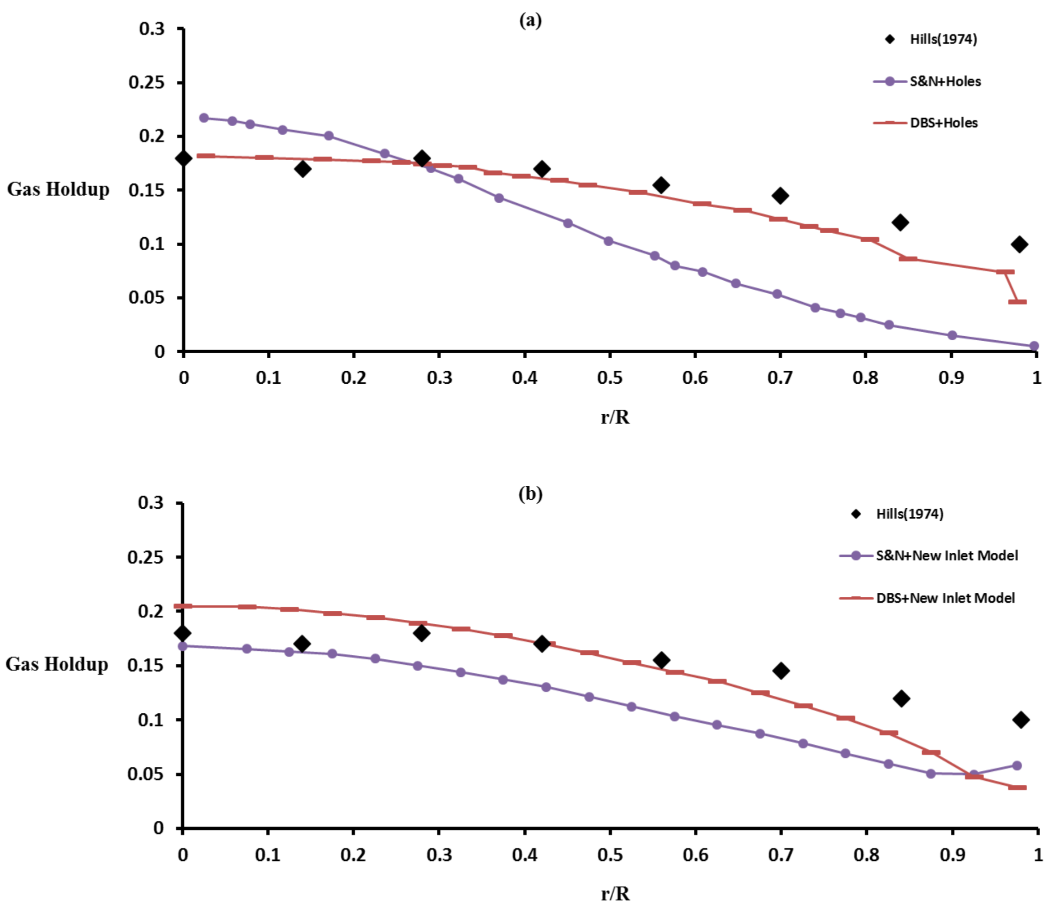

Figure 2-12 Radial distribution of gas holdup using different drag models in combined with (a) Holes model; (b) New Inlet Model (*Ug* = 0.038 m/s, *H* = 1.32 m).

4.2 Application in bubble columns of large diameters

To further verify the new inlet model for columns of large diameters, CFD simulation using the new inlet model is performed for the experimental system of Chen et al. (1999). Detail information is listed in Table 2-3.

Table 2-3 Bubble column parameters of Chen et al. (1999).

Column Diameter(m)	**Column Height(m)**	**Observation Height(m)**	**No. of holes on distributor**	**Diameter of holes(mm)**	ζ	**Superficial gas velocity(m/s)**
0.44	2.43	1.32	301	0.7	0.076	0.1

In this case, to avoid the liquid overflow from the top of the column, the column height is extended to 3 m. The space above the column height of 0.89 m is defined as the fully-developed region of the flow in terms of the experiments of CARPT/CT measurements of Chen et al. (1999). Since the column was under batch-operated conditions, the static liquid height with zero gas holdup is filled up to 1.7 m. The rest part of the column is the liquid-free region.

Figure 2-13 and Figure 2-14 illustrate the time-averaged radial distribution of gas holdup and liquid axial velocity. For the simulation using the uniform inlet condition, the gas holdup profile appears to be rather flat and the gas holdup is over-predicted, and the liquid axial velocity is under-predicted at the centre, which suggests that the uniform inlet boundary is not adequate to fully reflect the flow characteristics in the large-diameter bubble column. For the simulation using the new inlet model, the radial distribution of gas holdup and liquid axial velocity is in better agreement with experimental data. The difference may further attribute to the velocity gradient caused by the distributor is reflected in the new inlet model but neglected by the uniform inlet condition. Therefore, lift force model is required when the uniform inlet condition is applied.

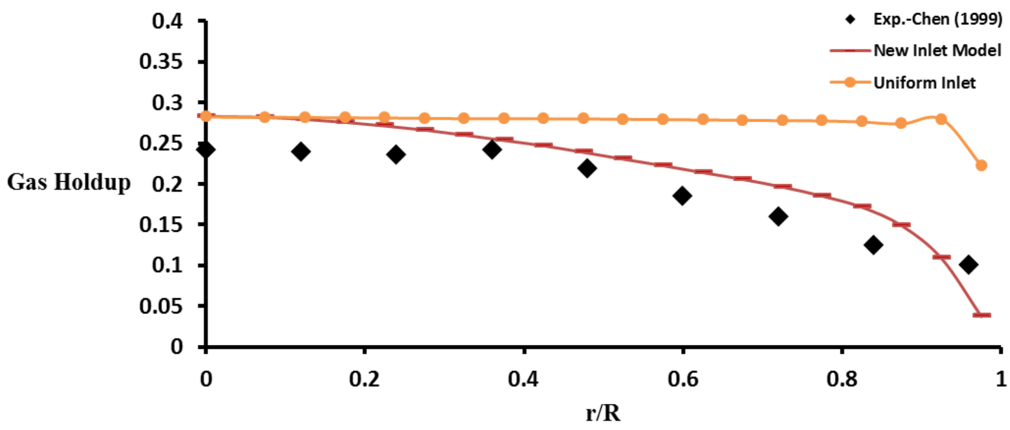

Figure 2-13 Radial profile of gas holdup in comparison with the CT data of Chen et al. (1999) (*Ug* = 0.1 m/s, *D* = 0.44 m).

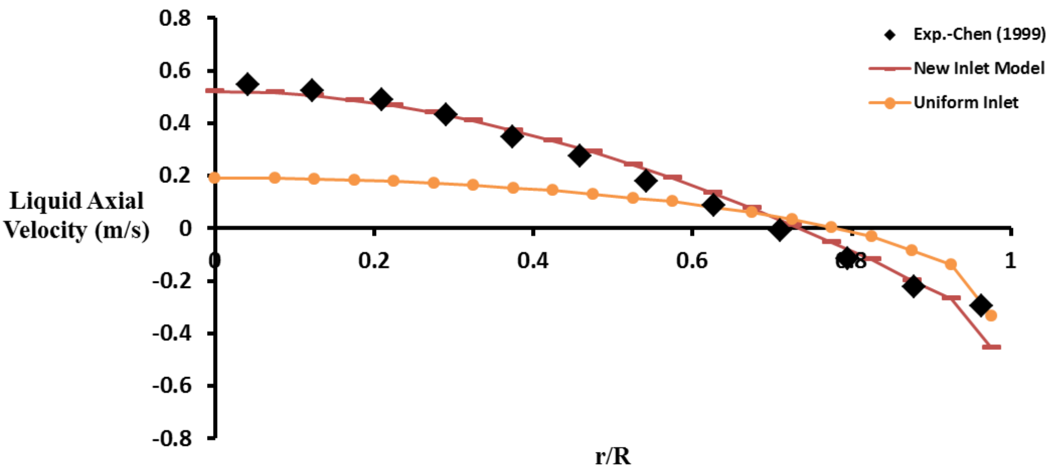

Figure 2-14 Radial profile of liquid axial velocity in comparison with the CARPT data of Chen et al. (1999) (*Ug* = 0.1 m/s, *D* = 0.44 m).

In order to further test the new inlet model in the modelling of large-diameter bubble columns, the experimental system of Menzel et al. (1990) with a column diameter of 600 mm was simulated. The superficial gas velocity is 0.072 m/s.

The simulation results of local gas holdup profiles along with the experiment data are illustrated in Figure 2-15. The above two cases demonstrated that the new inlet model is also suitable for bubble columns with large diameters.

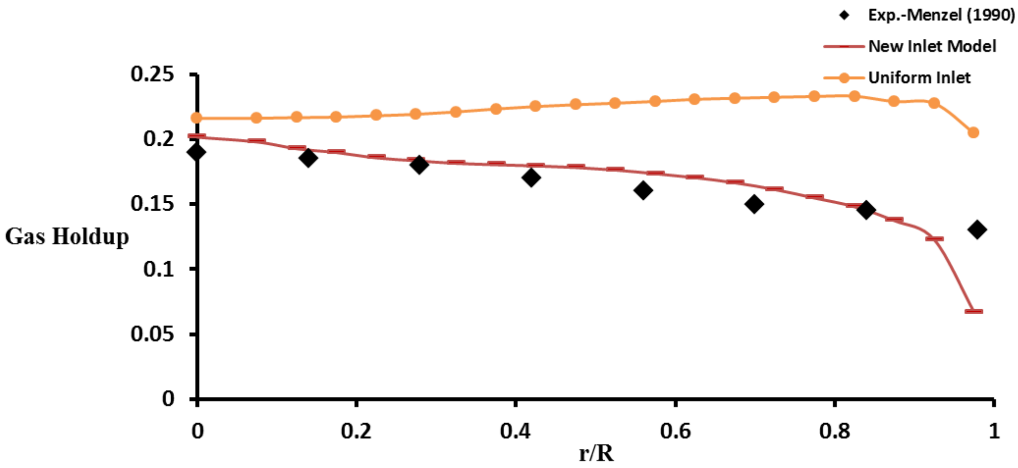

Figure 2-15 Radial profile of gas holdup in comparison with the experiment of Menzel et al. (1990) (Ug = 0.072 m/s, D = 0.6 m).

5. CONCLUSIONS

A new inlet model was proposed to approximate the effects caused by flow conditions and distributor geometries, and validated by the experiments in literature for the three bubble columns with diameters of 0.138 m, 0.44 m or 0.6 m. The simulation demonstrates that the uniform inlet boundary condition is inadequate in the prediction of both total and local gas holdup, in particular for higher gas flow rates, when the non-drag forces are not included in the simulation. The new inlet model is able to achieve the same level of accuracy as the hole case in which the full geometry of gas distributors is modelled. This is because the new inlet model can reasonably allocate the momentum onto the cross-section by the distribution functions proposed, and the effects of real geometries of distributors are considered as the parameters in the new inlet model. The new model is suitable for the simulation of both lab-scale and large size bubble column reactors, and able to reasonably predict the gas holdup profiles for different superficial gas velocities when the DBS drag model is used. The number of mesh cells can be reduced by approximately 10 times compared to the hole case, which is of practical significance for the simulation of industrial scale reactors.

References

AKHTAR, M. A., TADE, M. O. & PAREEK, V. K. 2006. Two-fluid Eulerian simulation of bubble column reactors with distributors. *Journal of Chemical Engineering of Japan,* 39**,** 831-841.

BAHADORI, F. & RAHIMI, R. 2007. Simulations of gas distributors in the design of shallow bubble column reactors. *Chemical Engineering & Technology,* 30**,** 443-447.

BAO, D., ZHANG, X., DONG, H. F., OUYANG, Z. L., ZHANG, X. P. & ZHANG, S. J. 2015. Numerical simulations of bubble behavior and mass transfer in CO2 capture system with ionic liquids. *Chemical Engineering Science,* 135**,** 76-88.

BEHKISH, A., LEMOINE, R., OUKACI, R. & MORSI, B. I. 2006. Novel correlations for gas holdup in large-scale slurry bubble column reactors operating under elevated pressures and temperatures. *Chemical Engineering Journal,* 115**,** 157-171.

BORDEL, S., MATO, R. & VILLAVERDE, S. 2006. Modeling of the evolution with length of bubble size distributions in bubble columns. *Chemical Engineering Science,* 61**,** 3663-3673.

CAMARASA, E., VIAL, C., PONCIN, S., WILD, G., MIDOUX, N. & BOUILLARD, J. 1999. Influence of coalescence behaviour of the liquid and of gas sparging on hydrodynamics and bubble characteristics in a bubble column. *Chemical Engineering and Processing,* 38**,** 329-344.

CHEN, J. H., YANG, N., GE, W. & LI, J. H. 2009. Modeling of Regime Transition in Bubble Columns with Stability Condition. *Industrial & Engineering Chemistry Research,* 48**,** 290-301.

CHEN, J. W., LI, F., DEGALEESAN, S., GUPTA, P., AL-DAHHAN, M. H., DUDUKOVIC, M. P. & TOSELAND, B. A. 1999. Fluid dynamic parameters in bubble columns with internals. *Chemical Engineering Science,* 54**,** 2187-2197.

CHEN, P., DUDUKOVIC, M. P. & SANYAL, J. 2005a. Three-dimensional simulation of bubble column flows with bubble coalescence and breakup. *Aiche Journal,* 51**,** 696-712.

CHEN, P., SANYAL, J. & DUDUKOVIC, M. P. 2005b. Numerical simulation of bubble columns flows: effect of different breakup and coalescence closures. *Chemical Engineering Science,* 60**,** 1085-1101.

DECKWER, W. D. 1992. Bubble Column Reactors. Chichester, UK: Wiley.

DEEN, N. G., SOLBERG, T. & HJERTAGER, B. H. 2000. Numerical simulation of gas–liquid flow in a square cross section bubble column. *14th International congress of chemical and process engineering (CHISA).* Praha, Czech Republic.

DEEN, N. G., SOLBERG, T. & HJERTAGER, B. H. 2001. Large eddy simulation of the gas-liquid flow in a square cross-sectioned bubble column. *Chemical Engineering Science,* 56**,** 6341-6349.

DELNOIJ, E., LAMMERS, F. A., KUIPERS, J. A. M. & VANSWAAIJ, W. P. M. 1997. Dynamic simulation of dispersed gas-liquid two-phase flow using a discrete bubble model. *Chemical Engineering Science,* 52**,** 1429-1458.

DHOTRE, M. T. & JOSHI, J. B. 2007. Design of a gas distributor: Three-dimensional CFD simulation of a coupled system consisting of a gas chamber and a bubble column. *Chemical Engineering Journal,* 125**,** 149-163.

GUAN, X. P., GAO, Y. X., TIAN, Z., WANG, L. J., CHENG, Y. W. & LI, X. 2015. Hydrodynamics in bubble columns with pin-fin tube internals. *Chemical Engineering Research & Design,* 102**,** 196-206.

HAQUE, M. W., NIGAM, K. D. P. & JOSHI, J. B. 1986. Optimum Gas Sparger Design for Bubble-Columns with a Low Height-to-Diameter Ratio. *Chemical Engineering Journal and the Biochemical Engineering Journal,* 33**,** 63-69.

HILLS, J. H. 1974. Radial Nonuniformity of Velocity and Voidage in a Bubble Column. *Transactions of the Institution of Chemical Engineers,* 52**,** 1-9.

HUNT, J. C. R., AUTON, T. R., SENE, K., THOMAS, N. H. & KOWE, R. ICHMT Int Seminar on Transient Phenomena in Multiphase Flow., May 24–30 1987 Dubrovnik, Yugoslavia. 103-125.

KRISHNA, R. & VAN BATEN, J. M. 2001. Eulerian simulations of bubble columns operating at elevated pressures in the churn turbulent flow regime. *Chemical Engineering Science*, 56**,** 6249-6258.

LABORDE-BOUTET, C., LARACHI, F., DROMARD, N., DELSART, O. & SCHWEICH, D. 2009. CFD simulation of bubble column flows: Investigations on turbulence models in RANS approach. *Chemical Engineering Science*, 64**,** 4399-4413.

LARACHI, F., DESVIGNE, D., DONNAT, L. & SCHWEICH, D. 2006. Simulating the effects of liquid circulation in bubble columns with internals. *Chemical Engineering Science*, 61**,** 4195-4206.

LI, G., YANG, X. G. & DAI, G. 2009. CFD simulation of effects of the configuration of gas distributors on gas-liquid flow and mixing in a bubble column. *Chemical Engineering Science,* 64**,** 5104-5116.

LI, W. L. & ZHONG, W. Q. 2015. CFD simulation of hydrodynamics of gas-liquid-solid three-phase bubble column. *Powder Technology,* 286**,** 766-788.

LUCAS, D., PRASSER, H. M. & MANERA, A. 2005. Influence of the lift force on the stability of a bubble column. *Chemical Engineering Science,* 60**,** 3609-3619.

LUCAS, D., RZEHAK, R., KREPPER, E., ZIEGENHEIN, T., LIAO, Y., KRIEBITZSCH, S. & APANASEVICH, P. 2016. A strategy for the qualification of multi-fluid approaches for nuclear reactor safety. *Nuclear Engineering and Design,* 299**,** 2-11.

LUCAS, D. & TOMIYAMA, A. 2011. On the role of the lateral lift force in poly-dispersed bubbly flows. *International Journal of Multiphase Flow,* 37**,** 1178-1190.

MASOOD, R. M. A., RAUH, C. & DELGADO, A. 2014. CFD simulation of bubble column flows: An explicit algebraic Reynolds stress model approach. *International Journal of Multiphase Flow,* 66**,** 11-25.

MENZEL, T., WEIDE, T. I. D., STAUDACHER, O., WEIN, O. & ONKEN, U. 1990. Reynolds Shear-Stress for Modeling of Bubble Column Reactors. *Industrial & Engineering Chemistry Research,* 29**,** 988-994.

MUDDE, R. F., HARTEVELD, W. K. & VAN DEN AKKER, H. E. A. 2009. Uniform Flow in Bubble Columns. *Industrial & Engineering Chemistry Research,* 48**,** 148-158.

RAMPURE, M. R., KULKARNI, A. A. & RANADE, V. V. 2007. Hydrodynamics of bubble column reactors at high gas velocity: Experiments and computational fluid dynamics (CFD) Simulations. *Industrial & Engineering Chemistry Research,* 46**,** 8431-8447.

RAMPURE, M. R., MAHAJANI, S. M. & RANADE, V. V. 2009. CFD Simulation of Bubble Columns: Modeling of Nonuniform Gas Distribution at Sparger. *Industrial & Engineering Chemistry Research,* 48**,** 8186-8192.

RANADE, V. V. & TAYALIA, Y. 2001. Modelling of fluid dynamics and mixing in shallow bubble column reactors: influence of sparger design. *Chemical Engineering Science,* 56**,** 1667-1675.

RIGOPOULOS, S. & JONES, A. 2003. A hybrid CFD - reaction engineering framework for multiphase reactor modelling: basic concept and application to bubble column reactors. *Chemical Engineering Science,* 58**,** 3077-3089.

SANKARANARAYANAN, K. & SUNDARESAN, S. 2002. Lift force in bubbly suspensions. *Chemical Engineering Science,* 57**,** 3521-3542.

SOKOLICHIN, A. & EIGENBERGER, G. 1999. Applicability of the standard k-epsilon turbulence model to the dynamic simulation of bubble columns: Part I. Detailed numerical simulations. *Chemical Engineering Science,* 54**,** 2273-2284.

SOKOLICHIN, A., EIGENBERGER, G. & LAPIN, A. 2004. Simulation of buoyancy driven bubbly flow: Established simplifications and open questions. *Aiche Journal,* 50**,** 24-45.

TABIB, M. V., ROY, S. A. & JOSHI, J. B. 2008. CFD simulation of bubble column - An analysis of interphase forces and turbulence models. *Chemical Engineering Journal,* 139**,** 589-614.

TOMIYAMA, A. 1998. Struggle with computational bubble dynamics. *Multiphase Science and Technology, Vol 10 Issue 4 1998***,** 369-405.

TROSHKO, A. A. & ZDRAVISTCH, F. 2009. CFD modeling of slurry bubble column reactors for Fisher-Tropsch synthesis. *Chemical Engineering Science,* 64**,** 892-903.

VAN BATEN, J. M. & KRISHNA, R. 2004. Scale effects on the hydrodynamics of bubble columns operating in the heterogeneous flow regime. *Chemical Engineering Research & Design,* 82**,** 1043-1053.

WANG, Q. G. & YAO, W. 2016. Computation and validation of the interphase force models for bubbly flow. *International Journal of Heat and Mass Transfer,* 98**,** 799-813.

WANG, T. F., WANG, J. F. & JIN, Y. 2006. A CFD-PBM coupled model for gas-liquid flows. *Aiche Journal,* 52**,** 125-140.

WIEMANN, D. & MEWES, D. 2005. Calculation of flow fields in two and three-phase bubble columns considering mass transfer. *Chemical Engineering Science,* 60**,** 6085-6093.

XIAO, Q., YANG, N. & LI, J. 2013. Stability-constrained multi-fluid CFD models for gas–liquid flow in bubble columns. *Chemical Engineering Science,* 100**,** 279-292.

YANG, N. 2012. A multi-scale framework for CFD modelling of multi-phase complex systems based on the EMMS approach. *Progress in Computational Fluid Dynamics,* 12**,** 220-229.

YANG, N., CHEN, J. H., ZHAO, H., GE, W. & LI, J. H. 2007. Explorations on the multi-scale flow structure and stability condition in bubble columns. *Chemical Engineering Science,* 62**,** 6978-6991.

YANG, N., WU, Z. Y., CHEN, J. H., WANG, Y. H. & LI, J. H. 2011. Multi-scale analysis of gas-liquid interaction and CFD simulation of gas-liquid flow in bubble columns. *Chemical Engineering Science,* 66**,** 3212-3222.

ZHANG, D., DEEN, N. G. & KUIPERS, J. A. M. 2006. Numerical simulation of the dynamic flow behavior in a bubble column: A study of closures for turbulence and interface forces. *Chemical Engineering Science,* 61**,** 7593-7608.

ZIEGENHEIN, T., RZEHAK, R., KREPPER, E. & LUCAS, D. 2013. Numerical Simulation of Polydispersed Flow in Bubble Columns with the Inhomogeneous Multi-Size-Group Model. *Chemie Ingenieur Technik*, 85**,** 1080-1091.

CHAPTER 3: MODELLING OF BREAKAGE RATE AND BUBBLE SIZE DISTRIBUTION IN BUBBLE COLUMNS ACCOUNTING FOR BUBBLE SHAPE VARIATIONS

SUMMARY

In the study of meso-scale structures of multi-phase flow in bubble columns, accurate modelling of the interaction between the turbulence eddies and particle/bubble groups is crucial for capturing the heat and mass transfer occurring between the bubbles and surrounding carrier fluid. This chapter focuses on the influence of bubble shape variations on bubble breakage due to the eddy collision with the bubbles in bubble column flows. An improved breakage model accounting for the variation of bubble shapes was proposed. The improved breakage model coupled with the widely adopted isotropic, homogeneous turbulence kinetic energy spectrums, that are currently available from the open literature, takes into account the different energy requirements in forming the daughter bubbles, i.e. the increase of in surface energy and the pressure head difference of the bubble and its surrounding turbulent eddies. The simulation results compared with experimental data have clearly demonstrated that the improved model effectively describes the various shapes of bubble breakage events, which may consequently have a strong impact on the interfacial area estimation that is crucial for calculation of the transfer rates of mass and heat transfer in the bubble columns.

1. INTRODUCTION

Bubble columns are widely used as multiphase contactors for carrying out gas-liquid reactions in chemical, petrochemical, biochemical, pharmaceutical and metallurgical industries, primarily because of the low costs involved in the construction, operation and maintenance process. In addition, bubble columns exhibit excellent heat and mass transfer characteristics, typically due to the increase of interface contact areas. In spite of their simplicity in mechanical design, fundamental properties of the two-phase hydrodynamics associated with the performance of bubble column reactors that are essential for scale-up and process optimisation, are still not fully understood because of the complex nature of multiphase flow, especially the continuous variations and deformation of bubble shapes in the process of bubble rising up through the bubble column.

The flow regime is one of the most fundamental studies in the bubble columns, because the flow characteristics are strongly related to the prevailing flow regime. In general, the flow regime in bubble columns can be classified as homogeneous regime, transition regime, heterogeneous regime and slug flow regime (Shah *et al.*, 1982). For fermentation process or cell culturing purposes, the bubble column usually operates at homogeneous regime. The homogeneous flow regime can be further distinguished into the mono-dispersed homogeneous regime and the poly-dispersed homogeneous flow regime, depending on the superficial velocities and the associated bubble size distributions (Besagni and Inzoli, 2016b). The mono-dispersed homogeneous regime may not exist if the large bubbles are aerated due to large diameter orifices on the sparger (Besagni and Inzoli, 2016a). The transition flow regime is characterized by large flow macro-structures with large eddies and a widened bubble size distribution (Guedon *et al.*, 2017), in which case, the turbulent eddies induced by the "coalescence-induced" large bubbles may make increasingly significant contributions to the turbulence generated in the column.

The time-dependent behaviour of flow patterns and features inside the bubble column are significantly influenced by the rising bubbles based on the experimental observations reported in the open literature (Pourtousi *et al.*, 2014). The bubbles induce the turbulence through the wake and interactions among the bubbles. These should be taken into account in CFD modelling of bubble column flows and the differences between different simulation methods have to be considered. Two major CFD modelling approaches currently adopted are the *Eulerian-Lagrangian* (E-L), which considers the dispersed phase as discrete entities (Delnoij et al., 1997, Sokolichin et al., 1997, Xue et al., 2017b, Xue et al., 2017a), and the *Eulerian-Eulerian* (E-E), which describes the dispersed phase as interpenetrating the continuous phase (Krishna et al., 1999, Lehr et al., 2002). It has been recognised that the use of both numerical approaches can lead to reliable prediction results only when the appropriate modelling for bubble-induced fluid motion are introduced. The E-E approach usually relies on the closure models that describe the gas–liquid interphase transport phenomena through a certain averaging. In the meantime, the associated closure models need to consider the effect of turbulence induced by bubble motions, the interphase momentum exchange caused by interactions between the gas-liquid two phases, and the bubbles size distribution, while these are closely related to the turbulence and the interphase interaction forces. A number of CFD studies have been conducted to assess the suitability of various turbulence models for CFD bubble columns (Masood et al., 2014, Sokolichin and Eigenberger, 1999, Laborde-Boutet et al., 2009, Tabib et al., 2008, Zhang et al., 2006) and the effect of interphase interactions (Yang et al., 2011, Xiao et al., 2013, Li and Zhong, 2015, Rzehak and Krepper, 2013, Pourtousi et al., 2014). The interphase interactions can be assumed to be induced through the composition of various forces such as the drag force that liquid exerts on the bubble surface due to viscosity (Deen et al., 2000, Krishna and van Baten, 2001, Ranade and Tayalia, 2001), the lift force which is caused by the shear flow around the bubbles and the virtual mass force due to the local acceleration (Sankaranarayanan and Sundaresan, 2002, Tomiyama, 1998, Delnoij et al., 1997, Sokolichin et al., 2004, Lucas et al., 2005, Lucas and Tomiyama, 2011, Tabib et al., 2008, Zhang et al., 2006, Rampure et al., 2007, Deen et al., 2001). These previous CFD studies on bubble column flow often employed the assumption of a unified bubble diameter, which can only generate reliable predictions when the bubble size is narrowly distributed. However, CFD modelling of gas-liquid two-phase flow behaviours has to take into account the bubble size distributions and the bubble-bubble interactions because these are very influential factors in the calculation of the gas-liquid interfacial area. There are different ways to consider the effect of bubble sizes. For example, based on Krishna and van Baten (2001), Guedon *et al.* (2017) explicitly classifies the bubbles into two groups in the simulations. On the contrary, Xiao *et al.* (2017) and Zhou *et al.* (2017) have applied the energy minimisation multi-scale EMMS based Dual-

Bubble-Size DBS drag model, which implicitly considered the bubble sizes and shapes by using a lumping coefficient C_D/d_b to replace the traditional drag coefficient closure. Also, a more direct way is to derive the bubble size distributions from the population balance equations (PBE) with the bubble-bubble and eddy-bubble interactions being controlled by bubble coalescence and breakup models. As the suitable prediction of the bubble breakage rate is critical when using the PBE to decide the bubble size distribution especially when mass transfer between two-phase interface is concerned, it becomes clear that a reliable model for estimation of breakage rate accounting for bubble shape variations is desirable for CFD modelling of bubble column flows.

For the bubble breakup process, Coulaloglou and Tavlarides (1977) assumed that the breakup process would occur if the energy carried by turbulent eddies impacting on the bubble is more than the surface energy contained by the bubble. Prince and Blanch (1990) acknowledged bubble breakup is caused by eddy-bubble collision but they proposed that bubble breakup can only be induced by eddies with approximately the same characteristic size as the bubbles. Eddies at a much larger length scale only transport the bubbles without causing breakage. Luo and Svendsen (1996) described the bubble breakup by considering both the length scale and the amount of energy contained by the arriving eddies. The minimum length scale of eddies that are responsible for breakup equals to 11.4 times those eddies corresponding to the dissipation with the Kolmogorov scale. The probability for bubble breakup is related to the critical ratio of surface energy increase of bubbles after breakup and the mean turbulent kinetic energy of the colliding eddies. When applying their model, it was found that very small eddies do not contain sufficient energy to cause the bubble breakup. Lehr *et al.* (2002) proposed a slightly different breakup mechanism from that proposed by Luo and Svendsen (1996). They considered the minimum length scale of eddies to be determined by the size of the smaller bubble after breakup, and the breakup process to be dependent on the inertial force of the arriving eddy and the interfacial force acting on the bubble. Based on the results of Luo and Svendsen (1996) and Lehr *et al.* (2002), Wang *et al.* (2003) proposed the model for bubble breakup, for which the constraints both the energy and the capillary pressure are imposed. The energy constraint requires the eddy energy to be greater than or equal to the increase of surface energy of bubbles after the breakage. The capillary constraint requires the dynamic pressure of the arriving eddy to exceed the capillary pressure of the bubble. The use of these two breakup criteria restricted the minimum size of the bubbles that can break, and hence yielded results in accordance with practical observations that were more interpretable than those obtained using Luo and Svendsen (1996). These two breakup criteria have also been adopted and extended in the recent studies reported by Zhao and Ge (2007) and Liao *et al.* (2015). Based on these previous work, Qin *et al.* (2016) and Yang and Xiao (2017) have developed EMMS-PBM model and successfully employed into CFD simulations of liquid-liquid and gas-liquid systems. The EMMS-PBM model features the use of a minimised micro-scale energy dissipation as the stability constraint and provides a unique way to close the equilibrium state of coalescence and breakage kernels of bubbles or drops.

As discussed above, the surface of bubbles may subject to different forces as they are exposed to the turbulent eddies. The deformation of bubble shapes has a fundamental impact on the estimation of the interfacial area of bubbles. In return, this will have major implications when applying the population balance model for CFD modelling of bubble coalescence and breakage. Few studies have considered the bubble shapes in bubble column CFD modelling especially for the cases of large elliptical or cap bubbles. Clark (1988) proposed a model to describe the deformation and surface oscillation of droplets. The model assumed the motion of the mass centre of the deformed drop to be acted by those interfacial forces. However, the model did not include the buoyancy force and added mass, which occurs when the drop or bubble accelerates relative to the continuous phase. For a gas-liquid system such as bubble columns, added mass force and buoyancy force are dominant factors and have to be taken into account. Han *et al.* (2016) considered the surface deformation and oscillation of bubble to be axisymmetric, i.e. the dynamics of bubble are formulated based on the motion of the centre of mass of the half bubble, and all interfacial forces act upon the centre of mass similar to the analogy of a translational mechanical system with a spring linking two parts with equal mass. This treatment method is still constrained to the cases of ellipsoidal bubbles without considering the actual shapes of the bubbles.

The aim of this paper is to consider the influence of bubble shape variations on bubble breakage in bubble column flows. A breakage model accounting for the variation of bubble shapes will be proposed, coupled with the breakage criterion of energy density increase during the entire breakup process. Section 2 will present the mathematical modelling adopted in the current study while section 3 will present the simulation results and discussion, focusing on the effect of considering the bubble shape variations on the prediction of key parameters including gas holdup, bubble number density and interfacial area. Section 4 will present the conclusions derived from the study.

2. MATHEMATICAL MODELLING

2.1 Governing equations

A 3D transient CFD model is used in this work to simulate the local hydrodynamics of the gas-liquid two-phase bubble column. A Eulerian-Eulerian approach is adopted to describe the flow behaviours for both phases, i.e. water as the continuous phase, and air as the dispersed phase. The mass and momentum balance equations are given by equations (3-1) and (3-2) respectively,

$$\frac{\partial(\rho_k \alpha_k)}{\partial t} + \nabla(\rho_k \alpha_k \boldsymbol{u}_k) = 0 \tag{3-1}$$

$$\frac{\partial(\rho_k \alpha_k \boldsymbol{u}_k)}{\partial t} + \nabla(\rho_k \alpha_k \boldsymbol{u}_k \boldsymbol{u}_k) = -\alpha_k \nabla p + \nabla \cdot \bar{\bar{\tau}}_k + \alpha_k \rho_k \boldsymbol{g} + \boldsymbol{F}_k \tag{3-2}$$

where ρ_k, α_k, $\boldsymbol{u}_k$, $\bar{\bar{\tau}}_k$, and $\boldsymbol{F}_k$ represent the density, volume fraction, velocity vector, viscous stress tensor and the inter-phase momentum exchange term for the k (liquid or gas) phase respectively. The sum of the volume fractions for both phases is equal to 1.

2.2 Interphase momentum transfer

In this study, drag force, lift force and added mass force are considered as the main interactions between the continuous liquid phase and the dispersed gas phase. The drag force is calculated using Equation (3-3),

$$\boldsymbol{F}_D = \frac{3}{4}\frac{C_D}{d_{eq}}\rho_l \alpha_g \left|\boldsymbol{u}_g - \boldsymbol{u}_l\right| \left(\boldsymbol{u}_g - \boldsymbol{u}_l\right) \tag{3-3}$$

where C_D is the drag coefficient, which can be obtained from the model by Grace *et al.* (1978). The Grace model is well suited for gas-liquid flows in which the bubbles exhibit a range of shapes, such as sphere, ellipsoid, and spherical-cap. However, instead of comparing the values of drag coefficients in the original Grace model, the drag coefficient can be applied directly according to the actual types of bubbles, as the variation of bubble shapes has been considered in the breakup model. The drag coefficients for different shapes of bubbles are calculated using equations (3-4) to (3-6),

$$C_{D,sphere} = \begin{cases} 24/Re_b & Re_b < 0.01 \\ 24\left(1+0.15Re_b^{0.687}\right)/Re_b & Re_b \geq 0.01 \end{cases} \tag{3-4}$$

$$C_{D,cap} = \frac{8}{3} \tag{3-5}$$

$$C_{D,ellipse} = \frac{4}{3}\frac{gd_{eq}}{U_t^2}\frac{\left(\rho_l - \rho_g\right)}{\rho_l} \tag{3-6}$$

where Re_b is the bubble Reynolds number given by $R_{eb} = \frac{\rho_l|\boldsymbol{u}_g - \boldsymbol{u}_l|d_{eq}}{\mu_l}$. U_t is the terminal velocity, calculated using the following relation given by Equation (3-7),

$$U_t = \frac{\mu_l}{\rho_l d} Mo^{-0.149}\left(J - 0.857\right) \tag{3-7}$$

where Mo is the Morton number defined by $Mo = \frac{\mu_l^4 g\left(\rho_l - \rho_g\right)}{\rho_l^2 \sigma^3}$. J is given by the piecewise function, calculated using the empirical expression (3-8).

$$J = \begin{cases} 0.94H^{0.757} & 2 < H < 59.3 \\ 3.42H^{0.441} & H > 59.3 \end{cases} \tag{3-8}$$

H in expression (3-6) is defined by Equation (3-9),

$$H = \frac{4}{3} Eo Mo^{-0.149} \left(\frac{\mu_l}{\mu_{ref}} \right)^{-0.14} \tag{3-9}$$

where Eo is the Eötvös number and $\mu_{ref} = 0.0009\, kg/\left(m \cdot s\right)$.

The lift force acting perpendicularly to the direction of relative motion of the two phases can be calculated by using Equation (3-10).

$$\boldsymbol{F}_{Lift} = C_L \rho_l \alpha_g \left(\boldsymbol{u}_g - \boldsymbol{u}_l\right) \times (\nabla \times \boldsymbol{u}_l) \tag{3-10}$$

where C_L is the lift coefficient and is estimated by the Tomiyama lift force correlation (Tomiyama, 1998), as described by the following empirical relation (3-11),

$$C_L = \begin{cases} \min\left[0.288 \tanh\left(0.121 Re_b\right), f\left(Eo'\right)\right] & Eo' \le 4 \\ f\left(Eo'\right) & 4 < Eo' < 10 \\ -0.29 & Eo' > 10 \end{cases} \tag{3-11}$$

where $f\left(Eo'\right) = 0.00105 Eo'^3 - 0.0159 Eo'^2 - 0.0204 Eo' + 0.474$. *Eo'* is the modified Eötvös number based on the maximum horizontal dimension of the deformable bubble, d_h, as defined and given respectively by Equations (3-12) and (3-13).

$$Eo' = \frac{g(\rho_l - \rho_g) d_h^2}{\sigma} \tag{3-12}$$

$$d_h = d(1 + 0.163 Eo^{0.757})^{1/3} \tag{3-13}$$

The virtual mass force is also significant when the gas phase density is much smaller than the liquid phase density. The virtual mass force will be applied to the bubbles when the inertia of the liquid phase mass encounters the accelerating bubbles. The virtual mass force can be calculated using Equation (3-14),

$$\boldsymbol{F}_{VM} = C_{VM}\rho_l\alpha_g\left(\frac{d_l\boldsymbol{u}_l}{dt} - \frac{d_l\boldsymbol{u}_g}{dt}\right) \tag{3-14}$$

where C_{VM} is the virtual mass coefficient. It should be noted with caution that the virtual mass coefficient may also be altered in accordance with the bubble shapes. The influence of the bubble shape variations on the virtual mass coefficient may require further investigation, and hence a common value of 0.5 is defined in this study.

2.3 Turbulence modelling

The turbulence generated in the bubble column can be thought of being the joint superposition of shear turbulence and bubble-induced turbulence, which is mainly influenced by the wake formed by shedding vortices from the bubbles and decays quickly due to the viscos dissipation. However, bubble-induced turbulence (bubbulence) may strongly interact with the carrier phase turbulence of the main flow. Taking into account the features of turbulence induced by rising bubbles in the bubble column, the standard $k \sim \varepsilon$ turbulence model with the consideration of bubble-induced turbulence by Sato and Sekoguchi (1975) is used for turbulence closure. The turbulent kinetic energy k_l and dissipation rate ε_l are computed by equations (3-15) and (3-16),

$$\frac{\partial(\alpha_l\rho_l k_l)}{\partial t}+\nabla\cdot(\alpha_l\rho_l k_l\boldsymbol{u}_k)=\nabla\cdot\left[\alpha_l\left(\mu_l+\frac{\mu_{eff,l}}{\sigma_k}\right)\nabla k_l\right]+\alpha_l\left(G_{k,l}-\rho_l\varepsilon_l\right)$$

(3-15)

$$\frac{\partial(\alpha_l\rho_l\varepsilon_l)}{\partial t}+\nabla\cdot(\alpha_l\rho_l\varepsilon_l\boldsymbol{u}_k)=\nabla\cdot\left[\alpha_l\left(\mu_l+\frac{\mu_{eff,l}}{\sigma_k}\right)\nabla\varepsilon_l\right]+\alpha_l\frac{\varepsilon_l}{k_l}\left(C_{1\varepsilon}G_{k,l}-C_{2\varepsilon}\rho_l\varepsilon_l\right)$$

(3-16)

where $G_{k,l}$ is the production of turbulent kinetic energy given by Equation (3-17).

$$G_{k,l}=\tau_l:\nabla\boldsymbol{u}_l \qquad (3\text{-}17)$$

The effective viscosity is composed of the contributions of turbulent viscosity and an extra term considering the effect of bubble-induced turbulence and is defined by Equation (3-18).

$$\mu_{eff,l}=\rho_l C_\mu\frac{k_l^2}{\varepsilon_l}+\rho_l C_{\mu,BIT}\alpha_g d_b\left|\boldsymbol{u}_g-\boldsymbol{u}_l\right| \qquad (3\text{-}18)$$

The Sato coefficient used is $C_{\mu,BI}$ = 0.6. In this work, the standard $k\sim\varepsilon$ model constants used are C_μ = 0.09, $C_{1\varepsilon}$ = 1.44, $C_{2\varepsilon}$ = 1.92, σ_k = 1.0, σ_ε = 1.3.

2.4 Bubble size distribution

The bubble size distribution is determined by using the population balance model with consideration of bubble coalescence and breakup. Bubbles are divided into several size groups with different shapes of equivalent diameters $d_{eq,i}$ and an equivalent phase with the Sauter mean diameter d_{32}, to represent the bubble classes. Sixteen bubble classes with equivalent diameters ranging from 1 to 32 mm are applied based on the geometric discretization method such that $V_i=2V_{i-1}$. The population balance equation is expressed by Equation (3-19),

$$\frac{\partial n_i}{\partial t} + \nabla \cdot (\tilde{\boldsymbol{u}}_i \cdot n_i) = S_i \tag{3-19}$$

where n_i is the number density for *i*-th group, $\tilde{u}_i$ is the mass average velocity vector, and S_i is the source term.

The source term, S_i, for the *i*-th group can be expressed as birth and death of bubbles due to coalescence and breakup respectively, given by Equation (3-20).

$$S_i = B_{coalescence,i} - D_{coalescence,i} + B_{breakup,i} - D_{breakup,i}$$
$$= \sum_{V_j=V_{min}}^{\frac{V_i}{2}} \Omega_C(V_j{:}V_i - V_j) - \sum_{V_j}^{V_{max}-V_i} \Omega_C(V_j{:}V_i) + \sum_{V_j=V_i}^{V_{max}} \Omega_B(V_j{:}V_i) - \Omega_B(V_i) \tag{3-20}$$

The local gas volume fraction can be calculated by Equation (3-21),

$$\alpha_g f_i = n_i V_i \tag{3-21}$$

where f_i is the *i*-th class fraction of total volume fraction, and V_i is the volume for the *i*-th class.

The Sauter mean diameter can be calculated as by using Equation (3-22).

$$\frac{1}{d_{32}} = \sum \frac{f_i}{d_{eq,i}} \tag{3-22}$$

For the coalescence between bubbles of size $d_{eq,i}$ and $d_{eq,j}$, the coalescence kernel used in this work was proposed by Luo (1993), as denoted by Equation (3-23).

$$\Omega_C\left(d_{eq,i} : d_{eq,j}\right) = \omega_C\left(d_{eq,i} : d_{eq,j}\right) p_c\left(d_{eq,i} : d_{eq,j}\right) \tag{3-23}$$

where ω_C is the frequency of collision and p_C is the probability of coalescence due to collision. The collision frequency is defined by Equation (3-24)

$$\omega_C\left(d_{eq,i}{:}d_{eq,j}\right) = n_i n_j \frac{\pi}{4}\left(d_{eq,i} + d_{eq,j}\right)^2 \overline{u}_{ij} \tag{3-24}$$

where $\overline{u}_{ij}$ is the characteristic velocity of two collision bubbles, denoted by Equation (3-25).

$$\overline{u}_{ij} = \left(\overline{u}_{d,i}^2 + \overline{u}_{d,j}^2\right)^{1/2} \tag{3-25}$$

The characteristic velocity of one individual bubble is given by (3-26).

$$\overline{u}_{d,i} = 1.43\left(\varepsilon d_{eq,i}\right)^{1/3} \tag{3-26}$$

The expression for the probability of coalescence is described using Equation (3-27),

$$p_C = \exp\left\{ -c_1 \frac{\left[0.75\left(1+x_{ij}^2\right)\left(1+x_{ij}^3\right)\right]^{1/2}}{\left(\rho_g/\rho_l + 0.5\right)^{1/2}\left(1+x_{ij}\right)^3} We_{ij}^{1/2} \right\} \tag{3-27}$$

where c_1 is a constant of order unity that usually equals to 1, $x_{ij} = d_{eq,i} / d_{eq,j}$, and the Weber number is defined by Equation (3-28).

$$We_{ij} = \frac{\rho_l d_{eq,i} \overline{u}_{ij}^2}{\sigma} \tag{3-28}$$

The breakup model used in this work is based on the work of Luo and Svendsen (1996). However, several improvements have been introduced for breakage rate prediction to produce more realistic breakup estimation. In Luo and Svendsen's model, the shape of breakage bubbles was assumed to be spherical. However, previous experimental studies have clearly indicated that the bubbles exist in various shapes and the dynamics of bubble motion strongly depend on the shape of bubbles (Grace et al., 1978, Tomiyama, 1998, Tomiyama et al., 1998). Figure 3-1 demonstrates the experimentally recorded breakup process of a spherical-cap bubble found in an operating bubble column used in an ongoing research project funded by NSFC. The spherical-cap bubble has collided with a bombarding eddy that was shredded from the previous bubbles. The spherical-cap bubble then becomes deformed and distorted and finally breaks into two ellipsoidal bubbles. The bubble shape has been neglected in almost previous studies for the simplification of models. However, the shape of the bubbles could potentially be a critical factor for accurately predicting the flow characteristics of the gas phase in CFD simulations.

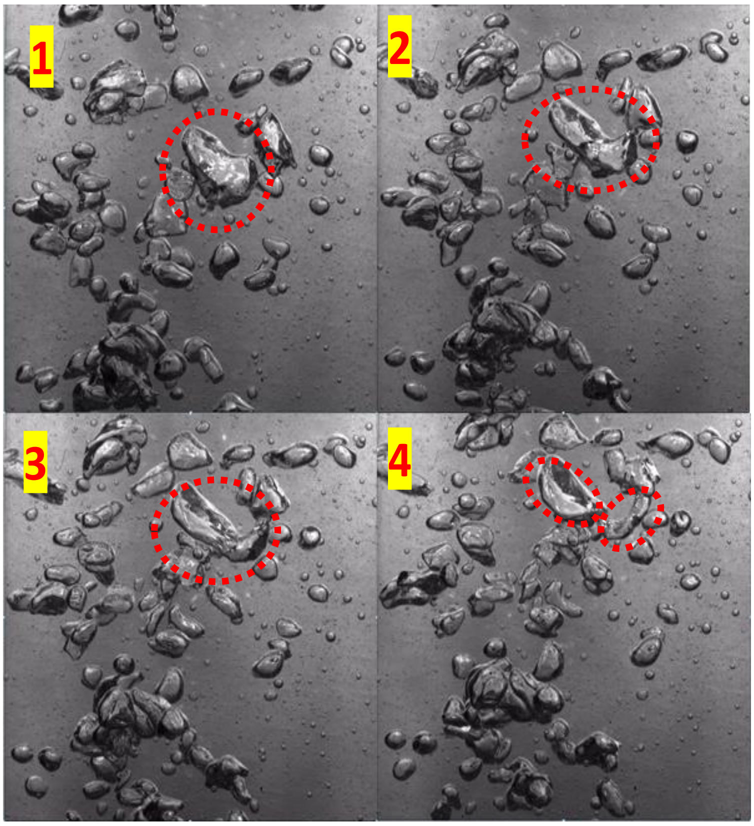

Figure 3-1 Time sequences of break-up of a rising bubble in a 150 mm diameter cylindrical bubble column (Ug = 0.02 m/s, total time duration: 0.03 s).

From experimental observations, the bubble shapes can be classified into different types: spherical, ellipsoidal and spherical-capped. The effects of different bubble shapes will be taken into account in the present study. As a result, an equivalent diameter, d_{eq}, is introduced to represent the size of these bubbles with various shapes. Also, due to the uncertainty of the spatial rotation of the bubbles, the contact angle of the bombarding eddies is very difficult to be determined. Therefore, instead of using the original bubble size d_i to calculate the sweep area of the collision tube, a nominal diameter, d_V, that approximately represents the size of the projected area of the bubble is defined by the following condition,

$$c \leq d_V \leq a \tag{3-29}$$

where c and a are the length of the short axis and long axis respectively. It seems that the eddy is more likely to bombards the bubble in the front rather than the rear directions. Therefore, the values of d_V are different in every computational cell when the breakage model is implemented into CFD modelling. The new imaginary collision tube is presented in Figure 3-2.

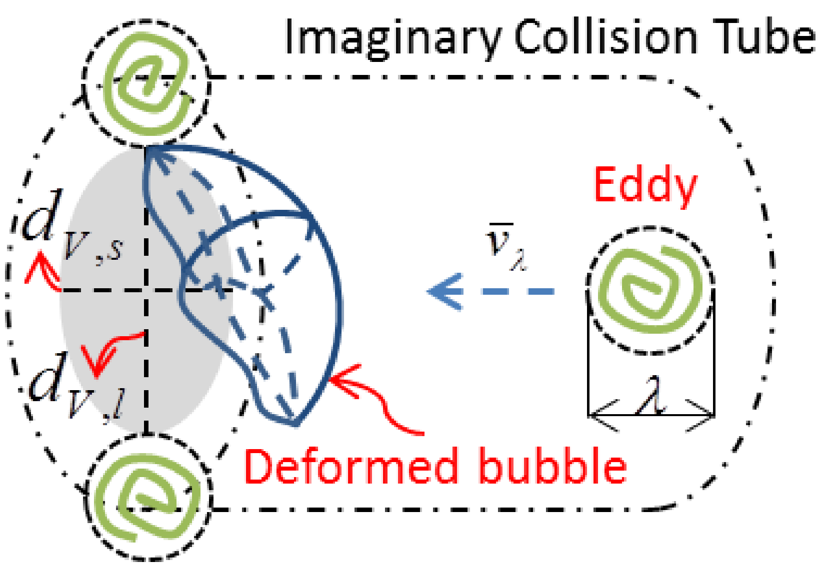

Figure 3-2 Sketch of a collision tube of an entering eddy moving through the tube with a mean velocity.

The breakup rate for one individual parent bubble breaking into two daughter bubbles can be calculated, given by Equation (3-30),

$$\Omega_B = \int_{\lambda_{\min}}^{d} \omega_B^T p_B \, d\lambda \tag{3-30}$$

where ω_B^T is the collision probability density which can be estimated from Luo and Svendsen (1996), as originally defined by Equation (3-31),

$$\omega_B^T = n_i n_\lambda \frac{\pi}{4} (d_i + \lambda)^2 \bar{v}_\lambda \tag{3-31}$$

In the original model, the cross-section of the collision tube is circular, no matter the bombarding eddy comes from which direction. However, once the bubble shapes are considered, the cross-section of the new collision tube is the projection of the ellipsoidal or the spherical-capped bubble on the moving direction of the bombarding eddy. Therefore, the collision probability density in the new collision tube can be approximately calculated by Equation (3-32),

$$\omega_B^T = n_i n_\lambda \frac{\pi}{4} \left(d_{V,s} + \lambda\right)\left(d_{V,l} + \lambda\right) \bar{v}_\lambda \tag{3-32}$$

where $d_{V,s}$ and $d_{V,l}$ denote to the short axis and the long axis of the projected area respectively. By considering the energy balance of the eddies being interpreted as discrete entities and as a spectrum function, the number density of eddies n_λ can be determined and hence the collision probability density becomes Equation (3-33),

$$\omega_B^T(\xi) = 0.923\left(1-\alpha_g\right)\left(\varepsilon d_{eq,i}\right)^{1/3} n_i \frac{\left(d_{V,s}/d_{eq,i} + \xi\right)\left(d_{V,l}/d_{eq,i} + \xi\right)}{d_{eq,i}^2 \xi^{11/3}} \tag{3-33}$$

where $\xi=\lambda/d_{eq,i}$ is the non-dimensional size of eddies that may contribute to the breakage of bubble size $d_{eq,i}$. The breakage probability function p_B used by Luo and Svendsen (1996) is given by Equation (3-34),

$$p_B = \exp(-\frac{e_s}{\bar{e}}) \tag{3-34}$$

where $\bar{e}$ is the mean turbulent kinetic energy for eddies of size λ and e_s is the increase in surface energy of bubbles after breakage. The mean turbulent kinetic energy can be determined by Equation (3-35).

$$\bar{e} = \rho_l \frac{\pi}{6} \lambda^3 \frac{\bar{u}_\lambda^2}{2} = \frac{\pi\beta}{12} \rho_l \left(\varepsilon d_{eq,i}\right)^{2/3} d_{eq,i}^3 \xi^{11/3} \tag{3-35}$$

By assuming the bubbles before and after breakage have deformed shapes with an equivalent diameter, when the parent bubble of size with $d_{eq,i}$ breaks into two bubbles of size $d_{eq,j}$ and $(d_{eq,i}^3 - d_{eq,j}^3)^{1/3}$, the increase in surface energy can be estimated using Equation (3-36),

$$e_s(d_{eq,i}, d_{eq,j}) = \sigma \cdot \pi d_{eq,i}^2 [f_V^{2/3} + (1 - f_V)^{2/3} - 1] \tag{3-36}$$

where the breakage volume fraction $f_V = d_{eq,j}^3 / d_{eq,i}^3$. However, since the effects of different shapes of bubbles are now taken into account, Equation (3-36) has to be re-written in a general form with regards to the surface area, S, of bubbles, which reflects the actual areas of the deformed daughter bubbles as described by Equation (3-37).

$$e_s = \sigma \cdot (S_{j,1} + S_{j,2} - S_i) \tag{3-37}$$

According to the models for bubble shapes proposed by Tomiyama *et al.* (1998), there are 3 main types that may be considered, including spherical, ellipsoidal and spherical-capped. The details of these 3 types of bubbles and their possible breakage footages are depicted in Figure 3-3.

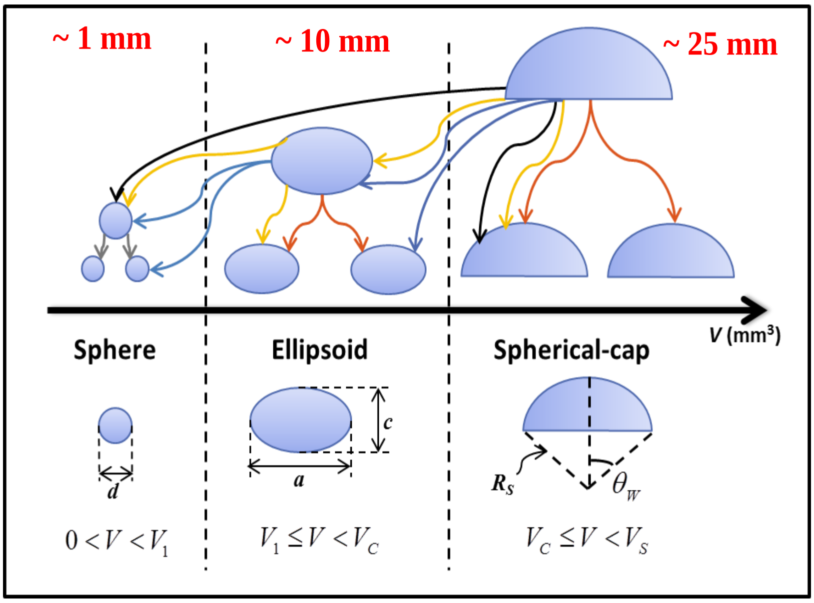

Figure 3-3 Classification of 3 types of bubbles and the possible breakage footage.

In order to emphasise that the volume is conserved when spherical bubble in the original model is converted into various shapes, the volume V is used in Figure 3-3. However, for readers' convenience, an equivalent diameter d_{eq} is used hereafter while the subscripts remain the same, i.e. $d_{eq,1}$ is the equivalent diameter of V_1. For an air-water system under atmospheric pressure and room temperature, $d_{eq,1}$ is roughly 1.16 mm for the pure system while $d_{eq,1}$ is approximately 1.36 mm for a slightly contaminated system. It is very important to point out that the volumes of ellipsoidal bubbles and spherical-cap bubbles should be equal to the volumes of their equivalent spherical bubbles with diameter d_{eq}. For bubbles with ellipsoidal shapes, by assuming in an oblate type of ellipsoid, as suggested by Batchelor (1967), the surface area can be calculated based on the following expression (3-38),

$$S_{ellipsoid} = \frac{\pi}{2} d_{eq}^2 E^{2/3} \left(1 + \frac{1}{2E\sqrt{E^2 - 1}} \ln(2E^2 - 1 + 2E\sqrt{E^2 - 1}) \right) \tag{3-38}$$

where the aspect ratio E can be expressed using an empirical correlation developed on the basis of experimental data of Besagni *et al.* (2016) and Besagni and Inzoli (2016a). The expression of the aspect ratio is given by Equation (3-39). It should be noticed that this correlation has only been validated in air-water dense bubbly flows. To use Equation (3-39) for other systems or for different operating conditions, more investigations and validations are strongly required. In addition, more experimental data to extend the discussion about the bubble aspect ratio in low Morton-number systems are described in Besagni *et al.* (2017).

$$E = \frac{a}{b} = 1 + 4.288 Ga^{-1/3} Eo^{1/2} \tag{3-39}$$

where Ga and Eo are the Galilei number and Eötvös number respectively, defined by Equation (3-40) and Equation (3-41).

$$Eo = \frac{g(\rho_l - \rho_g) d_{eq}^2}{\sigma} \tag{3-40}$$

$$Ga = \frac{\rho_l \sqrt{g d_{eq}} d_{eq}}{\mu_l} \tag{3-41}$$

The aspect ratio expressed in Equation (3-39) to characterise the bubble deformation has been intensively studied by different researchers. Wellek *et al.* (1966) proposed an empirical correlation to approximate the deformation of bubbles, which is consisted of dimensionless parameters including Weber number *We*, Reynolds number *Re*, Eötvös number *Eo*, Froude number *Fr*, and the ratio of dynamic viscosity. After a multiple regression process, they found the *Eo* number is the most important parameter which is able to approximate the bubble deformation in low viscosity systems. The idea of using *Eo* number to characterise the bubble deformation has been also adopted by Okawa *et al.* (2003), Tomiyama *et al.* (2002), Tsuchiya *et al.* (1990) and Besagni and Inzoli (2016a) among others. Moore (2006) derived an expression of the aspect ratio using the Webber number, based on the balance of the dynamic pressure and the capillary pressure at the bubble nose and side edge, respectively. The idea has also been extended by Sugihara *et al.* (2007) and Legendre *et al.* (2012). Some studies on the bubble deformations have attempted to introduce additional dimensionless parameters (Bozzano and Dente, 2001, Tripathi et al., 2015, Tsamopoulos et al., 2008, Clift et al., 1978, Legendre et al., 2012, Aoyama et al., 2016), such as Morton number *Mo*, Bond Number *Bo*, Archimedes number *Ar* and Tadaki number *Ta*, to correlate the aspect ratio or the conditions to distinguish different deformed bubbles. By carefully inspecting all these dimensionless numbers mentioned above, it can be seen clearly that the most important factors affecting the bubble deformations are mainly buoyancy, surface tension and viscosity. Thus, the dimensionless numbers used to correlate the aspect ratio should at least include these three key factors. The results using the correlation (3-39) compared with those data from the open literature have been plotted in Figure 3-4. It should be noted that the experimental data of the aspect ratio of bubbles greater than approximately 8 mm has rarely been documented. This is probably due to the fact that the experimental errors caused by large deformation and fast-changing of the shapes of large bubbles make it very difficult to determine the averaged aspect ratio. Under such circumstance, an approximation of 0.5 has been used for the aspect ratio of bubbles larger than 6 mm, which ensures the aspect ratio not to be infinitesimally small and the bubbles not able to be flatted without limitation. It can be seen from Figure 3-4 that the value of 0.5 is not much deviated from the correlation of Besagni & Inzoli and also agrees with the experimental data of Wang et al. (2014) It seems that Wellek's correlation, which has been adopted in Tomiyama's lift model, largely overestimates the aspect ratio especially when the bubble diameter is larger than 10 mm. This kind of overestimation means that the bubbles being depicted are extremely flat, which is much less likely to be continuously existed in the bubble column flows. On the contrary, although expressed using different dimensionless parameters, both the correlation by Besagni & Inzoli and the Equation (3-39) have shown much better agreements with the experimental data, which makes more sense in describing the bubbles' geometrical characteristics. This is very critical for the CFD modelling of gas-liquid two-phase flows, particularly when the flow characteristics are strongly affected by the bubble deformation and oscillation.

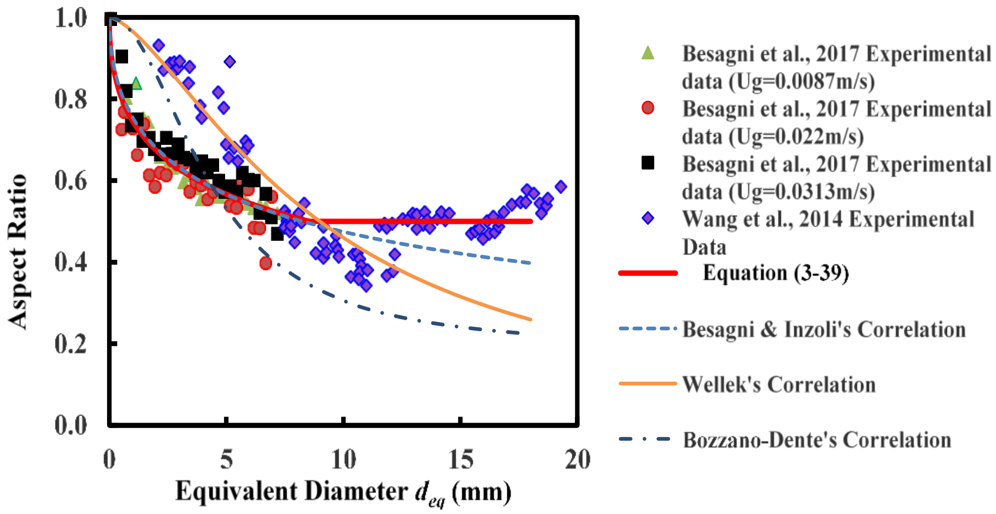

Figure 3-4 Aspect ratio correlation and comparison with the literature.

The boundary between ellipsoidal and spherical-cap bubbles, d_C, is estimated using Equation (3-42).

$$d_C = \sqrt{40\sigma \Big/ g\left(\rho_L - \rho_g\right)} \tag{3-42}$$

where d_c is found to be 17.3 mm for the air-water system. For a single spherical-cap bubble, the wake angle θ_W is assumed to be 50^o, following the work of Tomiyama (1998). As the volume of spherical-cap is equivalent to the volume of the equivalent spherical bubble, Equation (3-43) can be formulated as follows.

$$R_S^3 = \frac{d_{eq}^3 / 6}{\left(1-\cos\theta_W\right)^2 - \left(1-\cos\theta_W\right)^3 / 3} \tag{3-43}$$

The curved surface area for the front edge can be calculated using the following relation given by Equation (3-44).

$$S_{Cap} = 2\pi R^2\left(1-\cos\theta_W\right) \tag{3-44}$$

The experimental observations by Davenport *et al*. (1967) and Landel *et al.* (2008) have clearly indicated that the rear surface of a single spherical-cap bubble follows a constantly oscillating lenticular shape, resulting from the external perturbation acting on the rear surface. Such a lenticular shape rear surface can be considered to be essentially flat and the surface energy increase required to break up the rear surface can be neglected based on the consideration that when any arriving eddies bombard to the flat surface, the energy due to the surface tension force action will be far smaller than the kinetic energy carried by the turbulent eddies. The idea of neglecting the surface tension effects of rear surface has also been introduced by early research work of Batchelor (1967), based on a large amount of experimental observations. It should be noted with caution that these are rough approximations and more complicated crown bubble systems are not considered in the present work. The influence of the variation of bubble shapes on the increase in surface energy is further illustrated in Figure 3-8.

While the breakup model proposed by Luo and Svendsen (1996) only considered the surface energy requirement for breakup events, it should be noted that bubble breakage may also subject to the pressure head difference of the bubble and its surrounding eddies, especially when the breakage volume fraction is small. Therefore, on the basis of interaction force balance proposed by Lehr *et al.* (2002), the pressure energy requirement is also considered as a competitive breakup mechanism and a constraint which needs to be imposed. The same idea has been adopted by Zhao and Ge (2007), Liao *et al.* (2015), and Guo *et al.* (2016). The pressure energy term can be expressed using Equation (3-45),

$$e_P = \frac{\sigma}{\min(R_{C,j}, R_{C,k})} \tag{3-45}$$

where $R_{C,j}$ and $R_{C,k}$ are the radius of curvature of daughter bubbles. The theoretical prediction of surface energy and pressure energy requirement is shown in Figure 3-9.

As pointed out by Han *et al.* (2014), from a volume-based energy point of view, the surface energy density of the parent bubble should exceed the maximum of energy density increase during the entire breakup process. This is an important breakup criterion that has been adopted in this study. This criterion relates the size of parent bubble and the sizes of daughter bubbles at the same time, and hence restricts the generation of very small bubbles from the breakage as the energy density of daughter bubble will tends to infinity when its fraction or size tends to zero. Detailed information for the implementation of these two competitive breakup mechanisms under the consideration of bubble shape variations coupled with the energy density breakup criterion is described by a flowchart as shown in Figure 3-5.

The breakup frequency can be obtained by substituting equations (3-31) to (3-45) into Equation (3-30), which results in Equation (3-46)

$$\Omega_B = \begin{cases} 0.923(1-\alpha_g)n_i\left(\varepsilon/d_{eq,i}^2\right)^{1/3}\cdot\int_{\xi_{\min}}^{1}\frac{\left(d_{V,s}/d_{eq,i}+\xi\right)\left(d_{V,l}/d_{eq,i}+\xi\right)}{\xi^{11/3}}\exp\left(-\frac{12\sigma\left(S_j+S_k-S_i\right)}{\pi\beta\rho_l\varepsilon^{2/3}\xi^{11/3}d_{eq,i}^{11/3}}\right)d\xi, \\ \qquad when\ \frac{6\sigma\left(S_j+S_k-S_i\right)}{\pi d_{eq,i}^3}\geq\frac{\sigma}{\min\left(Rc_j,Rc_k\right)} \\ 0.923(1-\alpha_g)n_i\left(\varepsilon/d_{eq,i}^2\right)^{1/3}\cdot\int_{\xi_{\min}}^{1}\frac{\left(d_{V,s}/d_{eq,i}+\xi\right)\left(d_{V,l}/d_{eq,i}+\xi\right)}{\xi^{11/3}}\exp\left(-\frac{2\sigma}{\min\left(Rc_j,Rc_k\right)\beta\rho_l\varepsilon^{2/3}\xi^{2/3}d_{eq,i}^{2/3}}\right)d\xi, \\ \qquad when\ \frac{6\sigma\left(S_j+S_k-S_i\right)}{\pi d_{eq,i}^3}<\frac{\sigma}{\min\left(Rc_j,Rc_k\right)} \end{cases}$$

(3-46)

where $\xi_{\min}$ is the minimum breakage volume fraction that is able to satisfy the energy density criterion.

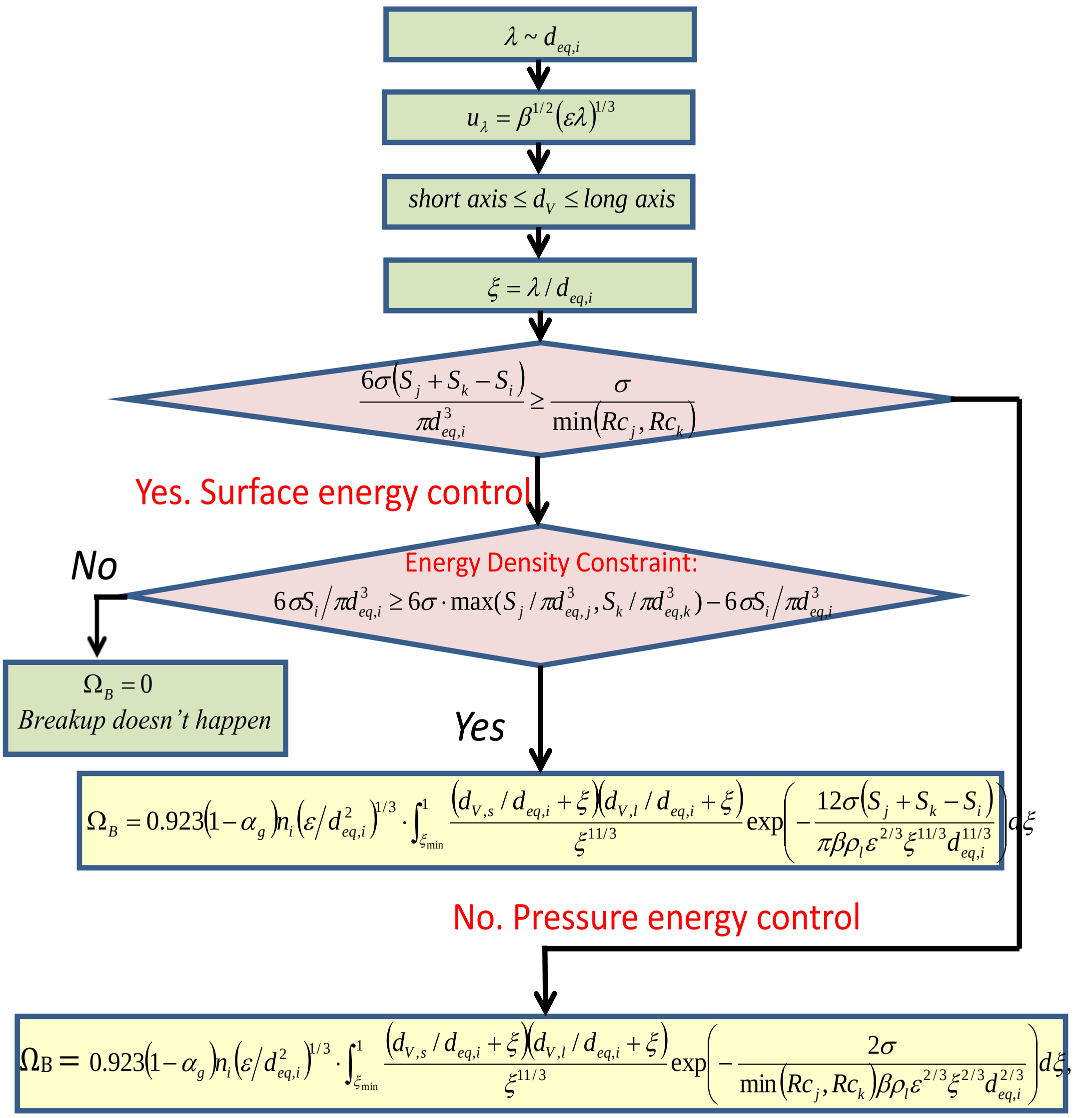

Figure 3-5 Flow chart for the improved breakup model.

3. NUMERICAL MODELLING

To validate the influence of variations in bubble shapes, numerical simulations have been carried out for the air-water bubble column systems used in Camarasa *et al.* (1999). Details of their experimental conditions are listed in Table 3-1.

Table 3-1 Details of experimental set-up.

Experiment	Diameter (m)	Height (m)	Superficial Velocity (m/s)	Static liquid Height (m)
Kulkarni *et al.* (2001)	0.15	0.8	0.0382	0.65
Camarasa *et al.* (1999)	0.1	2	0.0606	0.9

As shown in Figure 3-6, Grid 2 consists of 20(r)×40(θ)×100(z) equally distributed nodes in radial, circumferential and axial directions respectively, with no special grid refinements near the wall. The grid independence was tested in a coarser Grid 1 of 16(r)×32(θ)×80(z) nodes and a refined Grid 3 of 26(r)×48(θ)×126(z) nodes, in which case the total number of cells is doubled gradually. As shown in Figure 3-6, the grid independence test for these three set-ups has yielded similar results quantitatively though the gas-holdup for all three grids has been slightly over-predicted. The computed wall y+ values are within the range of 30-150 for all three grid configurations, which indicates that the standard wall functions can be used as near wall treatment. However, Grid 2 and Grid 3 present very similar results in the liquid axial velocity prediction while the coarser grid, Grid 1, has slightly deviated from both Grid 2 and Grid 3. Thus, Grid 2, as shown in Figure 3-6, has been employed throughout the subsequent simulations to investigate the effects of the improved breakup model.

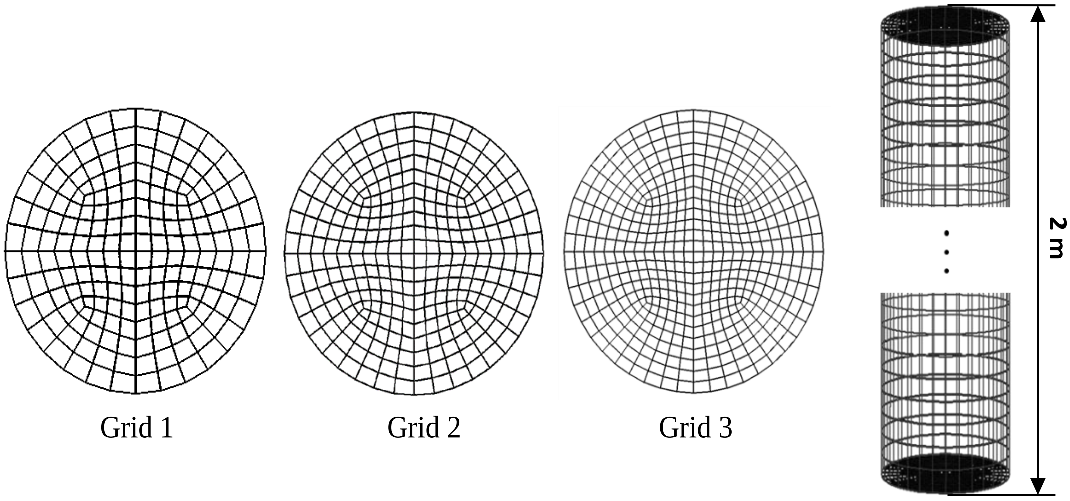

Figure 3-6 Mesh set-up at the bottom surface and main body of the column.

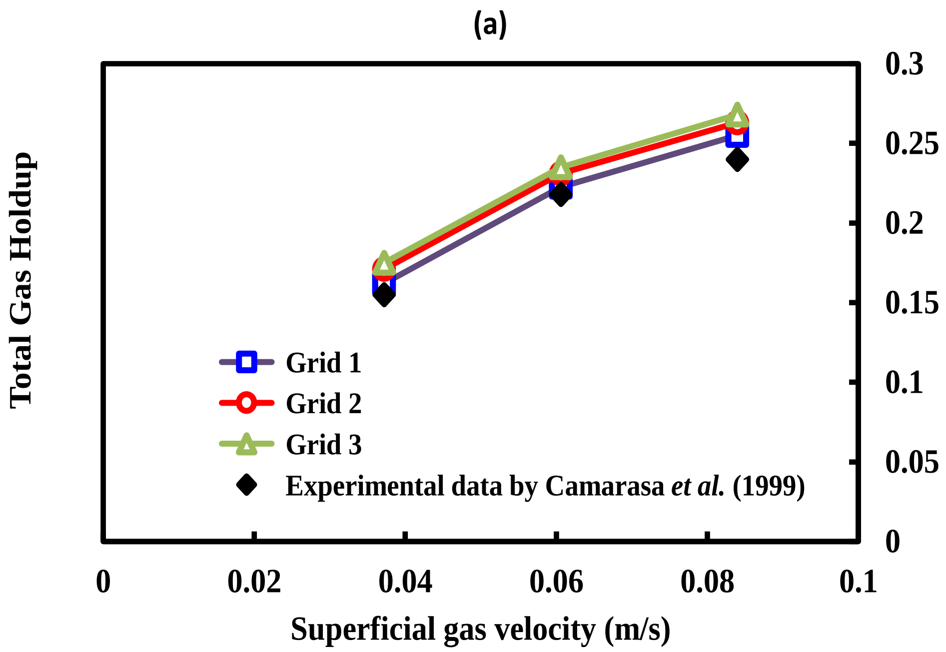

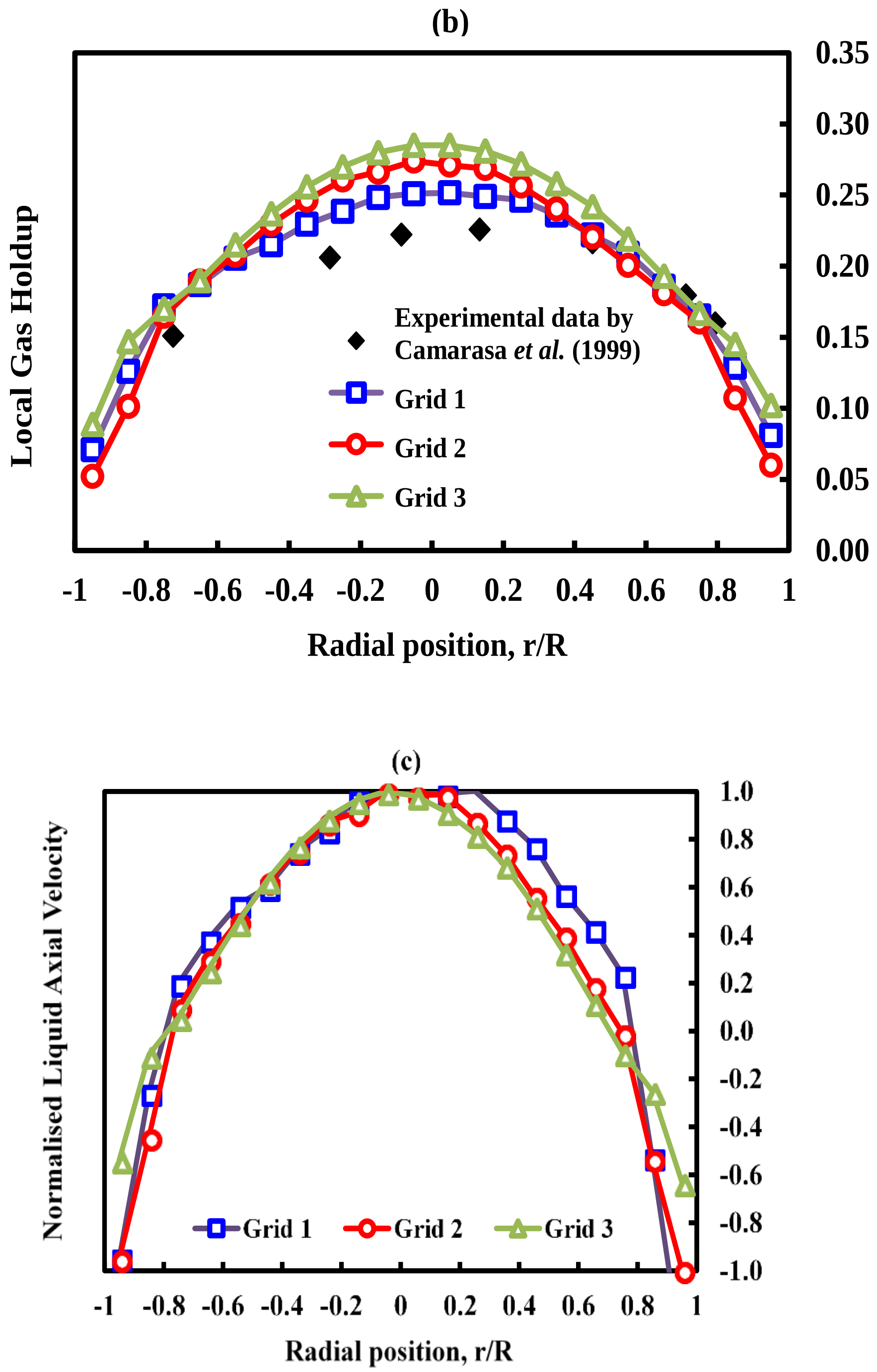

Figure 3-7 Comparison of simulated total gas holdup, local gas holdup and normalised liquid axial velocity profile with three different configurations.

ANSYS Fluent 3D pressure-based solver is employed in CFD-PBM modelling. Phase coupled SIMPLE scheme has been used for pressure-velocity coupling. The time step is set to be 0.001 seconds for all simulations, which is in accordance with the optimal value suggested by Guedon *et al.* (2017). Also, it is considered to be sufficient for illustrating the time-averaged characteristics of the flow fields by carrying out the data sampling statistics for typically 120 seconds after the quasi-steady state has been achieved. The improved breakup model is integrated into the simulations by using the user defined functions (UDF). All residual values including all phase bins are set to be below 1×10^{-4} as the convergence criteria.

The experiments by Camarasa *et al.* (1999) have used a multiple-orifice nozzle with 62 1-mm-diameter holes that uniformly spaced at the bottom of the bubble column as the gas sparger. The experimental results have shown an averaged bubble diameter near the sparger of approximately 4 mm for the superficial gas velocity at 0.0606 m/s. Therefore, for the inlet boundary conditions of the simulations, the volume fraction of gas phase with the fraction of 4-mm bubble class are both set to be 1. In this case, the evolution of bubble size distribution for the entire bubble column only relies on the bubble coalescence and breakage kernels. The turbulent intensity is assumed to be 5% with the turbulent viscosity ratio is 10 at the inlet. The treatment of the inlet velocity is different from using a constant superficial gas velocity, but a normal distributed velocity profile is applied by using the model proposed by Shi *et al.* (2017), which can be expressed as $\tilde{u}(r) = U_{max}\exp(-r^2/b)$, where U_{max} the maximum velocity, r the radial position and b the continuity coefficient. For example, for the gas distributor used by Camarasa *et al.* (1999) and the superficial gas velocity of 0.0606 m/s, the inlet model estimated value for U_{max} is about 0.1 m/s, and the value of b is about 2.2687×10^{-3} which guarantees the conservation of gas flow rate. Further information about the reasons, theoretical basis and the effects of using the inlet model can be found in the published work. The outlet boundary is set to be a pressure-outlet at the top. Since the gas phase at the outlet boundary is no longer bubbles, artificially setting the fractions of each bubble class seems to be inappropriate. Also, no-slip conditions are applied for both liquid and gas phases at the bubble column wall.

4. RESULTS AND DISCUSSION

To further illustrate the significance of considering the variation of bubble shapes, the theoretical comparison of the increase in surface energy for breakage of original spherical bubbles and various shapes of bubbles is shown in Figure 3-8. Various trends of increase in surface energy have been shown in Figure 3-8(a) for spherical-cap bubbles. It has been assumed in the modified breakup kernel that the surface energy change mainly concentrates at the front surface of the spherical-cap bubble while at the rear surface, the surface energy contribution can be ignored as the surface is nearly flat. In other words, a great percentage of formation of ellipsoidal bubbles means that higher surface energy is required to form such a daughter bubble compared with the formation of daughter bubbles based on spherical-capped shape. As a result, this scenario is more difficult to take place, which agrees with the physical phenomenon that the energy is less likely to be transferred from low energy density (spherical-capped parent bubble) to high energy density (ellipsoidal daughter bubble).

The theoretical predictions of surface energy and the pressure energy requirements for the breakage of ellipsoid and spherical-cap bubble are shown in Figure 3-9. It can be clearly seen from Figure 3-9 that the energy requirement for ellipsoid bubble shifts from pressure energy to surface energy with an increasing breakup volume fraction. This is likely attributed to the fact that the higher pressure head required inside a smaller bubble to resist the bombard from the surrounding eddies in order to sustain its own existence. However, the formation of spherical-capped daughter bubble mainly requires the surface energy. It can be conjectured that the surface energy required is mainly used for forming the large front surface of the spherical-cap bubbles. This would require further investigation.

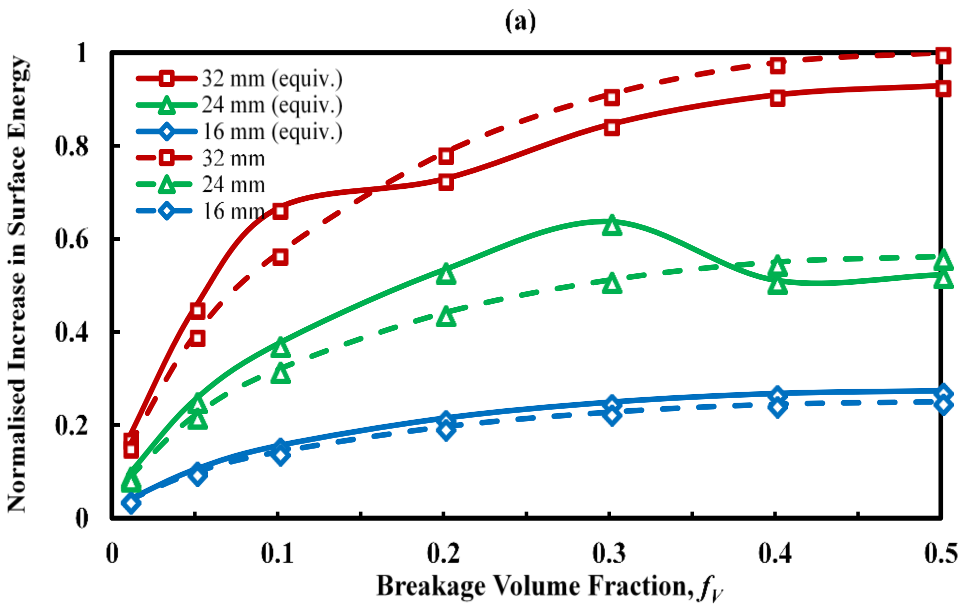

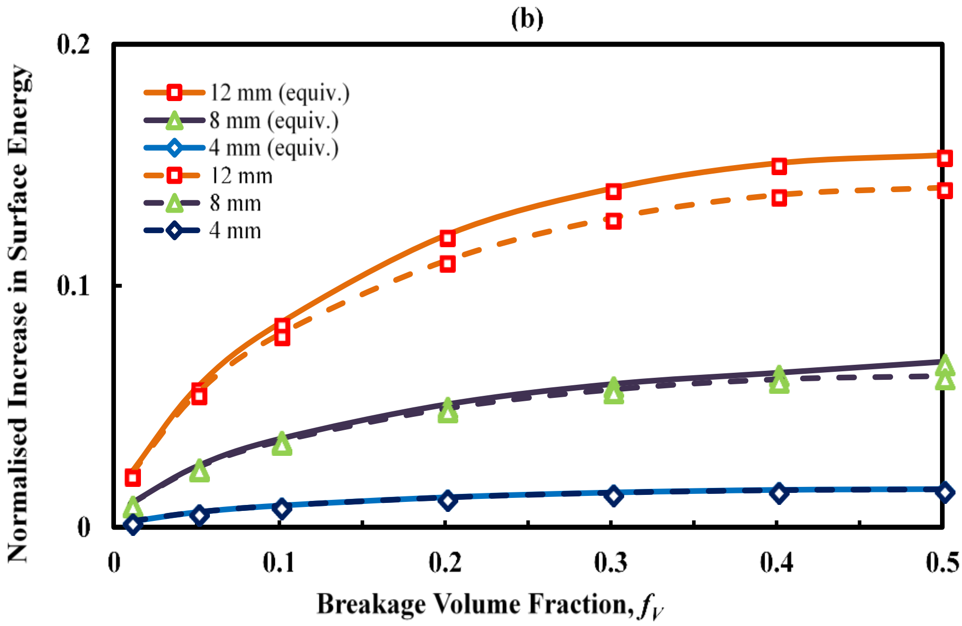

Figure 3-8 Increase in surface energy for breakage of original spherical bubbles and various shapes of bubbles.

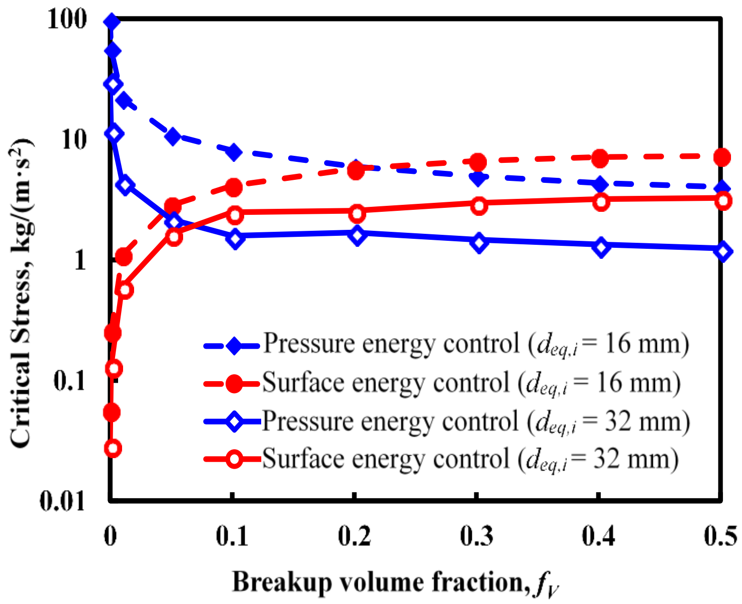

Figure 3-9 Two competitive control mechanism of the breakage of two types of bubbles: (a) Ellipsoid (b) Spherical-cap.

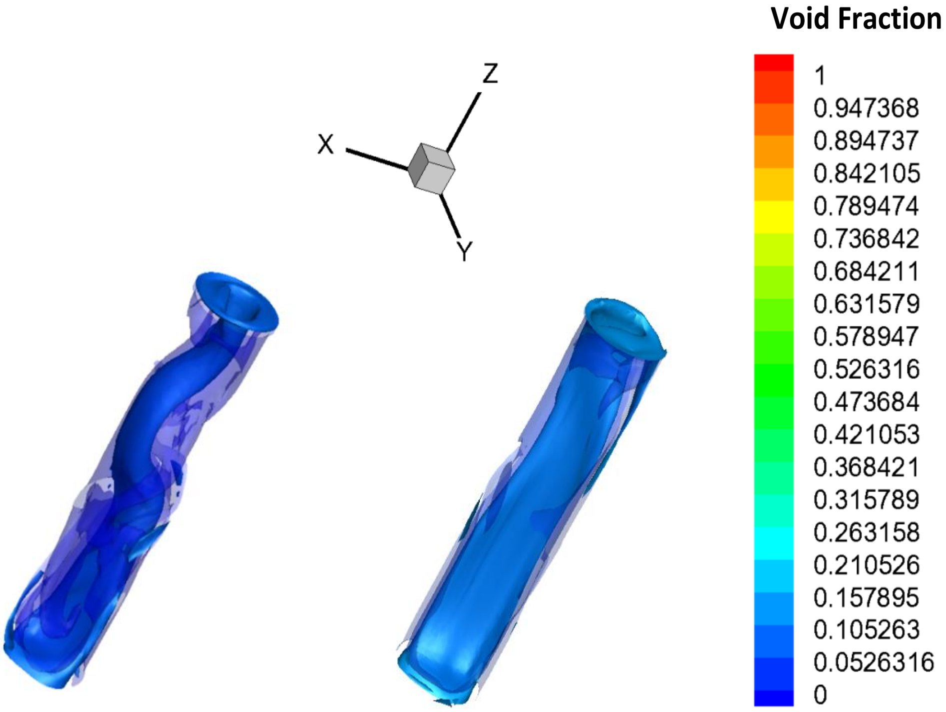

Figure 3-10 Iso-surfaces of time-average gas holdup obtained by using Luo & Svendsen model (left) and improved breakup model (right).

Figure 3-10 presents the iso-surfaces of time-average gas holdup for the simulation of a 15 cm diameter bubble column (Kulkarni *et al.*, 2001). It can be clearly seen from the Figure 3-that the overall flow pattern has changed significantly once the improved breakup model has been used. It is also noted that under-prediction of the gas holdup may occurs in the region nearing the bubble column wall no matter how the different breakup model is employed. This is likely attributed to the fact that the standard $k \sim \varepsilon$ turbulence model was employed in the simulation, resulting in underestimation of the gas holdup as the result of overestimation of the turbulence dissipation rate in the vicinity of the bubble column wall. Figure 3-11 presents the time-averaged turbulence dissipation rate. It should be noted here that even though the bubble-induced turbulence has been considered by using the Sato's model in the prediction of the turbulence dissipation rate, the turbulence dissipation rate used to evaluate the breakage rate of the bubbles, reflected from the turbulence spectrum which is still assumed to follow the classical Kolmogorov -5/3 law in sub-inertial range, was employed in the population balance model. This is obviously inappropriate. As pointed out by Mercado *et al.* (2010), Risso (2011), Riboux *et al.* (2013) and Prakash *et al.* (2016), the rising bubble induced turbulence in bubble columns is mainly caused by the agitation due to bubble wakes, which decays rapidly because of viscous dissipation. Such pseudo-turbulence has a different scaling behaviour on the energy spectrum with a slope of approximately the wave number to the power of -3. Thus, an improved expression of the breakup kernel may be required for further investigations.

It is believed that the breakup rate Ω_B, which is closely associated with the value of turbulence dissipation rate ε, directly affects the gas phase volume fraction. To highlight this deduction, the Small Perturbation Method (SPM) is applied to the dissipation term in the ε-equation of Equation (3-16), as defined by Equation (3-47),

$$\varepsilon = \varepsilon_0 + \varsigma \varepsilon_1 + \cdots \qquad (3\text{-}47)$$

where ς is the small perturbation parameter. When substituting Equation (3-47) with first order perturbation into the ε-equation and rewriting it in the cylindrical coordinates but neglecting the impacts of axial and circumferential components, Equation (3-48) can be obtained.

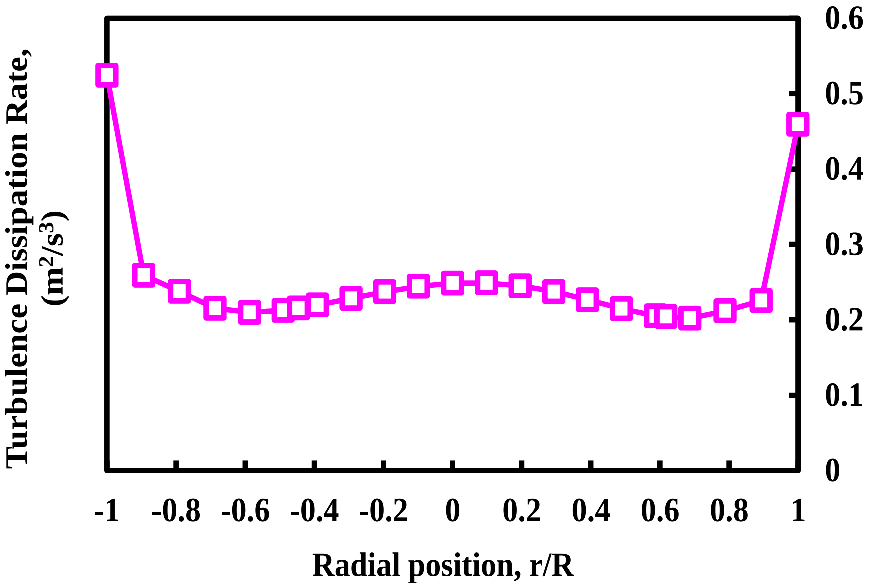

Figure 3-11 Radial distribution of time averaged turbulence dissipation rate for Case 1.

$$\frac{\partial}{\partial r}\left(\alpha\rho\left(\varepsilon_0+\varsigma\varepsilon_1\right)\vec{u}\right)=\frac{\partial}{\partial r}\left[\alpha\left(\mu+\frac{\mu_t}{\sigma_k}\right)\frac{\partial}{\partial r}\left(\varepsilon_0+\varsigma\varepsilon_1\right)\right] + \alpha\frac{\left(\varepsilon_0+\varsigma\varepsilon_1\right)}{k}\left(C_{1\varepsilon}G_k-C_{2\varepsilon}\rho\left(\varepsilon_0+\varsigma\varepsilon_1\right)\right) \tag{3-48}$$

The basic approximation by finding the zero order of ε term yields Equation (3-49),

$$\mathrm{O}\left(\varsigma^0\right):\ C_{01}\frac{\partial}{\partial r}\left(\alpha\frac{\partial\varepsilon_0}{\partial r}\right)+C_{02}\frac{\partial\left(\alpha\varepsilon_0\right)}{\partial r}+C_{03}\alpha\varepsilon_0+C_{04}\alpha\varepsilon_0^2=0 \tag{3-49}$$

while the first correction by finding the first order of ε term gives Equation (3-50),

$$\mathrm{O}\left(\varsigma^1\right):\ C_{11}\frac{\partial}{\partial r}\left(\alpha\frac{\partial\varepsilon_1}{\partial r}\right)+C_{12}\frac{\partial\left(\alpha\varepsilon_1\right)}{\partial r}+C_{13}\alpha\varepsilon_1+C_{14}\alpha\varepsilon_0\varepsilon_1=0 \tag{3-50}$$

where C_{ij} can be regarded as different constants. It can be seen clearly from the first correction that no matter how small the perturbation on the dissipation term is, the volume fraction term will inevitably generate an opposite feedback effect. The first two terms of Equation (3-50) are higher order terms, and their effects so small that can be represented by a small constant value written as C_2. By ignoring the signs of the constants, Equation (3-50) becomes $C_{13}\, \alpha\, \varepsilon_1 + C_{14}\, \alpha\, \varepsilon_0\, \varepsilon_1 = C_2$. If α is divided by both sides, the equation becomes $\varepsilon_1\, (C_{13} + C_{14}\, \varepsilon_0) = C_2 / \alpha$. In this case, small increase in ε_1 means the decrease in α, where ε_1 represents the small perturbation in turbulence dissipation rate and α is the gas holdup. This indicates that the overestimation of the dissipation term will indeed lead to the underestimation of gas volume fraction in the vicinity of the bubble column wall.

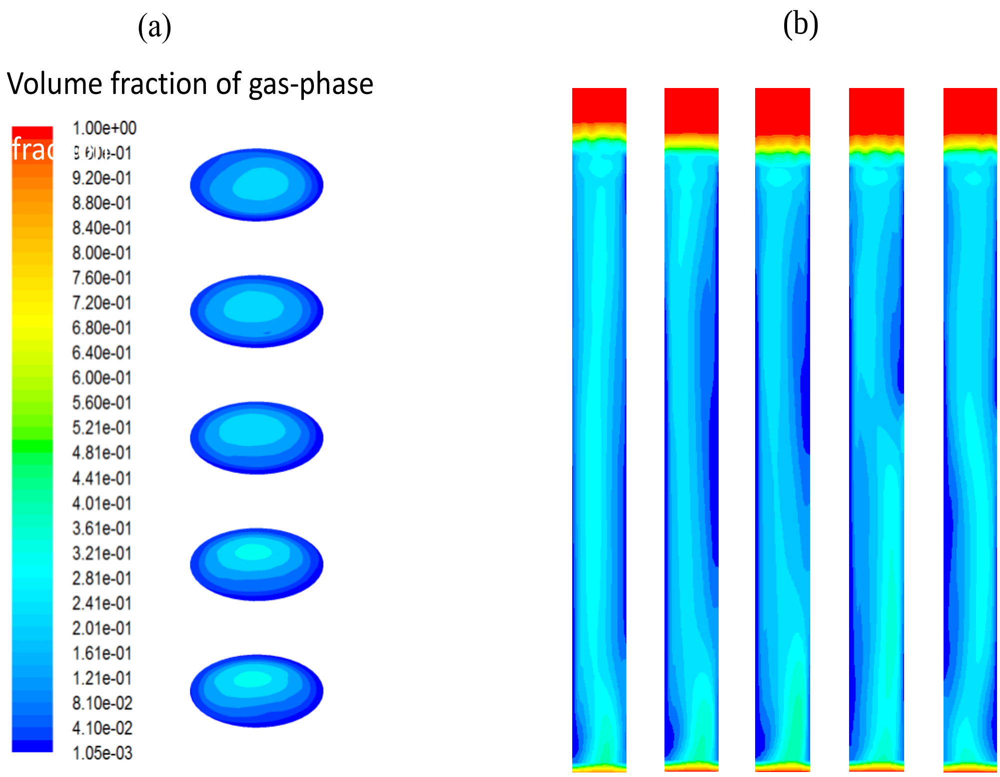

Figure 3-12 (a) Contours of time averaged gas holdup (from top to bottom: H=0.6, 0.5, 0.4, 0.3 and 0.2 m) and (b) bubble plume oscillation in time sequence (from left to right, physical time t =90 s, 95 s, 100 s, 105 s and 110 s).

Figure 3-12(a) shows the evolution of the time averaged gas holdup along the height of the bubble column, obtained by using the improved breakup model. It can be seen from Figure 3-12(a) that the high gas holdup takes place in the core of the bubble column though the holdup distributions slightly spread towards the column wall at the bottom. An explanation could be that the strong vorticity formed at the surrounding region of the wall entraps those of smaller bubbles. It can be also observed from Figure 3-12(b) that the bubble plume obtained in the CFD modelling clearly shows oscillation motions in time sequence, which reflects the transient characteristic of the dynamic behaviours of gas-liquid two-phase flow in the bubble columns.

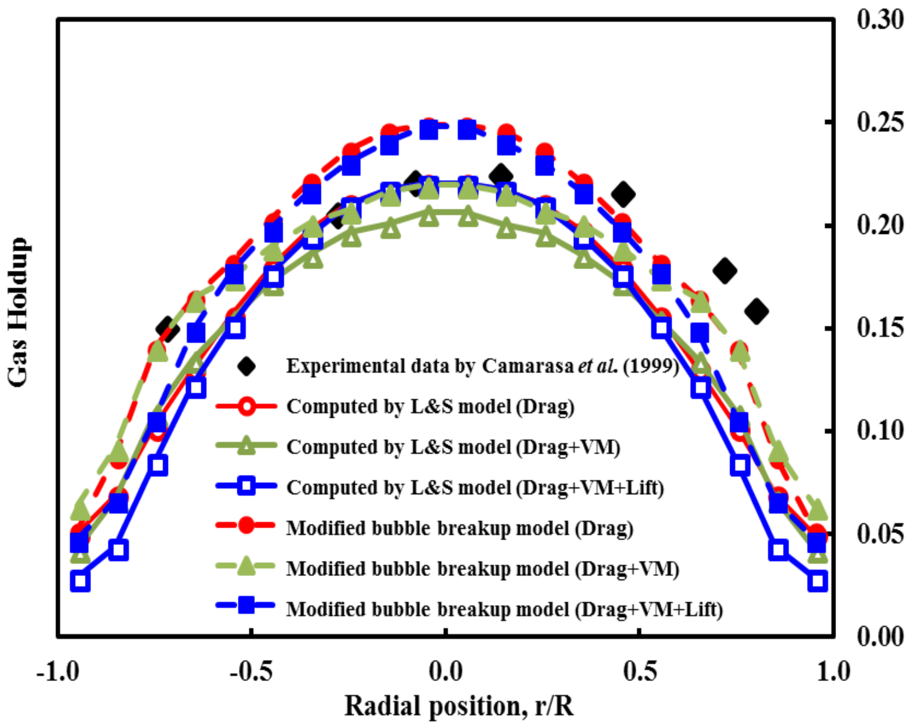

Figure 3-13 Effects of different interfacial force combinations coupled with improved breakup model and Luo and Svendsen's (L&S) breakup model.

Figure 3-13 shows the effects of implementing different combinations of interfacial forces coupled with both the improved breakup model and Luo and Svendsen's breakup model. The simulation results have clearly indicated that the use of the improved breakup model has obtained results consistent with the experimental data. However, small variations can be found among the use of different breakup models and different combinations of interfacial forces. In general, the gas holdup profiles predicted by using the Luo and Svendsen's breakup model are slightly lower than using the improved breakup model when the same interfacial forces are applied in the simulation. Although it appears that using the improved breakup model coupled with drag force and virtual mass force achieves the best agreement with the experimental data, this may only be valid for the simulation of particular industrial processes in which the effect of lift force is so insignificant that can be neglected. In general cases, the real physics of interphase momentum transfer still need to be considered sufficiently. It is noted that when the drag force, the virtual mass force and the lift force are considered simultaneously, the predicted gas flow distinctly moves towards the bubble column centre. This indicates that the influence of lift force could be significant when it is considered together with the drag force and virtual mass force.

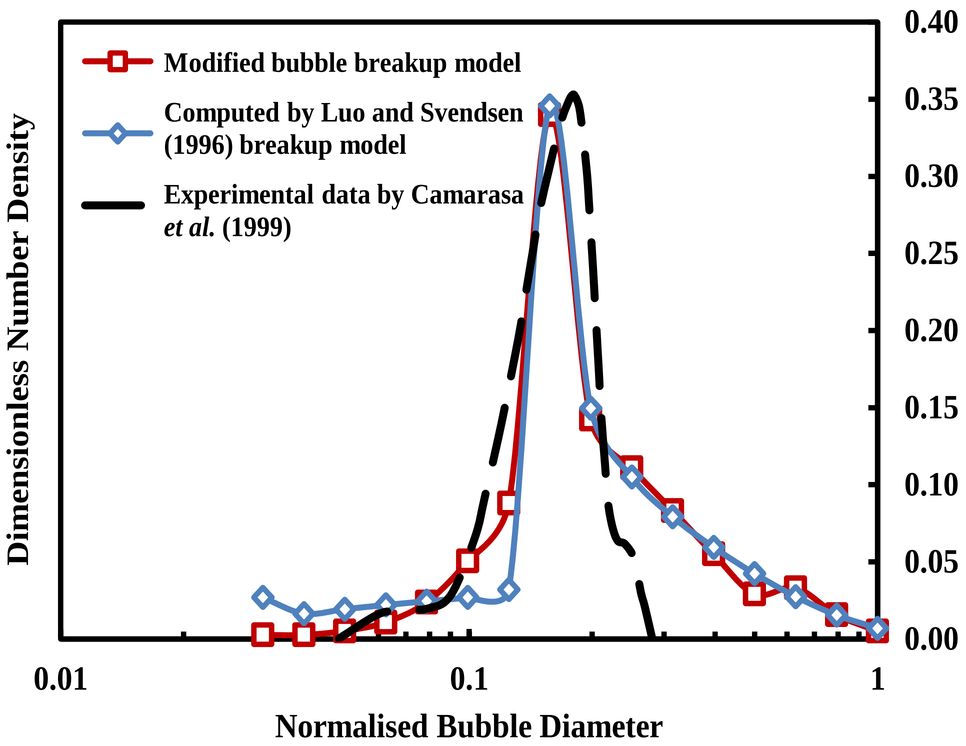

Figure 3-14 Dimensionless number density distribution of bubble groups.

Figure 3-14 presents the fraction of number density of each bubble class to the total number density of all bubbles. The x-coordinate of each data point represents the diameter of each bubble class normalised by the largest diameter of bubbles (32 mm) included in the simulation. The peak values obtained from the improved breakup model and Luo and Svendsen's breakup model are in the 8th bubble class from the left, which is equivalent to a bubble diameter of 5 mm. Although the experimental data shows the maximum number density at a slightly larger bubble class, the simulation results are in satisfactory overall agreement with the experimental data. Comparing the results of both models, it seems that a smoother number density distribution which better agrees with the experimental result can be found for small bubbles when the improved breakup model is coupled in the CFD simulation. This may be attributed to two main reasons. For both the 6th and the 7th bubble class, although not much difference can be found in the increase in surface energy when the breakage occurs, as shown in Figure 3-8, the generation of bubbles within these bubble classes may come from the breakage of large bubbles. However, when the bubble sizes are very small, such as the 1st to the 3rd bubble classes from the left, the consideration of energy density constraint and the pressure energy controlled breakup mechanism in the improved breakup model effectively restricts the over-breakage of these very small bubbles, due to the pressure head required in forming the smaller daughter bubbles being significantly large. On the contrary, a relatively small peak in the fraction of bubble number density appears at the boundary between ellipsoid and spherical-cap bubbles when using the improved breakup model, shown as the 3rd bubble class from the right. It is believed that this is very likely due to the effect of bubble shapes. As can be seen in Figure 3-8, the maximum requirement of increase in surface energy occurs when a larger spherical-cap bubble breaks into a smaller spherical-cap bubble and an ellipsoid bubble. Since the surface energy change mainly concentrates at the front surface of the spherical-cap bubble while at the rear surface, the surface energy contribution can be ignored as the surface is nearly flat. In other words, a great percentage of formation of ellipsoidal bubbles means that higher surface energy is required to form such a daughter bubble compared with the formation of daughter bubbles based on spherical-capped shape. As a result, this scenario is more difficult to take place, which agrees with the physical phenomenon that the energy is less likely to be transferred from low energy density (spherical-capped parent bubble) to high energy density (ellipsoidal daughter bubble). The breakage event is less likely to happen under this scenario and this could be the main reason that explains the appearance of the small peak at the boundary between ellipsoid and spherical bubbles.

Although the bubble shapes are considered to make more sense in physical interpretations in the newly proposed model, it is still based on the original model of Luo and Svendsen. It is believed that the fundamental issue in the breakage model is the characteristics of two-phase flow filed are still approximately described by the Kolmogorov -5/3 law of the turbulent kinetic energy spectrum. Except for the liquid shear turbulence, the bubble-induced turbulence due to the wake of ellipsoidal and spherical-capped bubbles may make significant contribution to the turbulence and the eddy-bubble interactions in the bubble column. However, the contribution from the bubble-induced turbulence has not been well reflected in the breakage model. This could be one of the main causes that will significantly improve the prediction of bubble size distribution.

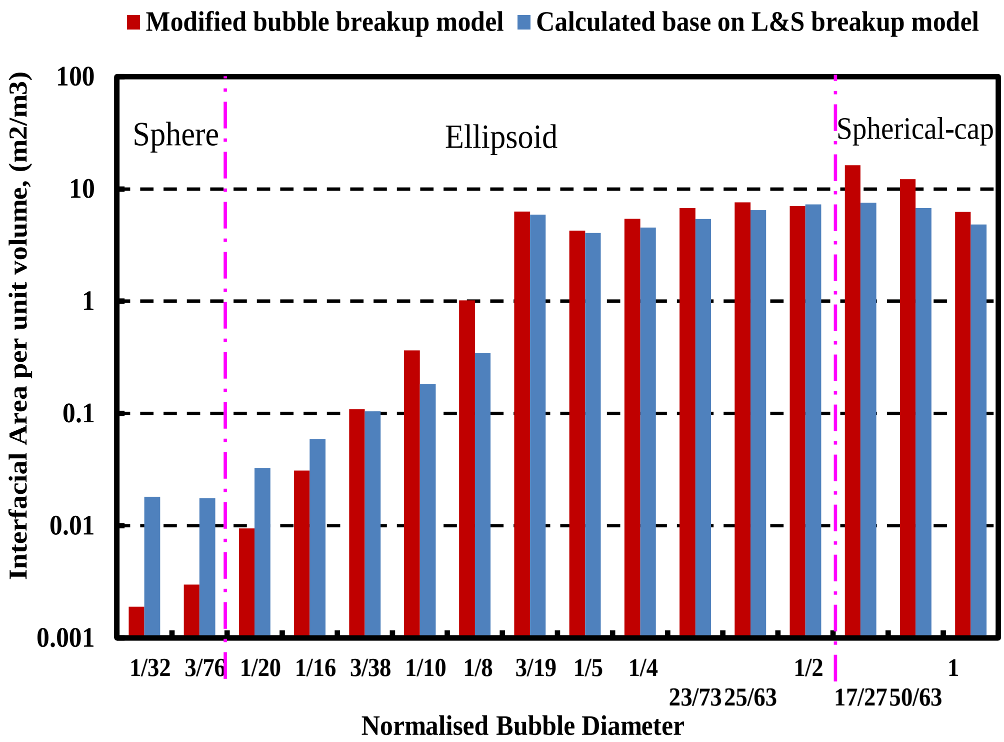

Figure 3-15 Comparison of simulated interfacial area in the bubble column.

Figure 3-15 presents the unit volume based interfacial area for each bubble class. The y-axis is shown in a $\log_{10}$ scale. Interfacial area is a key parameter that greatly affects the prediction of heat and mass transfer between bubbles and liquid phase in the bubble columns. It can be found that the difference in the interfacial area obtained by the improved breakup model and the original Luo and Svendsen's model is more apparent especially for bubble classes "1/32" to "1/20". Since these bubble classes represent very small bubbles, the difference is mainly due to the predicted number density, and hence the difference of their contribution to the total interfacial area is negligible. However, the influence of the bubble shapes is gradually reflected when the shape of the bubbles transforms from ellipsoid to spherical-cap, even if no significant difference is shown for the number density of bubble classes “17/27” to “1” predicted by both models. The consideration of ellipsoid and spherical-cap shapes of bubbles results in a significant increase in the prediction of interfacial area of bubbles and liquid phase. The total values of unit volume based interfacial area are shown in Table 3-2. It can be found that the increment obtained by the consideration of bubble shape variations reaches nearly 40 percent. Although this figure is based on statistical approximations of bubble shapes and will be slightly different from reality, it still suggests that the assumption of all bubbles defined by a spherical shape will underestimate the interfacial area to a great extent when mass and heat transfer is considered.

Table 3-2 Comparison of unit volume based interfacial area calculated from simulation results.

	Improved breakup model	**Original breakup model**
Interfacial area (m^2)	74.66	53.43

5. CONCLUSIONS

In the present study, an improved breakup model has been proposed based on the model for drop and bubble breakup presented by Luo and Svendsen (1996). The concluding remarks are as follows:

1. This improved breakup mode has taken into account the variation of bubble shapes, classified into spherical, deformed ellipsoid and spherical-cap, in the bubble columns.
2. A correlation on the aspect ratio of deformed ellipsoid bubbles, which takes into account the joint effect of buoyancy, viscosity and surface tension, has been proposed based on the experimental data of air-water systems in the bubble columns.
3. The pressure energy controlled breakup coupled with the modified breakage criteria has been considered in the modelling. The difference between the surface energy and pressure energy requirements for forming various daughter bubbles has been illustrated.
4. The energy density constraint has been applied to prevent the over-estimation of the breakage rate of small bubbles. The simulation results have shown an overall agreement with the experimental data reported in the open literature.

This study on the dynamic behaviours of various bubble shapes may lead to a more comprehensive understanding of the mass and heat transfer characteristics of the multi-phase reaction in the bubble column.

References

AOYAMA, S., HAYASHI, K., HOSOKAWA, S. & TOMIYAMA, A. 2016. Shapes of ellipsoidal bubbles in infinite stagnant liquids. *International Journal of Multiphase Flow,* 79**,** 23-30.

BATCHELOR, G. K. 1967. *An Introduction to Fluid Dynamics,* Cambridge University Press.

BESAGNI, G., BRAZZALE, P., FIOCCA, A. & INZOLI, F. 2016. Estimation of bubble size distributions and shapes in two-phase bubble column using image analysis and optical probes. *Flow Measurement and Instrumentation,* 52**,** 190-207.

BESAGNI, G. & INZOLI, F. 2016a. Bubble size distributions and shapes in annular gap bubble column. *Experimental Thermal and Fluid Science,* 74**,** 27-48.

BESAGNI, G. & INZOLI, F. 2016b. Comprehensive experimental investigation of counter-current bubble column hydrodynamics: Holdup, flow regime transition, bubble size distributions and local flow properties. *Chemical Engineering Science,* 146**,** 259-290.

BESAGNI, G., INZOLI, F., ZIEGENHEIN, T., HESSENKEMPER, H. & LUCAS, D. Bubble aspect ratio in dense bubbly flows: experimental studies in low Morton-number systems. 2017. 012014.

BOZZANO, G. & DENTE, M. 2001. Shape and terminal velocity of single bubble motion: a novel approach. *Computers & Chemical Engineering,* 25**,** 571-576.

CAMARASA, E., VIAL, C., PONCIN, S., WILD, G., MIDOUX, N. & BOUILLARD, J. 1999. Influence of coalescence behaviour of the liquid and of gas sparging on hydrodynamics and bubble characteristics in a bubble column. *Chemical Engineering and Processing,* 38**,** 329-344.

CLARK, M. M. 1988. Drop Breakup in a Turbulent-Flow .1. Conceptual and Modeling Considerations. *Chemical Engineering Science,* 43**,** 671-679.

CLIFT, R., GRACE, J. R. & WEBER, M. E. 1978. *Bubbles, Drops, and Particles,* Academic Press.

COULALOGLOU, C. A. & TAVLARIDES, L. L. 1977. Description of Interaction Processes in Agitated Liquid-Liquid Dispersions. *Chemical Engineering Science,* 32**,** 1289-1297.

DAVENPORT, W. G., BRADSHAW, A. V. & RICHARDSON, F. D. 1967. Behaviour of Spherical Cap Bubbles in Liquid Metals. *Journal of the Iron and Steel Institute,* 205**,** 1034.

DEEN, N. G., SOLBERG, T. & HJERTAGER, B. H. 2000. Numerical simulation of gas–liquid flow in a square cross section bubble column. *14th International congress of chemical and process engineering (CHISA).* Praha, Czech Republic.

DEEN, N. G., SOLBERG, T. & HJERTAGER, B. H. 2001. Large eddy simulation of the gas-liquid flow in a square cross-sectioned bubble column. *Chemical Engineering Science,* 56**,** 6341-6349.

DELNOIJ, E., LAMMERS, F. A., KUIPERS, J. A. M. & VANSWAAIJ, W. P. M. 1997. Dynamic simulation of dispersed gas-liquid two-phase flow using a discrete bubble model. *Chemical Engineering Science,* 52**,** 1429-1458.

GRACE, J. R., CLIFT, R. & WEBER, M. E. 1978. *Bubbles, Drops, and Particles,* Academic Press.

GUEDON, G. R., BESAGNI, G. & INZOLI, F. 2017. Prediction of gas-liquid flow in an annular gap bubble column using a bi-dispersed Eulerian model. *Chemical Engineering Science,* 161**,** 138-150.

GUO, X. F., ZHOU, Q., LI, J. & CHEN, C. X. 2016. Implementation of an improved bubble breakup model for TFM-PBM simulations of gas-liquid flows in bubble columns. *Chemical Engineering Science,* 152**,** 255-266.

HAN, L. C., FU, J., LI, M., GONG, S. G., GAO, N. N., ZHANG, C. & LUO, H. A. 2016. A theoretical unsteady-state model for k(L) of bubbles based on the framework of wide energy spectrum. *Aiche Journal,* 62**,** 1007-1022.

HAN, L. C., GONG, S. G., LI, Y. Q., GAO, N. N., FU, J., LUO, H. & LIU, Z. H. 2014. Influence of energy spectrum distribution on drop breakage in turbulent flows. *Chemical Engineering Science,* 117**,** 55-70.

KRISHNA, R., URSEANU, M. I., VAN BATEN, J. M. & ELLENBERGER, J. 1999. Influence of scale on the hydrodynamics of bubble columns operating in the churn-turbulent regime: experiments vs. Eulerian simulations. *Chemical Engineering Science,* 54**,** 4903-4911.

KRISHNA, R. & VAN BATEN, J. M. 2001. Eulerian simulations of bubble columns operating at elevated pressures in the churn turbulent flow regime. *Chemical Engineering Science,* 56**,** 6249-6258.

KULKARNI, A. A., JOSHI, J. B., KUMAR, V. R. & KULKARNI, B. D. 2001. Application of multiresolution analysis for simultaneous measurement of gas and liquid velocities and fractional gas hold-up in bubble column using LDA. *Chemical Engineering Science,* 56**,** 5037-5048.

LABORDE-BOUTET, C., LARACHI, F., DROMARD, N., DELSART, O. & SCHWEICH, D. 2009. CFD simulation of bubble column flows: Investigations on turbulence models in RANS approach. *Chemical Engineering Science,* 64**,** 4399-4413.

LANDEL, J. R., COSSU, C. & CAULFIELD, C. P. 2008. Spherical cap bubbles with a toroidal bubbly wake. *Physics of Fluids,* 20**,** 122101.

LEGENDRE, D., ZENIT, R. & VELEZ-CORDERO, J. R. 2012. On the deformation of gas bubbles in liquids. *Physics of Fluids,* 24.

LEHR, F., MILLIES, M. & MEWES, D. 2002. Bubble-size distributions and flow fields in bubble columns. *Aiche Journal,* 48**,** 2426-2443.

LI, W. L. & ZHONG, W. Q. 2015. CFD simulation of hydrodynamics of gas-liquid-solid three-phase bubble column. *Powder Technology,* 286**,** 766-788.

LIAO, Y. X., RZEHAK, R., LUCAS, D. & KREPPER, E. 2015. Baseline closure model for dispersed bubbly flow: Bubble coalescence and breakup. *Chemical Engineering Science,* 122**,** 336-349.

LUCAS, D., PRASSER, H. M. & MANERA, A. 2005. Influence of the lift force on the stability of a bubble column. *Chemical Engineering Science,* 60**,** 3609-3619.

LUCAS, D. & TOMIYAMA, A. 2011. On the role of the lateral lift force in poly-dispersed bubbly flows. *International Journal of Multiphase Flow,* 37**,** 1178-1190.

LUO, H. 1993. *Coalescence, Breakup and Liuqid Circulation in Bubble Column Reactors.* PhD thesis PhD thesis, PhD thesis from the Norwegian Institute of Technology.

LUO, H. & SVENDSEN, H. F. 1996. Theoretical model for drop and bubble breakup in turbulent dispersions. *Aiche Journal,* 42**,** 1225-1233.

MASOOD, R. M. A., RAUH, C. & DELGADO, A. 2014. CFD simulation of bubble column flows: An explicit algebraic Reynolds stress model approach. *International Journal of Multiphase Flow,* 66**,** 11-25.

MERCADO, J. M., GOMEZ, D. C., VAN GILS, D., SUN, C. & LOHSE, D. 2010. On bubble clustering and energy spectra in pseudo-turbulence. *Journal of Fluid Mechanics,* 650**,** 287-306.

MOORE, D. W. 2006. The velocity of rise of distorted gas bubbles in a liquid of small viscosity. *Journal of Fluid Mechanics,* 23**,** 749-766.

OKAWA, T., TANAKA, T., KATAOKA, I. & MORI, M. 2003. Temperature effect on single bubble rise characteristics in stagnant distilled water. *International Journal of Heat and Mass Transfer,* 46**,** 903-913.

POURTOUSI, M., SAHU, J. N. & GANESAN, P. 2014. Effect of interfacial forces and turbulence models on predicting flow pattern inside the bubble column. *Chemical Engineering and Processing: Process Intensification,* 75**,** 38-47.

PRAKASH, V. N., MERCADO, J. M., VAN WIJNGAARDEN, L., MANCILLA, E., TAGAWA, Y., LOHSE, D. & SUN, C. 2016. Energy spectra in turbulent bubbly flows. *Journal of Fluid Mechanics*, 791**,** 174-190.

PRINCE, M. J. & BLANCH, H. W. 1990. Bubble Coalescence and Break-up in Air-Sparged Bubble-Columns. *Aiche Journal,* 36**,** 1485-1499.

QIN, C. P., CHEN, C., XIAO, Q., YANG, N., YUAN, C. S., KUNKELMANN, C., CETINKAYA, M. & MULHEIMS, K. 2016. CFD-PBM simulation of droplets size distribution in rotor-stator mixing devices. *Chemical Engineering Science,* 155**,** 16-26.

RAMPURE, M. R., KULKARNI, A. A. & RANADE, V. V. 2007. Hydrodynamics of bubble column reactors at high gas velocity: Experiments and computational fluid dynamics (CFD) Simulations. *Industrial & Engineering Chemistry Research,* 46**,** 8431-8447.

RANADE, V. V. & TAYALIA, Y. 2001. Modelling of fluid dynamics and mixing in shallow bubble column reactors: influence of sparger design. *Chemical Engineering Science,* 56**,** 1667-1675.

RIBOUX, G., LEGENDRE, D. & RISSO, F. 2013. A model of bubble-induced turbulence based on large-scale wake interactions. *Journal of Fluid Mechanics*, 719**,** 362-387.

RISSO, F. 2011. Theoretical model for k(-3) spectra in dispersed multiphase flows. *Physics of Fluids,* 23.

RZEHAK, R. & KREPPER, E. 2013. CFD modeling of bubble-induced turbulence. *International Journal of Multiphase Flow,* 55**,** 138-155.

SANKARANARAYANAN, K. & SUNDARESAN, S. 2002. Lift force in bubbly suspensions. *Chemical Engineering Science,* 57**,** 3521-3542.

SATO, Y. & SEKOGUCHI, K. 1975. Liquid velocity distribution in two-phase bubble flow. *International Journal of Multiphase Flow,* 2**,** 79-95.

SHAH, Y. T., KELKAR, B. G., GODBOLE, S. P. & DECKWER, W. D. 1982. Design Parameters Estimations for Bubble Column Reactors. *Aiche Journal,* 28**,** 353-379.

SHI, W., YANG, N. & YANG, X. 2017. A kinetic inlet model for CFD simulation of large-scale bubble columns. *Chemical Engineering Science,* 158**,** 108-116.

SOKOLICHIN, A. & EIGENBERGER, G. 1999. Applicability of the standard k-epsilon turbulence model to the dynamic simulation of bubble columns: Part I. Detailed numerical simulations. *Chemical Engineering Science,* 54**,** 2273-2284.

SOKOLICHIN, A., EIGENBERGER, G. & LAPIN, A. 2004. Simulation of buoyancy driven bubbly flow: Established simplifications and open questions. *Aiche Journal,* 50**,** 24-45.

SOKOLICHIN, A., EIGENBERGER, G., LAPIN, A. & LUBBERT, A. 1997. Dynamic numerical simulation of gas-liquid two-phase flows - Euler/Euler versus Euler/Lagrange. *Chemical Engineering Science,* 52**,** 611-626.

SUGIHARA, K., SANADA, T., SHIROTA, M. & WATANABE, M. 2007. Behavior of single rising bubbles in superpurified water. *Kagaku Kogaku Ronbunshu,* 33**,** 402-408.

TABIB, M. V., ROY, S. A. & JOSHI, J. B. 2008. CFD simulation of bubble column - An analysis of interphase forces and turbulence models. *Chemical Engineering Journal,* 139**,** 589-614.

TOMIYAMA, A. 1998. Struggle with computational bubble dynamics. *Multiphase Science and Technology, Vol 10 Issue 4 1998***,** 369-405.

TOMIYAMA, A., MIYOSHI, K., TAMAI, H., ZUN, I. & SAKAFUCHI, T. 1998. A Bubble Tracking Method for the Prediction of Spatial-Evolution of Bubble Flow in a Vertical Pipe. *3rd International Conference on Multiphase Flow (ICMF 98).* Lyon, France.

TOMIYAMA, A., TAMAI, H., ZUN, I. & HOSOKAWA, S. 2002. Transverse migration of single bubbles in simple shear flows. *Chemical Engineering Science,* 57**,** 1849-1858.

TRIPATHI, M. K., SAHU, K. C. & GOVINDARAJAN, R. 2015. Dynamics of an initially spherical bubble rising in quiescent liquid. *Nature Communications,* 6.

TSAMOPOULOS, J., DIMAKOPOULOS, Y., CHATZIDAI, N., KARAPETSAS, G. & PAVLIDIS, M. 2008. Steady bubble rise and deformation in Newtonian and viscoplastic fluids and conditions for bubble entrapment. *Journal of Fluid Mechanics,* 601**,** 123-164.

TSUCHIYA, K., SONG, G. H. & FAN, L. S. 1990. Effects of Particle Properties on Bubble Rise and Wake in a 2-Dimensional Liquid-Solid Fluidized-Bed. *Chemical Engineering Science,* 45**,** 1429-1434.

WANG, T. F., WANG, J. F. & JIN, Y. 2003. A novel theoretical breakup kernel function for bubbles/droplets in a turbulent flow. *Chemical Engineering Science,* 58**,** 4629-4637.

WANG, X., KLAASEN, B., DEGREVE, J., BLANPAIN, B. & VERHAEGHE, F. 2014. Experimental and numerical study of buoyancy-driven single bubble dynamics in a vertical Hele-Shaw cell. *Physics of Fluids,* 26.

WELLEK, R. M., AGRAWAL, A. K. & SKELLAND, A. H. 1966. Shape of Liquid Drops Moving in Liquid Media. *Aiche Journal,* 12**,** 854-&.

XIAO, Q., WANG, J., YANG, N. & LI, J. H. 2017. Simulation of the multiphase flow in bubble columns with stability-constrained multi-fluid CFD models. *Chemical Engineering Journal,* 329**,** 88-99.

XIAO, Q., YANG, N. & LI, J. 2013. Stability-constrained multi-fluid CFD models for gas–liquid flow in bubble columns. *Chemical Engineering Science,* 100**,** 279-292.

XUE, J., CHEN, F. G., YANG, N. & GE, W. 2017a. Eulerian-Lagrangian simulation of bubble coalescence in bubbly flow using the spring-dashpot model. *Chinese Journal of Chemical Engineering,* 25**,** 249-256.

XUE, J., CHEN, F. G., YANG, N. & GE, W. 2017b. A Study of the Soft-Sphere Model in Eulerian-Lagrangian Simulation of Gas-Liquid Flow. *International Journal of Chemical Reactor Engineering,* 15**,** 57-67.

YANG, N., WU, Z. Y., CHEN, J. H., WANG, Y. H. & LI, J. H. 2011. Multi-scale analysis of gas-liquid interaction and CFD simulation of gas-liquid flow in bubble columns. *Chemical Engineering Science,* 66**,** 3212-3222.

YANG, N. & XIAO, Q. 2017. A mesoscale approach for population balance modeling of bubble size distribution in bubble column reactors. *Chemical Engineering Science,* 170**,** 241-250.

ZHANG, D., DEEN, N. G. & KUIPERS, J. A. M. 2006. Numerical simulation of the dynamic flow behavior in a bubble column: A study of closures for turbulence and interface forces. *Chemical Engineering Science,* 61**,** 7593-7608.

ZHAO, H. & GE, W. 2007. A theoretical bubble breakup model for slurry beds or three-phase fluidized beds under high pressure. *Chemical Engineering Science,* 62**,** 109-115.

ZHOU, R. T., YANG, N. & LI, J. H. 2017. CFD simulation of gas-liquid-solid flow in slurry bubble columns with EMMS drag model. *Powder Technology,* 314**,** 466-479.

CHAPTER 4: AN IMPROVED BUBBLE BREAKAGE MODEL ACCOUNTING THE EFFECT OF BUBBLE-INDUCED TURBULENCE ENERGY SPECTRUM DISTRIBUTION

SUMMARY

In the preceding Chapter, an improved breakup model has been proposed based on the model for drop and bubble presented by Luo and Svendsen (1996), which has taken into account the variation of bubble shapes. In fact, the interactions between the turbulent eddies and bubbles are significantly affected by the variation of bubble shapes as the bubble breakage is dependent on the collision between turbulent eddies and bubbles. Reasonably quantitative description of the interaction between the turbulence eddies and bubble groups is crucial for the prediction of the bubble size distribution in bubble columns when adopting the population balance model (PBM) as estimation of the heat and mass transfer across the interfaces between bubbles and carrier liquid will be significantly affected. Most currently adopted breakage kernels focus on the shear turbulence in the liquid phase and model the kinetic energy contained in the arrival eddies to hit the bubbles by using the classical single-phase turbulence Kolmogorov -5/3 scaling law. For bubble columns, eddies that hit the bubbles and cause the bubble breakage are those mainly generated by bubble-induced turbulence. This chapter focuses on the influence of κ^{-3} scaling of the bubble-induced turbulence energy spectrum on the bubble breakage due to the eddy-bubble collision in bubble columns and proposes a modified breakage model accounting for the the bubble-induced turbulence. The proposed breakage model has taken into

account the mean turbulent velocity of eddies under the influence of bubble-induced turbulence, and the characteristic wave number/length scale that corresponds to the bubble-induced turbulence. The simulation results compared with the experimental data have clearly demonstrated that the modified breakage model effectively describes bubble breakage events under the influence of bubble-induced turbulence in bubble columns. It was revealed that the interaction of bubbles with the bubble-induced turbulence eddies dominates the turbulence generated in in bubble column flows.

1. INTRODUCTION

Pseudo-turbulence induced by rising bubbles or so called bubbulence can be crucial in the numerical modelling of bubble column reactors. Although the energy cascade of pseudo-turbulence has not been fully understood, the difference of its behaviour from the homogeneous single-phase turbulence can be clearly observed from the turbulence energy spectrum. Many studies have focused on the breakage of fluid particles and a number of mathematical models have been proposed to describe the eddy-bubble interactions but the majority of these models are based on the classic Kolmogorov -5/3 scaling law for the inertial subrange to obtain the expression for the number density of eddies (Luo and Svendsen, 1996, Lehr et al., 2002, Andersson and Andersson, 2006, Wang et al., 2003, Hagesaether et al., 2002, Zhao and Ge, 2007, Han et al., 2011, Bhole et al., 2008, Jakobsen et al., 2005). This may be inappropriate when these breakup models are used to describe the bubble breakage phenomenon in bubble columns since the effect of pseudo-turbulence induced by rising bubbles may become predominant in these particular types of reactors.

The characteristics of the pseudo-turbulence induced by rising bubbles have come into the scope of research for only a few decades, but the concerns related to fluid disturbance induced by the sphere object were raised much earlier. The pioneering work of Batchelor (1967) presented the analytical description of axisymmetric irrotational flow due to a moving sphere and he deduced that the stream function behind the sphere decays with distance to the power of -3. Lance and Bataille (1991) have examined one dimensional energy spectra of bubble swarm for various values of void fractions and a given ratio of turbulent fluctuations of the liquid without bubble introduction to the bubble slip velocity, upflowing through a hydrodynamic tunnel with the grid located upstream for generating the turbulence and injecting the bubbles. They used both hot-wire and laser Doppler anemometry (LDA). They found from the measurements that the Kolmogorov power law scaling of -5/3 was gradually replaced by a slope of approximately -8/3 with the increase of the volume fraction of the gas phase. They attributed the change of slope to the wakes of bubbles, in which eddies produced were dissipated rapidly before the spectral transfer has even taken place. Therefore, based on the spectral energy balance of dissipation and production, they concluded that the exponent of power law scaling was approximately -3, which was close to the value of -8/3 they found from the experiments.

By contrast, a few experimental studies have reported the -5/3 behaviour for pseudo-turbulence (Mudde *et al.* (1997) Cui and Fan (2004). These studies show the energy spectrum slope in the range of inertia subrange the same as that of the energy spectrum of the homogeneous and isotropic turbulence in the single phase flow. Rensen *et al.* (2005) reported a slope close to but slightly less steep than -5/3. They attributed this to the energy enhancement at small scales, which is caused by the presence of microbubbles. However, it was not until the recent work of Mercado *et al.* (2010), Mendez-Diaz *et al.* (2013), Riboux *et al.* (2013) and Prakash *et al.* (2016) that the scaling behaviour of -3 for the inertial subrange was re-confirmed to be robust. As mentioned by Mercado *et al.* (2010), the signals from the bubbles should be separated from the liquid phase signal, and more importantly, the energy spectrum has to be calculated based on individual segments to reflect the liquid fluctuations rather than being based on averaging. Direct numerical simulation (DNS) conducted by Mazzitelli and Lohse (2009) also observed a slope of -5/3 for the energy spectrum of pseudo-turbulence. However, they only considered the bubbles as point-like particles, likely resulting in the finite-size effect and capillary phenomena being disregarded. Consequently, as highlighted by Mazzitelli and Lohse (2009), the -5/3 scaling law cannot properly reflect the real characteristics of the bubble column flows. Fully resolved simulations of freely rising deformable bubbles, such as those done by Sugiyama *et al.* (2001), Roghair *et al.* (2011) and Riboux *et al.* (2013), have clearly shown a slope of -3 to be the spectral scaling exponent for bubble-induced turbulence.

Though there is still no consensus reached for the power law scaling of bubble-induced turbulence in the bubble columns, most of recent progresses on bubble-induced turbulence have shown the convincing evidences that the scaling law of the pseudo-turbulence induced by the rising bubbles is different from the Kolmogorov -5/3 scaling, as has been demonstrated by Risso and Ellingsen (2002), Roig and de Tournemine (2007) and Risso *et al.* (2008). In particular, Risso *et al.* (2008) analogised the attenuation of wakes in a fixed array of spheres randomly distributed in space to that of bubbles within a homogeneous swarm, and have shown that the bubbles' wakes in pseudo-turbulence decay faster than standard turbulent flow with the same energy and integral length scale, even when the gas volume fraction is increased to 13%. In addition, different experimental approaches have been used to obtain the energy spectrum of the pseudo-turbulence induced by rising bubbles. Mercado *et al.* (2010) used a phase-sensitive constant-temperature anemometry (CTA), which is simultaneously calibrated by LDA, to measure the energy spectrum within the wake of the bubble swarm and obtained the energy spectrum of pseudo-turbulence with a κ^{-3} scaling. Riboux *et al.* (2010) measured the energy spectrum in the wake of a bubble swarm using PIV and also confirmed the scaling to be very close to -3. Risso (2011) proposed a theoretical model to explain the -3 scaling, which argues that the signals from the wakes of bubbles can be treated as the collective effect of localised random bursts with statistically independent strength and size. This study clearly distinguished between the spatial fluctuations that can be measured by PIV and time fluctuations of velocities that can be measured by CTA probe, and determined the κ^{-3} spectral density for both spatial and temporal parts. Although this is not the direct evidence that the Taylor hypothesis of "frozen turbulence" can be assumed to be applicable to the pseudo-turbulence, this work at least shows the similarity of κ^{-3} spectrum's behaviour both in time and in space. Prakash *et al.* (2016) also used a phase sensitive CTA probe to measure the velocity fluctuations of liquid phase, and they again reaffirmed that the κ^{-3} scaling is not only to hold for description of bubble-induced turbulence but also to be suitable for defining the generic feature of turbulent bubbly flows. Based on their experimental findings, they proposed an energy balance between the energy production due to the presence of bubbles and the viscous dissipation, i.e. the dissipation due to the bubbles counterbalances the production rate, a result consistent with the milestone finding of Lance and Bataille (1991).

Despite the ongoing discussions on the power law scaling for pseudo-turbulence, bubble-induced turbulence in current CFD modelling of bubbly flows is mainly considered by adding an extra contribution to the effective viscosity or by adding a generation source term in the turbulence models (Pfleger and Becker, 2001, Troshko and Hassan, 2001, Simonin, 1990, Sato and Sekoguchi, 1975, Rzehak and Krepper, 2013). To the best of the author's knowledge, the use of the bubble-induced turbulence energy spectra with -3 scaling law to characterise the mean fluctuation velocity of turbulent eddies and the turbulence dissipation rate for the estimation of bubble breakage rate when determining the number of turbulent eddies has rarely been documented in the CFD modelling of bubble column flows. Of particular relevance to the current study is the study carried out by Han *et al.* (2014), which proposed a theoretical model that considered the wide spectrum functions for the breakage of drop in turbulent flows. In their study, the energy spectrum function used in the breakage kernel was expanded to the energy-containing range and the dissipation range. In doing so, the crucial influence of the energy spectrum distribution on the evolution of the breakage frequency was successfully demonstrated. However, it should be noted that the Kolmogorov -5/3 scaling law is still applied in the inertial subrange for their model. The current work aims to consider the influence of by replacing -5/3 scaling law with -3 scaling in the inertial subrange on bubble breakage in bubble column flows. The influence of the energy-containing range and the dissipation range is not considered for the purpose of simplification. A breakage model accounting for the κ^{-3} scaling of the pseudo-turbulence energy spectrum induced by the rising bubbles is thus proposed. We argue that the eddies generated due to bubble wake induced turbulence contribute the most of bubble breakage events as such shed vortices from the preceding rising bubbles continuously hit or bombard the subsequent bubbles.

This chapter will be organised and presented in such a way. Section 2 will present the mathematical modelling adopted in the current study while section

3 will present the simulation results and discussion, focusing on the effect of considering the pseudo-turbulence spectrum on the prediction of key parameters including gas holdup, bubble breakage rate & particle size distribution function (PDF), and bubble number density. Section 4 will present the conclusions drawn from the current study.

2. Model Development

2.1 Energy spectrum function

Based on the model of Luo and Svendsen (1996), the number probability density of eddies, f_λ, can be obtained by equating the turbulent kinetic energy of the turbulent eddies to the kinetic energy contained in eddies of size between λ and λ+dλ and interpreting the eddies as discrete entities which are dependent on the wave number in the energy spectrum.

$$E_{eddies}(\lambda) = E_{spectra}(\lambda) \tag{4-1}$$

Hence, Equation (4-2) can be derived,

$$f_\lambda \left[\frac{1}{2}\left(\rho_L \frac{\pi}{6}\lambda^3\right)\bar{v}_\lambda^2\right] = E(\kappa)\rho_L(1-\alpha)\left(-\frac{d\kappa}{d\lambda}\right) \tag{4-2}$$

where ρ, λ, α, and κ are density, wave length, volume fraction and wave number respectively. It should be noticed that the mean eddy velocity, $\bar{v}_\lambda$, should also be related to the energy spectrum function, thus

$$\bar{v}_\lambda \sim \sqrt{\kappa E(\kappa)} \tag{4-3}$$

It is assumed that the turbulence is isotropic and that the eddy size of interest lies in the inertial subrange. An analytical approximation to estimate the lower and upper ends of the inertial subrange is given by Batchelor (1967), which is expressed by Equation (4-4),

$$\frac{1}{l} \ll \kappa \ll \frac{1}{\eta} \tag{4-4}$$

where l is the characteristic length scale and η is the Kolmogorov length scale defined as $\eta = (\nu^3/\varepsilon)^{1/4}$. Since the order of turbulence dissipation term is found to be $\varepsilon \sim u^3/l$, the ratio of the characteristic length to the Kolmogorov length scale should satisfy the following relation, given by Equation (4-5).

$$\frac{\eta}{l} \sim \left(\frac{ul}{\nu}\right)^{-\frac{3}{4}} \tag{4-5}$$

When the wave numbers fall into the order of $(l\eta)^{-1/2}$, it will lie within the inertial subrange, i.e.

$$\kappa \sim \left(\frac{1}{l\eta}\right)^{\frac{1}{2}} \sim \frac{1}{l}\left(\frac{ul}{\nu}\right)^{\frac{3}{8}} \tag{4-6}$$

It has been widely accepted and confirmed that the Kolmogorov -5/3 scaling law is held for single phase turbulence flows and it can be expressed by

$$E(\kappa) = C_\kappa \varepsilon^{\frac{2}{3}} \kappa^{-\frac{5}{3}} \tag{4-7}$$

where $C_\kappa \approx 1.5$.

Although Equation (4-7) is well-accepted for homogeneous single-phase turbulence, it may be inappropriate for description of the behaviour of the bubble-induced pseudo-turbulence flow in bubble columns. As has been pointed out in the preceding section, the bubble-induced turbulence becomes dominant especially in the core region of the bubble columns. For bubble-induced turbulence, Lance and Bataille (1991) and Prakash *et al.* (2016) have indicated that an equilibrium between the energy production and the dissipation can be established. The relation, in the form of the Fourier transform, can be approximated by

$$\upsilon E(\kappa)\kappa^2 \sim \frac{\alpha g U_r}{\kappa} \tag{4-8}$$

where $E(\kappa)$ is the Fourier transform of the kinetic energy divided by density and υ is the kinematic viscosity. The LHS of Equation (4-8) represents the energy dissipation term while the RHS represents the power input by bubbles, which equals to the work done by the buoyancy $\alpha g U_r$ divided by density. In this case, it is suggested that the energy input by the bubbles only passes over to higher wave numbers and the equilibrium can be achieved in a steady state. On the contrary, eddies within the wakes of bubble do not take part in the large-scale energy transfer for lower wave numbers. Thus, the Kolmogorov -5/3 scaling law may still be used to cover the range of lower wave numbers. The appropriateness of using the -5/3 slope for the lower wave number region, especially from the bubble breakage point of view, however, is still questionable. As pointed out by Han *et al.* (2014), the fluid particles that correspond to the lower wave numbers may also fall into the eddy containing region, for which the behaviour on the energy spectrum is different from the inertial subrange. The boundary between the energy containing range and the inertial range has not yet been clearly defined. This is true especially when the fluid particles that correspond to lower wave numbers are within the inertial subrange judging from the size and the "cross-over" effect is taken into account. In spite of the aforementioned considerations, the -5/3 scaling will be used for the lower wave numbers in the present study from engineering prediction perspectives. Therefore, the energy spectrum for the two-phase flow in the bubble columns can be expressed by

$$E(\kappa) = \delta_l C_\kappa \varepsilon^{\frac{2}{3}} \kappa^{-\frac{5}{3}} + \delta_b C_b \frac{\alpha g U_{slip}}{\nu} \kappa^{-3} \tag{4-9}$$

where δ_l and δ_b are switch functions. These two switch functions are adopted as the turbulence energy spectrum will be undergoing a transition on the slope of the spectrum at the position, approximately corresponding to the wave length which can be characterised by the characteristic length scale $\Lambda = d_b / C_D$ for the attenuated bubble wakes within the bubble swarm. C_D is the drag coefficient of a single bubble. Previous studies have illustrated that the drag coefficient for bubbles is strongly related to the shape of bubbles, such as Clift *et al.* (1978), Ishii and Zuber (1979). The use of the drag coefficient of a single bubble implicitly suggests that the regions under the influence of bubble wakes are very different for various shapes and sizes of bubbles. It appears that the corresponding critical wave number is not a constant parameter instead it is subjected to the local flow field. Thus, the Sauter mean diameter of bubbles can be used in computing the critical wave number. For two-way coupling, the value of the Sauter mean diameter should be the average of that at the previous and the present time-step. The critical wave number is thus expressed by

$$\kappa_{critical} = \frac{2\pi}{\Lambda} \tag{4-10}$$

where $\Lambda = d_{32} / C_D$ and $d_{32} = (d_{32,t-1} + d_{32,t}) / 2$. In this case, the values for C_l and C_b in Equation (4-9) are to be determined given a turbulence energy spectrum. Two criteria have been proposed in the present study. Firstly, due to the existence of different scaling in the inertial subrange, the functional form of the spectrum, Equation (4-9), behaviours to have a turning point (the critical wave number), where the continuity and the smooth transition of the turbulence energy spectrum may not be satisfied simultaneously. The continuity at this position requires $E(\kappa_{Critical})_{left} = E(\kappa_{Critical})_{right}$ while the smooth transition of the curve requires $E'(\kappa_{Critical})_{left} = E'(\kappa_{Critical})_{right}$. These two requirements can be expressed by Equation (4-11) and (4-12).

$$C_l \varepsilon^{\frac{2}{3}} \kappa_{Critical}^{-\frac{5}{3}} = C_b \frac{\alpha g U_{slip}}{\nu} \kappa^{-3} \tag{4-11}$$

$$-\frac{5}{3} C_l \varepsilon^{\frac{2}{3}} \kappa_{Critical}^{-\frac{8}{3}} = -3 C_b \frac{\alpha g U_{slip}}{\nu} \kappa_{Critical}^{-4} \tag{4-12}$$

Rearrangement of equations (4-11) and (4-12) yields

$$C_l = C_b \frac{\alpha g U_{slip}}{\nu} \kappa_{Critical}^{-\frac{4}{3}} \varepsilon^{-\frac{2}{3}} \tag{4-13}$$

$$C_l = \frac{9}{5} C_b \frac{\alpha g U_{slip}}{\nu} \kappa_{Critical}^{-\frac{2}{3}} \varepsilon^{-\frac{2}{3}}. \tag{4-14}$$

Equations (4-13) and (4-14) cannot hold at the same time. Considering that an abrupt change in the energy spectrum is unlikely to occur, the first condition, $E(\kappa_{Critical})_{left} = E(\kappa_{Critical})_{right}$, has to be satisfied at the very least, which leads to the use of Equation (4-11) as the continuity criterion. As the integration of the energy spectrum function over all wave numbers gives the turbulence kinetic energy, the following equation can be written by assuming κcritical to fall into the inertia subrange.

$$\frac{1}{2}\overline{u'^2} = \int_{\kappa_{min}}^{\kappa_{Critical}} C_l \varepsilon^{\frac{2}{3}} \kappa^{-\frac{5}{3}} d\kappa + \int_{\kappa_{Critical}}^{\kappa_{max}} C_b \frac{\alpha g U_{slip}}{\nu} \kappa^{-3} d\kappa \tag{4-15}$$

where $\kappa_{min} = 2\pi / D_{column}$ and $\kappa_{max} = 2\pi / \eta$ and κ_{max} and κ_{min} are used to indicate the two cut-off ends of the eddy sizes. By definition, in fully three-dimensional form, the turbulence kinetic energy, k, can be expressed by

$$k = \frac{1}{2}\left(\overline{u'^2} + \overline{v'^2} + \overline{w'^2}\right) \tag{4-16}$$

Although the large eddies generated by the bubble-induced turbulence are anisotropic, the local isotropy in the direction of the rising bubble wakes in the bubble columns may be assumed, i.e. $\overline{u'^2} = \overline{v'^2} = \overline{w'^2}$. Therefore, the energy conservation criterion to determine the energy spectrum function for gas-liquid two-phase flows in the bubble columns can be described by Equation (4-15). By considering the continuity and energy conservation criteria, equations (4-11) and (4-15), the coefficients C_κ and C_b can be determined. However, these two coefficients are subjected to parameters that can be obtained from the local flow field, which leads to different values in every computational cell in actual CFD simulations. The values of these two coefficients have to be updated once the local flow field has changed. This requires additional computational effort to keep these two coefficients updated in the entire computational domain. To better demonstrate the characteristics of the bubble-induced turbulence kinetic energy spectrum, the use of Equation (4-9) to represent the inertial subrange together with using non-dimensional functions f_L and f_η, as proposed by Pope (2000) and defined by equations (4-17) and (4-18) is proposed to characterise the whole energy spectrum covering from the energy-containing range and the dissipation range, which is given by Equation (4-19). Han *et al.* (2014) and Ghasempour *et al.* (2014) have also adopted the energy spectrum function proposed by Pope (2000). Comparisons of the predictions using our model that considers the bubble-induced turbulence with the results obtained by using the model energy spectrum function (Pope, 2000) together with direct numerical simulation (DNS) results for single phase flow (Gotoh *et al.*, 2002) are shown in Figure 4-1. Parameters used for plotting Figure 4-1 include α = 0.02, ε = 0.2 m^2/s^3, U_{Slip} = 0.2 m/s, and $\nu = 1 \times 10^{-6}$ m^2/s.

$$f_L(\kappa L) = \left(\frac{\kappa L}{[(\kappa L)^2 + C_L]^{1/2}}\right)^{\frac{5}{3}+p_0} \tag{4-17}$$

$$f_\eta(\kappa\eta) = exp\left\{-\beta\left\{\left[(\kappa\eta)^4 + C_\eta^4\right]^{1/4} - C_\eta\right\}\right\} \tag{4-18}$$

$$E(\kappa)_{wide} = E(\kappa)_{inertial} f_L(\kappa L) f_\eta(\kappa\eta) \tag{4-19}$$

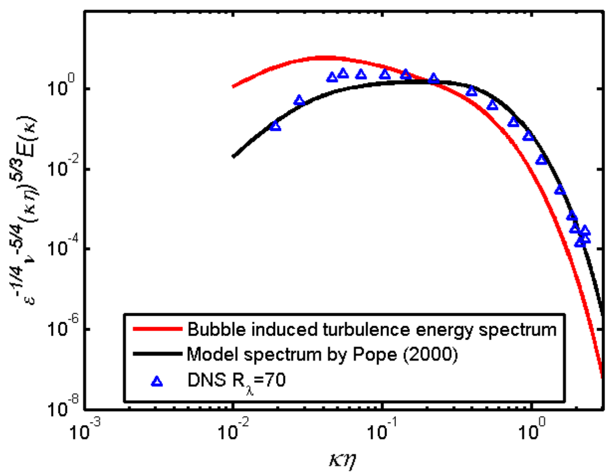

Figure 4-1 Comparison of results predicted by different energy spectrum models and the direct numerical simulation (DNS) results.

From the second-order velocity structure function, the mean turbulent velocity of eddies for single-phase turbulence can be expressed by

$$\bar{u}_\lambda = \beta(\varepsilon\lambda)^{\frac{1}{3}} \tag{4-20}$$

where β is a constant and can be found experimentally. A value of β = 2.0 has been suggested by Kuboi *et al.* (1972a), Kuboi *et al.* (1972b) and Saddoughi and Veeravalli (1994). In Luo and Svendsen (1996) model for drop and bubble breakup in turbulent dispersions, they also used the same value. Similarly, for the bubble-induced pseudo-turbulence due to the rising bubbles, the mean turbulent velocity of eddies by considering relation (4-3) can by expressed by

$$\bar{u}_\lambda = C_\lambda^{1/2}\sqrt{C_b\frac{\alpha g U_{slip}}{\nu}\lambda} \tag{4-21}$$

where the value of constant C_λ can be determined from the second-order structure function. However, since α and U_{Slip} are subjected to the local flow field and C_b is determined by continuity criterion (4-13) and energy balance criterion (4-15) when the mean turbulent eddy velocity is used to construct the breakage kernel, for the simplicity of the model, an trial value of 2.0 is adopted for C_λ.

2.2 Bubble size distribution

The bubble size distribution is determined by using the population balance equations (PBE) with consideration of bubble coalescence and breakup. Bubbles are classified into different size groups and d_i is the diameter of bubbles for *i*-th group. The population balance equation can be expressed by,

$$\frac{\partial n_i}{\partial t} + \nabla \cdot (\boldsymbol{u}_i n_i) = S_i \tag{4-22}$$

where n_i is the number density of bubbles for *i*-th group, $\vec{v}_i$ is the mass average velocity vector, and S_i is the source term. The source term can be expressed as the birth and death of bubbles due to coalescence and breakage, respectively, as shown in Equation (4-23).

$$S_i = B_{coalescence,i} - D_{coalescence,i} + B_{breakup,i} - D_{breakup,i}$$
$$= \sum_{V_j=V_{min}}^{V_i/2} \Omega_C(V_j: V_i - V_j) - \sum_{V_j}^{V_{max}-V_i} \Omega_C(V_j: V_i) + \sum_{V_j=V_i}^{V_{max}} \Omega_B(V_j: V_i) - \Omega_B(V_i) \tag{4-23}$$

The local gas volume fraction can be calculated by Equation (4-24),

$$\alpha_g f_i = n_i V_i \tag{4-24}$$

where f_i is the *i*-th class fraction of total volume fraction, and V_i is the volume for the *i*-th class.

The Sauter mean diameter d_{32} for the equivalent phase can be calculated by using Equation (4-25).

$$\frac{1}{d_{32}} = \sum_{i=1}^{N} \frac{f_i}{d_i} \tag{4-25}$$

For coalescence between bubbles of size d_i and d_j, the kernel used in the present study was the coalescence model proposed by Luo (1993), which is based on the drainage of liquid films between two collision bubbles. The detailed formulations can be found from Luo (1993) and Jakobsen *et al.* (2005). It should be noted that the use of bubble-induced energy spectrum leads to changes in the determination of the mean turbulent eddy velocity with which eddies hit bubbles and hence in the predicted coalescence rate when comparing with the use of classical -5/3 scaling law of the energy spectrum. The effect of such changes may not be as fundamental as those in applying the breakage model. Based on this consideration, no modifications are introduced for the coalescence model to address the influence of pseudo-turbulence generated by bubbles on the bubble breakage model.

Based on the binary breakage model by Luo and Svendsen (1996), the breakage rate for one individual parent bubble of size d_i breaking into daughter classes d_j can be expressed by Equation (4-26),

$$\Omega_B\left(d_i:d_j\right) = \int_{\lambda_{min}}^{d} \omega_B^T(d_i,\lambda)p_B\left(d_i,d_j,\lambda\right)d\lambda \tag{4-26}$$

where ω_B^T is the eddy-bubble collision probability density and p_B is the breakage probability function. It is assumed that only eddies with a size smaller than or equal to the bubble diameter can cause bubble breakage. Eddies with a much larger scale only transport the bubbles without causing breakage, an assumption that has been made in the previous studies (Prince and Blanch, 1990).

The eddy-bubble collision probability density can be expressed by Equation (4-27), based on the collision tube theory developed by Luo and Svendsen (1996). The collision tube theory considers that a number of eddies f_λ with a mean turbulent fluctuation velocity $\bar{u}_\lambda$ bombards a number of locally frozen bubbles n_i within the tube.

$$\omega_B^T(d_i,\lambda) = n_i f_\lambda \frac{\pi}{4}(d_i+\lambda)^2\bar{u}_\lambda \quad (4\text{-}27)$$

where f_λ and $\bar{u}_\lambda$ should be updated accordingly once the modified energy spectrum function of Equation (4-9) has been adopted. Since Equation (4-9) can be mathematically regarded as the linear superposition of two parts, spectrum function for liquid phase turbulence and for bubble-induced turbulence, these two parts can be treated separately for the simplification of further derivation. The breakage rate computed from the liquid phase turbulence energy spectrum would be the same as that of Luo and Svendsen (1996), except for the way of allocating the integration lower limit with the critical length scale Λ.

By substituting equations (4-9) and (4-21) into Equation (4-2), the expression of f_λ for the turbulence eddies induced by rising bubbles can be obtained, as shown by Equation (4-28),

$$f_\lambda = \frac{C_3(1-\alpha)}{\lambda^4} \quad (4\text{-}28)$$

where

$$C_3 = \frac{12}{\pi C_\lambda (2\pi)^2} \approx 0.0484. \quad (4\text{-}29)$$

Substituting equations (4-21) and (4-28) into Equation (4-27), the eddy-bubble collision probability density can be expressed by

$$\omega_B^T(d_i,\lambda) = C_4(1-\alpha)n_i \frac{(1+\xi)^2}{d_i\xi^3}\sqrt{C_b\frac{\alpha g U_{Slip}}{\nu}} \quad (4\text{-}30)$$

where $\xi = \lambda/d_i$ is the non-dimensional size of eddies that contributes to the breakage of parent bubble with size d_i, and

$$C_4 = \frac{\pi}{4}C_3(C_\lambda C_b)^{\frac{1}{2}}. \quad (4\text{-}31)$$

The conditional breakage probability function used by Luo and Svendsen (1996) is given by

$$P_B(d_i : d_j, \lambda) = exp\left(-\frac{e_s(d_i : d_j)}{\bar{e}(d_i, \lambda)}\right) \quad (4\text{-}32)$$

where e_s denotes the increase in surface energy and $\bar{e}$ is the mean turbulent kinetic energy for eddies with size λ. The increase in surface only relates to the sizes of parent and daughter bubbles, which can be written as

$$e_s(d_i : d_j) = \sigma \pi d_i^2 \left[f_V^{2/3} + (1 - f_V)^{2/3} - 1\right] = \sigma \pi d_i^2 C_f \quad (4\text{-}33)$$

where σ is the surface tension coefficient and C_f is the increase coefficient of surface area which only depends on the breakage volume fraction $f_V = d_j^3 / d_i^3$. By using the modified mean turbulent eddy fluctuation velocity given by Equation (4-20), the mean kinetic energy of an eddy with size λ can be described by

$$\bar{e}(d_i, \lambda) = \rho_l \frac{\pi}{6} \lambda^3 \frac{\bar{u}_\lambda^2}{2} = \frac{\pi}{12} C_\lambda \rho_l \lambda^5 C_b \frac{\alpha g U_{Slip}}{\nu} \quad (4\text{-}34)$$

Substituting equations (4-30) to (4-34) into Equation (4-25), the rate of breakage caused by bubble-induced turbulence eddies can be expressed by Equation (4-36),

$$\Omega_B(d_i : d_j) = C_4 (1 - \alpha) n_i \sqrt{C_b \frac{\alpha g U_{Slip}}{\nu}} \int_{\xi_{min}}^{\xi_{max}} \frac{(1 + \xi)^2}{\xi^3} exp\left(-\frac{12 \sigma C_f}{C_2 \rho_l C_b \frac{\alpha g U_{Slip}}{\nu} d_i^3 \xi^5}\right) d\xi \quad (4\text{-}35)$$

where the integration upper limit is defined by Equation (4-36).

$$\xi_{max} = \begin{cases} 1, & \Lambda \geq d_i \\ \frac{\Lambda}{d_i}, & \Lambda < d_i \end{cases} \quad (4\text{-}36)$$

When the integral length scale of the bombarding eddy is larger than or equal to the parent bubble diameter, the kinetic energy carried by eddies that interact with the parent bubbles can be defined by contribution from the portion which falls into the κ^{-3} scaling region on the energy spectrum. On the contrary, if the integral length scale of the bombarding eddy is smaller than the parent bubble diameter, the kinetic energy carried by the eddy due to the liquid-phase turbulence may partially contributes to the eddy-bubble collision. Under such situation, the breakup rate can be described by Equation (4-37),

$$\Omega_B\left(d_i:d_j\right) = 0.0923(1-\alpha)n_i(\varepsilon/d_i^2)^{\frac{1}{3}}\int_{\Lambda/d_i}^{1}\frac{(1+\xi)^2}{\xi^{\frac{11}{3}}}exp\left(-\frac{12\sigma C_f}{\beta\rho_l\varepsilon^{\frac{2}{3}}d_i^{\frac{5}{3}}\xi^{\frac{11}{3}}}\right)d\xi +$$

$$C_4(1-\alpha)n_i\sqrt{C_b\frac{\alpha g U_{Slip}}{\nu}}\int_{\xi_{min}}^{\Lambda/d_i}\frac{(1+\xi)^2}{\xi^{\frac{11}{3}}}exp\left(-\frac{12\sigma C_f}{\beta\rho_l C_b\frac{\alpha g U_{Slip}}{\nu}d_i^3\xi^5}\right)d\xi \quad (4\text{-}37)$$

where the integration lower limit should be the minimum size of eddies that fall into the inertial subrange of isotropic turbulence, defined by dimensionless form $\xi_{min}=11.4\eta/d_i$. Since binary breakage is assumed, Equation (4-37) is symmetrical with $f_V = 0.5$. Thus, the total breakage rate can be written as

$$\Omega_B(d_i) = \int_0^{0.5}\Omega_B\left(d_i:d_j\right)df_V \quad (4\text{-}38)$$

The dimensionless daughter size distribution probability density function can be defined by

$$\beta\left(d_i:d_j\right) = \frac{\Omega\left(d_i:d_j\right)}{\int_0^1\Omega_B\left(d_i:d_j\right)df_V} \quad (4\text{-}39)$$

The present model shows that the daughter bubble sizes resulting from a bubble breakage are not only functions of the parent bubble size, the energy dissipation rate, and the physical properties, but also of the typical characteristic length scale that corresponds to the bubble-induced turbulence. For bubble columns, this characteristic length scale will be the order of the rising bubble size as the induced turbulent eddies in the wake will have the sizes of the same order. Dimensionless daughter bubble size distributions for air-water system calculated on different turbulence energy dissipation rates are illustrated in

Figure 4-2. It can be seen clearly from Figure 4-2 that similar to the particle size distribution function (PDF) given by Luo and Svendsen (1996), the dimensionless daughter bubble size distribution is a U-shaped function and the lowest probability is found for equal-sized breakage. Parameters used for plotting Figure 4-2 include $\alpha = 0.1$, $U_{Slip} = 0.2$ m/s, and $\nu = 1 \times 10^{-6}$ m^2/s.

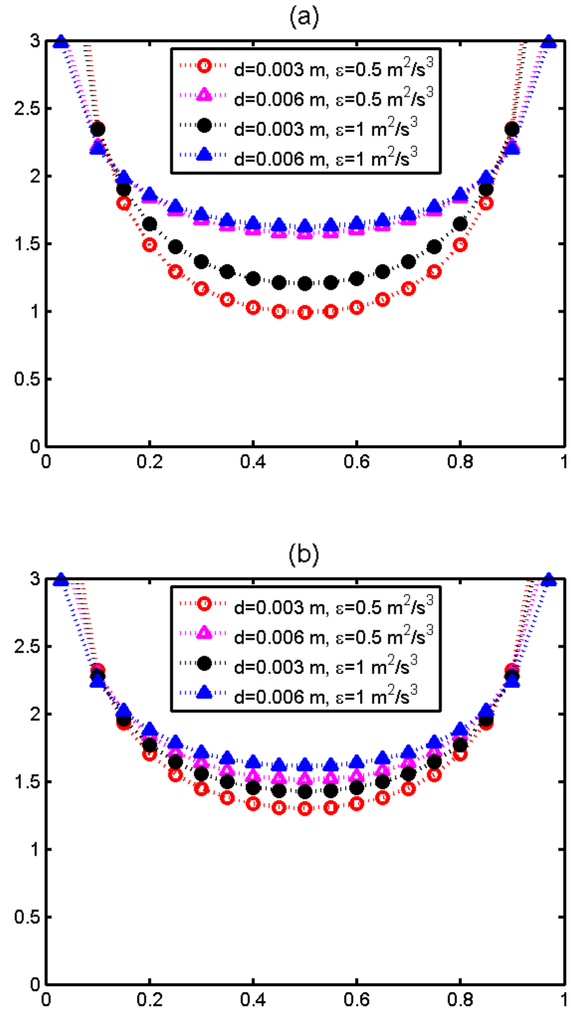

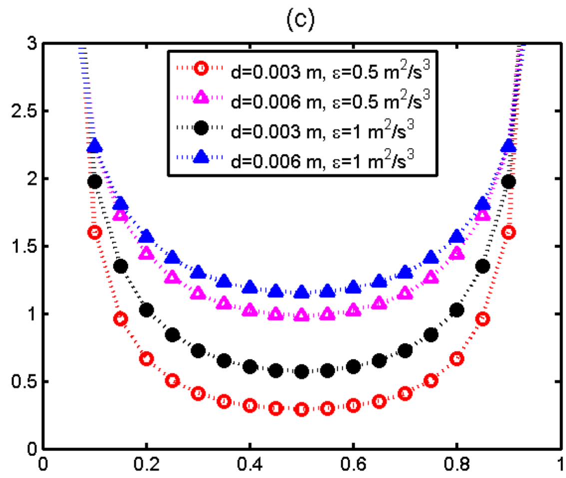

Figure 4-2 Effect of bubble size, energy dissipation rate per unit mass and characteristic length scale on the dimensionless daughter bubble size distribution: (a) Λ = 0.009 m, (b) Λ = 0.005 m, (c) Λ = 0.001 m. (where the symbols are used for distinguishing the different conditions).

Since the characteristic length scale is Λ = 0.009 m for Figure 4-2(a), both the 3 mm and 6 mm bubbles are under the influence of the bubble-induced -3 slope energy spectrum. On the contrary, the contribution from the bubble-induced turbulence is no longer significant for the PDFs as can be seen from Figure 4-2(c), where the corresponding length scale of Λ = 0.001 m is smaller than the bubble sizes. Therefore, the PDFs shown in Figure 4-2(c) are mainly influenced by liquid phase turbulence, resulting in similar distributions to the results of Luo and Svendsen (1996). Despite the difference existing in the contributions made from both bubble-induced turbulence and liquid phase turbulence, it can be seen from Figure 4-2 that the curves for a 6 mm diameter bubble are generally flatter than the curves for a 3 mm bubble, and the difference between the two given turbulent energy dissipation rates is smaller for larger bubbles. For those relatively large bubbles, the effect of turbulence energy dissipation rate becomes insignificant and the daughter bubble size distribution tends to become flat.

2.3 Numerical modelling and model validation

Governing Equations

It is found that the modified energy spectrum function and the PBEs for the gas-liquid two-phase flows in the bubble columns are very sensitive to the local parameters, such as volume fraction, bubble diameter, slip velocity and turbulence dissipation rate. Therefore, a full 3-D transient CFD model has been used in the present study to predict these key parameters. A two-fluid Eulerian-Eulerian approach is adopted to describe the flow behaviours for both phases i.e. water as continuous phase, and air as the dispersed phase. The mass and momentum conservations are given by equations (4-40) and (4-41), respectively,

$$\frac{\partial(\rho_k\alpha_k)}{\partial t} + \nabla\cdot(\rho_k\alpha_k\boldsymbol{u}_k) = 0 \tag{4-40}$$

$$\frac{\partial(\rho_k\alpha_k\boldsymbol{u}_k)}{\partial t} + \nabla\cdot(\rho_k\alpha_k\boldsymbol{u}_k\boldsymbol{u}_k) = -\alpha_k\nabla p + \nabla\cdot\boldsymbol{\tau}_k + \rho_k\alpha_k\boldsymbol{g} + \boldsymbol{F}_k \tag{4-41}$$

where ρ_k, α_k, $\boldsymbol{u}_k$, $\boldsymbol{\tau}_k$, and $\boldsymbol{F}_k$ represent the density, volume fraction, velocity vector, viscous stress tensor and the inter-phase momentum exchange term for the k (liquid or gas) phase, respectively. The sum of the volume fractions for both phases is equal to 1.

The turbulence generated in the bubble column can be thought of being the joint superposition of shear turbulence and bubble-induced turbulence. The bubble-induced turbulence is mainly contributed by the bubble wake generated by the shed vortices from the bubble surface and it decays quite rapidly due to the viscous dissipation. This induced turbulence has the feature of anisotropy. Thus, the adoption of the Boussinesq hypothesis of isotropic turbulent eddy viscosity may not be appropriate for the modelling of Reynolds stresses caused by this turbulence. Therefore, the Reynolds stress model (RSM) is required to reflect the anisotropic nature and individual Reynolds stresses $\overline{u_i' u_j'}$ are calculated by the Reynolds stresses transport equation. The RSM transport equations for the transport of the Reynolds stresses $\rho\overline{u_i' u_j'}$ employed in the present study can be written as

$$\frac{\partial\left(\alpha_l \rho_l \overline{u_i' u_j'}\right)}{\partial t} + \frac{\partial\left(\alpha_l \rho_l u_k \overline{u_i' u_j'}\right)}{\partial x_k} = \frac{\partial}{\partial x_k}\left(\alpha_l \left(\mu_l + \frac{\mu_t}{\sigma_k}\right)\frac{\partial \overline{u_i' u_j'}}{\partial x_k}\right)$$

$$+\alpha_l P_{ij} + \alpha_l \phi_{ij} - \tfrac{2}{3}\delta_{ij}\alpha_l \rho_l \varepsilon + \alpha_l S_{ij}^{BIT} \quad (4\text{-}42)$$

where ϕ_{ij} is the pressure-strain correlation, and the exact production term P' is given by Equation (4-43).

$$P_{ij} = -\rho_l \left(\overline{u_i' u_k'}\frac{\partial u_j}{\partial x_k} + \overline{u_j' u_k'}\frac{\partial u_i}{\partial x_k}\right) \quad (4\text{-}43)$$

As the scalar turbulence dissipation rate is used in Equation (4-44), a model transport equation, (4-44), is used to calculate ε.

$$\frac{\partial(\alpha_l \rho_l \varepsilon)}{\partial t} + \frac{\partial}{\partial x_i}(\alpha_l \rho_l \varepsilon \boldsymbol{u}_i) = \frac{\partial}{\partial x_j}\left[\alpha_l \left(\mu_l + \frac{\mu_t}{\sigma_\varepsilon}\right)\frac{\partial \varepsilon}{\partial x_j}\right] + \alpha_l \rho_l \frac{\varepsilon}{k}\left(C_{1\varepsilon}\overline{u'_i u'_j}\frac{\partial \boldsymbol{u}_i}{\partial x_k} - C_{2\varepsilon}\varepsilon\right) +$$

$$\alpha_l S_\varepsilon^{BIT} \quad (4\text{-}44)$$

k is calculated from the solved values of normal stress using the Reynolds stress transport equation as by Equation (4-45).

$$k = \tfrac{1}{2}\textstyle\sum_{i=1,2,3}\overline{u_i' u_j'} \quad (4\text{-}45)$$

The source term in Equation (4-42) represents the contribution to the Reynolds stresses due to bubble-induced turbulence. It should be noted that the bubble-induced turbulence has the feature of anisotropic. The widely accepted models for including bubble-induced turbulence are often based on the isotropic two-equation k-ε turbulence model, such as Troshko and Hassan (2001) and Rzehak and Krepper (2013). Only a few studies, e.g. Colombo and Fairweather (2015) and Parekh and Rzehak (2018), have partially considered the anisotropic feature. With caution, the effect of the bubble-induced turbulence on the Reynolds stresses through the source term S^{BIT} has been dropped off in the simulation but the influence of BIT on the bubble breakage rate and bubble size distribution is accounted in the bubble breakage model. The reason is that the shear turbulence may become dominant in the vicinity of the bubble column wall and the BIT is most likely to surpass the shear turbulence in the centre region of the bubble column. It has brought our attention, however, that the effect of BIT on the turbulence dissipation cannot be disregarded as this strongly affects the prediction of both the bubble coalescence and breakage kernels. Therefore, the proposed correlations of the source terms in the Reynolds stress turbulence model due to the bubble-induced turbulence will be further explored in Chapter 5.

Interphase momentum transfer

In this study, drag force, transverse lift force, added mass force, turbulent dispersion force and wall lubrication force are considered as the main interactions between the continuous liquid phase and dispersed gas phase. In order to compare the simulation results with literature, some forces may be temperately isolated to only reflect the effects of the bubble-induced energy spectrum function. The equations used for the interphase momentum transfer are listed in Table 4-1.

Table 4-1 Models for interphase momentum transfer.

Phase Interactions	Equations
Drag Schiller and Naumann Grace	$\boldsymbol{F}_D = \frac{3}{4}\frac{C_D}{d_b}\rho_l \alpha_g \lvert \boldsymbol{u}_g - \boldsymbol{u}_l \rvert (\boldsymbol{u}_g - \boldsymbol{u}_l)$ Schiller and Naumann model: $C_D = \begin{cases} 24(1+0.15R_e^{0.687})/R_e & R_e \le 1000 \\ 0.44 & R_e > 1000 \end{cases}$ $R_e = \frac{\rho_L \lvert \boldsymbol{u}_g - \boldsymbol{u}_L \rvert d_b}{\mu_L}$ Grace model: $C_D = max\left(C_{D,sphere},\ min\left(C_{D,ellipse},\ C_{D,cap}\right)\right),$ $C_{D,sphere} = \begin{cases} \frac{24}{R_{eb}} & R_{eb} < 1000 \\ \frac{24}{R_{eb}}(1+0.15R_{eb}^{0.687}) & R_{eb} \ge 1000 \end{cases},$ $C_{D,cap} = \frac{8}{3},\quad C_{D,ellipse} = \frac{4}{3}\frac{g d_{eq}}{U_t^2}\frac{(\rho_l - \rho_g)}{\rho_l},$ $Re_b = \frac{\rho_l \lvert \boldsymbol{u}_g - \boldsymbol{u}_l \rvert d_b}{\mu_l},\ U_t = \frac{\mu_l}{\rho_l d} M_O^{-0.149}(J - 0.857),$ $M_O = \frac{\mu_l^4 g(\rho_l - \rho_g)}{\rho_l^2 \sigma^3}, J = \begin{cases} 0.94H^{0.757} & 2 < H < 59.3 \\ 3.42H^{0.441} & H \ge 59.3 \end{cases},$ $H = \frac{4}{3}E_O M_O^{-0.149}\left(\frac{\mu_l}{\mu_{ref}}\right)^{-0.14}, \mu_{ref} = 0.0009\ kg/(ms)$
Lift Tomiyama	$\boldsymbol{F}_{lift} = C_L \rho_L \alpha_g (\boldsymbol{u}_g - \boldsymbol{u}_L) \times (\nabla \times \boldsymbol{u}_l)$ $C_L = \begin{cases} min[0.288tanh(0.121R_{eb}), f(E_O')] & E_O' \le 4 \\ f(E_O') & 4 < E_O' < 10 \\ -0.29 & E_O' > 10 \end{cases}$ $E_O' = \frac{g(\rho_l - \rho_g)d_h^2}{\sigma}, d_h = d(1 + 0.163E_O'^{0.757})^{1/3}$
Virtual mass	$\boldsymbol{F}_{VM} = C_{VM}\rho_L \alpha_g \left(\left.\frac{d\boldsymbol{u}_L}{dt}\right\rvert_l - \left.\frac{d\boldsymbol{u}_g}{dt}\right\rvert_g\right)$

Turbulent dispersion Burns model	$$\boldsymbol{F}_{td,l} = -\boldsymbol{F}_{td,g} = C_{TD}\frac{3\alpha_g}{4}\frac{\rho_l}{d_b}(\boldsymbol{u_l} - \boldsymbol{u_g})\frac{\nu_t}{\sigma_{TD}}\left(\frac{\nabla\alpha_l}{\alpha_l} - \frac{\nabla\alpha_g}{\alpha_g}\right)$$
Wall lubrication Tomiyama	$$\boldsymbol{F}_{wl} = C_{wl}\rho_L\alpha_g(\boldsymbol{u}_g - \boldsymbol{u}_L)\boldsymbol{n}_w$$ $$C_{wl} = max\left(0, \frac{C_{w1}}{d_b} + \frac{C_{w2}}{y_w}\right)$$

Numerical details

To validate the influence of bubble-induced pseudo-turbulence energy spectrum, numerical simulations have been conducted for the air-water bubble column systems as reported in Chen *et al.* (2005) and Guan and Yang (2017). Details of the experimental conditions are listed in Table 4-2.

Table 4-2 Details of experimental set-up.

Experiment	**Diameter (m)**	**Height (m)**	**Superficial Gas Velocity (m/s)**	**Static Liquid Height (m)**	**Observation Height (m)**
Chen *et al.* (1999)	0.44	2.44	0.1	0.9	1.32
Guan and Yang (2017)	0.15	1.6	0.05	1.2	0.8

As shown in Figure 4-3, the height of the bubble column is extended to 3 m to prevent overflow from the top for the case of Chen *et al.* (1999). Grid 2 consists of 28(r)×64(θ)×100(z) equally distributed nodes in radial, circumferential and axial directions respectively. The grid independence was tested in a coarser Grid 1 of 20(r)×40(θ)×80(z) nodes and a refined Grid 3 of 36(r)×72(θ)×126(z) nodes, in which case the total number of cells is doubled gradually. As shown in Figure 4-4, the grid independence test for these three set-ups has yielded similar results quantitatively. However, Grid 2 and Grid 3 present very similar results in the normalised liquid axial velocity prediction while the coarser grid, Grid 1, has slightly deviated from both Grid 2 and Grid 3. Thus, Grid 2 shown in Figure 4-3 has been employed throughout the subsequent simulations to investigate the effects of the improved breakup model.

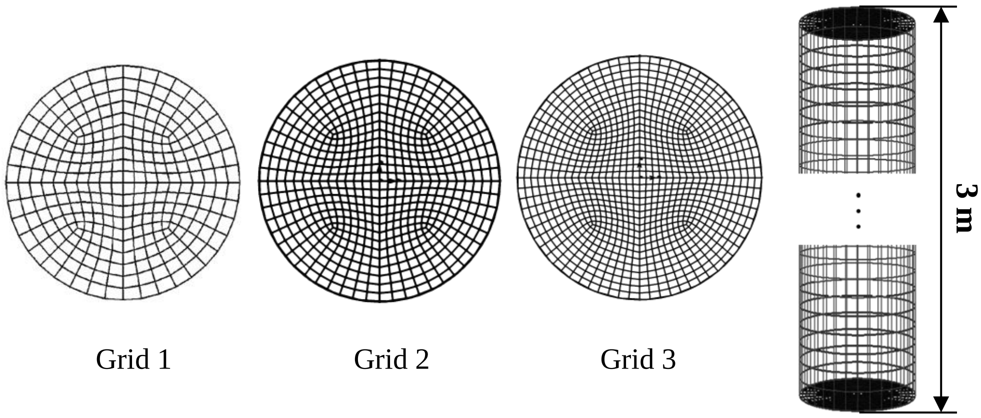

Figure 4-3 Mesh set-up at the bottom surface and main body of the column.

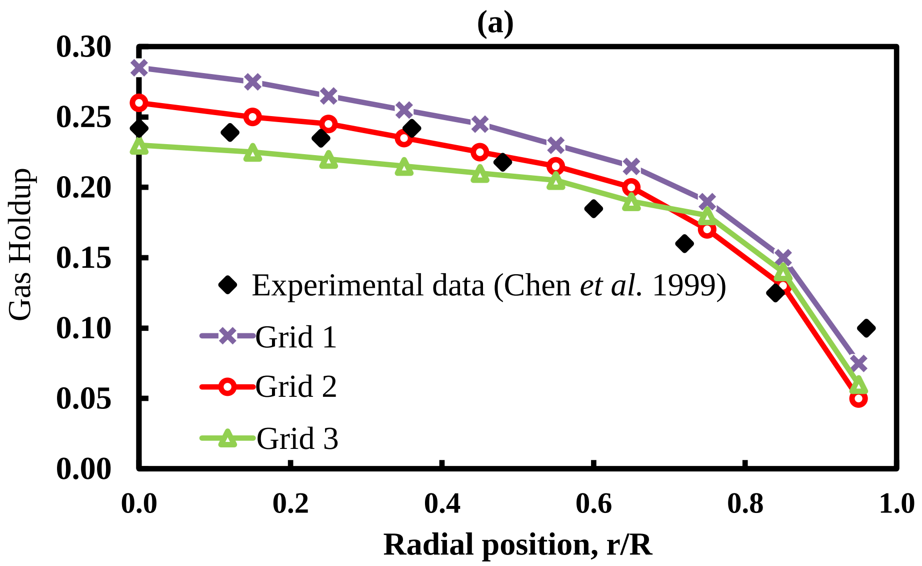

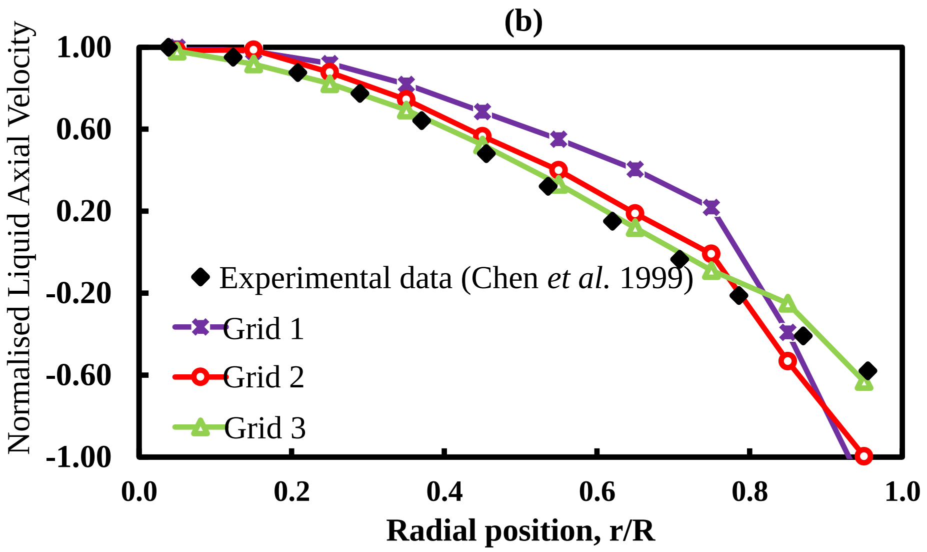

Figure 4-4 Grid sensitivity test results on radial distribution of (a) gas holdup and (b) normalised liquid axial velocity.

ANSYS Fluent 3D pressure-based solver is employed for CFD-PBM modelling. The time step is gradually increased from 0.001 seconds to 0.005 seconds for all simulations, which is considered to be sufficient for illustrating the time-averaged characteristics for the flow fields by carrying out the data sampling statistics for typically 120 seconds after the quasi-steady state has been achieved. For the population balance modelling, 9 discrete bubble classes have been used in total. The sizes of the bubble classes from small to large bubbles are increased in such a manner that $V_{i+1} = 4V_i$. The breakup model modified by the bubble-induced turbulence energy spectrum has been implemented into the simulations through the use of the user defined functions (UDF). Numerical execution of the incorporated UDF for the modified breakup model requires to separately compute the breakage frequency and bubble size distribution function, which involves numerical integrations for both first and double integrals. In this study, the methods adopted for numerical integrations have been carefully tested while the numerical results are compared with those obtained by using the Fluent built-in PBM module of Luo's breakup model. The volume fraction of gas phase is set to be 1.0 at the inlet. The gas inlet velocity is set to be equal to the superficial velocity, which means the effect of the gas chamber and the gas distributor has been neglected for the simplification of the problem. The outlet boundary is set to be a pressure-out let at the top of the column. No-slip conditions are applied for both liquid and gas phases at the bubble column wall.

3. RESULTS AND DISCUSSION

Successful prediction of the bubble breakage rate is crucial for correct prediction of the bubble size distribution in bubble column flow. It has been recognised based on the work reported in the existing literature (Chen, 2004, Chen et al., 2005) that the adoption of Luo and Svendsen's model usually underestimates the breakage rate, which is very likely caused by underestimation of the turbulent kinetic energy carried by those eddies that hit the bubbles. In order to achieve the better predictions, Chen (2004) artificially increased the breakage rate predicted by using Luo and Svendsen's model by a factor of 10 in the TFM-PBM model, showing the obtained numerical results to be in good agreement with the experimental data. This may have been an efficient way of solving engineering-related problems, but the predictive nature of CFD modelling has been overwritten. The tuning factor of 10 by which the bubble breakup rate is enhanced implies that the original breakup model is not able to properly estimate the bubble breakage frequency under certain operating conditions. Therefore, the fundamental nature of the original breakup model needed to be reconsidered. By revisiting the original breakup model, one can easily find that an important assumption was introduced in the bubble breakage rate kernel, i.e. the single-phase turbulence energy spectrum has been used to approximately represent the liquid phase energy spectrum in bubbly flow. As mentioned in the previous sections, this may not be an appropriate assumption in gas-liquid two-phase flows in bubble columns as there is no any turbulence presence until bubbles are injected into the bubble column through the gas distributor. The liquid phase turbulence is induced by the rising bubbles or bubble swarms. This type of bubble-induced turbulence could be predominant in the centre of the bubble column, especially when the bubbles are densely distributed. It can be found from the existing experimental work (Mercado et al., 2010, Prakash et al., 2016, Mendez-Diaz et al., 2013, Riboux et al., 2010, Murai et al., 2000, Bouche et al., 2014) and direct numerical simulations (Roghair et al., 2011, Sugiyama et al., 2001, Bunner and Tryggvason, 2003, Riboux et al., 2013) that the behaviour of bubble-induced turbulence on the turbulence energy spectrum is clearly in line with the κ^{-3} scaling in the inertial subrange, which is very close to the range that the size of bubbles is distributed (Risso et al., 2008, Roig and de Tournemine, 2007, Risso, 2011). Therefore, bubble-induced turbulence will be involved in most eddy-bubble collisions. In other words, the shed eddies from the preceding bubbles have the greater chances to collide with the rising bubbles. By considering this as the main mechanism of the eddy-bubble collision, the breakup model has been reconstructed and applied in simulations. It is notable from the breakup kernel (4-37) that there are no adjustable parameters in the entire model. The relevant modifications made are only due to the application of the bubble-induced turbulence energy spectrum. In order to directly compare the simulation results, the interphase momentum transfer term is set to be the same as that in Chen *et al.* (2005), where only the drag force is considered while the other forces are temperately redundant to reflect the effect on the breakup model. A comparison of the simulated time- and circumferential-averaged gas holdup and liquid axial velocity with the experimental data is shown in Figure 4-5.

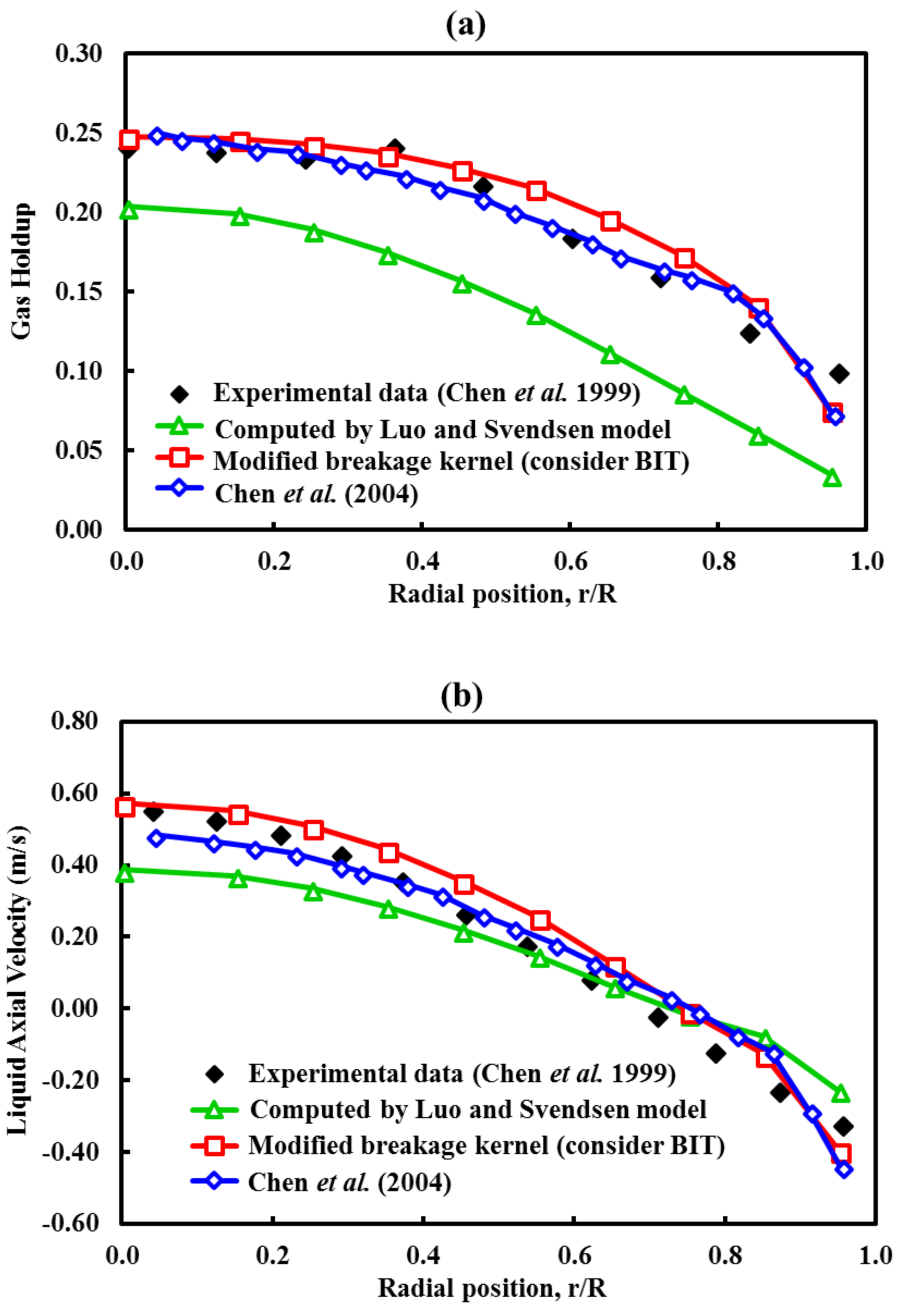

Figure 4-5 Radial distribution of time-averaged profiles: (a) gas holdup, and (b) liquid axial velocity.

Figure 4-5 shows the comparisons of the simulation results obtained by using different bubble breakup kernels. The simulation data are taken at axial position H = 1.32 m, which is the same as the observation height in the experiments. Predictions from the original breakup model show that both the predicted gas holdup and the liquid axial velocity profiles are underestimated. It is believed that the underestimation is due to the fact that the mechanism of eddy-bubble interactions were not correctly reflected in the original breakup model. In fact, the number density of bombarding eddies, which is a crucial parameter in predicting the collision frequency as pointed out by Ghasempour *et al.* (2014), is greatly affected by the application of the Kolmogorov -5/3 law of the energy spectrum. Once this approximation of using the single phase turbulence energy spectrum has been replaced by the κ^{-3} scaling for bubble-induced turbulence flows, the simulation results for both the gas holdup and the liquid axial velocity profiles achieve almost exactly the same degree of accuracy as the ones obtained by artificially enhancing the breakup rate, $\Omega_B'(d_i : d_j) = 10\Omega_B(d_i : d_j)$. However, it should be pointed out that this cannot be simply regarded as the result of using the bubble-induced turbulence energy spectrum which would affect the simulation results the same way as enhancing the breakage rate. If the daughter size distribution probability density function Equation (4-39) is considered, increasing the breakage rate has no influence on the daughter bubble size distribution. In addition, using the bubble-induced turbulence energy spectrum totally changes the daughter size distribution for each bubble class with dynamic changes in the critical length scale, as shown in Figure 4-2. Thus, the overall bubble size distribution for the entire gas-liquid contact region has been changed accordingly. The volume-based bubble size distribution is shown in Figure 4-6.

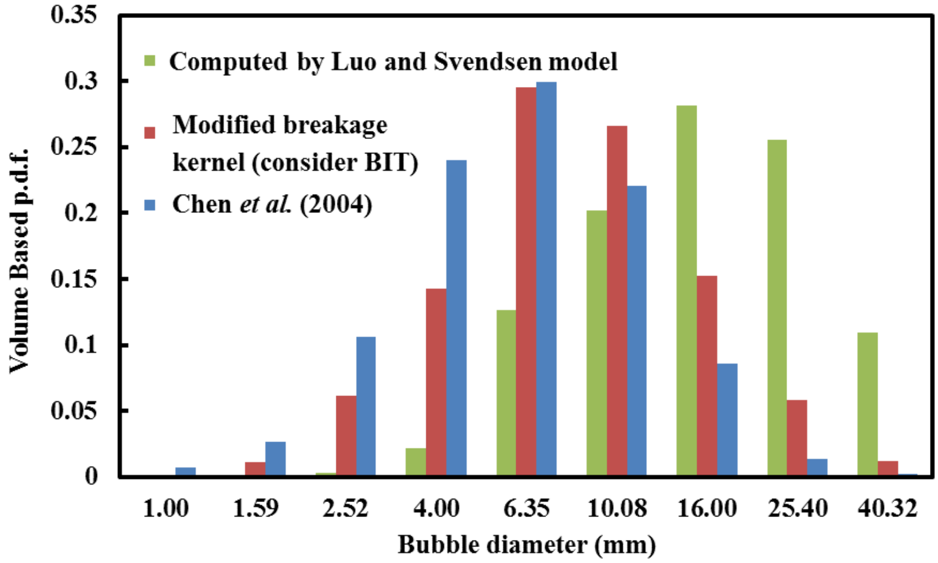

Figure 4-6 Bubble class volume-based probability distribution.

Figure 4-6 shows a comparison of the simulated results of overall bubble class probability distribution with different breakup kernels. The cumulative volume for each bubble class has been normalised by the total volume of all bubbles. Figure 4-6 illustrates that the peak value predicted by the original breakup model is shown to be at the 16mm bubble class, which is much greater than the predicted results of Chen *et al.* (2005). Thus, the breakage rate predicted by using the original breakup model is indeed far too small under this circumstance. The same point of view as the conclusion was drawn by Chen *et al.* (2005). After enhancing the breakage rate and applying the bubble-induced turbulence energy spectrum, the simulation results have shown that more than 90% of bubbles are within the medium size range (1.59 mm ~ 16 mm) with the bubbles mostly ellipsoidal in shape with a little variance in the aspect ratio. In addition, the peak values are at the 6.35 mm bubble class. Use of the bubble-induced turbulence energy spectrum has achieved an even smaller probability distribution for each bubble class under the peak value. Although there is still a considerably large number of small bubbles, their contributions to the total volume are much smaller than large bubbles. Several authors have used different breakage criteria to restrict the over-breakage of very small fluid particles, such as Wang *et al.* (2003), Han *et al.* (2011), Guo *et al.* (2016), Zhao and Ge (2007), Liao *et al.* (2015) and Andersson and Andersson (2006). Most of these studies have compared the requirements of the breakage of discrete fluid particles and the external conditions that the surrounding eddies can provide and have intensively studied the requirements for the breakage of discrete fluid particles. Although no breakage criteria being used in this study, the application of the bubble-induced turbulence energy spectrum has appropriately depicted the energy carried by eddies involved in the eddy-bubble collisions, as can be found from Equation (4-21). This may be one of the main reasons that lead to the smaller probability distribution of small bubbles.

The bubble breakage kernel with the use of bubble-induced turbulence energy spectrum has worked well in the simulations of bubble column used by Chen (2004) and Chen *et al.* (1999). Further CFD validations have been carried out for the bubble column used by Guan and Yang (2017). Figure 4-7 presents the time-averaged radial distribution of gas holdup and the equivalent bubble diameter distribution d_{32} at the observation height of H = 0.8 m. In general, the CFD simulations with the use of bubble-induced turbulence breakup model have achieved agreeable results in the prediction of key fluid dynamic parameters. The bubble size distribution, which is the main concern of using the population balance model, is illustrated in Figure 4-8. The data sets are normalised by the total volume of the gas bubbles individually. In comparison with the experimental results, it can be seen from the figure that the predicted bubble sizes fall into a well-accepted range of PDF distribution. The simulation result of bubble size distribution is quite convincing, as no artificial adjustments have been made in the breakage kernel. In addition, by appropriately considering the characteristics of bubble-induced turbulence of bubble column flows in the bubble breakage kernel, the simulation results have accurately reflected the predictive nature of CFD modelling. However, some differences can be found between the simulation and experimental results as can be observed from Figure 4-8. The reasons behind these differences may be attributed to the coalescence model. In coalescence models, such as those by Prince and Blanch (1990) or Luo (1993), it has been assumed that the mean turbulent approach velocity of bubbles that are carried by the fluid in bubble-bubble collisions is approximately the same as the mean turbulent velocity of eddies that have the same size as the bubbles, as defined by Equation (4-46). However, as the energy spectrum function of the bubble-induced turbulence is clearly distinguishable from the -5/3 single phase turbulence, bubbles that are mainly under the influence of the bubble-induced turbulence would behave in a different way, such as the behaviour shown in Equation (4-47). By considering the approach velocity of bubbles under the influence of bubble-induced turbulence in the coalescence model, the bubble-bubble collision density and the average contact time should be modified accordingly but this requires further investigation and validation.

$$\bar{v}_d = \beta(\varepsilon d)^{\frac{1}{3}} \tag{4-46}$$

$$\bar{v}_d = C_\lambda^{1/2}\sqrt{C_b \frac{\alpha g U_{Slip}}{\nu}}\, d \tag{4-47}$$

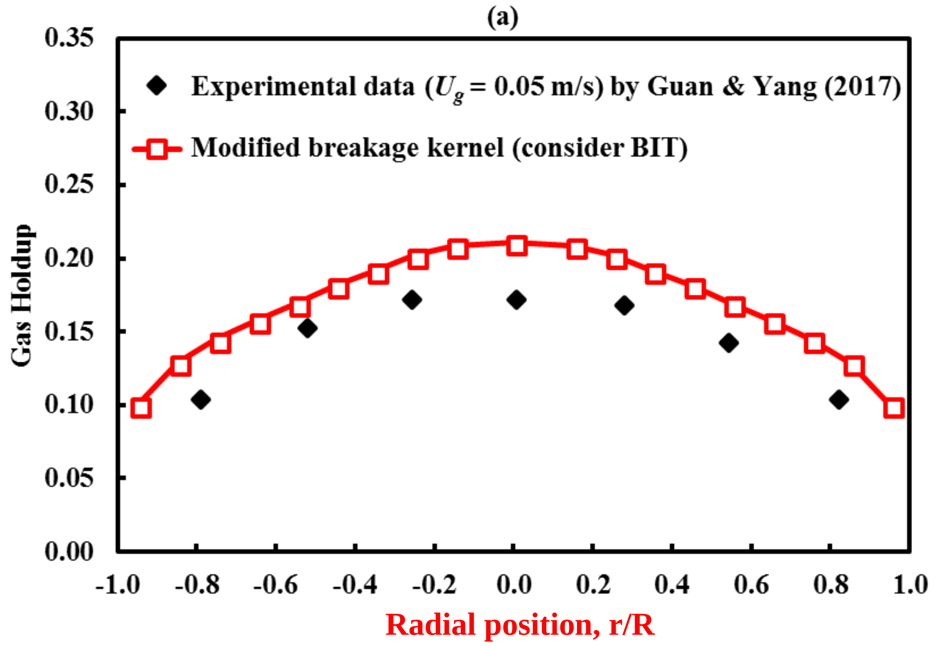

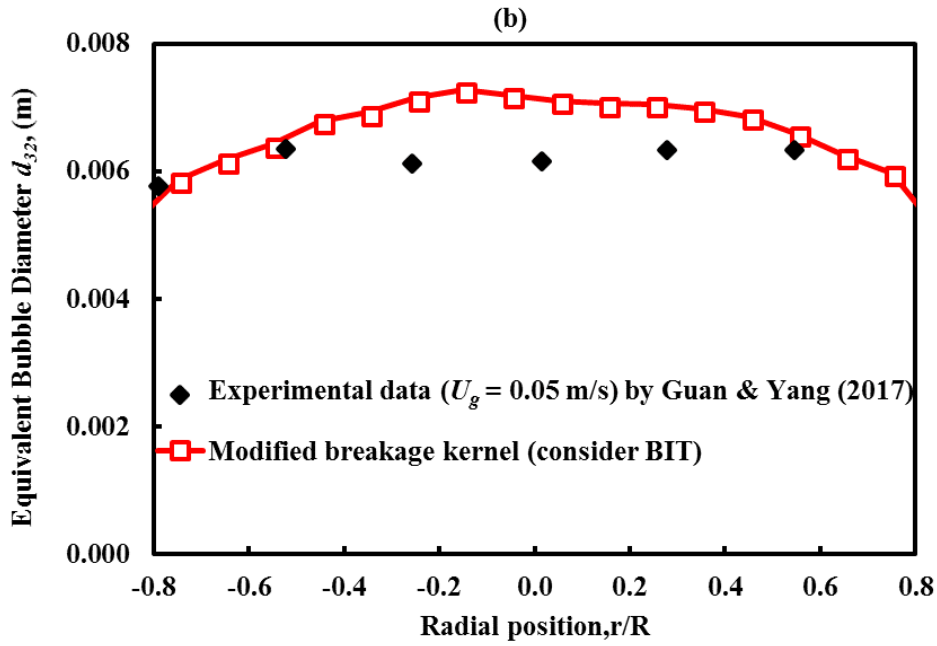

Figure 4-7 Simulation result of (a) Time-averaged radial distribution of gas holdup, and (b) radial distribution of equivalent bubble diameter d_{32}.

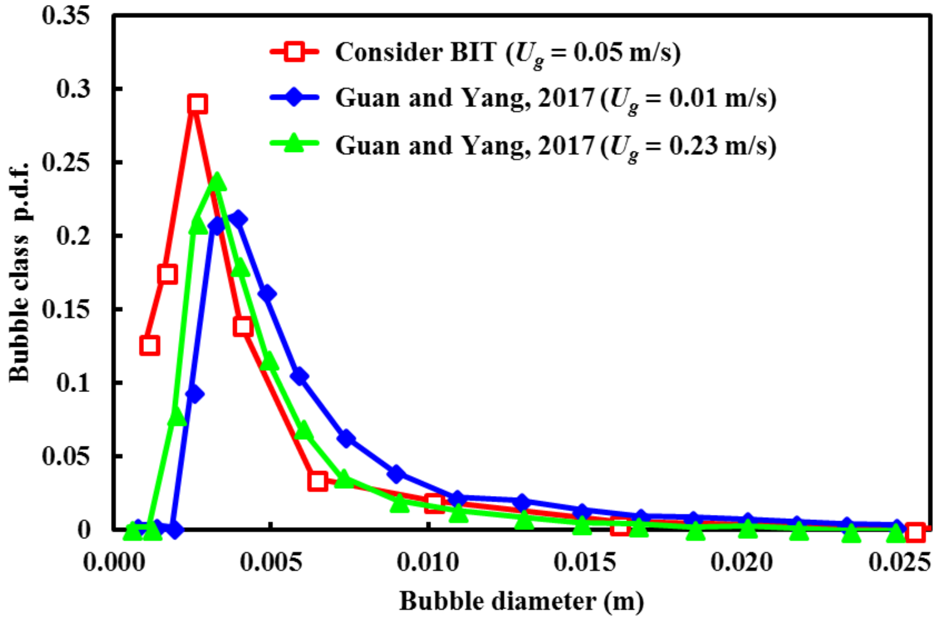

Figure 4-8 Comparison of predicted bubble probability distribution with experimental data.

4. CONCLUSIONS

A bubble breakage model that considers the effect of bubble-induced turbulence on the bubble breakage rate and bubble size distribution has been proposed for modelling bubble column flows, based on the model for drop and bubble breakup proposed by Luo and Svendsen (1996). The conclusions reached as the results of the present study are summarised as follows:

1. The contribution to the bubble breakage due to eddy turbulent kinetic energy using κ^{-3} scaling caused by bubble-induced turbulence and the Kolmogorov -5/3 law on the turbulence energy spectrum has been reflected in the proposed bubble breakage model.

2. The bubble breakage model has been modified by taking into account the bubble-induced turbulence and other factors such as the number density of

bombarding eddies, the mean turbulent velocity of eddies, the eddy-bubble collision density and the mean kinetic energy of the collision eddy.

3. The characteristic wave number that corresponds to the beginning boundary of the region which the bubble-induced turbulence dominates on the energy spectrum has been integrated into the bubble breakage model. This implicitly provides a well-defined physical interpretation for the bubbles with various sizes and shapes.

4. Theoretical predictions using the proposed bubble-induced turbulence breakage model have indicated that the dimensionless daughter bubble size distribution not only depends on the parent bubble size and the turbulence dissipation rate, but also is associated with the characteristic length scale that corresponds to the bubble-induced turbulence.

5. The proposed bubble breakage model has been validated for two cases of bubble column flows with diameters of D = 0.44 m and D = 0.15 m, respectively. The simulation results for both cases are consistent with the experimental data. This suggests that the bubble-induced turbulence breakage model may be appropriate for description of the mechanism of eddy-bubble interactions in the bubble columns when using the energy spectrum with κ^{-3} scaling, as no adjustable parameter is required in the bubble breakage kernel.

References

ANDERSSON, R. & ANDERSSON, B. 2006. Modeling the breakup of fluid particles in turbulent flows. *Aiche Journal,* 52**,** 2031-2038.

BATCHELOR, G. K. 1967. *An Introduction to Fluid Dynamics,* Cambridge University Press.

BHOLE, M. R., JOSHI, J. B. & RAMKRISHNA, D. 2008. CFD simulation of bubble columns incorporating population balance modeling. *Chemical Engineering Science,* 63**,** 2267-2282.

BOUCHE, E., ROIG, V., RISSO, F. & BILLET, A. M. 2014. Homogeneous swarm of high-Reynolds-number bubbles rising within a thin gap. Part 2. Liquid dynamics. *Journal of Fluid Mechanics,* 758**,** 508-521.

BUNNER, B. & TRYGGVASON, G. 2003. Effect of bubble deformation on the properties of bubbly flows. *Journal of Fluid Mechanics,* 495**,** 77-118.

CHEN, J. W., LI, F., DEGALEESAN, S., GUPTA, P., AL-DAHHAN, M. H., DUDUKOVIC, M. P. & TOSELAND, B. A. 1999. Fluid dynamic parameters in bubble columns with internals. *Chemical Engineering Science,* 54**,** 2187-2197.

CHEN, P. 2004. *Modeling the fluid dynamics of bubble column flows. Ph.D. Thesis.* Ph.D. Thesis.

CHEN, P., DUDUKOVIC, M. P. & SANYAL, J. 2005. Three-dimensional simulation of bubble column flows with bubble coalescence and breakup. *Aiche Journal,* 51**,** 696-712.

CLIFT, R., GRACE, J. R. & WEBER, M. E. 1978. *Bubbles, Drops, and Particles,* Academic Press.

COLOMBO, M. & FAIRWEATHER, M. 2015. Multiphase turbulence in bubbly flows: RANS simulations. *International Journal of Multiphase Flow,* 77**,** 222-243.

CUI, Z. & FAN, L. S. 2004. Turbulence energy distributions in bubbling gas-liquid and gas-liquid-solid flow systems. *Chemical Engineering Science,* 59**,** 1755-1766.

GHASEMPOUR, F., ANDERSSON, R., ANDERSSON, B. & BERGSTROM, D. J. 2014. Number Density of Turbulent Vortices in the Entire Energy Spectrum. *Aiche Journal,* 60**,** 3989-3995.

GOTOH, T., FUKAYAMA, D. & NAKANO, T. 2002. Velocity field statistics in homogeneous steady turbulence obtained using a high-resolution direct numerical simulation. *Physics of Fluids,* 14**,** 1065-1081.

GUAN, X. P. & YANG, N. 2017. Bubble properties measurement in bubble columns: From homogeneous to heterogeneous regime. *Chemical Engineering Research & Design,* 127**,** 103-112.

GUO, X. F., ZHOU, Q., LI, J. & CHEN, C. X. 2016. Implementation of an improved bubble breakup model for TFM-PBM simulations of gas-liquid flows in bubble columns. *Chemical Engineering Science,* 152**,** 255-266.

HAGESAETHER, L., JAKOBSEN, H. A. & SVENDSEN, H. F. 2002. A model for turbulent binary breakup of dispersed fluid particles. *Chemical Engineering Science,* 57**,** 3251-3267.

HAN, L. C., GONG, S. G., LI, Y. Q., GAO, N. N., FU, J., LUO, H. & LIU, Z. H. 2014. Influence of energy spectrum distribution on drop breakage in turbulent flows. *Chemical Engineering Science,* 117**,** 55-70.

HAN, L. C., LUO, H. A. & LIU, Y. J. 2011. A theoretical model for droplet breakup in turbulent dispersions. *Chemical Engineering Science,* 66**,** 766-776.

ISHII, M. & ZUBER, N. 1979. Drag Coefficient and Relative Velocity in Bubbly, Droplet or Particulate Flows. *Aiche Journal,* 25**,** 843-855.

JAKOBSEN, H. A., LINDBORG, H. & DORAO, C. A. 2005. Modeling of bubble column reactors: Progress and limitations. *Industrial & Engineering Chemistry Research,* 44**,** 5107-5151.

KUBOI, R., KOMASAWA, I. & OTAKE, T. 1972a. BEHAVIOR OF DISPERSED PARTICLES IN TURBULENT LIQUID FLOW. *Journal of Chemical Engineering of Japan,* 5**,** 349-355.

KUBOI, R., KOMASAWA, I. & OTAKE, T. 1972b. COLLISION AND COALESCENCE OF DISPERSED DROPS IN TURBULENT LIQUID FLOW. *Journal of Chemical Engineering of Japan,* 5**,** 423-424.

LANCE, M. & BATAILLE, J. 1991. Turbulence in the Liquid-Phase of a Uniform Bubbly Air Water-Flow. *Journal of Fluid Mechanics,* 222**,** 95-118.

LEHR, F., MILLIES, M. & MEWES, D. 2002. Bubble-size distributions and flow fields in bubble columns. *Aiche Journal,* 48**,** 2426-2443.

LIAO, Y. X., RZEHAK, R., LUCAS, D. & KREPPER, E. 2015. Baseline closure model for dispersed bubbly flow: Bubble coalescence and breakup. *Chemical Engineering Science,* 122**,** 336-349.

LUO, H. 1993. *Coalescence, Breakup and Liuqid Circulation in Bubble Column Reactors.* PhD thesis PhD thesis, PhD thesis from the Norwegian Institute of Technology.

LUO, H. & SVENDSEN, H. F. 1996. Theoretical model for drop and bubble breakup in turbulent dispersions. *Aiche Journal,* 42**,** 1225-1233.

MAZZITELLI, I. M. & LOHSE, D. 2009. Evolution of energy in flow driven by rising bubbles. *Physical Review E,* 79.

MENDEZ-DIAZ, S., SERRANO-GARCIA, J. C., ZENIT, R. & HERNANDEZ-CORDERO, J. A. 2013. Power spectral distributions of pseudo-turbulent bubbly flows. *Physics of Fluids,* 25.

MERCADO, J. M., GOMEZ, D. C., VAN GILS, D., SUN, C. & LOHSE, D. 2010. On bubble clustering and energy spectra in pseudo-turbulence. *Journal of Fluid Mechanics,* 650**,** 287-306.

MUDDE, R. F., GROEN, J. S. & VANDENAKKER, H. E. A. 1997. Liquid velocity field in a bubble column: LDA experiments. *Chemical Engineering Science,* 52**,** 4217-4224.

MURAI, Y., KITAGAWA, A., SONG, X. Q., OHTA, J. & YAMAMOTO, F. 2000. Inverse energy cascade structure of turbulence in a bubbly flow (Numerical analysis using Eulerian-Lagrangian model equations). *Jsme International Journal Series B-Fluids and Thermal Engineering,* 43**,** 197-205.

PAREKH, J. & RZEHAK, R. 2018. Euler-Euler multiphase CFD-simulation with full Reynolds stress model and anisotropic bubble-induced turbulence. *International Journal of Multiphase Flow,* 99**,** 231-245.

PFLEGER, D. & BECKER, S. 2001. Modelling and simulation of the dynamic flow behaviour in a bubble column. *Chemical Engineering Science,* 56**,** 1737-1747.

POPE, S. B. 2000. *Turbulent Flows,* Cambridge, Cambridge University Press.

PRAKASH, V. N., MERCADO, J. M., VAN WIJNGAARDEN, L., MANCILLA, E., TAGAWA, Y., LOHSE, D. & SUN, C. 2016. Energy spectra in turbulent bubbly flows. *Journal of Fluid Mechanics,* 791**,** 174-190.

PRINCE, M. J. & BLANCH, H. W. 1990. Bubble Coalescence and Break-up in Air-Sparged Bubble-Columns. *Aiche Journal,* 36**,** 1485-1499.

RENSEN, J., LUTHER, S. & LOHSE, D. 2005. The effect of bubbles on developed turbulence. *Journal of Fluid Mechanics,* 538**,** 153-187.

RIBOUX, G., LEGENDRE, D. & RISSO, F. 2013. A model of bubble-induced turbulence based on large-scale wake interactions. *Journal of Fluid Mechanics,* 719**,** 362-387.

RIBOUX, G., RISSO, F. & LEGENDRE, D. 2010. Experimental characterization of the agitation generated by bubbles rising at high Reynolds number. *Journal of Fluid Mechanics,* 643**,** 509-539.

RISSO, F. 2011. Theoretical model for k(-3) spectra in dispersed multiphase flows. *Physics of Fluids,* 23.

RISSO, F. & ELLINGSEN, K. 2002. Velocity fluctuations in a homogeneous dilute dispersion of high-Reynolds-number rising bubbles. *Journal of Fluid Mechanics,* 453**,** 395-410.

RISSO, F., ROIG, V., AMOURA, Z., RIBOUX, G. & BILLET, A. M. 2008. Wake attenuation in large Reynolds number dispersed two-phase flows. *Philosophical Transactions of the Royal Society a-Mathematical Physical and Engineering Sciences,* 366**,** 2177-2190.

ROGHAIR, I., MERCADO, J. M., ANNALAND, M. V., KUIPERS, H., SUN, C. & LOHSE, D. 2011. Energy spectra and bubble velocity distributions in pseudo-turbulence: Numerical simulations vs. experiments. *International Journal of Multiphase Flow,* 37**,** 1093-1098.

ROIG, V. & DE TOURNEMINE, A. L. 2007. Measurement of interstitial velocity of homogeneous bubbly flows at low to moderate void fraction. *Journal of Fluid Mechanics,* 572**,** 87-110.

RZEHAK, R. & KREPPER, E. 2013. CFD modeling of bubble-induced turbulence. *International Journal of Multiphase Flow,* 55**,** 138-155.

SADDOUGHI, S. G. & VEERAVALLI, S. V. 1994. Local Isotropy in Turbulent Boundary-Layers at High Reynolds-Number. *Journal of Fluid Mechanics,* 268**,** 333-372.

SATO, Y. & SEKOGUCHI, K. 1975. Liquid velocity distribution in two-phase bubble flow. *International Journal of Multiphase Flow,* 2**,** 79-95.

SIMONIN, O. Eulerian formulation for particle dispersion in turbulent two-phase flows. Proceedings of the Fifth Workshop on Two-Phase Flow Predictions, Erlangen, Germany, 1990.

SUGIYAMA, K., TAKAGI, S. & MATSUMOTO, Y. 2001. Multi-scale analysis of bubbly flows. *Computer Methods in Applied Mechanics and Engineering,* 191**,** 689-704.

TROSHKO, A. A. & HASSAN, Y. A. 2001. A two-equation turbulence model of turbulent bubbly flows. *International Journal of Multiphase Flow,* 27**,** 1965-2000.

WANG, T. F., WANG, J. F. & JIN, Y. 2003. A novel theoretical breakup kernel function for bubbles/droplets in a turbulent flow. *Chemical Engineering Science,* 58**,** 4629-4637.

ZHAO, H. & GE, W. 2007. A theoretical bubble breakup model for slurry beds or three-phase fluidized beds under high pressure. *Chemical Engineering Science,* 62**,** 109-115.

CHAPTER 5: MODELLING OF BUBBLE COALESCENCE IN BUBBLE COLUMNS ACCOUNTING FOR BUBBLE-INDUCED TURBULENCE

SUMMARY

Modelling of bubble breakage in bubble columns accounting for bubble wake induced turbulence has been explored and discussed in Chapter 4. Unlike the bubble breakup caused by collision between the turbulent eddies and bubbles, bubble coalescence takes place through the joint efforts of both bubble collision and bubble entrainment by turbulent eddies. This chapter will aim to partially address the issue of modelling of bubble coalescence affected by bubble-induced turbulence. In bubble coalescence kernels, especially for the bubble coalescence caused by turbulent fluctuations, the approaching velocities of two bubbles are usually approximated by the mean turbulent eddy velocity that corresponds to the size of each bubble. The mean turbulent eddy velocity is generally estimated based on the isotropic homogeneous shear turbulence. However, turbulence induced by the deformable rising bubbles through the wakes may play a significant role in the bubble column reactors as the turbulent eddies continuously collide with the rising bubbles. The turbulence energy spectrum of bubble-induced turbulence has been clearly demonstrated to exhibit a different scaling law from the classical Kolmogorov -5/3 scaling law for the isotropic homogeneous turbulence with a slope of -3. Also, this has been shown to be robust (Mercado et al., 2010, Risso, 2011, Riboux et al., 2010, Prakash et al., 2016). Thus, the influence of bubble-induced turbulence may need to be

considered in the bubble coalescence kernel. The present study implements the mean turbulent eddy velocity estimated based on the κ^{-3} power law scaling and the dissipation of bubbles' wake into the bubble coalescence model. CFD simulations using the modified bubble coalescence kernel, based on the coalescence model proposed by Prince and Blanch (1990), clearly illustrate the necessity of accounting for bubble-induced turbulence in the description of the bubble coalescence phenomenon.

1. INTRODUCTION

The bubble coalescence phenomenon can be easily described under the *Eulerian-Lagrangian* framework as the bubbles are modelled as individual particles. However, when using the two-fluid approach, the discrete bubbles are modelled as the dispersed phase, where the bubble breakage and coalescence can only be expressed by means of break-up or coalescence frequency and probability. In this case, the bubble coalescence kernel plays a significant role in determining the averaged bubble diameters, which strongly affect the interphase momentum exchange closures in CFD simulations. Thus, various models have been proposed and developed for a more comprehensive description of bubble coalescence.

For the bubble coalescence process, occurrence of direct contact and collisions between bubbles is the essential criteria for coalescence. Shinnar and Church (1960) proposed the classic film drainage model. According to the film drainage model, a liquid film is initially formed when two bubbles contact and deform due to the surrounding pressure; the liquid film begins to drain sequentially, leading to the film rupture and bubble coalescence. If the surrounding pressure is insufficient to overcome the viscous force of the thin film, the bubbles bounce back without coalescence. Therefore, the coalescence probability depends on the intrinsic contact time and drainage time between the bubbles. The expression of collision density was derived by analogy with molecule collision in the kinetic theory of gases, which considers a bubble travelling in a relative speed with respect to the other bubbles enclosed in the collision tube that has been virtually imagined to be stationary. Prince and Blanch (1990) proposed a collision model considering the effects of turbulent eddy fluctuation, buoyancy-driven and liquid viscous shear. In some cases, the effects of turbulence fluctuation may be considered to be more significant compared to the effects of buoyancy-driven and liquid viscous shear. Luo (1993) adopted this deduction and proposed a collision model that further considers the changes in the relative position of the mass centres of the two colliding bubbles during the liquid film drainage process.

When the coalescence models are implemented into CFD simulations together with the breakage model, a mismatch is often found for the bubble coalescence rate and the breakage rate, and hence empirical correlations are required to obtain acceptable agreements with experimental results. Chen (2004) and Chen *et al.* (2005) have reported that in churn-turbulent flow regimes, the model predicted bubble coalescence rate is about one order of magnitude higher than the predicted breakage rate. Wang *et al.* (2005a) and Wang *et al.* (2005b) have proposed correlations to consider two effects that relate to the prediction of the bubble coalescence rate. The distance between bubbles may be larger than the bubble turbulent path length and the coalescence rate should be multiplied by a coefficient smaller than 1 to account for such effect. On the contrary, the reduction of free space due to the bubbles occupying a specified volume may increase the coalescence rate. Bhole *et al.* (2008) have considered the slip velocity between the bubble and liquid eddy and have used a coefficient that is related to the bubble Stokes number to prevent the over-prediction of the bubble coalescence rate. Nguyen *et al.* (2013) have addressed the turbulent suppression phenomena in the coalescence model. It is believed that part of the energy of turbulent eddies has been dissipated by the surface of bubbles without causing breakage. In this case, the size of eddies that have been chosen as the characteristic length scale for bubble-bubble collision is greatly reduced, which further reduces the contact time and the coalescence efficiency. Yao and Morel (2004) and Mukin (2014) have suggested that coefficients for adjusting the model predicted coalescence rate are required in dense bubbly flows. Mitre *et al.* (2010) have addressed that the use of coefficients should depend on the combination of coalescence and breakup models as well as the superficial velocities. Xu *et al.* (2013) have employed a coefficient of 0.5 for the coalescence model and have suggested the use of RNG $k \sim \varepsilon$ turbulence model to avoid the overprediction of coalescence rate. Liao *et al.* (2015) summarised various previously proposed mechanisms of bubble collision induced coalescence including turbulence fluctuation, viscous shear stress, capture in turbulent eddies, buoyancy and wake interaction. When the coalescence frequency is derived, in addition to the inertial collision, Liao *et al.* (2015) adopted the viscous shear induced collision as presented by Lo and Zhang (2009). It seems that most of these considerations with regards to bubble coalescence focus on the bubble motions, whereas the effect of turbulent eddies, especially the ones induced by rising bubbles which are caused by bubble wakes and are encountered in bubble columns and bubble swarms, have rarely been considered. Of particular relevance to this study, Sun *et al.* (2004) have considered the effect of bubble wakes in a cylinder-wise tail region of ellipsoidal and spherical-cap bubbles. However, it seems that their considerations on the wake entrapment still favours using the empirical correlations rather than strictly following the turbulent kinetic energy of eddies as defined by the turbulence energy spectrum.

The present study will present and propose a coalescence model that considers the approaching velocities of the colliding bubbles and the dissipation rate of the bubble wakes under the influence of bubble-induced turbulence. Section 2 presents the mathematical modelling adopted for CFD simulations on gas-liquid two-phase bubble columns, especially focusing on the comparison of bubble coalescence under the influence of isotropic homogeneous turbulence and the bubble-induced turbulence. Section 3 presents the numerical details used in the simulations. Section 4 presents the theoretical analysis of the modified coalescence model and the simulation results with detailed discussion, while important concluding remarks are drawn in section 5.

2. Mathematical modelling

2.1 Governing equations

A 3D transient CFD model is used in this work to simulate the local hydrodynamics of the gas-liquid two-phase flow in bubble columns. A Eulerian-Eulerian approach is adopted to describe the flow behaviours for both phases, i.e. water as the continuous phase, and air as the dispersed phase. The mass and momentum balance equations are given by

$$\frac{\partial(\rho_k \alpha_k)}{\partial t} + \frac{\partial}{\partial x_i}\left(\rho_k \alpha_k \boldsymbol{u}_{i,k}\right) = 0 \tag{5-1}$$

$$\frac{\partial(\rho_k \alpha_k \boldsymbol{u}_{i,k})}{\partial t} + \frac{\partial}{\partial x_j}\left(\rho_k \alpha_k \boldsymbol{u}_{i,k} \boldsymbol{u}_{j,k}\right) = -\alpha_k \frac{\partial}{\partial x_i} p_k + \frac{\partial}{\partial x_j}\left[\alpha_k\left(\boldsymbol{\tau}_{ij,k} + \boldsymbol{\tau}_{ij,k}^{\boldsymbol{R_e}}\right)\right] + \alpha_k \rho_k g_i + \boldsymbol{F}_{i,k} \tag{5-2}$$

where ρ_k, α_k, $\boldsymbol{u}_{i,k}$, $\boldsymbol{\tau}_{ij,k}$, $\boldsymbol{\tau}_{ij,k}^{\boldsymbol{R_e}}$ and $\boldsymbol{F}_{i,k}$ represent the density, volume fraction, velocity vector, laminar stress tensor, turbulent stress tensor and the inter-phase momentum exchange term for the *k* (liquid or gas) phase, respectively. *p* and $\boldsymbol{g}$ are the pressure and the gravitational acceleration. The sum of the volume fractions for both phases is equal to 1.

Interphase momentum transfer

The above momentum equation needs to be closed by the interphase momentum transfer term, which can be regarded as the total effect of different forces acting on the gas and liquid interface. In this study, drag force, lift force and added mass force are considered as the main interactions. The adopted expressions for these interfacial forces are summarised as shown in Table 5-1.

Table 5-1 Interphase momentum transfer closures.

Force	Expressions
Drag	$\boldsymbol{F}_D = \frac{3}{4}\frac{C_D}{d_b}\rho_l\alpha_g\lvert\boldsymbol{u}_g - \boldsymbol{u}_l\rvert(\boldsymbol{u}_g - \boldsymbol{u}_l)$ Drag coefficient: Grace model (Clift *et al.*, 1978) $C_D = max\left(C_{D,sphere},\ min\left(C_{D,ellipse},\ C_{D,cap}\right)\right),$ $C_{D,sphere} = \begin{cases} \frac{24}{R_{eb}} & R_{eb} < 1000 \\ \frac{24}{R_{eb}}(1 + 0.15R_{eb}^{0.687}) & R_{eb} \geq 1000 \end{cases},$ $C_{D,cap} = \frac{8}{3},\quad C_{D,ellipse} = \frac{4}{3}\frac{gd_{eq}}{U_t^2}\frac{(\rho_l - \rho_g)}{\rho_l},$ $Re_b = \frac{\rho_l\lvert\boldsymbol{u}_g - \boldsymbol{u}_l\rvert d_b}{\mu_l},\ U_t = \frac{\mu_l}{\rho_l d}M_O^{-0.149}(J - 0.857),$ $M_O = \frac{\mu_l^4 g(\rho_l - \rho_g)}{\rho_l^2\sigma^3},\ J = \begin{cases} 0.94H^{0.757} & 2 < H < 59.3 \\ 3.42H^{0.441} & H \geq 59.3 \end{cases},$ $H = \frac{4}{3}E_O M_O^{-0.149}\left(\frac{\mu_l}{\mu_{ref}}\right)^{-0.14},\ \mu_{ref} = 0.0009\ kg/(ms)$

Lift	$\boldsymbol{F}_{Lift} = C_L \rho_l \alpha_g (\boldsymbol{u}_g - \boldsymbol{u}_l) \times (\nabla \times \boldsymbol{u}_l)$ Lift Coefficient: Tomiyama model (Tomiyama, 1998) $C_L = \begin{cases} min[0.288 tanh(0.121 R_{eb}), f(E_O')] & E_O' \leq 4 \\ f(E_O') & 4 < E_O' < 10 \\ -0.29 & E_O' > 10 \end{cases}$, $f(E_O') = 0.00105 E_O'^3 - 0.0159 E_O'^2 - 0.0204 E_O' + 0.474,$ $E_O' = \frac{g(\rho_l - \rho_g) d_h^2}{\sigma}, d_h = d(1 + 0.163 E_O'^{0.757})^{1/3}$
Added mass	$\boldsymbol{F}_{VM} = C_{VM} \rho_l \alpha_g \left(\frac{d_l \boldsymbol{u_l}}{dt} - \frac{d_l \boldsymbol{u_g}}{dt} \right)$, $C_{VM} = 0.5$
Turbulent Dispersion	Burns model (Burns *et al.*, 2004) $\boldsymbol{F_{td,l}} = -\boldsymbol{F_{td,g}} = C_{TD} \frac{3\alpha_g}{4} \frac{\rho_l}{d_b} (\boldsymbol{u_l} - \boldsymbol{u_g}) \frac{\nu_t}{\sigma_{TD}} \left(\frac{\nabla \alpha_l}{\alpha_l} - \frac{\nabla \alpha_g}{\alpha_g} \right)$
Wall Lubrication	$\boldsymbol{F_{wl}} = C_{wl} \rho_l \alpha_g \left| (\boldsymbol{u_l} - \boldsymbol{u_g})_{\|\|} \right|^2 \boldsymbol{n_w}$ Wall lubrication coefficient: Antal model (Antal *et al.*, 1991)

Turbulence modelling

The turbulence generated in the bubble column can be thought of as being the joint superposition of shear turbulence and bubble-induced turbulence. The bubble-induced turbulence is mainly influenced by the wake formed by shedding vortices from the bubbles and decays quite quickly. In this case, it seems that the flow features of interest in the present study are the result of anisotropy, and hence the Boussinesq hypothesis of isotropic turbulent eddy viscosity may not be appropriate for the modelling of Reynolds stresses. Therefore, the Reynolds stress model (RSM) is employed for the simulation of the liquid turbulence field in order to capture the anisotropic nature. In the RSM model, individual Reynolds stresses $\overline{u_i'u_j'}$ are solved via six Reynolds stress transport equations with an additional equation for the turbulence dissipation rate. When the bubble-induced turbulence is considered, the transport equations for the transport of the Reynolds stresses may be expressed as

$$\frac{\partial\left(\alpha_l\rho_l\overline{u_i'u_j'}\right)}{\partial t}+\frac{\partial\left(\alpha_l\rho_l u_k\overline{u_i'u_j'}\right)}{\partial x_k}=\frac{\partial}{\partial x_k}\left(\alpha_l\left(\mu_l+\frac{\mu_t}{\sigma_k}\right)\frac{\partial\overline{u_i'u_j'}}{\partial x_k}\right)$$

$$+\alpha_l P_{ij}+\alpha_l\phi_{ij}-\tfrac{2}{3}\delta_{ij}\alpha_l\rho_l\varepsilon+\alpha_l S_{ij}^{BIT} \tag{5-3}$$

where P_{ij} is the turbulence production that is given by

$$P_{ij}=-\rho_l\left(\overline{u_i'u_k'}\frac{\partial u_j}{\partial x_k}+\overline{u_j'u_k'}\frac{\partial u_i}{\partial x_k}\right) \tag{5-4}$$

and ϕ_{ij} is the pressure-strain correlation accounting for pressure fluctuations that redistribute the turbulent kinetic energy amongst the Reynolds stress components. It can be modelled according to the formulation proposed by Launder (1989):

$$\phi_{ij}=\phi_{ij,1}+\phi_{ij,2}+\phi_{ij,1}^{W}+\phi_{ij,2}^{W}$$

$$=-C_1\rho_l\frac{\varepsilon}{k}\left(\overline{u_i'u_j'}-\frac{2}{3}k\delta_{ij}\right)-C_2\rho_l\frac{\varepsilon}{k}\left(P_{ij}-\frac{1}{3}tr(P)\delta_{ij}\right)$$

$$-C_1^W\rho_l\frac{\varepsilon}{k}\left(\overline{u_k'u_m'}n_k n_m\delta_{ij}-\frac{3}{2}\overline{u_k'u_i'}n_k n_j-\frac{3}{2}\overline{u_k'u_j'}n_k n_i\right)\left(\frac{k^{3/2}}{\varepsilon}\frac{1}{C_l y_W}\right)^2$$

$$-C_2^W\left(\phi_{km,2}n_k n_m\delta_{ij}-\tfrac{3}{2}\phi_{ik,2}n_k n_j-\tfrac{3}{2}\phi_{jk,2}n_k n_i\right)\left(\tfrac{k^{3/2}}{\varepsilon}\tfrac{1}{C_l y_W}\right)^2. \tag{5-5}$$

In Equation (5-5), additional wall reflection terms are needed to account for the modification of the pressure field and blockage of the transfer of energy from the streamwise to the wall-normal direction observed in the presence of the bubble column walls with the quadratic wall damping function proposed by Naot and Rodi (1982). The reason is that the adoption of the linearly decreasing function may result in noteable wall effects near the axis of the bubble column as pointed out by Colombo and Fairweather (2015) for bubbly pipe flow. As the turbulence dissipation rate is used in Equation (5-5), a model transport equation is used to calculate ε, such as

$$\frac{\partial(\alpha_l \rho_l \varepsilon)}{\partial t} + \frac{\partial}{\partial x_i}(\alpha_l \rho_l \varepsilon \boldsymbol{u}_i) = \frac{\partial}{\partial x_j}\left[\alpha_l \left(\mu_l + \frac{\mu_t}{\sigma_\varepsilon}\right)\frac{\partial \varepsilon}{\partial x_j}\right] + \alpha_l \rho_l \frac{\varepsilon}{k}\left(C_{1\varepsilon}\overline{u'_l u'_J}\frac{\partial \boldsymbol{u_i}}{\partial x_k} - C_{2\varepsilon}\varepsilon\right) + \alpha_l S_\varepsilon^{BIT} \quad (5\text{-}6)$$

where the turbulent kinetic energy k is calculated from the solved values of normal stress using the Reynolds stress transport equation, such as

$$k = \frac{1}{2}\left(\sum_{i=1,2,3} u'_i u'_j\right). \quad (5\text{-}7)$$

The effect of bubble-induced turbulence is usually considered by the Sato and Sekoguchi (1975) model, which adds an extra term to the effective turbulent eddy viscosity term in two-equation models, such as $\mu_{eff} = \mu_l + \mu_t + \mu_{BIT}$. Pan *et al.* (1999) have achieved simulation results that are in good agreement with experimental data by using the Sato model, while Deen *et al.* (2001) have shown that the effect of inclusion of the viscosity due to the bubble-induced turbulence using the Sato model is not significant. Pfleger and Becker (2001), Troshko and Hassan (2001), and Simonin (1990) have also considered the effect of bubbles by adding different source terms to the k and ε equations of the liquid phase turbulence. However, the Reynolds stress model has abandoned the Boussinesq hypothesis of isotropic turbulent eddy viscosity and calculates the Reynolds stress terms directly, which leads to further difficulties for these types of models to be implemented into the RSM. It is noted that the effect of bubble-induced turbulence can be included in the turbulence closure of Reynolds stress model, such as Parekh and Rzehak (2018), who have used an anisotropic source term S_R^{BIT}. The source term S_R^{BIT} is obtained based on the decomposition of the k-

source term $S_k^{BIT} = C_{k,BIT} \boldsymbol{F}_L^{drag} \cdot (\boldsymbol{u}_G - \boldsymbol{u}_L)$ in the isotropic model of bubble-induced turbulence proposed by Rzehak and Krepper (2013a) and Rzehak and Krepper (2013b) for the two-equation turbulence closures. As the turbulence dissipation rate ε calculated by the RSM is also a scalar, the source term for ε remains the same as the one used in isotropic BIT model, such as $S_\varepsilon^{BIT} = C_{\varepsilon,BIT} \frac{S_k^{BIT}}{\tau}$. The decomposition of the production of turbulent kinetic energy leads to the velocity fluctuation in the direction of bubble's relative motion being almost twice as strong as the fluctuations in the perpendicular directions, which is in accordance with the experimental findings by Hosokawa and Tomiyama (2013). As the model has taken into account the anisotropic characteristic of the bubble-induced turbulence, it makes much more sense in physical interpretations. However, from the simulation results concerning the bubble-induced turbulence by Parekh and Rzehak (2018), the predictions with or without considering such anisotropy in the RSM show no significant differences. This may be attributed to the same assumption made in both models that all the energy lost by the bubble due to drag is converted to turbulent kinetic energy in its wake. However, this assumption may not be valid when the turbulence fluctuations caused by other forces such as the transverse lift or the added mass cannot be ignored. Also, the turbulence dissipation source S_ε^{BIT} is still treated as being isotropic and only based on dimensional analysis, which makes the selection of the characteristic time scale very sensitive to the simulation results, especially when the turbulence dissipation rate is further used to determine the bubble coalescence and breakage rate in population balance modelling. Considering all these factors, the bubble-induced turbulence source term is calculated using the following equation and then split amongst the normal Reynolds stress components. By using the approach of Lopez de Bertodano et al. (1990), the bubble-induced turbulence source is accommodated by the bubble rising direction:

$$S_{ij}^{BIT} = \begin{bmatrix} 1.0 & 0.0 & 0.0 \\ 0.0 & 0.5 & 0.0 \\ 0.0 & 0.0 & 0.5 \end{bmatrix} S_k^{BIT} . \tag{5-8}$$

It needs to be pointed out that the effect of bubble-induced turbulence in the bubble coalescence model has been shown to be important in determining the bubble size distribution. This will be discussed in the following section.

2.2 Bubble size distribution and Population Balance Model

Since the bubble size is used in the interphase momentum exchange closures, a non-uniform bubble size distribution is a better reflection of the local inhomogeneity of the fluid dynamics. The bubble size distribution can be modelled by the population balance equations (PBE) with consideration of bubble coalescence and breakage. Bubbles are classified into different size groups and d_i is the diameter of bubbles for i-th group. The population balance equation is expressed by

$$\frac{\partial n_i}{\partial t} + \nabla \cdot \left(\boldsymbol{u}_{b,i} \cdot n_i \right) = S_i \tag{5-9}$$

where n_i is the number density of bubbles for i-th group, $\boldsymbol{u}_{b,i}$ is the bubble velocity vector for the $\boldsymbol{i}$-th group, and S_i is the source term. The source term can be expressed as the birth and death of bubbles due to coalescence and breakage respectively, such as

$$S_i = B_{coalescence,i} - D_{coalescence,i} + B_{breakup,i} - D_{breakup,i}$$
$$= \sum_{V_j=V_{min}}^{V_i/2} \Omega_C\left(V_j: V_i - V_j\right) - \sum_{V_j}^{V_{max}-V_i} \Omega_C\left(V_j: V_i\right) + \sum_{V_j=V_i}^{V_{max}} \Omega_B\left(V_j: V_i\right) - \Omega_B(V_i)$$

(5-10)

The local gas volume fraction can be calculated by

$$\alpha_g f_i = n_i V_i \tag{5-11}$$

where f_i is the i-th class fraction of total volume fraction, and V_i is the volume for the i-th class.

The Sauter mean diameter d_{32} for the equivalent phase can be calculated by

$$\frac{1}{d_{32}} = \sum_{i=1}^{N} \frac{f_i}{d_i} \quad . \tag{5-12}$$

2.3 <u>Bubble Coalescence Model</u>

Model modifications considering the effect of BIT

For coalescence between bubbles of size d_i and d_j, the kernel used in the present study was the coalescence model proposed by Prince and Blanch (1990), which is based on the collision tube concept and the drainage of liquid films between two collision bubbles. Hagesaether *et al.* (2000) and Hagesaether *et al.* (2002) have adopted the model proposed by Prince and Blanch (1990) in the simulation of bubble columns and found that turbulence contribution dominates the collision rate in the system. In the present study, only the bubble coalescence due to shear turbulence and bubble-induced turbulence is considered. The coalescence rate of two bubbles of diameter d_i and d_j can be expressed by

$$\Omega_C = \omega_C^T p_C \tag{5-13}$$

where ω_C^T is the collision density due to the turbulence contribution and p_C is the coalescence probability. Since the turbulence considered in the present study is the shear turbulence due to the liquid velocity gradient and the bubble-induced turbulence, the difference between these two turbulence phenomena are reflected in the mean turbulent velocities and the turbulence dissipation in the wake of preceding bubbles.

The collision density relation proposed by Prince and Blanch (1990) can be expressed by

$$\omega_C^T \approx n_i n_j \frac{\pi}{4}\left(\frac{d_i+d_j}{2}\right)^2 \left(\bar{u}_i^2 + \bar{u}_j^2\right)^{1/2} \tag{5-14}$$

where $\overline{u_i}$ and $\overline{u_j}$ are the approaching velocities of two colliding bubbles. It is noted that the approaching velocities of two colliding bubbles are assumed to be approximately equal to the mean turbulent velocities of eddies with the same size of the bubbles. As indicated by Lamont and Scott (1970), the amplitude of turbulent velocity A is proportional to the wavenumber κ and the energy spectrum $E(\kappa)$, while $\overline{u_\iota}$ is proportional to A. As such, the mean turbulent velocity can be estimated from the turbulence kinetic energy spectrum $E(\kappa)$, which is written as

$$\bar{u}_i \approx \overline{u}_\lambda \sim \sqrt{\kappa E(\kappa)}. \tag{5-15}$$

As discussed in the introduction, bubble-induced turbulence plays a significant role in the turbulence generated in the bubble column. It has been shown that bubble-induced turbulence exhibits a different power law scaling in turbulence kinetic energy spectrum compared to the Kolmogorov -5/3 scaling law for isotropic and homogeneous turbulence (Mercado et al., 2010, Riboux et al., 2010, Risso, 2011, Prakash et al., 2016, Roghair et al., 2011). Following the theoretical analysis of Lance and Bataille (1991) on Kármán-Howarth equation, Prakash et al. (2016) proposed the equilibrium between energy input and energy dissipation in (one-dimensional) Fourier space. After simple mathematical manipulations, the energy spectrum function due to the bubble-induced turbulence can thus be written as

$$E_b(\kappa) = C_b \frac{\alpha g U_{Slip}}{\nu} \kappa^{-3} \tag{5-16}$$

where C_b is a model coefficient, α is the local gas holdup, gU_{Slip} is the work done on the surrounding fluid by bubbles due to buoyancy, ν is the kinematic viscosity of the carrier fluid, and wave number $\kappa = 2\pi / \lambda$. Therefore, the approaching velocity under the influence of bubble-induced turbulence can be expressed by

$$\bar{u}_{i,BIT} = C_\lambda^{1/2} \sqrt{C_b \frac{\alpha g U_{Slip}}{\nu}} \cdot d_i \tag{5-17}$$

where C_λ is also a model coefficient. Meanwhile, the approaching velocity in the original model of Prince and Blanch (1990), which considers the influence of shear turbulence, has been assumed to be expressed by

$$\bar{u}_i = 1.4(\varepsilon d_i)^{1/3}. \tag{5-18}$$

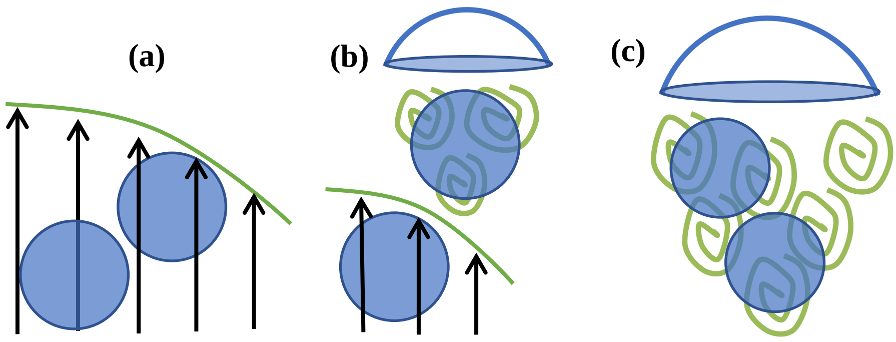

Figure 5-1 Bubble collision under the influence of (a) shear turbulence, (b) shear turbulence and bubble-induced turbulence, and (c) bubble-induced turbulence.

As shown in Figure 5-1, the collision between bubbles can be assumed to be the binary collision and the coalescence of bubbles may be considered to be influenced by either bubble-induced turbulence or shear turbulence, or by joint contributions from both turbulences, which leads to the approaching velocities of two colliding bubbles to be estimated based on the turbulence kinetic energy spectrum as given by

$$\bar{u}_i = \begin{cases} 1.4(\varepsilon d_i)^{1/3} & d_i < \Lambda \\ C_\lambda^{1/2}\sqrt{C_b\frac{\alpha g U_{Slip}}{\nu}}\cdot d_i & d_i \geq \Lambda \end{cases} . \tag{5-19}$$

It appears that C_λ and C_b are two model parameters that remain to be determined. Lance & Bataille (1991), Riboux *et al.* (2010) and Almeras *et al.* (2017) proposed that the characteristic length scale that corresponds to the bubble-induced turbulence can be approximately expressed as $\Lambda = d_{b,leading} / C_D$, where $d_{b,leading}$ is the diameter of the leading bubble that generates the wake. However, in the two-fluid model framework, the bubbles are not explicitly traced so that the value of this parameter can only be obtained by two-way coupling of the bubble diameter at the previous and the current timestep. Therefore, two relations must be satisfied at the characteristic length scale, such as

$$C_\kappa \varepsilon^{2/3}\Lambda^{5/3} = C_b\frac{\alpha g U_{Slip}}{\nu}\Lambda^3 \tag{5-20}$$

$$1.4(\varepsilon\Lambda)^{1/3} = C_\lambda^{1/2}\sqrt{C_b\frac{\alpha g U_{Slip}}{\nu}}\cdot\Lambda \quad . \tag{5-21}$$

The bubble collisions due to the joint influence of shear turbulence and bubble-induced turbulence have also affected the estimation of the coalescence probability. We assume that the bubble coalescence probability can still be approximated by

$$p_C \approx \exp\left(-\frac{\tau_{coal}}{\tau_{col}}\right) \tag{5-22}$$

where τ_{coal} and τ_{col} are the bubble coalescence time and the collision time respectively. The coalescence time can be derived based on the liquid file drainage model, which has been proposed by Prince and Blanch (1990) as

$$\tau_{coal,ij} = \left(\frac{r_{ij}^3 \rho_l}{16\sigma}\right)^{1/2} ln\left(\frac{h_0}{h_f}\right) \tag{5-23}$$

where the equivalent bubble radius $r_{ij} = \left(r_i^{-1} + r_j^{-1}\right)^{-1}/2$, σ is the surface tension, h_0 is the initial thickness of the liquid film between two bubbles and h_f is the final thickness. In the air-water system, $h_0 = 1 \times 10^{-4}$ m and $h_f = 1 \times 10^{-8}$ m.

The collision time is defined as the time that bubbles remain in contact, which depends on the bubble size and the turbulent intensity. Strong turbulence increases the probability that an eddy will separate the bubbles, while larger bubble sizes provide a larger contact area. Based on dimensional analysis, the collision time can be expressed by

$$\tau_{col,ij} = \frac{r_{ij}^{2/3}}{\varepsilon^{1/3}} \quad . \tag{5-24}$$

It is noted that the local turbulence dissipation rate ε, which is determined by the turbulence closure model, has contributions from both the shear turbulence and the bubble-induced turbulence. The latter contributes to the total turbulence dissipation surrounding the colliding bubbles and hence affects the bubble coalescence. Since the Reynolds stress terms or k and ε terms of bubble-induced turbulence have been included in the turbulence closure by using as the source terms, the dissipation rate of BIT can be considered as the generations due to all the energy lost by the rising bubbles. In particular, the drag force can be considered as the only source of turbulence generation due to bubbles (Kataoka and Serizawa, 1989, Troshko and Hassan, 2001, Rzehak and Krepper, 2013a, Parekh and Rzehak, 2018). Thus, all the energy lost by the bubbles due to the drag can be assumed to be only converted into turbulence kinetic energy inside the bubble wakes. Kataoka and Serizawa (1989) have indicated that generation of turbulence kinetic energy due to bubbles is directly related to the work of the interfacial force density per unit time. Interfacial work contributed from the drag force has been confirmed to be largely dominant in bubbly flows (Troshko and Hassan, 2001). Following these arguments, it has been suggested by Joshi *et al.* (2017) that the force and energy balances of a single bubble can be approximately expressed by

$$C_D \frac{\pi}{4} d_b^2 \rho_l \left|\boldsymbol{U}_{slip}\right| \boldsymbol{U}_{slip} = V_b \left(\rho_l - \rho_g\right) \boldsymbol{g} \tag{5-25}$$

$$C_D \frac{\pi}{4} d_b^2 \rho_l \left|\boldsymbol{U}_{slip}\right|^2 \boldsymbol{U}_{slip} = V_b \left(\rho_l - \rho_g\right) \boldsymbol{g} \left|\boldsymbol{U}_{slip}\right|. \tag{5-26}$$

For a bubble swarm, the number of bubble per unit volume is

$$N = \alpha_g / \frac{\pi}{6} d_b^3 \ . \tag{5-27}$$

Therefore, the frictional energy dissipation rate per unit liquid volume can be obtained by multiplying the LHS of Equation (5-26) by Equation (5-27), which gives

$$E_D / V_l = 1.5 \rho_l \alpha_g C_D \left|\boldsymbol{U}_{slip}\right|^3 / d_b \alpha_l \tag{5-28}$$

where V_l is the volume of the liquid phase. The energy dissipation per unit mass is thus given by

$$\varepsilon_w = 1.5 \alpha_g C_D \left|\boldsymbol{U}_{slip}\right|^3 / d_b \alpha_l \tag{5-29}$$

where ε_w is the turbulence energy dissipation rate due to the drag force and mainly dissipated in the wakes of bubbles. It is noted that other forces may have also contributed to the turbulence intensity in the wakes of bubbles, especially for those bubbles that rise in zigzag trajectories where the added mass and lift forces may have important contributions. Since the understanding behind these non-drag forces is still limited and their inclusion in the modelling will further complicate the estimation of the dissipation in the wakes of bubbles, the effects of these forces will be excluded and the turbulence dissipation of the wakes due to drag is considered. In this case, the turbulence dissipation rate ε required for estimation of the collision time $\tau_{col,ij}$ in Equation (5-24) can be obtained from Equation (5-5), while the bubble-induced turbulence dissipation source is given by

$$S_{\varepsilon}^{BIT} = C_{\varepsilon,BIT}\rho_l \frac{\varepsilon_W}{\tau_{BIT}} \tag{5-30}$$

where the coefficient $C_{\varepsilon,BIT}$ takes the value of 1 in the present study. The timescale τ_{BIT} can be modelled by $\tau_{BIT} = d_B/\sqrt{k}$ as proposed by Rzehak and Krepper (2013), where the bubble-induced turbulence generation is approximately at the length scale of the equivalent bubble size and such turbulence is shifted to smaller length scales observed in the experiments (Lance and Bataille, 1991, Shawkat et al., 2007). However, it is noted that the computed values of turbulence kinetic energy k represent the joint effect of shear turbulence and bubble-induced turbulence once the source terms S^k or S^R have been added. Therefore, a more appropriate correlation for the time-scale could be $\tau_{BIT} = d_B/U_{slip}$ where the slip velocity approximately equates to the velocity scale of the eddies in the wake of bubbles.

Model discussion

Since the modified coalescence model has taken into account the effect of bubble-induced turbulence and leads to the use of turbulence energy spectrum with the κ^{-3} power law scaling behaviour to modify the bubble approaching velocity and the turbulence dissipation, the modified coalescence kernel has been implemented in comparison with the original model by Prince and Blanch (1990).

It can be seen from Equation (5-6) that the turbulence dissipation rate ε, which includes the effect of both the shear turbulence and bubble-induced turbulence due to bubble's wakes, has been used in Equation (5-24). The turbulence dissipation due to bubble's wakes ε_w as suggested by Joshi *et al.* (2017) may significantly contribute to the local turbulent dissipation, especially for the case of the bubble column, where the bubble-induced turbulent kinetic energy decays quickly. Thus, the important variables that affect the turbulence dissipation in Equation (5-29) are the gas holdup α and the bubble diameter d_b, as the slip velocity usually changes little for a wide range of bubble diameters, while the drag coefficients can be well estimated based on d_b and U_{Slip} such as the use of Grace model (Clift et al., 1978). The influence of the dissipation rate due to shear turbulence, slip velocity, gas holdup and bubble diameter on the local turbulence dissipation rate has been comprehensively examined as shown in Figure 5-2.

In Figure 5-2, the transparent surface represents the condition that dissipation of shear turbulence ε_s =0.6 m^2/s^3. The local gas holdup ranges from 0.05 to 0.25 and the diameters of bubbles that induce the turbulence in its wake range from 0.005m to 0.015m. When the slip velocity is small, such as U_{Slip} = 0.1 m/s (see Figure 5-2(a)), the dissipation of shear turbulence contributes more towards the overall turbulent dissipation than that of the bubble-induced turbulence. With an increase in the bubble diameter, values of ε_w decrease and the contribution becomes smaller. However, this case is less likely to happen in the bubble columns, where large bubbles usually rise faster and leads to large slip velocity. As shown in Figure 5-2(b) for case of U_{Slip} = 0.2 m/s, which is usually true for those bubbles rising in the bubble column, the equivalent dissipation rate increases with the bubble diameter, revealing that the contribution from the bubble's wake becomes significant under this circumstance. The reason behind this is that the predictions of the drag coefficient also increase with the bubble diameter while this trend is kept consistently with further increasing in the slip velocity, as shown in Figure 5-2(c). However, the contribution of shear turbulence cannot be ignored, as a higher dissipation of shear turbulence leads to a higher equivalent dissipation rate in all three figures and the equivalent dissipation rate achieves its maximum at a certain point of gas holdup with a fixed bubble diameter.

For the original coalescence model by Prince and Blanch (P & B model), the coalescence rate is subjected to the diameters of two colliding bubbles and the local turbulence dissipation rate without considering the bubble-induced turbulence. Since the effect of bubble-induced turbulence has been taken into account in the modified coalescence model, it can be argued that the bubble diameter, which affects the induced turbulence in its wake, is one of the most important parameters that can characterise the BIT. The values of other parameters can be calculated either from the bubble diameter, such as characteristic length scale $\Lambda = d_b / C_D$, or be regarded as constants in the model.

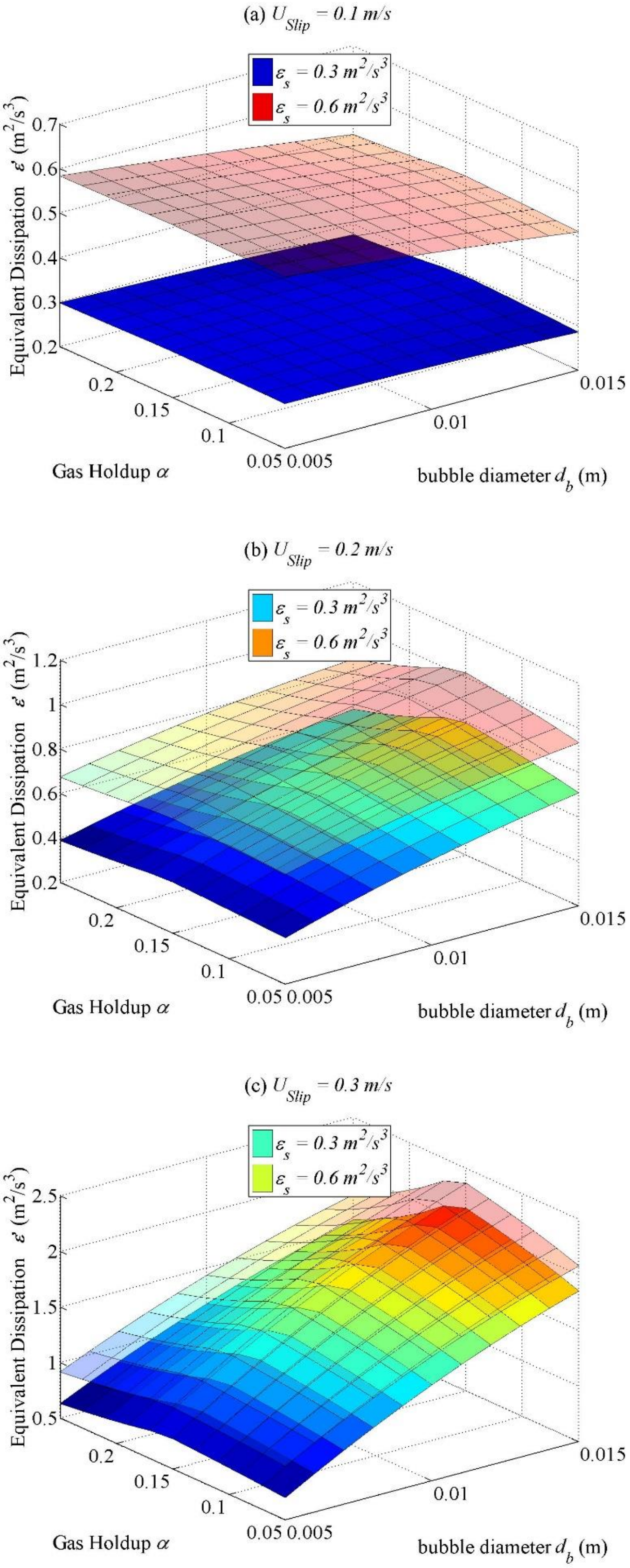

Figure 5-2 Effect of various parameters on the equivalent dissipation rate.

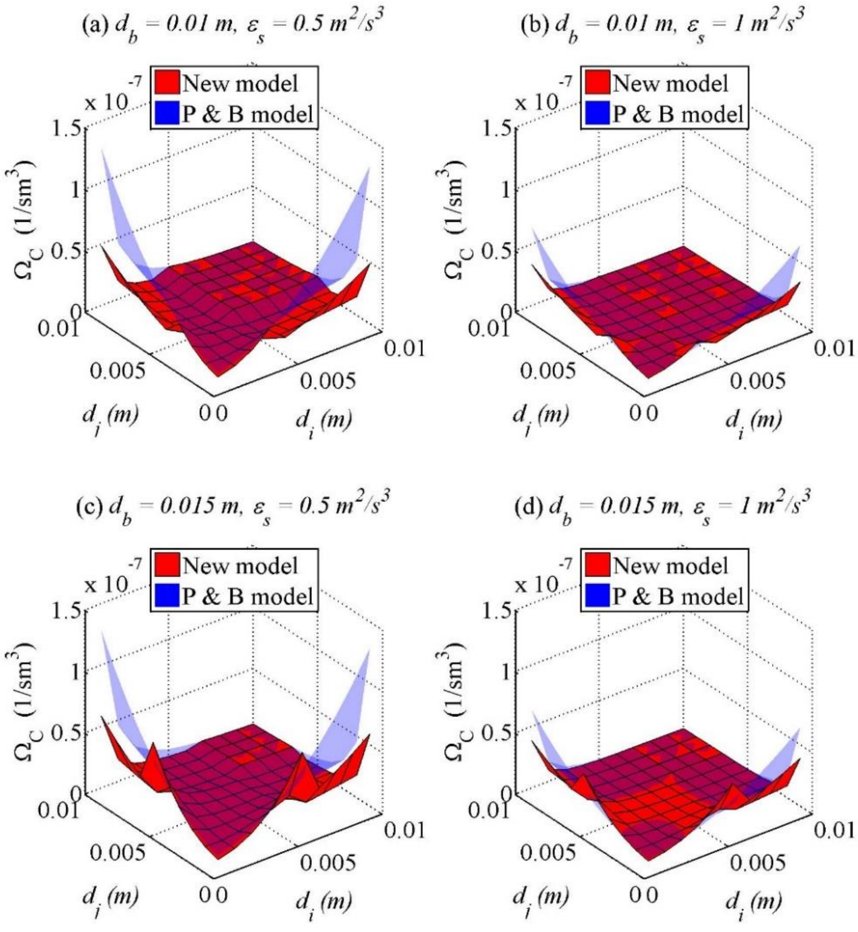

Figure 5-3 Effect of bubble diameter and dissipation of shear turbulence on the coalescence rate.

Figure 5-3 presents the effect of bubble-induced turbulence and the shear turbulence on the coalescence rate. For air-water system, the surface tension is taken as 0.072 N/m, density of water is taken as 1000 kg/m^3, viscosity of water is 0.001003 kg/m·s, and density of air is taken as 1.225 kg/m^3. The local volume fraction of gas is assumed to be 0.1, and the slip velocity is assumed to be 0.2 m/s. The diameters of both two colliding bubbles are ranging from 0.001 m to 0.01 m. In general, it seems that the modified bubble coalescence model has effectively lowered the over-prediction of the coalescence rate as pointed out by many researchers, such as Wang *et al.* (2005a), Bhole *et al.* (2008), and Yang and Xiao (2017). In particular, once the bubble-induced turbulence has been considered, the coalescence rate of one small bubble and one large bubble, such as d_i = 0.001 m and d_j = 0.01 m, has been significantly reduced. Although the bubble that under the influence of BIT may be with higher approaching velocity as calculated by Equation (5-15), the dissipation rate due to the contribution of BIT is also significant which makes the contact time to two bubbles much shorter. Meanwhile, the coalescence time is dependent on the sizes of two bubbles and the physical properties of the carrier fluid, which are not affected by the turbulence intensity. In this case, the shortened contact time reduces the coalescence efficiency. From Figure 5-3, it seems that the decrease in coalescence efficiency is more significant than the increase in collision density in most cases, which leads to the general decrease of the coalescence rate. However, for the modified coalescence model, sudden decrease of coalesce rate are found at the bubble diameters that approximately equal to the characteristic length scale. This is due to the sharp transition of the turbulence energy spectrum functions. It should be noticed that both the -5/3 and the -3 power law scaling behaviours are just approximations of the real energy spectrum within certain range. Considering that the transition on the real energy spectrum is indeed very smooth, a shape function may be required for these two energy spectrum functions in the future study, so that the coalescence rate around the characteristic length scale will be smoothened accordingly.

2.4 Bubble Breakage model

For the bubble breakage model, the effect of bubble-induced turbulence has been considered and presented in detail in Chapter 4. Although the use of the modified bubble breakage model accounting for BIT has shown to have a significant influence on the bubble size distribution in the simulation, the present study has attempted to separately examine these influences as the focus is centralised at the influence of BIT on the coalescence model. Thus, the Luo and Svendsen (1996) model is still used as the breakage kernel, which can be expressed as

$$\Omega_B = 0.923\left(1-\alpha_g\right)n_i\left(\varepsilon/d_i^2\right)^{1/3}\int_{\xi_{min}}^{1}\frac{(1+\xi)^2}{\xi^{11/3}}\exp\left(-\frac{12\sigma C_f}{\beta\rho_l\varepsilon^{2/3}d_i^{5/3}\xi^{11/3}}\right)d\xi, \tag{5-31}$$

where $\xi = \lambda / d_i$, the increase coefficient of surface area $C_f = f_V^{2/3} + (1 - f_V)^{2/3} - 1$, and the breakage volume fraction $f_V = d_j^3 / d_i^3$.

By considering the alternative of mean turbulent velocity due to bubble-induced turbulence and the turbulence dissipation in the wakes of bubbles, the effect of bubble-induced turbulence has been included in the bubble coalescence model. The performance of the modified bubble coalescence model will be theoretically assessed and shown in the following session of results and discussion. The modified bubble coalescence model coupled with the breakage model will be implemented into the CFD-PBM modelling, and the simulation results of key parameters especially the bubble size distributions are compared with the experimental data.

2.5 Numerical details

To validate the influence of bubble-induced turbulence on the bubble coalescence model, numerical simulations have been carried out for the air-water bubble column systems that have been reported in Kulkarni *et al.* (2007). Details of their experimental conditions are listed in Table 5-2.

Table 5-2 Details of experimental set-up by Kulkarni *et al.* (2007).

Diameter (m)	**Height (m)**	**Superficial Velocity (m/s)**	**Static liquid Height (m)**
0.15	1.2	0.02	0.9

ANSYS Fluent 3D pressure-based solver was employed in CFD-PBM modelling. The time step adopted in the simulations is gradually increased from 0.001 seconds to 0.005 seconds for all the simulations, which is considered to be sufficient for illustrating the time-averaged characteristics for the flow fields by carrying out the data sampling statistics for typically 120 seconds after the quasi-steady state has been achieved. For the population balance modelling, 15 discrete bubble classes have been used in total. The sizes of the bubble classes are gradually increased in such a manner that $V_{i+1} = \gamma V_i$, where γ is the ratio of volume increase and $\gamma = 2$ is suggested in the present study. The minimum diameter of all bubble classes is assumed to be 0.001 m. The modified bubble coalescence model has been implemented into the simulations by using the user defined function (UDF). The outlet boundary is set to be a pressure-out let at the top of the column. No-slip conditions are applied for both liquid and gas phases at the bubble column wall and standard wall function is used as wall treatment. The volume fraction of gas phase is set to be 1 at the inlet. The inlet velocity distribution is computed by using the kinetic inlet model as proposed in Chapter 2, which has taken into account the size and number of the holes and the through-hole velocities of the gas sparger.

The grid independency has been tested in coarse, medium and fine grids. As shown in Figure 5-4(a), Grid 2 consists of $20(r)\times40(\theta)\times100(z)$ equally distributed nodes in radial, circumferential and axial directions respectively, with no special grid refinements near the wall. The grid independence was tested in a coarser Grid 1 of $16(r)\times32(\theta)\times80(z)$ nodes and a refined Grid 3 of $26(r)\times48(\theta)\times126(z)$ nodes, in which case the total number of cells is doubled gradually. As shown in Figure 5-4(b), the grid independence test for these three set-ups has yielded similar results quantitatively though the gas-holdup for all three grids has been slightly over-predicted. The computed wall y+ values are within the range of 30-150 for all three grid configurations, which indicates that the standard wall functions can be used as near wall treatment. However, Grid 2 and Grid 3 present very similar results in the liquid axial velocity prediction while the coarser grid, Grid 1, has slightly deviated from both Grid 2 and Grid 3. Thus, Grid 2, as shown in Figure 3-6, has been employed throughout the subsequent simulations to investigate the effects of the improved breakup model.

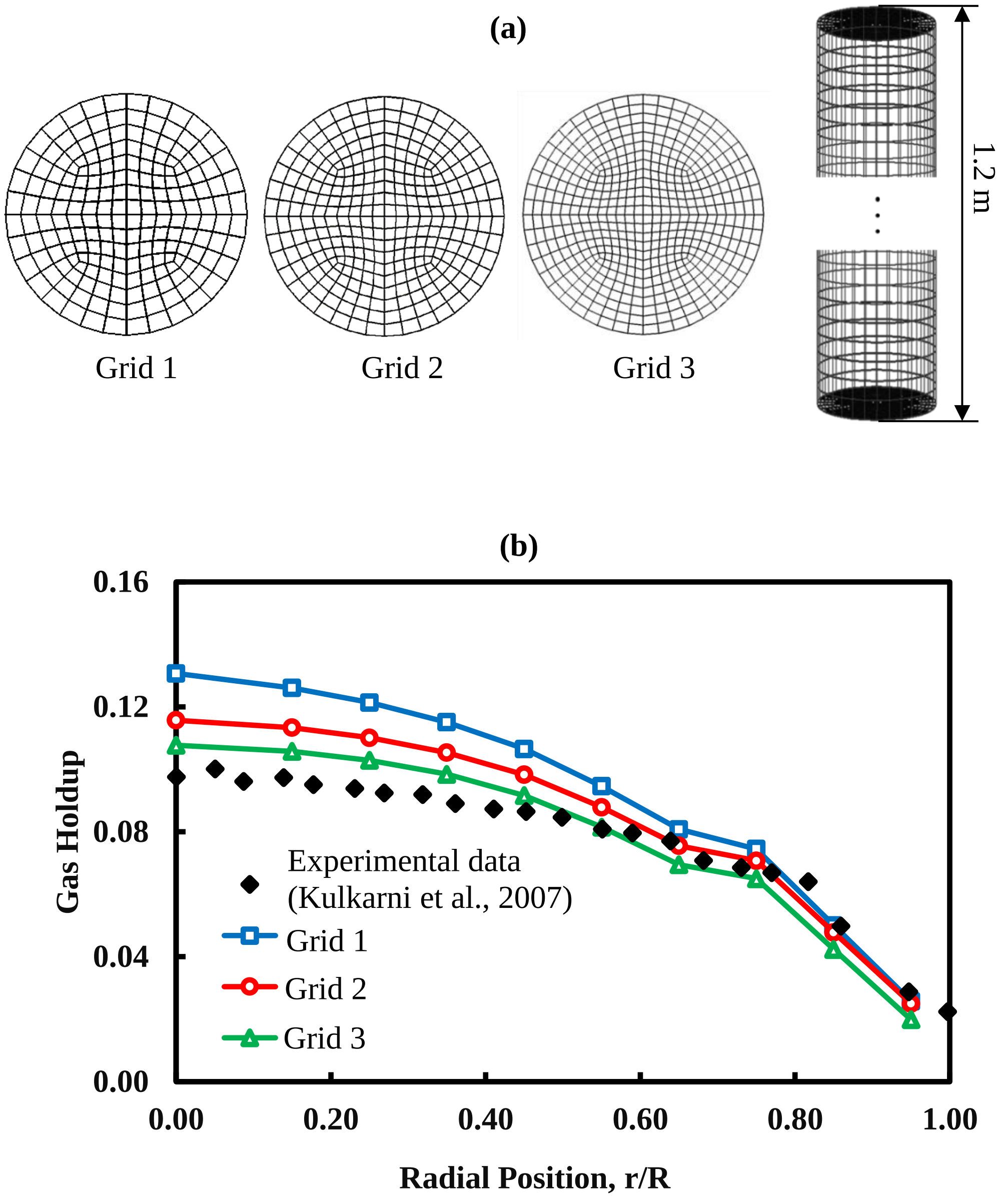

Figure 5-4 (a) Mesh setup; (b) comparison of simulated radial gas holdup distributions with three configurations.

Since the superficial gas velocity to be studied seems to be quite low (U_g = 0.02 m/s), which means the bubble coalescence and breakup is much less frequently to happen than operated in churn-turbulent flow regime, the bubble size distribution in the bulk phase may be largely affected by the initial distribution at the inlet. In this case, using a constant bubble diameter or uniformed bubble size distribution at the inlet boundary may neither be appropriate nor similar to the real distribution in the experiments. Actually, Polli *et al.* (2002) have shown that the bubble size distribution at the sparger region are in Gaussian distribution for many gas distributor configurations with a wide range of superficial velocities. Therefore, an empirical correlation can be proposed for crude estimation of the fractional distribution of bubble sizes at the inlet, such as $f_i = q \cdot exp\left(-\frac{(d_i-\overline{d})^2}{(\gamma^p d_{i,min}^3)^{2/3}}\right)$. In the proposed correlation, f_i and d_i are volume fraction and diameter of the i-th class at the inlet, $\overline{d}$ is the mean bubble diameter, γ is the ratio of volume increase, and $d_{i,min}$ is the minimum bubble diameter of all bubble classes. p and q are two model coefficients that satisfied the constraint of $\sum_{i=1}^{n} f_i = 1$. Theoretically, the initial bubble size distribution needs to associate with the number and size of holes of the gas distributor, the through-hole gas velocities and the physical properties of the fluids. However, it seems that all these parameters may not be fully available in different literatures. From simulation point of view, it may be a much practical way to only correlate f_i with easily obtained parameters such as mean bubble diameter or ratio of volume increase. For the bubble class used and the experimental systems performed in the present study, the distribution of f_i are presented in Table 5-3. The value of 0.005 m is taken as the mean bubble diameter at inlet, which is in accordance with Bhole *et al.* (2008).

Table 5-3 Fractional distribution of bubble classes at inlet.

d_i	f_i
0.001000	0.005421
0.001260	0.008965
0.001587	0.016101
0.002000	0.031198

0.002520	0.063597
0.003175	0.128705
0.004000	0.230525
0.005040	0.296091
0.006350	0.187729
0.008000	0.031198
0.010079	0.000468
0.012699	0.000000
0.016000	0.000000
0.020159	0.000000
0.025398	0.000000

3. RESULTS AND DISCUSSION

3.1 Verification of the modified bubble coalescence model

The experiments carried out by Kulkarni *et al.* (2007) have used a superficial gas velocities of 0.02 m/s, which means the reactor is operated at homogeneous bubbly flow regime. In this case, it seems that the phenomena of both the bubble coalescence and breakage were less frequently observed in the experiments. However, when the population balance models are applied into CFD simulations, especially once the bubble-induced turbulence has been considered, some improvements on the predictions of Sauter mean bubble diameter, bubble size distribution, and turbulence dissipation rate are still identified when comparing with the predictions by using the original model of Prince and Blanch (P & B model).

The radial distribution of time averaged gas holdup, liquid axial velocity and Sauter mean bubble diameter estimated by using both the original Prince and Blanch model and the modified coalescence model proposed in the present study have been compared with the experimental results (Kulkarni et al. (2007). The simulation results on the gas holdup and liquid axial velocity by both models are in generally good agreements with the

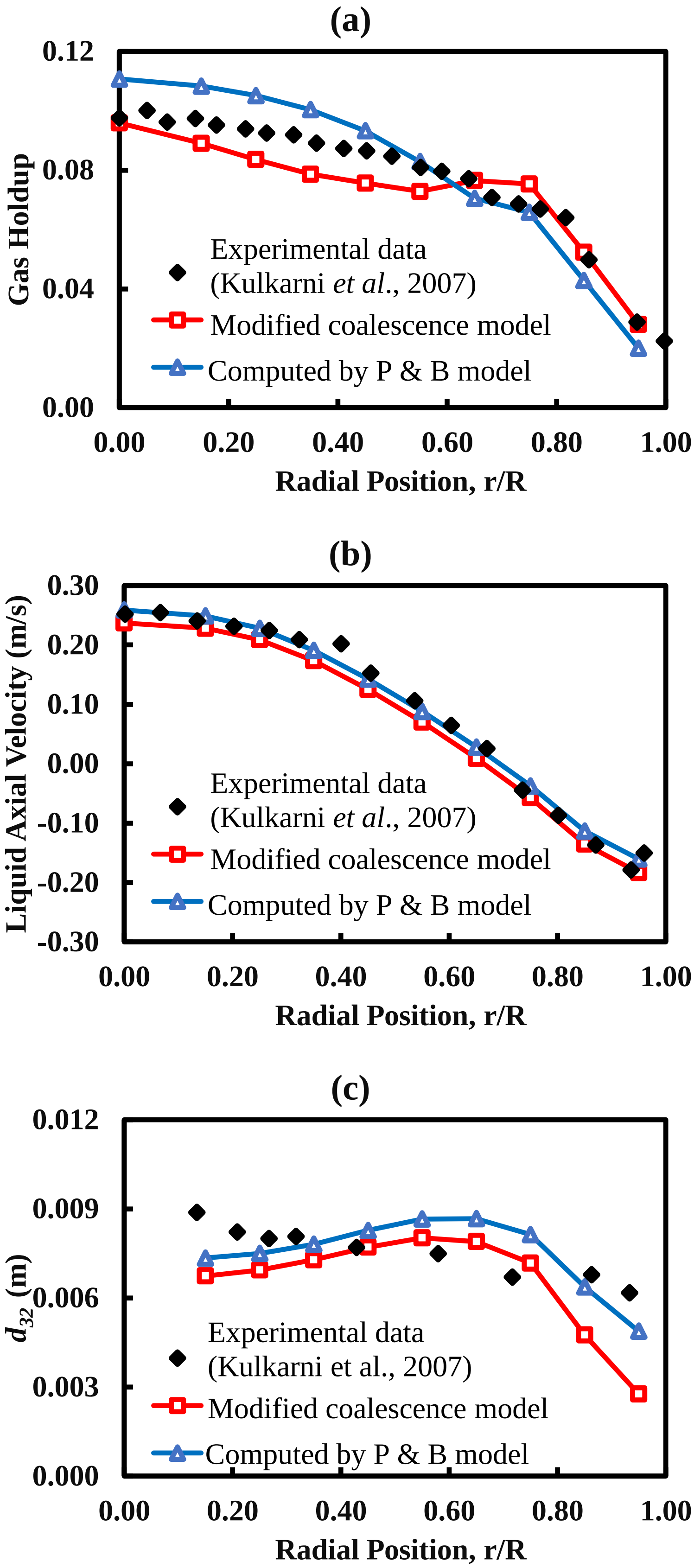

Figure 5-5 Radial distribution of time averaged parameters at *H/D* = 5: (a) gas holdup, (b) liquid axial velocity, and (c) bubble averaged diameter.

experimental data, which indicates that the numerical approaches used in the present study seems to be appropriate. The implementation of the bubble coalescence model into the simulations has shown the impact on the predicted distribution of gas bubbles in the bubble column. It can be seen from Figure 5-5(c) that the Sauter mean diameters predicted by using the original Prince and Blanch model deviates to a great extent from the experimental data at the region between the core part and the vicinity of the wall. The predictions made by the modified model gives out the reduced Sauter mean bubble diameters and has shown an improvement on bubble Sauter mean diameter distribution across the whole cross-section, reducing the overestimations by using the original model. As the reliable prediction of the bubble size distribution (BSD) has a strong impact on the interfacial area estimation that is crucial for calculation of the transfer rates of mass and heat transfer in the bubble columns, the predictions of bubble size distribution using the proposed model have also been compared with the experimental measurements as shown in Figure 5-6. The experimental data on bubble size distribution were taken from Kulkarni *et al.* (2004), in which the measurement was conducted by using LDA, and the averaged values of bubble size have been obtained from the measurements at various degrees in the plane of the column cross section perpendicular to column axis. The simulation results are the gas holdup-based probability distribution function (p.d.f.) of bubble classes of the entire bulk phase. It can be seen from the figure that the bubble size distribution of the entire bulk phase is totally different from the inlet BSD, which has illustrated that the evolution of bubble sizes, including bubble coalescence and breakage, has been developed in the transient simulation. Based on the same inlet BSD as shown in the figure, the BSD estimated by using the original Prince and Blanch model has greatly over-predicted the fractions of larger bubbles, which may have the implication that the bubble coalescence rate is much greater than the bubble breakage rate. This over-prediction on the larger bubbles may be partially attributed to the insufficient number of discrete bubble classes used for these larger bubbles in the simulation. A similar trend of overestimation of the coalescence rate has also been reported by several studies using uniform width of bubble classes, such as Bhole *et al.* (2008), Ekambara *et al.* (2008) and Yang and Xiao (2017). By considering the effect of bubble-induced turbulence, the modified coalescence model has reduced the over-estimation of the coalescence rate. The percentage difference on the predictions by using the modified coalescence model from the original model is also shown by the dash line in the figure, where the positive value means smaller than the original model and vice versa. For the small bubbles, both models have shown good agreements with the experimental data. However, 10 ~ 20% reductions by the modified coalescence model have been obtained for bubble sizes greater than 10 mm, which may significantly affect the overall gas holdup and the volume averaged bubble size.

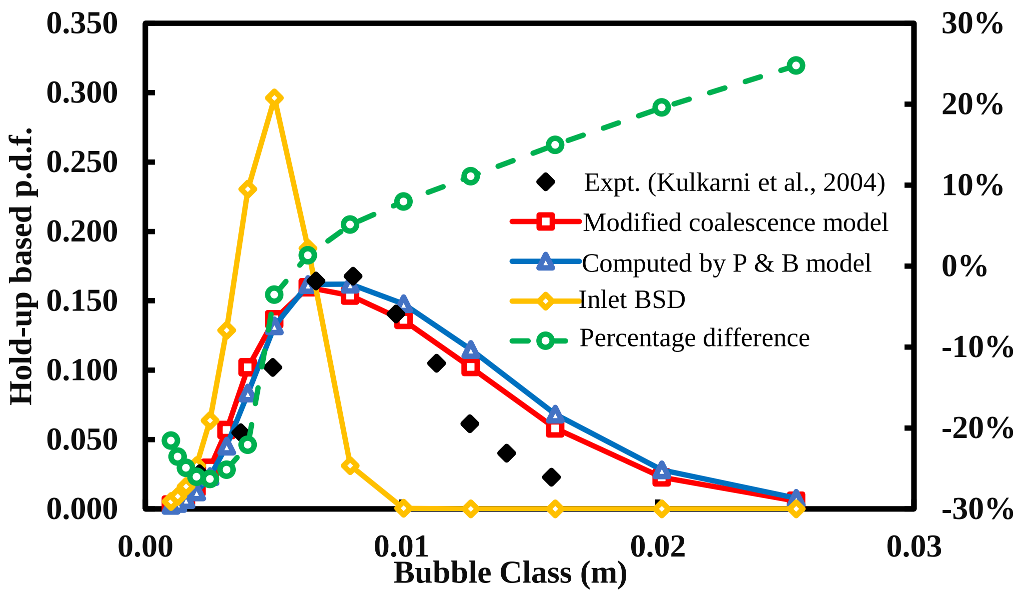

Figure 5-6 Hold-up based probability distribution of bubble classes. (solid line: left vertical axis; dash line: right vertical axis)

Since both the bubble-induced turbulence and the shear turbulence have been considered in the turbulence model and the modified coalescence model, one of the particular interested parameters would be the turbulence dissipation rate. The simulation results on the turbulence dissipation rate have been presented in Figure 5-7. It should be noted that the turbulence dissipation rate predicted in the present study is based on the predictions given by using the Reynolds turbulence model, and the source terms regarding the bubble-induced turbulence have been added to the RSM model. The bubble-induced turbulence, especially the anisotropic features of the BIT, has brought the difficulties in appropriately decomposing the source terms into different directions. Although the bubble-induced turbulence has been included in the modified coalescence model and it has been demonstrated to indeed improve the predictions on the bubble size distributions, it can be seen from Figure 5-7 that the predicted turbulence dissipation rate is still much lower than the experimental data at some radial positions, which indicates that the modification is still insufficient to fully resolve the turbulence characteristics in the bubble columns. A physical interpretation of overestimation of the bubble coalescence is that the low turbulence dissipation rate corresponds the low shear rate, which means that the turbulent eddies surrounding the bubbles will have lower possibilities to separate the two colliding bubbles apart and reduce their coalescence rate. In addition, the underestimated turbulence dissipation rate leads to larger collision time as can be from Equation (22), thus increasing the bubble coalescence probability. As the coalescence rate $\Omega_C \sim \exp\left(-\frac{t_{coal}}{\tau_{col}}\right)$, the larger collision time further leads to overestimation of the bubble coalescence rate. This could be one of the main reasons that explains the over-prediction on the Sauter mean bubble diameter. In this sense, further modification to better consider the effect of the bubble-induced turbulence in the turbulence closure is required, as it will further improve the prediction of bubble size distribution by applying the population balance model.

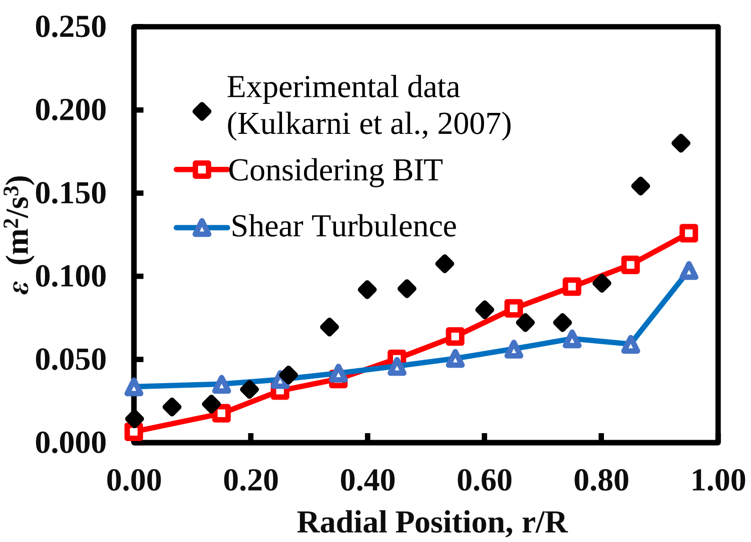

Figure 5-7 Radial distribution of turbulence dissipation rate.

3.2 Applications of modified bubble coalescence model

A typical application of the modified bubble coalescence model would be the rectangular cross-sectioned pseudo 2D bubble column, in which case the bubble coalescence happens frequently within the oscillating bubble plume. In the present study, the rectangular bubble column used in the work of Buwa and Ranade (2002) has been simulated by applying the modified coalescence model. The geometry of the rectangular bubble column is 0.2 m width × 1.2 m height × 0.05 m depth., which is the same as that used by Pfleger *et al.* (1999). Tap water is used as the liquid phase and filled up to a static height of 0.4 m. The air is pumped into the column through an 18 mm × 6 mm sintered disc gas distributor with a superficial gas velocity of 0.14 cm/s. In the CFD simulation, a fine grid as suggested by Buwa and Ranade (2002) that consists of 61 × 92 × 19 cells is used. The pressure outlet is used for the top. The inlet boundary has been simplified as a 24 mm width × 12 mm depth square section at the bottom centre while the sparging velocity being adjusted to maintain the gas flow rate consistent. The remaining surfaces are set to be the wall with no-slip conditions. For the population balance modelling, 8 classes of bubbles are used with the minimum size of $d_{\mathrm{i,min}}$ = 0.001 m and the ratio of volume increase γ = 1. The mean bubble diameter $\overline{d}$ at the inlet is estimated as 0.0025 m based on the experimental data and the values for the model coefficients take p = 1, q = 0.2452 of the inlet BSD. The timestep size for the transient simulation is fixed at 0.001s, and the time-dependent characteristics are averaged for 120 s after the quasi-steady state has been achieved. If no other specified, the observation height is fixed at 0.37 m from bottom.

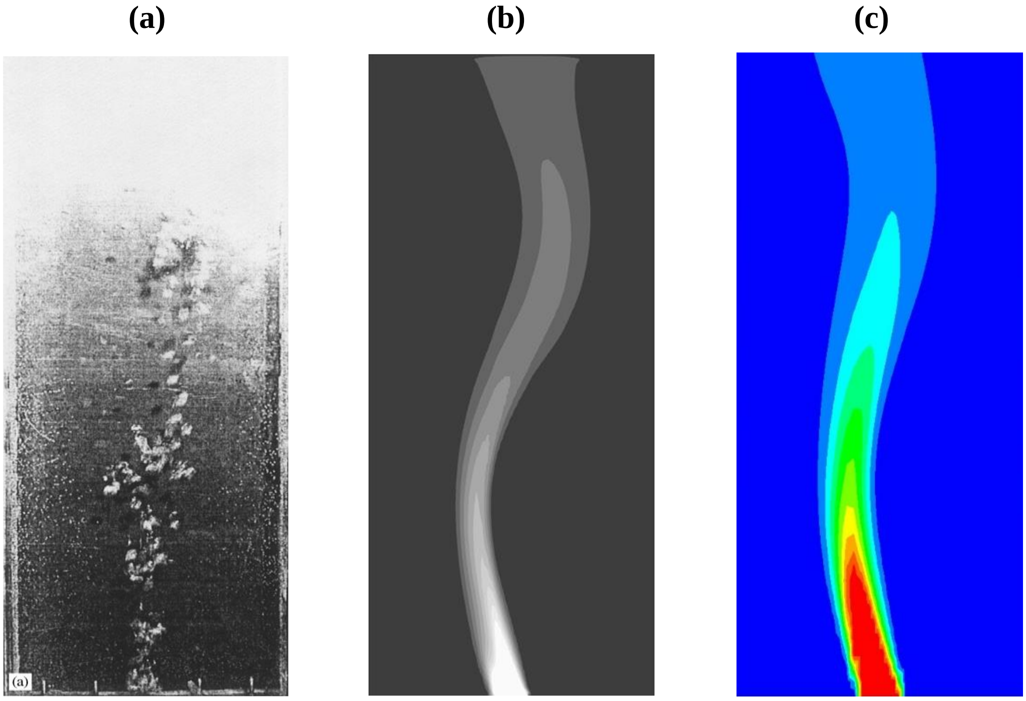

Figure 5-8 Snapshots of oscillating bubble plume (a) captured by highspeed camera, U_g = 0.16 cm/s; (b) predicted by Buwa and Ranade (2002), single bubble group d = 0.005 m, U_g = 0.16 cm/s; (c) predicted by using modified coalescence model, U_g = 0.14 cm/s.

Figure 5-8 shows the comparison of the oscillating bubble plume by using the modified coalescence model with the single bubble group predictions made by Buwa and Ranade (2002). 10 uniform contours in 0.0–0.1 are used to represent the gas holdup. It seems that the amplitudes of the plume oscillations are quite similar to each other, which suggests that the modelling approach used for the present case can be accepted. However, the snapshots are merely the reflection of instantaneous characteristics. The time-averaged characteristics are more important parameters for the design and the assessment of performance of the bubble columns. Therefore, the time-averaged gas holdup and the liquid axial velocity distributions are compared with the experimental data in Figure 5-9.

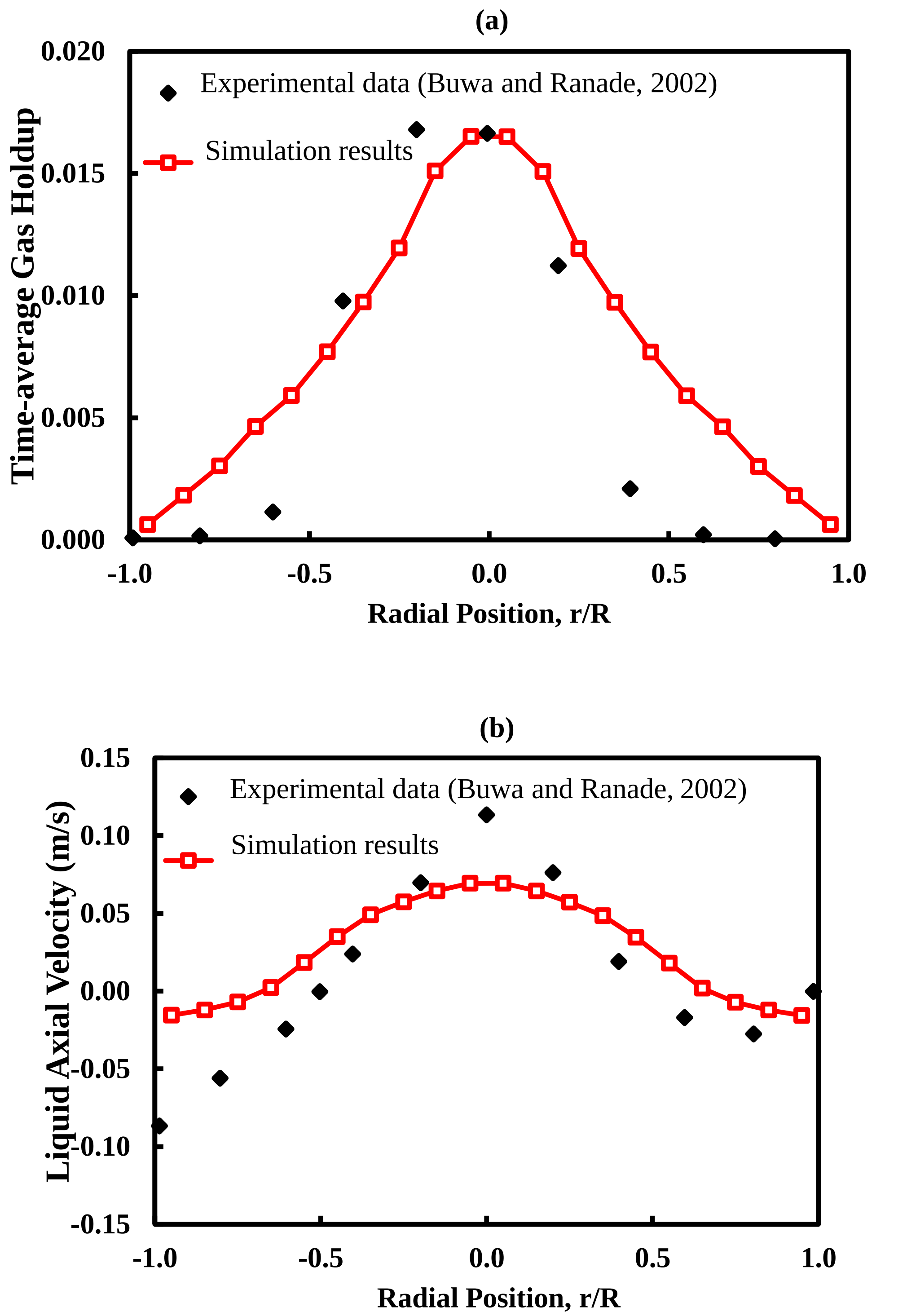

Figure 5-9 Radial distribution of time-averaged (a) gas holdup and (b) liquid axial velocity.

It seems that the estimation of gas holdup has achieved good agreements with the experimental data, while some underpredictions are found for the liquid axial velocity. This may be partially attributed to the simplification of the inlet boundary from small holes with high through-hole velocities on a sintered plate to a square inlet section with lower through-hole velocity. In this case, the liquid circulations are much lowered in the entire bubble column. Also, the underprediction of liquid axial velocity near the wall can be associated with the underestimation of the turbulence dissipation rate at the wall region. It is known that the liquid film drainage of two colliding bubbles are more difficult to be completed under high turbulence dissipation and vice versa. Therefore, the underestimation of turbulence dissipation leads to overprediction of the bubble coalescence rate and hence the number densities of larger bubbles are increased accordingly.

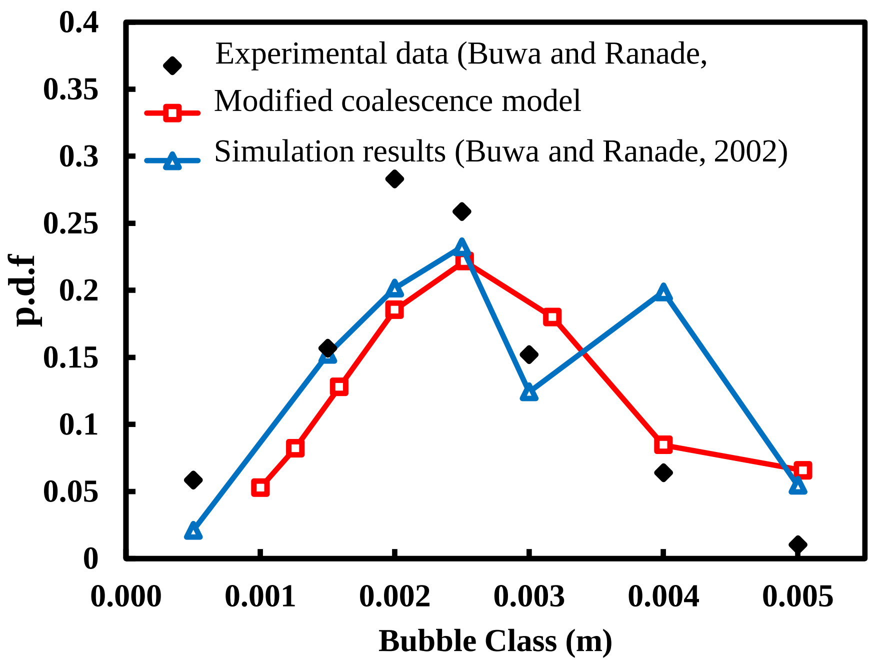

Figure 5-10 Comparison of holdup-based number density distribution of bubble classes.

Figure 5-10 compares holdup-based bubble size distribution predicted by considering the bubble-induced turbulence with the experimental data and the simulation results by Buwa and Ranade (2002). The experimental data and simulation results by Buwa and Ranade were presented in terms of bubble number fraction normalised with the corresponding bubble group width. Therefore, the original data can be easily converted to the holdup-based bubble size distribution. It seems that the simulation results by Buwa and Ranade largely overpredicts the values of p.d.f. for bubble classes larger than the mean bubble diameter at the inlet, while the modified coalescence model with considering the bubble-induced turbulence have successfully prevent this trend. However, some underpredictions are still shown for the number density of the bubble classes smaller than 0.0025 m, which clearly implies that the bubble breakup model also needs to be modified by considering the effects of bubble-induced turbulence.

4. CONCLUDING REMARKS

In the present study, a bubble coalescence model that includes effect of both the shear turbulence and the bubble-induced turbulence has been proposed based on the Prince and Blanch (1990) model. The concluding remarks are as follows:

1. The proposed model takes into account the influence of bubble-induced turbulence on the mean eddy turbulent velocity and hence the approaching velocity of colliding bubbles. The bubble collision under the influence of shear turbulence and the bubble-induced turbulence has been clearly illustrated.

2. The turbulence dissipation rate corresponding to the bubble-induced turbulence in the wake of bubble swarm has been used for estimating the bubble collision time. The model analysis shows a general trend of reduction of the predicted coalescence rate.

3. The CFD simulation results on gas hold-up radial distribution are in good agreements with the experimental data. The gas holdup-based bubble size distribution predicted by the modified bubble coalescence model compared with the experimental data has been improved for larger bubbles when comparing with the results obtained using Prince and Blanch (1990) model.

4. It has also been revealed from the simulation results that the implementation of bubble-induced turbulence into the population balance modelling has the impact on the prediction of bubble coalescence rate while this also affects the estimation of the turbulence dissipation rate in the carrier liquid phase. Thus, considering the effect of bubble-induced turbulence, especially covering its anisotropic feature, is required for the turbulence closure turbulence modelling of bubbly flow in the bubble columns.

References

ANTAL, S. P., LAHEY, R. T. & FLAHERTY, J. E. 1991. Analysis of phase distribution in fully developed laminar bubbly two-phase flow. *International Journal of Multiphase Flow,* 17**,** 635-652.

BHOLE, M. R., JOSHI, J. B. & RAMKRISHNA, D. 2008. CFD simulation of bubble columns incorporating population balance modeling. *Chemical Engineering Science,* 63**,** 2267-2282.

BURNS, A. D., FRANK, T., HAMILL, I. & SHI, J.-M. The Favre Averaged Drag Model for Turbulent Dispersion in Eulerian Multi-Phase Flows. Fifth International Conference on Multiphase Flow, ICMF-2004, 2004 Yokohama, Japan.

BUWA, V. V. & RANADE, V. V. 2002. Dynamics of gas-liquid flow in a rectangular bubble column: experiments and single/multi-group CFD simulations. *Chemical Engineering Science,* 57**,** 4715-4736.

CHEN, P. 2004. *Modeling the fluid dynamics of bubble column flows. Ph.D. Thesis.* Ph.D. Thesis.

CHEN, P., SANYAL, J. & DUDUKOVIC, M. P. 2005. Numerical simulation of bubble columns flows: effect of different breakup and coalescence closures. *Chemical Engineering Science,* 60**,** 1085-1101.

CLIFT, R., GRACE, J. R. & WEBER, M. E. 1978. *Bubbles, Drops, and Particles*, Academic Press.

COLOMBO, M. & FAIRWEATHER, M. 2015. Multiphase turbulence in bubbly flows: RANS simulations. *International Journal of Multiphase Flow,* 77**,** 222-243.

DEEN, N. G., SOLBERG, T. & HJERTAGER, B. H. 2001. Large eddy simulation of the gas-liquid flow in a square cross-sectioned bubble column. *Chemical Engineering Science,* 56**,** 6341-6349.

EKAMBARA, K., NANDAKUMAR, K. & JOSHI, J. B. 2008. CFD Simulation of Bubble Column Reactor Using Population Balance. *Industrial & Engineering Chemistry Research,* 47**,** 8505-8516.

HAGESAETHER, L., JAKOBSEN, H. A., HJARBO, K. & SVENDSEN, H. F. 2000. A coalescence and breakup module for implementation in CFD-codes. *In:* PIERUCCI, S. (ed.) *Computer Aided Chemical Engineering.* Elsevier.

HAGESAETHER, L., JAKOBSEN, H. A. & SVENDSEN, H. F. 2002. A model for turbulent binary breakup of dispersed fluid particles. *Chemical Engineering Science,* 57**,** 3251-3267.

HOSOKAWA, S. & TOMIYAMA, A. 2013. Bubble-induced pseudo turbulence in laminar pipe flows. *International Journal of Heat and Fluid Flow,* 40**,** 97-105.

JOSHI, J. B., NANDAKUMAR, K., EVANS, G. M., PAREEK, V. K., GUMULYA, M. M., SATHE, M. J. & KHANWALE, M. A. 2017. Bubble generated turbulence and direct numerical simulations. *Chemical Engineering Science,* 157**,** 26-75.

KATAOKA, I. & SERIZAWA, A. 1989. Basic equations of turbulence in gas-liquid two-phase flow. *International Journal of Multiphase Flow,* 15**,** 843-855.

KULKARNI, A. A., JOSHI, J. B. & RAMKRISHNA, D. 2004. Determination of bubble size distributions in bubble columns using LDA. *Aiche Journal,* 50**,** 3068-3084.

KULKARNI, A. A., KAMBARA, K. & JOSHI, J. B. 2007. On the development of flow pattern in a bubble column reactor: Experiments and CFD. *Chemical Engineering Science,* 62**,** 1049-1072.

LAMONT, J. C. & SCOTT, D. S. 1970. An eddy cell model of mass transfer into the surface of a turbulent liquid. *AIChE Journal,* 16**,** 513-519.

LANCE, M. & BATAILLE, J. 1991. Turbulence in the Liquid-Phase of a Uniform Bubbly Air Water-Flow. *Journal of Fluid Mechanics,* 222**,** 95-118.

LAUNDER, B. E. 1989. Second‐moment closure and its use in modelling turbulent industrial flows. *International Journal for Numerical Methods in Fluids,* 9**,** 963-985.

LIAO, Y. X., RZEHAK, R., LUCAS, D. & KREPPER, E. 2015. Baseline closure model for dispersed bubbly flow: Bubble coalescence and breakup. *Chemical Engineering Science,* 122**,** 336-349.

LO, S. & ZHANG, D. 2009. *Modelling of Break-Up and Coalescence in Bubbly Two-Phase Flows*.

LOPEZ DE BERTODANO, M., LEE, S. J., LAHEY, J. R. T. & DREW, D. A. 1990. The Prediction of Two-Phase Turbulence and Phase Distribution Phenomena Using a Reynolds Stress Model. *Journal of Fluids Engineering,* 112**,** 107-113.

LUO, H. 1993. *Coalescence, Breakup and Liuqid Circulation in Bubble Column Reactors.* PhD thesis PhD thesis, PhD thesis from the Norwegian Institute of Technology.

LUO, H. & SVENDSEN, H. F. 1996. Theoretical model for drop and bubble breakup in turbulent dispersions. *Aiche Journal,* 42**,** 1225-1233.

MERCADO, J. M., GOMEZ, D. C., VAN GILS, D., SUN, C. & LOHSE, D. 2010. On bubble clustering and energy spectra in pseudo-turbulence. *Journal of Fluid Mechanics,* 650**,** 287-306.

MITRE, J. F., TAKAHASHI, R. S. M., RIBEIRO, C. P. & LAGE, P. L. C. 2010. Analysis of breakage and coalescence models for bubble columns. *Chemical Engineering Science,* 65**,** 6089-6100.

MUKIN, R. V. 2014. Modeling of bubble coalescence and break-up in turbulent bubbly flow. *International Journal of Multiphase Flow,* 62**,** 52-66.

NAOT, D. & RODI, W. 1982. Calculation of secondary currents in channel flow. *Journal of the Hydraulics Division, ASCE,* 108**,** 948-968.

NGUYEN, V. T., SONG, C. H., BAE, B. U. & EUH, D. J. 2013. Modeling of bubble coalescence and break-up considering turbulent suppression phenomena in bubbly two-phase flow. *International Journal of Multiphase Flow,* 54**,** 31-42.

PAN, Y., DUDUKOVIC, M. P. & CHANG, M. 1999. Dynamic simulation of bubbly flow in bubble columns. *Chemical Engineering Science,* 54**,** 2481-2489.

PAREKH, J. & RZEHAK, R. 2018. Euler-Euler multiphase CFD-simulation with full Reynolds stress model and anisotropic bubble-induced turbulence. *International Journal of Multiphase Flow,* 99**,** 231-245.

PFLEGER, D. & BECKER, S. 2001. Modelling and simulation of the dynamic flow behaviour in a bubble column. *Chemical Engineering Science,* 56**,** 1737-1747.

PFLEGER, D., GOMES, S., GILBERT, N. & WAGNER, H. G. 1999. Hydrodynamic simulations of laboratory scale bubble columns fundamental studies of the Eulerian-Eulerian modelling approach. *Chemical Engineering Science,* 54**,** 5091-5099.

POLLI, M., DI STANISLAO, M., BAGATIN, R., ABU BAKR, E. & MASI, M. 2002. Bubble size distribution in the sparger region of bubble columns. *Chemical Engineering Science,* 57**,** 197-205.

PRAKASH, V. N., MERCADO, J. M., VAN WIJNGAARDEN, L., MANCILLA, E., TAGAWA, Y., LOHSE, D. & SUN, C. 2016. Energy spectra in turbulent bubbly flows. *Journal of Fluid Mechanics,* 791**,** 174-190.

PRINCE, M. J. & BLANCH, H. W. 1990. Bubble Coalescence and Break-up in Air-Sparged Bubble-Columns. *Aiche Journal,* 36**,** 1485-1499.

RIBOUX, G., RISSO, F. & LEGENDRE, D. 2010. Experimental characterization of the agitation generated by bubbles rising at high Reynolds number. *Journal of Fluid Mechanics,* 643**,** 509-539.

RISSO, F. 2011. Theoretical model for k(-3) spectra in dispersed multiphase flows. *Physics of Fluids,* 23.

ROGHAIR, I., MERCADO, J. M., ANNALAND, M. V., KUIPERS, H., SUN, C. & LOHSE, D. 2011. Energy spectra and bubble velocity distributions in pseudo-turbulence: Numerical simulations vs. experiments. *International Journal of Multiphase Flow,* 37**,** 1093-1098.

RZEHAK, R. & KREPPER, E. 2013a. CFD modeling of bubble-induced turbulence. *International Journal of Multiphase Flow,* 55**,** 138-155.

RZEHAK, R. & KREPPER, E. 2013b. Closure models for turbulent bubbly flows: A CFD study. *Nuclear Engineering and Design,* 265**,** 701-711.

SATO, Y. & SEKOGUCHI, K. 1975. Liquid velocity distribution in two-phase bubble flow. *International Journal of Multiphase Flow,* 2**,** 79-95.

SHAWKAT, M. E., CHING, C. Y. & SHOUKRI, M. 2007. On the liquid turbulence energy spectra in two-phase bubbly flow in a large diameter vertical pipe. *International Journal of Multiphase Flow,* 33**,** 300-316.

SHINNAR, R. & CHURCH, J. M. 1960. Statistical Theories of Turbulence In ... Predicting Particle Size in Agitated Dispersions. *Industrial and Engineering Chemistry,* 52**,** 253-256.

SIMONIN, O. Eulerian formulation for particle dispersion in turbulent two-phase flows. Proceedings of the Fifth Workshop on Two-Phase Flow Predictions, Erlangen, Germany, 1990.

SUN, X. D., KIM, S., ISHII, M. & BEUS, S. G. 2004. Modeling of bubble coalescence and disintegration in confined upward two-phase flow. *Nuclear Engineering and Design,* 230**,** 3-26.

TOMIYAMA, A. 1998. Struggle with computational bubble dynamics. *Multiphase Science and Technology, Vol 10 Issue 4 1998***,** 369-405.

TROSHKO, A. A. & HASSAN, Y. A. 2001. A two-equation turbulence model of turbulent bubbly flows. *International Journal of Multiphase Flow,* 27**,** 1965-2000.

WANG, T. F., WANG, J. F. & JIN, Y. 2005a. Population balance model for gas-liquid flows: Influence of bubble coalescence and breakup models. *Industrial & Engineering Chemistry Research,* 44**,** 7540-7549.

WANG, T. F., WANG, J. F. & JIN, Y. 2005b. Theoretical prediction of flow regime transition in bubble columns by the population balance model. *Chemical Engineering Science,* 60**,** 6199-6209.

XU, L. J., YUAN, B. R., NI, H. Y. & CHEN, C. X. 2013. Numerical Simulation of Bubble Column Flows in Churn-Turbulent Regime: Comparison of Bubble Size Models. *Industrial & Engineering Chemistry Research,* 52**,** 6794-6802.

YANG, N. & XIAO, Q. 2017. A mesoscale approach for population balance modeling of bubble size distribution in bubble column reactors. *Chemical Engineering Science,* 170**,** 241-250.

YAO, W. & MOREL, C. 2004. Volumetric interfacial area prediction in upward bubbly two-phase flow. *International Journal of Heat and Mass Transfer,* 47**,** 307-328.

CHAPTER 6: EXPERIMENTAL STUDIES ON THE BUBBLE-INDUCED TURBULENCE IN THE BUBBLE COLUMNS

SUMMARY

The simulation results obtained by considering the bubble-induced turbulence in the bubble breakage and coalescence models in the previous chapters have clearly demonstrated that the bubble-induced turbulence due to the rising bubble wakes is significantly different from the homogeneous isotropic single-phase turbulence. Bubble-induced turbulence plays a significant role in affecting the gas-liquid two-phase flow in the bubble columns. However, the fundamental understanding of bubble-induced turbulence is still very limited. A general consensus has not yet been reached especially with regards to the inhomogeneous characteristics of bubble-induced turbulence in both time and space, such as the characterisations of length/time scale, the energy transfer, the energy cascade, and the turbulence dissipation. In order to further understand these features of bubble-induced turbulence, quantitative experimental measurements are vital. Unlike bubbles or particles, there are no fixed shapes for turbulent eddies, which brings great difficulties in experimental studies to understand their particular behaviours. Therefore, the present study of bubble-induced turbulence can only be conducted using statistical tools such as the turbulent kinetic energy spectrum. In this chapter, the power law scaling behaviour of the bubble-induced turbulence on the energy spectrum will be investigated experimentally using Particle Imaging Velocimetry (PIV), high-speed camera and other measurement/data-processing techniques. In addition,

mathematical derivations for the spectrum function of bubble-induced turbulence will be performed based on both the *Kármán-Howarth* equation and dimensional analysis.

1. INTRODUCTION

In general, the turbulence energy spectrum can be approximately divided into an energy-containing range and universal equilibrium range, of which the latter includes an inertial subrange and dissipation range, based on the frequency or wavenumber of turbulent eddies. The turbulent kinetic energy gradually cascades from large eddies to small eddies in sequence. For the inertial subrange, the Kolmogorov -5/3 law, which can be expressed as $E(\kappa) \sim \varepsilon^{2/3}\kappa^{-5/3}$, has already been widely accepted for homogeneous and isotropic turbulence in single-phase flows.

The difference between the turbulence generated due to rising bubbles and homogeneous isotropic shear turbulence was originally illustrated by the pioneering work of Lance and Bataille (1991). They used both hot-wire and laser Doppler anemometry (LDA) in the up-flow through a hydrodynamic tunnel with the grid located upstream for generating the turbulence and injecting the bubbles. They examined the one-dimensional energy spectra of bubble swarm for various void fractions in comparison with a given ratio of turbulent fluctuations of the liquid without bubble introduction to the slip velocity. It was found from the measurements that the Kolmogorov power law scaling of -5/3 was gradually replaced by a slope of approximately -8/3 with the increase of the volume fraction of the gas phase. They attributed the change of slope to the wakes of bubbles, in which eddies produced were dissipated rapidly before the spectral transfer had even taken place. Therefore, based on the spectral energy balance of dissipation and production, they concluded that the exponent of power law scaling was approximately -3, which was close to the value of -8/3 they observed in their experiments.

Major breakthroughs on the study of behaviour of bubble-induced turbulence through the use of well-designed experiments have taken placed in the last decade. Risso *et al.* (2008) analogised the attenuation of wakes in a fixed array of spheres randomly distributed in space to that of bubbles within a homogeneous swarm and have shown that the bubbles' wakes in pseudo-turbulence decay faster than standard turbulent flow with the same energy and integral length scale. Mercado *et al.* (2010) used a phase-sensitive constant-temperature anemometry (CTA) to separate the velocity signals of bubbles from the liquid flow field, and hence re-confirmed the -3 scaling for bubble-induced turbulence that was concluded by Lance and Bataille. Mendez-Diaz *et al.* (2013) employed flying hot-film anemometry to perform measurements with gas fractions up to 6% and confirmed the power density distributions decay with a power of -3. It should be noted that the phase separation concept is vital in understanding the power law scaling behaviour of the bubble-induced turbulence. Otherwise, different results could be determined from the experiments. For example, based on the averaging of signals from both liquid and gas phases, a few experimental studies have reported the -5/3 behaviour for bubble generated pseudo-turbulence, such as Mudde *et al.* (1997) and Cui and Fan (2004). However, as mentioned by Mercado *et al.* (2010), the signals from the bubbles should be separated from the liquid phase signal, and more importantly, the energy spectrum has to be calculated based on individual segments to reflect the liquid fluctuations rather than being calculated based on averaging.

The separation concept also applies to the measurements obtained from Particle Imaging Velocimetry (PIV). For instance, Riboux *et al.* (2010) measured the turbulence energy spectrum in the wake of a bubble swarm using PIV and also confirmed that the power law scaling is very close to -3. In their experiments, one high-speed PIV camera was used to record the velocity information of the liquid phase and another synchronised camera was placed at a perpendicular position to trace the bubble trajectories. By doing so, the exact timing of the bubbles rising away from the fixed measuring window of the main camera could be found so that the measurements can trace the evolution of the bubble trajectories. Although this technique successfully measured the velocities induced at the bubbles rising passage, it only managed to take measurements from the single phase. Also, the measured velocities contained short delays and it was difficult to determine the intensity of the fluctuations in the wakes of individual bubbles compared with that in the swarm. Therefore, it seems that a more typical two-camera PIV system for simultaneous measurements of both the bubbles and the liquid phase in the bubble columns, such as the work by Broder and Sommerfeld (2002) and Poelma *et al.* (2007), is better suited to the purpose of understanding turbulence induced by rising bubbles. The details of the working principle of the simultaneous PIV measurements of both phases have been well documented by Poelma *et al.* (2007). It should be noted that Deen *et al.* (2000) used a two-camera PIV to measure the velocity field in a square bubble column and compared the results with that of a single-camera ensemble-averaged PIV measurement. The results clearly revealed that a proper discrimination of the displacement vectors for both phases was not possible in a single-camera setup, as the velocity difference between the phases is relatively small in bubble columns, even after applying filter functions, making the signals from both phases indistinguishable. Therefore, it should be emphasised that the separation of the signals from two phases is very important as the main concern is to only investigate the statistical characteristics of liquid phase turbulence (under the influence of bubbles). Based on the separation concept, similar PIV measurement results of -3 power law scaling for bubble-induced turbulence energy spectrum have been obtained by Murai *et al.* (2000) and Bouche *et al.* (2014) in both 2-D and 3-D bubble columns.

This chapter will be organised and presented in such a way: Section 2 will present the experimental methods for PIV measurements of the bubble-induced liquid-phase flow in the bubble column, while section 3 will present the results and discussion, focusing on the bubble-induced liquid-phase turbulence energy spectrum and the derivation of its κ^{-3} power law scaling behaviour. Section 4 will present the conclusions drawn from the current study.

2. EXPERIMENTAL METHOD

The testing section is a cylindrical bubble column with an inner diameter of 0.15 m and column height of 1 m. The column wall is made of transparent plexiglass with wall thickness of 0.5 cm. De-ionised water is used as the carrier fluid and the static liquid height is fixed at 0.6 m. The compressed air is pumped through a flowmeter with adjustable flow rate and finally into the gas chamber. The gas chamber is fully filled with 6mm beads so that the jet from the pipeline can be stabilised by being forced to rise through the multiple channels created by the stacking of beads. The gas is sparged into the main column through the gas distributor, which is a perforated plate with 32 holes of 1 mm in diameter in total while they are distributed with 16 evenly spaced each on 2 circles with the diameters of 75 mm and 100 mm, respectively. Since the PIV and high-speed camera are optical measurements, the reflection and refraction of lights in the surrounding environment should be minimised. In order to do so, a transparent square vessel is installed outside the main column with de-ionised water filled in the gap to reduce the effect of the curvature of the bubble column wall. The experimental set-up is illustrated in Figure 6-1.

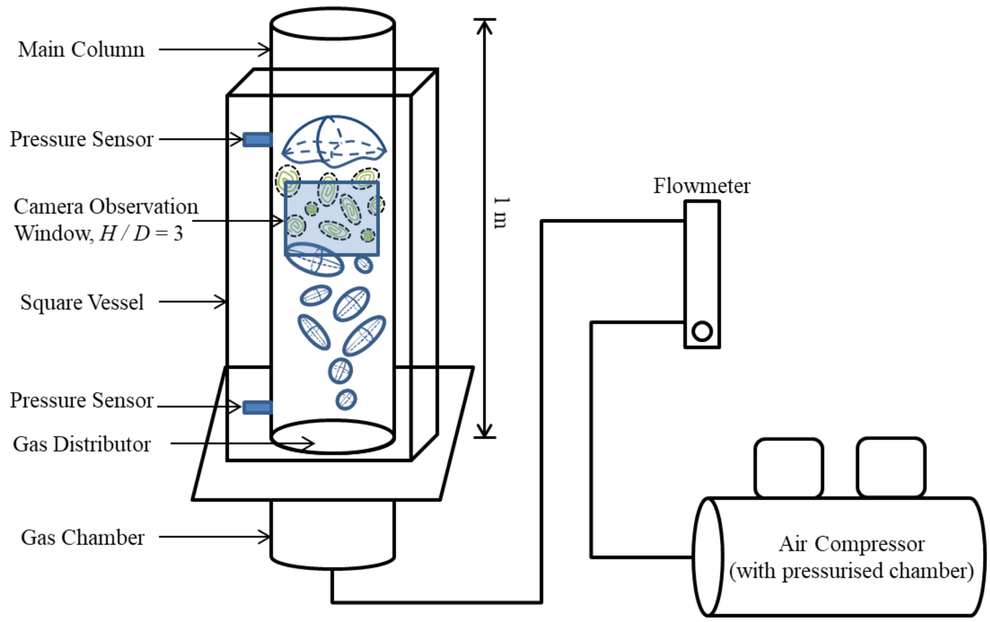

Figure 6-1 Experimental set-up of a 0.15 m diameter bubble column.

The PIV facility used in the experiments in the present study is made by Dantec Dynamics. The optical system consists of two cameras that are focused on the same field of view by using a mirror and a beam splitter plate, as shown in Figure 6-2. A calibration plate of 10 cm × 10 cm is used to calibrate the edges of the images acquired by two cameras. To ensure that the PIV camera only records the liquid phase information, tracer particles containing fluorescent dye and an appropriate cut-off filter are used. Similar approaches have been used in bubbly flow by Deen *et al.* (2000) and Lindken and Merzkirch (2002). The measuring volume is illuminated using a pulsed Nd:YAG laser ((New Wave Gemini, @532nm, 2×30 MJ, light sheet thickness approx. 0.5 mm). The scattered light from the tracer particles is captured by the PIV camera (Hi/Sense CCD camera, 2048 × 2048 pixels, fitted with a Nikon AF 50 mm F/1.8D lens). The strong reflection and scattering light of the dispersed bubbles requires the use of a neutral density filter to avoid over-exposure. As the tracer particles emit light at a higher wavelength than the original wavelength of the laser light source, the fluorescent light can pass through the filter, while the reflections and scattering at the original wavelength will be blocked.

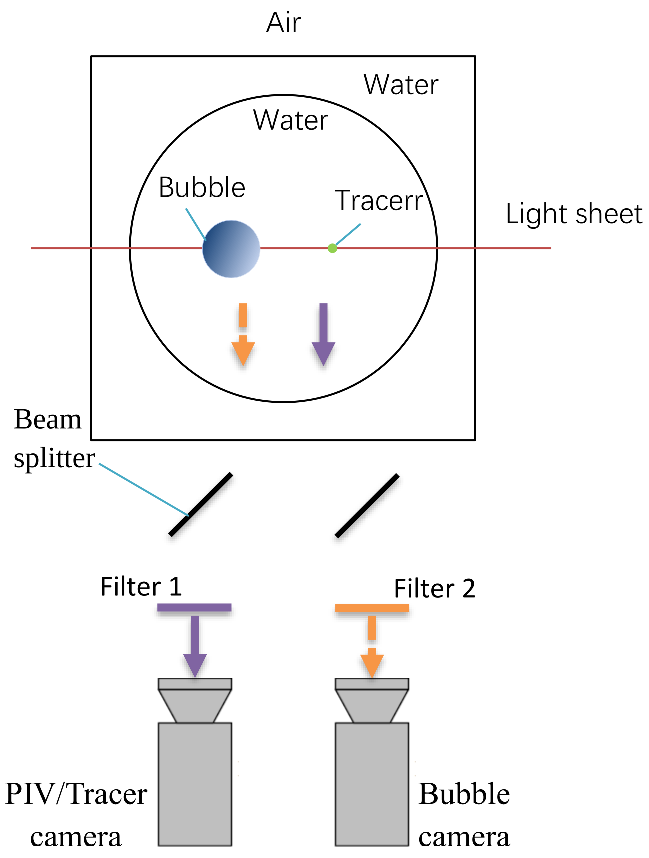

Figure 6-2 Schematic diagram of the simultaneous measurement of the fluid and dispersed phase.

In theory, the PIV camera records a pair of images with a short time delay, depending on the laser pulse delay time and the flow conditions. Although the PIV camera used in the present study can only capture image pairs at a relatively low frequency, the velocity vectors in the observing window at each specific point in time can still be obtained. It should be noted that the working principle of obtaining the turbulence energy spectrum from the PIV measurements is different from using LDV. For the experiments using LDV, the velocity signals are recorded in time series at a fixed point in space and hence the one-dimensional frequency spectrum can be directly obtained. As the Taylor hypothesis of "frozen turbulence" states that the spatial correlations can be approximated by the temporal correlations when the fluctuation velocity is much smaller than the mean velocity, the frequency spectrum can be turned into a wavenumber spectrum. However, a complete frequency spectrum cannot be obtained due to the limitation of the maximum frequency of the CCD camera used in the present study, as the information at frequencies higher than 5 Hz is simply lost. Therefore, an similar approach to the experiments by Riboux *et al.* (2010) has been used in the present study, which focuses on the direct acquisition of the wavelength spectrum in the wake of bubble swarm. It is assumed that the "frozen turbulence" still holds for the turbulence induced by swarm of bubbles. In this case, the velocity spatial fluctuations along the rising passage of the swarm of bubbles are approximately the same as the velocity fluctuations in time at each axial location. Therefore, the turbulence energy spectrum can be obtained from the measurements of the local liquid velocity at any fixed time. In PIV measurements, the local velocity is estimated from the displacement of tracer particles in each small segment of the entire image. The integration area used in the present study is fixed at 16 × 16 pixels with an overlap of 50%. For each image pair, the velocity vectors are computed by adaptive-correlating the interrogation areas, which subsequently determine the location of the displacement peak in the correlation field. The further processing of velocity data to plot the turbulence energy spectrum is shown in the results and discussion section.

As emphasised in the introduction, the important concept of separating the dispersed phase signals from the continuous phase velocity field is also applied in the present study. A high-speed camera is used for tracing the motion of the rising bubbles. The length and width of the measuring window are calibrated by placing a ruler at the front wall and the back wall of the square vessel. For the convenience of image processing, the size of view of the high-speed camera is adjusted to be slightly larger than that of the PIV camera in the present study. The recording rate is set to be 1000 frame-per-second (FPS), which makes the frequency two orders higher than the PIV camera. A pulsed light source is used for the illumination of image recording by the high-speed camera, while the interference on the over-exposure of the PIV camera can be avoided. The recorded images are processed by using the digital image analysis (DIA) technique developed based on the procedures proposed by Lau *et al.* (2013). The centre and axis length of bubbles are captured in the DIA processed images. Therefore, the exact timing that the bubbles rise away from the field of view and the approximate size of bubbles that corresponds to the generation of turbulent eddies can be detected. By doing so, the measured velocity field induced by bubbles or bubble swarm that just rise away can be used for the spectrum analysis without overlapping of the bubbles' velocity signals. This technique of measuring the liquid velocity field right in the wake of bubbles has been successfully used by Riboux *et al.* (2010) in turbulent bubbly flow.

3. RESULTS AND DISCUSSION

The digital image analysis technique is developed based on the procedures proposed by Lau *et al.* (2013). However, as the number density of the dispersed bubbles is quite low, only three main operations performed in the present study have shown satisfactory results. These three operations are image filtering, watershed transform and combination, as shown in Figure 6-3.

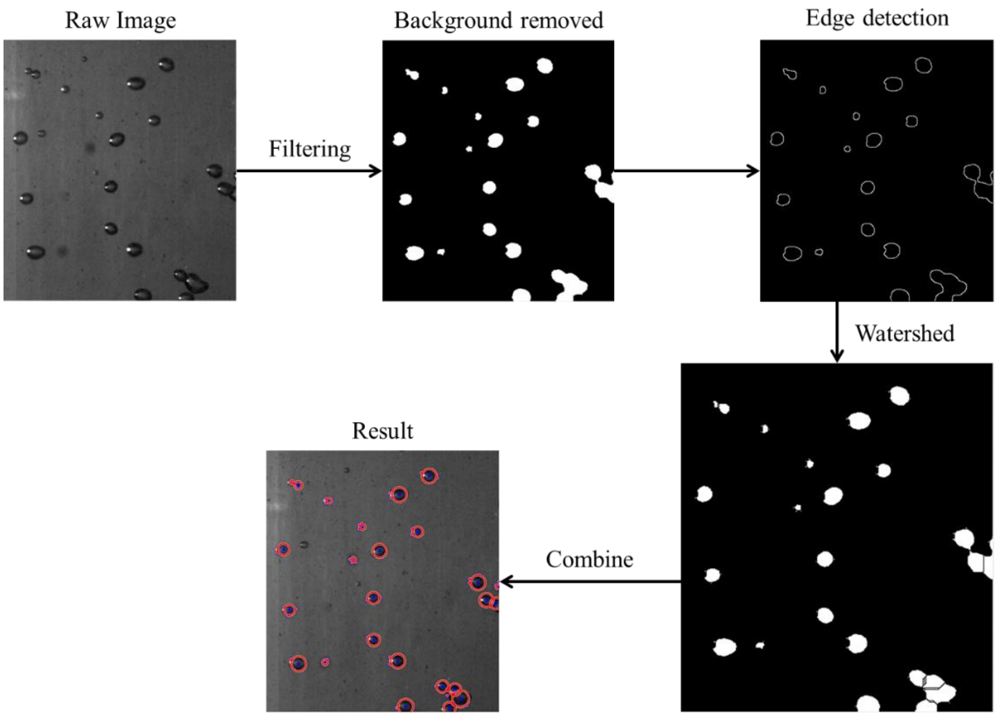

Figure 6-3 Image processing sequences to detect bubbles.

The raw images are firstly passed through a number of filters to remove the background noise. Since the background illumination is not uniformly distributed, it is necessary to correct the original image (I_0) using local thresholding. By assuming that the background illumination is homogeneous in local areas of the original image, I_0 is divided in blocks (16 mm × 16 mm) and each block is independently thresholded by employing the filter function proposed by Otsu (1979).

$$I_{local\ threshold} = \begin{cases} 0 & if\ I_0(i,j) > I_{Otsu} \\ 1 & if\ I_0(i,j) > I_{Otsu} \end{cases} \quad (6\text{-}1)$$

where I_{Otsu} is the automatic threshold level. The local threshold image is then subtracted from the original image to yield image without background. Some bubbles that are not in the plane of focus will be filtered in this step. It is noted that some pixels on the edge of bubbles may be mistakenly filtered out, which results in the disconnection of the edge of bubbles. The disconnection of the edges will lead to further errors when the edge detection algorithm is applied. Therefore, mathematical morphology operations of dilation and erosion are used to reconnect the edges and make sure that the bubbles are represented by sealed circles or ellipses. Whenever necessary, the filtered image can be easily converted to a binary image using an appropriate threshold value chosen from the histogram of the image grey scales.

The edges of the bubble objects in the filtered image can be highlighted by using an edge detection algorithm proposed by Canny (1986). The detected edges are used for both enhancing the distinction between bubbles and background and the application of the watershed transform. For individual bubbles, bubble properties such as the centre and the equivalent diameter are easily captured by the recognition algorithm. However, distinguishing between overlapping bubbles seems to be difficult and the separation of these overlapping bubbles is required. The watershed transform algorithm is a region-based segmentation method proposed by Meyer (1994). It can be explained by considering the analogy with a water flooding process on a grey scale image. The water level keeps rising from two local minima till a dam/dividing line is found such that the bubbles can be divided into each other. The working principle of watershed transform has been clearly illustrated by Lau *et al.* (2013). However, a typical error of the watershed transform is that it sometimes over-divides the overlapping bubbles when the detected edge contains multiple minima. For example, it can be seen from Figure 6-3 that the bubble with a slight necking located at the right-down corner of the raw image has been treated as the overlapping bubbles divided by an edge in the watershed image because the bubble surface keeps oscillating under the influence of surrounding eddies. The watershed algorithm mistakenly divides this bubble into two bubbles. Although this kind of error cannot be avoided, the total area is kept consistent while the separated bubbles are individually represented by circular/ellipsoidal shapes. Therefore, the gas holdup can be determined by calculating the ratio of area occupied by bubbles and the total area.

Various kinds of error will take place during the entire image analysis process. These errors come from the non-uniform lighting, image distortion, filtering, bubble separation, recognition, and approximating the fractional area as volumetric holdup. Although it is difficult to calculate the errors from each step, the overall error can still be found. In order to do so, multiple groups of image series with time interval of 1 second have been processed to calculate the averaged gas holdup. The result of computed overall gas holdup shows that the relative error is within 10% from the total gas holdup measurements by using pressure sensors, which means that the image processing techniques used in the present study is quite reliable.

By analysing the images captured by the high-speed camera, the exact timing of the bubbles just rising away from the field of view and the equivalent bubble diameter that correspond to the generation of bubble-induced turbulence can be found. Therefore, at approximately the same time (with short delays due to the low frequency of the PIV camera), the image captured by the PIV camera is believed to contain the information of liquid phase turbulence that is mainly generated due to the bubbles just rise away. The velocity vectors can be found by finding the displacements of the fluorescent tracer particles between a pair of images. In order to determine the energy spectra on the main direction of bubbles motion, the velocity components and velocity fluctuations in the vertical direction decomposed from the velocity vectors are shown in Figure 6-4.

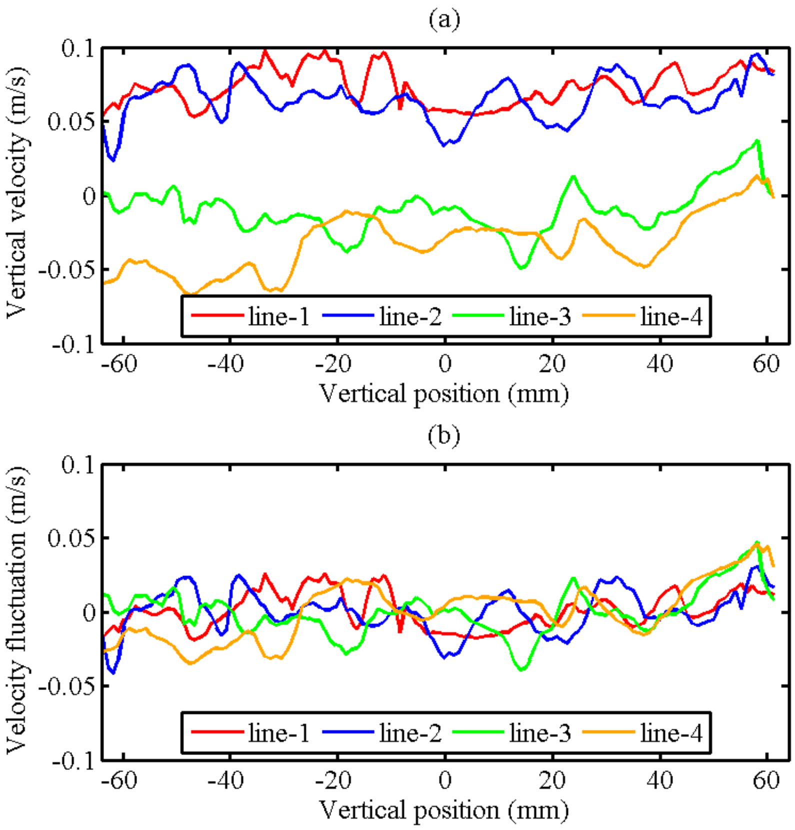

Figure 6-4 (a) Vertical liquid velocity and (b) velocity fluctuation at different radial positions.

As shown in Figure 6-4, polylines represent the vertical velocity components and fluctuations of the liquid phase at different horizontal positions on the PIV image. The centre of the image is allocated at the height of H / D = 3. The size of the image is approximately 128 mm × 128 mm, which leads to approximately 1mm size for each interrogation cell. The horizontal positions for line-1 to line-4 are selected as 26 mm, 55 mm, 74 mm and 95 mm from the left edge of the present PIV image, according to the existence of the preceding bubbles that just rise away from the measurement window. The velocity fluctuations are calculated by subtracting the mean of each data set from the vertical velocities, such as $u'_z = u_z - \overline{U}_z$. The fluctuation is slightly higher at the top of the measurement window, which is closer to the rear of the bubbles or bubble swarm. The autocorrelation function in vertical direction can be defined as

$$f(z) = \frac{\overline{(u\prime_z)_A(u\prime_z)_B}}{\tilde{u}_z^2}, \tag{6-2}$$

where A and B refer to two points in the vertical column and the turbulence intensity $\tilde{u}_z$ can be defined as

$$\tilde{u}_z = \sqrt{\overline{u}'^2_z}. \tag{6-3}$$

When two points A and B are very close to each other, they can be considered to be under the influence of the same turbulent eddy. In this case, the velocity fluctuations are closely related, and the value of autocorrelation approximately equals to 1. With the increase of the distance between these two points, they might under the influence of different turbulent eddies. Therefore, it is expected that the correlation of velocity fluctuations is gradually diminished, and the values of autocorrelation function approach to 0. To demonstrate this trend clearly, the autocorrelation of line-2 is presented in Figure 6-5. It is noted that the curve has been cut-off at 64 mm away from the starting point. This is limited by the size of PIV measurement window, which leads to the loss of information in low wavenumber region ($\kappa = 2\pi / \lambda$) on the energy spectrum. However, this information loss may not be so important as the power law scaling behaviour has mainly taken place within the inertia subrange, while the low wavenumber region may have already been very close to the energy containing range. Taking all these considerations into account, the spatial spectra of the vertical velocity S_{zz} can be calculated using a fast Fourier transform (FFT) of the autocorrelation for each vertical column of the two-dimensional PIV velocity measurements. The one-dimensional energy spectra in the wake of bubbles are presented in Figure 6-6.

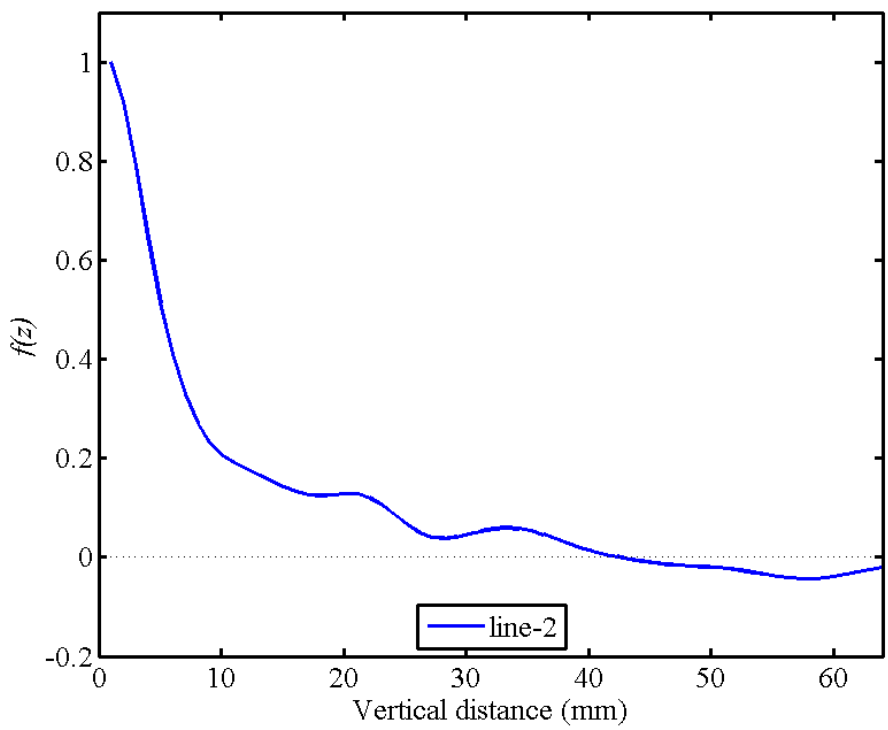

Figure 6-5 Autocorrelation function in vertical direction.

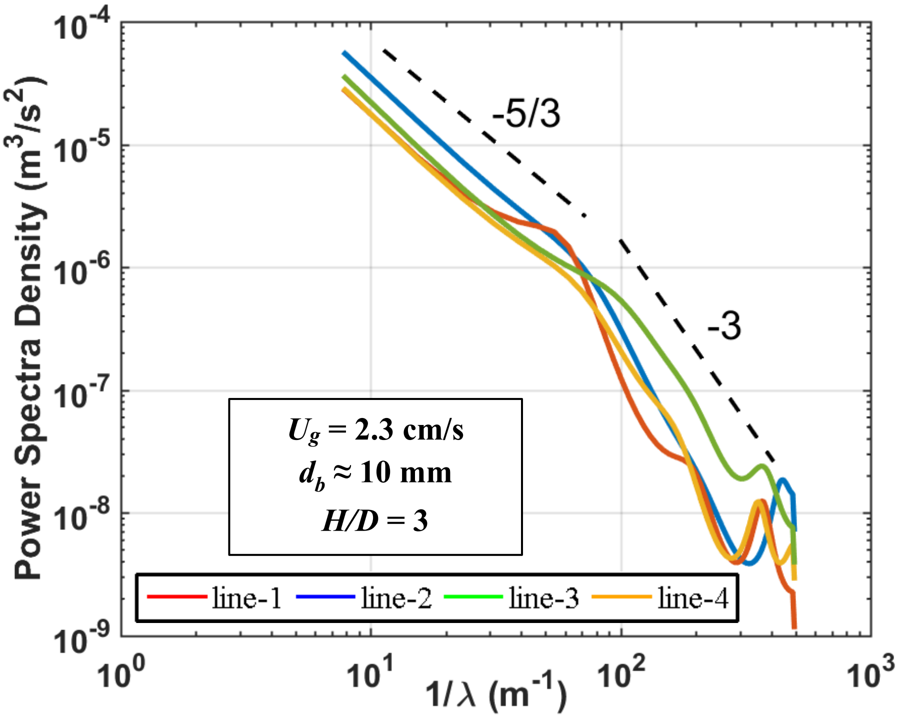

Figure 6-6 One-dimensional energy spectra in the wake of bubbles.

It can be clearly seen from Figure 6-6 that a slope of -3 can be found for all selected vertical columns in the wake of bubbles. This trend agrees with the experimental results of Mercado *et al.* (2010), Mendez-Diaz *et al.* (2013), Riboux *et al.* (2010), and Prakash *et al.* (2016). The experimental results clearly show that the bubble-induced turbulence indeed exists, and its power law scaling behaviour is totally different from the homogeneous isotropic single-phase turbulence. It can also be found that the characteristic length scale that corresponds to the slope -3 scaling is approximately the same as the size of bubbles that generate the wake. As shown by Risso (2011) and Riboux *et al.* (2013), this length scale that corresponds to the slope -3 scaling can be approximated as $\Lambda \sim d_b / C_D$, where C_D is the bubble drag coefficient. This implicitly states that the characteristic length scale is also affected by the shape factor of the preceding bubbles. For turbulent eddies with wavelength much larger than the characteristic length scale, the slope of -5/3 is still observed. This indicates that the shear turbulence and bubble-induced turbulence both exists in bubble column turbulent bubbly flows. However, the influence of bubbles is only on the turbulent eddies that are approximately the same size or smaller than the size of bubbles.

Although the existence of bubble-induced κ^{-3} power law scaling behaviour has been confirmed by the experimental results reported in the literature and results obtained in the present study, the theoretical derivation of exact expression of the bubble-induced turbulence energy spectrum function has rarely been documented. Of particular relevance is the work by Risso (2011) that analogies the signal of bubbles as localised random bursts and shows that the collective effect of each individual burst can exhibit an intermediate subrange evolving as κ^{-3} scaling. However, this result was derived using rather complicated numerical methods. Therefore, the mathematical derivation of the bubble-induced turbulence energy spectrum function by using dimensional analysis techniques is shown in the present study. Approach 1 follows the same approach presented by Kolmogorov to obtain the -5/3 law or also known as K41 theory (Kolmogoroff, 1941, Kolmogorov, 1991), Approach 2 employs the Taylor's expansion on the second-order velocity structure function, and Approach 3 starts from the *Kármán-Howarth* equation on the basis of the pioneering work by Lance and Bataille (1991).

Approach 1

For the second-order structure function of velocity fluctuations, it is associated with the turbulence dissipation rate ε and the characteristic length scale l for shear turbulence, such as

$$\overline{[\vec{u}(r+\Delta r)-\vec{u}(r)]^2} \sim (\varepsilon \cdot l)^{2/3} \quad . \tag{6-4}$$

It is easy to find that the dimensions for second-order structure function should be m^2/s^2. Therefore, the same dimensions apply to the bubble-induced turbulence. It is believed that the work done by rising bubbles gU_r (m^2/s^3), the kinematic viscosity ν (m^2/s) that is closely associated with the dissipation of turbulence, and the length scale l (m) are key parameters that relate to the second-order term of velocity fluctuations for bubble-induced turbulence. Assuming the combinations of these parameters are

$$(\Delta u)^2 \sim (gU_r)^a \cdot \nu^b \cdot l^c, \tag{6-5}$$

which suggests that $(\mathrm{m}^2/\mathrm{s}^3)^a(\mathrm{m}^2/\mathrm{s})^b\mathrm{m}^c = \mathrm{m}^2/\mathrm{s}^2$. By balancing the exponents of m and s,

$$\begin{cases} m: 2a+2b+c=2 \\ s: -3a-b=-2 \end{cases} \tag{6-6}$$

It is easy to find a solution: a = 1, b = -1, c = 2. According to Buckingham's π theorem in dimensional analysis, there should be two solutions for four meaningful physical variables (Δu, gU_r, ν, and l) and two basic physical dimensions (m and s) involved. Therefore, the other solution gives a = 2/3, b = 0, c = 2/3, which is equivalent to the combination of shear turbulence due to the work done by bubbles gU_r has the same dimensions as the turbulence dissipation ε. Considering that the shear turbulence and bubble-induced turbulence both existed in the turbulent bubbly flow, the second-order structure function of velocity fluctuations may be the combination of both expressions, such as

$$\overline{[\vec{u}(r+\Delta r)-\vec{u}(r)]^2} \sim (1-\alpha)(\varepsilon \cdot l)^{2/3} + \alpha \frac{gU_r}{\nu} \cdot l_d^2. \qquad (6\text{-}7)$$

In general, it is reasonable to assume that the spectrum function takes the form of a power function with negative exponent, due to its fast decreasing trend with increasing wavenumber, such as $E(\kappa) \sim \kappa^{-n}$.

According to definition, the integral of spectrum function is associated with the turbulent kinetic energy, such as

$$\frac{1}{2}\overline{u'^2} \sim \int_0^\infty E(\kappa)d\kappa \sim \int_0^\infty \kappa^{-n} d\kappa = -\frac{1}{1-n}\kappa^{-n+1} = C \cdot E(\kappa) \cdot \kappa. \qquad (6\text{-}8)$$

Let $C\kappa E(\kappa) = (1-\alpha)\varepsilon^{2/3}\kappa^{-2/3} + \alpha \frac{gU_r}{\nu} \cdot \kappa_d^{-2}$, which gives

$$E(\kappa) = C_\kappa (1-\alpha)\varepsilon^{2/3}\kappa^{-5/3} + C_b \alpha \frac{gU_r}{\nu} \cdot \kappa_d^{-2} \cdot \kappa^{-1} \ . \qquad (6\text{-}9)$$

When the wavenumber is within the range that corresponds to bubble-induced turbulence, such as $\kappa = \kappa_d$, the spectrum function only for bubble-induced turbulence can be written as

$$E(\kappa)_{BIT} = C_b \alpha \frac{gU_r}{\nu} \kappa^{-3}. \qquad (6\text{-}10)$$

Approach 2

Furthermore, if the second-order structure function can be expanded using Taylor's expansion, such as

$$\overline{[\vec{u}(r+\Delta r)-\vec{u}(r)]^2} = \left(\frac{\partial \overline{\vec{u}'}}{\partial r}\right)^2 \Delta r^2 + O^4 \qquad (6\text{-}11)$$

where O^4 represents cut-off terms whose orders are higher than 4. Although it seems that the bubble-induced turbulence is anisotropic, local homogeneity within each small segment of the bubbles ringing passage may still be assumed in the bubble columns. Under this consideration, the manipulation of using Taylor's expansion in all directions should be valid.

According to the definition, the turbulence dissipation rate can be written as

$$\varepsilon = \nu \overline{\frac{\partial u_i'}{\partial x_j} \frac{\partial u_j'}{\partial x_i}} \ . \tag{6-12}$$

If one-dimension is concerned, it is reasonable to assume that $\frac{\partial u_i'}{\partial x_j}$ is approximately the same order of magnitude as $\frac{\partial u_j'}{\partial x_i}$. Until this step, it seems that the isotropic feature may not be so important as it is the only consideration based on the magnitude of velocity fluctuations. Therefore, the turbulence dissipation rate can be approximately written as

$$\varepsilon \sim \nu \left(\frac{\partial \overline{\vec{u}'}}{\partial r}\right)^2 \tag{6-13}$$

which gives $\left(\frac{\partial \overline{\vec{u}'}}{\partial r}\right)^2 \sim \left(\frac{\varepsilon}{\nu}\right)$. Hence, Equation (6-11) becomes

$$\overline{[\vec{u}(r + \Delta r) - \vec{u}(r)]^2} \sim \left(\frac{\varepsilon}{\nu}\right) \cdot \Delta r^2. \tag{6-14}$$

As the turbulence dissipation has the same dimensions as the work done by rising bubbles such as $\varepsilon \sim gU_r$, and the short distance Δr between two points can be represented by the characteristic length scale l_d for the wake of bubbles, the second-order structure function for bubble-induced turbulence can be expressed as

$$\overline{[\vec{u}(r + \Delta r) - \vec{u}(r)]^2} \sim \left(\frac{gU_r}{\nu}\right) \cdot l_d^2. \tag{6-15}$$

Approach 3

If starting from the *Kármán-Howarth* equation, as suggested by Pope (2000), the spectral energy balance at high wavenumbers can be written as

$$\frac{\partial}{\partial t} E(\kappa) + 2\nu\kappa^2 E(\kappa) = \frac{\partial}{\partial \kappa} T(\kappa, t) + \Pi(\kappa, t) \tag{6-16}$$

where $E(\kappa)$ is the turbulence energy spectrum, $2\nu\kappa^2 E(\kappa)$ is the dissipation term,

T is the spectral energy transfer and Π is the production term associated with bubble wakes. From a dimensional analysis perspective, the dimensions for the dissipation term $2\nu\kappa^2 E(\kappa)$ would be $\frac{m^2}{s} \cdot m^{-2} \cdot \frac{m^3}{s^2} = m^3/s^3$. Therefore, the same dimensions apply to the production term. If the production spectrum Π is assumed to be local in the spectral space, it can be assumed to be a combination of the wavenumber and the energy dissipation rate in the bubble wakes ε_w, which leads to the estimation of $\Pi \approx \kappa^{-1}\varepsilon_w$. It is also noted that the dissipation in the bubble wakes should have the same dimensions as the work input by bubbles, such as $\varepsilon_w \sim gU_r$. Recalling that the main concern is at high wavenumbers, especially within the inertia subrange, the change in the spectral transfer is almost negligible, which has been illustrated by Pope (2000). In a steady state, Equation (6-16) can be further interpreted as the rapid dissipation of bubble-induced turbulence due to viscosity is approximately equivalent to the production of energy in the bubble wakes, such as

$$2\nu\kappa^2 E(\kappa) \sim \kappa^{-1} g U_r \tag{6-17}$$

which gives a crude relation of the turbulence energy spectrum

$$E(\kappa) \sim \frac{\alpha g U_r}{\nu\kappa^3} \tag{6-18}$$

where the volume fraction α represents the time averaged state of existence of the bubble wakes. The results obtained from this approach agree with the conclusions drawn by Prakash *et al.* (2016), which made the analysis on the basis of Fourier transform. However, it is noted that different interpretations on the *Kármán-Howarth* equation have been made and the dimensional analysis technique has been considered in the present study.

4. CONCLUSIONS

Experimental measurements on the velocity field in the wakes of bubbles have been performed by using a combination of PIV and high-speed camera. The following concluding remarks can be drawn from the present study:

1. The experimental data has been processed using digital image analysis techniques and codes have been developed to obtain the energy spectrum for the bubble-induced turbulence.
2. The experimental results are consistent with previous results reported in literature and re-confirms the existence of the κ^{-3} power law scaling range in the wakes of bubbles.
3. Mathematical derivations for the spectrum function of bubble-induced turbulence have been performed in three different ways including dimensional analysis, Taylor's expansion on the second order structure function and applying the *Kármán-Howarth* equation. The theoretical analyses clearly demonstrate that the scaling exponent for bubble-induced turbulence has to be -3 to the wavenumber κ of turbulent eddies generated in the bubble wakes.

Reference

BOUCHE, E., ROIG, V., RISSO, F. & BILLET, A. M. 2014. Homogeneous swarm of high-Reynolds-number bubbles rising within a thin gap. Part 2. Liquid dynamics. *Journal of Fluid Mechanics,* 758**,** 508-521.

BRODER, D. & SOMMERFELD, M. 2002. An advanced LIF-PLV system for analysing the hydrodynamics in a laboratory bubble column at higher void fractions. *Experiments in Fluids,* 33**,** 826-837.

CANNY, J. 1986. A Computational Approach to Edge Detection. *IEEE Transactions on Pattern Analysis and Machine Intelligence,* PAMI-8**,** 679-698.

CUI, Z. & FAN, L. S. 2004. Turbulence energy distributions in bubbling gas-liquid and gas-liquid-solid flow systems. *Chemical Engineering Science,* 59**,** 1755-1766.

DEEN, N., HJERTAGER, B. & SOLBERG, T. 2000. *Comparison of PIV and LDA Measurement Methods Applied to the Gas-Liquid Flow in a Bubble Column*.

KOLMOGOROFF, A. 1941. The local structure of turbulence in incompressible viscous fluid for very large Reynolds numbers. *Comptes Rendus De L Academie Des Sciences De L Urss,* 30**,** 301-305.

KOLMOGOROV, A. N. 1991. The Local-Structure of Turbulence in Incompressible Viscous-Fluid for Very Large Reynolds-Numbers. *Proceedings of the Royal Society of London Series a-Mathematical Physical and Engineering Sciences,* 434**,** 9-13.

LANCE, M. & BATAILLE, J. 1991. Turbulence in the Liquid-Phase of a Uniform Bubbly Air Water-Flow. *Journal of Fluid Mechanics,* 222**,** 95-118.

LAU, Y. M., DEEN, N. G. & KUIPERS, J. A. M. 2013. Development of an image measurement technique for size distribution in dense bubbly flows. *Chemical Engineering Science,* 94**,** 20-29.

LINDKEN, R. & MERZKIRCH, W. 2002. A novel PIV technique for measurements in multiphase flows and its application to two-phase bubbly flows. *Experiments in Fluids,* 33**,** 814-825.

MENDEZ-DIAZ, S., SERRANO-GARCIA, J. C., ZENIT, R. & HERNANDEZ-CORDERO, J. A. 2013. Power spectral distributions of pseudo-turbulent bubbly flows. *Physics of Fluids,* 25.

MERCADO, J. M., GOMEZ, D. C., VAN GILS, D., SUN, C. & LOHSE, D. 2010. On bubble clustering and energy spectra in pseudo-turbulence. *Journal of Fluid Mechanics,* 650**,** 287-306.

MEYER, F. 1994. Topographic Distance and Watershed Lines. *Signal Processing,* 38**,** 113-125.

MUDDE, R. F., GROEN, J. S. & VANDENAKKER, H. E. A. 1997. Liquid velocity field in a bubble column: LDA experiments. *Chemical Engineering Science,* 52**,** 4217-4224.

MURAI, Y., SONG, X. Q., TAKAGI, T., ISHIKAWA, M., YAMAMOTO, F. & OHTA, J. 2000. Inverse energy cascade structure of turbulence in a bubbly flow (PIV measurement and results). *Jsme International Journal Series B-Fluids and Thermal Engineering,* 43**,** 188-196.

OTSU, N. 1979. A Threshold Selection Method from Gray-Level Histograms. *IEEE Transactions on Systems, Man, and Cybernetics,* 9**,** 62-66.

POELMA, C., WESTERWEEL, J. & OOMS, G. 2007. Particle-fluid interactions in grid-generated turbulence. *Journal of Fluid Mechanics,* 589**,** 315-351.

POPE, S. B. 2000. *Turbulent Flows,* Cambridge, Cambridge University Press.

PRAKASH, V. N., MERCADO, J. M., VAN WIJNGAARDEN, L., MANCILLA, E., TAGAWA, Y., LOHSE, D. & SUN, C. 2016. Energy spectra in turbulent bubbly flows. *Journal of Fluid Mechanics,* 791**,** 174-190.

RIBOUX, G., LEGENDRE, D. & RISSO, F. 2013. A model of bubble-induced turbulence based on large-scale wake interactions. *Journal of Fluid Mechanics,* 719**,** 362-387.

RIBOUX, G., RISSO, F. & LEGENDRE, D. 2010. Experimental characterization of the agitation generated by bubbles rising at high Reynolds number. *Journal of Fluid Mechanics,* 643**,** 509-539.

RISSO, F. 2011. Theoretical model for k(-3) spectra in dispersed multiphase flows. *Physics of Fluids,* 23.

RISSO, F., ROIG, V., AMOURA, Z., RIBOUX, G. & BILLET, A. M. 2008. Wake attenuation in large Reynolds number dispersed two-phase flows. *Philosophical Transactions of the Royal Society a-Mathematical Physical and Engineering Sciences,* 366**,** 2177-2190.

CHAPTER 7: RECAPITULATION AND RECOMMENDATIONS

1. NUMERICAL MODELLING OF BUBBLE COLUMN REACTORS

The aims of this PhD project are to investigate the interactions of the deformable rising bubbles and their surrounding eddies in turbulent bubbly flows by using numerical modelling. Several models have been proposed and successfully implanted into CFD simulations to address the effects of inlet conditions, bubble deformations, and κ^{-3} power law scaling of turbulence energy spectrum due to bubble-induced turbulence on the predictions of important parameters for design and scale-up of bubble column reactors. The parameters studied include but not limited to the gas holdup and liquid axial velocity, the bubble coalescence and breakage rate, and turbulence kinetic energy and dissipation rate. A CFD-PBM approach has been applied for exploring the effects of various shapes of bubbles during the bubble breakup process. The same approach has been subsequently applied to systematically evaluate the effects of bubble-induced turbulence and its κ^{-3} power law scaling behaviour on the models of bubble breakage and coalescence, respectively. In addition, the experimental study on the spatial fluctuations of liquid axial velocity in the wake of bubbles and the analysis based on the experimental results have validated the theoretical basis for the numerical simulations, i.e. the existence of the κ^{-3} power law scaling is responsible for the bubble-induced turbulence in the range of small wavelength but this may also include inertia subrange on the turbulence energy spectrum. The main accomplishments of this project can be summarised as:

(1) Numerical simulations of the large-scale bubble columns were successfully conducted with consideration of the effect of the gas velocity profiles at the inlet boundary. The influence of gas inlet conditions including uniform inlet, the kinetic inlet model, and real distributor holes have been examined while the simulation results are in general agreement with the experimental data when using kinetic inlet model and the real distributor holes.

(2) The shapes of bubbles are classified into spherical, ellipsoidal, and spherical-capped. The aspect ratio of the ellipsoidal bubbles has been correlated based on a number of experimental measurements reported in the open literature. The new correlation suggests that the aspect ratio is mainly affected by the buoyancy, surface tension and viscosity. The increase in surface energy has been significantly altered when the bubble shapes are explicitly considered in the breakage kernel. The pressure-energy controlled breakage has been introduced in competition with the surface-energy controlled breakage.

(3) The effects of bubble-induced turbulence have been included in the expressions of the turbulence energy spectrum function, the mean turbulent eddy velocity, and the number density of the bombarding eddies. The modified breakage kernel has been successfully implemented into the CFD simulations and the predicted bubble breakage rate has been greatly enhanced.

(4) The effects of bubble-induced turbulence have been considered in the bubble coalescence model by modifying the approaching velocities of two colliding bubbles. Since both the bubble breakage and coalescence

model are significantly affected by the turbulence dissipation rate calculated by the turbulence model, the turbulence generation due to bubble-induced turbulence has been added to the turbulence model by using the source terms.

(5) The experiments on the one-dimensional spectra in the wake of bubbles have been performed by using the combination of Particle Imaging Velocimetry and digital image analysis based on the high-speed imaging. The dimensional analysis and interpretation for bubble-induced turbulence that exhibits a κ^{-3} scaling law in terms of the experiments have been presented based on the turbulence dissipation rate and characteristic length that reflects the feature of bubble wake induced turbulence.

The specific realisations of the above claims are described in detail in the following section.

2. Specific Realisations

A kinetic inlet model was proposed in Chapter 2 to approximate the effects caused by flow conditions and distributor geometries, and validated by the experiments in literature for the three bubble columns with diameters of 0.138 m, 0.44 m or 0.6 m. The simulation demonstrates that the uniform inlet boundary condition is inadequate in the prediction of both total and local gas holdup, in particular for higher gas flow rates, when the non-drag forces are not included in the simulation. The implementation of the new inlet model is able to achieve the same level of simulation accuracy as the case which the complete geometry of gas distributors including the distributed holes is modelled. This is because the new inlet model can reasonably allocate the momentum onto the cross-section by the distribution functions proposed, and the effects of real geometries of distributors are considered as the parameters in the new inlet model. The new model is suitable for the simulation of both lab-scale and large size bubble column reactors, and able to reasonably predict the gas holdup profiles for different superficial gas velocities when the DBS drag model is used. The number of mesh cells can be reduced by approximately 10 times compared to the case that the complete geometry of the distributor is modelled, very much beneficial to the simulation of industrial scale reactors.

An improved breakup model has been proposed based on the model for drop and bubble presented by Luo and Svendsen (1996). The improved breakup model has taken into account the variation of bubble shapes, in which the bubbles are classified into spherical, deformed ellipsoid and spherical-cap, in the bubble columns. A correlation on the aspect ratio of deformed ellipsoid bubbles, which considers the joint effect of buoyancy, viscosity and surface tension, has been proposed based on the experimental data of air-water systems for the bubble columns. The pressure-energy controlled breakup coupled with the modified breakage criteria has been considered in the modelling. The difference between the surface energy and pressure energy requirements for forming various daughter bubbles has been illustrated. The energy density constraint has been applied to prevent the over-estimation of the breakage rate of small bubbles. The simulation results have shown an overall agreement with the experimental data reported in the open literature.

The effect of bubble-induced turbulence on the bubble breakage rate and bubble size distribution has been considered for modelling bubble column flows in Chapter 4. The contributions to the bubble breakage due to eddy turbulent kinetic energy using κ^{-3} scaling caused by bubble-induced turbulence and the Kolmogorov -5/3 law on the turbulence energy spectrum has been reflected in the proposed bubble breakage model. The bubble breakage model has been modified by taking into account the bubble-induced turbulence and related parameters such as the number density of bombarding eddies, the mean turbulent velocity of eddies, the eddy-bubble collision density and the mean kinetic energy of the collision eddy. The characteristic wave number that corresponds to the beginning boundary of the region which the bubble-induced turbulence dominates on the energy spectrum has been integrated into the bubble breakage model. This implicitly provides a well-defined physical interpretation for the bubbles with various sizes and shapes. Theoretical predictions using the proposed breakage model that accounts for bubble-induced turbulence have indicated that the dimensionless daughter bubble size distribution not only depends on the parent bubble size and the turbulence dissipation rate, but also is associated with the characteristic length scale that corresponds to the bubble-induced turbulence. The simulation results of bubble size distribution are in consistent with the results obtained by Chen et al., (2004) in which the breakage rate has been artificially increased by 10 times, indicating that the modified breakage model may be appropriate for description of the mechanism of eddy-bubble interactions in the bubble columns when using the energy spectrum with κ^{-3} scaling, with no adjustable parameter is required in the modified bubble breakage kernel.

In Chapter 5, a bubble coalescence model that includes effect of both the shear turbulence and the bubble-induced turbulence has been proposed based on the Prince and Blanch (1990) model. The proposed model takes into account the influence of bubble-induced turbulence on the mean eddy turbulent velocity and hence the approaching velocity of colliding bubbles. The bubble collision under the influence of shear turbulence and the bubble-induced turbulence has been clearly illustrated. The turbulence generation and dissipation in the wake of bubbles has also been included in the Reynolds stress turbulence model using the source terms of S^{R}, S^{k} and S^{ε}. The turbulence dissipation rate considering the joint effect of shear turbulence and bubble-induced turbulence has been used for estimating the bubble collision time. The model analysis shows a general trend of reduction of the predicted coalescence rate.

Experimental measurements on the velocity field in the wakes of bubbles have been performed by using a combination of the PIV and high-speed camera, which has been described in Chapter 6. The experimental data has been processed using the digital image analysis techniques and the codes for treating and filtering the experimental data have been developed to obtain the energy spectrum for the bubble-induced turbulence. By emphasising the separation of velocity signals of the bubbles from the liquid flow field in data processing, it has been firmly reaffirmed that the experimental results have been consist with the previous findings reported in the open literature, i.e. the existence of the κ^{-3} power law scaling range in the wakes of bubbles. Mathematical derivations for the spectrum function of bubble-induced turbulence have been performed in three different ways including dimensional analysis, Taylor's expansion on the second order structure function and applying the Kármán-Howarth equation. The theoretical analyses clearly demonstrate that the scaling exponent for bubble-induced turbulence behaves -3 to the wavenumber κ of turbulent eddies generated in the bubble wakes.

3. RECOMMENDATIONS FOR FUTURE WORK

This PhD project has concentrated on one key issue, the gas-liquid interactions of the turbulent bubbly flows in bubble column reactors, and has investigated the effects of various shapes of rising bubbles due to deformation and the turbulent eddies generated in the wakes of rising bubbles on the bubble coalescence, bubble breakage, bubble size distributions, turbulence kinetic energy, dissipation rate and other related hydrodynamic parameters. However, there are still some remaining difficulties in understanding the nature and the effects of the bubble-induced turbulence that require further investigations. These to the best knowledge of this thesis' author can be summarised as follows:

(1) In corresponding to the anisotropic feature of the bubble-induced turbulence, the turbulence generation source terms for the Reynolds stress equations also have to be anisotropic. Although the current models have considered the decomposition of isotropic source term S^k into S^R in all three directions, the expression of S^k is still based on the work done by drag force in the direction of the main flow. However, it is believed that the turbulence generations in two transverse directions are strongly affected by the forces acting on the transverse directions, such as lift and wall lubrication forces. Therefore, the effects of transverse forces need to be considered in the turbulence generation term S^R to appropriately address the anisotropic nature of the bubble-induced turbulence. Although the dissipation source term S^ε can be calculated by the dissipation in the wake of bubble ε_w divided by some time scale t, it seems that there is not such a widely accepted expression for this time

scale. It is suggested that the time scale should only correspond to that of the turbulent eddies in the wake of bubbles. Therefore, the in-depth understanding regarding the characteristic time scale of the bubble-induced turbulence is further required.

(2) It is believed that the liquid shear turbulence and the bubble-induced turbulence both exist and appear on the turbulence kinetic energy spectrum. However, it should be noted that no matter the Kolmogorov -5/3 law for shear turbulence or the κ^{-3} power scaling law for bubble-induced turbulence, they are only suitable for description of a certain range of bubbly flow turbulence in the actual turbulence kinetic energy spectrum. Although the characteristic length scale $\Lambda = d_b / C_D$ that corresponds to the maximum size of turbulent eddies induced by the rising bubble has been used in the current work to separate the shear turbulence and the bubble-induced turbulence on the energy spectrum, it should be noted that this distinction is also an approximation. In fact, it is very difficult to obtain the exact distinction as the values may subject to different preceding bubbles and those eddies surrounding the bubbles. Also, how the energy cascade from the large-scale turbulence structure to the dissipated eddies induced by the rising bubbles is still unclear, which further prevents from allocating the distinction of these two kinds of turbulence. Thus, if shear turbulence and bubble-induced turbulence can be considered in competition with each other, it is suggested that the EMMS (Energy-Minimisation Multi-Scale) paradigm can be used here to theoretically resolve the above-mentioned difficulties in understanding the bubble-induced turbulence energy

spectrum. The total energy dissipation can be decomposed into macro-scale, meso-scale and micro-scale, with the dissipation in each scale can be calculated. When the system tends to be steady, a postulated stability condition of the meso-scale dissipation due to the compromise in competition of shear turbulence and bubble-induced turbulence may achieve its maximum in the inertia subrange.

(3) The CFD simulations conducted in the current work are based on the two-fluid model with either two-equation $k \sim \varepsilon$ turbulence model or the Reynolds stress turbulence model. Clearly, the local turbulence structures still have not been resolved sufficiently using these simulation approaches. In order to further understand the inherent structures of the two-phase turbulence, large eddy simulation (LES) may be a more promising modelling strategy. However, the eddy viscosity term due to shear turbulence is often considered in the open literature, while the explicit consideration of the effects of bubble-induced turbulence or the κ^{-3} power law scaling on turbulence energy spectrum have rarely been documented. The lack of reliable correlations of the bubble-induced turbulence on the eddy viscosity term has impeded the further implementation of the LES to investigate the turbulent bubbly flow. Development of two-phase LES model that considers the joint effects of shear turbulence and bubble-induced turbulence is strongly suggested, which will assist to accurately depict the gas-liquid interactions in the bubble column reactors.

LIST OF PUBLICATIONS

Journal articles

SHI, W., YANG, N. & YANG, X. 2017. A kinetic inlet model for CFD simulation of large-scale bubble columns. *Chemical Engineering Science*, 158, 108-116.

SHI, W., YANG, J., LI, G., YANG, X., ZONG, Y. & CAI, X. 2018. Modelling of breakage rate and bubble size distribution in bubble columns accounting for bubble shape variations. *Chemical Engineering Science*, 187, 391-405.

SHI, W., YANG, J., LI, G., ZONG, Y. & YANG, X. 2018. CFD-PBM Modelling of Gas-Liquid Two-Phase Flow in Bubble Column Reactors with an Improved Breakup Kernel Accounting for Bubble Shape Variations. *Heat Transfer Engineering*. (Accepted, in press)

Book Chapter

SHI, W., YANG, J., LI, G., ZONG, Y. & YANG, X. 2018. Modelling of Bubbly Flow in Bubble Column Reactors with an Improved Breakup Kernel Accounting for Bubble Shape Variations. *Heat and Mass Transfer – Volume 1,* IntechOpen. ISBN: 978-953-51-6135-6. (Accepted, in press)

Conference Proceeding

SHI, W., LI, G., YANG, J., ZONG, Y. & YANG, X. 2017. CFD-PBM Modelling of Gas-Liquid Two-Phase Flow in Bubble Column Reactors with an Improved Breakup Kernel Accounting for Bubble Shape Variations, 13th International Conference on Heat Transfer, Fluid Mechanics and Thermodynamics, Slovenia. (Outstanding Paper Award)

Chemical Engineering Science 158 (2017) 108–116

Contents lists available at ScienceDirect

Chemical Engineering Science

journal homepage: www.elsevier.com/locate/ces

A kinetic inlet model for CFD simulation of large-scale bubble columns

Weibin Shi[a,b], Ning Yang[a,*], Xiaogang Yang[b]

[a] State Key Laboratory of Multiphase Complex Systems, Institute of Process Engineering, Chinese Academy of Sciences, P.O. Box 353, Beijing 100190, PR China

[b] International Doctoral Innovation Centre (IDIC), The University of Nottingham Ningbo, University Park, Ningbo 315100, PR China

ARTICLE INFO

Keywords:
CFD modelling
Bubble columns
DBS drag model
Gas distributor
New inlet model
Large-scale

ABSTRACT

For the simulation of industrial-scale bubble column reactors, while modelling the gas distributor as uniform inlets oversimplifies the inhomogeneity introduced by inlets, the direct simulation of the full geometry of gas distributor or sparger brings about enormous pre-processing work and huge computational cost. A new inlet model is therefore proposed in this paper to simplify the modelling of gas distributor and meanwhile maintain the simulation accuracy. The new inlet model is validated by the comparison of the model prediction with experiments and the CFD simulation incorporating the full geometry of gas distributor for bubble columns of small or large diameters. Comparisons of three different inlet boundary conditions, i.e., the direct simulation of gas distributor, the uniform inlet, and the new inlet model, are made in the simulation of the total gas holdup, the radial profiles of gas holdup at different cross-sections along the column height, and the axial velocity of liquid at various superficial gas velocities. The results indicate that the new inlet model is capable of achieving a good balance between simulation accuracy and computational cost for the CFD simulation of large-scale bubble column reactors.

1. Introduction

Bubble columns and their variants have been extensively utilized in chemical or process industries for gas-liquid or gas-liquid-solid reactions, such as oxidation, chlorination, alkylation, polymerization, hydrogenation, and fermentation. These reactors provide higher heat and mass transfer rates while maintaining lower operation and maintenance costs. For the design and scale-up of various processes, a large number of experimental studies have been carried out to investigate the hydrodynamics of gas-liquid flow in bubble columns at different operational parameters. However, these experimental studies (Deckwer, 1992) are usually carried out in lab-scale columns of diameters less than 0.5 m. Experiments on large-diameter columns are seldom reported due to the difficulty or complexity in experimental measurements. With the rapid development of computer technology and computational science in the past two decades, CFD is becoming a powerful tool in understanding the complexity of hydrodynamics. A number of studies have been conducted on various aspects of CFD simulation, e.g., the impact of turbulence models (Laborde-Boutet et al., 2009; Masood et al., 2014; Sokolichin and Eigenberger, 1999), drag forces (Li and Zhong, 2015; Xiao et al., 2013; Yang et al., 2011), lift forces (Lucas et al., 2016; Wang and Yao, 2016) and bubble breakage and coalescence models (Bordel et al., 2006; Chen et al., 2005b; Wang et al., 2006), and the coupling of CFD simulation with mass transfer (Bao et al., 2015; Wiemann and Mewes, 2005) or reaction kinetics (Rigopoulos and Jones, 2003; Troshko and Zdravistch, 2009; Van Baten and Krishna, 2004). Hitherto there are two main issues in CFD simulation of bubble columns. The first one is the sensitivity of simulation on closure models of interfacial momentum exchange, in particular, the drag force and other forces including lift or virtual mass force exerted by the surrounding liquid to the bubbles. There have been some studies regarding the effects of the lift coefficient C_L (Delnoij et al., 1997; Lucas et al., 2005; Lucas and Tomiyama, 2011; Sankaranarayanan and Sundaresan, 2002; Sokolichin et al., 2004; Tomiyama, 1998), and of the virtual mass force (Delnoij et al., 1997; Hunt et al., 1987). However, successful simulations have been reported in literature for either including lift and virtual mass forces (Deen et al., 2001; Rampure et al., 2007; Tabib et al., 2008; Zhang et al., 2006) or only using the drag force (Deen et al., 2000; Krishna and van Baten, 2001; Ranade and Tayalia, 2001). Actually the lift coefficient or lift force, as a result of pressure or velocity gradient, can generally be used to adjust the simulation of radial distribution of gas holdup, especially when the uniform inlet condition is applied. The physical basis of these non-drag forces still requires further investigation. In this study we temporarily isolate these effects from that of drag force and inlet conditions. The second issue is the

* Corresponding author.
E-mail address: nyang@ipe.ac.cn (N. Yang).

http://dx.doi.org/10.1016/j.ces.2016.10.005
Received 11 April 2016; Received in revised form 29 September 2016; Accepted 6 October 2016
Available online 07 October 2016
0009-2509/

Nomenclature

C_D	effective drag coefficient for a bubble around a swarm, dimensionless
d_b	bubble diameter, m
U_g	superficial gas velocity, m/s
U_l	superficial liquid velocity, m/s
u	velocity vector, m/s
k	turbulent kinetic energy, m^2/s^2
g	gravity acceleration, m/s^2
H	distance from the bottom surface, m
F^D	drag force, N/m^3
t	time, s
P_T	total pressure, MPa
P_S	vapour pressure of the liquid, MPa
D_C	column diameter, m
X^W	weight fraction of the primary liquid in the mixture, w/w

Greek letters

α	phase volume fraction, gas holdup
ε	turbulence dissipation rate
μ	molecular dynamic viscosity, Pa s
μ_t	turbulence dynamic viscosity, Pa s
ρ	fluid density, kg/m^3
σ	surface tension, N/s
Γ	gas distributor parameter

Abbreviations

DBS	double-bubble-size
EMMS	energy-minimization multi-scale
CARPT	Computer-automated radioactive particle tracking
CT	Computed tomography

Subscripts

g	gas
l	liquid

simplification of gas distributor or sparger as a uniform inlet or the high computational cost arising from the direct modelling of the full geometry of gas distributors. The latter issue is less covered in literature but still a challenge for the simulation of industrial-scale columns.

Gas distributors or spargers are reported to have great influence on flow behaviours. Hills (1974) and Camarasa et al. (1999) showed that the gas holdup, liquid velocity, bubble size and bubble velocity altered significantly when using different gas distributors, e.g., the sieve plates of various configurations, the porous plates, the multi- or single- orifice nozzles. Mudde et al. (2009) presented a densely arranged multi-needle sparger to obtain a uniform bubble injection, and found that the homogeneous flow regime was extended up to a gas fraction of 55%. Haque et al. (1986) reported that the mixing time and total gas holdup were significantly affected by sparger designs. Moreover, Dhotre and Joshi (2007) stated that the distributor of different configurations generated the initial bubbles of a certain size and gas holdup, which in turn influenced the overall flow pattern. Some researchers have studied the effect of distributors by using CFD modelling. Ranade and Tayalia (2001) modelled a shallow bubble column of single- or double-ring spargers, and the simulation indicated that the fluid dynamics and mixing in shallow bubble column reactors were controlled by sparger configuration. Akhtar et al. (2006) simulated the perforated plates with different open areas, indicating that including the real gas distributors in simulation can lead to asymmetric flow patterns which were otherwise smoothened when a uniform gas source was used in CFD simulation. Dhotre and Joshi (2007) studied the influence of the size, location, opening area and hole diameter of nozzles on the flow pattern of CFD simulation. They analysed the flow pattern within the gas chamber under the distributor and velocities through all the holes, and found that the chamber configurations affected the uniformity of gas distribution in the sparger region of bubble columns. It appears that an interaction exists between the chamber and sparger, which may affect the stability of the plume. Bahadori and Rahimi (2007) investigated the influence of the number of orifices on gas hold-up and liquid phase velocity by CFD modelling. They reported that increasing the number of orifices in the sparger increased the total gas holdup in a shallow bubble column and each local orifice contributed to liquid circulation and mixing. Li et al. (2009) reported that the distributor configurations had strong impact on the asymmetric flow and mixing characteristics in the vicinity of gas distributor. Rampure et al. (2009) included the plenum area under the gas distributor into the CFD simulation. They modelled the perforated plate as a porous zone and adopted empirical correlations to obtain the model input parameters. Compared to the cases using uniform inlet conditions or directly modelling the gas distributors, the purpose of this study is to develop a new kinetic inlet model which could equivalently reflect the kinetic information of gas velocity gradient and the inhomogeneity introduced through the inlet, without the need to directly model the real inlet geometry. It may provide a simpler way without the necessity to simulate the perforated plate as well as the gas chamber underneath, while the simulation accuracy is still guaranteed.

Direct modelling of the full geometry of gas distributor or specifying the mass sources at the real positions of holes has been reported in literature (Tabib et al., 2008; Ziegenhein et al., 2013). However, this may also lead to a significant increase in pre-processing work, grid number and complexity as well as computational cost. For example, when the number of holes in a gas distributor is around 60 and the hole diameter is larger than 2 mm, it is possible to include every single hole in the simulation of lab-scale bubble columns. Nevertheless, the gas distributors used in industrial-scale columns are far more complicated, involving hundreds of holes with the size around 1 mm. Chen et al. (2005a) used 0.7 mm- or 1.32 mm-diameter holes on perforated plate and stated that it was impossible to include the gas distributor into the simulation due to the fact that the direct modelling of gas distributor would require millions of cells. The computational cost would become unaffordable if more complicated geometries (e.g., heat exchange tubes or internals) need to be investigated, or more transport equations need to be solved, e.g., the three-fluid model for gas, liquid and solid phases, or the population balance equations for bubble coalescence and break-up, or species transport equations to incorporate mass transfer and reaction kinetics.

Some previous CFD studies attempted to simplify the gas distributor as a uniform inlet across the whole bottom surface since this may greatly reduce the number of grids and computational cost. However, this simplification may cause some under-prediction of gas holdup for large diameter columns, which will be further elucidated in this study. Therefore, as a compromise of these two methods, the objective of this work is to propose a new inlet model which is able to reflect the non-uniformity of the gas inlet and achieve the reasonable simulation and meanwhile reduce the computational cost. Section 2 will present the computational models to be used in the simulations and demonstrate the new inlet model. Numerical details in CFD simulations conducted in this work will be given in Section 3. Section 4 provides the simulations utilizing the new inlet model in small- and large-diameter columns. The simulation validates the new model function, demonstrating its capability to achieve the balance between simulation accuracy and computational cost in CFD simulation of large-scale bubble column reactors.

2. Mathematical formulation

2.1. Computational models

The equations of Eulerian-Eulerian approach used in this work are given as below, consisting of mass and momentum balance equations to describe the hydrodynamics of the continuous liquid or disperse gas phases:

$$\frac{\partial(\alpha_k\rho_k)}{\partial t} + \nabla\cdot(\alpha_k\rho_k\vec{u}_k) = 0\ (k\ =\ \text{liquid or gas}) \tag{1}$$

$$\frac{\partial(\alpha_k\rho_k\vec{u}_k)}{\partial t} + \nabla\cdot(\alpha_k\rho_k\vec{u}_k\vec{u}_k)\ =\ -\alpha_k\nabla P\ +\ \nabla\cdot\overline{\overline{\tau}}_k + \alpha_k\rho_k g +\ F_k^D \tag{2}$$

Closure laws are required for the phase interaction forces. In this study, only the drag force is employed as it is considered to be the predominant interfacial force in gas-liquid flows in bubble columns (Laborde-Boutet et al., 2009; Larachi et al., 2006). The drag force is formulated as:

$$F_g^D = -F_l^D = \frac{3}{4}\alpha_g\frac{C_D}{d_b}\rho_l|\vec{u}_g - \vec{u}_l|(\vec{u}_g - \vec{u}_l) \tag{3}$$

In the equation above, C_D/d_b is a critical lumped parameter in CFD simulation. It can be either calculated from several correlations in literature, or be derived from the DBS drag model (Yang, 2012; Yang et al., 2011). The DBS model extended the energy minimization multi-scale (EMMS) approach for gas-solid fluidization to gas-liquid flows, and its physical background and further details can be found in the previous publications (Chen et al., 2009; Xiao et al., 2013; Yang, 2012; Yang et al., 2007, 2011). The lumped ratio was formulated by Xiao et al. (2013) as:

$$C_D/d_b = \begin{cases} 431.14 - 6729.02U_g + 35092.2U_g^2, & U_g \le 0.101\ m\cdot s^{-1} \\ 122.49 - 553.94U_g + 741.24U_g^2, & U_g > 0.101\ m\cdot s^{-1} \end{cases} \tag{4}$$

The standard k-ε model for the two-phase mixture is employed as given below:

$$\frac{\partial}{\partial t}(\rho_m k) + \nabla\cdot(\rho_m\vec{u}_m k) = \nabla\cdot\left(\frac{\mu_{t,m}}{\sigma_k}\nabla k\right) + G_{k,m} - \rho_m\varepsilon \tag{5}$$

$$\frac{\partial}{\partial t}(\rho_m\varepsilon) + \nabla\cdot(\rho_m\vec{u}_m\varepsilon) = \nabla\cdot\left(\frac{\mu_{t,m}}{\sigma_\varepsilon}\nabla\varepsilon\right) + \frac{\varepsilon}{k}(C_{1\varepsilon}G_{k,m} - C_{2\varepsilon}\rho_m\varepsilon) \tag{6}$$

2.2. A new inlet model

As mentioned in the introduction section, the CFD modelling of large-scale bubble columns by employing the actual geometry of gas distributor may impose an insurmountable difficulty due to the constraint of mesh generation and computational cost. It would be desired and practical if a kinetic model could be introduced to incorporate the flow behaviour but avoid modelling the actual geometry of gas distributor. A new inlet model is proposed here to account for the effect of entrance velocity gradient with an attractive benefit of significant reduction of the number of mesh cells. This model attempts to take the number and size of the perforated holes into consideration for a particular type of gas distributor, i.e., the perforated plates. For this type of distributor, the gas flows through each perforated hole to form jet arrays, generating a velocity fluctuation around the holes along the radial direction due to the entrainment of the carrier fluid. Although these local jet flows may not essentially affect the hydrodynamic behaviours if the height to dimension ratio H/D is larger enough, there can be a very strong influence on the flow pattern in the non-fully-developed region. Moreover, Guan et al. (2015) reported that the flow pattern in bubble columns with internal tubes was always not fully developed due to the existence of internal tube banks. In this case, the inlet condition may play important roles.

Behkish et al. (2006) proposed a correlation of gas holdup in bubble columns or slurry bubble columns based on 3881 experimental data points. The model parameters included the pressure, temperature, gas superficial velocity, solid concentration, particle density/concentration, reactor size, and gas sparger characteristics. Rearranging the correlation of Behkish et al. (2006) leads to

$$\tilde{u}_s = 2.24\times10^2\times\alpha^{1.8}\times\left(\frac{\mu_L^{0.313}\sigma_L^{0.486}}{\rho_L^{0.747}\rho_G^{0.319}}\right)\times\left(\frac{P_T - P_S}{P_T}\right)^{0.365}\times \left(\frac{D_C}{D_C + 1}\right)^{0.211}\times\Gamma^{-0.095}\times e^{0.436X_W} \tag{7}$$

where u_s is the superficial gas velocity, α is the gas holdup, and Γ represents the gas distributor parameter. Other parameters are either the physical properties or operational parameters. The local gas holdup is a function of radial position and can be correlated by an exponential function of radial position, as will be demonstrated in Eq. (14) in the following sections. Hence if we apply Eq. (7) to the local radial positions, it can be deduced that the local gas velocity could also be expressed as an exponential function of radial position. In general, the fluctuating trend and magnitude of local jet flows could be averaged and approximated by a normal distribution-like function which defines the local gas velocity at a given point on the inlet boundary. Thus, it may be reasonable to assume that the entrance velocity for the gas distributor could be approximated by the exponential function. Based on this consideration, we thus propose the simplified inlet model. It should be pointed out that this approximate approach should be distinguished from the method of modelling the real holes. The new inlet model for a perforated plate could then be formulated as:

$$\tilde{u}_s = \begin{cases} \left(1.5 + \frac{\Gamma}{100}\right)U_g\cdot e^{\frac{-r^2}{b}}, & Ug \le 0.12m/s \\ \left(0.75 + \frac{\Gamma}{100}\right)U_g\cdot e^{\frac{-r^2}{b}}, & Ug > 0.12m/s \end{cases} \tag{8}$$

which is also subject to the continuity function:

$$Q = \sum\frac{\pi}{4}d_i^2\cdot u_i = \frac{\pi}{4}D^2\cdot U_g = \int_0^R\tilde{u}_s\cdot 2\pi r dr \tag{9}$$

Table 1
Parameters of 5 typical perforated plates.

Configuration	Hole number	Do (mm)	Dc (m)	do/Dc	ζ	Γ	Umax (m/s)	b
1	61	0.4	0.14	0.0029	0.0498	72.8416	0.2228	0.0026
2	121	1.32	0.14	0.0094	1.0757	23.6553	0.1737	0.0038
3	225	1.32	0.19	0.0069	1.086	43.9871	0.1940	0.0060
4	241	3	0.45	0.0067	1.0711	59.9278	0.2099	0.0280
5	301	0.77	0.45	0.0017	0.0881	46.7722	0.1968	0.0326

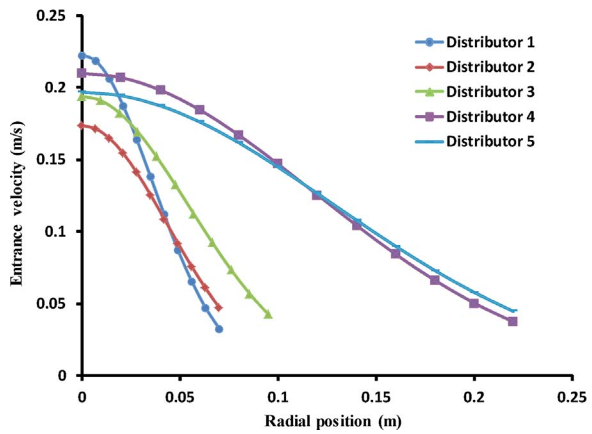

Fig. 1. Inlet gas velocity profile for different geometrical parameters (Ug=0.1 m/s).

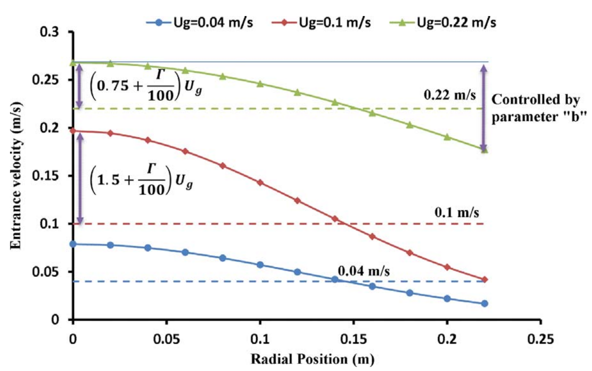

Fig. 2. Inlet gas velocity profile for Distributor 5 (Ug=0.04, 0.1, 0.22 m/s).

where d_i and u_i are the diameter and the through hole velocity of i-th inlet hole respectively, r is the non-dimensional radial position, and the parameter b can be determined by solving the continuity function Eq. (9). Γ is a lumped coefficient representing the influence of gas distributor configurations and defined by Behkish et al. (2006) as:

$$\Gamma = K_d \times N_O d_O^{\alpha} \tag{10}$$

$K_d$is the distributor coefficient that equals 1.364 for perforated plates, N_O is the number of orifice holes on the plate, and d_O is the diameter of orifice holes. The index α depends on the value of ζ, the free area of the distributor:

$$\zeta = N_O\left(\frac{d_O}{D_C}\right)^2 \times 100 \tag{11}$$

For perforated plates,
$\alpha = 0.017$, when $\zeta<0.055$;.
$\alpha = 0.303$, when$0.055 \le \zeta \le 0.3$;.
$\alpha = 0.293$, when $\zeta>0.3$.

Table 1 lists the distributor parameters for five typical perforated plates. The gas velocity distribution at the inlet is illustrated in Fig. 1 for five different gas distributors at U_g=0.1 m/s, and Fig. 2 shows the velocity profile of distributor 5 at different superficial velocities.

It should be pointed out that an exact inlet model could also be correlated from the CFD simulation of the actual configuration including the gas plenum chamber and the gas distributor with consideration of the liquid height above the gas distributor, such as the work of Rampure et al. (2009). However, Dhotre and Joshi (2007) reported that the gas velocity profile at the holes was not only dependent on the superficial velocity and the number and diameter of orifice holes, but also on the pressure drop of distributor and liquid bulk phase as well as the chamber geometry. Actually an exact simulation of the velocity profile around holes also requires the inclusion of the two-phase flow above the distributor or even an iteration process between the gas chamber and the bulk region of two-phase flow, which is far more complicated and beyond the scope of this study. Here we propose a simplified function to replace the inlet velocity distribution which is only a function of distributor geometry and superficial gas velocity for engineering application.

For these five perforated plates with different geometrical configurations in Fig. 1, the maximum at the centre of the column are approximately twice the superficial velocity according to the Hagen-Poiseuille's Law. The effects of model parameters are illustrated in Fig. 2. The maximum value is determined by geometrical parameters, i.e., the ratio $(0.75 + \Gamma/100)$ or $(1.5 + \Gamma/100)$. The slopes of the curve are dependent on the parameter b which can be obtained by solving the continuity function. We may assume that the flow near the distributor region could be approximated by a free-stream flow in a pipe. When the flow rate is relatively lower (0.04–0.1 m/s), the pressure loss is linear with the velocity so that the steepness of the profiles increases. According to Law of Blasius, the sum of viscous shear stress and turbulent stress τ_w can be expressed as $\tau_w = 0.03325\rho U^{7/4}(\upsilon/R)^{1/4}$. Hence when the flow enters the fully-developed heterogeneous (churn-turbulent) regime ($U_g > 0.12$ m/s), the velocity profiles in the cross-sections close to the entrance of bubble columns tend to be flat and the velocity gradient is restricted to the near wall region.

It should also be pointed out that the new inlet model proposed here has only been tested for perforated plates in which holes are uniformly distributed at the whole cross-section in concentric circles or in a triangular pitch, with the size of holes not exceeding 4 mm and the number of holes more than 60. Although further validation is required, the proposed model is potentially capable of representing distributor configurations beyond this range or other types of gas distributors such as porous plates or multiple-orifice nozzles.

3. Simulation details

To validate the effect of the new inlet model, simulations have been carried out for the air-water bubble columns of Hills (1974). The detail information is listed in Table 2.

The average size of cells is about 7 mm for the case of Grid 1 (Fig. 3) which is equivalent to $14(r)\times36(\theta)\times150(z)$ nodes and results in approximately sixty thousand cells in total. The grid sensitivity was further tested in the two stages with a grid refinement of a factor of about 1.3 in all directions. Grid 2 generates twice the total number of cells of Grid 1, and Grid 3 doubles the total number of cells of Grid 2 in a similar manner.

3D pressure-based solver of Ansys Fluent® is used in this work. The time step is set to be 0.0005 s in the beginning. When the physical time reaches 10 s, the time step increases to 0.001 s till the flow time reaches 30 s, and then the time step is fixed to be 0.005 s. The quasi-steady state is considered to be achieved after 80 s. Data sampling statistics for the next 80 s is considered to be sufficient to illustrate the time-averaged characteristics of the flow fields. The new inlet model is

Table 2
Details of experimental setup in Hills (1974).

Column Diameter (m)	Column Height (m)	Observation Height (m)	No. of holes on distributor	Diameter of holes (mm)	ζ	Superficial gas velocity (m/s)
0.138	1.37	0.6	61	0.4	0.0498	0.038–0.127

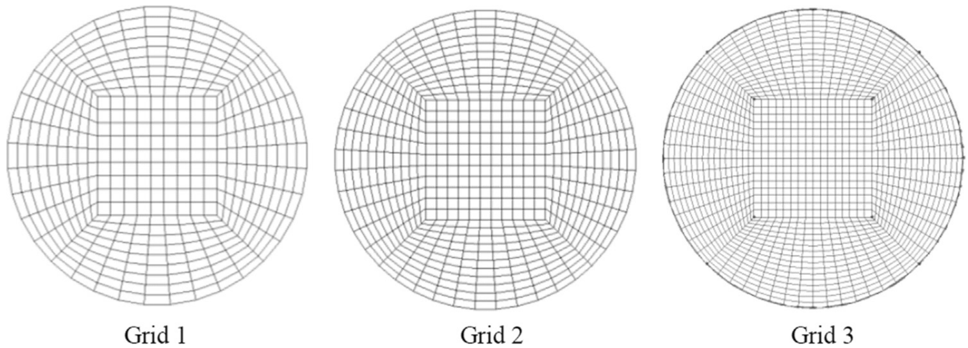

Fig. 3. Mesh set-up at bottom surface.

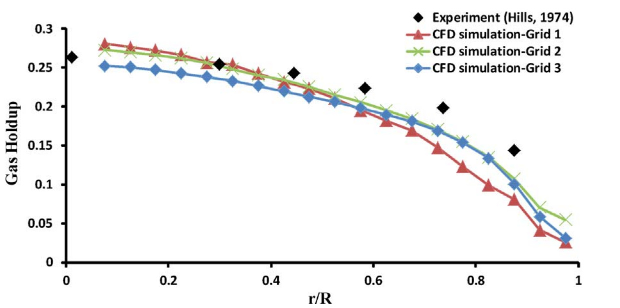

Fig. 4. Comparison of simulated gas holdup profile with three different grids (Ug=0.064 m/s).

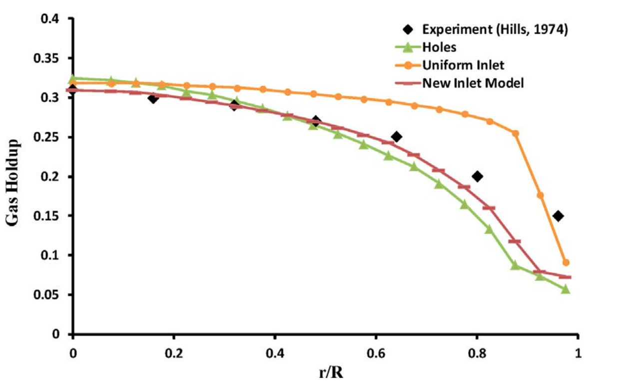

Fig. 5. Radial distribution of gas holdup using different inlet conditions (Ug=0.095 m/s, H=0.6 m, H/D=4.35).

integrated into the user define function (UDF). The volume fraction of gas phase is set to be 1 at inlet. The outlet boundary is set as a pressure outlet at the top. Non-slip conditions are applied for both liquid and gas phases at the vessel wall. A grid sensitivity test has been conducted for Grid 1, Grid 2 and Grid 3, and they can yield quantitatively the similar results (Fig. 4), and Grid 2 is used in the succeeding simulations to investigate the effects of inlet models.

4. Results and discussion

4.1. Validation of the new inlet model

Three cases for different superficial gas velocities are simulated for the Hills system: 0.038, 0.095 and 0.127 m/s, representing the homogenous, transitional, or heterogeneous regimes respectively. The prediction of gas holdup distribution by using the new inlet model is compared with experimental data of Hills (1974) and the simulation of Yang et al. (2011) and Xiao et al. (2013) in which all the gas inlet holes were included.

Fig. 5 compares the time-averaged gas holdup distribution for three different inlet models at superficial gas velocity Ug=0.095 m/s. "Holes" means that all the orifices at the gas distributor are modelled so that the gas is introduced through each orifice holes. "Uniform Inlet" means that the distributor geometry is not modelled and the gas is introduced uniformly through the whole bottom surface of the column. "New Inlet Model" denotes that the gas is introduced through the profile functions of the new inlet model. Although all the three inlet models achieved reasonable agreements with experimental data, it can be seen that the gas holdup distribution curve tends to be flat for the "Uniform Inlet" case whereas the other two fit the experimental data better.

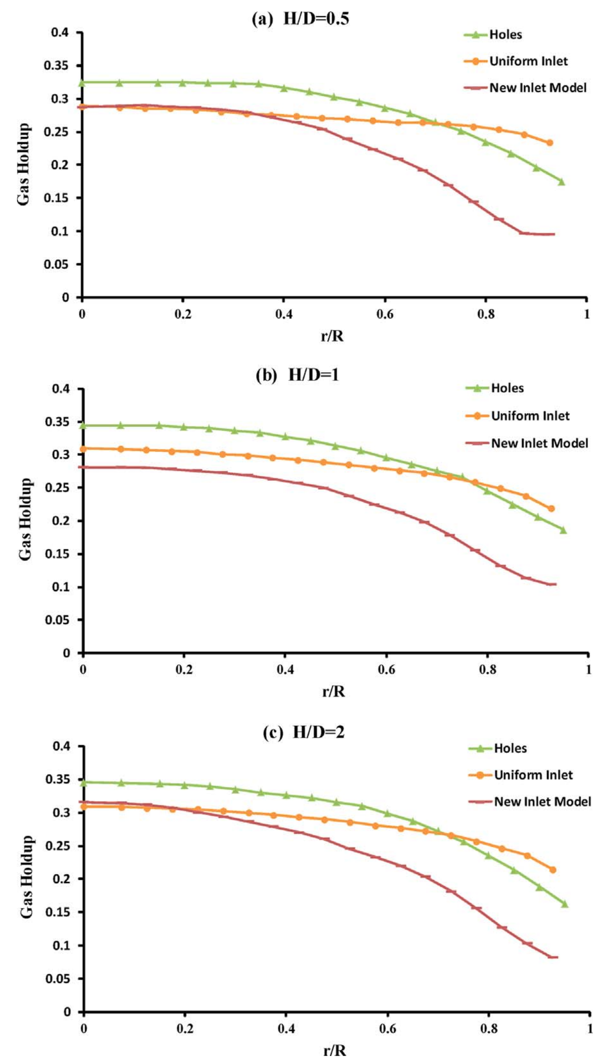

Fig. 6. Gas holdup radial distribution along the column height (from the top to bottom: H/D=0.5, 1, 2; Ug=0.095 m/s).

Fig. 6 presents the evolution of gas holdup profiles along the

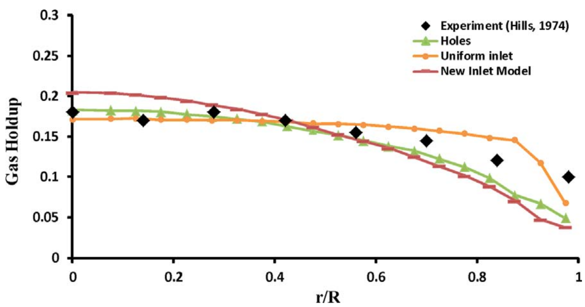

Fig. 7. Radial distribution of gas holdup using different inlet conditions (Ug=0.038 m/s, H=0.6 m).

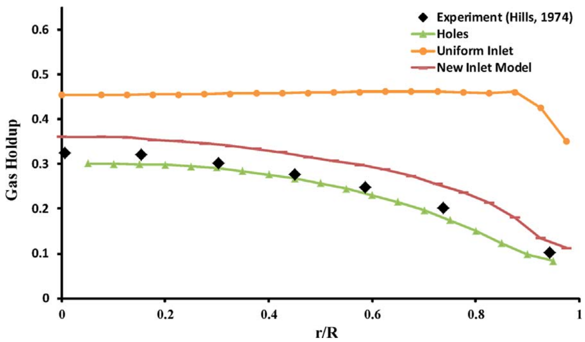

Fig. 8. Radial distribution of gas holdup using different inlet conditions (Ug=0.127 m/s, H=0.6 m).

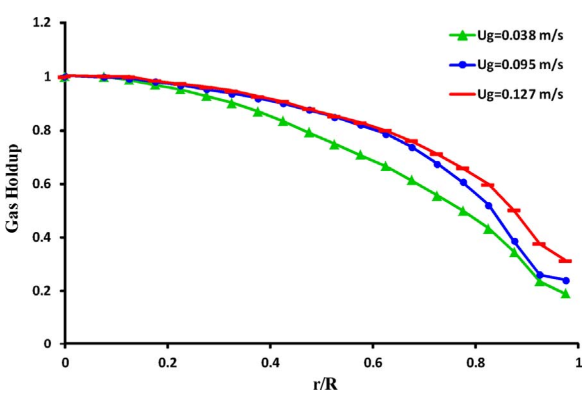

Fig. 9. Radial distribution of normalized gas holdup profile using new inlet model (H=0.6 m).

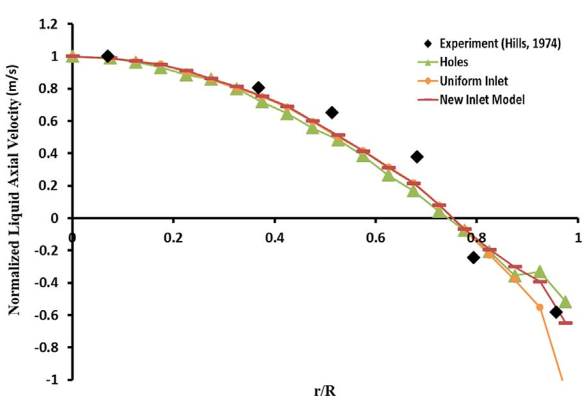

Fig. 10. Radial distribution of normalized axial liquid velocity (Ug=0.95 m/s, H=0.6 m).

column height for the three gas inlet conditions. Since the experimental data of lower H/D ratios is not available, only the simulation results are plotted in the figure. For the "Holes" case, the gas holdup turns out to be a monotonous parabolic profile when H/D=0.5. This reflects the

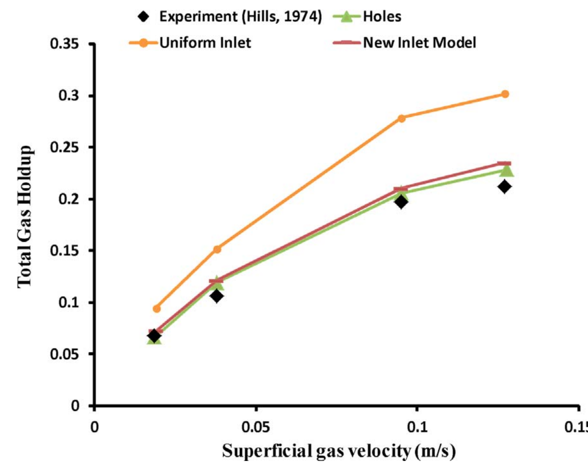

Fig. 11. Comparison of simulated total gas holdup profiles with experiments of Hills (1974).

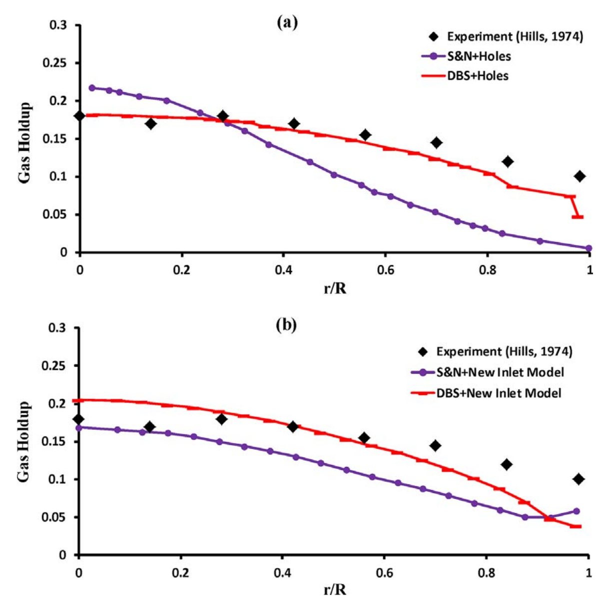

Fig. 12. Radial distribution of gas holdup using different drag models in combined with (a) Holes model; (b) New Inlet Model (Ug=0.038 m/s, H=1.32 m).

influence of gas momentum distribution formed by the orifice holes on the sparger. The parabolic profile holds coherently and even rises slightly as a whole with increasing the H/D ratio. On the one hand, for the uniform inlet condition, it allows the gas to be introduced from the entire bottom surface, and the gas holdup profile is shown to be consistently flat at all cross-sections, showing the uniform momentum distribution. On the other hand, the performance of new inlet model is between the "Holes" and "Uniform Inlet" cases. For the new inlet model, it captures the performance of the "Holes" case to some extent, especially the pattern of inlet gas momentum distribution and the resulting parabolic shape of gas holdup profile, even though the absolute magnitudes are not exactly the same. The reason for the difference is that the direct simulation of holes on the sparger actually introduces much higher gas injection velocity at each inlet hole and consequently affects the sparging region. However, the difference becomes smaller for higher H/D, as shown in Fig. 5 (H=0.6 m, H/D=4.35).

The simulations in Figs. 5 and 6 also indicate that, for the new inlet model, the difference in radial profiles for H/D=2 (Fig. 6c) and H/D =4.35 (Fig. 5) is smaller. This implies that the influence of the inlet condition (or gas distributor) is marginal for higher H/D, and the evolution of radial distribution along the height does not change

Table 3
Bubble column parameters of Chen et al. (1999).

Column Diameter (m)	Column Height (m)	Observation Height (m)	No. of holes on distributor	Diameter of holes (mm)	ζ	Superficial gas velocity (m/s)
0.44	2.43	1.32	301	0.7	0.076	0.1

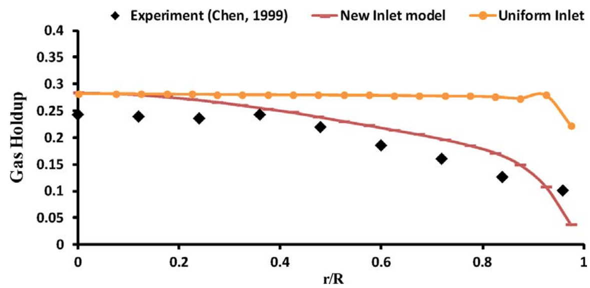

Fig. 13. Radial profile of gas holdup in comparison with the CT data of Chen et al. (1999) (Ug=0.1 m/s, D=0.44 m).

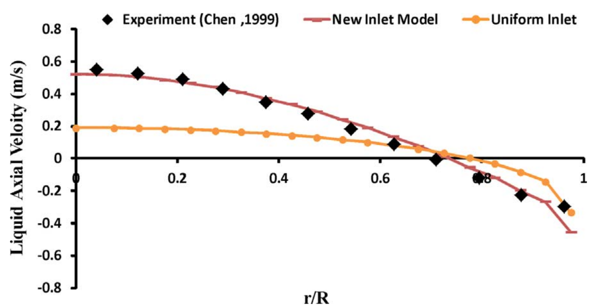

Fig. 14. Radial profile of liquid axial velocity in comparison with the CARPT data of Chen et al. (1999) (Ug=0.1 m/s, D=0.44 m).

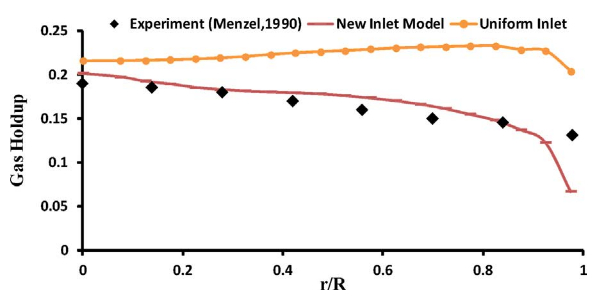

Fig. 15. Radial profile of gas holdup in comparison with the experiment of Menzel et al. (1990) (Ug=0.072 m/s, D=0.6 m).

noticeably for each specific distributor.

Figs. 7 and 8 present the radial distribution of gas holdup at Ug=0.038 m/s and Ug=0.127 m/s respectively. The results indicate that the uniform inlet overestimates the gas holdup at higher gas flow rate. While the "Holes" model performs the best, the new inlet model can also yield reasonable simulation. It should be pointed out that some previous studies have used the uniform inlet condition and also obtained good simulation results. This issue is complicated and, to our knowledge, it is related to two aspects. Firstly, the performance of uniform inlet is problem-dependent and a critical evaluation is still lacking on the simulation of different operating conditions and column geometries. Secondly, the simulation is also pertinent to the models of drag force or non-drag forces such as lift and virtual mass force. Some studies involved the lift force for the cases of the uniform inlet conditions, and hence the radial profile of gas holdup becomes parabolic. However, the simulation is also sensitive to the choice of lift coefficient. This article only focuses on the inlet conditions and the effects of non-drag forces have been omitted. We cautiously point out that the interaction between inlet conditions and physical models may be important, but has not yet been analysed or reported in literature.

Although the simulation of the new inlet model in Figs. 7 and 8 did not perfectly fit the experimental data, acceptable agreement is achieved with the error less than 20% for the majority part of the curves. The new inlet model reasonably allocates the gas momentum onto the cross-section at the bottom by the distribution profile functions, and hence the prediction can qualitatively capture the main characteristics of the experiments and the "Holes" case.

Fig. 9 presents the gas holdup profile normalized by the centreline values at three different superficial gas velocities (Ug=0.038, 0.095 and 0.127 m/s). It can be seen that the three profiles of gas holdup bear some analogy. In this case, it is reasonable to establish the following equation for gas holdup:

$$\frac{\partial \alpha}{\partial t} + \vec{u}\cdot\nabla\alpha = D\nabla^2\alpha \tag{12}$$

.

The first term vanishes in the fully developed region, and hence in radial direction

$$u_r\cdot\frac{\partial \alpha}{\partial r} = D\frac{\partial}{\partial r}\left(\frac{\partial \alpha}{\partial r}\right) \tag{13}$$

By solving Eq. (13), we obtain:

$$\frac{\partial \alpha}{\partial r} = C\cdot e^{\frac{u_r}{D}r} \tag{14}$$

where C and D are coefficients. Eq. (14) indicates that the gas holdup gradient in radial direction can be expressed in the form of an exponential function. It is reasonable to deduce that the similar expression holds for the inlet condition.

Fig. 10 shows the profile of normalized axial liquid velocity (relative to the centreline liquid velocity) along the radial direction. The normalized axial liquid velocity profiles are very similar and all of them are close to the experiment results, indicating that inlet conditions do not affect the flow pattern of liquid-phase. However, it should be pointed out that the simulated absolute centreline liquid velocities with all the inlet conditions are lower than experiments. This may be relevant to the simplified treatments for holes of sparger. For the "Holes" case, the hole diameter of the distributor was enlarged from 0.4 to 2 mm while maintaining the original number of holes in order to decrease the mesh number and mesh skewness. Therefore, the gas velocity at holes is actually lower than that of real cases, which may lead to the underestimation of liquid axial centreline velocity. The simulation is similar to the results of Yang et al. (2011).

Fig. 11 compares the simulated total gas holdup and the experiments for three different gas inlet models. The uniform inlet overestimates the total gas holdup especially at higher superficial gas velocities, whereas the other two models give good simulation. In the "Holes" case, the increase of gas holdup slows down with increasing superficial gas velocity. In the meantime, unlike the uniform inlet case, the new inlet model does not change this dampening tendency and can achieve similar effect that can only be obtained by the multi-hole inlet boundary. In conjunction with the DBS drag model, the new inlet model shows great adaptability for the prediction of both the total and the radial distribution of gas holdup without the need of adjusting modelling parameters.

It can be inferred from Figs. 5–11 that, on one hand, including exactly the real number and size of holes into the simulation is necessary to acquire accurate prediction for all the three superficial velocities, but this requires approximately 700,000 cells for a lab-scale hollow bubble column. On the other hand, utilizing the new inlet model as an approximation can achieve acceptable agreements with experimental data in all the three cases, and the total cell number is reduced to approximately 60,000. The computational cost was apparently reduced to a great extent (approximately one tenth of the "Holes" case) without much sacrifice of the simulation accuracy. This may be of more significance for pilot- or industrial-scale bubble column reactors in which a large number of internals of complex geometry may reside, and in such cases the total number of cells could easily soar up to as many as tens of millions or even hundreds of millions. The new inlet model greatly reduces the grid number and unbearable computational cost by orders-of-magnitude.

It should be pointed out that the drag model is the predominant factor for the accuracy of simulation compared to the inlet boundary conditions. For example, the Schiller-Naumann (S & N) drag model still largely under-predicts the gas holdup, even if the "Holes" model or the new inlet model is employed, as shown in Fig.12. For the two different inlet boundary conditions, the DBS drag model consistently shows the better agreement with the experiments than the Schiller-Naumann drag model, which was also reported in our previous publications (Xiao et al., 2013; Yang, 2012; Yang et al., 2011).

4.2. Application in bubble columns of large diameters

To further verify the new inlet model for columns of large diameters, CFD simulation using the new inlet model is performed for the experimental system of Chen et al. (1999). Detail information is listed in Table 3.

In this case, to avoid the liquid overflow from the top of the column, the column height is extended to 3 m. The space above the column height of 0.89 m is defined as the fully-developed region of the flow in terms of the experiments of CARPT/CT measurements of Chen et al. (1999). Since the column was under batch-operated conditions, the static liquid height with zero gas holdup is filled up to 1.7 m. The rest part of the column is the liquid-free region.

Figs. 13 and 14 illustrate the time-averaged radial distribution of gas holdup and liquid axial velocity. For the simulation using the uniform inlet condition, the gas holdup profile appears to be rather flat and the gas holdup is over-predicted, and the liquid axial velocity is under-predicted at the centre, which suggests that the uniform inlet boundary is not adequate to fully reflect the flow characteristics in the large-diameter bubble column. For the simulation using the new inlet model, the radial distribution of gas holdup and liquid axial velocity is in better agreement with experimental data. The difference may be attributed to the velocity gradients caused by these two inlet models. The practical velocity gradient can be reasonably reflected in the new inlet model but neglected in the uniform inlet condition. In the latter case, additional radial force models may be required to recover the effects caused by the practical velocity gradient, e.g., tuning the lift coefficient.

In order to further test the new inlet model in the modelling of large-diameter bubble columns, the experimental system of Menzel et al. (1990) with a column diameter of 600 mm was simulated. The superficial gas velocity is 0.072 m/s. The simulation results of local gas holdup profiles along with the experiment data are illustrated in Fig. 15. The above two cases demonstrated that the new inlet model is also suitable for bubble columns with large diameters.

5. Conclusions

A new inlet model was proposed to approximate the effects caused by flow conditions and distributor geometries, and validated by the experiments in literature for the three bubble columns with diameters of 0.138 m, 0.44 m or 0.6 m. The simulation demonstrates that the uniform inlet boundary condition is inadequate in the prediction of both total and local gas holdup, in particular for higher gas flow rates, when the non-drag forces are not included in the simulation. The new inlet model is able to achieve the same level of accuracy as the hole case in which the full geometry of gas distributors is modelled. This is because the new inlet model can reasonably allocate the momentum onto the cross-section by the distribution functions proposed, and the effects of real geometries of distributors are considered as the parameters in the new inlet model. The new model is suitable for the simulation of both lab-scale and large size bubble column reactors, and able to reasonably predict the gas holdup profiles for different superficial gas velocities when the DBS drag model is used. The number of mesh cells can be reduced by approximately 10 times compared to the hole case, which is of practical significance for the simulation of industrial scale reactors.

Acknowledgements

The authors wish to thank the long-term support from National Natural Science Foundation of China (NSFC) (Grant nos. 91434121 and 91534118) and Ministry of Science and Technology of China (Grant no. 2013BAC12B01). Weibin Shi would also like to acknowledge the Ph.D. scholarship of the International Doctoral Innovation Centre (IDIC) of University of Nottingham Ningbo China and the support of EPSRC (Grant no. EP/G037345/1).

References

Akhtar, M.A., Tade, M.O., Pareek, V.K., 2006. Two-fluid Eulerian simulation of bubble column reactors with distributors. J. Chem. Eng. Jpn. 39, 831–841.
Bahadori, F., Rahimi, R., 2007. Simulations of gas distributors in the design of shallow bubble column reactors. Chem. Eng. Technol. 30, 443–447.
Bao, D., Zhang, X., Dong, H.F., Ouyang, Z.L., Zhang, X.P., Zhang, S.J., 2015. Numerical simulations of bubble behavior and mass transfer in CO_2 capture system with ionic liquids. Chem. Eng. Sci. 135, 76–88.
Behkish, A., Lemoine, R., Oukaci, R., Morsi, B.I., 2006. Novel correlations for gas holdup in large-scale slurry bubble column reactors operating under elevated pressures and temperatures. Chem. Eng. J. 115, 157–171.
Bordel, S., Mato, R., Villaverde, S., 2006. Modeling of the evolution with length of bubble size distributions in bubble columns. Chem. Eng. Sci. 61, 3663–3673.
Camarasa, E., Vial, C., Poncin, S., Wild, G., Midoux, N., Bouillard, J., 1999. Influence of coalescence behaviour of the liquid and of gas sparging on hydrodynamics and bubble characteristics in a bubble column. Chem. Eng. Process. 38, 329–344.
Chen, J.H., Yang, N., Ge, W., Li, J.H., 2009. Modeling of regime transition in bubble columns with stability condition. Ind. Eng. Chem. Res. 48, 290–301.
Chen, J.W., Li, F., Degaleesan, S., Gupta, P., Al-Dahhan, M.H., Dudukovic, M.P., Toseland, B.A., 1999. Fluid dynamic parameters in bubble columns with internals. Chem. Eng. Sci. 54, 2187–2197.
Chen, P., Dudukovic, M.P., Sanyal, J., 2005a. Three-dimensional simulation of bubble column flows with bubble coalescence and breakup. AIChE J. 51, 696–712.
Chen, P., Sanyal, J., Dudukovic, M.P., 2005b. Numerical simulation of bubble columns flows: effect of different breakup and coalescence closures. Chem. Eng. Sci. 60, 1085–1101.
Deckwer, W.D., 1992. Bubble Column Reactors. Wiley, Chichester, UK.
Deen, N.G., Solberg, T., Hjertager, B.H., 2000. Numerical simulation of gas–liquid flow in a square cross section bubble column, in: Proceedings of the 14th International congress of chemical and process engineering (CHISA), Praha, Czech Republic.
Deen, N.G., Solberg, T., Hjertager, B.H., 2001. Large eddy simulation of the gas-liquid flow in a square cross-sectioned bubble column. Chem. Eng. Sci. 56, 6341–6349.
Delnoij, E., Lammers, F.A., Kuipers, J.A.M., vanSwaaij, W.P.M., 1997. Dynamic simulation of dispersed gas-liquid two-phase flow using a discrete bubble model. Chem. Eng. Sci. 52, 1429–1458.
Dhotre, M.T., Joshi, J.B., 2007. Design of a gas distributor: three-dimensional CFD simulation of a coupled system consisting of a gas chamber and a bubble column. Chem. Eng. J. 125, 149–163.
Guan, X.P., Gao, Y.X., Tian, Z., Wang, L.J., Cheng, Y.W., Li, X., 2015. Hydrodynamics in bubble columns with pin-fin tube internals. Chem. Eng. Res. Des. 102, 196–206.
Haque, M.W., Nigam, K.D.P., Joshi, J.B., 1986. Optimum gas sparger design for bubble-columns with a low height-to-diameter ratio. Chem. Eng. J. Biochem. Eng. J. 33, 63–69.
Hills, J.H., 1974. Radial nonuniformity of velocity and voidage in a bubble column. Trans. Inst. Chem. Eng. 52, 1–9.
Hunt, J.C.R., Auton, T.R., Sene, K., Thomas, N.H., Kowe, R., 1987. ICHMT Int Seminar on Transient Phenomena in Multiphase Flow., Dubrovnik, Yugoslavia, pp. 103–125.
Krishna, R., van Baten, J.M., 2001. Eulerian simulations of bubble columns operating at elevated pressures in the churn turbulent flow regime. Chem. Eng. Sci. 56,

6249–6258.
Laborde-Boutet, C., Larachi, F., Dromard, N., Delsart, O., Schweich, D., 2009. CFD simulation of bubble column flows: investigations on turbulence models in RANS approach. Chem. Eng. Sci. 64, 4399–4413.
Larachi, F., Desvigne, D., Donnat, L., Schweich, D., 2006. Simulating the effects of liquid circulation in bubble columns with internals. Chem. Eng. Sci. 61, 4195–4206.
Li, G., Yang, X.G., Dai, G., 2009. CFD simulation of effects of the configuration of gas distributors on gas-liquid flow and mixing in a bubble column. Chem. Eng. Sci. 64, 5104–5116.
Li, W.L., Zhong, W.Q., 2015. CFD simulation of hydrodynamics of gas-liquid-solid three-phase bubble column. Powder Technol. 286, 766–788.
Lucas, D., Tomiyama, A., 2011. On the role of the lateral lift force in poly-dispersed bubbly flows. Int. J. Multiph. Flow. 37, 1178–1190.
Lucas, D., Prasser, H.M., Manera, A., 2005. Influence of the lift force on the stability of a bubble column. Chem. Eng. Sci. 60, 3609–3619.
Lucas, D., Rzehak, R., Krepper, E., Ziegenhein, T., Liao, Y., Kriebitzsch, S., Apanasevich, P., 2016. A strategy for the qualification of multi-fluid approaches for nuclear reactor safety. Nucl. Eng. Des. 299, 2–11.
Masood, R.M.A., Rauh, C., Delgado, A., 2014. CFD simulation of bubble column flows: an explicit algebraic Reynolds stress model approach. Int. J. Multiph. Flow 66, 11–25.
Menzel, T., Weide, T.I.D., Staudacher, O., Wein, O., Onken, U., 1990. Reynolds shear-stress for modeling of bubble column reactors. Ind. Eng. Chem. Res. 29, 988–994.
Mudde, R.F., Harteveld, W.K., van den Akker, H.E.A., 2009. Uniform flow in bubble columns. Ind. Eng. Chem. Res. 48, 148–158.
Rampure, M.R., Kulkarni, A.A., Ranade, V.V., 2007. Hydrodynamics of bubble column reactors at high gas velocity: experiments and computational fluid dynamics (CFD) Simulations. Ind. Eng. Chem. Res. 46, 8431–8447.
Rampure, M.R., Mahajani, S.M., Ranade, V.V., 2009. CFD simulation of bubble columns: modeling of nonuniform gas distribution at sparger. Ind. Eng. Chem. Res. 48, 8186–8192.
Ranade, V.V., Tayalia, Y., 2001. Modelling of fluid dynamics and mixing in shallow bubble column reactors: influence of sparger design. Chem. Eng. Sci. 56, 1667–1675.
Rigopoulos, S., Jones, A., 2003. A hybrid CFD – reaction engineering framework for multiphase reactor modelling: basic concept and application to bubble column reactors. Chem. Eng. Sci. 58, 3077–3089.
Sankaranarayanan, K., Sundaresan, S., 2002. Lift force in bubbly suspensions. Chem. Eng. Sci. 57, 3521–3542.
Sokolichin, A., Eigenberger, G., 1999. Applicability of the standard k-epsilon turbulence model to the dynamic simulation of bubble columns: part I. Detailed numerical simulations. Chem. Eng. Sci. 54, 2273–2284.
Sokolichin, A., Eigenberger, G., Lapin, A., 2004. Simulation of buoyancy driven bubbly flow: established simplifications and open questions. AIChE J. 50, 24–45.
Tabib, M.V., Roy, S.A., Joshi, J.B., 2008. CFD simulation of bubble column - An analysis of interphase forces and turbulence models. Chem. Eng. J. 139, 589–614.
Tomiyama, A., 1998. Struggle with computational bubble dynamics. Multiph. Sci. Technol. 10 (4), 369–405.
Troshko, A.A., Zdravistch, F., 2009. CFD modeling of slurry bubble column reactors for Fisher-Tropsch synthesis. Chem. Eng. Sci. 64, 892–903.
Van Baten, J.M., Krishna, R., 2004. Scale effects on the hydrodynamics of bubble columns operating in the heterogeneous flow regime. Chem. Eng. Res. Des. 82, 1043–1053.
Wang, T.F., Wang, J.F., Jin, Y., 2006. A CFD-PBM coupled model for gas-liquid flows. AlChE J. 52, 125–140.
Wang, Q.G., Yao, W., 2016. Computation and validation of the interphase force models for bubbly flow. Int. J. Heat Mass Transfer 98, 799–813.
Wiemann, D., Mewes, D., 2005. Calculation of flow fields in two and three-phase bubble columns considering mass transfer. Chem. Eng. Sci. 60, 6085–6093.
Xiao, Q., Yang, N., Li, J., 2013. Stability-constrained multi-fluid CFD models for gas–liquid flow in bubble columns. Chem. Eng. Sci. 100, 279–292.
Yang, N., 2012. A multi-scale framework for CFD modelling of multi-phase complex systems based on the EMMS approach. Prog. Comput. Fluid Dyn. 12, 220–229.
Yang, N., Chen, J.H., Zhao, H., Ge, W., Li, J.H., 2007. Explorations on the multi-scale flow structure and stability condition in bubble columns. Chem. Eng. Sci. 62, 6978–6991.
Yang, N., Wu, Z.Y., Chen, J.H., Wang, Y.H., Li, J.H., 2011. Multi-scale analysis of gas-liquid interaction and CFD simulation of gas-liquid flow in bubble columns. Chem. Eng. Sci. 66, 3212–3222.
Zhang, D., Deen, N.G., Kuipers, J.A.M., 2006. Numerical simulation of the dynamic flow behavior in a bubble column: a study of closures for turbulence and interface forces. Chem. Eng. Sci. 61, 7593–7608.
Ziegenhein, T., Rzehak, R., Krepper, E., Lucas, D., 2013. Numerical simulation of polydispersed flow in bubble columns with the inhomogeneous multi-size-group model. Chem. Ing. Tech. 85, 1080–1091.

Chemical Engineering Science 187 (2018) 391–405

Contents lists available at ScienceDirect

Chemical Engineering Science

journal homepage: www.elsevier.com/locate/ces

Modelling of breakage rate and bubble size distribution in bubble columns accounting for bubble shape variations

Weibin Shi [a], Jie Yang [b], Guang Li [a], Xiaogang Yang [a,*], Yuan Zong [c], Xinyue Cai [a]

[a] Department of Mechanical, Materials and Manufacturing Engineering, The University of Nottingham Ningbo China, University Park, Ningbo 315100, PR China
[b] School of Mathematical Sciences, The University of Nottingham Ningbo China, University Park, Ningbo 315100, PR China
[c] State Key Laboratory of Chemical Engineering, East China University of Science and Technology, Shanghai 200237, PR China

HIGHLIGHTS

- A modified model for prediction of bubble breakage rate was proposed.
- Variation of bubble shapes and different energy requirements were considered.
- Impact of bubble orientation on eddy-bubble collision process was considered.
- Effect of the bubble breakage on the change of bubble interfacial area was demonstrated.

GRAPHICAL ABSTRACT

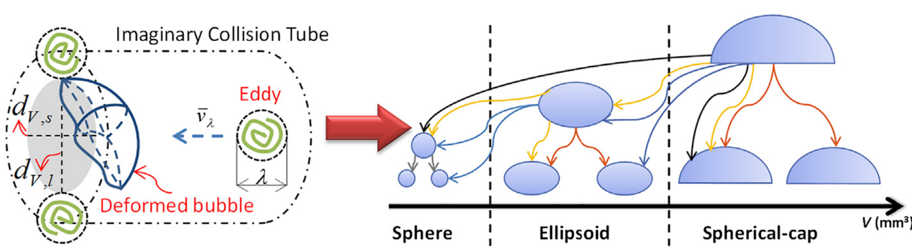

ARTICLE INFO

Article history:
Received 11 January 2018
Received in revised form 6 May 2018
Accepted 8 May 2018

Keywords:
CFD simulation
Bubble column
Breakup model
Bubble shapes
Breakage criterion

ABSTRACT

In the study of meso-scale structures of multi-phase flow in bubble columns, accurate modelling of the interaction between the turbulence eddies and particle/bubble groups is crucial for capturing the heat and mass transfer occurring between the bubbles and surrounding carrier fluid. This work focuses on the influence of bubble shape variations on bubble breakage due to the eddy collision with the bubbles in bubble column flows. An improved breakage model accounting for the variation of bubble shapes was proposed. The improved breakage model coupled with the widely adopted isotropic, homogeneous turbulence kinetic energy spectrums, that are currently available from the open literature, takes into account the different energy requirements in forming the daughter bubbles, i.e. the increase of in surface energy and the pressure head difference of the bubble and its surrounding turbulent eddies. The simulation results compared with experimental data have clearly demonstrated that the improved model effectively describes the various shapes of bubble breakage events, which may consequently have a strong impact on the interfacial area estimation that is crucial for calculation of the transfer rates of mass and heat transfer in the bubble columns.

1. Introduction

Bubble columns are widely used as multiphase contactors for carrying out gas-liquid reactions in chemical, petrochemical, biochemical, pharmaceutical and metallurgical industries, primarily because of the low costs involved in the construction, operation and maintenance process. In addition, bubble columns exhibit excellent heat and mass transfer characteristics, typically due to the increase of interface contact areas. In spite of their simplicity in mechanical design, fundamental properties of the two-phase hydrodynamics associated with the performance of bubble column reactors that are essential for scale-up and process optimisation, are still not fully understood because of the complex nature of multiphase flow, especially the continuous variations and deformation of bubble shapes in the process of bubble rising up through the bubble column.

* Corresponding author.
E-mail address: Xiaogang.Yang@nottingham.edu.cn (X. Yang).

https://doi.org/10.1016/j.ces.2018.05.013

Nomenclature

a	long half axis length of an ellipse, m
c	short half axis length of an ellipse, m
C_D	effective drag coefficient for a bubble around a swarm, dimensionless
D	bubble column diameter, m
d	bubble diameter, m
d_{eq}	equivalent bubble diameter, m
d_V	length of virtual axis, m
Eo	Eötvös number, dimensionless
$\bar{e}$	mean turbulence kinetic energy, kg·m^2/s^2
e_s	increase in surface energy, kg·m^2/s^2
F_D	drag force, N/m^3
F_{Lift}	lift force, N/m^3
F_{VM}	virtual mass force, N/m^3
f_V	breakage volume fraction, dimensionless
g	gravity acceleration, m/s^2
H	distance from the bottom surface, m
k	turbulence kinetic energy, m^2/s^2
Mo	Morton number, dimensionless
n	number density per unit volume, m^{-3}
t	time, s
Rc	radius of curvature, m
Re	Reynolds number, dimensionless
S	surface area, m^2
U	superficial velocity, m/s
U_t	terminal velocity, m/s
$\bar{u}_\lambda$	mean velocity of turbulence eddies, m/s
u	velocity vector, m/s
V	volume, m^3

Greek letters

α	phase volume fraction, gas holdup
ε	turbulence dissipation rate, m^2/s^3
λ	characteristic length scale of eddy, m
μ	molecular dynamic viscosity, Pa·s
μ_{eff}	effective turbulence dynamic viscosity, Pa·s
υ	kinematic viscosity, m^2/s
ρ	fluid density, kg/m^3
σ	surface tension, N/m
τ	shear stress, Pa

Subscripts

b	bubble
g	gas
i	i-th class bubble
j/k	daughter bubble
l	liquid/long axis
s	short axis/surface

The flow regime is one of the most fundamental studies in the bubble columns, because the flow characteristics are strongly related to the prevailing flow regime. In general, the flow regime in bubble columns can be classified as homogeneous regime, transition regime, heterogeneous regime and slug flow regime (Shah et al., 1982). For fermentation process or cell culturing purposes, the bubble column usually operates at homogeneous regime. The homogeneous flow regime can be further distinguished into the mono-dispersed homogeneous regime and the poly-dispersed homogeneous flow regime, depending on the superficial velocities and the associated bubble size distributions (Besagni and Inzoli, 2016b). The mono-dispersed homogeneous regime may not exist if the large bubbles are aerated due to large diameter orifices on the sparger (Besagni and Inzoli, 2016a). The transition flow regime is characterized by large flow macro-structures with large eddies and a widened bubble size distribution (Guedon et al., 2017), in which case, the turbulent eddies induced by the "coalescence-induced" large bubbles may make increasingly significant contributions to the turbulence generated in the column.

The time-dependent behaviour of flow patterns and features inside the bubble column are significantly influenced by the rising bubbles based on the experimental observations reported in the open literature (Pourtousi et al., 2014). The bubbles induce the turbulence through the wake and interactions among the bubbles. These should be taken into account in CFD modelling of bubble column flows and the differences between different simulation methods have to be considered. Two major CFD modelling approaches currently adopted are the *Eulerian-Lagrangian* (E-L), which considers the dispersed phase as discrete entities (Delnoij et al., 1997; Sokolichin et al., 1997; Xue et al., 2017a, 2017b), and the *Eulerian-Eulerian* (E-E), which describes the dispersed phase as interpenetrating the continuous phase (Krishna et al., 1999; Lehr et al., 2002). It has been recognised that the use of both numerical approaches can lead to reliable prediction results only when the appropriate modelling for bubble induced fluid motion are introduced. The E-E approach usually relies on the closure models that describe the gas–liquid interphase transport phenomena through a certain averaging. In the meantime, the associated closure models need to consider the effect of turbulence induced by bubble motions, the interphase momentum exchange caused by interactions between the gas-liquid two phases, and the bubbles size distribution, while these are closely related to the turbulence and the interphase interaction forces. A number of CFD studies have been conducted to assess the suitability of various turbulence models for CFD bubble columns (Laborde-Boutet et al., 2009; Masood et al., 2014; Sokolichin and Eigenberger, 1999; Tabib et al., 2008; Zhang et al., 2006) and the effect of interphase interactions (Li and Zhong, 2015; Pourtousi et al., 2014; Rzehak and Krepper, 2013; Xiao et al., 2013; Yang et al., 2011). The interphase interactions can be assumed to be induced through the composition of various forces such as the drag force that liquid exerts on the bubble surface due to viscosity (Deen et al., 2000; Krishna and van Baten, 2001; Ranade and Tayalia, 2001), the lift force which is caused by the shear flow around the bubbles and the virtual mass force due to the local acceleration (Deen et al., 2001; Delnoij et al., 1997; Lucas et al., 2005; Lucas and Tomiyama, 2011; Rampure et al., 2007; Sankaranarayanan and Sundaresan, 2002; Sokolichin et al., 2004; Tabib et al., 2008; Tomiyama, 1998; Zhang et al., 2006). These previous CFD studies on bubble column flow often employed the assumption of a unified bubble diameter, which can only generate reliable predictions when the bubble size is narrowly distributed. However, CFD modelling of gas-liquid two-phase flow behaviours has to take into account the bubble size distributions and the bubble-bubble interactions because these are very influential factors in the calculation of the gas-liquid interfacial area. There are different ways to consider the effect of bubble sizes. For example, based on Krishna and van Baten (2001), Guedon et al. (2017) explicitly classifies the bubbles into two groups in the simulations. On the contray, Xiao et al. (2017) and Zhou et al. (2017) have applied the energy minimisation multi-scale EMMS based Dual-Bubble-Size DBS drag model, which implicitly considered the bubble sizes and shapes by using a lumping coefficient C_D/d_B to replace the traditional drag coefficient closure. Also, a more direct way is to derive the bubble size distributions from the population balance equations (PBE) with the bubble-bubble and eddy-bubble interactions being controlled by bubble coalescence and breakup models. As the suitable prediction of the bubble breakage rate is critical when using the PBE to decide the bubble size distribution especially when mass transfer between two phase interface is concerned, it becomes clear that a reliable model for estimation of breakage rate accounting for bubble shape variations is desirable for CFD modelling of bubble column flows.

For the bubble breakup process, Coulaloglou and Tavlarides (1977) assumed that the breakup process would occur if the energy carried by turbulent eddies impacting on the bubble is more than the surface energy contained by the bubble. Prince and Blanch (1990) acknowledged bubble breakup is caused by eddy-bubble collision but they proposed that bubble breakup can only be induced by eddies with approximately the same characteristic size as the bubbles. Eddies at a much larger length scale only transport the bubbles without causing breakage. Luo and Svendsen (1996) described the bubble breakup by considering both the length scale and the amount of energy contained by the arriving eddies. The minimum length scale of eddies that are responsible for breakup equals to 11.4 times those eddies corresponding to the dissipation with the Kolmogorov scale. The probability for bubble breakup is related to the critical ratio of surface energy increase of bubbles after breakup and the mean turbulent kinetic energy of the colliding eddies. When applying their model, it was found that very small eddies do not contain sufficient energy to cause the bubble breakup. Lehr et al. (2002) proposed a slightly different breakup mechanism from that proposed by Luo and Svendsen (1996). They considered the minimum length scale of eddies to be determined by the size of the smaller bubble after breakup, and the breakup process to be dependent on the inertial force of the arriving eddy and the interfacial force acting on the bubble. Based on the results of Luo and Svendsen (1996) and Lehr et al. (2002), Wang et al. (2003) proposed the model for bubble breakup, for which the constraints both the energy and the capillary pressure are imposed. The energy constraint requires the eddy energy to be greater than or equal to the increase of surface energy of bubbles after the breakage. The capillary constraint requires the dynamic pressure of the arriving eddy to exceed the capillary pressure of the bubble. The use of these two breakup criteria restricted the minimum size of the bubbles that can break, and hence yielded results in accordance with practical observations that were more interpretable than those obtained using Luo and Svendsen (1996). These two breakup criteria have also been adopted and extended in the recent studies reported by Zhao and Ge (2007) and Liao et al. (2015). Based on these previous work, Qin et al. (2016) and Yang and Xiao (2017) have developed EMMS-PBM model and successfully employed into CFD simulations of liquid-liquid and gas-liquid systems. The EMMS-PBM model features the use of a minimised micro-scale energy dissipation as the stability constraint and provides a unique way to close the equilibrium state of coalescence and breakage kernels of bubbles or drops.

As discussed above, the surface of bubbles may subject to different forces as they are exposed to the turbulent eddies. The deformation of bubble shapes has a fundamental impact on the estimation of the interfacial area of bubbles. In return, this will have major implications when applying the population balance model for CFD modelling of bubble coalescence and breakage. Few studies have considered the bubble shapes in bubble column CFD modelling especially for the cases of large elliptical or cap bubbles. Clark (1988) proposed a model to describe the deformation and surface oscillation of droplets. The model assumed the motion of the mass centre of the deformed drop to be acted by those interfacial forces. However, the model did not include the buoyancy force and added mass, which occurs when the drop or bubble accelerates relative to the continuous phase. For a gas-liquid system such as bubble columns, added mass force and buoyancy force are dominant factors and have to be taken into account. Han et al. (2016) considered the surface deformation and oscillation of bubble to be axisymmetric, i.e. the dynamics of bubble are formulated based on the motion of the centre of mass of the half bubble, and all interfacial forces act upon the centre of mass similar to the analogy of a translational mechanical system with a spring linking two parts with equal mass. This treatment method is still constrained to the cases of ellipsoidal bubbles without considering the actual shapes of the bubbles.

The aim of this paper is to consider the influence of bubble shape variations on bubble breakage in bubble column flows. A breakage model accounting for the variation of bubble shapes will be proposed, coupled with the breakage criterion of energy density increase during the entire breakup process. Section 2 will present the mathematical modelling adopted in the current study while Section 3 will present the simulation results and discussion, focusing on the effect of considering the bubble shape variations on the prediction of key parameters including gas holdup, bubble number density and interfacial area. Section 4 will present the conclusions derived from the study.

2. Mathematical modelling

2.1. Governing equations

A 3D transient CFD model is used in this work to simulate the local hydrodynamics of the gas-liquid two-phase bubble column. A Eulerian-Eulerian approach is adopted to describe the flow behaviours for both phases, i.e. water as the continuous phase, and air as the dispersed phase. The mass and momentum balance equations are given by Eqs. (1) and (2) respectively,

$$\frac{\partial(\rho_k \alpha_k)}{\partial t} + \nabla(\rho_k \alpha_k \mathbf{u}_k) = 0 \tag{1}$$

$$\frac{\partial(\rho_k \alpha_k \mathbf{u}_k)}{\partial t} + \nabla(\rho_k \alpha_k \mathbf{u}_k \mathbf{u}_k) = -\alpha_k \nabla p + \nabla \cdot \tau \equiv_k + \alpha_k \rho_k \mathbf{g} + \mathbf{F}_k \tag{2}$$

where ρ_k, α_k, $\mathbf{u}_k$, $\tau \equiv_k$, and $\mathbf{F}_k$ represent the density, volume fraction, velocity vector, viscous stress tensor and the inter-phase momentum exchange term for the k (liquid or gas) phase respectively. The sum of the volume fractions for both phases is equal to 1.

2.2. Interphase momentum transfer

In this study, drag force, lift force and added mass force are considered as the main interactions between the continuous liquid phase and the dispersed gas phase. The drag force is calculated using Eq. (3),

$$\mathbf{F}_D = \frac{3}{4}\frac{C_D}{d_{eq}}\rho_l \alpha_g |\mathbf{u}_g - \mathbf{u}_l|(\mathbf{u}_g - \mathbf{u}_l) \tag{3}$$

where C_D is the drag coefficient, which can be obtained from the model by Grace et al. (1978). The Grace model is well suited for gas-liquid flows in which the bubbles exhibit a range of shapes, such as sphere, ellipsoid, and spherical-cap. However, instead of comparing the values of drag coefficients in the original Grace model, the drag coefficient can be applied directly according to the actual types of bubbles, as the variation of bubble shapes has been considered in the breakup model. The drag coefficients for different shapes of bubbles are calculated using Eqs. (4)–(6),

$$C_{D,sphere} = \begin{cases} 24/Re_b & Re_b < 0.01 \\ 24(1 + 0.15Re_b^{0.687})/Re_b & Re_b \geqslant 0.01 \end{cases} \tag{4}$$

$$C_{D,cap} = \frac{8}{3} \tag{5}$$

$$C_{D,ellipse} = \frac{4}{3}\frac{gd_{eq}}{U_t^2}\frac{(\rho_l - \rho_g)}{\rho_l} \quad (6)$$

where Re_b is the bubble Reynolds number given by $R_{eb} = \frac{\rho_l|\boldsymbol{u}_g - \boldsymbol{u}_l|d_{eq}}{\mu_l}$. U_t is the terminal velocity, calculated using the following relation given by Eq. (7),

$$U_t = \frac{\mu_l}{\rho_l d} Mo^{-0.149}(J - 0.857) \quad (7)$$

where Mo is the Morton number defined by $Mo = \frac{\mu_l^4 g(\rho_l - \rho_g)}{\rho_l^2 \sigma^3}$. J is given by the piecewise function, calculated using the empirical expression (8).

$$J = \begin{cases} 0.94H^{0.757} & 2 < H < 59.3 \\ 3.42H^{0.441} & H > 59.3 \end{cases} \quad (8)$$

H in expression (6) is defined by Eq. (9),

$$H = \frac{4}{3} Eo Mo^{-0.149}\left(\frac{\mu_l}{\mu_{ref}}\right)^{-0.14} \quad (9)$$

where Eo is the Eötvös number and $\mu_{ref} = 0.0009\ \mathrm{kg/(m \cdot s)}$.

The lift force acting perpendicularly to the direction of relative motion of the two phases can be calculated by using Eq. (10).

$$\boldsymbol{F}_{Lift} = C_L \rho_l \alpha_g (\boldsymbol{u}_g - \boldsymbol{u}_l) \times (\nabla \times \boldsymbol{u}_l) \quad (10)$$

where C_L is the lift coefficient and is estimated by the Tomiyama lift force correlation (Tomiyama, 1998), as described by the following empirical relation (11),

$$C_L = \begin{cases} \min[0.288\tanh(0.121Re_b), f(Eo')] & Eo' \leqslant 4 \\ f(Eo') & 4 < Eo' < 10 \\ -0.29 & Eo' > 10 \end{cases} \quad (11)$$

where $f(Eo') = 0.00105Eo'^3 - 0.0159Eo'^2 - 0.0204Eo' + 0.474$. Eo' is the modified Eötvös number based on the maximum horizontal dimension of the deformable bubble, d_h, as defined and given respectively by Eqs. (12) and (13).

$$Eo' = \frac{g(\rho_l - \rho_g)d_h^2}{\sigma} \quad (12)$$

$$d_h = d(1 + 0.163Eo^{0.757})^{1/3} \quad (13)$$

The virtual mass force is also significant when the gas phase density is much smaller than the liquid phase density. The virtual mass force will be applied to the bubbles when the inertia of the liquid phase mass encounters the accelerating bubbles. The virtual mass force can be calculated using Eq. (14),

$$\boldsymbol{F}_{VM} = C_{VM}\rho_l \alpha_g \left(\frac{d_l \boldsymbol{u}_l}{dt} - \frac{d_l \boldsymbol{u}_g}{dt}\right) \quad (14)$$

where C_{VM} is the virtual mass coefficient. It should be noted with caution that the virtual mass coefficient may also be altered in accordance with the bubble shapes. The influence of the bubble shape variations on the virtual mass coefficient may require further investigation, and hence a common value of 0.5 is defined in this study.

2.3. Turbulence modelling

The turbulence generated in the bubble column can be thought of being the joint superposition of shear turbulence and bubble induced turbulence, which is mainly influenced by the wake formed by shedding vortices from the bubbles and decays quickly due to the viscos dissipation. However, bubble induced turbulence (bubbulence) may strongly interact with the carrier phase turbulence of the main flow. Taking into account the features of turbulence induced by rising bubbles in the bubble column, the standard $k \sim \varepsilon$ turbulence model with the consideration of bubble induced turbulence by Sato and Sekoguchi (1975) is used for turbulence closure. The turbulent kinetic energy k_l and dissipation rate ε_l are computed by Eqs. (15) and (16),

$$\frac{\partial(\boldsymbol{\alpha_l \rho_l k_l})}{\partial t} + \nabla \cdot (\boldsymbol{\alpha_l \rho_l k_l u_k}) = \boldsymbol{\nabla} \cdot \left[\boldsymbol{\alpha_l}\left(\boldsymbol{\mu_l} + \frac{\boldsymbol{\mu_{eff,l}}}{\boldsymbol{\sigma_k}}\right)\boldsymbol{\nabla k_l}\right] + \boldsymbol{\alpha_l}(\boldsymbol{G_{k,l}} - \boldsymbol{\rho_l \varepsilon_l}) \quad (15)$$

$$\frac{\partial(\boldsymbol{\alpha_l \rho_l \varepsilon_l})}{\partial t} + \boldsymbol{\nabla} \cdot (\boldsymbol{\alpha_l \rho_l \varepsilon_l u_k}) = \nabla \cdot \left[\boldsymbol{\alpha_l}\left(\boldsymbol{\mu_l} + \frac{\boldsymbol{\mu_{eff,l}}}{\boldsymbol{\sigma_k}}\right)\nabla \boldsymbol{\varepsilon_l}\right] + \boldsymbol{\alpha_l}\frac{\boldsymbol{\varepsilon_l}}{\boldsymbol{k_l}} \times (\boldsymbol{C_{1\varepsilon} G_{k,l}} - \boldsymbol{C_{2\varepsilon}\rho_l \varepsilon_l}) \quad (16)$$

where $G_{k,l}$ is the production of turbulent kinetic energy given by Eq. (17).

$$G_{k,l} = \tau_l : \nabla \boldsymbol{u}_l \quad (17)$$

The effective viscosity is composed of the contributions of turbulent viscosity and an extra term considering the effect of bubble induced turbulence and is defined by Eq. (18).

$$\mu_{eff,l} = \rho_l C_\mu \frac{k_l^2}{\varepsilon_l} + \rho_l C_{\mu,BIT}\alpha_g d_b |\boldsymbol{u}_g - \boldsymbol{u}_l| \quad (18)$$

The Sato coefficient used is $C_{\mu,BI}$ = 0.6. In this work, the standard $k \sim \varepsilon$ model constants used are C_μ = 0.09, $C_{1\varepsilon}$ = 1.44, $C_{2\varepsilon}$ = 1.92, σ_k = 1.0, σ_ε = 1.3.

2.4. Bubble size distribution

The bubble size distribution is determined by using the population balance model with consideration of bubble coalescence and breakup. Bubbles are divided into several size groups with different shapes of equivalent diameters $d_{eq,i}$ and an equivalent phase with the Sauter mean diameter d_{32}, to represent the bubble classes. Sixteen bubble classes with equivalent diameters ranging from 1 to 32 *mm* are applied based on the geometric discretization method such that $V_i = 2V_{i-1}$. The population balance equation is expressed by Eq. (19),

$$\frac{\partial n_i}{\partial t} + \nabla \cdot (\tilde{\boldsymbol{u}}_i \cdot n_i) = S_i \quad (19)$$

where n_i is the number density for i-th group, $\tilde{u}_i$ is the mass average velocity vector, and S_i is the source term.

The source term, S_i, for the i-th group can be expressed as birth and death of bubbles due to coalescence and breakup respectively, given by Eq. (20).

$$S_i = B_{coalescence,\ i} - D_{coalescence,\ i} + B_{breakup,\ i} - D_{breakup,\ i} = \sum_{d_{eq,j}=d_{eq,\min}}^{d_{eq,i}/2} \Omega_C(d_{eq,j} : d_{eq,i} - d_{eq,j}) - \sum_{d_{eq,j}}^{d_{eq,\max} - d_{eq,i}} \Omega_C(d_{eq,j} : d_{eq,i}) + \sum_{d_j = d_i}^{d_{\max}} \Omega_B(d_{eq,j} : d_{eq,i}) - \Omega_B(d_{eq,i}) \quad (20)$$

The local gas volume fraction can be calculated by Eq. (21),

$$\alpha_g f_i = n_i V_i \quad (21)$$

where f_i is the i-th class fraction of total volume fraction, and V_i is the volume for the i-th class.

The Sauter mean diameter can be calculated as by using Eq. (22).

$$\frac{1}{d_{32}} = \sum \frac{f_i}{d_{eq,i}} \quad (22)$$

For the coalescence between bubbles of size $d_{eq,i}$ and $d_{eq,j}$, the coalescence kernel used in this work was proposed by Luo (1993), as denoted by Eq. (23).

$$\Omega_C(d_{eq,i} : d_{eq,j}) = \omega_C(d_{eq,i} : d_{eq,j}) p_c(d_{eq,i} : d_{eq,j}) \tag{23}$$

where ω_C is the frequency of collision and p_C is the probability of coalescence due to collision. The frequency is defined by Eq. (24),

$$\omega_C(d_{eq,i} : d_{eq,j}) = n_i n_j \frac{\pi}{4}(d_{eq,i} + d_{eq,j})^2 \bar{u}_{ij} \tag{24}$$

where $\bar{u}_{ij}$ is the characteristic velocity of two collision bubbles, denoted by Eq. (25).

$$\bar{u}_{ij} = (\bar{u}_{d,i}^2 + \bar{u}_{d,j}^2)^{1/2} \tag{25}$$

The characteristic velocity of one individual bubble is given by (26).

$$\bar{u}_{d,i} = 1.43(\varepsilon d_{eq,i})^{1/3} \tag{26}$$

The expression for the probability of coalescence is described using Eq. (27),

$$p_C = \exp\left\{-c_1 \frac{\left[0.75(1+x_{ij}^2)(1+x_{ij}^3)\right]^{1/2}}{(\rho_g/\rho_l + 0.5)^{1/2}(1+x_{ij})^3} We_{ij}^{1/2}\right\} \tag{27}$$

where c_1 is a constant of order unity that usually equals to 1, $x_{ij} = d_{eq,i}/d_{eq,j}$, and the Weber number is defined by Eq. (28).

$$We_{ij} = \frac{\rho_l d_{eq,i} \bar{u}_{ij}^2}{\sigma} \tag{28}$$

The breakup model used in this work is based on the work of Luo and Svendsen (1996). However, several improvements have been introduced for breakage rate prediction to produce more realistic breakup estimation. In Luo and Svendsen's model, the shape of breakage bubbles was assumed to be spherical. However, previous experimental studies have clearly indicated that the bubbles exist in various shapes and the dynamics of bubble motion strongly depend on the shape of bubbles (Grace et al., 1978; Tomiyama, 1998; Tomiyama et al., 1998). Figure demonstrates the experimentally recorded breakup process of a spherical-cap bubble found in an operating bubble column used in an ongoing research project funded by NSFC. The spherical-cap bubble has collided with a bombarding eddy that was shredded from the previous bubbles. The spherical-cap bubble then becomes deformed and distorted and finally breaks into two ellipsoidal bubbles. The bubble shape has been neglected in almost previous studies for the simplification of models. However, the shape of the bubbles could potentially be a critical factor for accurately predicting the flow characteristics of the gas phase in CFD simulations.

From experimental observations (see Fig. 1), the bubble shapes can be classified into different types: spherical, ellipsoidal and spherical-capped. The effects of different bubble shapes will be taken into account in the present study. As a result, an equivalent diameter, d_{eq}, is introduced to represent the size of these bubbles with various shapes. Also, due to the uncertainty of the spatial rotation of the bubbles, the contact angle of the bombarding eddies is very difficult to be determined. Therefore, instead of using the original bubble size d_i to calculate the sweep area of the collision tube, a nominal diameter, d_V, that approximately represents the size of the projected area of the bubble is defined by the following condition,

$$c \leqslant d_V \leqslant a \tag{29}$$

where c and a are the length of the short axis and long axis respectively. It seems that the eddy is more likely to bombards the bubble in the front rather than the rear directions. Therefore, the values of d_V are different in every computational cell when the breakage model is implemented into CFD modelling. The new imaginary collision tube is presented in Fig. 2.

The breakup rate for one individual parent bubble breaking into two daughter bubbles can be calculated, given by Eq. (30),

$$\Omega_B = \int_{\lambda_{\min}}^{d} \omega_B^T p_B \, d\lambda \tag{30}$$

where ω_B^T is the collision probability density which can be estimated from Luo and Svendsen (1996), as originally defined by Eq. (31),

$$\omega_B^T = n_i n_\lambda \frac{\pi}{4}(d_i + \lambda)^2 \bar{v}_\lambda \tag{31}$$

In the original model, the cross-section of the collision tube is circular, no matter the bombarding eddy comes from which direction. However, once the bubble shapes are considered, the cross-section of the new collision tube is the projection of the ellipsoidal or the spherical-capped bubble on the moving direction of the bombarding eddy. Therefore, the collision probability density in the new collision tube can be approximately calculated by Eq. (32),

$$\omega_B^T = n_i n_\lambda \frac{\pi}{4}(d_{V,s} + \lambda)(d_{V,l} + \lambda)\bar{v}_\lambda \tag{32}$$

where $d_{V,s}$ and $d_{V,l}$ denote to the short axis and the long axis of the projected area respectively. By considering the energy balance of the eddies being interpreted as discrete entities and as a spectrum function, the number density of eddies n_λ can be determined and hence the collision probability density becomes Eq. (33),

$$\omega_B^T(\xi) = 0.923(1-\alpha_g)(\varepsilon d_{eq,i})^{1/3} n_i \frac{(d_{V,s}/d_{eq,i} + \xi)(d_{V,l}/d_{eq,i} + \xi)}{d_{eq,i}^2 \xi^{11/3}} \tag{33}$$

where $\xi = \lambda/d_{eq,i}$ is the non-dimensional size of eddies that may contribute to the breakage of bubble size $d_{eq,i}$. The breakage probability function p_B used by Luo and Svendsen (1996) is given by Eq. (34),

$$p_B = \exp\left(-\frac{e_s}{\bar{e}}\right) \tag{34}$$

where $\bar{e}$ is the mean turbulent kinetic energy for eddies of size λ and e_s is the increase in surface energy of bubbles after breakage. The mean turbulent kinetic energy can be determined by Eq. (35).

$$\bar{e} = \rho_l \frac{\pi}{6}\lambda^3 \frac{\bar{u}_\lambda^2}{2} = \frac{\pi\beta}{12}\rho_l(\varepsilon d_{eq,i})^{2/3} d_{eq,i}^3 \xi^{11/3} \tag{35}$$

By assuming the bubbles before and after breakage have deformed shapes with an equivalent diameter, when the parent bubble of size with $d_{eq,i}$ breaks into two bubbles of size $d_{eq,j}$ and $(d_{eq,i}^3 - d_{eq,j}{}^3)^{1/3}$, the increase in surface energy can be estimated using Eq. (36),

$$e_s(d_{eq,i}, d_{eq,j}) = \sigma \cdot \pi d_{eq,i}^2 [f_V^{2/3} + (1-f_V)^{2/3} - 1] \tag{36}$$

where the breakage volume fraction $f_V = d_{eq,j}^3 / d_{eq,i}^3$. However, since the effects of different shapes of bubbles are now taken into account, Eq. (36) has to be re-written in a general form with regards to the surface area, S, of bubbles, which reflects the actual areas of the deformed daughter bubbles as described by Eq. (37).

$$e_s = \sigma \cdot (S_{j,1} + S_{j,2} - S_i) \tag{37}$$

According to the models for bubble shapes proposed by Tomiyama et al. (1998), there are 3 main types that may be considered, including spherical, ellipsoidal and spherical-capped. The details of these 3 types of bubbles and their possible breakage footages are depicted in Fig. 3.

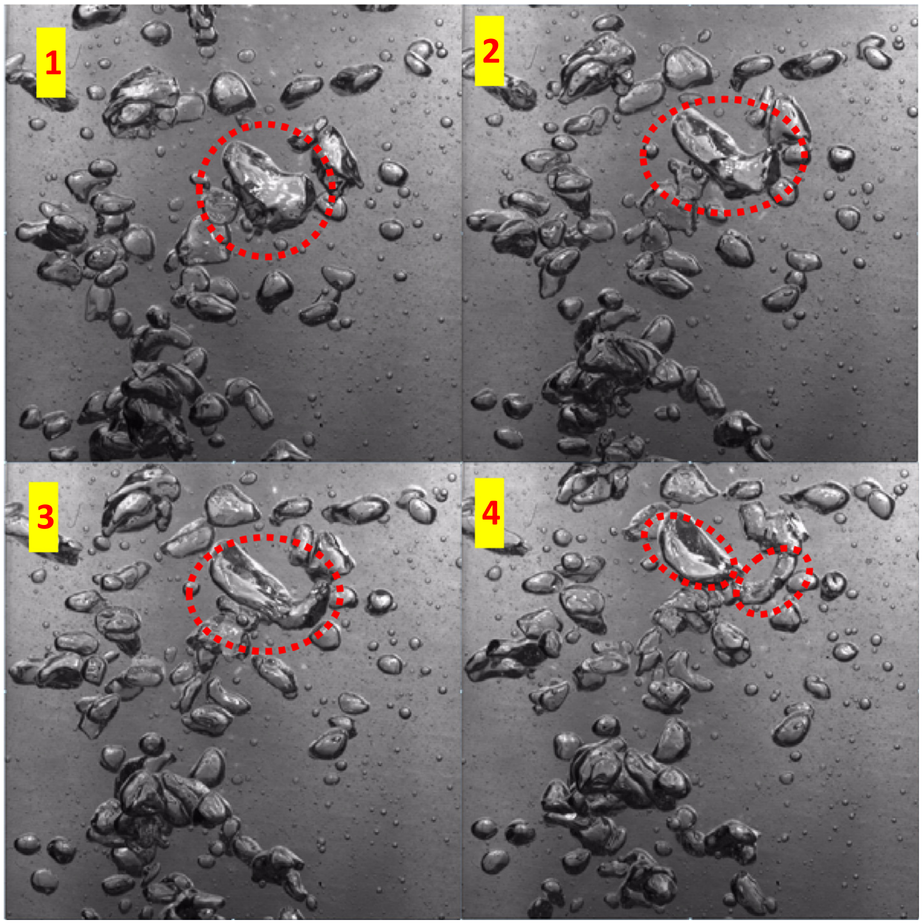

Fig. 1. Time sequences of break-up of a rising bubble in a 150 mm diameter cylindrical bubble column (Ug = 0.02 m/s).

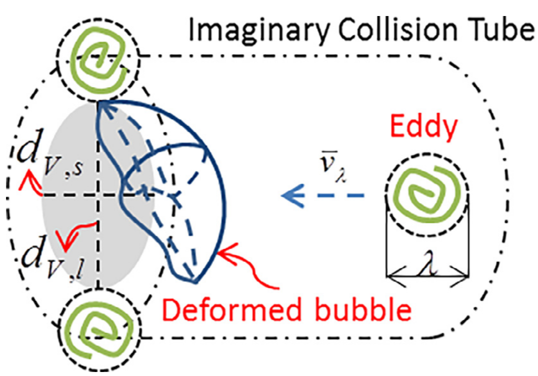

Fig. 2. Sketch of a collision tube of an entering eddy moving through the tube with a mean velocity.

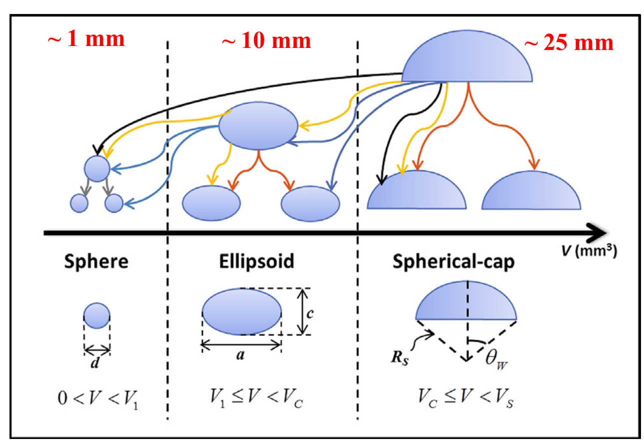

Fig. 3. Classification of 3 types of bubbles and the possible breakage footage.

In order to emphasise that the volume is conserved when spherical bubble in the original model is converted into various shapes, the volume V is used in Fig. 3. However, for readers' convenience, an equivalent diameter d_{eq} is used hereafter while the subscripts remain the same, i.e. $d_{eq,1}$ is the equivalent diameter of V_1. For an air-water system under atmospheric pressure and room temperature, $d_{eq,1}$ is roughly 1.16 mm for the pure system while $d_{eq,1}$ is approximately 1.36 mm for a slightly contaminated system. It is very important to point out that the volumes of ellipsoidal bubbles and spherical-cap bubbles should be equal to the volumes of their equivalent spherical bubbles with diameter d_{eq}. For bubbles with ellipsoidal shapes, by assuming in an oblate type of ellipsoid, as suggested by Batchelor (1967), the surface area can be calculated based on the following expression (38),

$$S_{ellipsoid} = \frac{\pi}{2} d_{eq}^2 E^{2/3} \left(1 + \frac{1}{2E\sqrt{E^2-1}} \ln\left(2E^2 - 1 + 2E\sqrt{E^2-1}\right) \right) \tag{38}$$

where the aspect ratio E can be expressed using an empirical correlation developed on the basis of experimental data of Besagni et al. (2016) and Besagni and Inzoli (2016a). The expression of the aspect ratio is given by Eq. (39). It should be noticed that this correlation has only been validated in air-water dense bubbly flows. To use Eq. (39) for other systems or for different operating conditions, more investigations and validations are strongly required. In addition, more experimental data to extend the discussion about the bubble aspect ratio in low Morton-number systems are described in Besagni et al. (2017).

$$E = \frac{a}{b} = 1 + 4.288 Ga^{-1/3} Eo^{1/2} \tag{39}$$

where Ga and Eo are the Galilei number and Eötvös number respectively, defined by Eqs. (40) and (41).

$$Eo = \frac{g(\rho_l - \rho_g) d_{eq}^2}{\sigma} \tag{40}$$

$$Ga = \frac{\rho_l \sqrt{g d_{eq}} d_{eq}}{\mu_l} \tag{41}$$

The aspect ratio expressed in Eq. (39) to characterise the bubble deformation has been intensively studied by different researchers. Wellek et al. (1966) proposed an empirical correlation to approximate the deformation of bubbles, which is consisted of dimensionless parameters including Weber number We, Reynolds number Re, Eötvös number Eo, Froude number Fr, and the ratio of dynamic viscosity. After a multiple regression process, they found the Eo number is the most important parameter which is able to approximate the bubble deformation in low viscosity systems. The idea of using Eo number to characterise the bubble deformation has been also adopted by Okawa et al. (2003), Tomiyama et al. (2002), Tsuchiya et al. (1990) and Besagni and Inzoli (2016a) among others. Moore (2006) derived an expression of the aspect ratio using the Webber number, based on the balance of the dynamic pressure and the capillary pressure at the bubble nose and side edge, respectively. The idea has also been extended by Sugihara et al. (2007) and Legendre et al. (2012). Some studies on the bubble deformations have attempted to introduce additional dimensionless parameters (Aoyama et al., 2016; Bozzano and Dente, 2001; Clift et al., 1978; Legendre et al., 2012; Tripathi et al., 2015; Tsamopoulos et al., 2008), such as Morton number Mo, Bond Number Bo, Archimedes number Ar and Tadaki number Ta, to correlate the aspect ratio or the conditions to distinguish different deformed bubbles. By carefully inspecting all these dimensionless numbers mentioned above, it can be seen clearly that the most important factors affecting the bubble deformations are mainly buoyancy, surface tension and viscosity. Thus, the dimensionless numbers used to correlate the aspect ratio should at least include these three key factors. The results using the correlation (39) compared with those data from the open literature have been plotted in Fig. 4. It should be noted that the experimental data of the aspect ratio of bubbles greater than approximately 8 mm has rarely been documented. This is probably due to the fact that the experimental errors caused by large deformation and fast-changing of the shapes of large bubbles make it very difficult to determine the averaged aspect ratio. Under such circumstance, an approximation of 0.5 has been used for the aspect ratio of bubbles larger than 6 mm, which ensures the aspect ratio not to be infinitesimally small and the bubbles not able to be flatted without limitation. It can be seen from Fig. 4 that the value of 0.5 is not much deviated from the correlation of Besagni et al. (2017) and also agrees with the experimental data of Wang et al. (2014) It seems that Wellek's correlation, which has been adopted in Tomiyama's lift model, largely overestimates the aspect ratio especially when the bubble diameter is larger than 10 mm. This kind of overestimation means that the bubbles being depicted are extremely flat, which is much less likely to be continuously existed in the bubble column flows. On the contrary, although expressed using different dimensionless parameters, both the correlation by Besagni & Inzoli and the Eq. (39) have shown much better agreements with the experimental data, which makes more sense in describing the bubbles' geometrical characteristics. This is very critical for the CFD modelling of gas-liquid two-phase flows, particularly when the flow characteristics are strongly affected by the bubble deformation and oscillation.

The boundary between ellipsoidal and spherical-cap bubbles, d_C, is estimated using Eq. (42).

$$d_C = \sqrt{40\sigma / g(\rho_L - \rho_g)} \tag{42}$$

where d_c is found to be 17.3 mm for the air-water system. For a single spherical-cap bubble, the wake angle θ_W is assumed to be 50°, following the work of Tomiyama (1998). As the volume of spherical-cap is equivalent to the volume of the equivalent spherical bubble, Eq. (43) can be formulated as follows.

$$R_S^3 = \frac{d_{eq}^3/6}{(1-\cos\theta_W)^2 - (1-\cos\theta_W)^3/3} \tag{43}$$

The curved surface area for the front edge can be calculated using the following relation given by Eq. (44).

$$S_{Cap} = 2\pi R^2 (1 - \cos\theta_W) \tag{44}$$

The experimental observations by Davenport et al. (1967) and Landel et al. (2008) have clearly indicated that the rear surface of a single spherical-cap bubble follows a constantly oscillating lenticular shape, resulting from the external perturbation acting on the rear surface. Such a lenticular shape rear surface can be considered to be essentially flat and the surface energy increase required to break up the rear surface can be neglected based on the consideration that when any arriving eddies bombard to the flat surface, the energy due to the surface tension force action will be far smaller than the kinetic energy carried by the turbulent eddies. The idea of neglecting the surface tension effects of rear surface has also been introduced by early research work of Batchelor (1967), based on a large amount of experimental observations. It should be noted with caution that these are rough approximations and more complicated crown bubble systems are not considered in the present work. The influence of the variation of bubble shapes on the increase in surface energy is further illustrated in Fig. 8.

While the breakup model proposed by Luo and Svendsen (1996) only considered the surface energy requirement for breakup events, it should be noted that bubble breakage may also subject to the pressure head difference of the bubble and its surrounding eddies, especially when the breakage volume fraction is small. Therefore, on the basis of interaction force balance proposed by Lehr et al. (2002), the pressure energy requirement is also considered as a competitive breakup mechanism and a constraint which needs to be imposed. The same idea has been adopted by Zhao and Ge (2007), Liao et al. (2015), and Guo et al. (2016). The pressure energy term can be expressed using Eq. (45),

$$e_P = \frac{\sigma}{\min(R_{C,j}, R_{C,k})} \tag{45}$$

where $R_{C,j}$ and $R_{C,k}$ are the radius of curvature of daughter bubbles. The theoretical prediction of surface energy and pressure energy requirement is shown in Fig. 9.

As pointed out by Han et al. (2014), from a volume-based energy point of view, the surface energy density of the parent bubble should exceed the maximum of energy density increase during the entire breakup process. This is an important breakup criterion that has been adopted in this study. This criterion relates the size of parent bubble and the sizes of daughter bubbles at the same

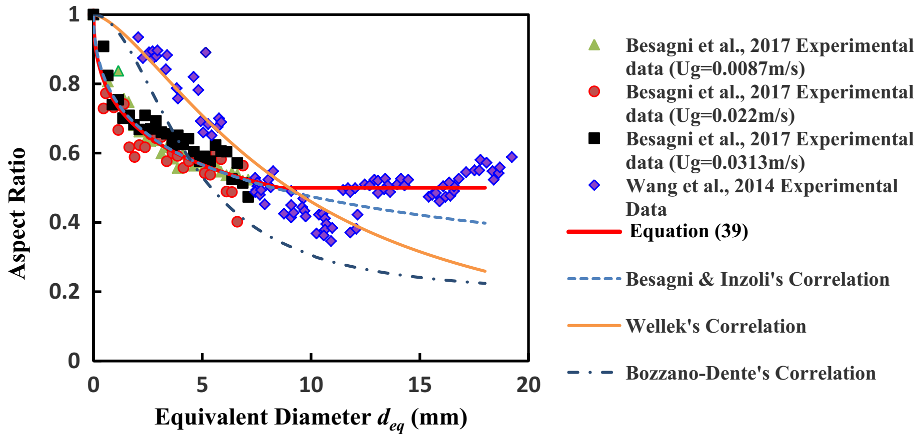

Fig. 4. Aspect ratio correlation and comparison with the literature.

time, and hence restricts the generation of very small bubbles from the breakage as the energy density of daughter bubble will tends to infinity when its fraction or size tends to zero. Detailed information for the implementation of these two competitive breakup mechanisms under the consideration of bubble shape variations coupled with the energy density breakup criterion is described by a flowchart as shown in Fig. 5.

The breakup frequency can be obtained by substituting Eqs. (31)–(45) into Eq. (30), which results in Eq. (46)

$$\Omega_B = \begin{cases} 0.923(1-\alpha_g)n_i(\varepsilon/d_{eq,i}^2)^{1/3}\cdot\int_{\xi_{\min}}^{1}\frac{(d_{V,s}/d_{eq,i}+\xi)(d_{V,l}/d_{eq,i}+\xi)}{\xi^{11/3}}\exp\left(-\frac{12\sigma(S_j+S_k-S_i)}{\pi\beta\rho_l\varepsilon^{2/3}\xi^{11/3}d_{eq,i}^{11/3}}\right)d\xi, & When\ \frac{6\sigma(S_j+S_k-S_i)}{\pi d_{eq,i}^3}\geqslant\frac{\sigma}{\min(Rc_j,Rc_k)} \\ 0.923(1-\alpha_g)n_i(\varepsilon/d_{eq,i}^2)^{1/3}\cdot\int_{\xi_{\min}}^{1}\frac{(d_{V,s}/d_{eq,i}+\xi)(d_{V,l}/d_{eq,i}+\xi)}{\xi^{11/3}}\exp\left(-\frac{2\sigma}{\min(Rc_j,Rc_k)\beta\rho_l\varepsilon^{2/3}\xi^{2/3}d_{eq,i}^{2/3}}\right)d\xi, & When\ \frac{6\sigma(S_j+S_k-S_i)}{\pi d_{eq,i}^3}<\frac{\sigma}{\min(Rc_j,Rc_k)} \end{cases} \tag{46}$$

where $\xi_{\min}$ is the minimum breakage volume fraction that is able to satisfy the energy density criterion.

3. Numerical modelling

To validate the influence of variations in bubble shapes, numerical simulations have been carried out for the air-water bubble column systems used in Camarasa et al. (1999). Details of their experimental conditions are listed in Table 1.

As shown in Fig. 6, Grid 2 consists of $20(\mathrm{r})\times 40(\theta)\times 100(\mathrm{z})$ equally distributed nodes in radial, circumferential and axial directions respectively, with no special grid refinements near the wall. The grid independence was tested in a coarser Grid 1 of $16(\mathrm{r})\times 32(\theta)\times 80(\mathrm{z})$ nodes and a refined Grid 3 of $26(\mathrm{r})\times 48(\theta)\times 126(\mathrm{z})$ nodes, in which case the total number of cells is doubled gradually. As shown in Fig. 6, the grid independence test for these three setups has yielded similar results quantitatively though the gas-holdup for all three grids has been slightly over-predicted. The computed wall y+ values are within the range of 30–150 for all three grid configurations, which indicates that the standard wall functions can be used as near wall treatment. However, Grid 2 and Grid 3 present very similar results in the liquid axial velocity prediction while the coarser grid, Grid 1, has slightly deviated from both Grid 2 and Grid 3. Thus, Grid 2, as shown in Fig. 6, has been employed throughout the subsequent simulations to investigate the effects of the improved breakup model (see Fig. 7).

ANSYS Fluent 3D pressure-based solver is employed in CFD-PBM modelling. Phase coupled SIMPLE scheme has been used for pressure-velocity coupling. The time step is set to be 0.001 s for all simulations, which is in accordance with the optimal value suggested by Guedon et al. (2017). Also, it is considered to be sufficient for illustrating the time-averaged characteristics of the flow fields by carrying out the data sampling statistics for typically 120 s after the quasi-steady state has been achieved. The improved breakup model is integrated into the simulations by using the user defined functions (UDF). All residual values including all phase bins are set to be below 1×10^{-4} as the convergence criteria.

The experiments by Camarasa et al. (1999) have used a multiple-orifice nozzle with 62 1-mm-diameter holes that uniformly spaced at the bottom of the bubble column as the gas sparger. The experimental results have shown an averaged bubble diameter near the sparger of approximately 4 mm for the superficial gas velocity at 0.0606 m/s. Therefore, for the inlet boundary conditions of the simulations, the volume fraction of gas phase with the fraction of 4-mm bubble class are both set to be 1. In this case, the evolution of bubble size distribution for the entire bubble column only relies on the bubble coalescence and breakage kernels. The turbulent intensity is assumed to be 5% with the turbulent viscosity ratio is 10 at the inlet. The treatment of the inlet velocity is different from using a constant superficial gas velocity, but a normal distributed velocity profile is applied by using the model proposed by Shi et al. (2017), which can be expressed as $\tilde{u}(r) = U_{max}\exp(-r^2/b)$, where U_{max} the maximum velocity, r the radial position and b the continuity coefficient. For example, for the gas distributor used by Camarasa et al. (1999) and the superficial gas velocity of 0.0606 m/s, the inlet model estimated value for U_{max} is about 0.1 m/s, and the value of b is about 2.2687×10^{-3} which guarantees the conservation of gas flow rate. Further information about the reasons, theoretical basis and the effects of using the inlet model can be found in the published work. The outlet boundary is set to be a pressure-outlet at the top. Since the gas phase at the outlet boundary is no longer bubbles, artificially setting the fractions of each bubble class seems to be inappropriate. Also, no-slip conditions are applied for both liquid and gas phases at the bubble column wall.

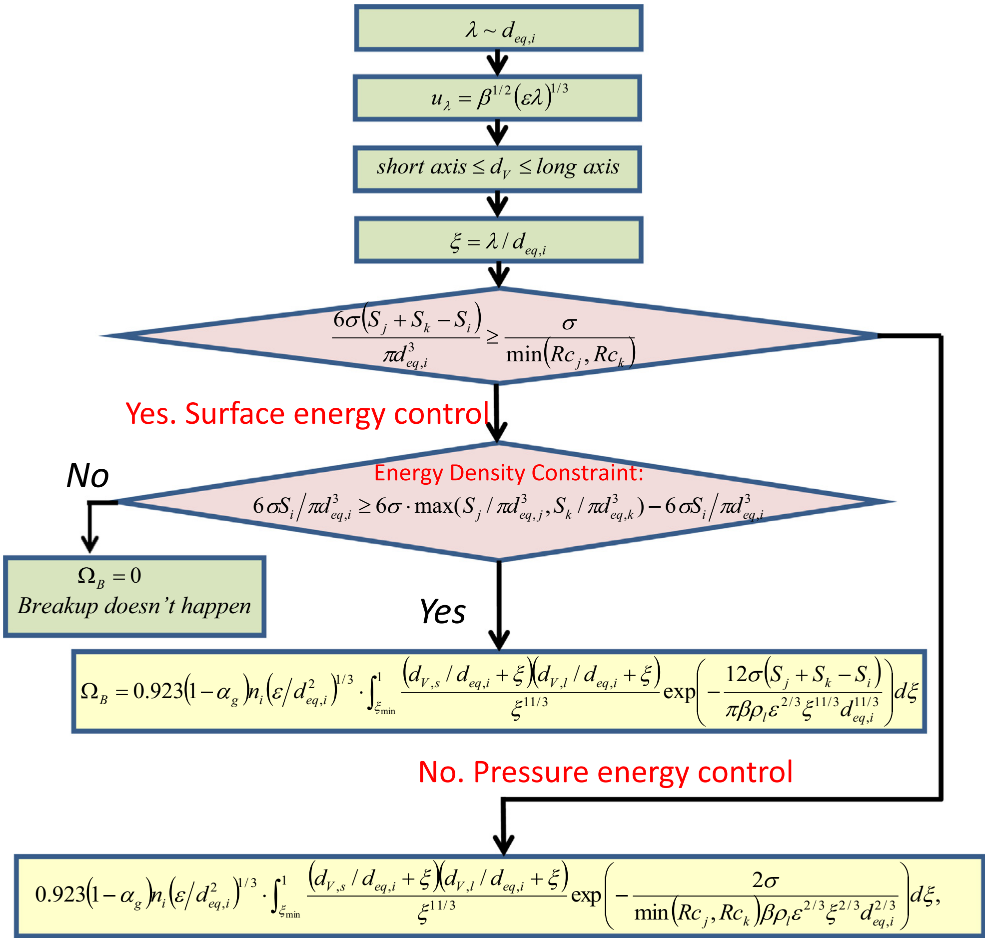

Fig. 5. Flow chart for the improved breakup model.

Table 1
Details of experimental set-up.

Experiment	Diameter (m)	Height (m)	Superficial Velocity (m/s)	Static liquid Height (m)
Kulkarni et al. (2001)	0.15	0.8	0.0382	0.65
Camarasa et al. (1999)	0.1	2	0.0606	0.9

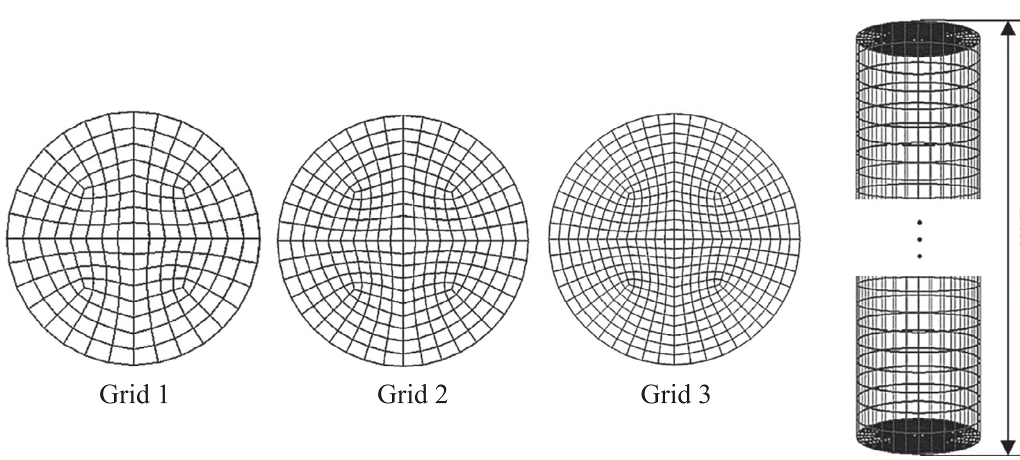

Fig. 6. Mesh set-up at the bottom surface and main body of the column.

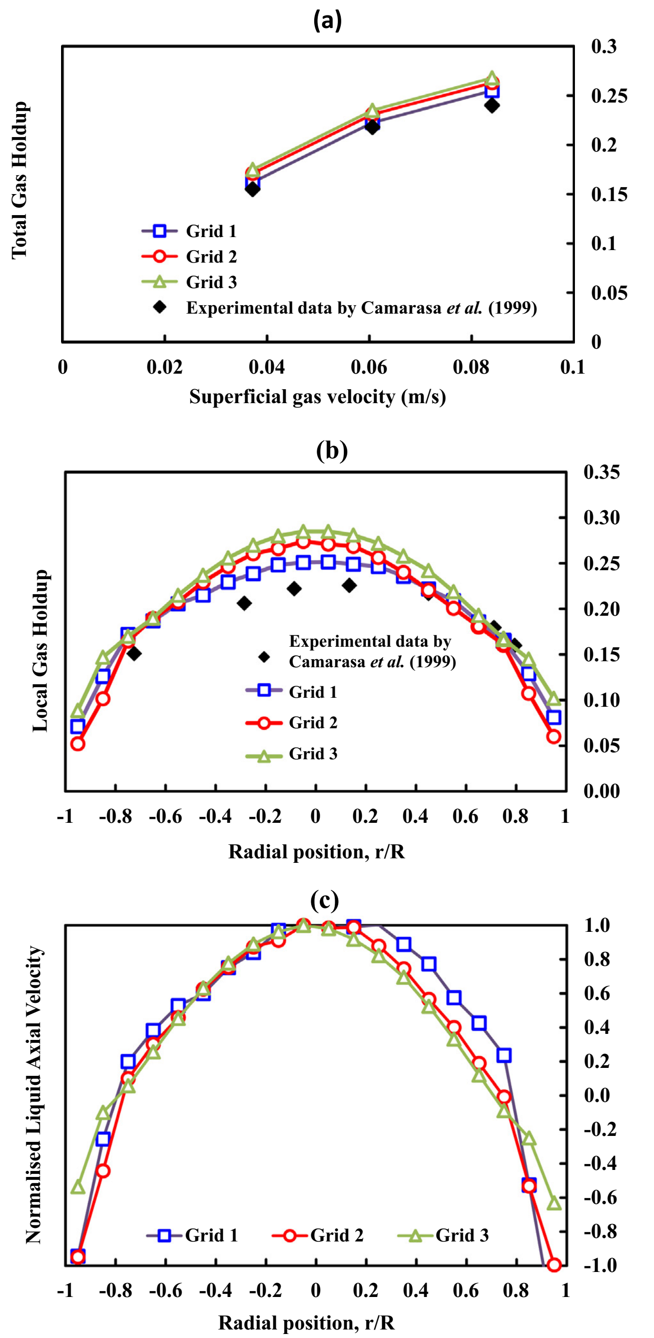

Fig. 7. Comparison of simulated total gas holdup, local gas holdup and normalised liquid axial velocity profile with three different configurations.

4. Results and discussion

To further illustrate the significance of considering the variation of bubble shapes, the theoretical comparison of the increase in surface energy for breakage of original spherical bubbles and various shapes of bubbles is shown in Fig. 8. Various trends of increase in surface energy have been shown in Fig. 8(a) for spherical-cap bubbles. It has been assumed in the modified breakup kernel that the surface energy change mainly concentrates at the front surface of the spherical-cap bubble while at the rear surface, the surface energy contribution can be ignored as the surface is nearly flat. In other words, a great percentage of formation of ellipsoidal bubbles means that higher surface energy is required to form such a

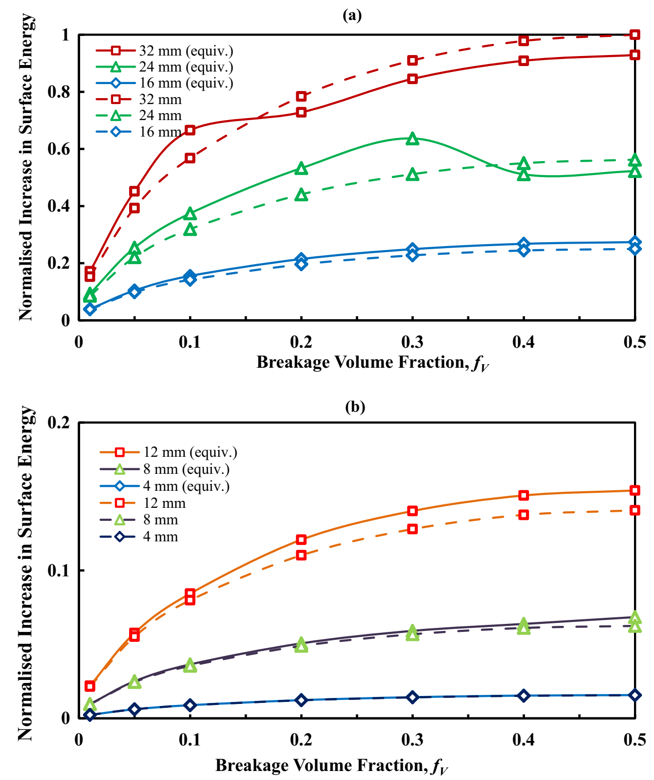

Fig. 8. Increase in surface energy for breakage of original spherical bubbles and various shapes of bubbles.

daughter bubble compared with the formation of daughter bubbles based on spherical-capped shape. As a result, this scenario is more difficult to take place, which agrees with the physical phenomenon that the energy is less likely to be transferred from low energy density (spherical-capped parent bubble) to high energy density (ellipsoidal daughter bubble).

The theoretical predictions of surface energy and the pressure energy requirements for the breakage of ellipsoid and spherical-cap bubble are shown in Fig. 9. It can be clearly seen from Fig. 9 that the energy requirement for ellipsoid bubble shifts from pressure energy to surface energy with an increasing breakup volume fraction. This is likely attributed to the fact that the higher pressure

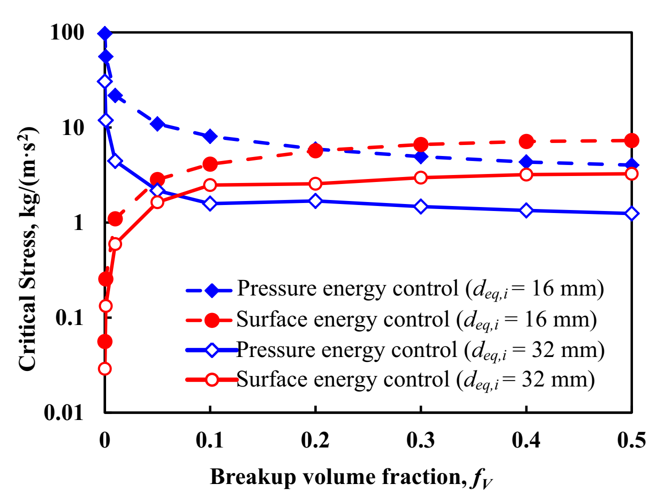

Fig. 9. Two competitive control mechanism of the breakage of two types of bubbles: (a) Ellipsoid (b) Spherical-cap.

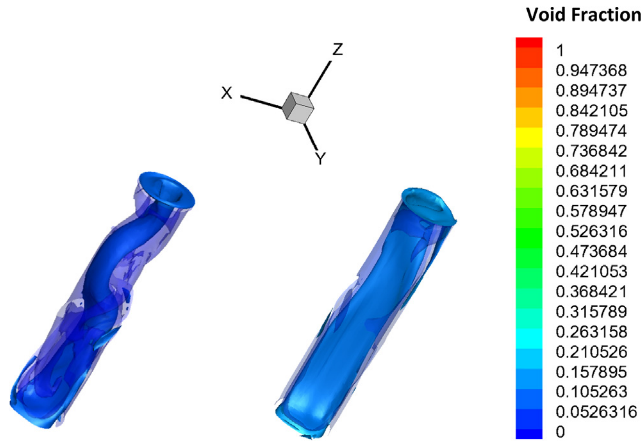

Fig. 10. Iso-surfaces of time-average gas holdup obtained by using Luo & Svendsen model (left) and improved breakup model (right).

head required inside a smaller bubble to resist the bombard from the surrounding eddies in order to sustain its own existence. However, the formation of spherical-capped daughter bubble mainly requires the surface energy. It can be conjectured that the surface energy required is mainly used for forming the large front surface of the spherical-cap bubbles. This would require further investigation.

Fig. 10 presents the iso-surfaces of time-average gas holdup for the simulation of a 15 cm diameter bubble column (Kulkarni et al., 2001). It can be clearly seen from the figure that the overall flow pattern has changed significantly once the improved breakup model has been used. It is also noted that under-prediction of the gas holdup may occurs in the region nearing the bubble column wall no matter how the different breakup model is employed. This is likely attributed to the fact that the standard $k \sim \varepsilon$ turbulence model was employed in the simulation, resulting in underestimation of the gas holdup as the result of overestimation of the turbulence dissipation rate in the vicinity of the bubble column wall. Fig. 11 presents the time-averaged turbulence dissipation rate. It should be noted here that even though the bubble induced turbulence has been considered by using the Sato's model in the prediction of the turbulence dissipation rate, the turbulence dissipation rate used to evaluate the breakage rate of the bubbles, reflected from the turbulence spectrum which is still assumed to follow the classical Kolmogorov $-5/3$ law in sub-inertial range, was employed in the population balance model. This is obviously inappropriate. As pointed out by Mercado et al. (2010), Risso (2011), Riboux et al. (2013) and Prakash et al. (2016), the rising bubble induced turbulence in bubble columns is mainly caused by the agitation due to bubble wakes, which decays rapidly

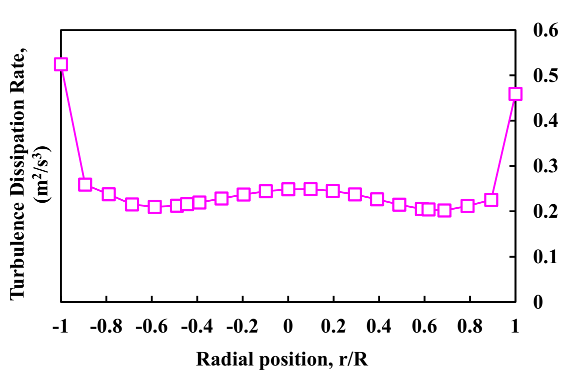

Fig. 11. Radial distribution of time averaged turbulence dissipation rate for Case 1.

because of viscous dissipation. Such pseudo-turbulence has a different scaling behaviour on the energy spectrum with a slope of approximately the wave number to the power of -3. Thus, an improved expression of the breakup kernel may be required for further investigations.

It is believed that the breakup rate Ω_B, which is closely associated with the value of turbulence dissipation rate ε, directly affects the gas phase volume fraction. To highlight this deduction, the Small Perturbation Method (SPM) is applied to the dissipation term in the ε-equation of Eq. (16), as defined by Eq. (47),

$$\varepsilon = \varepsilon_0 + \varsigma\varepsilon_1 + \cdots \tag{47}$$

where ς is the small perturbation parameter. When substituting Eq. (47) with first order perturbation into the ε-equation and rewriting it in the cylindrical coordinates but neglecting the impacts of axial and circumferential components, Eq. (48) can be obtained.

$$\frac{\partial}{\partial r}(\alpha\rho(\varepsilon_0 + \varsigma\varepsilon_1)\vec{u}) = \frac{\partial}{\partial r}\left[\alpha\left(\mu + \frac{\mu_t}{\sigma_k}\right)\frac{\partial}{\partial r}(\varepsilon_0 + \varsigma\varepsilon_1)\right] + \alpha\frac{(\varepsilon_0 + \varsigma\varepsilon_1)}{k}(C_{1\varepsilon}G_k - C_{2\varepsilon}\rho(\varepsilon_0 + \varsigma\varepsilon_1)) \tag{48}$$

The basic approximation by finding the zero order of ε term yields Eq. (49),

$$O(\varsigma^0) : C_{01}\frac{\partial}{\partial r}\left(\alpha\frac{\partial\varepsilon_0}{\partial r}\right) + C_{02}\frac{\partial(\alpha\varepsilon_0)}{\partial r} + C_{03}\alpha\varepsilon_0 + C_{04}\alpha\varepsilon_0^2 = 0 \tag{49}$$

while the first correction by finding the first order of ε term gives Eq. (50),

$$O(\varsigma^1) : C_{11}\frac{\partial}{\partial r}\left(\alpha\frac{\partial\varepsilon_1}{\partial r}\right) + C_{12}\frac{\partial(\alpha\varepsilon_1)}{\partial r} + C_{13}\alpha\varepsilon_1 + C_{14}\alpha\varepsilon_0\varepsilon_1 = 0 \tag{50}$$

where C_{ij} can be regarded as different constants. It can be seen clearly from the first correction that no matter how small the perturbation on the dissipation term is, the volume fraction term will inevitably generate an opposite feedback effect. The first two terms of Eq. (50) are higher order terms, and their effects are small, which can be represented by a small constant value written as C_2. By ignoring the signs of the constants, Eq. (50) becomes $C_{13}\ \alpha\ \varepsilon_1 + C_{14}\ \alpha\ \varepsilon_0\ \varepsilon_1 = C_2$. If α is divided by both sides, the equation becomes $\varepsilon_1\ (C_{13} + C_{14}\ \varepsilon_0) = C_2/\alpha$. In this case, small increase in ε_1 means the decrease in α, where ε_1 represents the small perturbation in turbulence dissipation rate and α is the gas holdup. This indicates that the overestimation of the dissipation term will indeed lead to the underestimation of gas volume fraction in the vicinity of the bubble column wall.

Fig. 12(a) shows the evolution of the time averaged gas holdup along the height of the bubble column, obtained by using the improved breakup model. It can be seen from Fig. 12(a) that the high gas holdup takes place in the core of the bubble column though the holdup distributions slightly spread towards the column wall at the bottom. An explanation could be that the strong vorticity formed at the surrounding region of the wall entraps those of smaller bubbles. It can be also observed from Fig. 12(b) that the bubble plume obtained in the CFD modelling clearly shows oscillation motions in time sequence, which reflects the transient characteristic of the dynamic behaviours of gas-liquid two-phase flow in the bubble columns.

Fig. 13 shows the effects of implementing different combinations of interfacial forces coupled with both the improved breakup model and Luo and Svendsen's breakup model. The simulation results have clearly indicated that the use of the improved breakup model has obtained results consistent with the experimental data. However, small variations can be found among the use of different breakup models and different combinations of interfacial forces. In general, the gas holdup profiles predicted by using the Luo and

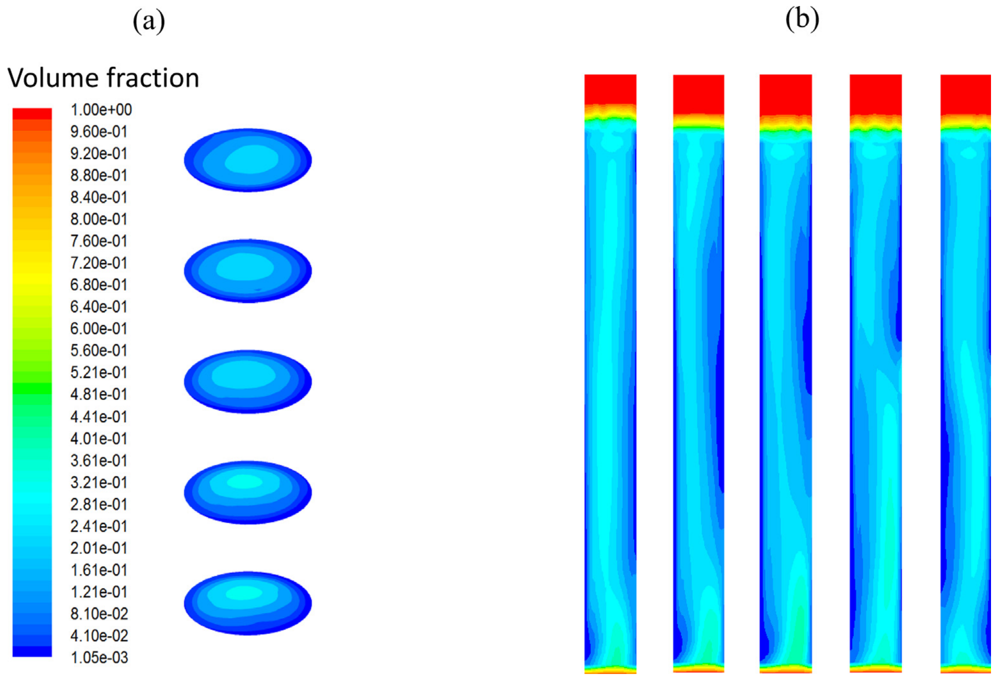

Fig. 12. (a) Contours of time averaged gas holdup (from top to bottom: H = 0.6, 0.5, 0.4, 0.3 and 0.2 m) and (b) bubble plume oscillation in time sequence (from left to right, physical time t = 90 s, 95 s, 100 s, 105 s and 110 s).

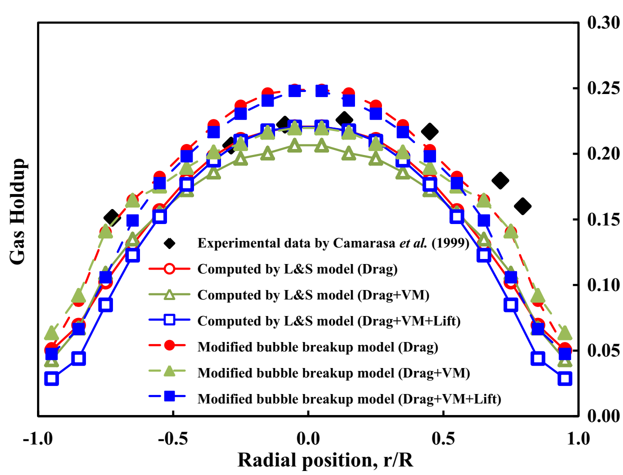

Fig. 13. Effects of different interfacial force combinations coupled with improved breakup model and Luo and Svendsen's (L&S) breakup model.

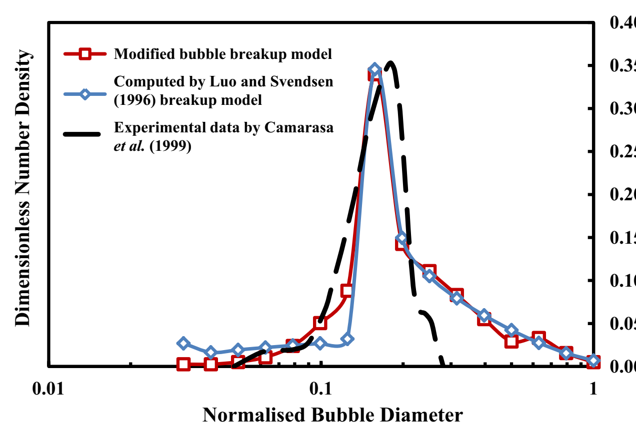

Fig. 14. Dimensionless number density distribution of bubble groups.

Svendsen's breakup model are slightly lower than using the improved breakup model when the same interfacial forces are applied in the simulation. Although it appears that using the improved breakup model coupled with drag force and virtual mass force achieves the best agreement with the experimental data, this may only be valid for the simulation of particular industrial processes in which the effect of lift force is so insignificant that can be neglected. In general cases, the real physics of interphase momentum transfer still need to be considered sufficiently. It is noted that when the drag force, the virtual mass force and the lift force are considered simultaneously, the predicted gas flow distinctly moves towards the bubble column centre. This indicates that the influence of lift force could be significant when it is considered together with the drag force and virtual mass force.

Fig. 14 presents the fraction of number density of each bubble class to the total number density of all bubbles. The x-coordinate of each data point represents the diameter of each bubble class normalised by the largest diameter of bubbles (32 mm) included in the simulation. The peak values obtained from the improved breakup model and Luo and Svendsen's breakup model are in the 8th bubble class from the left, which is equivalent to a bubble diameter of 5 mm. Although the experimental data shows the maximum number density at a slightly larger bubble class, the simulation results are in satisfactory overall agreement with the experimental data. Comparing the results of both models, it seems that a smoother number density distribution which better agrees with the experimental result can be found for small bubbles when the improved breakup model is coupled in the CFD simulation. This may be attributed to two main reasons. For both the 6th and the 7th bubble class, although not much difference can be found in the increase in surface energy when the breakage occurs, as shown in Fig. 8, the generation of bubbles within these bubble classes may come from the breakage of large bubbles. However, when the bubble sizes are very small, such as the 1st to the 3rd bubble classes from the left, the consideration of energy density constraint and the pressure energy controlled breakup mechanism in the improved breakup model effectively restricts the over-breakage of these very small bubbles, due to the pressure head required in forming the smaller daughter bubbles being significantly large. On the contrary, a relatively small peak in the fraction of bubble number density appears at the boundary between ellipsoid and spherical-cap bubbles when using the improved breakup model, shown as the 3rd bubble class from the right. It is believed that this is very likely due to the effect of bubble shapes. As can be seen in Fig. 8, the maximum requirement of increase in surface energy occurs when a larger spherical-cap bubble breaks into a smaller spherical-cap bubble and an ellipsoid bubble. Since the surface energy change mainly concentrates at the front surface of the spherical-cap bubble while at the rear surface, the surface energy contribution can be ignored as the surface is nearly flat. In other words, a great percentage of formation of ellipsoidal bubbles means that higher surface energy is required to form such a daughter bubble compared with the formation of daughter bubbles based on spherical-capped shape. As a result, this scenario is more difficult to take place, which agrees with the physical phenomenon that the energy is less likely to be transferred from low energy density (spherical-capped parent bubble) to high energy density (ellipsoidal daughter bubble). The breakage event is less likely to happen under this scenario and this could be the main reason that explains the appearance of the small peak at the boundary between ellipsoid and spherical bubbles.

Although the bubble shapes are considered to make more sense in physical interpretations in the newly proposed model, it is still based on the original model of Luo and Svendsen. It is believed that the fundamental issue in the breakage model is the characteristics of two-phase flow filed are still approximately described by the Kolmogorov $-5/3$ law of the turbulent kinetic energy spectrum. Except for the liquid shear turbulence, the bubble induced turbulence due to the wake of ellipsoidal and spherical-capped bubbles may make significant contribution to the turbulence and the eddy-bubble interactions in the bubble column. However, the contribution from the bubble induced turbulence has not been well reflected in the breakage model. This could be one of the main causes that will significantly improve the prediction of bubble size distribution.

Fig. 15 presents the unit volume based interfacial area for each bubble class. The y-axis is shown in a $\log_{10}$ scale. Interfacial area is a key parameter that greatly affects the prediction of heat and mass transfer between bubbles and liquid phase in the bubble columns. It can be found that the difference in the interfacial area obtained by the improved breakup model and the original Luo and Svendsen's model is more apparent especially for bubble classes "1/32" to "1/20". Since these bubble classes represent very small bubbles, the difference is mainly due to the predicted number density, and hence the difference of their contribution to the total interfacial area is negligible. However, the influence of the bubble shapes is gradually reflected when the shape of the bubbles transforms from ellipsoid to spherical-cap, even if no significant difference is shown for the number density of bubble classes "17/27" to "1" predicted by both models. The consideration of ellipsoid and spherical-cap shapes of bubbles results in a significant increase in the prediction of interfacial area of bubbles and liquid phase. The total values of unit volume based interfacial area are shown in Table 2. It can be found that the increment obtained by the consideration of bubble shape variations reaches nearly 40 percent. Although this figure is based on statistical approximations of bubble shapes and will be slightly different from reality, it still suggests that the assumption of all bubbles defined by a spherical shape will underestimate the interfacial area to a great extent when mass and heat transfer is considered.

Table 2
Comparison of unit volume based interfacial area calculated from simulation results.

	Improved breakup model	Original breakup model
Interfacial area (m^2)	74.66	53.43

5. Conclusions

In the present study, an improved breakup model has been proposed based on the model for drop and bubble breakup presented by Luo and Svendsen (1996). The concluding remarks are as follows:

1. This improved breakup mode has taken into account the variation of bubble shapes, classified into spherical, deformed ellipsoid and spherical-cap, in the bubble columns.
2. A correlation on the aspect ratio of deformed ellipsoid bubbles, which takes into account the joint effect of buoyancy, viscosity and surface tension, has been proposed based on the experimental data of air-water systems in the bubble columns.

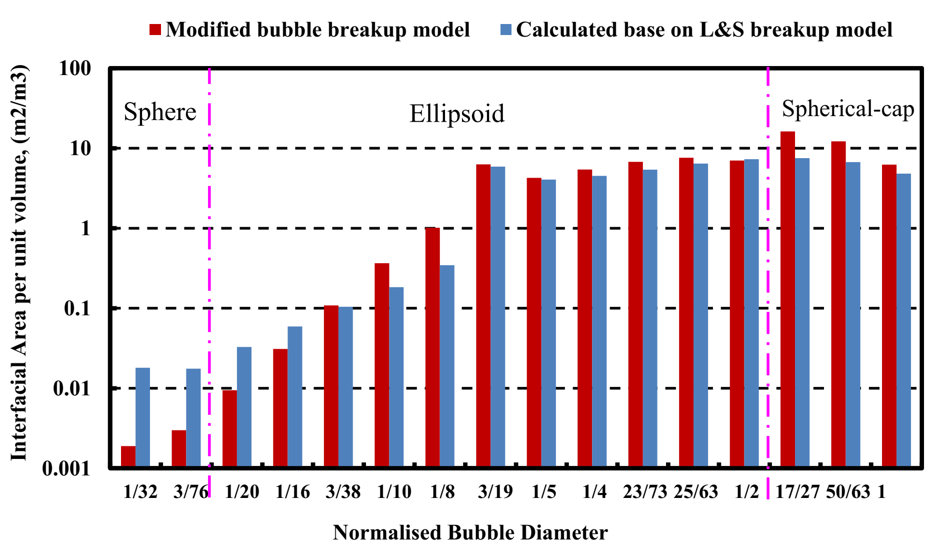

Fig. 15. Comparison of simulated interfacial area in the bubble column.

3. The pressure energy controlled breakup coupled with the modified breakage criteria has been considered in the modelling. The difference between the surface energy and pressure energy requirements for forming various daughter bubbles has been illustrated.
4. The energy density constraint has been applied to prevent the over-estimation of the breakage rate of small bubbles. The simulation results have shown an overall agreement with the experimental data reported in the open literature.
5. This study on the dynamic behaviours of various bubble shapes may lead to a more comprehensive understanding of the mass and heat transfer characteristics of the multi-phase reaction in the bubble column.

Acknowledgements

This work was financially supported by the National Natural Science Foundation of China (Grant Nos. 91534118, 21761132026). Weibin Shi and Xinyue Cai would also like to acknowledge the Ph.D. scholarship of the International Doctoral Innovation Centre (IDIC) of the University of Nottingham Ningbo China and the support of EPSRC (Grant no. EP/G037345/1).

References

Aoyama, S., Hayashi, K., Hosokawa, S., Tomiyama, A., 2016. Shapes of ellipsoidal bubbles in infinite stagnant liquids. Int. J. Multiph. Flow 79, 23–30.
Batchelor, G.K., 1967. An Introduction to Fluid Dynamics. Cambridge University Press.
Besagni, G., Brazzale, P., Fiocca, A., Inzoli, F., 2016. Estimation of bubble size distributions and shapes in two-phase bubble column using image analysis and optical probes. Flow Meas. Instrum. 52, 190–207.
Besagni, G., Inzoli, F., 2016a. Bubble size distributions and shapes in annular gap bubble column. Exp. Therm. Fluid Sci. 74, 27–48.
Besagni, G., Inzoli, F., 2016b. Comprehensive experimental investigation of counter-current bubble column hydrodynamics: holdup, flow regime transition, bubble size distributions and local flow properties. Chem. Eng. Sci. 146, 259–290.
Besagni, G., Inzoli, F., Ziegenhein, T., Hessenkemper, H., Lucas, D., 2017. Bubble aspect ratio in dense bubbly flows: experimental studies in low Morton-number systems, p. 012014.
Bozzano, G., Dente, M., 2001. Shape and terminal velocity of single bubble motion: a novel approach. Comput. Chem. Eng. 25, 571–576.
Camarasa, E., Vial, C., Poncin, S., Wild, G., Midoux, N., Bouillard, J., 1999. Influence of coalescence behaviour of the liquid and of gas sparging on hydrodynamics and bubble characteristics in a bubble column. Chem. Eng. Process. 38, 329–344.
Clark, M.M., 1988. Drop breakup in a turbulent-flow. 1. Conceptual and modeling considerations. Chem. Eng. Sci. 43, 671–679.
Clift, R., Grace, J.R., Weber, M.E., 1978. Bubbles, Drops, and Particles. Academic Press.
Coulaloglou, C.A., Tavlarides, L.L., 1977. Description of interaction processes in agitated liquid-liquid dispersions. Chem. Eng. Sci. 32, 1289–1297.
Davenport, W.G., Bradshaw, A.V., Richardson, F.D., 1967. Behaviour of spherical cap bubbles in liquid metals. Journal of the Iron and Steel Institute 205, 1034.
Deen, N.G., Solberg, T., Hjertager, B.H., 2000. Numerical simulation of gas–liquid flow in a square cross section bubble column. In: 14th International Congress of Chemical and Process Engineering (CHISA), Praha, Czech Republic.
Deen, N.G., Solberg, T., Hjertager, B.H., 2001. Large eddy simulation of the gas-liquid flow in a square cross-sectioned bubble column. Chem. Eng. Sci. 56, 6341–6349.
Delnoij, E., Lammers, F.A., Kuipers, J.A.M., vanSwaaij, W.P.M., 1997. Dynamic simulation of dispersed gas-liquid two-phase flow using a discrete bubble model. Chem. Eng. Sci. 52, 1429–1458.
Grace, J.R., Clift, R., Weber, M.E., 1978. Bubbles, Drops, and Particles. Academic Press.
Guedon, G.R., Besagni, G., Inzoli, F., 2017. Prediction of gas-liquid flow in an annular gap bubble column using a bi-dispersed Eulerian model. Chem. Eng. Sci. 161, 138–150.
Guo, X.F., Zhou, Q., Li, J., Chen, C.X., 2016. Implementation of an improved bubble breakup model for TFM-PBM simulations of gas-liquid flows in bubble columns. Chem. Eng. Sci. 152, 255–266.
Han, L.C., Fu, J., Li, M., Gong, S.G., Gao, N.N., Zhang, C., Luo, H.A., 2016. A theoretical unsteady-state model for k(L) of bubbles based on the framework of wide energy spectrum. Aiche J. 62, 1007–1022.
Han, L.C., Gong, S.G., Li, Y.Q., Gao, N.N., Fu, J., Luo, H., Liu, Z.H., 2014. Influence of energy spectrum distribution on drop breakage in turbulent flows. Chem. Eng. Sci. 117, 55–70.
Krishna, R., Urseanu, M.I., van Baten, J.M., Ellenberger, J., 1999. Influence of scale on the hydrodynamics of bubble columns operating in the churn-turbulent regime: experiments vs. Eulerian simulations. Chem. Eng. Sci. 54, 4903–4911.
Krishna, R., van Baten, J.M., 2001. Eulerian simulations of bubble columns operating at elevated pressures in the churn turbulent flow regime. Chem. Eng. Sci. 56, 6249–6258.
Kulkarni, A.A., Joshi, J.B., Kumar, V.R., Kulkarni, B.D., 2001. Application of multiresolution analysis for simultaneous measurement of gas and liquid velocities and fractional gas hold-up in bubble column using LDA. Chem. Eng. Sci. 56, 5037–5048.
Laborde-Boutet, C., Larachi, F., Dromard, N., Delsart, O., Schweich, D., 2009. CFD simulation of bubble column flows: investigations on turbulence models in RANS approach. Chem. Eng. Sci. 64, 4399–4413.
Landel, J.R., Cossu, C., Caulfield, C.P., 2008. Spherical cap bubbles with a toroidal bubbly wake. Phys. Fluids 20, 122101.
Legendre, D., Zenit, R., Velez-Cordero, J.R., 2012. On the deformation of gas bubbles in liquids. Physics of Fluids 24.
Lehr, F., Millies, M., Mewes, D., 2002. Bubble-size distributions and flow fields in bubble columns. Aiche J. 48, 2426–2443.
Li, W.L., Zhong, W.Q., 2015. CFD simulation of hydrodynamics of gas-liquid-solid three-phase bubble column. Powder Technol. 286, 766–788.
Liao, Y.X., Rzehak, R., Lucas, D., Krepper, E., 2015. Baseline closure model for dispersed bubbly flow: bubble coalescence and breakup. Chem. Eng. Sci. 122, 336–349.
Lucas, D., Prasser, H.M., Manera, A., 2005. Influence of the lift force on the stability of a bubble column. Chem. Eng. Sci. 60, 3609–3619.
Lucas, D., Tomiyama, A., 2011. On the role of the lateral lift force in poly-dispersed bubbly flows. Int. J. Multiph. Flow 37, 1178–1190.
Luo, H., 1993. Coalescence, Breakup and Liuqid Circulation in Bubble Column Reactors. PhD thesis from the Norwegian Institute of Technology, Trondheim, Norway.
Luo, H., Svendsen, H.F., 1996. Theoretical model for drop and bubble breakup in turbulent dispersions. Aiche J. 42, 1225–1233.
Masood, R.M.A., Rauh, C., Delgado, A., 2014. CFD simulation of bubble column flows: an explicit algebraic Reynolds stress model approach. Int. J. Multiph. Flow 66, 11–25.
Mercado, J.M., Gomez, D.C., Van Gils, D., Sun, C., Lohse, D., 2010. On bubble clustering and energy spectra in pseudo-turbulence. J. Fluid Mech. 650, 287–306.
Moore, D.W., 2006. The velocity of rise of distorted gas bubbles in a liquid of small viscosity. J. Fluid Mech. 23, 749–766.
Okawa, T., Tanaka, T., Kataoka, I., Mori, M., 2003. Temperature effect on single bubble rise characteristics in stagnant distilled water. Int. J. Heat Mass Transfer 46, 903–913.
Pourtousi, M., Sahu, J.N., Ganesan, P., 2014. Effect of interfacial forces and turbulence models on predicting flow pattern inside the bubble column. Chem. Eng. Process. Process Intensifier 75, 38–47.
Prakash, V.N., Mercado, J.M., van Wijngaarden, L., Mancilla, E., Tagawa, Y., Lohse, D., Sun, C., 2016. Energy spectra in turbulent bubbly flows. J. Fluid Mech. 791, 174–190.
Prince, M.J., Blanch, H.W., 1990. Bubble coalescence and break-up in air-sparged bubble-columns. Aiche J. 36, 1485–1499.
Qin, C.P., Chen, C., Xiao, Q., Yang, N., Yuan, C.S., Kunkelmann, C., Cetinkaya, M., Mulheims, K., 2016. CFD-PBM simulation of droplets size distribution in rotor-stator mixing devices. Chem. Eng. Sci. 155, 16–26.
Rampure, M.R., Kulkarni, A.A., Ranade, V.V., 2007. Hydrodynamics of bubble column reactors at high gas velocity: experiments and computational fluid dynamics (CFD) simulations. Ind. Eng. Chem. Res. 46, 8431–8447.
Ranade, V.V., Tayalia, Y., 2001. Modelling of fluid dynamics and mixing in shallow bubble column reactors: influence of sparger design. Chem. Eng. Sci. 56, 1667–1675.
Riboux, G., Legendre, D., Risso, F., 2013. A model of bubble-induced turbulence based on large-scale wake interactions. J. Fluid Mech. 719, 362–387.
Risso, F., 2011. Theoretical model for k(-3) spectra in dispersed multiphase flows. Physics of Fluids 23.
Rzehak, R., Krepper, E., 2013. CFD modeling of bubble-induced turbulence. Int. J. Multiph. Flow 55, 138–155.
Sankaranarayanan, K., Sundaresan, S., 2002. Lift force in bubbly suspensions. Chem. Eng. Sci. 57, 3521–3542.
Sato, Y., Sekoguchi, K., 1975. Liquid velocity distribution in two-phase bubble flow. Int. J. Multiph. Flow 2, 79–95.
Shah, Y.T., Kelkar, B.G., Godbole, S.P., Deckwer, W.D., 1982. Design parameters estimations for bubble column reactors. Aiche J. 28, 353–379.
Shi, W., Yang, N., Yang, X., 2017. A kinetic inlet model for CFD simulation of large-scale bubble columns. Chem. Eng. Sci. 158, 108–116.
Sokolichin, A., Eigenberger, G., 1999. Applicability of the standard k-epsilon turbulence model to the dynamic simulation of bubble columns: Part I. Detailed numerical simulations. Chem. Eng. Sci. 54, 2273–2284.
Sokolichin, A., Eigenberger, G., Lapin, A., 2004. Simulation of buoyancy driven bubbly flow: established simplifications and open questions. Aiche J. 50, 24–45.
Sokolichin, A., Eigenberger, G., Lapin, A., Lubbert, A., 1997. Dynamic numerical simulation of gas-liquid two-phase flows – Euler/Euler versus Euler/Lagrange. Chem. Eng. Sci. 52, 611–626.
Sugihara, K., Sanada, T., Shirota, M., Watanabe, M., 2007. Behavior of single rising bubbles in superpurified water. Kagaku Kogaku Ronbunshu 33, 402–408.

Tabib, M.V., Roy, S.A., Joshi, J.B., 2008. CFD simulation of bubble column – an analysis of interphase forces and turbulence models. Chem. Eng. J. 139, 589–614.

Tomiyama, A., 1998. Struggle with computational bubble dynamics. Multiphase Science and Technology, 10(4), 369–405.

Tomiyama, A., Miyoshi, K., Tamai, H., Zun, I., Sakafuchi, T., 1998. A bubble tracking method for the prediction of spatial-evolution of bubble flow in a vertical pipe. In: 3rd International Conference on Multiphase Flow (ICMF 98), Lyon, France.

Tomiyama, A., Tamai, H., Zun, I., Hosokawa, S., 2002. Transverse migration of single bubbles in simple shear flows. Chem. Eng. Sci. 57, 1849–1858.

Tripathi, M.K., Sahu, K.C., Govindarajan, R., 2015. Dynamics of an initially spherical bubble rising in quiescent liquid. Nat. Commun. 6.

Tsamopoulos, J., Dimakopoulos, Y., Chatzidai, N., Karapetsas, G., Pavlidis, M., 2008. Steady bubble rise and deformation in Newtonian and viscoplastic fluids and conditions for bubble entrapment. J. Fluid Mech. 601, 123–164.

Tsuchiya, K., Song, G.H., Fan, L.S., 1990. Effects of particle properties on bubble rise and wake in a 2-dimensional liquid-solid fluidized-bed. Chem. Eng. Sci. 45, 1429–1434.

Wang, T.F., Wang, J.F., Jin, Y., 2003. A novel theoretical breakup kernel function for bubbles/droplets in a turbulent flow. Chem. Eng. Sci. 58, 4629–4637.

Wang, X., Klaasen, B., Degreve, J., Blanpain, B., Verhaeghe, F., 2014. Experimental and numerical study of buoyancy-driven single bubble dynamics in a vertical Hele-Shaw cell. Phys. Fluids 26.

Wellek, R.M., Agrawal, A.K., Skelland, A.H., 1966. Shape of liquid drops moving in liquid media. Aiche J. 12. 854-&.

Xiao, Q., Wang, J., Yang, N., Li, J.H., 2017. Simulation of the multiphase flow in bubble columns with stability-constrained multi-fluid CFD models. Chem. Eng. J. 329, 88–99.

Xiao, Q., Yang, N., Li, J., 2013. Stability-constrained multi-fluid CFD models for gas–liquid flow in bubble columns. Chem. Eng. Sci. 100, 279–292.

Xue, J., Chen, F.G., Yang, N., Ge, W., 2017a. Eulerian-Lagrangian simulation of bubble coalescence in bubbly flow using the spring-dashpot model. Chin. J. Chem. Eng. 25, 249–256.

Xue, J., Chen, F.G., Yang, N., Ge, W., 2017b. A study of the soft-sphere model in eulerian-lagrangian simulation of gas-liquid flow. Int. J. Chem. Reactor Eng. 15, 57–67.

Yang, N., Wu, Z.Y., Chen, J.H., Wang, Y.H., Li, J.H., 2011. Multi-scale analysis of gas-liquid interaction and CFD simulation of gas-liquid flow in bubble columns. Chem. Eng. Sci. 66, 3212–3222.

Yang, N., Xiao, Q., 2017. A mesoscale approach for population balance modeling of bubble size distribution in bubble column reactors. Chem. Eng. Sci. 170, 241–250.

Zhang, D., Deen, N.G., Kuipers, J.A.M., 2006. Numerical simulation of the dynamic flow behavior in a bubble column: a study of closures for turbulence and interface forces. Chem. Eng. Sci. 61, 7593–7608.

Zhao, H., Ge, W., 2007. A theoretical bubble breakup model for slurry beds or three-phase fluidized beds under high pressure. Chem. Eng. Sci. 62, 109–115.

Zhou, R.T., Yang, N., Li, J.H., 2017. CFD simulation of gas-liquid-solid flow in slurry bubble columns with EMMS drag model. Powder Technol. 314, 466–479.

CFD-PBM MODELLING OF GAS-LIQUID TWO-PHASE FLOW IN BUBBLE COLUMN REACTORS WITH AN IMPROVED BREAKUP KERNEL ACCOUNTING FOR BUBBLE SHAPE VARIATIONS

Shi W.[a], Li G.[a], Yang J[b], Zong Y.[c], and Yang X.[a]*
*Author for correspondence
E-mail: Xiaogang.Yang @ nottingham.edu.cn
[a] Department of Mechanical, Materials and Manufacturing Engineering,
The University of Nottingham Ningbo China, Ningbo, 315100, PR China
[b] School of Mathematical Sciences,
The University of Nottingham Ningbo China, Ningbo, 315100, PR China,
[c] State Key Laboratory of Chemical Engineering,
East China University of Science and Technology, Shanghai 200237, PR China

ABSTRACT

The breakup model developed by Luo and Svendsen (1993) implemented into CFD modelling of gas-liquid two-phase flows assumes that the bubble shapes are spherical. The simulation results usually yield an unreliable prediction of the break-up of very small bubbles. To the best knowledge of the authors, incorporation of the bubble shape variation into the break-up model has been rarely documented. The current study intends to propose and implement an improved bubble breakup model which accounts for variation of bubble shapes when solving the population balance equations for CFD simulation of gas-liquid two-phase flows in bubble columns.

1. INTRODUCTION

Some previous CFD studies often employ the assumption of an unified bubble diameter, which can only generate accurate predictions if the bubble size distribution is narrow. However, numerical modelling of gas-liquid two-phase flow behaviours has to take into account the bubble size distributions and the bubble-bubble interactions. These are very influential factors in the calculation of the gas-liquid interfacial area, which will further affect the mass and heat transfer between two phases. The multiple size groups (MUSIG) model describes the bubble sizes as being directly derived from the population balance equations (PBE), and the eddy/bubble-bubble interactions being controlled by bubble coalescence and breakup models.

For the bubble breakup process, Coulaloglou and Tavlarides [1] assumed that the breakup process would occur if the energy from turbulent eddies acting on the fluid particle is more than the surface energy it contains. Prince and Blanch [2] acknowledged that bubble breakup was caused by eddy-bubble collision and proposed that the bubble breakup can only be induced by eddies with approximately the same characteristic length. Eddies at a much larger length scale only transport the bubbles without causing breakup. Luo and Svendsen [3] described the bubble breakup by considering both the length scale and the amount of energy contained by the arriving eddies. The minimum length scale of eddies that are responsible for breakup equals to 11.4 times the Kolmogorov scale. The probability for bubble breakup is related to the critical ratio of surface energy increase of bubbles after breakup and the mean turbulent kinetic energy of the colliding eddy. Therefore, very small eddies do not contain sufficient energy to cause the bubble breakup. Lehr, Millies and Mewes [4] proposed a slightly different breakup mechanism from Luo and Svendsen [3]. They considered the minimum length scale of eddies to be determined by the size of the smaller bubble after breakup, and the breakup process to depend on the inertial force of the arriving eddy and the interfacial force of the bubble. Based on the results of Luo and Svendsen [3] and Lehr, Millies and Mewes [4], Wang, Wang and Jin [5] proposed the energy constraint and the capillary constraint criteria for the breakup model. The energy constraint requires the eddy energy to be larger than or equal to the increase of surface energy of bubbles after the breakage. The capillary constraint requires the dynamic pressure of the eddy to exceed the capillary pressure of the bubble. The use of these two breakup criteria actually restricted the minimum size of the bubbles that can break, and hence showed more accurate results than Luo and Svendsen [3]. These two breakup criteria have also been adopted in more recent work by Zhao and Ge [6] and Liao, Rzehak, Lucas and Krepper [7].

2. MATHEMATICAL MODELLING

2.1 Governing equations

A 3D transient CFD model is employed in this work to simulate the local hydrodynamics of the gas-liquid two-phase bubble column. An Eulerian-Eulerian approach is adopted to describe the flow behaviours for both phases, i.e. water as the continuous phase, and air as the dispersed phase.

The mass and momentum balance equations are given by equation (1) and (2) respectively,

$$\frac{\partial(\rho_k\alpha_k)}{\partial t}+\nabla(\rho_k\alpha_k\vec{u}_k)=0 \tag{1}$$

$$\frac{\partial(\rho_k\alpha_k\vec{u}_k)}{\partial t}+\nabla(\rho_k\alpha_k\vec{u}_k\vec{u}_k) = -\alpha_k\nabla p+\nabla\cdot\overline{\overline{\tau}}_k+\alpha_k\rho_k\vec{g}+\vec{F}_k \tag{2}$$

where ρ_k, α_k, $\vec{u}_k$, $\overline{\overline{\tau}}_k$, and $\vec{F}_k$ represent the density, volume fraction, velocity vector, viscous stress tensor and the inter-phase momentum exchange term for the k (k liquid or gas) phase respectively. The sum of the volume fractions for both phases is equal to 1.

The standard $k \sim \varepsilon$ turbulence model is used for turbulence closure. The turbulent kinetic energy k_l and dissipation rate ε_l are computed by equation (3) and (4),

$$\frac{\partial(\alpha_l \rho_l k_l)}{\partial t} + \nabla \cdot (\alpha_l \rho_l k_l \vec{u}_l) = \nabla \cdot \left[\alpha_l \left(\mu_l + \frac{\mu_{t,l}}{\sigma_k} \right) \nabla k_l \right] + \alpha_l (G_{k,l} - \rho_l \varepsilon_l) \tag{3}$$

$$\frac{\partial(\alpha_l \rho_l \varepsilon_l)}{\partial t} + \nabla \cdot (\alpha_l \rho_l \varepsilon_l \vec{u}_l) = \nabla \cdot \left[\alpha_l \left(\mu_l + \frac{\mu_{t,l}}{\sigma_k} \right) \nabla \varepsilon_l \right] + \alpha_l \frac{\varepsilon_l}{k_l} (C_{1\varepsilon} G_{k,l} - C_{2\varepsilon} \rho_l \varepsilon_l) \tag{4}$$

where $G_{k,l}$ is the production of turbulent kinetic energy and $\mu_{t,l}$ is the turbulent viscosity. In this work, the standard $k \sim \varepsilon$ model constants used are C_μ = 0.09, $C_{1\varepsilon}$ = 1.44, $C_{2\varepsilon}$ = 1.92, σ_k = 1.0, σ_ε = 1.3.

2.2 Bubble size distribution

The bubble size distribution is determined using the MUSIG model, i.e. population balance model with consideration of bubble coalescence and breakup. Bubbles are divided into several size groups with different diameters d_i and an equivalent phase with the Sauter mean diameter to represent the bubble classes. In this study, 16 bubble classes with diameters ranging from 1 to 32 mm are applied based on the geometric discretization method such that $V_i = 2V_{i-1}$. The population balance equation is expressed by equation (5),

$$\frac{\partial n_i}{\partial t} + \nabla \cdot (\vec{v}_i \cdot n_i) = S_i \tag{5}$$

where n_i is the number density for *i*-th group, $\vec{v}_i$ is the mass average velocity vector, and S_i is the source term.

The source term, S_i, for the *i*-th group can be expressed as the birth and death of bubbles due to coalescence and breakup respectively, given by equation (6)

$$S_i = B_{coalescence,i} - D_{coalescence,i} + B_{breakup,i} - D_{breakup,i} = \sum_{d_j = d_{\min}}^{d_i/2} \Omega_C(d_j : d_i - d_j) - \sum_{d_j}^{d_{\max} - d_i} \Omega_C(d_j : d_i) + \sum_{d_j = d_i}^{d_{\max}} \Omega_B(d_j : d_i) - \Omega_B(d_i) \tag{6}$$

The local gas volume fraction can be calculated by equation (7),

$$\alpha_g f_i = n_i V_i \tag{7}$$

where f_i is the *i*-th class fraction of total volume fraction, and V_i is the volume for the *i*-th class.

For the coalescence between two bubbles, the coalescence kernel used in this study was proposed by Luo [8]. As this is not the main concern of this work, further details will not be presented here.

The breakup model used in this work is based on the work of Luo and Svendsen [3]. However, several improvements have been introduced in this study to produce a more realistic breakup model. In Luo and Svendsen's model, the shape of breakage bubbles was assumed to be spherical. However, previous experimental studies, such as Grace, Clift and Weber [9] and Tomiyama [10], have found that the bubbles exist in various shapes and the dynamics of bubble motion strongly depend on the shape of the bubbles. For example, Figure 1 demonstrates the experimentally recorded variation in bubble shapes found in an operating bubble column. The bubble shape has been neglected in previous studies for the simplification of models. However, the shape of the bubbles could potentially be a critical factor for accurately predicting the flow characteristics of the gas phase in CFD simulations.

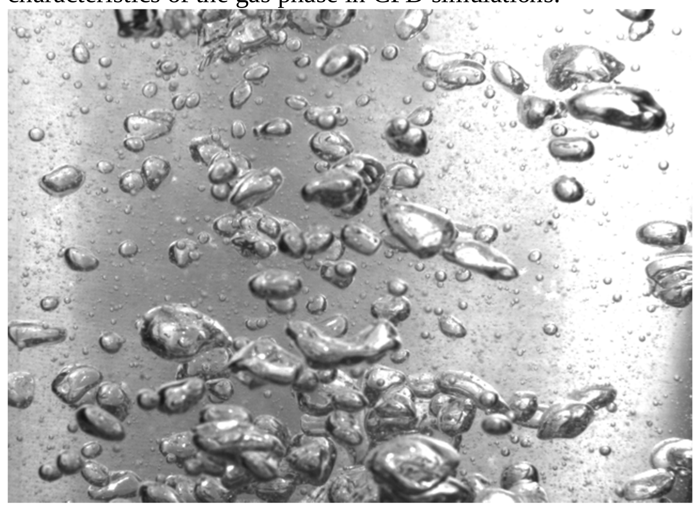

Figure 1 Instantaneous photo of rising bubbles in a 150 mm diameter cylindrical bubble column (*Ug*=0.02 m/s).

From experimental observations, the bubble shapes can be classified into different types. Thus, the effects of different bubble shapes are taken into account in this study. Due to the uncertainty of the spatial rotation of the bubbles, the contact angle of the bombarding eddy is very difficult to be determined. Therefore, instead of the original bubble size, d_i, the equivalent diameter that approximately represents the size of the projected area of the bubble is expressed by equation (8),

$$c \le d_{eq} \le a \tag{8}$$

where *c* and *a* are the length of the short axis and long axis respectively.

The breakup rate for one individual parent bubble breaking into two daughter bubbles is expressed by equation (9),

$$\Omega_B = \int_{\lambda_{\min}}^{d} \omega_B^T p_B d\lambda \tag{9}$$

where ω_B^T is the collision probability density. It can be expressed by using equation (10),

$$\omega_B^T(\xi) = 0.923(1 - \alpha_g)(\varepsilon d_i)^{1/3} n_i \frac{(d_{eq,i}/d_i + \xi)^2}{d_i^2 \xi^{11/3}} \tag{10}$$

where $\xi = \lambda / d_i$, characterising the sizes of eddies that may contribute to the breakage of bubble size d_i. The breakage probability function p_B used by Luo and Svendsen [3] is re-expressed in equation (11),

$$p_B = \exp(-\frac{e_s}{\bar{e}}) \quad (11)$$

where $\bar{e}$ is the mean turbulent kinetic energy for eddies of size λ and e_s is the increase in surface energy of bubbles after breakage. The mean turbulent kinetic energy can be determined by equation (12).

$$\bar{e} = \rho_l \frac{\pi}{6}\lambda^3 \frac{\bar{v}_\lambda^2}{2} = \frac{\pi\beta}{12}\rho_l (\varepsilon d_i)^{2/3} d_i^3 \xi^{11/3} \quad (12)$$

By assuming the bubbles before and after breakage are all in spherical shape, when the parent bubble of size d_i breaks into two bubbles of size d_j and $(d_i^3 - d_j^3)^{1/3}$, the increase in surface energy was originally described by equation (13),

$$e_s = \sigma \cdot \pi d_i^2 [f_V^{2/3} + (1-f_V)^{2/3} - 1] \quad (13)$$

However, since the effects of different shapes of bubbles are taken into account, equation (13) can be re-written in a general form with regards to the surface area, S, of bubbles, as described by equation (14).

$$e_s = \sigma \cdot (S_{j,1} + S_{j,2} - S_i) \quad (14)$$

According to the models for bubble shapes by Tomiyama, Miyoshi, Tamai, Zun and Sakafuchi [11], there are 3 main types of bubbles that exist in the given conditions in this work, such as the sphere, ellipsoid and spherical-cap. The details of these 3 types of bubbles and their possible breakage footages are given in Figure 2.

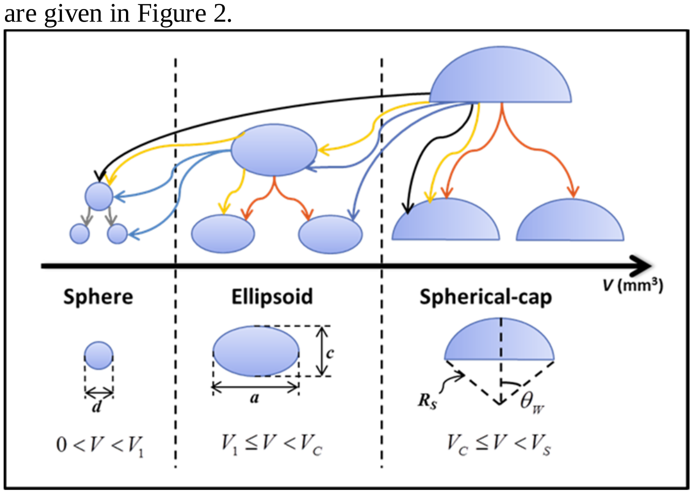

Figure 2 Classification of 3 types of bubbles and the possible breakage footage.

For an air-water system under atmospheric pressure and room temperature, the boundary between spherical bubbles and ellipsoid bubbles, d_1, is 1.16 mm for the pure system and d_1 is 1.36 mm for a slightly contaminated system. The boundary between ellipsoidal and spherical-cap bubbles, d_c, is 17.3 mm under the same conditions. It is very important to point out that the volumes of ellipsoidal bubbles and spherical-cap bubbles are equal to the volumes of their original spherical bubbles with diameter d. For bubbles with ellipsoidal shapes, by assuming an oblate type of ellipsoid, the surface area can be calculated by equation (15),

$$S_{ellipsoid} = \frac{\pi}{2} d^2 E^{1/3}\left(1 + \frac{1}{2E\sqrt{E^2-1}}\ln(2E^2 - 1 + 2E\sqrt{E^2-1})\right) \quad (15)$$

where the aspect ratio E can be expressed using empirical correlation described by Wellek, Agrawal and Skelland [12], as given by equation (16),

$$E = a/b = 1 + 0.163 Eo^{0.757} \quad (16)$$

where Eo is the Eötvös number.

For a single spherical-cap bubble, the wake angle θ_W is also assumed to be 50^o in this work, which is the same as Tomiyama [10]. The curved surface area for the front edge can be calculated using equation (17),

$$S_{Cap} = 2\pi R^2 (1 - \cos\theta_W) \quad (17)$$

where R is the radius of the completed sphere.

It can be seen from the experimental observations by Davenport, Bradshaw and Richardson [13] and Landel, Cossu and Caulfield [14] that the rear surface of a single spherical-cap bubble turns out to be in a constantly oscillating lenticular shape, resulting from the external perturbation acting on the rear surface. However, the lenticular shape rear surface can be considered to be essentially flat, due to the surface energy acting on the curvature which can be averaged over time and hence being neglected. It should be noted that these are rough approximations and more complicated crown bubble systems are not considered in this work. The influence of the variation of bubble shapes on the increase in surface energy is further illustrated in Figure 6.

While the original breakup model only considered the surface energy requirement for breakup events, bubble breakage may also be subjected to the pressure head difference of the bubble and its surrounding eddies, especially when the breakage volume fraction is small. Therefore, on the basis of interaction force balance proposed by Lehr, Millies and Mewes [4], the pressure energy requirement is also considered as a competitive breakup mechanism in this work. The same idea has been adopted by Zhao and Ge [6], Liao, Rzehak, Lucas and Krepper [7], and Guo, Zhou, Li and Chen [15]. The pressure energy requirement can be expressed using equation (18),

$$e_P = \frac{\sigma}{\min(R_{C,j}, R_{C,k})} \cdot \frac{\pi(\min(d_j, d_k))^3}{6} \quad (18)$$

where $R_{C,j}$ and $R_{C,k}$ are the radius of curvature of daughter bubbles. The theoretical prediction of surface energy and pressure energy requirement is shown in Figure 7.

Wang, Wang and Jin [5] proposed the breakage criteria in two aspects: capillary constraint and energy constraint. Due to the consideration of various bubble shapes and the competitive breakup mechanisms, these two constraints cannot be applied to this work directly. Slight modifications are made as follows. When the pressure head of the bombarding eddy is greater than the capillary pressure of the parent bubble, the parent bubble will start to deform. However, as previously mentioned, the breakup event may be subjected to two competitive breakup mechanisms. The energy constraint will be satisfied when the eddy contained energy exceeds either the surface energy or the pressure energy requirement for forming the daughter bubbles. These two modified breakup criteria will be embedded, together with the previously mentioned surface energy requirement and pressure energy requirement, into the simulation.

The breakup frequency can be obtained by substituting equation (10) ~ (18) into equation (9) and expressed by equation (19),

$$\Omega_B = \begin{cases} 0.923(1-\alpha_g)n_i\left(\dfrac{\varepsilon}{d_i^2}\right)^{1/3}\displaystyle\int_{\xi_{\min}}^{1}\frac{(d_{eq,i}/d_i+\xi)^2}{\xi^{11/3}}\exp\left(-\frac{12\sigma(S_j+S_k-S_i)}{\pi\beta\rho_L\varepsilon^{2/3}\xi^{11/3}d_i^{11/3}}\right)d\xi, \\ \qquad when\ \dfrac{6\sigma(S_j+S_k-S_i)}{\pi d_i^2}\geq\dfrac{\sigma}{\min(R_{C,j},R_{C,k})}. \\ 0.923(1-\alpha_g)n_i\left(\dfrac{\varepsilon}{d_i^2}\right)^{1/3}\displaystyle\int_{\xi_{\min}}^{1}\frac{(d_{eq,i}/d_i+\xi)^2}{\xi^{11/3}}\exp\left(-\frac{2\sigma(\min(d_j,d_k))^2}{\min(R_{C,j},R_{C,k})\beta\rho_L\varepsilon^{2/3}\xi^{11/3}d_i^{11/3}}\right)d\xi, \\ \qquad when\ \dfrac{6\sigma(S_j+S_k-S_i)}{\pi d_i^2}<\dfrac{\sigma}{\min(R_{C,j},R_{C,k})}. \end{cases} \tag{19}$$

where $\xi_{\min}$ is the minimum breakage volume fraction that is able to satisfy both the capillary and the energy constraints.

2.3 Interphase momentum transfer

In this study, drag force, lift force and added mass force are considered as the main interactions between the continuous liquid phase and the dispersed gas phase. The drag force coefficient can be obtained from the model by Grace model [9]. The Grace model is well suited for gas-liquid flows in which the bubbles exhibit a range of shapes, such as sphere, ellipsoid, and spherical-cap. However, instead of comparing the values of drag coefficients in the original Grace model, the drag coefficient can be applied directly according to the actual types of bubbles, as the variation of bubble shapes is considered in the breakup model. Since there are not any further modifications, detailed calculation of the drag force coefficients can be found from Grace, Clift and Weber [9]. The lift coefficient is applied by using the Tomiyama lift force correlation [10]. The virtual mass force coefficient is 0.5 in the present study.

2.4 Numerical modelling

To validate the influence of variations in bubble shape, numerical simulations have been carried out for the air-water bubble column of Kulkarni, Joshi, Kumar and Kulkarni [16], denoted by Case 1, and Camarasa, Vial, Poncin, Wild, Midoux and Bouillard [17], denoted by Case 2. Detailed information is provided in Table 1.

Table 1 Details of experimental set-up.

	Diameter (m)	Height (m)	Superficial Velocity (m/s)	Static liquid Height (m)
Case 1	0.15	0.8	0.0382	0.65
Case 2	0.1	2	0.0606	0.9

As shown in Figure 4, Grid 2 consists of $20(r)\times 40(\theta)\times 100(z)$ nodes in radial, circumferential and axial directions respectively. The grid independence was tested in a coarser Grid 1 of $16(r)\times 32(\theta)\times 80(z)$ nodes and a refined Grid 3 of $26(r)\times 48(\theta)\times 126(z)$ nodes, in which case the total number of cells is doubled gradually. The grid independence test for these three set-ups has yielded similar results quantitatively, even though the overall trend of over-prediction has shown for all three grids, as shown in Figure 5. Thus, Grid 2 shown in Figure 4 is used in the subsequent simulations to investigate the effects of the improved breakup model.

3D pressure-based solver of Fluent® 6.3 is employed for this work. The time step is set to be 0.001 seconds for all simulations. It is considered to be sufficient to illustrate the time-averaged characteristics of the flow fields by carrying out the data sampling statistics for typically 120 seconds after the quasi-steady state is achieved. The improved breakup model is integrated into the simulations by using the user defined function (UDF). The flow chart of the improved breakup model is shown in Figure 3.At inlet boundary, the volume fraction of gas phase is set to be 1 and the velocity profile is applied by using a kinetic inlet model proposed by Shi, Yang and Yang [18]. The outlet boundary is set to be pressure-outlet at the top. No-slip conditions are applied for both liquid and gas phases at the vessel wall.

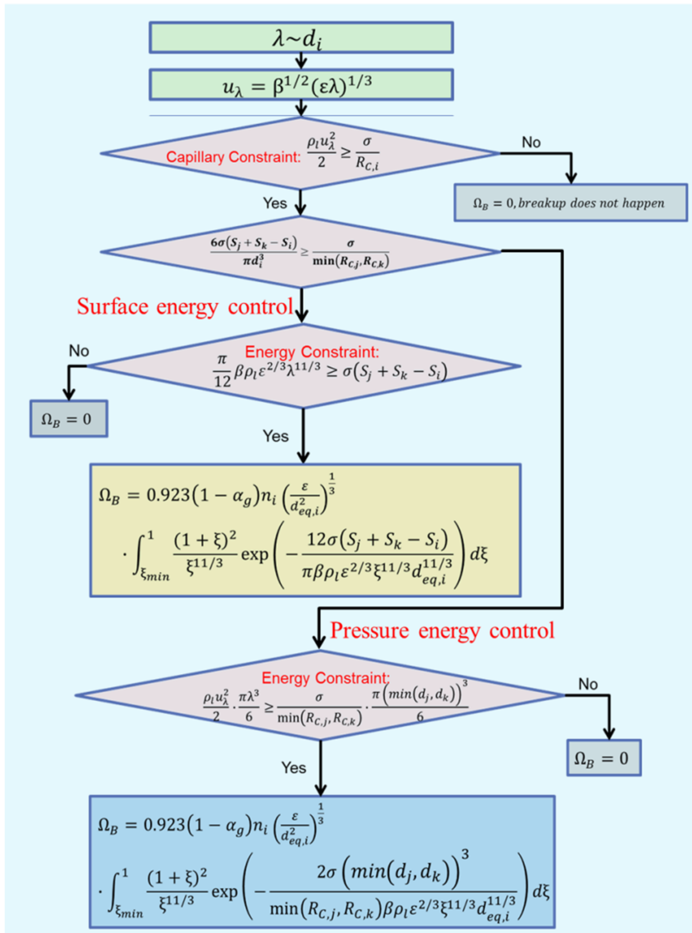

Figure 3 Flow chart of the improved bubble breakup model.

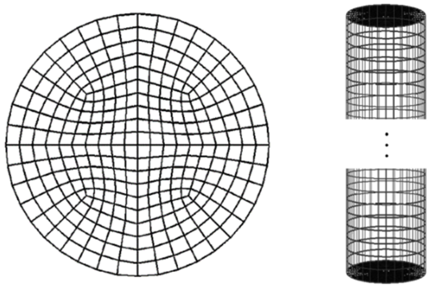

Figure 4 Mesh set-up at the bottom surface and the main body of the column.

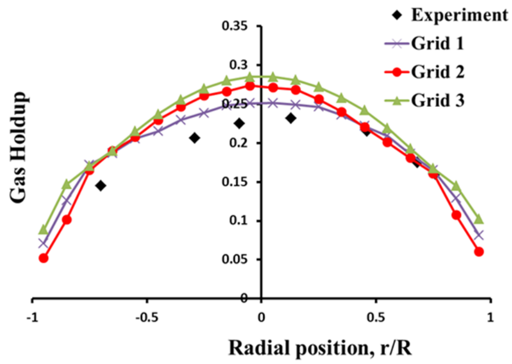

Figure 5 Comparison of simulated gas holdup profile for Case1 with three different grid configurations.

3. RESULTS AND DISCUSSION

To further illustrate the significance of considering the variation of bubble shapes, the theoretical comparison of the increase in surface energy for breakage of original spherical bubbles and various shapes of bubbles is drawn in Figure 6.

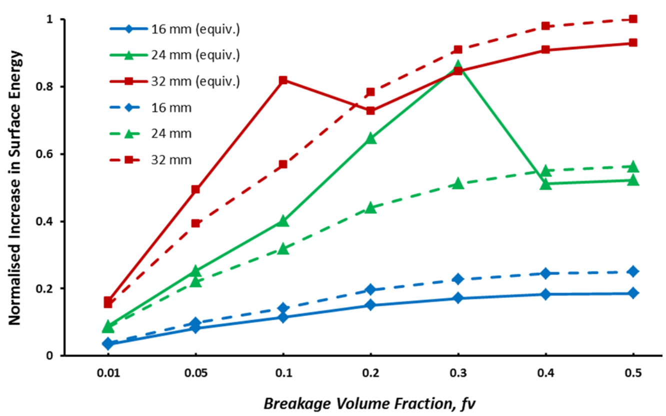

Figure 6 Normalised increase in surface energy for breakage of original spherical bubbles and various shapes of bubbles.

The theoretical predictions of surface energy and the pressure energy requirements for the breakage of ellipsoid and spherical-cap bubble are shown in Figure 7(a) and Figure 7(b) respectively. It can be clearly seen from the Figure 7(a) that the energy requirement for ellipsoid bubble shifts from pressure energy to surface energy with increasing breakup volume fraction. This may be attributed to the situation of the higher pressure head being required inside a smaller bubble to resist the surrounding eddy pressure in order to sustain its own existence. However, as shown in Figure 7(b), the spherical-cap bubble requires mostly surface energy. This may mainly be due to the requirement of forming the large front surface of spherical-cap bubbles.

Figure 8 compares the time averaged gas holdup predicted by the original breakup model and the improved breakup model. It can be seen that the improved breakup model has achieved results very similar to the experimental data at the column centre, while under-estimation is shown near the column wall. Since the standard $k\sim\varepsilon$ turbulence model is still applied in this work, the underestimation of gas holdup may be due to the overestimation of turbulence dissipation rate at this region.

Figure 9 shows the radial distribution of time averaged turbulence dissipation rate predicted by the improved breakup model. It can be seen from equation (19) that the breakup rate Ω_B is at least equivalent to the dissipation rate ε of the order of -1/3, which means the higher dissipation rate near the wall will certainly lead to a lower breakup rate. It is believed that the breakup rate will affect the gas phase volume fraction directly. Moreover, if the Small Perturbation Method can be used to the dissipation term in the equation (4), the dissipation term can be written as:

$$\varepsilon = \varepsilon_0 + \varsigma\varepsilon_1 + \cdots \qquad (20)$$

where ς is the small perturbation term that being introduced.

When equation (20) is substituted back into the ε-equation, it can be rewritten in the following cylindrical coordinates if the impacts of axial and circumferential directions can be neglected, as defined in equation (21). The basic approximation can be obtained by finding the zero order of ε term from equation (21), as described by equation (22). The first correction can be obtained by finding the first order of ε term, as denoted by equation (23).

$$\frac{\partial}{\partial r}\left(\alpha\rho(\varepsilon_0+\varsigma\varepsilon_1)\bar{u}\right) = \qquad (21)$$

$$\frac{\partial}{\partial r}\left[\alpha\left(\mu+\frac{\mu_t}{\sigma_k}\right)\frac{\partial}{\partial r}(\varepsilon_0+\varsigma\varepsilon_1)\right]+\alpha\frac{(\varepsilon_0+\varsigma\varepsilon_1)}{k}\left(C_{1\varepsilon}G_k-C_{2\varepsilon}\rho(\varepsilon_0+\varsigma\varepsilon_1)\right)$$

$$\mathrm{O}(\varsigma^0):\ C_{01}\frac{\partial}{\partial r}\left(\alpha\frac{\partial\varepsilon_0}{\partial r}\right)+C_{02}\frac{\partial(\alpha\varepsilon_0)}{\partial r}+C_{03}\alpha\varepsilon_0+C_{04}\alpha\varepsilon_0^2=0 \qquad (22)$$

$$\mathrm{O}(\varsigma^1):\ C_{11}\frac{\partial}{\partial r}\left(\alpha\frac{\partial\varepsilon_1}{\partial r}\right)+C_{12}\frac{\partial(\alpha\varepsilon_1)}{\partial r}+C_{13}\alpha\varepsilon_1+C_{14}\alpha\varepsilon_0\varepsilon_1=0 \qquad (23)$$

It can be seen from the first correction that no matter how small the perturbation on the dissipation term is, the volume fraction term will inevitably generate an opposite feedback effect. This indicates that the overestimation of the dissipation term will indeed lead to the underestimation of gas volume fraction near the wall.

(a)

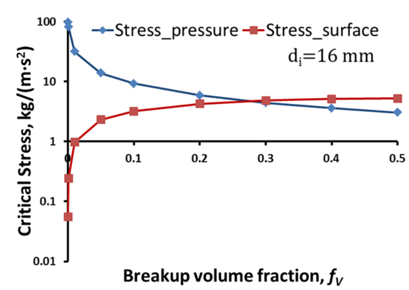

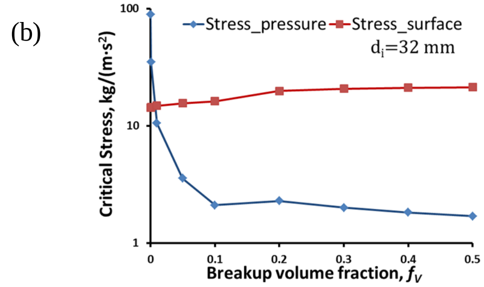

Figure 7 Two competitive control mechanism of the breakage of two types of bubbles: (a) Ellipsoid (b) Spherical-cap.

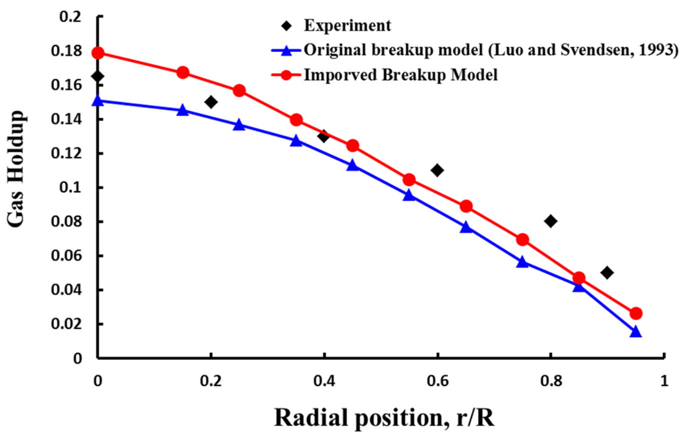

Figure 8 Comparison of the original breakup model and the improved breakup model for Case 1.

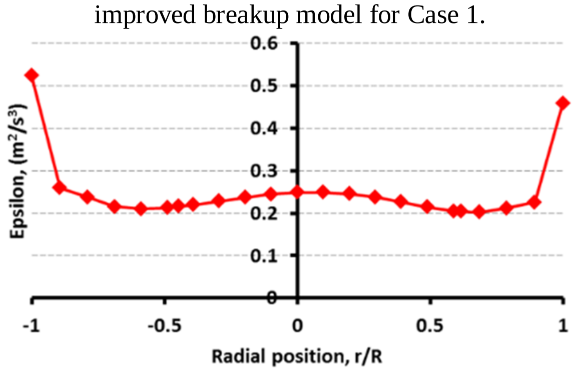

Figure 9 Radial distribution of time averaged turbulence dissipation rate for Case 1.

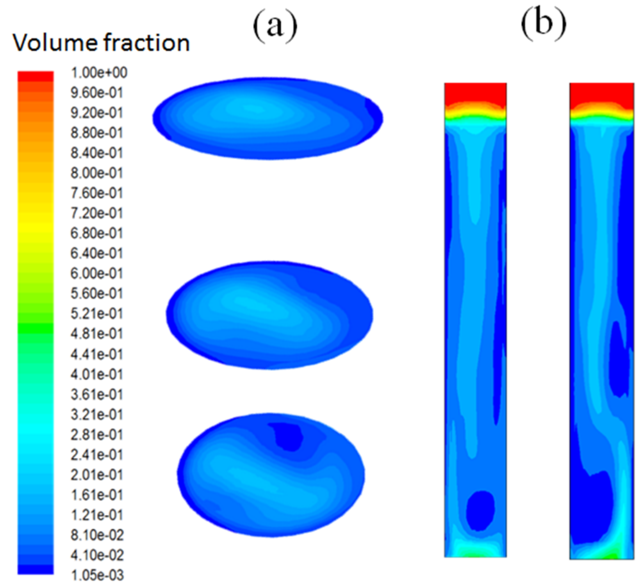

Figure 10 Contours of time averaged gas holdup CASE 1: (a) Aerial view of z-plane: from top to bottom: H=0.6, 0.45, and 0.3 m; (b) x-plane: original breakup model (left) and improved breakup model (right).

Figure 10(a) shows the time averaged gas holdup development obtained by using the improved breakup model. It can be seen from Figure 10(a) that the gas flow is mostly centralised at the column centre even though it moves towards the column wall slightly at the bottom. This is due to the strong vorticity formed at the surrounding region. It can also be observed from Figure 10(b) that the overall flow pattern obtained by the improved breakup model demonstrates significant differences from the original breakup model by Luo and Svendsen [3].

Figure 11 shows the radial distribution of time averaged gas holdup at different cross sections in the axial direction for Case 2. It may be deduced from the Figure 11 that the time averaged flow characteristics in the fully developed region ($H/D>5$) are very similar regardless of the axial positions, and the inlet conditions do not affect this similarity. This result concurs with some previous experimental findings. Figure 12 presents the interfacial area in the bulk region for each bubble group obtained from simulation. Interfacial area is a key parameter that largely affects the prediction of heat and mass transfer between gas and liquid phase in the bubble columns. Although the differences in the simulated interfacial area between the improved breakup model and the original breakup model is not significant when the bubble size is relatively small (bubble volume smaller than 1.309×10^{-5} m^3), the influence of the bubble shapes is gradually reflected when the shape of the bubbles transforms from ellipsoid to spherical-cap, resulting in an increasingly larger interfacial area for large bubbles. The total values of interfacial area in the bulk region are shown in Table 2.

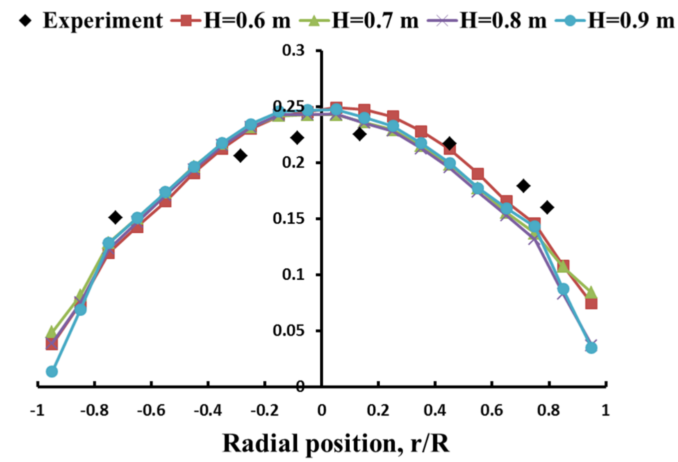

Figure 11 Radial distribution of time averaged gas holdup at different cross sections for Case 2.

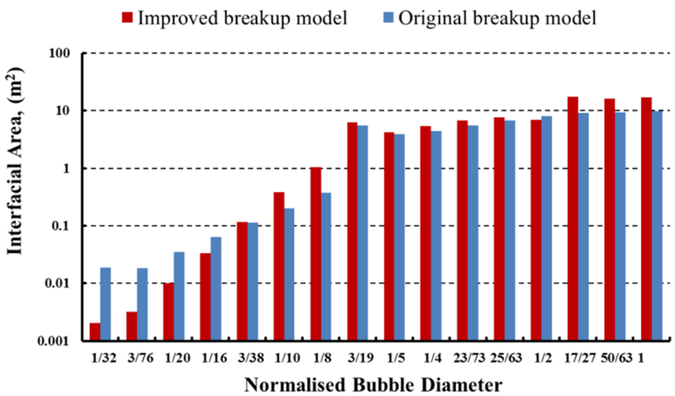

Figure 12 Comparison of simulated interfacial area in the bubble column.

Table 2 Comparison of interfacial area obtained from simulation.

	Improved breakup model	Original breakup model
Interfacial area (m^2)	88.86	62.97

4. CONCLUSIONS

In the present study, an improved breakup model has been proposed based on the classic breakup model of Luo and Svendsen [3]. The improved breakup mode has taken into account the variation of bubble shapes, such as spherical, ellipsoid and spherical-cap in the bubble columns. In addition, the pressure energy controlled breakup coupled with modified breakage criteria has been considered in the present work. The simulation results have achieved very similar findings compared with experimental data. The difference between the surface energy and pressure energy requirements for forming various daughter bubbles has been illustrated. The capillary and energy constraints have been applied to prevent the over-breakage of small bubbles. This study on the dynamic behaviours of various bubble shapes may lead to a more comprehensive understanding of the mass and heat transfer characteristics of the multi-phase reaction in the bubble column.

ACKNOWLEDGEMENTS

The authors gratefully acknowledge the support provided by the National Natural Science Foundation of China (Grant no. 91534118). Weibin Shi would also like to acknowledge the Ph.D. scholarship of the International Doctoral Innovation Centre (IDIC) of University of Nottingham Ningbo China and the support of EPSRC (Grant no. EP/G037345/1).

REFERENCES

[1] C.A. Coulaloglou, L.L. Tavlarides, Description of Interaction Processes in Agitated Liquid-Liquid Dispersions, Chem Eng Sci 32 (1977) 1289-1297.

[2] M.J. Prince, H.W. Blanch, Bubble Coalescence and Break-up in Air-Sparged Bubble-Columns, Aiche J 36 (1990) 1485-1499.

[3] H. Luo, H.F. Svendsen, Theoretical model for drop and bubble breakup in turbulent dispersions, Aiche J 42 (1996) 1225-1233.

[4] F. Lehr, M. Millies, D. Mewes, Bubble-size distributions and flow fields in bubble columns, Aiche J 48 (2002) 2426-2443.

[5] T.F. Wang, J.F. Wang, Y. Jin, A novel theoretical breakup kernel function for bubbles/droplets in a turbulent flow, Chem Eng Sci 58 (2003) 4629-4637.

[6] H. Zhao, W. Ge, A theoretical bubble breakup model for slurry beds or three-phase fluidized beds under high pressure, Chem Eng Sci 62 (2007) 109-115.

[7] Y.X. Liao, R. Rzehak, D. Lucas, E. Krepper, Baseline closure model for dispersed bubbly flow: Bubble coalescence and breakup, Chem Eng Sci 122 (2015) 336-349.

[8] H. Luo, Coalescence, Breakup and Liuqid Circulation in Bubble Column Reactors, PhD thesis from the Norwegian Institute of Technology, Trondheim, Norway, 1993.

[9] J.R. Grace, R. Clift, M.E. Weber, Bubbles, Drops, and Particles, Academic Press1978.

[10] A. Tomiyama, Struggle with computational bubble dynamics, Multiphase Science and Technology, Vol 10 Issue 4 1998 (1998) 369-405.

[11] A. Tomiyama, K. Miyoshi, H. Tamai, I. Zun, T. Sakafuchi, A Bubble Tracking Method for the Prediction of Spatial-Evolution of Bubble Flow in a Vertical Pipe, 3rd International Conference on Multiphase Flow (ICMF 98)Lyon, France, 1998.

[12] R.M. Wellek, A.K. Agrawal, A.H. Skelland, Shape of Liquid Drops Moving in Liquid Media, Aiche J 12 (1966) 854-&.

[13] W.G. Davenport, A.V. Bradshaw, F.D. Richardson, Behaviour of Spherical Cap Bubbles in Liquid Metals, J Iron Steel I 205 (1967) 1034-1042.

[14] J.R. Landel, C. Cossu, C.P. Caulfield, Spherical cap bubbles with a toroidal bubbly wake, Phys Fluids 20 (2008).

[15] X.F. Guo, Q. Zhou, J. Li, C.X. Chen, Implementation of an improved bubble breakup model for TFM-PBM simulations of gas-liquid flows in bubble columns, Chem Eng Sci 152 (2016) 255-266.

[16] A.A. Kulkarni, J.B. Joshi, V.R. Kumar, B.D. Kulkarni, Application of multiresolution analysis for simultaneous measurement of gas and liquid velocities and fractional gas hold-up in bubble column using LDA, Chem Eng Sci 56 (2001) 5037-5048.

[17] E. Camarasa, C. Vial, S. Poncin, G. Wild, N. Midoux, J. Bouillard, Influence of coalescence behaviour of the liquid and of gas sparging on hydrodynamics and bubble characteristics in a bubble column, Chem Eng Process 38 (1999) 329-344.

[18] W. Shi, N. Yang, X. Yang, A kinetic inlet model for CFD simulation of large-scale bubble columns, Chem Eng Sci 158 (2017) 108-116.